BEILSTEIN JOURNAL OF ORGANIC CHEMISTRY

Dyes in modern organic chemistry

Edited by Heiko Ihmels

Light-up probes for G-quadruplex DNA

Imprint

Beilstein Journal of Organic Chemistry
www.bjoc.org
ISSN 1860-5397
Email: journals-support@beilstein-institut.de

The *Beilstein Journal of Organic Chemistry* is published by the Beilstein-Institut zur Förderung der Chemischen Wissenschaften.

Beilstein-Institut zur Förderung der Chemischen Wissenschaften
Trakehner Straße 7–9
60487 Frankfurt am Main
Germany
www.beilstein-institut.de

BEILSTEIN JOURNAL OF ORGANIC CHEMISTRY

Dyes in modern organic chemistry

Heiko Ihmels

Editorial

Open Access

Address:
University of Siegen, Department of Chemistry and Biology, and Center of Micro- and Nanochemistry and Engineering, Adolf-Reichwein-Str. 2, 57068 Siegen, Germany

Email:
Heiko Ihmels - ihmels@chemie.uni-siegen.de

Keywords:
dyes

Beilstein J. Org. Chem. **2019,** *15,* 2798–2800.
doi:10.3762/bjoc.15.272

Received: 21 October 2019
Accepted: 08 November 2019
Published: 20 November 2019

This article is part of the thematic issue "Dyes in modern organic chemistry".

Guest Editor: H. Ihmels

Research on organic dyes constitutes a cornerstone in organic chemistry. It started already in 1856 with Perkin's seminal synthesis of mauveine [1]. Since then, dye chemistry evolved into a highly interdisciplinary research area in organic chemistry. Especially the immediate commercialization of Perkin's discovery in a dye firm demonstrated already at that time the strong relationship between research on dyes and industrial chemistry [2-4]. As a result, the success and strength of several chemical companies are originally based on dye chemistry. Although the traditional dyeing of textiles, hair, food, cosmetics, photography or printer colors, etc. is still highly relevant, organic dyes also contribute as essential components in modern applications such as in OLEDs [5,6], solar cells [7,8], organic semiconductors [9], NLO materials [10], photopolymerization [11], or Chemistry 4.0 [12].

From its very beginning, dye chemistry is strongly connected to the scientific developments in organic synthesis. Especially the obvious success and profitability of commercial dyes certainly stimulated the research activities to design and synthesize novel colorants with desirable properties, such as bright and beautiful absorption and emission colors, color fastness, persistence, as well as high molar extinction coefficients and emission quantum yields. Along these lines, numerous new methods and synthetic routes were developed to either functionalize established dye cores or to design new classes of dyes [13,14]. To add to that, efforts were spent to isolate and identify dyes that are found in nature, thus establishing important classes of dyes based on natural products [15,16]. At the same time, dyes themselves turned out to be useful tools in organic synthesis, for example, in traditional photosensitization or in a more recent topical approach as efficient and highly versatile photocatalysts [17-19].

The investigation of dyes is also at the heart of physical organic chemistry. Specifically, the seminal studies to understand the relationship between structure and color are considered highlights in chemistry and contributed significantly to the development of theoretical and computational chemistry [20]. In the same way, essential dye properties, such as aggregation [21,22] or solvatochromism [23], are still in the focus of current physical organic research.

The analytical sciences also depend very much on the availability of appropriate dyes with characteristic properties. Traditionally, organic dyes are the basis of well-established color indica-

tors for qualitative and quantitative analysis. Nowadays, we cannot imagine research in the life sciences or in medical diagnostics without the sophisticated applications of organic dyes as fluorescent probes, dye labels, two-photon absorption probes or chemosensors [24-30].

After all, dye chemistry is literally an "evergreen" in scientific research, and consequently, its significant contributions to scientific developments and breakthroughs is well-documented in several Nobel prizes that are directly or indirectly linked to the synthesis or application of dyes, such as – just to name a few – the ones awarded to A. von Baeyer (1905), H. Fischer (1930), P. Karrer (1937), O. Shimomura, M. Chalfie, R. Tsien (2008), and E. Betzig, S. Hell, W. Moerner (2014).

Although the above mentioned aspects and examples clearly show that dye chemistry is a mature and essential topic in organic chemistry, it still constitutes a vibrant research area because of the continuous need for specifically designed dyes with custom-made optical properties for diverse topical applications. Hence, this special issue aimed at the compilation of the latest trends in the chemistry of organic dyes and it covers the diverse modern aspects with a special focus on organic synthesis, photochemical and photophysical studies, as well as on applications in (bio)analytical chemistry, materials science, biology, and medicine.

I greatly enjoyed acting as guest editor of this thematic issue in the *Beilstein Journal of Organic Chemistry*. With sincere gratitude I would like to thank all authors for their excellent contributions, the referees for their constructive suggestions and the staff of the Beilstein-Institut for their continuous support.

Heiko Ihmels

Siegen, October 2019

References

1. Garfield, S. *Mauve. How One Man Invented a Color that Changed the World;* Norton and Company: New York, NY, USA, 2001.
2. Hunger, K., Ed. *Industrial Dyes, Chemistry, Properties, Applications;* Wiley-VCH: Weinheim, Germany, 2003.
3. Kuenemann, M. A.; Szymczyk, M.; Chen, Y.; Sultana, N.; Hinks, D.; Freeman, H. S.; Williams, A. J.; Fourches, D.; Vinueza, N. R. *Chem. Sci.* **2017,** *8,* 4334–4339. doi:10.1039/c7sc00567a
4. Gill, M.; Mustroph, H. *Chem. Unserer Zeit* **2014,** *48,* 424–438. doi:10.1002/ciuz.201400631
5. Bui, T.-T.; Goubard, F.; Ibrahim-Ouali, M.; Gigmes, D.; Dumur, F. *Beilstein J. Org. Chem.* **2018,** *14,* 282–308. doi:10.3762/bjoc.14.18
6. Wong, M. Y.; Zysman-Colman, E. *Adv. Mater. (Weinheim, Ger.)* **2017,** *29,* 1605444. doi:10.1002/adma.201605444
7. Cole, J. M.; Pepe, G.; Al Bahri, O. K.; Cooper, C. B. *Chem. Rev.* **2019,** *119,* 7279–7327. doi:10.1021/acs.chemrev.8b00632
8. Yum, J.-H.; Chen, P.; Grätzel, M.; Nazeeruddin, M. K. *ChemSusChem* **2008,** *1,* 699–707. doi:10.1002/cssc.200800084
9. Gsänger, M.; Bialas, D.; Huang, L.; Stolte, M.; Würthner, F. *Adv. Mater. (Weinheim, Ger.)* **2016,** *28,* 3615–3645. doi:10.1002/adma.201505440
10. Rajeshirke, M.; Sekar, N. *Dyes Pigm.* **2019,** *163,* 675–683. doi:10.1016/j.dyepig.2018.12.063
11. Corrigan, N.; Yeow, J.; Judzewitsch, P.; Xu, J.; Boyer, C. *Angew. Chem., Int. Ed.* **2019,** *58,* 5170–5189. doi:10.1002/anie.201805473
12. Strehmel, B.; Schmitz, C.; Cremanns, K.; Göttert, J. *Chem. – Eur. J.* **2019,** *25,* 12855–12864. doi:10.1002/chem.201901746
13. Zollinger, H. *Color Chemistry;* Wiley-VCH: Weinheim, Germany, 2003.
14. Christie, R. *Color Chemistry;* RSC Publishing: Cambridge, UK, 2014.
15. Duval, R.; Duplais, C. *Nat. Prod. Rep.* **2017,** *34,* 161–193. doi:10.1039/c6np00111d
16. Yusuf, M.; Shabbir, M.; Mohammad, F. *Nat. Prod. Bioprospect.* **2017,** *7,* 123–145. doi:10.1007/s13659-017-0119-9
17. Bogdos, M. K.; Pinard, E.; Murphy, J. A. *Beilstein J. Org. Chem.* **2018,** *14,* 2035–2064. doi:10.3762/bjoc.14.179
18. Zhou, Q.-Q.; Zou, Y.-Q.; Lu, L.-Q.; Xiao, W.-J. *Angew. Chem.* **2019,** *131,* 1600–1619. doi:10.1002/ange.201803102
19. Marzo, L.; Pagire, S. K.; Reiser, O.; König, B. *Angew. Chem.* **2018,** *130,* 10188–10228. doi:10.1002/ange.201709766
20. Fabian, J.; Hartmann, H. *Light Absorption of Organic Colorants;* Springer: Berlin, 2012. doi:10.1007/978-3-642-67587-4
21. Hestand, N. J.; Spano, F. C. *Chem. Rev.* **2018,** *118,* 7069–7163. doi:10.1021/acs.chemrev.7b00581
22. Würthner, F.; Kaiser, T. E.; Saha-Möller, C. R. *Angew. Chem., Int. Ed.* **2011,** *50,* 3376–3410. doi:10.1002/anie.201002307
23. Machado, V. G.; Stock, R. I.; Reichardt, C. *Chem. Rev.* **2014,** *114,* 10429–10475. doi:10.1021/cr5001157
24. Kozma, E.; Kele, P. *Org. Biomol. Chem.* **2019,** *17,* 215–233. doi:10.1039/c8ob02711k
25. Wang, L.; Frei, M. S.; Salim, A.; Johnsson, K. *J. Am. Chem. Soc.* **2019,** *141,* 2770–2781. doi:10.1021/jacs.8b11134
26. Gao, P.; Pan, W.; Li, N.; Tang, B. *Chem. Sci.* **2019,** *10,* 6035–6071. doi:10.1039/c9sc01652j
27. Li, Z.; Askim, J. R.; Suslick, K. S. *Chem. Rev.* **2019,** *119,* 231–292. doi:10.1021/acs.chemrev.8b00226
28. Wu, D.; Sedgwick, A. C.; Gunnlaugsson, T.; Akkaya, E. U.; Yoon, J.; James, T. D. *Chem. Soc. Rev.* **2017,** *46,* 7105–7123. doi:10.1039/c7cs00240h
29. Amin, M. A.; Nandi, S.; Mondal, P.; Mahata, T.; Ghosh, S.; Bhattacharyya, K. *Phys. Chem. Chem. Phys.* **2017,** *19,* 12620–12627. doi:10.1039/c7cp02228j
30. Kelley, S. O. *Acc. Chem. Res.* **2017,** *50,* 503–507. doi:10.1021/acs.accounts.6b00497

BEILSTEIN JOURNAL OF ORGANIC CHEMISTRY

Azologization of serotonin 5-HT$_3$ receptor antagonists

Karin Rustler[1], Galyna Maleeva[2], Piotr Bregestovski[2,3,4] and Burkhard König[*1]

Full Research Paper

Open Access

Address:
[1]Institute of Organic Chemistry, University of Regensburg, 93053 Regensburg, Germany, [2]Aix-Marseille University, INSERM, INS, Institut de Neurosciences des Systèmes, 13005 Marseille, France, [3]Department of Normal Physiology, Kazan State Medical University, Kazan, Russia and [4]Institute of Neurosciences, Kazan State Medical University, Kazan, Russia

Email:
Burkhard König* - burkhard.koenig@ur.de

* Corresponding author

Keywords:
azobenzene; 5-HT$_3$R; ion currents; photopharmacology; serotonin

Beilstein J. Org. Chem. **2019,** *15,* 780–788.
doi:10.3762/bjoc.15.74

Received: 28 January 2019
Accepted: 14 March 2019
Published: 25 March 2019

This article is part of the thematic issue "Dyes in modern organic chemistry".

Guest Editor: H. Ihmels

Abstract

The serotonin 5-hydroxytryptamine 3 receptor (5-HT$_3$R) plays a unique role within the seven classes of the serotonin receptor family, as it represents the only ionotropic receptor, while the other six members are G protein-coupled receptors (GPCRs). The 5-HT$_3$ receptor is related to chemo-/radiotherapy provoked emesis and dysfunction leads to neurodevelopmental disorders and psychopathologies. Since the development of the first serotonin receptor antagonist in the early 1990s, the range of highly selective and potent drugs expanded based on various chemical structures. Nevertheless, on-off-targeting of a pharmacophore's activity with high spatiotemporal resolution as provided by photopharmacology remains an unsolved challenge bearing additionally the opportunity for detailed receptor examination. In the presented work, we summarize the synthesis, photochromic properties and in vitro characterization of azobenzene-based photochromic derivatives of published 5-HT$_3$R antagonists. Despite reported proof of principle of direct azologization, only one of the investigated derivatives showed antagonistic activity lacking isomer specificity.

Introduction

5-Hydroxytryptamine (5-HT), commonly known as serotonin [1,2] or enteramine [3,4], is a monoamine neurotransmitter and hormone which is produced in the brain and in intestines and regulates a large variety of physiological functions in the mammalian central and peripheral nervous system [1,5]. In the central nervous system (CNS), it modulates sleep–wake cycles, emesis, appetite, mood, memory, breathing, cognition and numerous other functions [6-9]. In the gastrointestinal (GI) tract, it causes peristalsis via either smooth muscle contraction or enteric nerve depolarization [10]. It is also found in the platelets, where it is presumably involved in blood coagulation and vasoconstriction. Furthermore, serotonin is one of the first neurotransmitters to appear during development [11] and may have an organizing function in the development of the mammalian CNS being involved in cell division, differentiation, survival, neuronal migration [12,13] and synaptogenesis [14]. Dysfunction of the 5-HT receptor (5-HTR) signalling during early developmental stages my lead to altered

cognitive ability, neurodevelopmental disorders, and increased incidence of psychopathologies such as autism and schizophrenia [15,16].

Serotonin operates via seven classes of 5-HT receptors of which six are G protein-coupled receptors (GPCRs) and only one, the 5-HT_3R, is a ligand-gated cation channel [5,6,17]. When this receptor was identified and cloned [18-20], it became clear that 5-HT_3 takes a unique position as pentameric ligand-gated cation-selective ion channel belonging to the Cys-loop receptor subfamily. In vertebrates, this family also includes nicotinic acetylcholine receptors (nAChRs), γ-aminobutyric acid type A receptors ($GABA_A$Rs), and glycine receptors (GlyRs). To date, five subunits of the 5-HT_3 receptor are identified (5-HT_3A–5-HT_3E) [21]. Functional receptors are either constructed as 5-HT_3A homopentamers or as heteropentamers containing 5-HT_3A and 5-HT_3B receptor subunits [22-24].

5-HT_3 receptors are highly expressed in the brainstem, especially in areas involved in the vomiting reflex and in the dorsal horn of the spinal cord [25]. These receptors are also expressed presynaptically providing regulation of the neurotransmitters release [21,22].

Besides targeting of 5-HT_3Rs for the treatment of psychiatric disorders, they are object to counteract postoperative nausea and chemo-/radiotherapy provoked emesis [26-29]. In the early 1990s, the first potent and selective 5-HT_3 receptor antagonist ondansetron was initially developed [26]. Since then the development of 5-HT_3R antagonists progressed. The first-generation antagonists are structurally categorized in three major classes: (I) carbazole derivatives (e.g., ondansetron), (II) indazoles (e.g., granisetron), and (III) indoles (e.g., dolasetron) [26,30]. Generally, 5-HT_3R antagonists share a basic amine, a rigid (hetero-)aromatic system and a carbonyl group or isosteric equivalent which is coplanar to the aromatic system. Although the antagonists show a general structural motive, they differ in their binding affinities, dose responses, and side effects [22].

To improve prospective antagonists and obtain a systematic tool for receptor investigation, spatial and temporal restriction of ligand binding and concomitant activity regulation is desirable. Fuelled by light, the growing field of photopharmacology provides a noninvasive method to trigger a drug's pharmacological response on demand [31-33]. To introduce photoresponsiveness into a biological system, different approaches are feasible, e.g., the use of caged ligands (CL) [34-37], photoswitchable tethered ligands (PTLs) [38-40], photoswitchable orthogonal remotely tethered ligands (PORTLs) [41] or photochromic ligands (PCLs) [31,42]. The latter ones represent small molecules, which can either be engineered via extension of the chemical structure of a known pharmacophore towards a photochromic moiety or via replacement of certain parts of the biomolecule to generate a photochromic hybrid biomolecule. In this context, various photochromic scaffolds including dithienylethenes, fulgi(mi)des, and azobenzenes are investigated [31,42]. The latter ones were already discovered in 1834 by E. Mitscherlich [43] but it took around another 100 years till G. S. Hartley [44] revealed their photo-induced *trans–cis* isomerization representing the time of birth of the azobenzene photoswitch. Benefiting of their accessible synthesis, large change in polarity and geometry upon switching, excellent photochromic properties and tuneability, azobenzenes are amongst the most widely used photochromic scaffolds [31,42,45-47]. Since their first use in a biological environment in the late 1960s for the photoregulation of the enzymatic activity of chymotrypsin [48], their applications in biology widely expanded towards receptor control [49-52] and fields as bacterial growth [53], vision restoration [53-55], the respiratory chain [56] and lipids [57,58]. Owing to the reported serotonin antagonists' chemical structures, the use of azobenzene as photochromic scaffold in the presented work seemed axiomatic. Therefore, the primary design of our photochromic derivatives is based on the direct "azologization" [59] of reported non-photochromic antagonists [60,61] via replacement of the benzene-ring connecting amide bond and thioether, respectively, by an azo bridge.

Results and Discussion

Design and synthesis of azobenzene-based photochromic modulators

The reported [60,61] scaffolds of 5-HT_3R antagonists are based on an aromatic system either connected to a purine/pyrimidine moiety via a thioether bridge or a quinoxaline moiety via an amide bond. Referring to this work performed by the groups of DiMauro [60] and Jensen [61], we envisioned that the replacement of the thioether or amide bond (Scheme 1) by an azo bridge would result in highly active photochromic serotonin 5-HTR antagonists controllable by irradiation with light. Based on the suggested receptor binding mode reported for one potent non-photochromic antagonist (lead structure of **16c**) [61] we expected the extended *trans*-isomer as biologically active configuration whereas its bent *cis*-isomer should be inactive.

Synthesis of the quinoxaline-based azobenzenes

The synthesis of the unsubstituted quinoxaline-based azobenzene derivatives **5a** and **5b** is based on a Baeyer [62]–Mills [63] reaction (Scheme 2). Therefore, nitrosoquinoxaline **3** was synthesized in a two-step procedure starting from 2-chloroquinoxaline (**1**), which was transformed into its oxime **2** using hydroxylammonium chloride [64]. The subsequent oxidation

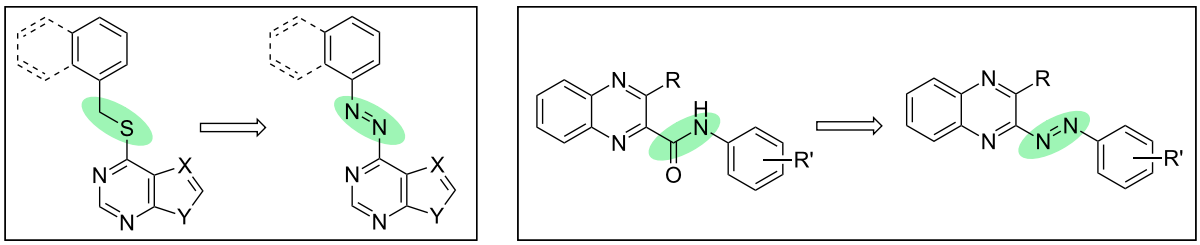

Scheme 1: Approach of the direct azologization of reported [60,61] serotonin 5-HT_3R antagonists via replacement of a thioether or amide bond by an azo bridge.

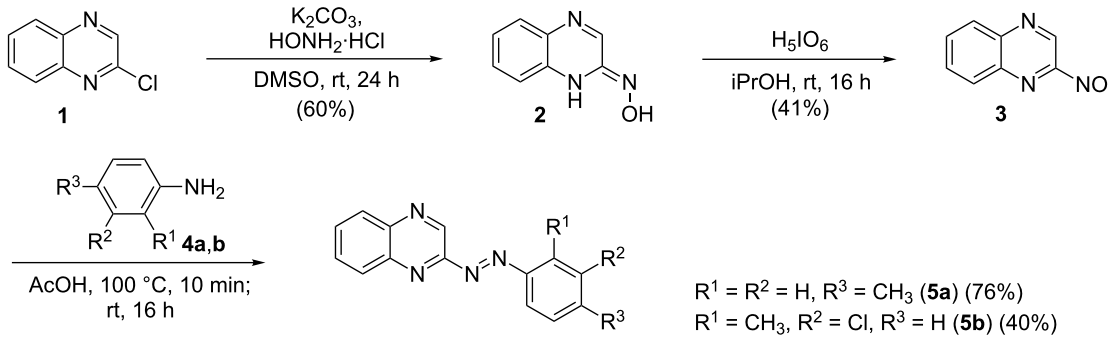

Scheme 2: Synthesis of the differently substituted quinoxaline azobenzene derivatives **5a** and **5b** via Baeyer [62]–Mills [63] reaction [64,65].

was performed using periodic acid as oxidant [65]. The subsequent reaction with differently substituted anilines in acetic acid [65] provided both quinoxaline azobenzene derivatives in good yields.

The methoxy-substituted quinoxaline azobenzene derivative **12a** was synthesized via a different synthetic route depicted in Scheme 3. In a first step, *p*-toluidine (**4a**) was diazotized using sodium nitrite and subsequently reacted with the 2-chloroacetyl-

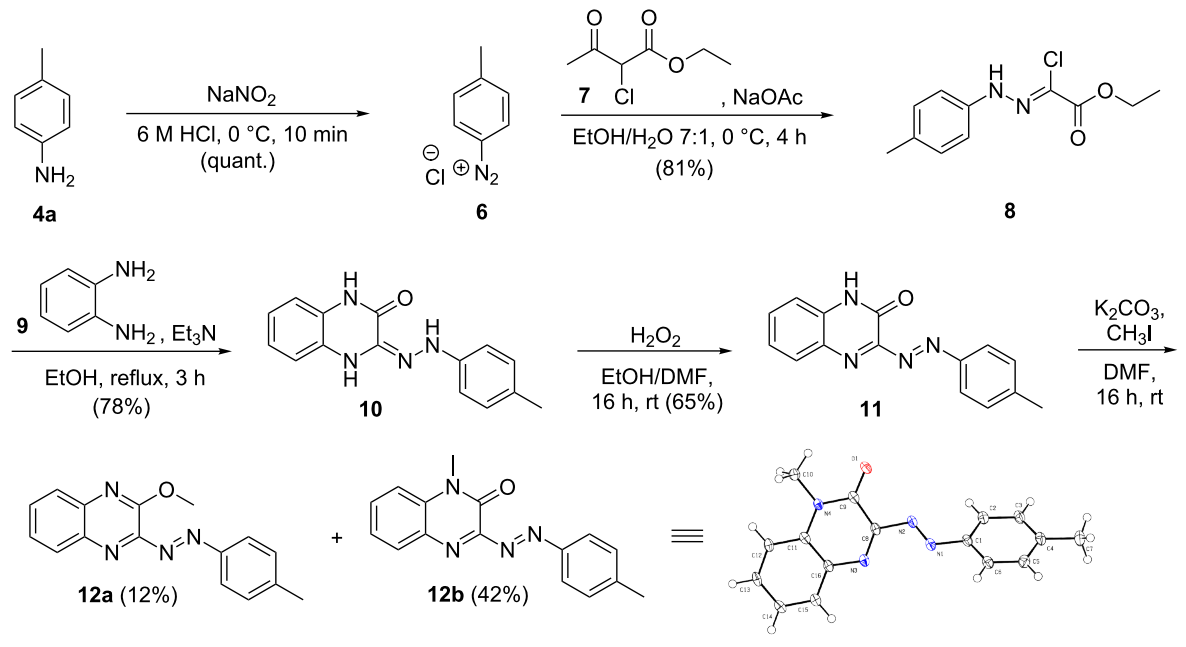

Scheme 3: Synthesis of the methoxy-substituted quinoxaline derivative **12a** via diazotization [66-69].

acetone ester derivative **7** providing hydrazine **8** [66]. Upon reaction of the chloro-ester **8** with phenylenediamine (**9**) in the presence of triethylamine the quinoxaline moiety was formed [67]. Oxidation of the hydrazine derivative **10** using hydrogen peroxide under an oxygen atmosphere afforded the quinoxaline azobenzene derivative **11** [68]. Subsequent methylation using methyl iodide [69] mainly resulted in the formation of the *N*-methylated non-photochromic product **12b** but in low yields also the desired photochromic methoxy-substituted quinoxaline azobenzene derivative **12a**.

Synthesis of the purine and thienopyrimidine-based derivatives

Scheme 4 depicts the general procedure applied for the synthesis of differently substituted purine- and thienopyrimidine azobenzene derivatives. Differently substituted non-photochromic antagonists were chosen as lead structures delivering photochromic derivatives with varying electronic and thus photochromic properties. The respective arylamines **13a**–**c** were converted into their corresponding hydrazines **14a**–**c** via diazonium-salt formation using sodium nitrite and subsequent reduction using tin(II) chloride [70]. The following nucleophilic substitution at a chloro-substituted purine (**15a**,**b**) or thienopyrimidine (**15c**), respectively, and subsequent oxidation of the hydrazine moiety afforded the corresponding azobenzene derivatives **16a**–**d** [71].

Synthesis of azobenzene-extended thiopurine derivatives

To further tune the photochromism and compare the properties of direct azologization to azo-extension, two additional derivatives of the in vitro most promising naphthalene azopurine **16c** were synthesized either by keeping the original thioether (Scheme 5) or replacing it by an amide bond (Scheme 6) known as common structural feature of 5-HT_3R antagonists.

Scheme 5 reflects the synthesis of the azo-extended thiomethylpurine **23** starting with the synthesis of hydroxymethylazobenzene **19** [72] in a Baeyer [62]–Mills [63] reaction and subsequent nucleophilic substitution using cyanuric chloride (**20**) [73] providing chloromethyl azobenzene **21**. The introduction of the thiopurine moiety in **23** was accomplished upon reaction of **21** with dihydropurinethione **22** [74].

The amide-linked derivative of thiomethylpurine azobenzene **23** was synthesized via Baeyer [62]–Mills [63] formation of the carboxylated azobenzene **25** starting from aminobenzoic acid **24** and nitrosobenzene (**18**) [75]. Activation using thionyl chlo-

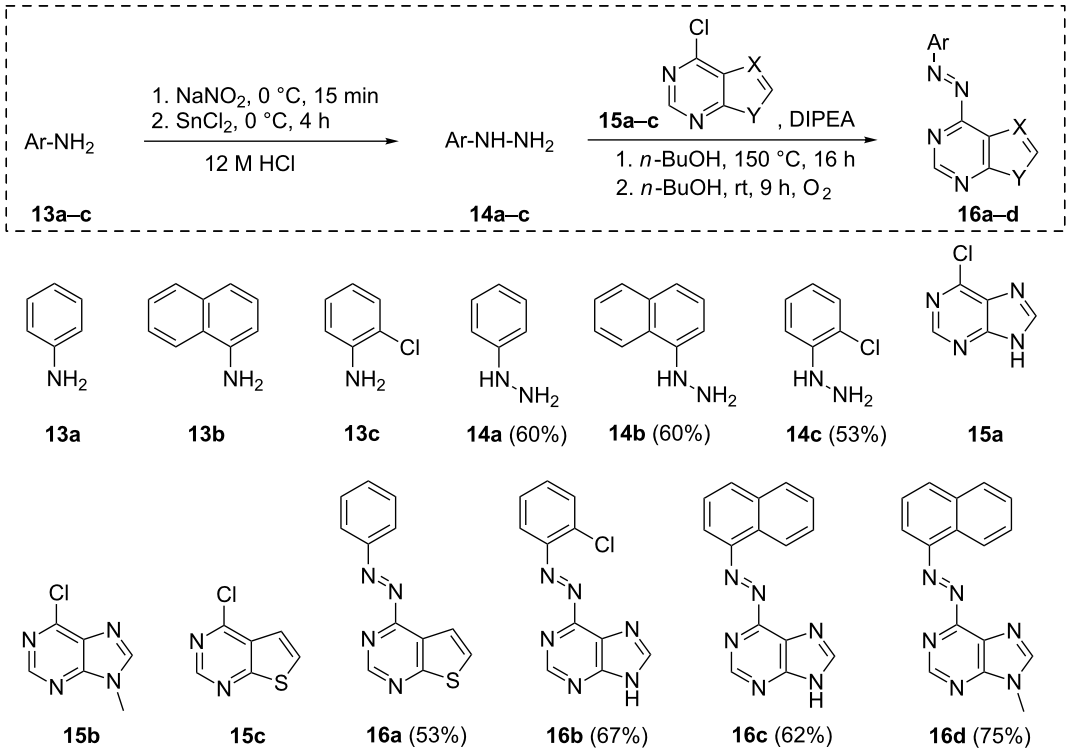

Scheme 4: General procedure for the synthesis of purine- and thienopyrimidine-substituted arylazobenzenes and depiction of the corresponding structures [70,71].

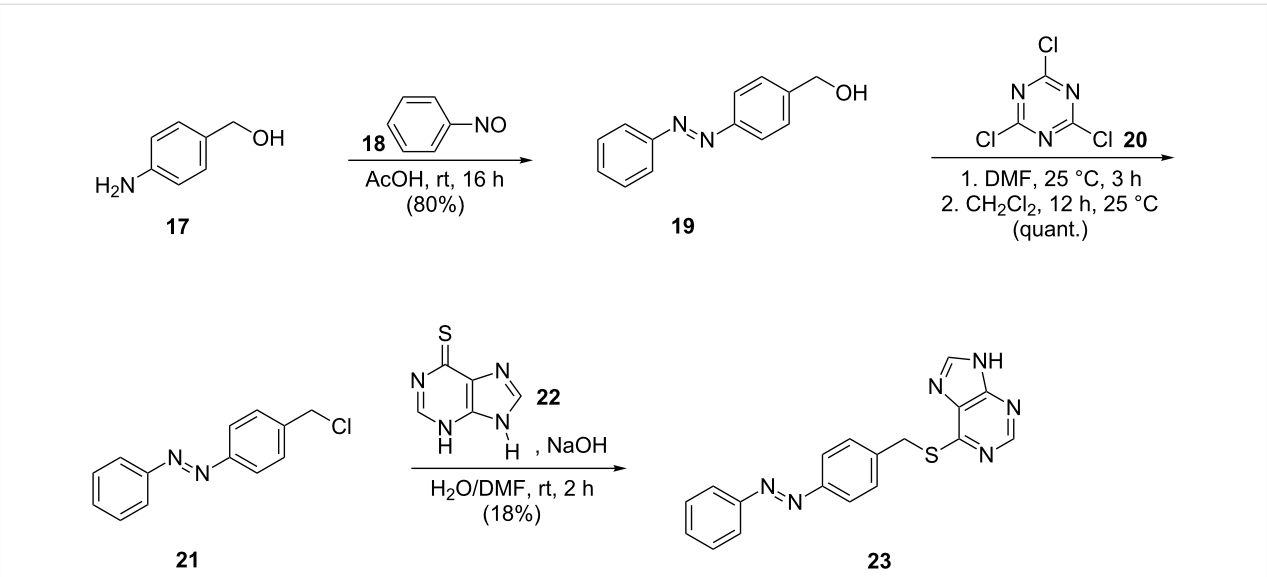

Scheme 5: Synthesis of the thiomethyl-linked purine azobenzene **23** [62,63,72-74].

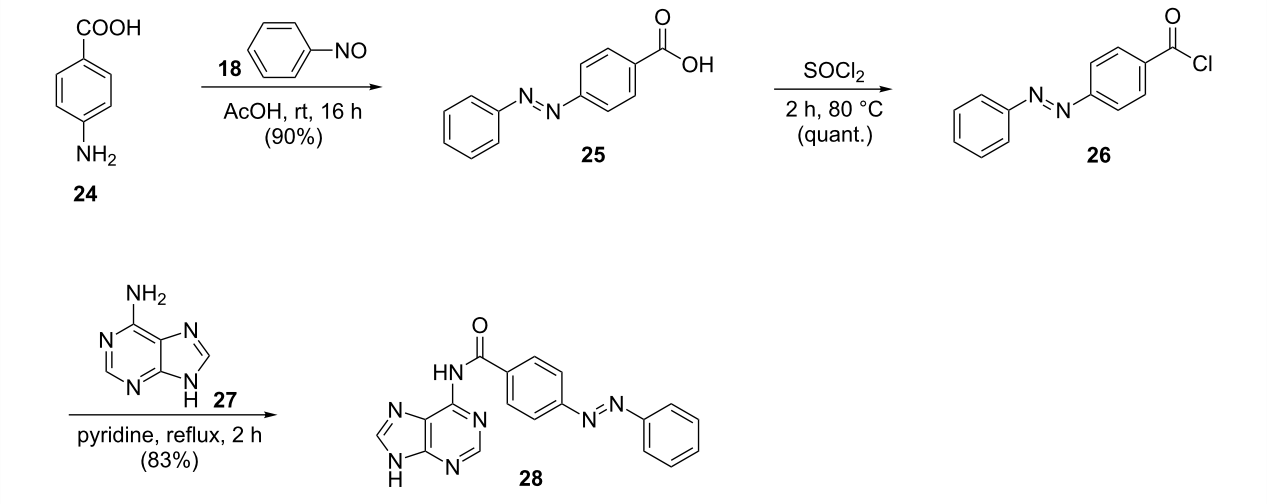

Scheme 6: Synthesis of the amide-linked azobenzene purine **28** [62,63,75-77].

ride [76] afforded the acid chloride **26** and allowed amide-bond formation [77] for the generation of **28** (Scheme 6).

Photochromic properties

The investigation of the photochromic properties of the potential 5-HT_3R antagonists **5a**, **5b**, **12a**, **16a**–**d**, **23**, and **28** was performed in DMSO and depending on their solubility in phosphate buffer + 0.1% DMSO (**16a**–**d**) by UV–vis absorption spectroscopy. The compounds were dissolved at 50 µM in the respective solvent and irradiated with the indicated wavelengths to generate a substantial amount of their *cis*-isomer. This process can be followed by a decrease of the *trans*-absorption maximum at around 350–400 nm and an increase in absorption at around 450–500 nm in the UV–vis spectrum representing the *cis*-isomer (Figure 1, black arrows). The absorption bands of the *trans* and *cis*-isomers of compounds **12a**, **16c**, and **16d** overlap to such an extent, that no new maximum representing the *cis*-isomer was observed and thus *cis–trans* isomerization only occurs thermally and is not triggerable by irradiation with visible light. Back-isomerization was triggered by irradiation with visible light (**5a**, **5b**, **16a**, **16b**, **23**, and **28**) of the indicated wavelength or by thermal relaxation (**5a**, **5b**, **12a**, **16a**–**d**, **23**, and **28**). The irradiation times were determined by following the UV–vis spectrum upon isomerization until no more changes in absorption were observed and the photostationary state (PSS) was reached. The points of intersec-

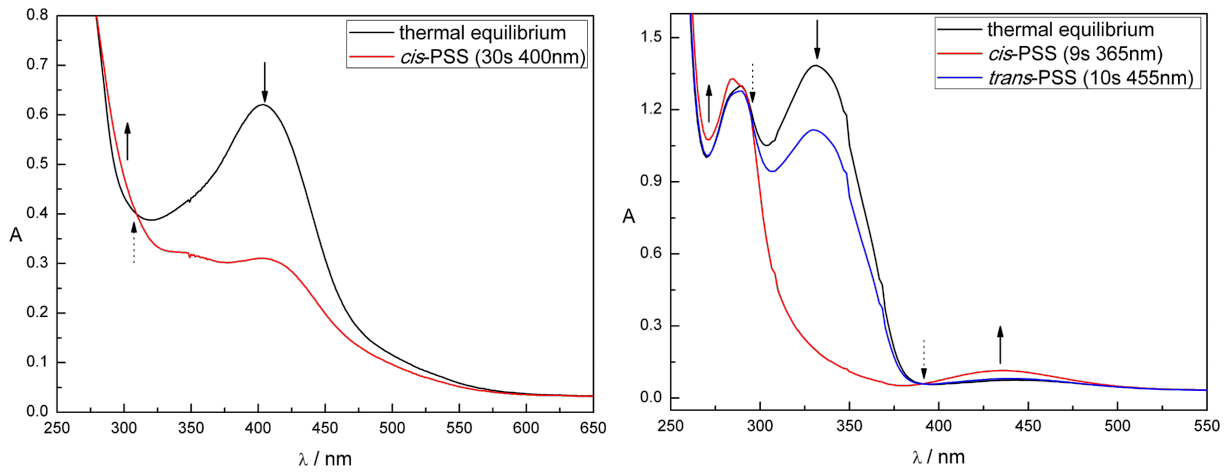

Figure 1: UV–vis absorption spectra measured at 50 µM in DMSO. Left: purine derivative **16c**; right: azo-extended derivative **23**.

tion in the absorption spectrum upon switching (= isosbestic points) indicate a clear two-component switching between *trans* and *cis*-species without any degradation or formation of a side-product (Figure 1, dotted black arrows). The UV–vis absorption spectra of all compounds are depicted in Supporting Information File 1, Figures S1–S10 and the data are summarized in Table S1 and Table S2. A comparison of the differently substituted purine azobenzene derivatives revealed the beneficial effect of an *o*-chloro substitution on the photochromic properties of **16b** compared to **16c** as the electron density at the nitrogen-rich purine core is reduced. Further reduction of the electron density was achieved by using a thienopyrimidine (**16a**) instead of a purine core (**16b–d**). Nevertheless, the photochromic properties of those heterocyclic, especially purine-based azobenzenes, are rather poor. In addition to direct azologization, two azo-extended purine derivatives **23** and **28** were synthesized resulting in excellent photochromic properties. Figure 1 compares exemplarily the UV–vis absorption spectra of the naphthalene-azo-purine **16c** (left) and its azo-extended azobenzene thioether purine **23** (right). The determination of the thermal half-lives (THL) of the *cis*-isomers of compounds **5a**, **5b**, **12a**, **16a–d**, **23**, and **28** was accomplished by monitoring the increase in absorbance which corresponds to the evolution of the *trans*-isomer after irradiation and exposure to dark. In contrast to the heterocyclic compounds **5a**, **5b**, **12a**, and **16a–d** with a thermal half-life in the seconds to minutes range, the azo-extended compounds **23** and **28** showed only slow thermal back-isomerization (day range) at room temperature. Depending on the desired application, both properties may be of benefit. For thermally instable compounds, only one wavelength for switching is required. In case of thermally stable *cis*-isomers constant irradiation to maintain a substantial amount of the *cis*-isomer can be avoided.

Patch-clamp studies

The synthesized azo antagonist derivatives **5a**, **5b**, **12a**, **16a–d**, **23**, and **28** were tested for their inhibitory activity using the patch-clamp technique on heterologously expressed ionotropic homopentameric 5-HT_3A receptors. Only upon addition of **16c** the amplitude of the 5-HT_3A mediated currents was decreased (Figure 2, left). Application of a 50 µM solution of *trans*-**16c** in its thermal equilibrium decreased the amplitude of 5-HT induced currents on 54 ± 3% (n = 4). However, irradiation-induced *trans–cis* isomerization with light of λ = 530 nm and 455 nm, respectively, had no significant effect on the amplitude of 5-HT_3A-mediated currents (Figure 2, right).

Conclusion

In the presented work, we address the design, synthesis, photochromic characterization and in vitro investigation of in total nine azobenzene-based derivatives of reported 5-HT_3R antagonists. Initially, seven photoligands (**5a**, **5b**, **12a**, and **16a–d**) either based on quinoxaline (**5a**, **5b**, and **12a**) or purine derivatives (**16a–d**) with varying electronic and thus photochromic properties were synthesized by direct azologization of the respective leads. Especially the purine-based azobenzenes displayed high solubility in aqueous media. The beneficial effect of substituents reducing the overall electron density of the purine moiety (**16a**, **16b**) resulted in higher photostationary states and better band separation compared to **16c** and **16d**. Still, only one compound (**16c**) showed antagonistic activity in patch-clamp studies. This might be explained by the fact that its corresponding non-photochromic lead is the inhibitory most active reported [61] antagonist among the investigated ones. The partial rigidization of the thioether via incorporation of an azo bridge might result in a vast loss of activity. Thereby, azologization of the less potent leads resulted in complete loss of

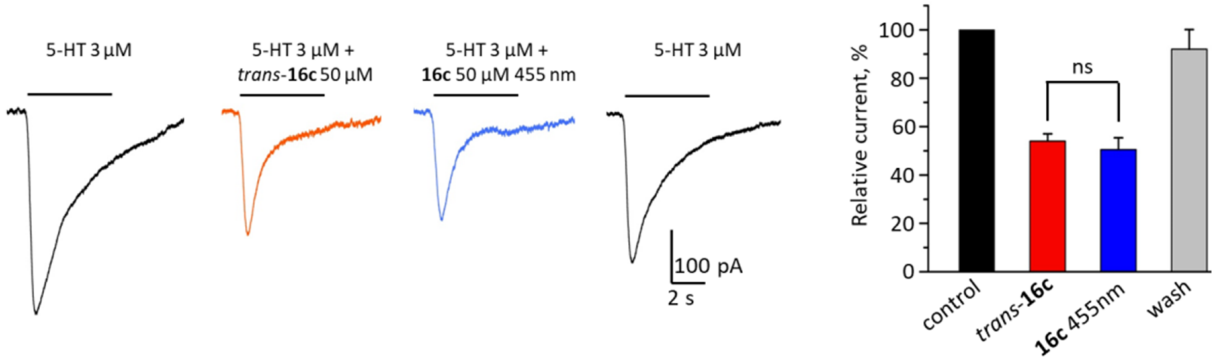

Figure 2: On the left panel representative traces of currents induced by the application of 3 µM 5HT (black trace), by 3 µM 5HT and 50 µM *trans*-**16c** (red trace), by 5HT and **16c** under constant irradiation (455 nm, blue trace), and again by pure 5HT – wash-out of the studied compound (black trace) are shown. On the right panel, a graph representing the relative amplitudes of currents in control (black column), at application of *trans*-**16c** (red column), at application of **16c** irradiated with blue light (blue column) and at wash-out (gray column) are shown. $P > 0.05$, paired t-test.

inhibitory activity (**5a**, **5b**, **12a**, **16a**, **16b**, **16d**) and only the originally most potent derivative **16c** kept recordable antagonistic activity. The missing significant difference in activity upon irradiation-induced *trans–cis* isomerization of **16c** is probably due to its moderate photochromic properties and slow *trans–cis* isomerization (Figure 1, left). During the patch-clamp analysis, the cells are continuously superfused with external solution resulting in a fast exchange of the surrounding media and co-applied tested compounds. Thus, the *cis*-PSS of **16c** might not be reached by irradiation within the short time of compound application despite continuous irradiation. Therefore, two azobenzene-extended derivatives (**23** and **28**) with improved photochromic properties were synthesized but lost antagonistic activity probably due to their increased steric demand.

In ongoing studies, detailed molecular modelling is used to design potential photochromic antagonists fitting the requirements of the receptor's binding pocket. Regarding the analysis method, compounds will be optimized towards either thermally stable *cis*-isomers to be tested separately upon prior irradiation or faster switching compounds.

Supporting Information

Supporting Information File 1

Detailed photochromic characterization (UV–vis absorption spectra, cycle performances, thermal half-lives) and NMR spectra of all synthesized compounds are provided. The file contains crystal structures of compounds **12b** and **16a** and experimental procedures.
[https://www.beilstein-journals.org/bjoc/content/supplementary/1860-5397-15-74-S1.pdf]

Acknowledgements

The authors are grateful for financial support to ERA SynBIO grant MODULIGHTOR (PCIN-2015-163-C02-01), the Bundesministerium für Bildung und Forschung (BMBF) and the Russian Science Foundation (grant number: 18-15-00313). We are also grateful to Dr. S. Lummis for kind providing with cDNA of $5HT_3A$ subunit. KR thanks Josef Kiermaier and Wolfgang Söllner for mass spectrometry analysis. KR thanks the X-ray department for crystal structure analysis.

ORCID® iDs

Karin Rustler - https://orcid.org/0000-0001-6548-1333
Galyna Maleeva - https://orcid.org/0000-0002-1379-1521
Piotr Bregestovski - https://orcid.org/0000-0003-2699-7825
Burkhard König - https://orcid.org/0000-0002-6131-4850

References

1. Barnes, N. M.; Neumaier, J. F. *Tocris Sci. Rev. Ser.* **2015,** *34,* 1–16.
2. Rapport, M. M. *J. Biol. Chem.* **1949,** *180,* 961–969.
3. Erspamer, V.; Asero, B. *Nature* **1952,** *169,* 800–801. doi:10.1038/169800b0
4. Erspamer, V. *Naunyn-Schmiedebergs Arch. Exp. Pathol. Pharmakol.* **1940,** *196,* 343–365. doi:10.1007/bf01861121
5. Barnes, N. M.; Sharp, T. *Neuropharmacology* **1999,** *38,* 1083–1152. doi:10.1016/s0028-3908(99)00010-6
6. Berger, M.; Gray, J. A.; Roth, B. L. *Annu. Rev. Med.* **2009,** *60,* 355–366. doi:10.1146/annurev.med.60.042307.110802
7. Davis, J. M.; Alderson, N. L.; Welsh, R. S. *Am. J. Clin. Nutr.* **2000,** *72,* 573S–578S. doi:10.1093/ajcn/72.2.573s
8. Ray, R. S.; Corcoran, A. E.; Brust, R. D.; Kim, J. C.; Richerson, G. B.; Nattie, E.; Dymecki, S. M. *Science* **2011,** *333,* 637–642. doi:10.1126/science.1205295
9. McCorvy, J. D.; Roth, B. L. *Pharmacol. Ther.* **2015,** *150,* 129–142. doi:10.1016/j.pharmthera.2015.01.009
10. Gershon, M. D.; Wade, P. R.; Kirchgessner, A. L.; Tamir, H. *Neuropsychopharmacology* **1990,** *3,* 385–395.

11. Lauder, J. M. *Ann. N. Y. Acad. Sci.* **1990,** *600,* 297–313. doi:10.1111/j.1749-6632.1990.tb16891.x
12. Azmitia, E. C. *Brain Res. Bull.* **2001,** *56,* 413–424. doi:10.1016/s0361-9230(01)00614-1
13. Vitalis, T.; Cases, O.; Passemard, S.; Callebert, J.; Parnavelas, J. G. *Eur. J. Neurosci.* **2007,** *26,* 331–344. doi:10.1111/j.1460-9568.2007.05661.x
14. Matsukawa, M.; Nakadate, K.; Ishihara, I.; Okado, N. *Neuroscience* **2003,** *122,* 627–635. doi:10.1016/j.neuroscience.2003.08.047
15. Engel, M.; Smidt, M. P.; van Hooft, J. A. *Front. Cell. Neurosci.* **2013,** *7,* No. 76.
16. Whitaker-Azmitia, P. M. *Brain Res. Bull.* **2001,** *56,* 479–485. doi:10.1016/s0361-9230(01)00615-3
17. Hoyer, D.; Clarke, D. E.; Fozard, J. R.; Hartig, P. R.; Martin, G. R.; Mylecharane, E. J.; Saxena, P. R.; Humphrey, P. P. A. *Pharmacol. Rev.* **1994,** *46,* 157–203.
18. Derkach, V.; Surprenant, A.; North, R. A. *Nature* **1989,** *339,* 706–709. doi:10.1038/339706a0
19. Maricq, A. V.; Peterson, A. S.; Brake, A. J.; Myers, R. M.; Julius, D. *Science* **1991,** *254,* 432–437. doi:10.1126/science.1718042
20. Kilpatrick, G. J.; Jones, B. J.; Tyers, M. B. *Nature* **1987,** *330,* 746–748. doi:10.1038/330746a0
21. Lummis, S. C. R. *J. Biol. Chem.* **2012,** *287,* 40239–40245. doi:10.1074/jbc.r112.406496
22. Thompson, A. J.; Lummis, S. C. R. *Curr. Pharm. Des.* **2006,** *12,* 3615–3630. doi:10.2174/138161206778522029
23. Davies, P. A.; Pistis, M.; Hanna, M. C.; Peters, J. A.; Lambert, J. J.; Hales, T. G.; Kirkness, E. F. *Nature* **1999,** *397,* 359–363. doi:10.1038/16941
24. Dubin, A. E.; Huvar, R.; D'Andrea, M. R.; Pyati, J.; Zhu, J. Y.; Joy, K. C.; Wilson, S. J.; Galindo, J. E.; Glass, C. A.; Luo, L.; Jackson, M. R.; Lovenberg, T. W.; Erlander, M. G. *J. Biol. Chem.* **1999,** *274,* 30799–30810. doi:10.1074/jbc.274.43.30799
25. Miquel, M.-C.; Emerit, M. B.; Nosjean, A.; Simon, A.; Rumajogee, P.; Brisorgueil, M.-J.; Doucet, E.; Hamon, M.; Vergé, D. *Eur. J. Neurosci.* **2002,** *15,* 449–457. doi:10.1046/j.0953-816x.2001.01872.x
26. Smith, H. S.; Cox, L. R.; Smith, E. J. *Ann. Palliat. Med.* **2012,** *1,* 115–120. doi:10.3978/j.issn.2224-5820.2012.07.07
27. Miller, P. S.; Smart, T. G. *Trends Pharmacol. Sci.* **2010,** *31,* 161–174. doi:10.1016/j.tips.2009.12.005
28. Barnes, N. M.; Hales, T. G.; Lummis, S. C. R.; Peters, J. A. *Neuropharmacology* **2009,** *56,* 273–284. doi:10.1016/j.neuropharm.2008.08.003
29. Walstab, J.; Rappold, G.; Niesler, B. *Pharmacol. Ther.* **2010,** *128,* 146–169. doi:10.1016/j.pharmthera.2010.07.001
30. Ho, K.-Y.; Gan, T. J. *Curr. Opin. Anaesthesiol.* **2006,** *19,* 606–611. doi:10.1097/01.aco.0000247340.61815.38
31. Szymański, W.; Beierle, J. M.; Kistemaker, H. A. V.; Velema, W. A.; Feringa, B. L. *Chem. Rev.* **2013,** *113,* 6114–6178. doi:10.1021/cr300179f
32. Lerch, M. M.; Hansen, M. J.; van Dam, G. M.; Szymanski, W.; Feringa, B. L. *Angew. Chem., Int. Ed.* **2016,** *55,* 10978–10999. doi:10.1002/anie.201601931
33. Broichhagen, J.; Frank, J. A.; Trauner, D. *Acc. Chem. Res.* **2015,** *48,* 1947–1960. doi:10.1021/acs.accounts.5b00129
34. Mayer, G.; Heckel, A. *Angew. Chem., Int. Ed.* **2006,** *45,* 4900–4921. doi:10.1002/anie.200600387
35. Deiters, A. *ChemBioChem* **2010,** *11,* 47–53. doi:10.1002/cbic.200900529
36. Curley, K.; Lawrence, D. S. *Pharmacol. Ther.* **1999,** *82,* 347–354. doi:10.1016/s0163-7258(98)00055-2
37. Lemke, E. A. *ChemBioChem* **2010,** *11,* 1825–1827. doi:10.1002/cbic.201000364
38. Reiner, A.; Isacoff, E. Y. Photoswitching of Cell Surface Receptors Using Tethered Ligands. In *Photoswitching Proteins;* Cambridge, S., Ed.; Methods in Molecular Biology, Vol. 1148; Humana Press: New York, USA; pp 45–68. doi:10.1007/978-1-4939-0470-9_4
39. Donthamsetti, P. C.; Winter, N.; Schönberger, M.; Levitz, J.; Stanley, C.; Javitch, J. A.; Isacoff, E. Y.; Trauner, D. *J. Am. Chem. Soc.* **2017,** *139,* 18522–18535. doi:10.1021/jacs.7b07659
40. Lin, W.-C.; Tsai, M.-C.; Rajappa, R.; Kramer, R. H. *J. Am. Chem. Soc.* **2018,** *140,* 7445–7448. doi:10.1021/jacs.8b03942
41. Broichhagen, J.; Damijonaitis, A.; Levitz, J.; Sokol, K. R.; Leippe, P.; Konrad, D.; Isacoff, E. Y.; Trauner, D. *ACS Cent. Sci.* **2015,** *1,* 383–393. doi:10.1021/acscentsci.5b00260
42. Brieke, C.; Rohrbach, F.; Gottschalk, A.; Mayer, G.; Heckel, A. *Angew. Chem., Int. Ed.* **2012,** *51,* 8446–8476. doi:10.1002/anie.201202134
43. Mitscherlich, E. *Ann. Pharm. (Lemgo, Ger.)* **1834,** *12,* 311–314. doi:10.1002/jlac.18340120282|
44. Hartley, G. S. *Nature* **1937,** *140,* 281–282. doi:10.1038/140281a0
45. Dong, M.; Babalhavaeji, A.; Samanta, S.; Beharry, A. A.; Woolley, G. A. *Acc. Chem. Res.* **2015,** *48,* 2662–2670. doi:10.1021/acs.accounts.5b00270
46. Beharry, A. A.; Sadovski, O.; Woolley, G. A. *J. Am. Chem. Soc.* **2011,** *133,* 19684–19687. doi:10.1021/ja209239m
47. Weston, C. E.; Richardson, R. D.; Haycock, P. R.; White, A. J. P.; Fuchter, M. J. *J. Am. Chem. Soc.* **2014,** *136,* 11878–11881. doi:10.1021/ja505444d
48. Kaufman, H.; Vratsanos, S. M.; Erlanger, B. F. *Science* **1968,** *162,* 1487–1489. doi:10.1126/science.162.3861.1487
49. Deal, W. J.; Erlanger, B. F.; Nachmansohn, D. *Proc. Natl. Acad. Sci. U. S. A.* **1969,** *64,* 1230–1234. doi:10.1073/pnas.64.4.1230
50. Volgraf, M.; Gorostiza, P.; Numano, R.; Kramer, R. H.; Isacoff, E. Y.; Trauner, D. *Nat. Chem. Biol.* **2006,** *2,* 47–52. doi:10.1038/nchembio756
51. Volgraf, M.; Gorostiza, P.; Szobota, S.; Helix, M. R.; Isacoff, E. Y.; Trauner, D. *J. Am. Chem. Soc.* **2007,** *129,* 260–261. doi:10.1021/ja067269o
52. Hauwert, N. J.; Mocking, T. A. M.; Da Costa Pereira, D.; Kooistra, A. J.; Wijnen, L. M.; Vreeker, G. C. M.; Verweij, E. W. E.; De Boer, A. H.; Smit, M. J.; De Graaf, C.; Vischer, H. F.; de Esch, I. J. P.; Wijtmans, M.; Leurs, R. *J. Am. Chem. Soc.* **2018,** *140,* 4232–4243. doi:10.1021/jacs.7b11422
53. Wegener, M.; Hansen, M. J.; Driessen, A. J. M.; Szymanski, W.; Feringa, B. L. *J. Am. Chem. Soc.* **2017,** *139,* 17979–17986. doi:10.1021/jacs.7b09281
54. Polosukhina, A.; Litt, J.; Tochitsky, I.; Nemargut, J.; Sychev, Y.; De Kouchkovsky, I.; Huang, T.; Borges, K.; Trauner, D.; Van Gelder, R. N.; Kramer, R. H. *Neuron* **2012,** *75,* 271–282. doi:10.1016/j.neuron.2012.05.022
55. Tochitsky, I.; Polosukhina, A.; Degtyar, V. E.; Gallerani, N.; Smith, C. M.; Friedman, A.; Van Gelder, R. N.; Trauner, D.; Kaufer, D.; Kramer, R. H. *Neuron* **2014,** *81,* 800–813. doi:10.1016/j.neuron.2014.01.003
56. Simeth, N. A.; Kneuttinger, A. C.; Sterner, R.; König, B. *Chem. Sci.* **2017,** *8,* 6474–6483. doi:10.1039/c7sc00781g

57. Frank, J. A.; Franquelim, H. G.; Schwille, P.; Trauner, D. *J. Am. Chem. Soc.* **2016,** *138,* 12981–12986. doi:10.1021/jacs.6b07278
58. Pernpeintner, C.; Frank, J. A.; Urban, P.; Roeske, C. R.; Pritzl, S. D.; Trauner, D.; Lohmüller, T. *Langmuir* **2017,** *33,* 4083–4089. doi:10.1021/acs.langmuir.7b01020
59. Schoenberger, M.; Damijonaitis, A.; Zhang, Z.; Nagel, D.; Trauner, D. *ACS Chem. Neurosci.* **2014,** *5,* 514–518. doi:10.1021/cn500070w
60. Sparling, B. A.; DiMauro, E. F. *Bioorg. Med. Chem. Lett.* **2017,** *27,* 3207–3218. doi:10.1016/j.bmcl.2017.04.073
61. Trattnig, S. M.; Harpsøe, K.; Thygesen, S. B.; Rahr, L. M.; Ahring, P. K.; Balle, T.; Jensen, A. A. *J. Biol. Chem.* **2012,** *287,* 25241–25254. doi:10.1074/jbc.m112.360370
62. Baeyer, A. *Ber. Dtsch. Chem. Ges.* **1874,** *7,* 1638–1640. doi:10.1002/cber.187400702214
63. Mills, C. *J. Chem. Soc., Trans.* **1895,** *67,* 925–933. doi:10.1039/ct8956700925
64. von Wantoch Rekowski, M.; Pyriochou, A.; Papapetropoulos, N.; Stößel, A.; Papapetropoulos, A.; Giannis, A. *Bioorg. Med. Chem.* **2010,** *18,* 1288–1296. doi:10.1016/j.bmc.2009.12.027
65. Harsányi, K.; Gönczi, C.; Korbonits, D. *Justus Liebigs Ann. Chem.* **1973,** 190–194. doi:10.1002/jlac.197319730203
66. Murarka, S.; Martín-Gago, P.; Schultz-Fademrecht, C.; Al Saabi, A.; Baumann, M.; Fansa, E. K.; Ismail, S.; Nussbaumer, P.; Wittinghofer, A.; Waldmann, H. *Chem. – Eur. J.* **2017,** *23,* 6083–6093. doi:10.1002/chem.201603222
67. Colotta, V.; Catarzi, D.; Varano, F.; Cecchi, L.; Filacchioni, G.; Galli, A.; Costagli, C. *Arch. Pharm. (Weinheim, Ger.)* **1997,** *330,* 387–391. doi:10.1002/ardp.19973301206
68. Párkányi, C.; Abdelhamid, A. O.; Shawali, A. S. *J. Heterocycl. Chem.* **1984,** *21,* 521–524. doi:10.1002/jhet.5570210251
69. Pierau, S.; Dale, G. Novel Compounds having an anti-bacterial Activity. WO Pat. Appl. WO2006021448 A1, March 2, 2006.
70. Wang, X.; Chen, Y.-F.; Yan, W.; Cao, L.-L.; Ye, Y.-H. *Molecules* **2016,** *21,* No. 1574. doi:10.3390/molecules21111574
71. Kolarski, D.; Szymanski, W.; Feringa, B. L. *Org. Lett.* **2017,** *19,* 5090–5093. doi:10.1021/acs.orglett.7b02361
72. Stawski, P.; Sumser, M.; Trauner, D. *Angew. Chem., Int. Ed.* **2012,** *51,* 5748–5751. doi:10.1002/anie.201109265
73. del Barrio, J.; Horton, P. N.; Lairez, D.; Lloyd, G. O.; Toprakcioglu, C.; Scherman, O. A. *J. Am. Chem. Soc.* **2013,** *135,* 11760–11763. doi:10.1021/ja406556h
74. Laufer, S. A.; Domeyer, D. M.; Scior, T. R. F.; Albrecht, W.; Hauser, D. R. J. *J. Med. Chem.* **2005,** *48,* 710–722. doi:10.1021/jm0408767
75. Meng, F.-N.; Li, Z.-Y.; Ying, Y.-L.; Liu, S.-C.; Zhang, J.; Long, Y.-T. *Chem. Commun.* **2017,** *53,* 9462–9465. doi:10.1039/c7cc04599a
76. Coleman, G. H.; Nichols, G.; McCloskey, C. M.; Anspon, H. D. *Org. Synth.* **1945,** *25,* 87–89. doi:10.15227/orgsyn.025.0087
77. Liu, C. F.; Zeng, Y.; Lu, X. W. Peptide Nucleic Acid Monomers and Oligomers. WO Pat. Appl. WO2010027326 A1, March 2, 2006.

License and Terms

BEILSTEIN JOURNAL OF ORGANIC CHEMISTRY

Diaminoterephthalate–α-lipoic acid conjugates with fluorinated residues

Leon Buschbeck, Aleksandra Markovic, Gunther Wittstock and Jens Christoffers*

Full Research Paper

Open Access

Address:
Institut für Chemie, Universität Oldenburg, Carl von Ossietzky-Str. 9–11, D-26129 Oldenburg, Germany

Email:
Jens Christoffers* - jens.christoffers@uol.de

* Corresponding author

Keywords:
chromophore; diaminoterephthalate; fluorine surface marker; fluorescence dye; lipoic acid; self-assembled monolayers

Beilstein J. Org. Chem. **2019,** *15,* 981–991.
doi:10.3762/bjoc.15.96

Received: 28 February 2019
Accepted: 18 April 2019
Published: 26 April 2019

This article is part of the thematic issue "Dyes in modern organic chemistry".

Guest Editor: H. Ihmels

Abstract

Two bifunctional diaminoterephthalate (DAT) fluorescence dyes were prepared in a three-step sequence including one deprotection reaction. One functional unit is α-lipoic acid (ALA) for binding the dye to gold surfaces. It was introduced to the DAT scaffold by an amidation reaction. The other functional unit is a *para*-(trifluoromethyl)benzyl group for facile detection of the surface-bound material by X-ray photoelectron spectroscopy (XPS). This residue was introduced by reductive amination of the DAT scaffold with the respective benzaldehyde derivative. In one compound (60% yield over three steps) the ALA unit is directly bound to the DAT as a relatively electron-withdrawing amide. In solution (CH_2Cl_2), this material shows strong fluorescence (quantum yield 57% with emission at 495 nm, absorption maximum at 420 nm). The other compound (57% yield over three steps) possesses a propylene spacer between the ALA and the DAT units for electronic decoupling, thus, bathochromic shifts are observed (absorption at 514 nm, emission at 566 nm). The quantum yield is, however, lower (4%). Self-assembled monolayers on a gold surface of both compounds were prepared and characterized by high-resolution XPS of the C 1s, O 1s, S 2p, N 1s and F 1s emissions. The high signal-to-noise ratios of the F 1s peaks indicated that trifluoromethylation is an excellent tool for the detection of surface-bound materials by XPS.

Introduction

Diaminoterephthalates (DATs) are powerful fluorescence dyes [1,2] with outstanding properties such as high quantum yields and pronounced stability against photobleaching [3-5]. Although being structurally relatively simple, this class of dyes is so far underrated in the literature. The chromophore, which is accessed from succinyl succinates and primary amines [6,7], can be regarded as a molecular scaffold [8], which can be orthogonally equipped with different functional units [9] by simple transformations. Thus, different applications in materials science [10] and life sciences [11,12] can be addressed by

tailored functional DATs. As an example for an application in biochemistry, Figure 1 shows a compound with cyclooctyne and maleimide as functional units. It was used as a "turn-on" fluorescence probe for cross-linking proteins [13]. The highly reactive cyclooctyne residue undergoes 1,3-dipolar cycloadditions with organoazides (copper-free click reactions) [14]. The second functional unit, the maleimide moiety, is a reactive probe for mercaptane, which could be, e.g., a protein holding a cysteine residue on its surface [15-17]. The successful ligation by conjugated addition can be followed by the changes of the fluorescence quantum yields (i.e., "turn-on effect") [11-13].

Modification of solid surfaces by defined layers of organic compounds raised significant interest in the last century. Those modifications can be fairly simple as in the case of alkanethiolate layers on gold [18] yet have a number of applications in sensorics [19], microcontact printing [20], dip-pen nanolithography [21], microfluidics [22], and protection of nanoparticles [23]. Initially, surface modification aimed on controlling physical properties of surfaces [24,25], while nowadays chemical surface properties can be tuned to yield platforms for the study of electron transfer [26,27] or for building surface molecular devices for different purposes, commonly called integrated molecular systems [19]. These molecular systems are mainly used for pH sensing [28-30], inorganic- [31-33], organic- and biosensors [34,35]. Self-assembled monolayers (SAMs) can also be triggered electrochemically to perform reactions on the surfaces. These "dynamic" surfaces allow the "turn-on" of active states upon application of electrochemical potentials, for instance, for the addition of compounds to surfaces or for the control of cell adhesion [36-38].

Characterization of such integrated molecular systems constitutes a substantial challenge (as compared to the structural characterization of soluble organic compounds) because (1) different compounds are potentially present on the surface and cannot be separated; (2) some powerful techniques, especially NMR and MS with soft ionizations are not applicable; and (3) the total amount of material is extremely small (i.e., about 10^{-9} mol·cm^{-2}) [39]. X-ray photoelectron spectroscopy (XPS) is one of the few suitable methods for detection of surface-immobilized compounds and changes on the surfaces. However, due to similar chemical shifts in binding energies, fragments of larger organic compounds are not easily distinguished. Labeling molecular entities with elements possessing large excitation cross sections like fluorine, chlorine, or bromine [40] represents an approach that can greatly simplify the detection of molecular reactions (cleavage, anchoring) in monolayers after their assembly on surfaces.

In the course of our project on surface modifications by redox-active SAMs, we envisioned a bifunctionalized DAT as suitable building block. Surface binding to a metal support, e.g., gold, should be accomplished by an α-lipoic acid (ALA) residue. Furthermore, a fluorine-substituted moiety bound to DAT shall facilitate detection by XPS.

Results and Discussion

Synthesis. The preparation of DAT–ALA conjugate **3** with a fluorinated residue started from mono-carbamate-protected diethyl DAT **1** (Scheme 1). Compound **1** was accessed in three steps from diethyl succinate according to Wu et al. [41]. Reductive amination with trifluoromethylated benzaldehyde was accomplished with a mixture of $ZnCl_2$ and $NaBH_3CN$ [42] yielding the respective *N*-benzylated compound **2** in good yield. After subsequent *N*-Boc-deprotection with TFA (product **4** in quantitative yield), the primary amino function was amidated with racemic α-lipoic acid (ALA) in the presence of COMU–DIPEA [COMU = (1-cyano-2-ethoxy-2-oxoethylideneaminooxy)(dimethylamino)(morpholino)carbenium hexafluorophosphate, DIPEA = ethyldiisopropylamine] [43] as coupling reagent to the first title compound **3** in 71% yield. Due to the electron-withdrawing amide group, the chromophore is relatively electron deficient (absorption at 420 nm and emission at 495 nm).

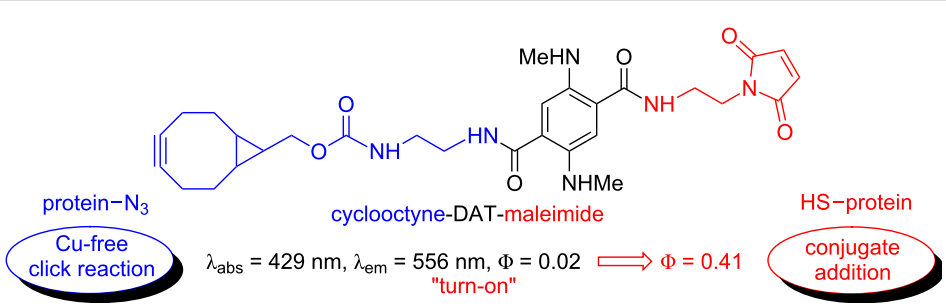

Figure 1: Bifunctional DAT as a cross-linker for proteins. The compound is a turn-on-probe, i.e., the fluorescence quantum yield Φ = 2% increased upon reaction with the target to Φ = 41%.

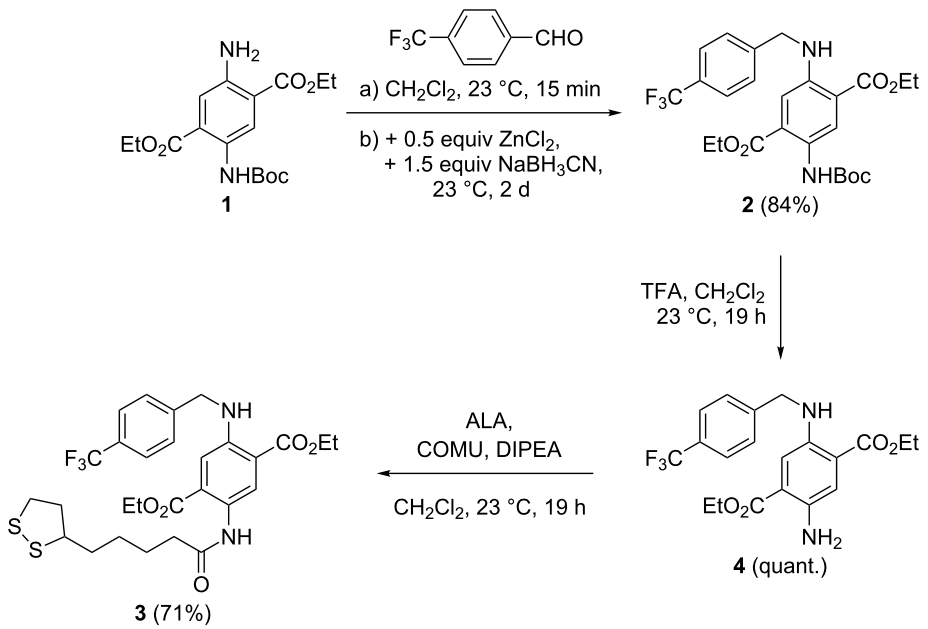

Scheme 1: Preparation of DAT–ALA conjugate **3** with fluorinated benzyl residue.

In order to achieve a bathochromic shift of absorption and emission bands, the DAT and ALA moieties should be electronically decoupled by introduction of a propylene spacer. Therefore, we started the synthesis with compound **5** (Scheme 2), which was accessed from compound **1** in two steps by reductive amination with *N*-Alloc-3-aminopropanal and subsequent *N*-Boc deprotection as reported recently [44]. Reductive amination with trifluoromethylated benzaldehyde was accomplished as described for compound **2** and furnished product **6** in 91% yield. The Alloc-protecting group was then cleaved (95% yield of product **8**) in a palladium-catalyzed allylic substitution reaction with morpholine as a scavenger of the allylic cation [45,46]. Finally, the primary amine **8** was coupled with ALA in the presence of COMU–DIPEA to furnish the second title com-

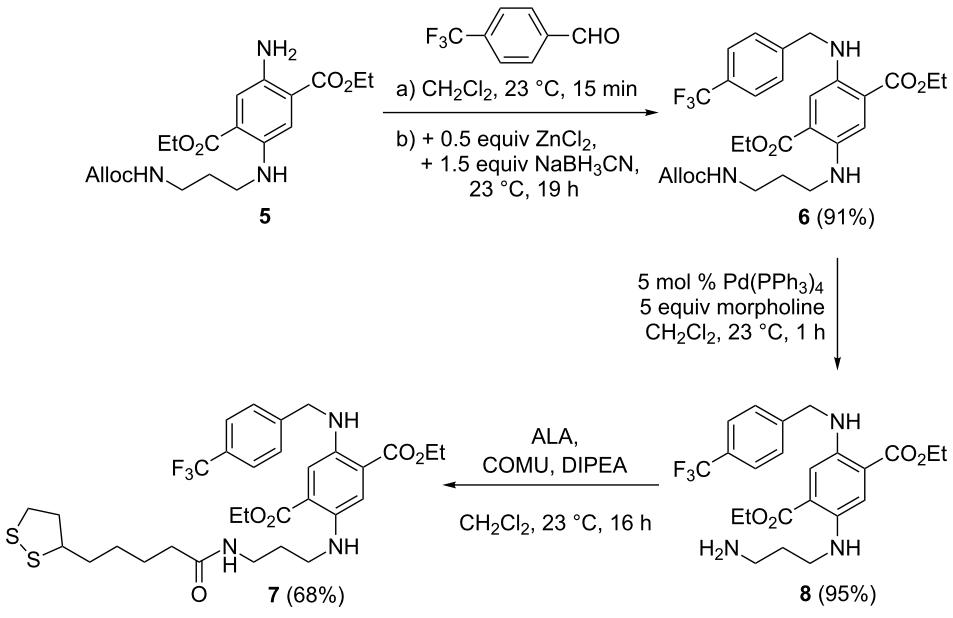

Scheme 2: Preparation of conjugate **7** consisting of fluorinated DAT and ALA moieties with an additional propylene linker unit.

pound **7** in 68% yield. Indeed, a bathochromic shift of the spectral data was observed (absorption at 514 nm and emission at 566 nm).

Spectroscopy. Being typical push–pull aromatic systems, all DAT derivatives are colored materials (yellow, orange, or red) showing pronounced fluorescence in solution (Table 1). The absorption and emission wavelengths are sensitively tuned by the electron-accepting or electron-donating nature of the nitrogen-substituents at the aromatic ring. In Table 1, compound **1** with an NH_2 and NHBoc group is the most electron-deficient one with absorption and emission wavelength at 408 nm and 487 nm, respectively (Stokes shift ca. 80 nm). A bathochromic shift of 16 nm of both, absorption and emission wavelengths, is achieved by introduction of a benzyl residue at one nitrogen atom (compound **2**). If the Boc group is replaced by the slightly more electron-withdrawing carboxamide as in compound **3**, this bathochromic shift (compared to compound **1**) is only ca. 10 nm. Without an *N*-acceptor moiety, i.e., *N*-monoalkyl (compounds **4** and **5**) or *N*,*N*′-dialkyl substitution (compounds **6**–**8**), a stronger bathochromic shift is observed towards the absorption at 451–473 nm (514 nm for compound **7**, which is exceptionally high) and emission at 547–567 nm. The quantum yields of compounds **1**–**4** range between 0.21 and 0.57, for compounds **5**–**8** with propylene linker, the quantum yields are between 0.04–0.13. Interestingly, target compound **3** has the highest (0.57), target compound **7** the lowest (0.04) quantum yield.

XPS characterization of SAMs. SAMs were prepared from compounds **3** and **7** exploiting the strong binding affinity of the ALA residue to gold surfaces [52]. The resulting layers of compound **3** (SAM **3**) and **7** (SAM **7**) were characterized by XPS of the C 1s, O 1s, S 2p, N 1s and F 1s emissions (Figure 2 for SAM **3**, Figure 3 for SAM **7**).

The largest contributions of the C 1s spectra at 284.4 eV (SAM **3**) and 284.7 eV (SAM **7**) correspond to the carbon atoms of the alkyl chains, the aromatic ring and the carbon bound to sulfur atoms (Table 2). The peak at 285.5 eV (SAM **3** and SAM **7**) corresponds to the carbon atoms with a higher binding energy due to the bond to one more electronegative atom (*C*−O and *C*−N) [53]. Figure 2 and Figure 3 show further C 1s peaks lying at binding energies of 288.5 eV, 290.6 eV, and 292.6 eV (SAM **3**) and 288.5 eV, 290.9 eV, and 292.7 eV (SAM **7**). The first component at 288.5 eV corresponds to the carbonyl carbon atom in the amide and ester functions, which are bond to two electronegative elements (O=*C*−O and O=*C*−N) that shift the binding energies to higher values. The broad contributions at 290.6 eV (SAM **3**) and 290.9 eV (SAM **7**) originate from multi-electron excitations, i.e., from shake-up process at aromatic systems [54]. The components at 292.6 eV and 292.7 eV correspond to the carbon bound to three fluorine atoms causing a strong shift of binding energies outside the range typical for most organic compounds.

The O 1s spectrum of the monolayers consist of two components at 531.5 eV and 533.2 eV (SAM **3**) and 531.6 eV and 533.3 eV (SAM **7**) for oxygen atoms involved in the *O*=C and *O*−C bonds, respectively [55]. The slight deviation from the peak area ratio of 3:2 for I(531.5 eV)/I(533.5 eV), which is expected from the molecular structure of compounds **3** and **7**, may be caused by residual adsorbed water that also causes an O 1s component at 533.0–533.5 eV [57,58].

The main doublet in the S 2p spectra of both monolayers at 161.8 eV corresponds to sulfur bound to gold [59]. Although, S 2p spectra were recorded first among all spectra there is indication of radiation damage by the doublet at 163.3 eV in SAM **7** (Figure 3) [60-62]. This signal is not found in monolayers from SAM **3** (Figure 2).

Table 1: Spectroscopic properties of diaminoterephthalates **1**–**8**; solvent CH_2Cl_2.

Compound	λ_{max} [nm]	lg ε [$dm^3 \cdot mol^{-1} \cdot cm^{-1}$]	λ_{em} [nm][a]	Φ[b]
1	408	3.87	487	0.21
2	424	3.88	503	0.36
3	420	3.67	495	0.57
4	451	3.72	547	0.21
5	455	3.77	553	0.13
6	473	3.83	567	0.12
7	514	3.58	566	0.04
8[c]	464	3.58	566	0.09

[a]Excitation at λ_{max} of the absorption band. [b]Quantum yields were determined according to the Parker Rees method [47-49] using rhodamine B in EtOH as standard [λ_{max} = 544 nm, lg ε [$dm^3 \cdot mol^{-1} \cdot cm^{-1}$] = 3.23, λ_{em} = 569 nm, Φ = 0.46] [50,51]. [c]In MeOH as solvent.

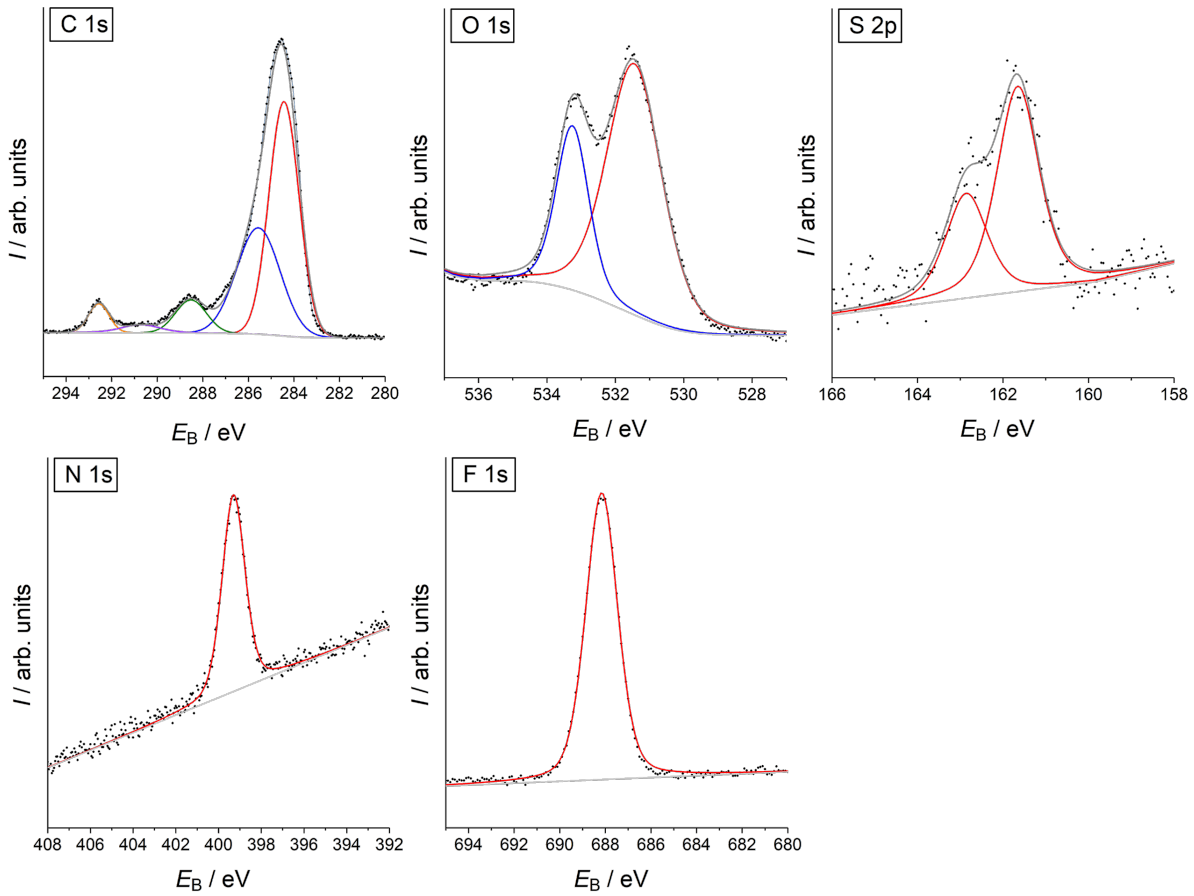

Figure 2: High-resolution XPS of SAM **3**.

Table 2: Binding energies of the C 1s, O 1s, S 2p, N 1s, and F 1s photoemission lines of SAM **3** and SAM **7**.

XPS line	SAM **3** E_B [eV]	SAM **7** E_B [eV]	Assignment	References
C 1s	284.4	284.7	*C*–C, *C*–S	[53]
	285.5	285.5	*C*–O, *C*–N	[53]
	288.5	288.5	O=*C*–O, O=*C*–N	[53]
	290.6	290.9	multi electron excitations	[54]
	292.6	292.7	CF_3	[55]
O 1s	531.5	531.6	*O*=C	[56]
	533.2	533.3	*O*–C and residual water	[56-58]
S $2p_{3/2}$	161.8	161.8	R–*S*–Au	[59]
	–	163.3	radiation damage	[60-62]
S $2p_{1/2}$	162.9	163.0	R–*S*–Au	[59]
	–	164.6	radiation damage	[60-62]
N 1s	399.3	399.3	*N*–aryl	[63]
F 1s	688.2	688.4	CF_3	[55]

There is only one N 1s component at 399.3 eV which corresponds to all nitrogen atoms at both SAMs [63]. Fluorine atoms in the F_3C group are detected at binding energies of 688.2 eV (SAM **3**) and 688.4 eV (SAM **7**) in agreement with the literature [55], which is a typical value for the F_3C group. The high signal-to-noise ratio, especially in comparison to the S 2p and

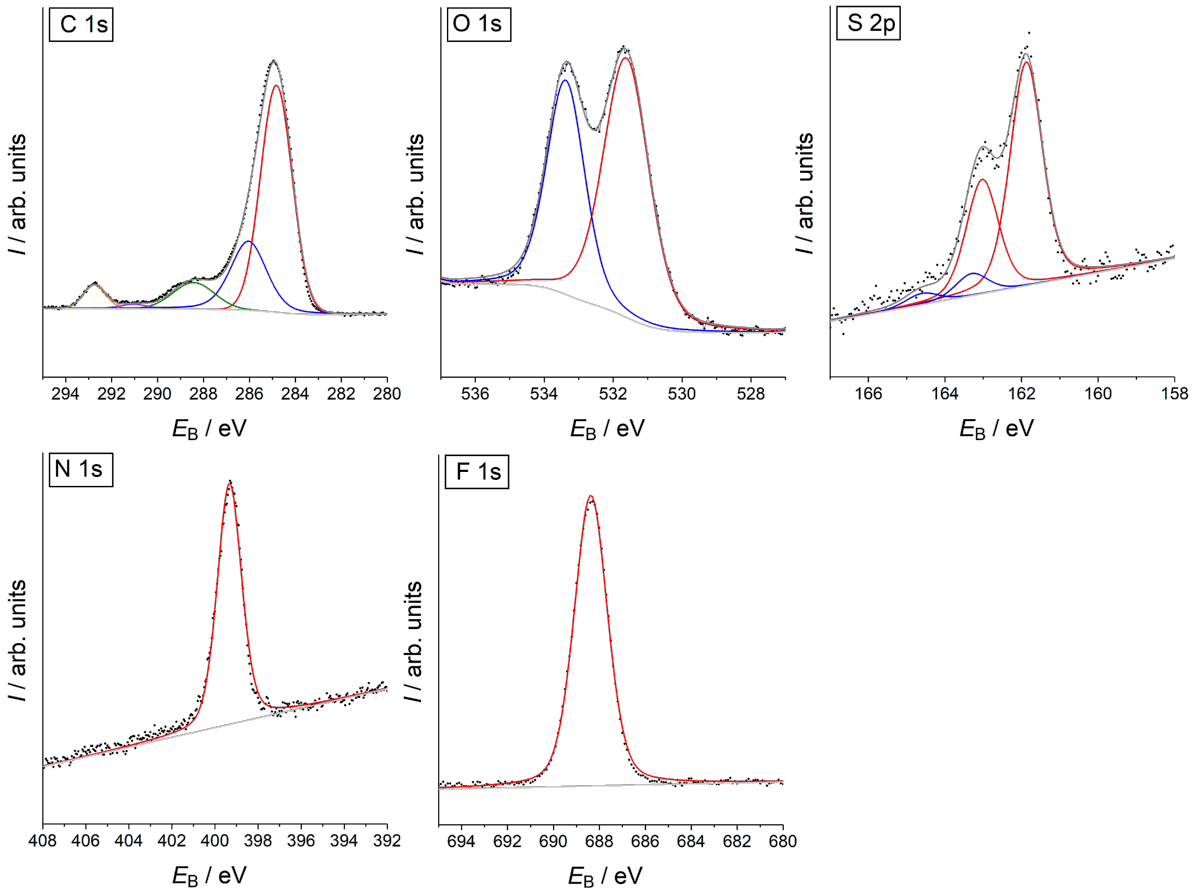

Figure 3: High-resolution XPS of SAM **7**.

N 1s signals, illustrates its suitability for molecular surface labeling.

Conclusion

Two bifunctional diaminoterephthalate (DAT) fluorescence dyes have been prepared. One functional unit is α-lipoic acid (ALA) for binding the dye to gold surfaces. The other carries a trifluoromethyl group for facile detection of the surface-bound material by X-ray photoelectron spectroscopy (XPS). In the first of two target structures, compound **3**, the fluorinated residue was introduced by reductive amination of mono-*N*-Boc-protected diethyl DAT **1** with *para*-(trifluoromethyl)-substituted benzaldehyde. After *N*-deprotection, the ALA unit was introduced by amidation using a standard coupling protocol (with COMU–DIPEA). Compound **3** was accessed in 60% yield over three steps. In solution (CH_2Cl_2), **3** shows strong fluorescence (quantum yield Φ = 57%) at λ_{em} = 495 nm when irradiated at its absorption maximum at λ_{max} = 420 nm. In order to achieve bathochromic shifts of the wavelengths, the electron-withdrawing ALA-amide unit was electronically decoupled from the DAT chromophore by introducing a propylene spacer. Thus, diethyl DAT was first equipped with an *N*-Alloc-protected 3-aminopropyl side chain at one nitrogen function following a literature protocol. This compound, **5**, was then submitted to reductive amination with *para*-(trifluoromethyl)benzaldehyde. After Alloc deprotection, the side chain was amidated with ALA following the same COMU–DIPEA protocol as described for **3**. The second target compound **7** was obtained in 59% yield over three steps. Indeed, the emission and absorption wavelengths in solution (CH_2Cl_2) of compound **7** were bathochromically shifted (λ_{max} = 514 nm, λ_{em} = 566 nm). However, the quantum yield of **7** was on the other hand significantly lower (Φ = 4%). Self-assembled monolayers (SAMs) of both compound **3** and **7** were prepared on a gold surface. The elemental compositions of these two SAMs were characterized by high-resolution XPS of the C 1s, O 1s, S 2p, N 1s and F 1s emissions. As is indicated by the high signal-to-noise ratio of the F 1s peaks, the trifluoromethylation is an excellent tool for the detection of surface-bound materials by XPS.

Experimental

General experimental methods: Preparative column chromatography was carried out using Merck SiO_2 (35–70 µm, type 60 A) with hexanes (mixture of isomers, bp. 64–71 °C), CH_2Cl_2, EtOAc and MeOH as eluents. TLC was performed on aluminum plates coated with SiO_2 F_{254}. ^1H and ^{13}C NMR spectra were recorded on a Bruker Avance DRX 500 instrument. Multiplicities of carbon signals were determined with DEPT experiments. HRMS spectra of products were obtained with Waters Q-TOF Premier (ESI) or Thermo Scientific DFS (EI) spectrometers. IR spectra were recorded on a Bruker Tensor 27 spectrometer equipped with a diamond ATR unit. UV–vis spectra were recorded with a Shimadzu UV-1800, fluorescence spectra with a Shimadzu RF-5301PC spectrometer. Compounds **1** [41] and **5** [44] were prepared according to literature procedures. All other starting materials were commercially available.

XPS of SAMs were recorded with ESCALAB 250 iX (Thermo Fisher, East Grinsted, UK) using a monochromatized Al K_α excitation (1486.6 eV) and the magnetic lens mode. Data acquisition and spectra processing was performed with the Avantage software v. 5.52. After recording a survey spectrum, high-resolution spectra were obtained from the O 1s, F 1s, N 1s, C 1s and S 2p region with a pass energy of 30 eV, a step size of 0.05 eV and 50 ms dwell time. In order to avoid radiation damage of the SAMs, which becomes evident by the appearance of a second S 2p doublet at 163.3 eV/164.5 eV [60-62], 35 scans were averaged from different regions of the same sample (area scan). The peak-fit analysis used the "smart background" from Avantage software and sum of Gaussian and Lorentzian contributions for each spectral component. The area ratio between S $2p_{3/2}$ and S $2p_{1/2}$ emissions from each state was fixed to 2:1. The graphs show the experimental points as dot, the sum curve as black line, the background as grey line and the spectral components as colored lines.

Diethyl 2-(*tert*-butoxycarbonyl)amino-5-[4-(trifluoromethyl)benzylamino]terephthalate (2): In a similar manner as described in [44], a solution of DAT **1** (0.567 mmol, 200 mg, 1.0 equiv) in CH_2Cl_2 (3 mL) was added dropwise to a cooled (ice-water bath) suspension of 4-(trifluoromethyl)benzaldehyde (0.850 mmol, 148 mg, 1.5 equiv) in CH_2Cl_2 (3 mL). After stirring the mixture for 15 min at ambient temperature, it was cooled (ice-water bath) and $ZnCl_2$ (0.23 mmol, 39 mg, 0.5 equiv) and $NaBH_3CN$ (0.85 mmol, 53 mg, 1.5 equiv) were added. Subsequently, the mixture was stirred for 2 d at ambient temperature, then diluted with water (25 mL) and extracted with CH_2Cl_2 (3 × 25 mL). The combined organic layers were dried ($MgSO_4$) and evaporated after filtration. The residue was recrystallized (from hexanes/EtOAc 8:1, 20 mL) to furnish the title compound **2** (244 mg, 0.478 mmol, 84%) as an orange solid. Mp 210 °C. R_f = 0.31 (SiO_2, hexanes/CH_2Cl_2 1:3); ^1H NMR (500 MHz, $CDCl_3$) δ 1.30 (t, *J* = 7.1 Hz, 3H), 1.42 (t, *J* = 7.1 Hz, 3H), 1.51 (s, 9H), 4.28 (q, *J* = 7.1 Hz, 2H), 4.38 (q, *J* = 7.1 Hz, 2H), 4.50 (d, *J* = 5.6 Hz, 2H), 7.16 (s, 1H), 7.48 (d, *J* = 8.0 Hz, 2H), 7.59 (d, *J* = 8.1 Hz, 2H), 7.91 (t, *J* = 5.6 Hz, 1H), 8.86 (s, 1H), 9.49 (br. s, 1H) ppm; $^{13}C\{^1H\}$ NMR (125 MHz, $CDCl_3$) δ 14.12 (CH_3), 14.48 (CH_3), 28.53 (3 CH_3), 47.19 (CH_2), 61.28 (CH_2), 61.63 (CH_2), 80.23 (C), 113.61 (CH), 115.86 (C), 121.08 (C), 122.82 (C), 124.28 (q, *J* = 272.0 Hz, C), 125.76 (q, *J* = 3.6 Hz, 2 CH), 127.53 (2 CH), 129.67 (q, *J* = 32.3 Hz, C), 130.31 (C), 143.34 (C), 144.74 (C), 153.25 (C), 167.29 (C), 168.17 (C) ppm; IR (ATR): 3310 (w), 2983 (w), 1715 (m), 1676 (m), 1620 (w), 1542 (m), 1469 (w), 1422 (m), 1393 (w), 1368 (w), 1326 (m), 1241 (m), 1217 (s), 1159 (s), 1107 (vs), 1066 (m), 1043 (w), 1022 (s), 907 (w), 870 (w), 830 (m), 786 (m), 764 (w), 700 (w), 654 (w), 610 (w), 596 (w), 575 (w) cm^{-1}; MS (EI, 70 eV) *m/z* (%): 510 (17) [M^+], 453 (54), 435 (17), 410 (100), 388 (16), 362 (12), 251 (21), 158 (20); HRMS (EI): [M^+] calcd for $C_{25}H_{29}F_3N_2O_6^+$, 510.1972; found, 510.1972; UV–vis (CH_2Cl_2): λ_{max} (lg ε) = 424 nm (3.88); fluorescence (CH_2Cl_2): λ_{em} = 503 nm, λ_{ex} = 424 nm, Φ = 0.36; $C_{25}H_{29}F_3N_2O_6$ (510.51 $g \cdot mol^{-1}$).

Diethyl 2-amino-5-[4-(trifluoromethyl)benzylamino]terephthalate (4): In a similar manner as described in [44], TFA (3 mL) was added dropwise to a cooled (ice-water bath) solution of carbamate **2** (0.402 mmol, 205 mg) in CH_2Cl_2 (3 mL). The mixture was stirred for 19 h at ambient temperature and then poured into saturated aqueous $NaHCO_3$ solution (50 mL). After stirring for 5 min at ambient temperature, it was extracted with CH_2Cl_2 (3 × 50 mL). The combined organic layers were dried ($MgSO_4$) and evaporated after filtration. Chromatography of the residue (SiO_2, hexanes/EtOAc 6:1 with 1 vol % NEt_3, R_f = 0.31) furnished the title compound **4** (171 mg, 0.417 mmol, quant.) as an orange-red solid. Mp 98–99 °C; ^1H NMR (500 MHz, $CDCl_3$) δ 1.30 (t, *J* = 7.1 Hz, 3H), 1.39 (t, *J* = 7.1 Hz, 3H), 4.27 (q, *J* = 7.1 Hz, 2H), 4.34 (q, *J* = 7.1 Hz, 2H), 4.46 (s, 2H), 7.12 (s, 1H), 7.38 (s, 1H), 7.50 (d, *J* = 8.0 Hz, 2H), 7.59 (d, *J* = 8.1 Hz, 2H) ppm, signals for three NH protons were not observed; $^{13}C\{^1H\}$ NMR (125 MHz, $CDCl_3$) δ 14.28 (CH_3), 14.42 (CH_3), 47.73 (CH_2), 60.93 (CH_2), 61.93 (CH_2), 113.88 (CH), 117.33 (C), 117.83 (C), 119.99 (CH), 124.35 (q, *J* = 271.9 Hz, C), 125.68 (q, *J* = 3.6 Hz, 2 CH), 127.64 (2 CH), 129.53 (q, *J* = 32.5 Hz, C), 139.79 (C), 141.69 (C), 143.85 (C), 167.44 (C), 167.82 (C) ppm; IR (ATR): 3421 (w), 2988 (w), 2904 (w), 1679 (s), 1619 (w), 1563 (w), 1514 (m), 1474 (w), 1441 (w), 1416 (w), 1367 (w), 1329 (m), 1289 (m), 1280 (w), 1265 (w), 1207 (vs), 1158 (m), 1102 (vs), 1062 (s), 1018 (m), 878 (w), 844 (w), 827 (w), 787 (m), 729 (w), 655 (w), 596 (w) cm^{-1}; MS (EI, 70 eV) *m/z* (%): 410 (100) [M^+], 362 (16), 251

(42), 204 (22), 158 (52), 132 (18); HRMS (EI): [M^+] calcd for $C_{20}H_{21}F_3N_2O_4^+$, 410.1448; found, 410.1447; UV–vis (CH_2Cl_2): λ_{max} (lg ε) = 451 nm (3.72); fluorescence (CH_2Cl_2): λ_{em} = 547 nm, λ_{ex} = 451 nm, Φ = 0.21; $C_{20}H_{21}F_3N_2O_4$ (410.39 g·mol^{-1}).

***rac*-Diethyl 2-[5-(1,2-dithiolan-3-yl)pentanoylamino]-5-[4-(trifluoromethyl)benzylamino]terephthalate (3):** In a similar manner as described in [44], DIPEA (1.05 mmol, 136 mg, 3.0 equiv) and COMU (1.05 mmol, 450 mg, 3.0 equiv) were added successively to a cooled (ice-water bath) solution of *rac*-α-lipoic acid (0.698 mmol, 144 mg, 2.0 equiv) in CH_2Cl_2 (8 mL). After stirring for 1 h at ambient temperature a solution of amine **4** (0.346 mmol, 142 mg, 1.0 equiv) in CH_2Cl_2 (8 mL) was added to the again cooled solution. The mixture was then stirred for 19 h at ambient temperature. It was subsequently diluted with water (50 mL) and extracted with CH_2Cl_2 (3 × 50 mL). The combined organic layers were dried ($MgSO_4$), filtered and all volatile materials were removed under reduced pressure. The residue was chromatographed (SiO_2, hexanes/EtOAc 6:1, R_f = 0.25) to yield compound **3** (148 mg, 0.247 mmol, 71%) as a bright yellow solid. Mp 86–88 °C; ^{1}H NMR (500 MHz, $CDCl_3$) δ 1.31 (t, *J* = 7.1 Hz, 3H), 1.41 (t, *J* = 7.1 Hz, 3H), 1.46–1.59 (m, 2H), 1.66–1.81 (m, 4H), 1.91 (dq, *J* = 13.6 Hz, *J* = 7.0 Hz, 1H), 2.37–2.48 (m, 3H), 3.07–3.12 (m, 1H), 3.14–3.19 (m, 1H), 3.54–3.60 (m, 1H), 4.29 (q, *J* = 7.1 Hz, 2H), 4.37 (q, *J* = 7.1 Hz, 2H), 4.51 (d, *J* = 5.3 Hz, 2H), 7.18 (s, 1H), 7.48 (d, *J* = 8.1 Hz, 2H), 7.59 (d, *J* = 8.1 Hz, 2H), 8.03 (t, *J* = 5.3 Hz, 1H), 9.21–9.22 (m, 1H), 10.40–10.42 (m, 1H) ppm; ^{13}C{^{1}H} NMR (125 MHz, $CDCl_3$) δ 14.11 (CH_3), 14.42 (CH_3), 25.40 (CH_2), 28.98 (CH_2), 34.81 (CH_2), 38.25 (CH_2), 38.60 (CH_2), 40.35 (CH_2), 47.11 (CH_2), 56.52 (CH), 61.30 (CH_2), 61.81 (CH_2), 113.49 (CH), 115.62 (C), 121.26 (C), 124.20 (CH), 124.26 (q, *J* = 271.9 Hz, C), 125.79 (q, *J* = 3.4 Hz, 2 CH), 127.50 (2 CH), 129.73 (C), 129.76 (q, *J* = 32.3 Hz, C), 143.18 (C), 145.52 (C), 167.56 (C), 168.09 (C), 171.21 (C) ppm; IR (ATR): 3387 (w), 3304 (w), 2981 (w), 2932 (w), 1715 (m), 1680 (s), 1657 (m), 1621 (w), 1543 (s), 1500 (w), 1473 (w), 1448 (w), 1415 (m), 1367 (w), 1329 (s), 1264 (m), 1216 (vs), 1160 (s), 1108 (s), 1094 (s), 1068 (s), 1019 (m), 912 (w), 896 (w), 866 (w), 827 (m), 791 (m), 667 (w), 633 (w), 588 (w), 577 (w) cm^{-1}; MS (EI, 70 eV) *m/z* (%): 598 (18) [M^+], 551 (26), 418 (16), 405 (30), 158 (55), 73 (100), 66 (24); HRMS (EI): [M^+] calcd for $C_{28}H_{33}F_3N_2O_5S_2^+$, 598.1777; found, 598.1776; UV–vis (CH_2Cl_2): λ_{max} (lg ε) = 420 nm (3.67); fluorescence (CH_2Cl_2): λ_{em} = 495 nm, λ_{ex} = 420 nm, Φ = 0.57; $C_{28}H_{33}F_3N_2O_5S_2$ (598.71 g·mol^{-1}).

Diethyl 2-[3-(allyloxycarbonylamino)propylamino]-5-[4-(trifluoromethyl)benzylamino]terephthalate (6): A solution of DAT **5** (0.254 mmol, 100 mg, 1.0 equiv) in CH_2Cl_2 (2 mL) was added to a cooled (ice-water bath) suspension of 4-(trifluoromethyl)benzaldehyde (0.38 mmol, 66 mg, 1.5 equiv) in CH_2Cl_2 (2 mL). After stirring the mixture for 15 min at ambient temperature, it was cooled again (ice-water bath) and $ZnCl_2$ (0.13 mmol, 18 mg, 0.5 equiv) and after 30 min $NaBH_3CN$ (0.38 mmol, 66 mg, 1.5 equiv) were added and the resulting mixture was further stirred at ambient temperature for 19 h. It was then diluted with water (25 mL) and extracted with CH_2Cl_2 (2 × 25 mL). The combined organic layers were dried ($MgSO_4$) and evaporated after filtration. Chromatography of the residue (SiO_2, hexanes/EtOAc 3:1, R_f = 0.24) furnished title compound **6** (128 mg, 0.232 mmol, 91%) as an orange-red solid. Mp 127–128 °C; ^{1}H NMR (500 MHz, $CDCl_3$) δ 1.28 (t, *J* = 7.1 Hz, 3H), 1.41 (t, *J* = 7.1 Hz, 3H), 1.88 (pent, *J* = 6.7 Hz, 2H), 3.23 (t, *J* = 6.6 Hz, 2H), 3.33 (q, *J* = 6.3 Hz, 2H), 4.24 (q, *J* = 7.1 Hz, 2H), 4.37 (q, *J* = 7.1 Hz, 2H), 4.46 (s, 2H), 4.35 (d, *J* = 4.6 Hz, 2H), 4.89 (br.s, 1H), 5.19 (d, *J* = 10.4 Hz, 1H), 5.29 (dd, *J* = 17.2 Hz, *J* = 1.4 Hz, 1H), 5.91 (ddt, *J* = 16.9 Hz, *J* = 10.7 Hz, *J* = 5.6 Hz, 1H), 6.80 (br. s, 1H), 7.18 (s, 1H), 7.30 (s, 1H), 7.38 (br. s, 1H), 7.49 (d, *J* = 8.0 Hz, 2H), 7.58 (d, *J* = 8.1 Hz, 2H) ppm; ^{13}C{^{1}H} NMR (125 MHz, $CDCl_3$) δ 14.22 (CH_3), 14.46 (CH_3), 29.72 (CH_2), 39.19 (CH_2), 41.13 (CH_2), 47.72 (CH_2), 60.83 (CH_2), 61.07 (CH_2), 65.63 (CH_2), 114.15 (CH), 114.81 (CH), 116.88 (C), 117.52 (C), 117.68 (CH), 124.35 (q, *J* = 271.9 Hz, C), 125.64 (q, *J* = 3.5 Hz, 2 CH), 127.60 (2 CH), 123.49 (q, *J* = 32.3 Hz, C), 133.09 (C), 140.59 (C), 141.65 (C), 144.07 (C), 156.44 (C), 167.87 (C), 168.08 (C) ppm; IR (ATR): 3378 (w), 3323 (w), 2992 (w), 2942 (w), 2882 (w), 1676 (s), 1623 (w), 1529 (s), 1475 (w), 1457 (w), 1420 (m), 1392 (w), 1368 (w), 1331 (m), 1267 (w), 1203 (vs), 1159 (m), 1106 (vs), 1070 (s), 1022 (m), 940 (w), 921 (w), 875 (w), 860 (w), 826 (w), 790 (m), 631 (w), 602 (w) cm^{-1}; MS (EI, 70 eV) *m/z* (%): 551 (86) [M^+], 493 (100), 423 (12), 376 (62), 334 (35), 244 (13), 158 (30); HRMS (EI): [M^+] calcd for $C_{27}H_{32}F_3N_3O_6^+$, 551.2238; found, 551.2236; UV–vis (CH_2Cl_2): λ_{max} (lg ε) = 473 nm (3.83); fluorescence (CH_2Cl_2): λ_{em} = 567 nm, λ_{ex} = 473 nm, Φ = 0.12; $C_{27}H_{32}F_3N_3O_6$ (551.56 g·mol^{-1}).

Diethyl 2-[(3-aminopropyl)amino]-5-[4-(trifluoromethyl)benzylamino]terephthalate (8): Under exclusion of air and moisture, morpholine (1.17 mmol, 102 mg, 5.0 equiv) was added to a solution of carbamate **6** (0.234 mmol, 129 mg, 1.0 equiv) in abs. CH_2Cl_2 (3 mL). The mixture was degassed (three cycles of freeze, pump and thaw). Then $Pd(PPh_3)_4$ (12 µmol, 14 mg, 0.05 equiv) was added and the mixture was stirred for 1 h at ambient temperature under an inert atmosphere. After adding charcoal (2 mg), it was stirred for 5 min at ambient temperature and then filtered. The filtrate was evaporated and the residue chromatographed (SiO_2, EtOAc/MeOH 6:1 with 1 vol % NEt_3, R_f = 0.15) to furnish title compound **8**

(104 mg, 0.222 mmol, 95%) as red solid. Mp 189–191 °C; ^{1}H NMR (500 MHz, DMSO-d_6) δ 1.18 (t, J = 7.1 Hz, 3H), 1.33 (t, J = 7.1 Hz, 3H), 1.71 (pent, J = 6.8 Hz, 2H), 2.70 (t, J = 6.9 Hz, 2H), 3.51 (q, J = 6.2 Hz, 2H), 4.16 (q, J = 7.1 Hz, 2H), 4.33 (q, J = 7.1 Hz, 2H), 4.48 (d, J = 5.7 Hz, 2H), 6.68 (t, J = 4.6 Hz, 1H), 7.08 (s, 1H), 7.24 (s, 1H), 7.33 (t, J = 5.8 Hz, 1H), 7.57 (d, J = 8.1 Hz, 2H), 7.69 (d, J = 8.2 Hz, 2H) ppm, signals for two NH protons were not detected; ^{13}C{^{1}H} NMR (125 MHz, DMSO-d_6) δ 13.81 (CH_3), 14.12 (CH_3), 30.54 (CH_2), 38.45 (CH_2), 40.24 (CH_2), 46.48 (CH_2), 60.49 (CH_2), 60.79 (CH_2), 113.42 (CH), 114.35 (CH), 115.84 (C), 117.06 (C), 124.39 (q, J = 271.8 Hz, C), 125.30 (q, J = 3.5 Hz, 2 CH), 127.37 (2 CH), 127.29 (q, J = 31.6 Hz, C), 139.46 (C), 140.80 (C), 145.07 (C), 166.88 (C), 167.04 (C) ppm; IR (ATR): 3392 (m), 3250 (br), 2907 (br), 2751 (w), 2680 (w), 2600 (w), 2522 (w), 1669 (s), 1621 (w), 1530 (s), 1474 (w), 1418 (w), 1390 (w), 1368 (w), 1338 (m), 1310 (w), 1276 (m), 1215 (vs), 1152 (s), 1106 (vs), 1070 (s), 1043 (w), 1019 (m), 961 (m), 879 (w), 828 (w), 786 (m), 748 (w), 605 (w), 576 (w) cm^{-1}; MS (EI, 70 eV) *m/z* (%): 467 (100) [M$^+$], 423 (21), 410 (16), 376 (50), 232 (18), 158 (49); HRMS (EI): [M$^+$] calcd for $C_{23}H_{28}F_3N_3O_4^+$, 467.2026; found, 467.2012; UV–vis (MeOH): λ_{max} (lg ε) = 464 nm (3.58); fluorescence (MeOH): λ_{em} = 566 nm, λ_{ex} = 464 nm, Φ = 0.09; $C_{23}H_{28}F_3N_3O_4$ (467.49 g·mol^{-1}).

***rac*-Diethyl 2-{3-[5-(1,2-dithiolan-3-yl)pentanoylamino]propylamino}-5-[4-(trifluoromethyl)benzylamino]terephthalate (7):** *rac*-α-Lipoic acid (0.21 mmol, 44 mg, 2.0 equiv) and COMU (0.320 mmol, 137 mg, 3.0 equiv) were successively added to a solution of DIPEA (0.32 mmol, 41 mg, 3.0 equiv) in CH_2Cl_2 (2 mL) and the solution was stirred for 1 h at ambient temperature. The solution was added dropwise to a suspension of amine **8** (107 µmol, 50.0 mg, 1.0 equiv) in CH_2Cl_2 (2 mL) and the mixture was stirred for 16 h at ambient temperature. It was diluted with water (25 mL) and the mixture was extracted with CH_2Cl_2 (2 × 25 mL). The combined organic layers were dried ($MgSO_4$), filtered and all volatile materials were removed under reduced pressure. The residue was chromatographed (SiO_2, hexanes/EtOAc 1:2, R_f = 0.23) to yield compound **7** (48 mg, 73 µmol, 68%) as a red resin. ^{1}H NMR (500 MHz, $CDCl_3$) δ 1.28 (t, J = 7.1 Hz, 3H), 1.33–1.48 (m, 2H), 1.41 (t, J = 7.1 Hz, 3H), 1.59–1.73 (m, 4H), 1.85–1.93 (m, 3H), 2.17 (dt, J = 7.6 Hz, J = 1.6 Hz, 2H), 2.40–2.49 (m, 1H), 3.07–3.14 (m, 1H), 3.15–3.18 (m, 1H), 3.23 (t, J = 6.5 Hz, 2H), 3.40 (q, J = 6.5 Hz, 2H), 3.52–3.60 (m, 1H), 4.24 (q, J = 7.1 Hz, 2H), 4.37 (q, J = 7.1 Hz, 2H), 4.46 (s, 2H), 5.74 (t, J = 5.3 Hz, 1H), 7.18 (s, 1H), 7.30 (s, 1H), 7.50 (d, J = 8.1 Hz, 2H), 7.58 (d, J = 8.1 Hz, 2H) ppm, signals for three NH-protons could not be detected; ^{13}C{^{1}H} NMR (125 MHz, $CDCl_3$) δ 14.26 (CH_3), 14.51 (CH_3), 25.53 (CH_2), 29.06 (CH_2), 29.30 (CH_2), 34.77 (CH_2), 36.65 (CH_2), 38.03 (CH_2), 38.61 (CH_2), 40.37 (CH_2), 41.73 (CH_2), 47.71 (CH_2), 56.54 (CH), 60.92 (CH_2), 61.14 (CH_2), 114.22 (CH), 114.80 (CH), 116.91 (C), 117.50 (C), 124.34 (q, J = 272.3 Hz, C), 125.66 (q, J = 3.6 Hz, 2 CH), 127.60 (2 CH), 129.49 (q, J = 32.2 Hz, C), 140.68 (C), 141.56 (C), 144.02 (C), 167.93 (C), 168.07 (C), 172.99 (C) ppm; IR (ATR): 2980 (w), 2933 (w), 2866 (w), 1726 (w), 1682 (m), 1618 (w), 1607 (w), 1575 (w), 1529 (m), 1463 (w), 1418 (w), 1371 (w), 1325 (m), 1258 (w), 1216 (m), 1195 (s), 1164 (m), 1118 (s), 1104 (s), 1083 (s), 1065 (m), 1017 (w), 993 (w), 839 (vs), 790 (m), 739 (w), 632 (w), 608 (w) cm^{-1}; HRMS (ESI, pos. mode): [M + H$^+$] calcd for $C_{31}H_{41}F_3N_3O_5S_2^+$, 656.2434; found, 656.2440; UV–vis (CH_2Cl_2): λ_{max} (lg ε) = 514 nm (3.58); fluorescence (CH_2Cl_2): λ_{em} = 514 nm, λ_{ex} = 566 nm, Φ = 0.04; $C_{31}H_{40}F_3N_3O_5S_2$ (655.79 g·mol^{-1}).

Preparation of SAMs of compounds 3 and 7: Gold surfaces were prepared onto cleaned glass slides as the support by depositing 0.5 nm of chromium by electron-beam evaporation as adhesion layer and 200 nm of gold by resistive heating using an evaporation chamber (minicoater, Tectra GmbH, Frankfurt, Germany). The thickness was monitored by means of a quartz crystal microbalance (Tectra GmbH, Frankfurt, Germany). The gold substrates were freshly prepared prior to each experiment. Compound **3** or compound **7** were dissolved in 20 mL ethanol (analytical grade, Fisher Chemicals) and diluted to a final concentration of 3 × 10^{-4} mol·L^{-1}. The gold substrates were immersed in the ethanolic solutions of compound **3** or compound **7** immediately after preparation of the gold layer. The gold substrates were left in the ethanolic solution for self-assembly over 24 h, then removed and rinsed with copious amounts of ethanol (analytical grade, Fisher Chemicals) and eventually dried in an argon stream.

Supporting Information

Supporting Information File 1

Copies of NMR spectra of all reported compounds.
[https://www.beilstein-journals.org/bjoc/content/supplementary/1860-5397-15-96-S1.pdf]

Acknowledgements

This study was supported by a grant (GRK 1885/2) from the Deutsche Forschungsgemeinschaft (DFG) and by the graduate school Nanoenergy funded by the Ministry of Science and Culture of the State of Lower Saxony. MTBE was obtained as a generous gift from Evonik Industries, Marl, Germany. The XPS facility has been co-funded by the DFG (INST 184/144-1 FUGG).

ORCID® iDs

Aleksandra Markovic - https://orcid.org/0000-0002-5706-0325
Gunther Wittstock - https://orcid.org/0000-0002-6884-5515

References

1. Liebermann, H. *Justus Liebigs Ann. Chem.* **1914,** *404,* 272–321. doi:10.1002/jlac.19144040303
2. Christoffers, J. *Eur. J. Org. Chem.* **2018,** 2366–2377. doi:10.1002/ejoc.201701447
3. Shimizu, M.; Asai, Y.; Takeda, Y.; Yamatani, A.; Hiyama, T. *Tetrahedron Lett.* **2011,** *52,* 4084–4089. doi:10.1016/j.tetlet.2011.05.087
4. Shimizu, M.; Fukui, H.; Natakani, M.; Sakaguchi, H. *Eur. J. Org. Chem.* **2016,** 5950–5956. doi:10.1002/ejoc.201601067
5. Tang, B.; Wang, C.; Wang, Y.; Zhang, H. *Angew. Chem., Int. Ed.* **2017,** *56,* 12543–12547. doi:10.1002/anie.201706517
Angew. Chem. **2017,** *129,* 12717–12721. doi:10.1002/ange.201706517
6. Sinnreich, J. *Synthesis* **1980,** 578–580. doi:10.1055/s-1980-29132
7. Zhang, Y.; Starynowicz, P.; Christoffers, J. *Eur. J. Org. Chem.* **2008,** 3488–3495. doi:10.1002/ejoc.200800211
8. Pflantz, R.; Christoffers, J. *Chem. – Eur. J.* **2009,** *15,* 2200–2209. doi:10.1002/chem.200802151
9. Freimuth, L.; Christoffers, J. *Chem. – Eur. J.* **2015,** *21,* 8214–8221. doi:10.1002/chem.201500494
10. Christoffers, J.; Freimuth, L.; Rozzi, C.; Lienau, C. *Synthesis* **2015,** *47,* 1325–1328. doi:10.1055/s-0034-1379963
11. Wache, N.; Schröder, C.; Koch, K.-W.; Christoffers, J. *ChemBioChem* **2012,** *13,* 993–998. doi:10.1002/cbic.201200027
12. Wache, N.; Scholten, A.; Klüner, T.; Koch, K.-W.; Christoffers, J. *Eur. J. Org. Chem.* **2012,** 5712–5722. doi:10.1002/ejoc.201200879
13. Wallisch, M.; Sulmann, S.; Koch, K.-W.; Christoffers, J. *Chem. – Eur. J.* **2017,** *23,* 6535–6543. doi:10.1002/chem.201700774
14. Jewett, J. C.; Bertozzi, C. R. *Chem. Soc. Rev.* **2010,** *39,* 1272–1279. doi:10.1039/b901970g
15. Wu, D.; Cheung, S.; Devocelle, M.; Zhang, L.-J.; Chen, Z.-L.; O'Shea, D. F. *Chem. Commun.* **2015,** *51,* 16667–16670. doi:10.1039/c5cc06137g
16. Haimi, P.; Sikorskaite-Gudziuniene, S.; Baniulis, D. *Proteomics* **2015,** *15,* 1777–1780. doi:10.1002/pmic.201400022
17. Dietz, L.; Bosque, A.; Pankert, P.; Ohnesorge, S.; Merz, P.; Anel, A.; Schnölzer, M.; Thierse, H.-J. *Proteomics* **2009,** *9,* 4298–4308. doi:10.1002/pmic.200900051
18. Ulman, A. *Chem. Rev.* **1996,** *96,* 1533–1554. doi:10.1021/cr9502357
19. Gooding, J. J.; Mearns, F.; Yang, W.; Liu, J. *Electroanalysis* **2003,** *15,* 81–96. doi:10.1002/elan.200390017
20. Wilbur, J. L.; Kumar, A.; Biebuyck, H. A.; Kim, E.; Whitesides, G. M. *Nanotechnology* **1996,** *7,* 452–457. doi:10.1088/0957-4484/7/4/028
21. Ahn, Y.; Hong, S.; Jang, J. *J. Phys. Chem. B* **2006,** *110,* 4270–4273. doi:10.1021/jp055778r
22. Li, Y.; Yuan, B.; Ji, H.; Han, D.; Chen, S.; Tian, F.; Jiang, X. *Angew. Chem., Int. Ed.* **2007,** *46,* 1094–1096. doi:10.1002/anie.200603844
Angew. Chem. **2007,** *119,* 1112–1114. doi:10.1002/ange.200603844
23. Jadhav, S. A. *J. Mater. Chem.* **2012,** *22,* 5894–5899. doi:10.1039/c2jm14239b
24. Zhang, X.; Shi, F.; Niu, J.; Jiang, Y.; Wang, Z. *J. Mater. Chem.* **2008,** *18,* 621–633. doi:10.1039/b711226b
25. Laibinis, P. E.; Whitesides, G. M.; Allara, D. L.; Tao, Y.-T.; Parikh, A. N.; Nuzzo, R. G. *J. Am. Chem. Soc.* **1991,** *113,* 7152–7167. doi:10.1021/ja00019a011
26. Smalley, J. F.; Finklea, H. O.; Chidsey, C. E. D.; Linford, M. R.; Creager, S. E.; Ferraris, J. P.; Chalfant, K.; Zawodzinsk, T.; Feldberg, S. W.; Newton, M. D. *J. Am. Chem. Soc.* **2003,** *125,* 2004–2013. doi:10.1021/ja028458j
27. Eckermann, A. L.; Feld, D. J.; Shaw, J. A.; Meade, T. J. *Coord. Chem. Rev.* **2010,** *254,* 1769–1802. doi:10.1016/j.ccr.2009.12.023
28. Bardea, A.; Katz, E.; Willner, I. *Electroanalysis* **2000,** *12,* 731–735. doi:10.1002/1521-4109(200006)12:10<731::aid-elan731>3.0.co;2-6
29. Beulen, M. W. J.; van Veggel, F. C. J. M.; Reinhoudt, D. N. *Chem. Commun.* **1999,** 503–504. doi:10.1039/a809790i
30. Hickman, J. J.; Ofer, D.; Laibinis, P. E.; Whitesides, G. M.; Wrighton, M. S. *Science* **1991,** *252,* 688–691. doi:10.1126/science.252.5006.688
31. Yang, W.; Gooding, J. J.; Hibbert, D. B. *Analyst* **2001,** *126,* 1573–1577. doi:10.1039/b102898g
32. Yang, W.; Jaramillo, D.; Gooding, J. J.; Hibbert, D. B.; Zhang, R.; Willett, G. D.; Fisher, K. J. *Chem. Commun.* **2001,** 1982–1983. doi:10.1039/b106730n
33. Yang, W.; Gooding, J. J.; Hibbert, D. B. *J. Electroanal. Chem.* **2001,** *516,* 10–16. doi:10.1016/s0022-0728(01)00649-0
34. Gooding, J. J.; Erokhin, P.; Losic, D.; Yang, W.; Policarpio, V.; Liu, J.; Ho, F. M.; Situmorang, M.; Hibbert, D. B.; Shapter, J. G. *Anal. Sci.* **2001,** *17,* 3–9. doi:10.2116/analsci.17.3
35. Gooding, J. J.; Hibbert, D. B. *TrAC, Trends Anal. Chem.* **1999,** *18,* 525–533. doi:10.1016/s0165-9936(99)00133-8
36. Yousaf, M. N.; Mrksich, M. *J. Am. Chem. Soc.* **1999,** *121,* 4286–4287. doi:10.1021/ja983529t
37. Zhao, C.; Witte, I.; Wittstock, G. *Angew. Chem., Int. Ed.* **2006,** *45,* 5469–5471. doi:10.1002/anie.200601151
Angew. Chem. **2006,** *118,* 5595–5597. doi:10.1002/ange.200601151
38. Lesch, A.; Vaske, B.; Meiners, F.; Momotenko, D.; Cortés-Salazar, F.; Girault, H. H.; Wittstock, G. *Angew. Chem., Int. Ed.* **2012,** *51,* 10413–10416. doi:10.1002/anie.201205347
Angew. Chem. **2012,** *124,* 10559–10563. doi:10.1002/ange.201205347
39. Gooding, J. J.; Ciampi, S. *Chem. Soc. Rev.* **2011,** *40,* 2704–2718. doi:10.1039/c0cs00139b
40. Scofield, J. H. *J. Electron Spectrosc. Relat. Phenom.* **1976,** *8,* 129–137. doi:10.1016/0368-2048(76)80015-1
41. Wu, Z.-Q.; Jiang, X.-K.; Zhu, S.-Z.; Li, Z.-T. *Org. Lett.* **2004,** *6,* 229–232. doi:10.1021/ol036108b
42. Penning, M.; Christoffers, J. *Eur. J. Org. Chem.* **2012,** 1809–1818. doi:10.1002/ejoc.201101645
43. Hjelmgaard, T.; Faure, S.; Staerk, D.; Taillefumier, C.; Nielsen, J. *Eur. J. Org. Chem.* **2011,** 4121–4132. doi:10.1002/ejoc.201100232
44. Buschbeck, L.; Christoffers, J. *J. Org. Chem.* **2018,** *83,* 4002–4014. doi:10.1021/acs.joc.8b00347
45. Jimmidi, R.; Shroff, G. K.; Satyanarayana, M.; Reddy, B. R.; Kapireddy, J.; Sawant, M. A.; Sitaswad, S. L.; Arya, P.; Mitra, P. *Eur. J. Org. Chem.* **2014,** 1151–1156. doi:10.1002/ejoc.201301769
46. Pachamuthu, K.; Zhu, X.; Schmidt, R. R. *J. Org. Chem.* **2005,** *70,* 3720–3723. doi:10.1021/jo0482357
47. Parker, C. A.; Rees, W. T. *Analyst* **1960,** *85,* 587–600. doi:10.1039/an9608500587
48. Demas, J. N.; Crosby, G. A. *J. Phys. Chem.* **1971,** *75,* 991–1024. doi:10.1021/j100678a001

49. Fery-Forgues, S.; Lavabre, D. *J. Chem. Educ.* **1999,** *76,* 1260–1264. doi:10.1021/ed076p1260
50. Snare, M. J.; Treloar, F. E.; Ghiggino, K. P.; Thistlethwaite, P. J. *J. Photochem.* **1982,** *18,* 335–346. doi:10.1016/0047-2670(82)87023-8
51. Casey, K. G.; Quitevis, E. L. *J. Phys. Chem.* **1988,** *92,* 6590–6594. doi:10.1021/j100334a023
52. Capitao, D.; Sahli, R.; Raouafi, N.; Limoges, B.; Fave, C.; Schöllhorn, B. *ChemElectroChem* **2016,** *3,* 1422–1428. doi:10.1002/celc.201600260
53. Desimoni, E.; Brunetti, B. *Chemosensors* **2015,** *3,* 70–117. doi:10.3390/chemosensors3020070
54. Gardella, J. A., Jr.; Ferguson, S. A.; Chin, R. L. *Appl. Spectrosc.* **1986,** *40,* 224–232. doi:10.1366/0003702864509565
55. Chinwangso, P.; Lee, H. J.; Lee, T. R. *Langmuir* **2015,** *31,* 13341–13349. doi:10.1021/acs.langmuir.5b03392
56. López, G. P.; Castner, D. G.; Ratner, B. D. *Surf. Interface Anal.* **1991,** *17,* 267–272. doi:10.1002/sia.740170508
57. Spitzer, A.; Lüth, H. *Surf. Sci.* **1985,** *160,* 353–361. doi:10.1016/0039-6028(85)90779-4
58. Zhang, X.; Ptasinska, S. *J. Phys. Chem. C* **2014,** *118,* 4259–4266. doi:10.1021/jp411977p
59. Duwez, A.-S. *J. Electron Spectrosc. Relat. Phenom.* **2004,** *134,* 97–138. doi:10.1016/j.elspec.2003.10.005
60. Laibinis, P. E.; Graham, R. L.; Biebuyck, H. A.; Whitesides, G. M. *Science* **1991,** *254,* 981–983. doi:10.1126/science.254.5034.981
61. Graham, R. L.; Bain, C. D.; Biebuyck, H. A.; Laibinis, P. E.; Whitesides, G. M. *J. Phys. Chem.* **1993,** *97,* 9456–9464. doi:10.1021/j100139a033
62. Heister, K.; Zharnikov, M.; Grunze, M.; Johansson, L. S. O.; Ulman, A. *Langmuir* **2001,** *17,* 8–11. doi:10.1021/la001101d
63. Han, M. G.; Im, S. S. *Polymer* **2000,** *41,* 3253–3262. doi:10.1016/s0032-3861(99)00531-5

License and Terms

BEILSTEIN JOURNAL OF ORGANIC CHEMISTRY

Remarkable effect of alkynyl substituents on the fluorescence properties of a BN-phenanthrene

Alberto Abengózar, David Sucunza, Patricia García-García* and Juan J. Vaquero*

Full Research Paper

Open Access

Address:
Departamento de Química Orgánica y Química Inorgánica, Instituto de Investigación Química "Andrés M. del Río" (IQAR), Universidad de Alcalá, 28871-Alcalá de Henares, Madrid, Spain

Email:
Patricia García-García* - patricia.garciagarci@uah.es;
Juan J. Vaquero* - juanjose.vaquero@uah.es

* Corresponding author

Keywords:
alkyne; BN-phenanthrene; cross-coupling; fluorescence; heterocycles

Beilstein J. Org. Chem. **2019,** *15,* 1257–1261.
doi:10.3762/bjoc.15.122

Received: 02 February 2019
Accepted: 21 May 2019
Published: 06 June 2019

This article is part of the thematic issue "Dyes in modern organic chemistry".

Guest Editor: H. Ihmels

Abstract

A series of BN-phenanthrenes with substituents of a diverse nature have been synthesized by palladium-catalyzed cross-coupling reactions of a common chloro-substituted precursor, which was made from readily available materials in only four steps. Evaluation of the photophysical properties of the prepared compounds unveiled an impressive effect of the presence of alkynyl substituents on the fluorescence quantum yield, which improved from 0.01 in the parent compound to up to 0.65 in derivatives containing a triple bond.

Introduction

BN-polycyclic aromatic hydrocarbons (BN-PAHs) have received increasing interest over the past few years [1-5], particularly in the field of materials science [6]. The presence of a polarized B–N bond induces significant changes in the photophysical properties of these compounds when compared to their PAH analogues containing only non-polar C=C bonds. This fact opens up new opportunities for creating improved optoelectronic devices [7-15].

The introduction of substituents is known to have a substantial influence on the photophysical properties of PAHs. However, although some particular examples of the impact of substituents on the behaviour of BN-PAHs have been reported [16-21], systematic studies are not usually performed, probably due to the difficulties associated with their synthesis and the lack of general methods for their functionalization [22].

We have recently designed an efficient synthesis for one of the simplest BN-PAHs, namely BN-phenanthrene **1a** [23]. We are interested in evaluating the reactivity [24] and properties of **1a** in greater detail as this could provide valuable information that leads to a better understanding of the behaviour of

BN-aromatics. Interestingly, **1a** turned out to be weakly fluorescent [23], in contrast to other BN-phenanthrene isomers described previously [25,26]. The presence of aryl or amino substituents at C1, which can be introduced via bromination and subsequent palladium-catalyzed cross coupling, does not have a significant impact on the fluorescence of these compounds (Figure 1) [23]. In order to gain a deeper understanding of the photophysical properties of the BN-phenanthrene core, we decided to evaluate the influence of substituents located in other positions. We were particularly interested in the effect of alkynyl substituents, as their presence in PAHs is known to alter the fluorescence properties thereof markedly [27-29]. In this regard, we have recently described a methodology for the synthesis of a chloro-substituted BN-benzo[*c*]phenanthrene and its subsequent derivatization via palladium-catalyzed cross-coupling reactions [30], and we envisioned that this reaction could be used to prepare C7 substituted BN-phenanthrenes (Figure 1).

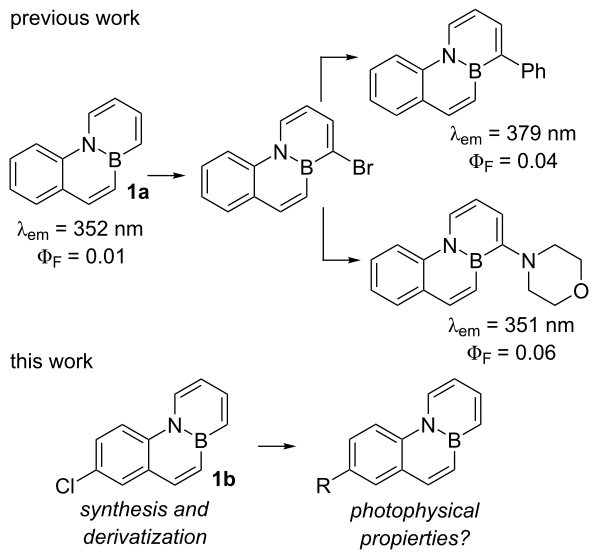

Figure 1: BN-phenanthrene **1a** and synthesis of substituted derivatives proposed in this work.

Herein we report the synthesis of chloro-substituted BN-phenanthrene **1b**, its derivatization via palladium-catalyzed cross-coupling reactions and the significant effect of the substituents on the fluorescence properties of the compounds prepared.

Results and Discussion

Our first aim was to synthesise the Cl-substituted BN-phenanthrene **1b** (Scheme 1), following a synthetic sequence analogous to that described previously by us for preparation of the parent BN-phenanthrene **1a** [23]. Thus, an initial Buchwald–Hartwig amination between 2-bromo-5-chlorostyrene and 3-butenylamine was the initial step. This coupling was performed at 70 °C, as a higher yield was obtained at this temperature (71% at 80 °C, 24 h vs 82% at 70 °C, 48 h). Substrate **2** was then cyclized with vinyl trifluoroborate. The optimal conditions to obtain **3** were found to be heating at 110 °C for 72 h. Lower temperatures and/or shorter times led to incomplete conversions in the borylative cyclization of **2**. Ring-closing metathesis of **3** proceeded efficiently in the presence of 10 mol % of the second-generation Grubbs catalyst to yield dihydro-BN-phenanthrene **4**, which was oxidized to **1b** under the conditions previously optimized for the synthesis of the parent BN-phenanthrene **1a** [23].

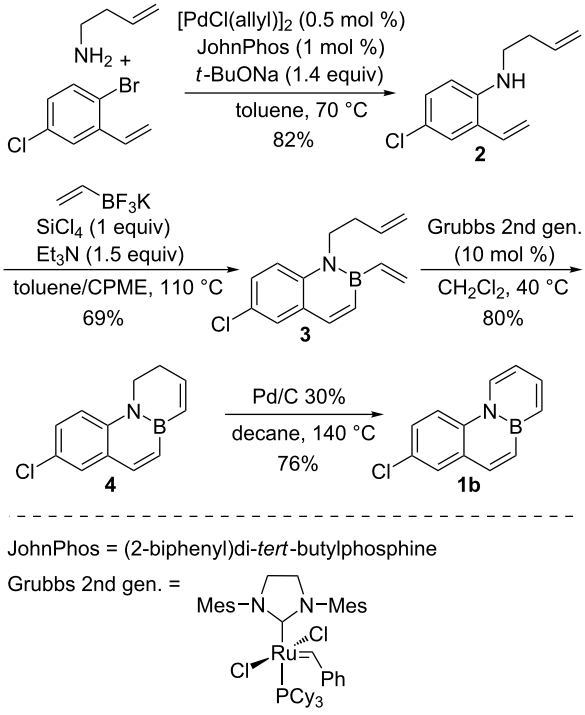

Scheme 1: Synthesis of Cl-substituted BN-phenanthrene **1b**.

Next, we explored the preparation of various substituted BN-phenanthrenes by means of palladium-catalyzed cross-coupling reactions of **1b**, under conditions optimized for a related BN-benzo[*c*]phenanthrene [30]. Gratifyingly, Suzuki coupling and Buchwald–Hartwig amination yielded the corresponding aryl- and amino-substituted BN-phenanthrenes **1c** and **1d** in good yields (Scheme 2).

Moreover, Sonogashira couplings efficiently proceed to provide alkynyl-substituted BN-phenanthrenes **1e** and **1f** in excellent yields (Scheme 3). These results confirm the value of palladium-catalyzed cross-coupling reactions of chloro-substituted BN-arenes as a useful tool for the preparation of derivatives functionalized with a range of substituents of a different nature.

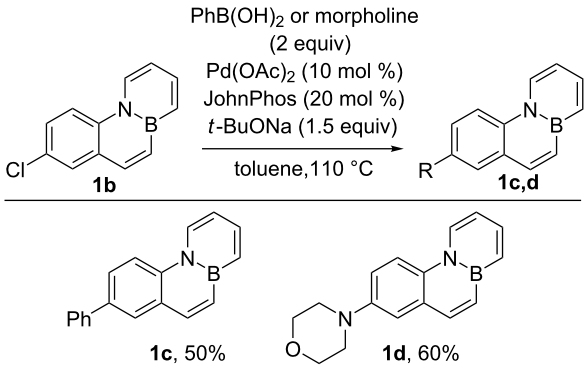

Scheme 2: Palladium-catalyzed cross-couplings of Cl-substituted BN-phenanthrene **1b**.

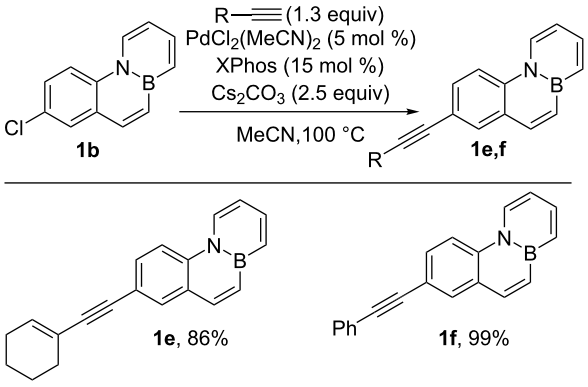

Scheme 3: Pd-catalyzed Sonogashira reactions of Cl-substituted BN-phenanthrene **1b**.

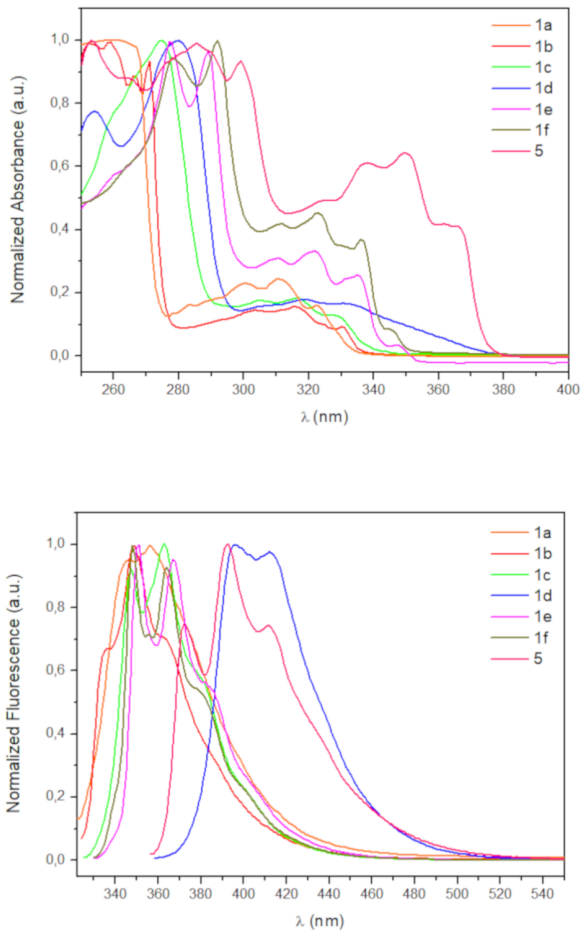

Figure 2: UV–vis absorption (top) and emission (bottom) spectra for BN-phenanthrenes **1** and **5** in cyclohexane (≈0.02 mM).

Once we had developed a useful method for the synthesis of the functionalized BN-phenanthrenes **1**, we focussed on our initial goal of evaluating the influence of different substituents on the photophysical properties thereof. The absorption and emission spectra of the parent BN-phenanthrene **1a** and the derivatives prepared in this work are shown in Figure 2. 1-(Phenylethynyl)-4a-aza-10a-boraphenanthrene (**5**), which was previously prepared in our group by bromination of **1a** and subsequent coupling [23], was also included in this comparative study. The absorption and emission data for these compounds are summarized in Table 1, and a picture of their solutions under UV irradiation are shown in Figure 3.

Table 1: UV–vis and fluorescence data for BN-phenanthrenes **1a–f** and **5**.[a]

Compound	ε ($M^{-1}cm^{-1}$)	$\lambda_{abs\ max}$ (nm)	λ_{em} (nm)	Φ_f[b]
1a	5488	310	356	0.01
1b	7715	316	349	0.03
1c	7482	316	363	0.17
1d	4331	319	395	0.19
1e	18283	322	351	0.44
1f	19392	323	348	0.65
5	15851	350	392	0.45

[a]All experiments were performed in cyclohexane solution (≈0.01–0.02 mM). The excitation wavelength match the absorption maxima for each compound. [b]Quantum yields reported relative to 9,10-diphenylanthracene (Φ_f = 0.93).

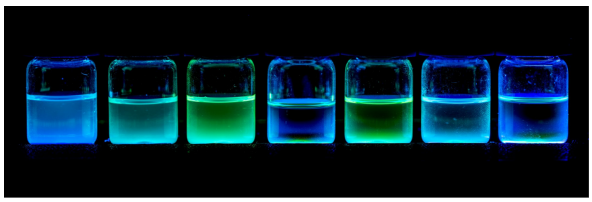

Figure 3: Solutions of **1a–f** and **5** (from left to right) under UV irradiation.

The emission maxima were not significantly affected by the presence of substituents, except for 7-amino substituted BN-phenanthrene **1d** and 1-alkynyl substituted BN-phenanthrene **5**, whose emission maxima are slightly red-shifted (395 and 392 nm vs 356 nm for unsubstituted **1a**). In contrast, 7-alkynyl-substituted BN-phenanthrenes **1e** and **1f** show emission maxima analogous to that of the parent BN-phenanthrene **1a**. With regard to the fluorescence quantum yield, phenyl and morpholine substituents at C7 (**1c** and **1d**) provide a significant increase when compared to the parent compound (0.17 and 0.19 vs 0.01). This enhancement is higher than that observed when these same substituents are located at C1 (see Figure 1) [23]. More interestingly, the presence of alkynyl substituents at C7 gives rise to a marked increase in the fluorescence quantum yield (0.44 and 0.65), particularly when the triple bond is bonded to a phenyl ring (**1f**). A similar increase ($\Phi_f = 0.45$) is observed when the alkynyl group is attached to C1 (**5**), thus indicating that the positive influence of the triple bond on the fluorescence quantum yield of BN-phenanthrene seems to be a general effect, irrespective of its position. It should be noted that the introduction of ethynyl groups into the all-carbon phenanthrene skeleton results in a slight increase in the fluorescence quantum yields compared to that of phenanthrene [27]. However, the effect observed here for BN-phenanthrenes is much more pronounced [31]. We have also evaluated the emission of **1f** in different solvents. The emission maxima are almost unaffected by the nature of the solvent [32], whereas the fluorescence quantum yield decreases in more polar solvents (0.29 in CH_2Cl_2, 0.19 in THF, 0.39 in 1,4-dioxane, 0.26 in MeCN)

Conclusion

We have successfully prepared a chloro-substituted BN-phenanthrene derivative that serves as a useful intermediate for the synthesis of a range of BN-phenanthrenes substituted with groups of diverse nature at C-7. This efficient post-functionalization methodology allows the influence of substituents on the photophysical properties of the BN-phenanthrene core to be studied. Substituted derivatives show an improved quantum yield with respect to the parent BN-phenanthrene, an effect that is particularly noteworthy for alkynyl substituents. A BN-phenanthrene bearing the triple bond at C-1 shows a similar increase in the quantum yield, thus suggesting that the influence of the alkynyl substituent is not limited to a particular position. We consider that this discovery may have important implications in the discovery of novel BN-arenes with improved properties. Further studies into the effect of alkynyl substituents on the fluorescence of BN-arenes are currently ongoing in our laboratories.

Supporting Information

Supporting Information File 1

Experimental details and NMR spectra for all new compounds.
[https://www.beilstein-journals.org/bjoc/content/supplementary/1860-5397-15-122-S1.pdf]

Acknowledgements

We are grateful to the Ministerio de Economía y Competitividad (MINECO), AEI and FEDER (project CTQ2017-85263-R, FPU predoctoral grant for A.A. and "Ramón y Cajal" contract for P.G.G.), Instituto de Salud Carlos III (FEDER funds, ISCIII RETIC REDINREN RD16/0009/0015), and University of Alcalá (project CCGP2017-EXP012) for financial support.

ORCID® iDs

David Sucunza - https://orcid.org/0000-0002-3307-4204
Patricia García-García - https://orcid.org/0000-0003-3671-5828
Juan J. Vaquero - https://orcid.org/0000-0002-3820-9673

References

1. Wang, X.-Y.; Wang, J.-Y.; Pei, J. *Chem. – Eur. J.* **2015,** *21,* 3528–3539. doi:10.1002/chem.201405627
2. Campbell, P. G.; Marwitz, A. J. V.; Liu, S.-Y. *Angew. Chem.* **2012,** *124,* 6178–6197. doi:10.1002/ange.201200063
   Campbell, P. G.; Marwitz, A. J. V.; Liu, S.-Y. *Angew. Chem., Int. Ed.* **2012,** 51, 6074–6092. doi:10.1002/anie.201200063
3. Bosdet, M. J. D.; Piers, W. E. *Can. J. Chem.* **2009,** *87,* 8–29. doi:10.1139/v08-110
4. Giustra, Z. X.; Liu, S.-Y. *J. Am. Chem. Soc.* **2018,** *140,* 1184–1194. doi:10.1021/jacs.7b09446
5. Bélanger-Chabot, G.; Braunschweig, H.; Roy, D. K. *Eur. J. Inorg. Chem.* **2017,** 4353–4368. doi:10.1002/ejic.201700562
6. Wang, J.-Y.; Pei, J. *Chin. Chem. Lett.* **2016,** *27,* 1139–1146. doi:10.1016/j.cclet.2016.06.014
7. Nakatsuka, S.; Yasuda, N.; Hatakeyama, T. *J. Am. Chem. Soc.* **2018,** *140,* 13562–13565. doi:10.1021/jacs.8b08197
8. Zhang, W.; Zhang, F.; Tang, R.; Fu, Y.; Wang, X.; Zhuang, X.; He, G.; Feng, X. *Org. Lett.* **2016,** *18,* 3618–3621. doi:10.1021/acs.orglett.6b01659
9. Li, G.; Zhao, Y.; Li, J.; Cao, J.; Zhu, J.; Sun, X. W.; Zhang, Q. *J. Org. Chem.* **2015,** *80,* 196–203. doi:10.1021/jo502296z

10. Hashimoto, S.; Ikuta, T.; Shiren, K.; Nakatsuka, S.; Ni, J.; Nakamura, M.; Hatakeyama, T. *Chem. Mater.* **2014,** *26,* 6265–6271. doi:10.1021/cm503102d
11. Wang, X.; Zhang, F.; Liu, J.; Tang, R.; Fu, Y.; Wu, D.; Xu, Q.; Zhuang, X.; He, G.; Feng, X. *Org. Lett.* **2013,** *15,* 5714–5717. doi:10.1021/ol402745r
12. Wang, X.-Y.; Zhuang, F.-D.; Wang, J.-Y.; Pei, J. *Chem. Commun.* **2015,** *51,* 17532–17535. doi:10.1039/c5cc06927k
13. Wang, X.-Y.; Zhuang, F.-D.; Wang, R.-B.; Wang, X.-C.; Cao, X.-Y.; Wang, J.-Y.; Pei, J. *J. Am. Chem. Soc.* **2014,** *136,* 3764–3767. doi:10.1021/ja500117z
14. Wang, X.-Y.; Zhuang, F.-D.; Zhou, X.; Yang, D.-C.; Wang, J.-Y.; Pei, J. *J. Mater. Chem. C* **2014,** *2,* 8152–8161. doi:10.1039/c4tc01369g
15. Wang, X.-Y.; Lin, H.-R.; Lei, T.; Yang, D.-C.; Zhuang, F.-D.; Wang, J.-Y.; Yuan, S.-C.; Pei, J. *Angew. Chem.* **2013,** *125,* 3199–3202. doi:10.1002/ange.201209706
Wang, X.-Y.; Lin, H.-R.; Lei, T.; Yang, D.-C.; Zhuang, F.-D.; Wang, J.-Y.; Yuan, S.-C.; Pei, J. *Angew. Chem., Int. Ed.* **2013,** 52*,* 3117–3120. doi:10.1002/anie.201209706
16. Zhang, W.; Fu, Y.; Qiang, P.; Hunger, J.; Bi, S.; Zhang, W.; Zhang, F. *Org. Biomol. Chem.* **2017,** *15,* 7106–7111. doi:10.1039/c7ob01679d
17. Huang, H.; Pan, Z.; Cui, C. *Chem. Commun.* **2016,** *52,* 4227–4230. doi:10.1039/c6cc00161k
18. Wang, X.-Y.; Yang, D.-C.; Zhuang, F.-D.; Liu, J.-J.; Wang, J.-Y.; Pei, J. *Chem. – Eur. J.* **2015,** *21,* 8867–8873. doi:10.1002/chem.201501161
19. Liu, X.; Wu, P.; Li, J.; Cui, C. *J. Org. Chem.* **2015,** *80,* 3737–3744. doi:10.1021/jo5029437
20. Sun, F.; Lv, L.; Huang, M.; Zhou, Z.; Fang, X. *Org. Lett.* **2014,** *16,* 5024–5027. doi:10.1021/ol502339h
21. Bosdet, M. J. D.; Piers, W. E.; Sorensen, T. S.; Parvez, M. *Angew. Chem.* **2007,** *119,* 5028–5031. doi:10.1002/ange.200700591
Bosdet, M. J. D.; Piers, W. E.; Sorensen, T. S.; Parvez, M. *Angew. Chem., Int. Ed.* **2007,** 46*,* 4940–4943. doi:10.1002/anie.200700591
22. Morgan, M. M.; Piers, W. E. *Dalton Trans.* **2016,** *45,* 5920–5924. doi:10.1039/c5dt03991f
23. Abengózar, A.; García-García, P.; Sucunza, D.; Frutos, L. M.; Castaño, O.; Sampedro, D.; Pérez-Redondo, A.; Vaquero, J. J. *Org. Lett.* **2017,** *19,* 3458–3461. doi:10.1021/acs.orglett.7b01435
24. Abengózar, A.; Fernández-González, M. A.; Sucunza, D.; Frutos, L. M.; Salgado, A.; García-García, P.; Vaquero, J. J. *Org. Lett.* **2018,** *20,* 4902–4906. doi:10.1021/acs.orglett.8b02040
25. Bosdet, M. J. D.; Jaska, C. A.; Piers, W. E.; Sorensen, T. S.; Parvez, M. *Org. Lett.* **2007,** *9,* 1395–1398. doi:10.1021/ol070328y
26. Lu, J.-S.; Ko, S.-B.; Walters, N. R.; Kang, Y.; Sauriol, F.; Wang, S. *Angew. Chem.* **2013,** *125,* 4642–4646. doi:10.1002/ange.201300873
Lu, J.-S.; Ko, S.-B.; Walters, N. R.; Kang, Y.; Sauriol, F.; Wang, S. *Angew. Chem., Int. Ed.* **2013,** 52*,* 4544–4548. doi:10.1002/anie.201300873
27. Hakoda, Y.; Aoyagi, M.; Irisawa, K.-i.; Kato, S.-i.; Nakamura, Y.; Yamaji, M. *Photochem. Photobiol. Sci.* **2016,** *15,* 1586–1593. doi:10.1039/c6pp00291a
28. Yamaji, M.; Maeda, H.; Nanai, Y.; Mizuno, K. *Chem. Phys. Lett.* **2012,** *536,* 72–76. doi:10.1016/j.cplett.2012.03.108
29. Maeda, H.; Maeda, T.; Mizuno, K.; Fujimoto, K.; Shimizu, H.; Inouye, M. *Chem. – Eur. J.* **2006,** *12,* 824–831. doi:10.1002/chem.200500638
30. Abengózar, A.; García-García, P.; Sucunza, D.; Pérez-Redondo, A.; Vaquero, J. J. *Chem. Commun.* **2018,** *54,* 2467–2470. doi:10.1039/c7cc09264d
31. Abengózar, A.; García-García, P.; Sucunza, D.; Sampedro, D.; Pérez-Redondo, A.; Vaquero, J. J. *Org. Lett.* **2019,** *21,* 2550–2554. doi:10.1021/acs.orglett.9b00448
32. See Supporting Information File 1 for details.

License and Terms

BEILSTEIN JOURNAL OF ORGANIC CHEMISTRY

Selenophene-containing heterotriacenes by a C–Se coupling/cyclization reaction

Pierre-Olivier Schwartz[1,2], Sebastian Förtsch[1,3], Astrid Vogt[1], Elena Mena-Osteritz[1] and Peter Bäuerle[*1]

Full Research Paper

Open Access

Address:
[1]Institute of Organic Chemistry II and Advanced Materials, University of Ulm, Albert-Einstein-Allee 11, 89081 Ulm, Germany, [2]Alsachim, 160 Rue Tobias Stimmer, 67400 Illkirch-Graffenstaden, France and [3]DuPont, August-Wolff-Straße 13, 29699 Bomlitz, Germany

Email:
Peter Bäuerle[*] - peter.baeuerle@uni-ulm.de

* Corresponding author

Keywords:
conducting polymer; C–S coupling; C–Se coupling; heteroacene; selenophene

Beilstein J. Org. Chem. **2019,** *15,* 1379–1393.
doi:10.3762/bjoc.15.138

Received: 21 March 2019
Accepted: 07 June 2019
Published: 24 June 2019

This article is part of the thematic issue "Dyes in modern organic chemistry".

Guest Editor: H. Ihmels

Abstract

A new novel family of tricyclic sulfur and/or selenium-containing heterotriacenes **2**–**4** with an increasing number of selenium (Se) atoms is presented. The heterotriacene derivatives were synthesized in multistep synthetic routes and the crucial cyclization steps to the stable and soluble fused systems were achieved by copper-catalyzed C–S and C–Se coupling/cyclization reactions. Structures and packing motifs in the solid state were elucidated by single crystal X-ray analysis and XRD powder measurements. Comparison of the optoelectronic properties provides interesting structure–property relationships and gives valuable insights into the role of heteroatoms within the series of the heterotriacenes. Electrooxidative polymerization led to the corresponding poly(heterotriacene)s **P2**–**P4**.

Introduction

In recent years, great interest has been devoted to the development of new π-conjugated polycyclic molecules, in particular to polycyclic aromatic hydrocarbons (PAH) such as acenes [1], phenacenes [2], or nanographenes [3]. Corresponding heteroacenes incorporating heteroatoms such as nitrogen or sulfur represent encouraging alternatives to PAHs providing manageable electronic properties and increased chemical stability [4,5]. In this respect, series of heteroacenes consisting of fused five-membered heterocycles such as thienoacenes [6,7] or *S*,*N*-heteroacenes [8] were investigated and successfully used as building blocks for high-performance organic electronic materials and devices [9-16]. Among the different heteroatoms that can be introduced into heteroacenes and in contrast to corresponding thiophene-based systems, selenium (Se) has only sparingly been used most probably because of the high price of selenophene itself, the limited number of commercially available derivatives, and the less explored chemistry. Nevertheless, the implementation of selenophenes as heteroanalogues of thio-

phene-based materials is highly attractive, because molecules containing selenophene fragments instead of thiophene showed promising optical and electrochemical properties [17-19] and improved charge transport characteristics [20]. With respect to fused selenoloacenes, only the shortest parent system consisting of two fused heterocycles, mixed thieno[3,2-*b*]selenophene [21,22] and selenolo[3,2-*b*]selenophene [23], were described and represent analogues to the well-known thieno[3,2-*b*]thiophene [24]. Three fused selenophenes only were implemented in larger heteroacenes and analyzed towards their optical properties [25] whereupon the unsubstituted parent system, diselenolo[3,2-*b*:2',3'-*d*]selenophene (DSS), is still unknown. Cheng et al. published a synthesis of various heterotriacenes including two selenophenes bridged with other elements such as silicon, germanium, nitrogen, and carbon [26]. Very recently, Wang et al. released selenophene-based heteroacenes via trimethylsilyl (TMS)-substituted selenolotriacenes, which served as intermediate building blocks [27].

In continuation of our work on heteroacenes, we now report synthesis and characterization of fused tricyclic selenium or selenophene-containing heteroacenes **2**–**4**, which represent the so far unknown unsubstituted parent systems of the selenolotriacenes synthesized by Wang et al. [27] and are analogues of the well-known dithieno[3,2-*b*:2',3'-*d*]thiophene (**1**, DTT) [24]. These triacenes **2**–**4** contain an increasing number of selenium atoms and for their synthesis not only selenophene was used as starting material, but also ring fusion to selenophene was achieved by Cu-catalyzed C–Se cross-coupling reaction [28]. The detailed geometric structure and the packing behaviour in the solid state of triacenes **2**–**4** have been elucidated by single crystal X-ray structure analysis and X-ray diffraction on powders. Furthermore, the systematically varied structures of triacenes **1**–**4** allow for investigation of the influence of the number and position of selenium atoms or selenophene rings on the physical and electronic properties in fused systems (Figure 1).

Results and Discussion

Syntheses. Several routes for the synthesis of dithienothiophene **1**, which is mostly built up by oxidative dehydrocoupling of 3,3'-dithienyl sulfide or ring-closure reactions of brominated thiophenes with ethyl mercaptoacetate, are described in literature [24]. For comparability to the selenophene-containing triacenes **2**–**4**, we reinvestigated the synthesis of DTT **1** by using a Cu-catalyzed C–S cross-coupling reaction with potassium sulfide (K_2S) as sulfur source [29]. The best results for this C–S ring-closure reaction were achieved by reacting 3,3'-diiodo-2,2'-bithiophene (**5**) [30] with the system K_2S and copper iodide (CuI) as catalyst in acetonitrile at 140 °C in a Schlenck tube to give DTT **1** in 66% yield. In the same way, trimethylsilyl (TMS)-protected diiodobithiophene **6** [31] gave 2,6-bis(trimethylsilyl)dithienothiophene **7** [32] in 73% yield, which was subsequently deprotected by tetrabutylammonium fluoride (TBAF) to form target DTT **1** in 91% yield (Scheme 1).

Triacene dithieno[3,2-*b*:2',3'-*d*]selenophene (DTS, **2**) was successfully prepared as well from diiodinated bithiophene **5** in 51% yield after purification in a C–Se cross-coupling/cyclization reaction with selenourea as selenium source, copper oxide nanoparticles as catalyst, and potassium hydroxide as base in DMSO (Scheme 1). This method has been previously used for the synthesis of symmetrical diaryl selenides from aryl halides [28]. Attempts to use the corresponding 3,3'-dibromo-2,2'-bithiophene as starting material for the synthesis of either DTS **2** with the same reagents as aforementioned or DTT **1** with thiourea or thioacetate in a Pd-catalyzed reaction [33] led in both cases to substantially lower yields.

For the synthesis of selenolotriacenes (DST) **3** and (DSS) **4** we followed the same strategies and applied the above described Cu-catalyzed C–S and C–Se cross-coupling/cyclization reactions, respectively. In both cases, the synthesis started from TMS-protected diiodinated 2,2'-biselenophene **11**, which was prepared from 2-iodo-5-(trimethylsilyl)selenophene (**10**) in 59% yield by lithiation with LDA, halogen-dance reaction [34], and subsequent oxidative dehydrocoupling with $ZnCl_2$ and $CuCl_2$. Selenophene precursor **10** itself was readily obtained in 68% yield from selenophene (**9**) in a one-pot procedure by successive lithiation with *n*-BuLi and quenching with trimethylsilyl chloride and iodine, respectively. We reacted biselenophene **11** with K_2S as sulfur source and catalytic amounts of CuI in acetonitrile at 140 °C (vide supra) to afford TMS-protected DST **12** in 97% yield, which was subsequently deprotected with TBAF to parent DST **3** in 91% yield after purification. The trimethylsilyl-substituted precursor **12** was recently synthesized

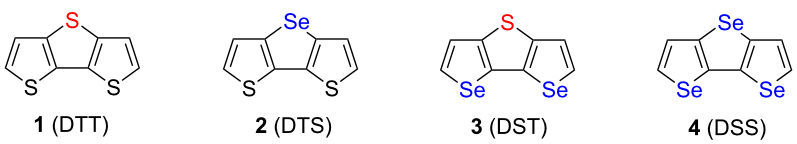

Figure 1: Heterotriacenes DTT **1**, DTS **2**, DST **3**, and DSS **4** with varying number of selenium atoms and fused selenophene rings.

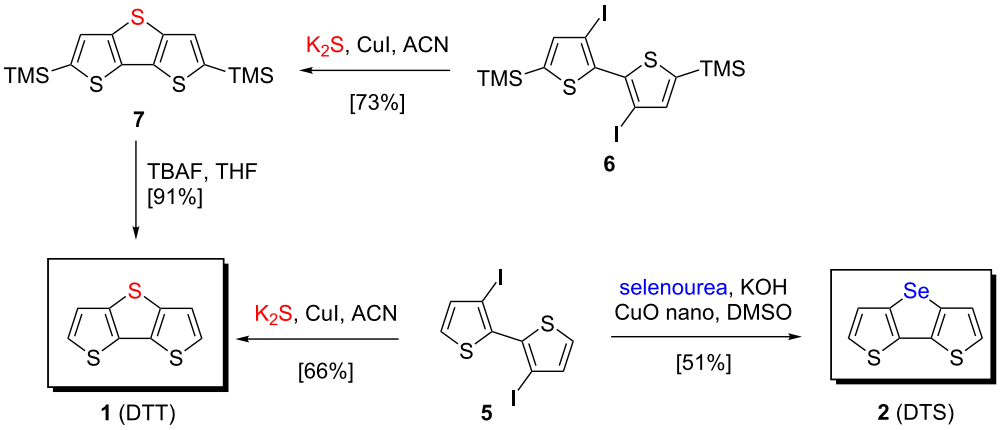

Scheme 1: Synthesis of heterotriacenes DTT **1** and DTS **2** via copper-catalyzed cross-coupling reactions.

by Wang et al. from the corresponding dibromobiselenophene and benzene sulfonyl sulfide as sulfur source (50% yield) [27].

In parallel, TMS-protected iodinated biselenophene **11** was subjected to selenourea, copper oxide nanoparticles, and potassium hydroxide in DMSO to isolate diselenolo[3,2-*b*:2',3'-*d*]selenophene (DSS, **4**) in 48% yield after purification (Scheme 2). Other selenation reagents such as selenium powder or disodium selenide were tested as well, but were not successful in order to giving increased yields of DSS **4**. In all reactions and optimization attempts, the TMS-groups were relatively quickly cleaved off from starting material **11** and dehalogenation was in parallel observed as competitive reaction pathway. Thus, mostly diiodobiselenophene **13** and 2,2'-biselenophene were isolated as main products. Independent reaction of deprotected diiodobiselenophene **13**, which was alongside prepared from TMS-biselenophene **11** by deprotection with TBAF in 66% yield, with selenourea and copper oxide nanoparticles surprisingly did not lead to any targeted DSS **4** in the attempted C–Se cross-coupling reaction.

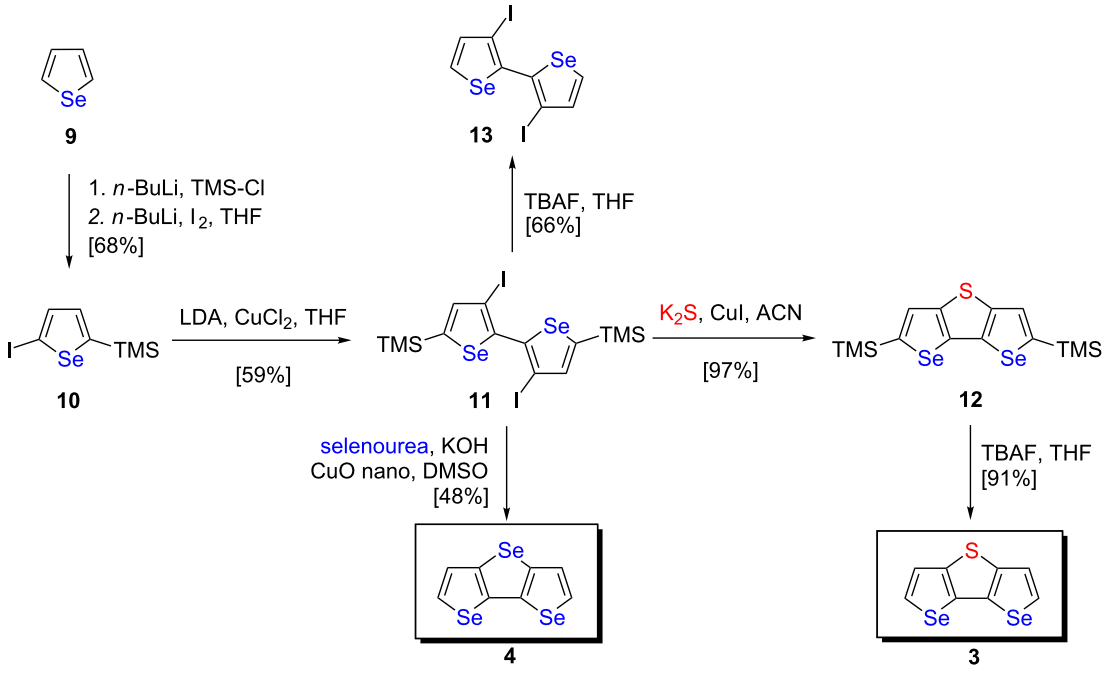

Scheme 2: Synthesis of selenolotriacenes DST **3** and DSS **4**.

The structures of the prepared novel selenolotriacenes **2**–**4** and known DTT **1** were characterized by means of NMR spectroscopy (Supporting Information File 1, Figures S1–S4), high-resolution mass spectrometry, and elemental analysis. In the ^{1}H NMR spectra, the influence of the selenium atoms in triacenes DST **3** and DSS **4** results in substantial deshielding of the protons compared to bithiophene-based derivates **1** and **2**, which is in accordance with data for selenophene compared to thiophene [35].

Single crystal X-ray structure analysis

Single crystals of heterotriacenes DTS **2**, DST **3**, and DSS **4** suitable for X-ray structure analysis were obtained and details of the refinements are summarized in Tables S1-S3 (Supporting Information File 1). X-ray structure analysis of DTT **1** was already published by Brédas et al. [36,37]. Single crystals of DTS **2** and DSS **4** as very thin crystalline needles were obtainned by careful sublimation. Both heterotriacenes crystallized in the monoclinic space group $P2_1/c$ with 18 molecules in the unit cell (DTS **2**: a = 5.978(3), b = 29.005(11), c = 21.173(8) Å; α = 90°, β = 91.903(19)°, γ = 90°, V = 3669(3) Å^3; DSS **4**: a = 6.108(3), b = 29.049(17), c = 21.949(11) Å; α = 90°, β = 91.815 (12)°, γ = 90°, V = 3892(3) Å^3). The molecules in both crystals evidenced some rotational disorder. Single crystals of heterotriacene DST **3** were obtained by diffusion of *n*-hexane into a solution of DST **3** in dichloromethane. Triacene DST **3** crystallized in the monoclinic space group $P2_1/n$ with four equivalent molecules in the unit cell (a = 6.02748(19), b = 10.6662(3), c = 12.9279(4) Å; α = 90°, β = 96.747(3)°, γ = 90°) resulting in a unit cell volume of 825.38(4) Å^3. The geometry of heterotriacene DST **3** is shown in the top and side view in Figure 2a and 2b, and for comparison purposes, bond lengths and angles from all four X-ray structure analyses of heterotriacenes **1**–**4** are summarized in Table 1.

The molecular volume in the crystals continuously increased from DTT **1** to DSS **4** (190.8 Å^3, 203.8 Å^3, 206.3 Å^3, and 216.2 Å^3) mostly due to the larger van der Waals radii of the selenium versus sulfur atoms (190 vs 180 pm) [38]. Bond distances and angles showed the expected differences between selenophene and thiophene rings: C–Se bonds are elongated by 0.16 to 0.17 Å compared to the C–S bonds and consequently the

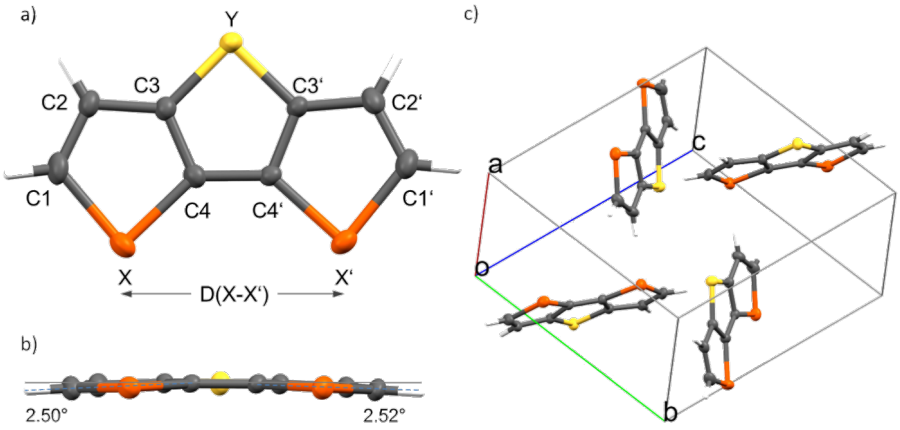

Figure 2: Single crystal X-ray structure analysis of selenolotriacene DST **3**, (a) individual molecule and atom numbering (top view); (b) side view. (c) Herringbone-type packing structure of the four molecules in the unit.

Table 1: Bond distances, bond angles, and distances D of the outer heteroatoms obtained from the single crystal X-ray structure analysis of heterotriacenes **1** to **4**.

Hetero-triacene	Bond distance (Å) C_1–C_2/C_2–C_3/C_3–C_4/C_4–$C_{4'}$	Bond distance (Å) C_1–X/X–C4/C_3–Y	Angles (°) C_1XC_4/$C_3YC_{3'}$/$XC_4C_{4'}$	D(X–X') (Å)	Angle (°) $C_1YC_{1'}$
DTT **1**[a]	1.36/1.42/1.38–9/1.42	1.73/1.72/1.74	91/90/137	3.94	105
DTS **2**	1.35–6/1.41/1.37–8/1.44	1.73/1.72–3/1.88–9	91/86/135	3.87	100
DST **3**	1.35/1.42–3/1.38/1.42	1.87–8/1.87/1.74	86.5/91.5/137	4.145	109
DSS **4**	1.34–5/1.41–2/1.36–8/1.43	1.88/1.88/1.89–91	86/87/134	4.08	104

[a]Data taken from reference [36,37].

C–Se–C bond angles in selenophene rings are compressed to 86–87° compared to the C–S–C bond angle in the thiophene rings (90–91.5°) [39]. The C–Y "bridging" bonds always appeared elongated when compared to corresponding C–X bond distances. Remarkably, the distances between the external heteroatoms D(X–X') are reduced by 0.07 Å in heteroacenes **2** and **4** containing Se atoms at the bridge position (Y) compared to **1** and **3**, while the inner bond distance (C_4–$C_{4'}$) barely change (0.01(2) Å). Although the molecular geometry of the heterotriacenes should be expected planar, a slight curvature of the π-system was found for DST **3**, whose α-carbon atoms are bent relative to the central thiophene plane by about 2.5 degrees (Figure 2b). This effect might be due to strong intermolecular π–π interactions in pairs of molecules (Figure 2b), because a completely flat geometry of the isolated molecule DST **3** (in the gas phase) was obtained from theoretical calculations (vide infra).

Molecules of DST **3** order in a typical herringbone fashion, where the terminal hydrogen atoms form hydrogen bond-like C–H heteroatom interactions (2.819 Å with S and 3.028 Å with Se) in a face-to-edge orientation (Figure 3c, Table S4a in Supporting Information File 1) [40]. We found as well several non-bonding S–Se contacts (3.644 Å) with four neighboring molecules in all crystallographic axes, which are slightly shorter than the sum of the van der Waals radii (3.70 Å), implying a 3-dimensional electronic coupling between the molecules of DST **3** in the crystal (Figure 3c, Table S2 in Supporting Information File 1). A similar situation has also been observed for DTS **2** (Figure S5, Table S1, and Table S5 in Supporting Information File 1) and DSS **4** (Figure S8, Table S3, and Table S6 in Supporting Information File 1).

In the case of DTT **1** only three non-bonding contacts between sulfur atoms in the b-axis direction were found which imply a 1-dimensional intermolecular electronic coupling in the molecular columns separated from each other by distances of 3.57 Å [36,37]. On the contrary, a much higher number of non-bonding contacts per molecule in all three space directions were identified for DTS **2** (10 contacts), DST **3** (8 contacts), and DSS **4** (14 contacts), respectively. Furthermore, in heterotriacenes **2**, **3**, and **4** we identified partial overlap of stacked and offset molecules leading to π–π interactions with distances as close as 3.42 Å for DST **3** (Figure 3a and b), 3.24 to 3.49 Å for DTS **2** (Figure S6a–c in Supporting Information File 1), and 3.28 to 3.58 Å for DSS **4** (Figure S8a–c in Supporting Information File 1). Interestingly, the symmetry of the formed dimers showed some differences: in DTT **1** the molecules overlap in a parallel orientation whereas in DST **3** an antiparallel orientation of the molecules in the dimer was found. The degree of overlap was determined to 73% and 64% for DTT **1** and DST **3**, respectively. Less degree of overlap (43–53% and 45–52%) and a mixture of both, parallel and antiparallel stacked dimers, were found in the X-ray structure analysis of heterotriacenes **2** (Figure S6b,c) and **4** (Figure S8b and S8c in Supporting Information File 1), respectively.

XRD powder measurements

For completion, we performed XRD measurements on microcrystalline powders of all derivatives (Supporting Information File 1, Figure S9). At first glance, the stronger intensity of the signals for DTT **1** and DST **3** clearly evidences a higher crystallinity compared to triacenes DTS **2** and DSS **4**. XRD plots of heterotriacenes **1** to **3** obtained from the corresponding single crystal structure analysis were compared to the X-ray powder

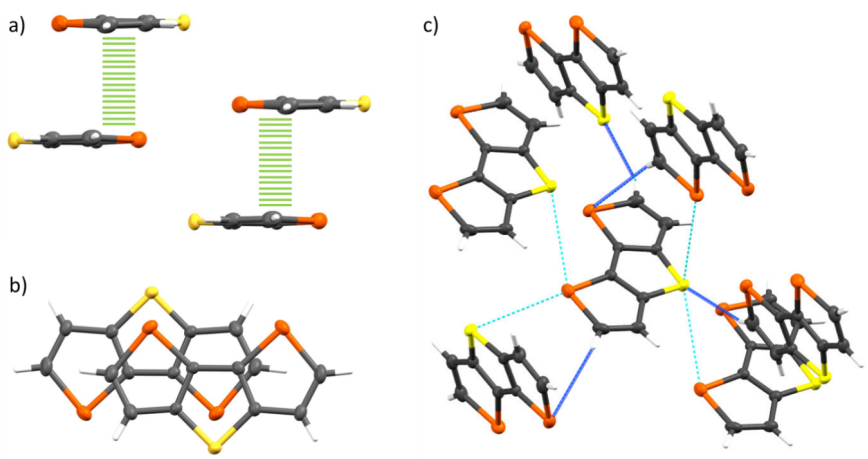

Figure 3: Single crystal X-ray structure analysis of selenolotriacene DST **3**: (a) partial overlap of stacked and displaced molecules leading to π–π interactions with distances down to 3.42 Å (side view); (b) and top view (64% molecular overlap). (c) Intermolecular interactions between heteroatoms and hydrogen-heteroatoms (labelled cyan and blue, respectively).

diffraction spectra (Figures S10, S11 and S12, in Supporting Information File 1). Whereas no correlation of the main peaks was found for DTT **1**, DTS **2** showed a better relationship between the powder and single crystal derived powder spectra. A very good correlation with almost no systematic error in peak positions can be clearly identified in the case of heterotriacene DST **3** (Figure S12, Supporting Information File 1) indicating a similar dominating crystalline phase in the microcrystalline powder and in the single crystal. Relevant signals at expected strong π–π intermolecular distances of 3.5–3.3 Å (2Θ = 25–26°), at offset π–π intermolecular distances of 4.1 Å (2Θ = 21.5°), and at herringbone intermolecular interaction distances of 8.2 Å (2Θ = 10.8°) were found and correlated with the Miller indices obtained in the X-ray single crystal structure analysis. XRD plots of DST **2** and DSS **4** showed strong diffusion scattering vs signal intensity which we assign to a high degree of amorphous phases. The crystallite sizes determined were quite similar for **1**, **2**, and **3** (66 nm, 76 nm, and 72 nm), respectively, except for DSS **4** which were smaller with 52 nm. The lack of correlation between the spectra for DTT **1** (Figure S10 in Supporting Information File 1) accounts for a completely different crystalline phase in the XRD vs the multicrystalline powder spectrum. Nevertheless, the high crystallinity observed in XRD measurements of heterotriacenes **1** and **3** rationalize their unexpected higher melting point compared to **2** and **4**.

Quantum chemical calculations

Quantum chemical DFT and TDDFT calculations (CAMB3LYP and B3LYP with the functional 6-31G^{++} (d,p)) were performed for the ground and excited state of heterotriacenes **1**–**4** in order to investigate their geometry and electronic properties. The optimized geometry of DTT **1** is shown in Figure 4, and most relevant corresponding bond distances and angles for all derivatives are summarized in Table 2. The comparative analysis of the alternating double-single bonds in the π-system of the heterotriacenes **1**–**4** evidenced only a slight increase of the interring bond (C_4–$C_{4'}$) for DTS **2** (1.43 Å) and consequently a smallest bite angle ($C_1YC_{1'}$ = 100°) despite the longest C–Se bond in the series (1.88 Å). The C-heteroatom distances vary for S (1.73–1.75 Å) to Se (1.85–1.88 Å) with the peculiarity that the longer distances in both cases correspond to the C_3–Y bond. This was already observed in the X-ray structure analysis. The distances between the external heteroatoms D (X–X') are reduced by introducing the bigger Se atom in the bridge position (Y) and in all cases are shorter than the ones obtained from the crystal structure analysis.

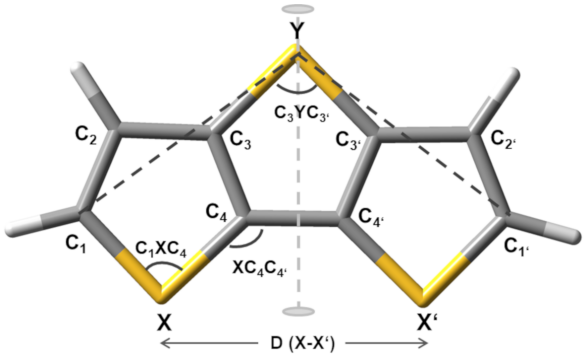

Figure 4: DFT quantum chemical calculated geometry of DTT **1** and general atom labelling for all heterotriacenes **1**–**4** discussed.

The analysis of the theoretical calculations gave also insight into the electronic properties of the heterotriacene series. The energies of the calculated frontier orbitals and electronic transitions are summarized in Table 3. In this respect, the energy of the HOMO slightly destabilizes from DTT **1** to DSS **4** in accordance to the decreasing aromatic character of the selenophene-based derivatives. A strong influence of the selenium atoms on the HOMO-1 and the LUMO can be observed (Figure 5, left and Table 3): the heavier selenium atoms gradually stabilize the LUMO and strongly destabilize HOMO-1. The calculated energy gap decreases from thiophene-based DTT **1** to selenium-containing derivative DSS **4** in accordance with the trend found for the experimentally determined optical energy gaps (vide supra).

TDDFT calculations on heteroacenes **1**–**4** revealed the coexistence of two electronic transitions in a very narrow range of the spectrum: HOMO → LUMO transition, S_1, whose transition dipole is oriented along the long-axis of the molecule and a

Table 2: DFT quantum chemical calculations on the geometry of heterotriacenes **1**–**4**.

Heterotriacene	Bond distance (Å) C_1–C_2/C_2–C_3/C_3–C_4/C_4–$C_{4'}$	Bond distance (Å) C_1–X/X–C_4/C_3–Y	Angles (°) C_1XC_4/$C_3YC_{3'}$/$XC_4C_{4'}$	(Å) D(X–X')	Angle (°) $C_1YC_{1'}$
DTT **1**	1.36/1.42/1.38/1.42	1.74/1.73/1.75	91/90/135	3.88	104
DTS **2**	1.36/1.42/1.38/1.43	1.74/1.73/1.88	91/87/134	3.84	100
DST **3**	1.36/1.43/1.38/1.42	1.88/1.85/1.75	87/90/136	4.10	108
DSS **4**	1.36/1.43/1.38/1.42	1.87/1.85/1.88	87/87/134	4.00	104

Table 3: DFT and TDDFT quantum chemical calculations on heterotriacenes **1–4**.

Hetero-triacene	HOMO-1 [eV]	HOMO [eV]	LUMO [eV]	S_1 [nm/eV] (f)	S_2 [nm/eV] (f)	E_g [eV]
DTT **1**	−7.59	−7.23	−0.19	274/4.52 (0.38)	254/4.87 (0.17)	7.04
DTS **2**	−7.42	−7.22	−0.24	278/4.45 (0.34)	265/4.69 (0.17)	6.98
DST **3**	−7.39	−7.21	−0.30	283/4.39 (0.34)	268/4.63 (0.18)	6.91
DSS **4**	−7.26	−7.20	−0.36	288/4.31 (0.31)	278/4.46 (0.19)	6.84

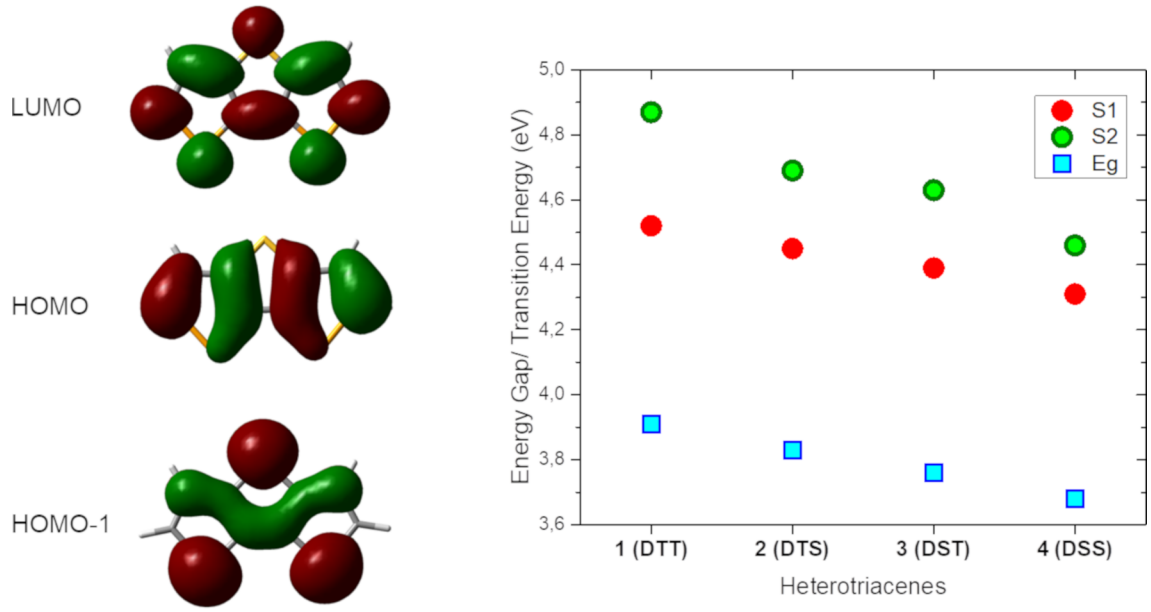

Figure 5: Representative electron density of frontier orbitals LUMO, HOMO, and HOMO-1 for heterotriacene DSS **4** (left). Energy of the first S_1 (red dot) and second S_2 (green dot) electronic transition calculated with TD-DFT and experimental energy gap (blue squares) of heterotriacenes **1** to **4** (right).

HOMO-1 → LUMO transition, S_2, whose transition dipole orients perpendicular to the long axis of the molecule (Table 3). In Figure 5 (right), the transition energies of S_1 and S_2 as well as the experimentally determined energy gaps are depicted for the heterotriacenes under investigation. The dependence of both transitions energies on the heteroatom character of the triacenes is shown. Both transitions gradually bathochromically shift from DTT **1** to DSS **4**, with stronger stabilization of the S_2 transition which is coherent with the large atomic contribution from the heteroatoms to the involved molecular orbitals HOMO-1 and LUMO (vide supra). We can conclude that the theoretically calculated transitions S_1 and S_2 are reflected in the experimentally obtained absorption spectra (Figure 6) being responsible for the slightly different shape of their fine structure. The latter has been analyzed through Gaussian deconvolution of the absorption spectra and the two expected transitions for heterotriacene DTT **1** are shown (Figure 6, right).

Optical properties

The optical properties of the four heterotriacenes were investigated by UV–vis and fluorescence spectroscopy in dichloromethane solution (Figure 6, left and Table 4). The absorption spectra in the series of DTT **1** to DSS **4** showed one main absorption band exhibiting vibronic fine structure according to the planar π-conjugated system. Gaussian deconvolution of the experimental spectra exemplarily shown for DDT **1** (Figure 6, right) evidenced the coexistence of two electronic transitions under the absorption curve in correlation with the theoretical calculations (vide infra). The absorption maxima are continuously red-shifted from DTT **1** to DSS **4** the more selenium atoms are present in the heteroacene (292–312 nm). This finding can be explained by the slightly lower aromaticity of the selenophene rings compared to thiophenes as a result from the slightly lower electronegativity (EN 2.55 vs 2.58) and significantly greater polarizability of selenium compared to sulfur

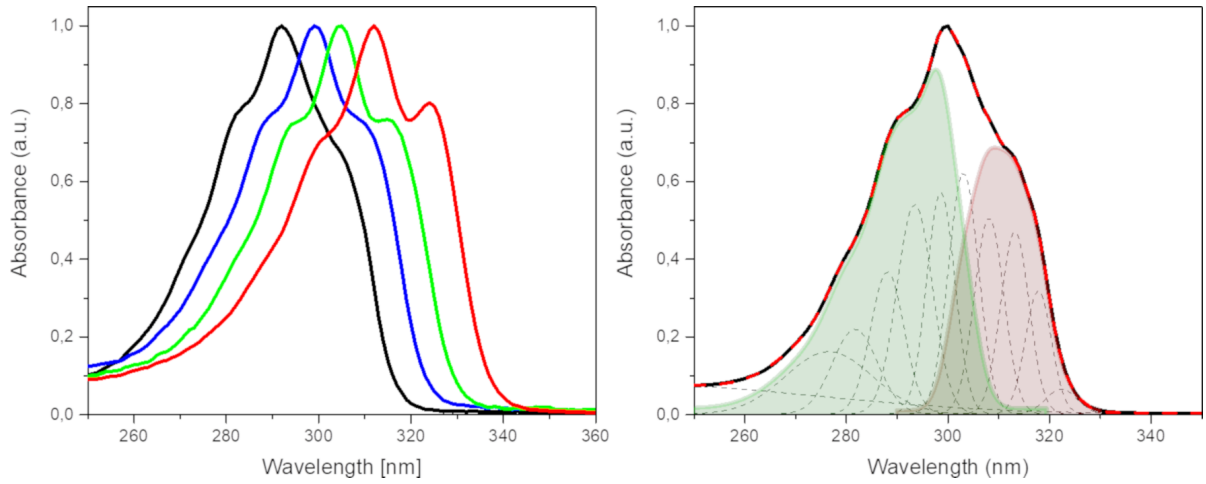

Figure 6: Normalized absorption spectra of heteroacenes DTT **1** (black line), DTS **2** (blue line), DST **3** (green line), and DSS **4** (red line) in dichloromethane (left). Gaussian deconvolution analysis of the absorption spectrum of DTT **1** (right): Gaussian deconvolution peaks (doted black lines), S_1 transition (light red curve, balanced sum of the first 5 Gaussians), S_2 transition (light green curve, balanced sum of Gaussians 6 to 10), and complete cumulative peak-fit (doted red line).

Table 4: Thermal, optical, and electrochemical properties of heterotriacenes **1**–**4**.

Heterotriacene	Mp [°C]	λ_{abs} [nm][a]	ε [L mol^{-1} cm^{-1}]	E_g^{opt} [eV][b]	E_p^{ox} [V]	HOMO [eV][c]	LUMO [eV][d]
DTT **1**	69.8	292	26800	3.91	0.94	−5.92	−2.01
DTS **2**	62.1	299	22100	3.83	0.84	−5.87	−2.04
DST **3**	120.6	305, 315	28400	3.76	0.82	−5.82	−2.06
DSS **4**	90.1	312, 324	20830	3.67	0.80	−5.80	−2.13

[a]Measured in dichloromethane solution (10^{-4} M). [b]Estimated using the onset of the UV–vis spectrum in solution by $E_g^{opt} = 1240/\lambda_{onset}$. [c]Estimated from the onset of the respective oxidation waves, Fc/Fc^+ value set to −5.1 eV vs vacuum [45]. [d]Determined from the optical band gap and HOMO.

atoms (P 3.77 Å^3 vs 2.9 Å^3) [41-43]. This effect is also obvious in a red-shift of the absorption maximum from 2,2'-bithiophene **5** (304 nm) to 2,2'-biselenophene **6** (328 nm) [44] as non-bridged counterparts of DTT **1**/DST **3** and DTS **2**/DSS **4**, respectively, which is explained in theoretical studies by a higher quinoidal character of the oligoselenophenes and a higher twisting barrier of the interring C–C bonds compared to oligothiophenes. The optical energy gaps, E_g, are in accordance with the observed trend and decrease from 3.91 eV for DTT **1** to 3.67 eV for DSS **4** due to a stabilization of the HOMO energy level with increasing number of selenium atoms in the heteroacene (vide infra). The extinction coefficients are as well sensitive to the heteroatom in the bridge for pair DTT **1**/DTS **2** (26,800 to 22,100 L mol^{-1} cm^{-1}) and DST **3**/DSS **4** (28,400 to 20,830 L mol^{-1} cm^{-1}). No fluorescence was observed for each of the four heteroacenes DTT **1** to DSS **4** neither in DCM nor in THF.

Electrochemical properties and electropolymerization

The redox properties of the heterotriacenes **1**–**4** were investigated by means of cyclic voltammetry in the electrolyte tetrabutylammonium hexafluorophosphate ($TBAPF_6$)/acetonitrile (Table 4, Figure S13 in Supporting Information File 1). The voltammogram of DDT **1** revealed one irreversible oxidation signal at 0.94 V (vs Fc^+/Fc), which is in accordance to literature values [46]. Because selenophenes are slightly less aromatic than thiophenes with increasing number of selenium atoms a continuous decrease of the anodic peak potential was observed going from **2** (0.84 V) over **3** (0.82 V) to **4** (0.80 V). In comparison, dithienopyrrole (DTP), a corresponding nitrogen-bridged 2,2'-bithiophene, with a peak potential of 0.49 V, is much easier to oxidize due to the electron-rich character of the pyrrole ring [47]. The HOMO energy levels were determined from the onset of the oxidation wave and accordingly gradually de-

creased from **1** to **4** (−5.92 eV to −5.80 eV) (Table 4, Figure 7). Due to the absence of reduction waves in the cyclic voltammograms, the LUMO energy levels were calculated from E_g^{opt} and the HOMO energy and decrease with increasing amount of selenium atoms in the heterotriacenes.

Because of the structural similarity of heterotriacenes **1**–**4** to 2,2'-bithiophene and 2,2'-biselenophene, which can be oxidatively polymerized to polythiophenes [48-50] or polyselenophenes [51], respectively, we were interested in the electropolymerization of heterotriacenes **1**–**4** to the corresponding conjugated polymers **P1**–**P4**. Hence, monomers **1**–**4** were subjected to potentiodynamic polymerization in dichloromethane/$TBAPF_6$ as electrolyte and the redox and optical properties of the obtained films were determined. Electropolymer P(DTT) **P1** has already been reported in literature and the findings agree well with our results [46,51]. In Figure 8, exemplarily the electropolymerization of heterotriacene DST **2** (left) and subsequent electrochemical characterization of polymer P(DTS) **P2** at various scan rates in a monomer-free electrolyte is shown

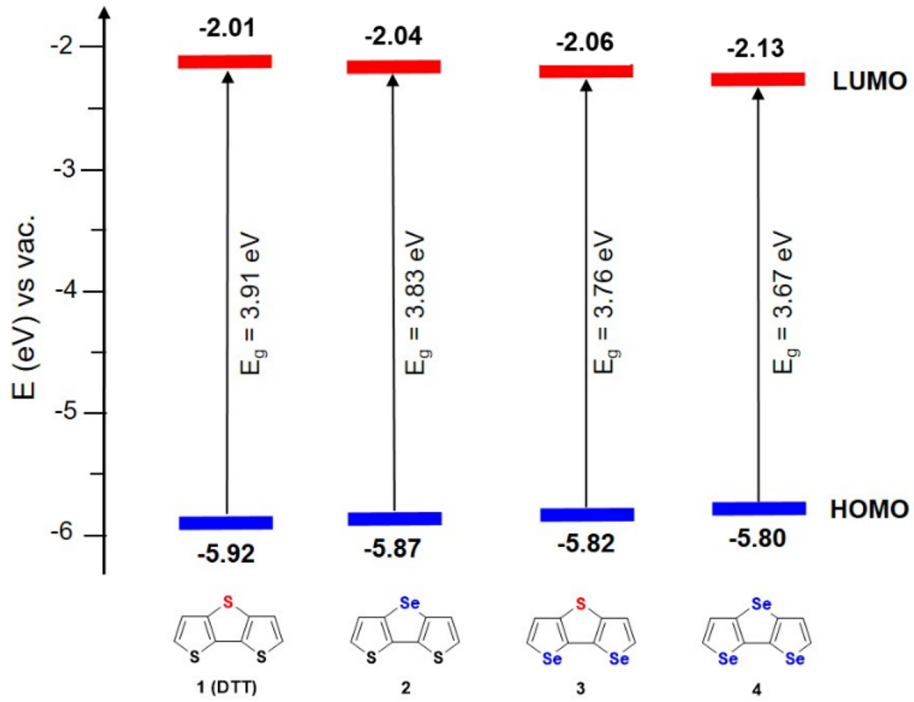

Figure 7: Energy diagram of the frontier molecular orbitals of heterotriacenes **1**–**4**.

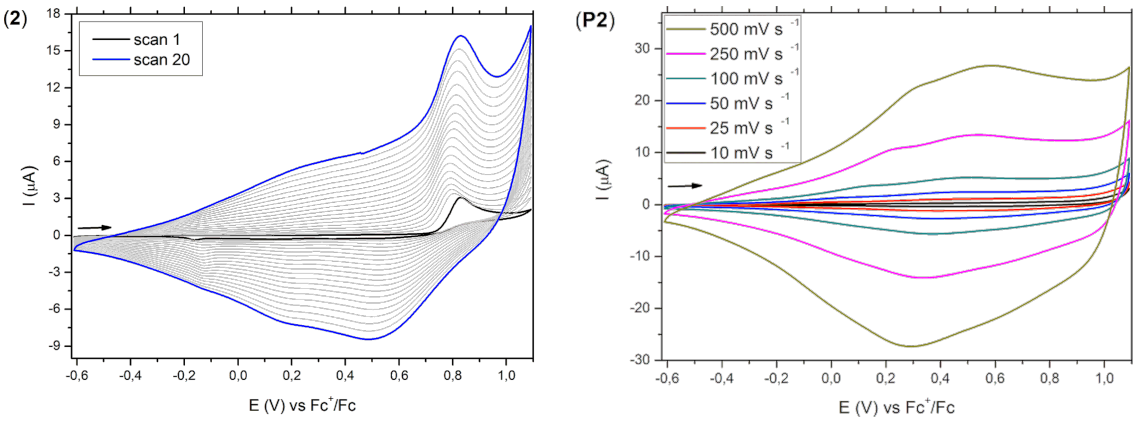

Figure 8: Multisweep voltammograms for the electrochemical polymerization of monomeric heterotriacene DST **2** in CH_2Cl_2/$TBAPF_6$ (0.1 M) at a scan rate of 100 mV s^{-1} (left) and electrochemical characterization of the corresponding polymer P(DTS) **P2** in CH_2Cl_2/$TBAPF_6$ (0.1 M) using different scan rates (right).

(right). The other examples for **P1**, **P3**, and **P4** are shown in Supporting Information File 1, Figure S14. After the oxidation of the monomer in the first scan, polymerization starts by coupling of the emerging radical cations via the more reactive α-positions forming a film on the surface of the working electrode (Scheme 3). Calculations on radical cations of heterotriacenes **1–4** clearly showed that spin density is by far highest at the α- and low at the β-positions. Therefore, we assume that coupling and polymerization of the radical cations occurs via the α-positions leading to mostly linear conjugated systems without branching. In subsequent scans, broad cathodic and anodic signals emerged and with increasing number of cycles the respective currents continuously increased indicating the steady growth of polymer film. After 20 sweeps, homogeneous films of polymers **P1–P4** were obtained (observed by optical microscopy) which were then electrochemically and spectroelectrochemically characterized (Table 5 and Table S7 in Supporting Information File 1).

Cyclic voltammograms of polymers **P1–P4** in a monomer-free electrolyte showed broad and unstructured redox waves typical for conducting polymers reflecting the inhomogeneity of the material containing various electrophoric moieties due to variations in the (conjugated) chain length and conformational issues [52]. As well the relatively large shifts of the peak potentials with increasing scan rate, which are due to reduced diffusion of counter ions through the film, hinder the exact determination of redox potentials and trends among the derivatives of the series. Nevertheless, onset potentials, which reflect the starting transition between semiconducting and conducting state of the polymer, are indicative and for all four polymers **P1–P4** are located in the same range at −0.12 V to −0.18 V and vary only little. Therefore, the effect of the selenium atoms, which we saw for the oxidation of the corresponding monomers **1–4**, i.e., a lowering of the oxidation potential with increasing number of selenium atoms (vide supra), seems to be blurred for the polymers. Published data for P(DTT) **P1** is very similar showing an onset potential of −0.12 V vs Fc/Fc^+ (calculated from 0.37 V vs Ag/AgCl) [46,52]. The redox characteristic of **P1–P4** is slightly more negative compared to the non-bridged counterparts, namely poly(bithiophene) [48-50] and poly(biselenophene) [51] (both show E_{onset} at ca. −0.0 V vs Fc/Fc^+) indicating that the chalcogenide bridges do not much influence the electrochemical properties of the corresponding conjugated polymers. The related poly(dithienopyrrole) P(DTP) in contrast is more electron-rich and much easier to oxidize (E_{onset} = −0.54 V vs Fc/Fc^+) [47]. Additionally, we evaluated the electrochemical stability of polymers **P1**–**P4.** After performing 30 sweeps, about 18–19% of the electroactivity was degraded for the bithiophene-based poly(heterotriacenes) P(DTT) **P1** and P(DTS) **P2** and only 3–8% for the biselenophene-based counterparts P(DST) **P3** and P(DSS) **P4** which is similar to P(DTP) [47] (Figure S15 in Supporting Information File 1).

The optical properties of polyheterotriacenes **P1**–**P4** were determined via spectroelectrochemistry using a previously described setup with a platinum working electrode and UV–vis–NIR spectra were recorded in reflectance mode [53]. At the beginning of the measurements a potential of −500 mV (vs Ag/AgCl) was applied in order to obtain the neutral polymer films with-

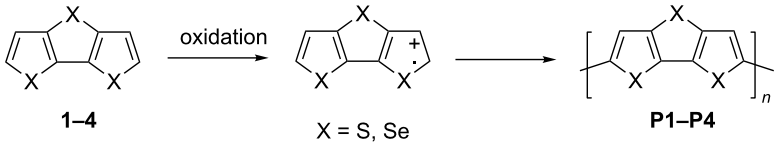

Scheme 3: Oxidative polymerization of heterotriacenes **1**–**4** to corresponding conjugated polymers **P1–P4**.

Table 5: Electrochemical properties of poly(heterotriacenes) **P1**–**P4** and film loss after conducting 30 scans in a monomer-free electrolyte solution.

Poly(heterotriacene)	E_{pa}[a] [V]	E_{pc}[b] [V]	E_{onset} [V]	HOMO [eV]	Film loss [%][c]
P(DTT) **P1**	0.45	0.39	−0.18	−4.92	18
P(DTS) **P2**	0.51	0.37	−0.15	−4.95	19
P(DST) **P3**	[d]	0.33	−0.17	−4.93	8
P(DSS) **P4**	[d]	0.27	−0.12	−4.98	3
P(DTP) [33]	0.18	0.19	−0.54	−4.56	6

Potentials are referenced vs Fc^+/Fc. [a]E_{pa}: anodic peak potential (scan rate 100 mV/s). [b]E_{pc}: cathodic peak potential (scan rate 100 mV/s). [c]Determined as the difference of exchanged charges during the oxidation in scan 2 and scan 30, respectively. [d]Could not be determined.

out any oxidized parts. Then, the potentials were gradually increased until the oxidized polymers were obtained in their polaronic/bipolaronic states. In the neutral state, the most intense and broad bands of the π–π* transition showed absorption maxima in the range of 532 nm for P(DTT) **P1** to 478 nm for P(DSS) **P4** which is comparable to P(DTP) (524 nm) [47]. The deviation of the absorption of P(DTT) **P1** to the literature value (480 nm) [46] can most likely be attributed to differences in the polymerization procedures. The optical energy gaps have been determined from the onset absorptions and show decreasing values from P(DTT) **P1** (E_g = 1.79 eV) to **P2**–**P4** (E_g = 1.66–1.67 eV). The oxidized polymers gave as expected very broad and flat absorption bands from the visible to the NIR regime of the spectra (400–1600 nm) which is typical for conducting polymers, but hamper the determination of maxima (Table S7, Figure S16 in Supporting Information File 1).

Conclusion

In summary, we presented the synthesis and characterization of novel selenolotriacenes DTS **2**, DST **3**, and DSS **4** in comparison to known DTT **1**, in which a varying number and sequence of fused thiophene and selenophene rings is implemented. For their preparation, efficient multistep synthesis routes with good overall yields based on recently published transition metal-catalyzed C–S and C–Se coupling/cyclization reactions in the crucial cyclization steps of iodinated bithiophene and biselenophene precursors. Heterotriacenes **1**–**4** turned out to be stable and well soluble systems, which allowed for the determination of thermal, optical, and electrochemical properties. By single crystal X-ray structure analysis the geometric structure and packing motifs of selenolotriacenes **2**–**4** were determined. Quantum chemical calculations allowed for a deeper understanding of the geometric and electronic structure of the heterotriacenes. The optoelectronic properties were determined and valuable structure–property relationships were deduced giving insight into the role of the number and relative position of the S and Se heteroatoms in the equally long fused conjugated triacenes. Electrooxidative polymerization of triacenes **1**–**4** led to corresponding conducting polymers **P1**–**P4**, which were electrochemically and spectroelectrochemically characterized and the properties compared to the non-bridged counterparts.

Experimental

Instruments and measurements

NMR spectra were recorded on a Bruker Avance 400 (^{1}H NMR: 400 MHz, ^{13}C NMR: 100 MHz), normally at 25 °C. Chemical shift values (δ) are expressed in parts per million using the solvent (^{1}H NMR, δ_H = 7.26 and ^{13}C NMR, δ_C = 77.0 for $CDCl_3$) as internal standard. The splitting patterns are designated as follows: s (singlet), d (doublet), t (triplet), m (multiplet). Coupling constants (*J*) relate to proton-proton couplings. GC–MS measurements were performed on a Shimadzu GCMS-QP2010 SE instrument. Melting points were measured via differential scanning calorimetric measurements (DSC) on a Mettler Toledo DSC823e under argon atmosphere at a heating rate of 10 °C/min. Elemental analyses were performed on an Elementar Vario EL instrument. High resolution MALDI–MS was measured on a Fourier Transform Ion Cyclotron Resonance (FT-ICR) mass spectrometer solariX from Bruker Daltonics equipped with a 7.0 T superconducting magnet and interfaced to an Apollo II Dual ESI/MALDI source. Single crystals were analysed on a Bruker SMART APEX-II CCD diffractometer (λ(Mo Kα)-radiation, graphite monochromator, ω and 4 scan mode) and corrected for absorption using the SADABS program [53]. The structures were solved by direct methods and refined by a full-matrix least squares technique on F^2 with anisotropic displacement parameters for non-hydrogen atoms. The hydrogen atoms were placed in calculated positions and refined within the riding model with fixed isotropic displacement parameters (U_{ISO}(H) = 1.2Ueq(C)). All calculations were carried out using the SHELXL program package in Olex2 (v. 1.2.10) [54]. Crystallographic data have been deposited with the Cambridge Crystallographic Data Center: DTS **2** CCDC 1897412; DST **3** CCDC 1025419; DSS **4** CCDC 1898450. UV–vis measurements were carried out in dry DCM in 1 cm cuvettes and recorded on a Perkin Elmer UV/VIS/NIR Lambda 19 spectrometer. Cyclic voltammetry experiments were performed with a computer-controlled Autolab PGSTAT30 potentiostat in a three-electrode single compartment cell (3 mL). The platinum working electrode consisted of a platinum wire sealed in a soft glass tube with a surface of A = 0.785 mm^2, which was polished down to 0.25 µm with Buehler polishing paste prior to use to guarantee reproducible surfaces. The counter electrode consisted of a platinum wire and the reference electrode was an Ag/AgCl reference electrode. All potentials were internally referenced to the ferrocene/ferricenium couple (Fc/Fc^+). For the measurements, concentrations of 10^{-3} M of the electroactive species were used in freshly distilled and deaerated dichloromethane (Lichrosolv, Merck) purified with a Braun MB-SPS-800 and 0.1 M (n-Bu)$_4$NPF$_6$ (Fluka; recrystallized twice from ethanol). Spectroelectrochemical measurements of the polymer films were carried out in a 0.1 M solution of (n-Bu)$_4$NPF$_6$ in dry DCM. The applied setup has been described in the literature [55]. A platinum working electrode, a Ag/AgCl reference electrode, and a platinum sheet as the counter electrode were used and measurements were conducted in reflectance mode. During recording the UV–vis–NIR spectra, the applied potential was kept constant. Instrumental artefacts due to the change of the detector were removed and marked in the spectra. Quantum chemical calculations were performed with the Gaussian 09 package: DFT and TDDFT with the B3LYP and CAMB3LYP functional and 6-31++(d,p) basis-set [56].

Materials

Iodine, zinc(II) chloride, copper(II) chloride, potassium hydroxide, chlorotrimethylsilane, copper(I) iodide, and potassium phosphate were purchased from Merck. Diisopropylamine, bis(dibenzylideneacetone)palladium(0), tetrabutylammonium fluoride, selenourea, and copper oxide nanoparticles were purchased from Sigma-Aldrich. *n*-Butyllithium in *n*-hexane (1.6 M) was purchased from Acros Organics, selenophene from TCI, 3-bromothiophene from Fluorochem, potassium thioacetate from Alfa Aesar, potassium sulfide from Caesar & Loretz, and 1,1'-bis(diphenylphosphino)ferrocene (dppf) from Frontier Scientific. Absolute tetrahydrofuran, dichloromethane, and toluene were provided from Sigma-Aldrich and purified using a Büchi MB SPS-800. Dimethyl sulfoxide, acetonitrile, and acetone were purchased from Merck and Sigma-Aldrich, purified, and dried by standard methods prior to use. All synthetic steps were carried out under an argon atmosphere and all glassware used for reactions was dried prior to use. Column chromatography was performed on glass columns packed with silica gel, Merck Silica 60, particle size 40–63 µm (Macherey-Nagel). Thin-layer chromatography was performed on aluminum plates, pre-coated with silica gel Merck Si60 F254. 3,3'-Diiodo-2,2'-bithiophene (**5**) [30] and 5,5-bis(trimethylsilyl)-3,3'-diiodo-2,2'-bithiophene (**6**) [31] were prepared according to literature procedures.

Synthesis

2,6-Bis(trimethylsilyl)dithieno[3,2-*b*:2',3'-*d*]thiophene (7) [20]. To a solution of 3,3'-diiodo-5,5'-bis(trimethylsilyl)-2,2'-bithiophene (**6**, 500 mg, 0.89 mmol) in dry acetonitrile (7 mL) was added copper(I) iodide (17 mg, 89 µmol, 10 mol %) and dipotassium sulfide (196 mg, 1.8 mmol) at rt. The mixture was heated to 140 °C and stirred for 16 hours. After cooling to rt, the reaction was quenched with water and the resulting mixture was extracted three times with diethyl ether. The combined organic layer was dried over Na_2SO_4 and concentrated under vacuum. The residue was purified by column chromatography (SiO_2, petroleum ether) to give DTT (**7**) as a white solid (0.22 g, 0.65 mmol, 73%). Mp 94.6 °C (DSC); ^{1}H NMR ($CDCl_3$) δ (ppm) = 7.34 (s, 2H), 0.37 (s, 18H); ^{13}C NMR ($CDCl_3$) δ (ppm) 144.2, 142.5, 135.6, 127.1, 0.0; anal. calcd for C, 49.41; H, 5.88; S, 28.24; found: C, 48.65; H, 5.64; S, 29.18. The analytical data are in accordance with literature [32].

Dithieno[3,2-*b*:2',3'-*d*]thiophene (DTT, 1) prepared from **7**. To a solution of 2,6-bis(trimethylsilyl)dithieno[3,2-*b*:2',3'-*d*]thiophene (**7**, 92 mg, 0.27 mmol) in THF (2 mL) a solution of tetrabutylammonium fluoride trihydrate (184 mg, 0.6 mmol) in 1 mL THF was added. The mixture was stirred for 1.5 hours, filtrated, and concentrated under vacuum. The crude product was purified by column chromatography (SiO_2, petroleum ether) to afford DTT **1** as a white solid (48 mg, 0.245 mmol, 91%). Mp 69.6 °C (DSC); ^{1}H NMR ($CDCl_3$) δ (ppm) 7.36 (d, ^3J = 5.2 Hz, 2H), 7.29 (d, ^3J = 5.2 Hz, 2H); ^{13}C NMR ($CDCl_3$) δ (ppm) 141.7, 131.0, 126.0, 120.9; anal. calcd for C, 48.95; H, 2.05; S, 49.00; found: C, 49.06; H, 2.10; S 49.24. The analytical data are in accordance with literature [57].

Dithieno[3,2-*b*:2',3'-*d*]thiophene (DTT, 1) prepared from **5**. To a solution of 3,3'-diiodo-2,2'-bithiophene (**5**, 500 mg, 1.2 mmol) in dry acetonitrile (14 mL) was added copper(I) iodide (23 mg, 0.12 mmol, 10 mol %) and dipotassium sulfide (264 mg, 2.4 mmol) at rt. The mixture was heated to 140 °C and stirred for 16 hours. After cooling to rt, the reaction was quenched with water and the resulting mixture was extracted three times with diethyl ether. The combined organic layer was dried over Na_2SO_4 and concentrated under vacuum. The residue was purified by column chromatography (SiO_2, petroleum ether) to provide DTT **1** as a white solid (152 mg, 0.8 mmol, 66%). The analytical data was the same as described above.

Selenolo[3,2-*b*:4,5-*b'*]dithiophene (2). To a stirred solution of 3,3'-diiodo-2,2'-bithiophene (**5**, 200 mg, 0.48 mmol) and selenourea (118 mg, 0.96 mmol) in dry dimethyl sulfoxide (1.5 mL) at rt was added copper(I) oxide nanoparticles (4 mg, 48 µmol, 10 mol %) followed by potassium hydroxide (54 mg, 0.96 mmol). The mixture was heated at 80 °C for 20 hours, before a second portion of selenourea (118 mg, 0.96 mmol), copper(I) oxide (4 mg, 48 µmol, 10 mol %), and potassium hydroxide (54 mg, 0.96 mmol) was added. After stirring at 80 °C for another 20 hours, the reaction mixture was cooled to rt and a 1:1 mixture of dichloromethane/water was added. The combined organic extracts were collected, dried with anhydrous $MgSO_4$ and concentrated under vacuum. The crude product was purified by column chromatography (SiO_2, petroleum ether) and the product-enriched fractions were further purified by HPLC (*n*-hexane/CH_2Cl_2 8:2) to afford the desired heterotriacene DTS **2** as a white solid (59 mg, 0.24 mmol, 51%). Mp 62.1 °C (DSC); ^{1}H NMR ($CDCl_3$) δ (ppm) 7.34 (d, ^3J = 5.2 Hz, 2H), 7.33 (d, ^3J = 5.2 Hz, 2H); ^{13}C NMR ($CDCl_3$) δ (ppm) 139.2, 132.4, 125.5, 123.7; anal. calcd for C, 39.51; H, 1.66; S, 26.37; found: C, 39.51; H, 1.63; S: 26.18. HRMS (APCI) *m*/*z*: [M^+] calcd for $C_8H_4S_2Se$, 243.89129; found, 243.89155; δ*m*/*m* = 1.07 ppm.

5-Iodo-2-(trimethylsilyl)selenophene (10). Selenophene (**9**, 2.00 g, 15 mmol) was dissolved under argon in dry THF (11 mL) and *n*-BuLi (1.6 M in hexane, 9.5 mL, 15 mmol) was added dropwise at −78 °C. The milky solution was stirred at −78 °C for 45 min. Chlorotrimethylsilane (2 mL, 16 mmol) was added and the mixture was stirred for one more hour. Then, another portion of *n*-BuLi (1.6 M, 10 mL, 16 mmol) was added.

After stirring for one hour at −78 °C, a solution of elemental iodine (3.8 g, 15 mmol) in THF (8 mL) was added dropwise at −65 to −55 °C within 15 min. The solution was stirred for another hour at rt and remaining iodine was reduced with a sodium thiosulfate solution (10 mL). The mixture was quenched with water and extracted three times with diethyl ether. The organic layers were combined, dried over $MgSO_4$, and concentrated under vacuum. The brown crude product was purified by column chromatography (SiO_2; petroleum ether) to obtain pure selenophene **10** as a light yellow liquid (3.4 g, 10.3 mmol, 68%); ^{1}H NMR ($CDCl_3$) δ (ppm) 7.54 (d with ^{77}Se-satellites, $^3J_{Se\text{-}H}$ = 11.6 Hz, $^3J_{H\text{-}H}$ = 3.6 Hz, 1H), 7.53 (d with ^{77}Se-satellites, $^3J_{Se\text{-}H}$ = 11.6 Hz, $^3J_{H\text{-}H}$ = 3.6 Hz, 1H), 0.29 (s, 9H); ^{13}C NMR ($CDCl_3$) δ (ppm) 156.6, 141.8, 138.0, 79.9, 0.4; HRMS (APCI) *m*/*z*: [M^+] calcd for $C_7H_{11}ISeSi$, 329.88343; found, 329.88409; δ*m*/*m* = 2.0 ppm.

3,3'-Diiodo-5,5'-bis(trimethylsilyl)-2,2'-biselenophene (11). *n*-BuLi (1.6 M in hexane, 4.6 mL, 7.3 mmol) was added dropwise to a solution of diisoproylamine (1.2 mL, 8.6 mmol) in dry THF (4 mL) at 0 °C and stirred for one hour. 5-Iodo-2-(trimethylsilyl)selenophene (**10**, 2.0 g, 6.1 mmol) was dissolved in dry THF (7.5 mL) and the LDA solution was added dropwise within 30 min. The mixture was stirred at −78 °C for 1.5 hours after complete addition of LDA and then a solution of zinc(II) chloride (1.0 g, 7.3 mmol) dissolved in 5.6 mL dry THF was added. After stirring for one hour at 0 °C, copper(II) chloride (986 mg, 7.3 mmol) was added in one portion and the resulting mixture was stirred at −78 °C for 3 hours, then at rt for 18 hours. The solvent was removed under reduced pressure. The crude product was purified by column chromatography (SiO_2; petroleum ether) to obtain pure biselenophene **11** (1.47 g; 2.2 mmol, 59%) as a pale yellow solid. Mp 107.1 °C (DSC); ^{1}H NMR ($CDCl_3$) δ (ppm) 7.49 (s, with ^{77} Se-satellites, $^3J_{Se\text{-}H}$ = 6.0 Hz, 2H), 0.34 (s, 18H); ^{13}C NMR ($CDCl_3$) δ (ppm) 153.4, 146.2, 144.33, 87.4, 0.2; anal. calcd for C, 25.62; H 3.07; found: C, 25.77; H: 2.89; HRMS (APCI) *m*/*z*: [M^+] calcd for $C_{14}H_{20}I_2Se_2Si_2$, 657.75199; found, 657.75033; δ*m*/*m* = 2.52 ppm.

2,6-Bis(trimethylsilyl)bisselenolo[3,2-*b*:2',3'-*d*]thiophene (12). To a solution of 3,3'-diiodo-5, 5'-bis(trimethylsilyl)-2,2'-biselenophene (**11**, 514 mg, 0.78 mmol) in dry and well-degassed acetonitrile (15 mL) copper(I) iodide (30 mg, 0.16 mmol, 20 mol %) and dipotassium sulfide (346 mg, 3.14 mmol) was added at rt. The mixture was heated to 140 °C and stirred for 20 hours. After cooling to rt, the reaction was quenched with water and the resulting mixture was extracted three times with diethyl ether. The combined organic layer was dried over $MgSO_4$ and concentrated under vacuum. The residue was purified by column chromatography (alumina, petroleum ether) to obtain biselenolothiophene **12** as an orange solid (331 mg, 0.76 mmol, 97%). Mp 111.7 °C (DSC); ^{1}H NMR ($CDCl_3$) δ (ppm) 7.63 (s, with ^{77}Se-satellites, $^3J_{Se\text{-}H}$ = 6.8 Hz, 2H), 0.34 (s, 18H); ^{13}C NMR ($CDCl_3$) δ (ppm) 149.4, 145.2, 138.3, 129.4, 0.3; anal. calcd for C, 38.70; H, 4.64; S, 7.38; found: C, 38.60; H, 4.45; S, 7.49. The analytical data are in accordance with literature [27].

Bisselenolo[3,2-*b*:2',3'-*d*]thiophene (DST, 3). To a solution of 2,6-bis(trimethylsilyl)bisselenolo[3,2-*b*:2',3'-*d*]thiophene (**12**, 153 mg, 0.35 mmol) in THF (4 mL) was added tetrabutylammonium fluoride trihydrate (391 mg, 1.23 mmol) in 2 mL THF. The mixture was stirred for 2 hours, then filtrated and concentrated under vacuum. The crude product was purified by column chromatography (SiO_2, petroleum ether) to afford bisselenolothiophene **3** as a lightly yellow solid (94 mg, 0.32 mmol, 91%). Mp 120.5 °C (DSC); ^{1}H NMR ($CDCl_3$) δ (ppm) 7.95 (d with ^{77}Se-satellites, $^2J_{Se\text{-}H}$ = 48.6 Hz, $^3J_{H\text{-}H}$ = 5.7 Hz, 2H), 7.53 (d with ^{77}Se-satellites, $^3J_{Se\text{-}H}$ = 5.8Hz, $^3J_{H\text{-}H}$ = 5.6 Hz, 2H); ^{13}C NMR ($CDCl_3$) δ (ppm) 142.7, 133.9, 129.7, 123.4. anal. calcd for C, 33.12; H, 1.36; S, 11.05; found: C, 33.70; H, 1.52; S, 11.64. HRMS (APCI) *m/z*: [M^+] calcd for $C_8H_4SSe_2$, 291.83583; found, 291.83625; δ*m*/*m* = 1.1 ppm.

Bisselenolo[3,2-*b*:2',3'-*d*]selenophene (DSS, 4). To a stirred solution of 3,3'-diiodo-5,5'-bis(trimethylsilyl)-2,2'-biselenophene (**11**, 100 mg, 0.15 mmol) and selenourea (28 mg, 0.23 mmol) in dry dimethyl sulfoxide (0.8 mL) under argon at rt was added copper oxide nanoparticles (1.2 mg, 10 mol %) followed by potassium hydroxide (26 mg, 0.46 mmol). The mixture was heated at 80 °C for 18 hours, cooled to rt, and a 1:1 mixture of dichloromethane/water was added. The combined organic extracts were collected, dried with anhydrous $MgSO_4$, and concentrated under vacuum. The crude product was purified by column chromatography (SiO_2, deactivated with 3% triethylamine, petroleum ether) to afford bisselenoloselenophene **4** as a lightly grey solid (25 mg, 70 μmol, 48%). Mp 90.1 °C (DSC); ^{1}H NMR ($CDCl_3$) δ (ppm) 7.94 (d with ^{77}Se-satellites, $^2J_{Se\text{-}H}$ = 48.4 Hz, $^3J_{H\text{-}H}$ = 5.6 Hz, 2H), 7.56 (d with ^{77}Se-satellites, $^3J_{Se\text{-}H}$ = 5.6 Hz, $^3J_{H\text{-}H}$ = 5.6 Hz, 2H); ^{13}C NMR ($CDCl_3$) δ (ppm) 140.7, 135.5, 129.6, 126.1; HRMS (APCI) *m*/*z*: [M^+] calcd for $C_8H_4Se_3$, 337.78158; found, 337.782251; δ*m*/*m* = 2.75 ppm.

3,3'-Diiodo-2,2'-biselenophene (13). To a stirred solution of 3,3'-diiodo-5,5'-bis(trimethylsilyl)-2,2'-biselenophene (**11**, 400 mg, 0.61 mmol) in THF (7 mL) at 0 °C under argon was added dropwise tetrabutylammonium fluoride trihydrate (400 mg, 1.3 mmol) in 1 mL THF. The mixture was warmed to rt and stirred for 1.5 hours. At the end of the reaction, the mixture was filtrated and concentrated under vacuum. The crude

product was purified by column chromatography (SiO_2, *n*-hexane/DCM 10:1) to afford biselenophene **13** as a white solid (202 mg, 0.4 mmol, 66%). ^{1}H NMR ($CDCl_3$) δ (ppm) 8.08 (d with ^{77}Se-satellites, $^2J_{Se-H}$ = 44 Hz, $^3J_{H-H}$ = 5.8 Hz, 2H); 7.36 (d with ^{77}Se-satellites, $^3J_{Se-H}$ = 12 Hz, $^3J_{H-H}$ = 5.8 Hz, 2H); ^{13}C NMR ($CDCl_3$) δ (ppm) 141.7, 138.4, 135.1, 86.6. HRMS (APCI): *m*/*z*: [M^+] calcd for $C_8H_4Se_3$, 513.67274; found, 513.67374; δ*m*/*m* = 1.6 ppm.

Supporting Information

Supporting Information File 1

Additional spectral and crystallographic data.
[https://www.beilstein-journals.org/bjoc/content/supplementary/1860-5397-15-138-S1.pdf]

Acknowledgements

We gratefully acknowledge P. Martin, M. Hartkorn, C. Lorenz, and J. Pommerenke for preparative help; M. Lechner, Institute of Inorganic Chemistry II, and S. Blessing, Institute of Inorganic Chemistry I, University of Ulm, for X-ray measurements.

ORCID® iDs

Peter Bäuerle - https://orcid.org/0000-0003-2017-4414

References

1. Anthony, J. E. *Chem. Rev.* **2006,** *106,* 5028–5048. doi:10.1021/cr050966z
2. Shimo, Y.; Mikami, T.; Hamao, S.; Goto, H.; Okamoto, H.; Eguchi, R.; Gohda, S.; Hayashi, Y.; Kubozono, Y. *Sci. Rep.* **2016,** *6,* 21008. doi:10.1038/srep21008
3. Narita, A.; Wang, X.-Y.; Feng, X.; Müllen, K. *Chem. Soc. Rev.* **2015,** *44,* 6616–6643. doi:10.1039/c5cs00183h
4. Bunz, U. H. F.; Engelhart, J. U.; Lindner, B. D.; Schaffroth, M. *Angew. Chem., Int. Ed.* **2013,** *52,* 3810–3821. doi:10.1002/anie.201209479
5. Mori, T.; Nishimura, T.; Yamamoto, T.; Doi, I.; Miyazaki, E.; Osaka, I.; Takimiya, K. *J. Am. Chem. Soc.* **2013,** *135,* 13900–13913. doi:10.1021/ja406257u
6. Zhang, X.; Côté, A. P.; Matzger, A. J. *J. Am. Chem. Soc.* **2005,** *127,* 10502–10503. doi:10.1021/ja053326m
7. Okamoto, T.; Kudoh, K.; Wakamiya, A.; Yamaguchi, S. *Chem. – Eur. J.* **2007,** *13,* 548–556. doi:10.1002/chem.200601064
8. Wetzel, C.; Brier, E.; Vogt, A.; Mishra, A.; Mena-Osteritz, E.; Bäuerle, P. *Angew. Chem., Int. Ed.* **2015,** *54,* 12334–12338. doi:10.1002/anie.201502840
9. Mishra, A.; Popovic, D.; Vogt, A.; Kast, H.; Leitner, T.; Walzer, K.; Pfeiffer, M.; Mena-Osteritz, E.; Bäuerle, P. *Adv. Mater. (Weinheim, Ger.)* **2014,** *26,* 7217–7223. doi:10.1002/adma.201402448
10. Qin, P.; Kast, H.; Nazeeruddin, M. K.; Zakeeruddin, S. M.; Mishra, A.; Bäuerle, P.; Grätzel, M. *Energy Environ. Sci.* **2014,** *7,* 2981–2985. doi:10.1039/c4ee01220h
11. Wetzel, C.; Mishra, A.; Mena-Osteritz, E.; Liess, A.; Stolte, M.; Würthner, F.; Bäuerle, P. *Org. Lett.* **2014,** *16,* 362–365. doi:10.1021/ol403153z
12. Chung, C.-L.; Chen, C.-Y.; Kang, H.-W.; Lin, H.-W.; Tsai, W.-L.; Hsu, C.-C.; Wong, K.-T. *Org. Electron.* **2016,** *28,* 229–238. doi:10.1016/j.orgel.2015.10.030
13. Wetzel, C.; Mishra, A.; Mena-Osteritz, E.; Walzer, K.; Pfeiffer, M.; Bäuerle, P. *J. Mater. Chem. C* **2016,** *4,* 3715–3725. doi:10.1039/c5tc03539b
14. Huang, C.; Liao, X.; Gao, K.; Zuo, L.; Lin, F.; Shi, X.; Li, C.-Z.; Liu, H.; Li, X.; Liu, F.; Chen, Y.; Chen, H.; Jen, A. K.-Y. *Chem. Mater.* **2018,** *30,* 5429–5434. doi:10.1021/acs.chemmater.8b02276
15. Leitner, T. D.; Vogt, A.; Popović, D.; Mena-Osteritz, E.; Walzer, K.; Pfeiffer, M.; Bäuerle, P. *Mater. Chem. Front.* **2018,** *2,* 959–968. doi:10.1039/c7qm00542c
16. Mishra, A.; Wetzel, C.; Singhal, R.; Bäuerle, P.; Sharma, G. D. *J. Phys. Chem. C* **2018,** *122,* 11262–11269. doi:10.1021/acs.jpcc.8b02348
17. Osuna, R. M.; Ortiz, R. P.; Okamoto, T.; Suzuki, Y.; Yamaguchi, S.; Hernández, V.; López Navarrete, J. T. *J. Phys. Chem. B* **2007,** *111,* 7488–7496. doi:10.1021/jp067262t
18. Haid, S.; Mishra, A.; Uhrich, C.; Pfeiffer, M.; Bäuerle, P. *Chem. Mater.* **2011,** *23,* 4435–4444. doi:10.1021/cm201392c
19. Haid, S.; Mishra, A.; Weil, M.; Uhrich, C.; Pfeiffer, M.; Bäuerle, P. *Adv. Funct. Mater.* **2012,** *22,* 4322–4333. doi:10.1002/adfm.201201018
20. Otsubo, T.; Takimiya, K. In *Handbook of Thiophene-based Materials, Perepichka;* Perepichka, I. F.; Perepichka, D. F., Eds.; John Wiley & Sons Ltd.: Chichester, UK, 2009; pp 321–340.
21. Yasuike, S.; Kurita, J.; Tsuchiya, T. *Heterocycles* **1997,** *45,* 1891–1894. doi:10.3987/com-97-7911
22. Mishra, S. P.; Javier, A. E.; Zhang, R.; Liu, J.; Belot, J. A.; Osaka, I.; McCullough, R. D. *J. Mater. Chem.* **2011,** *21,* 1551–1561. doi:10.1039/c0jm00602e
23. Heeney, M.; Zhang, W.; Tierney, S.; McCulloch, I. *Polymers comprising fused selenophene*. PCT Int. Appl. WO2008077465A2, July 3, 2008.
24. Cinar, M. E.; Ozturk, T. *Chem. Rev.* **2015,** *115,* 3036–3140. doi:10.1021/cr500271a
25. Okamoto, T.; Kudoh, K.; Wakamiya, A.; Yamaguchi, S. *Org. Lett.* **2005,** *7,* 5301–5304. doi:10.1021/ol0523650
26. Pao, Y.-C.; Chen, Y.-L.; Chen, Y.-T.; Cheng, S.-W.; Lai, Y.-Y.; Huang, W.-C.; Cheng, Y.-J. *Org. Lett.* **2014,** *16,* 5724–5727. doi:10.1021/ol502793e
27. Xu, W.; Wang, M.; Ma, Z.; Shan, Z.; Li, C.; Wang, H. *J. Org. Chem.* **2018,** *83,* 12154–12163. doi:10.1021/acs.joc.8b02107
28. Reddy, V. P.; Kumar, A. V.; Rao, K. R. *J. Org. Chem.* **2010,** *75,* 8720–8723. doi:10.1021/jo102017g
29. You, W.; Yan, X.; Liao, Q.; Xi, C. *Org. Lett.* **2010,** *12,* 3930–3933. doi:10.1021/ol101619s
30. Harschneck, T.; Zhou, N.; Manley, E. F.; Lou, S. J.; Yu, X.; Butler, M. R.; Timalsina, A.; Turrisi, R.; Ratner, M. A.; Chen, L. X.; Chang, R. P. H.; Facchetti, A.; Marks, T. J. *Chem. Commun.* **2014,** *50,* 4099–4101. doi:10.1039/c3cc49620a
31. Guo, X.; Puniredd, S. R.; Baumgarten, M.; Pisula, W.; Müllen, K. *J. Am. Chem. Soc.* **2012,** *134,* 8404–8407. doi:10.1021/ja302957s
32. San Miguel, L.; Porter, W. W., III; Matzger, A. J. *Org. Lett.* **2007,** *9,* 1005–1008. doi:10.1021/ol0630393
33. Oechsle, P.; Paradies, J. *Org. Lett.* **2014,** *16,* 4086–4089. doi:10.1021/ol501752f
34. Schnürch, M.; Spina, M.; Khan, A. F.; Mihovilovic, M. D.; Stanetty, P. *Chem. Soc. Rev.* **2007,** *36,* 1046–1057. doi:10.1039/b607701n

35. Schatz, J. *Sci. Synth.* **2002,** *9,* 423.
36. Bertinelli, F.; Palmieri, P.; Stremmenos, C.; Pelizzi, G.; Taliani, C. *J. Phys. Chem.* **1983,** *87,* 2317–2322. doi:10.1021/j100236a017
37. Castañeda, R.; Khrustalev, V. N.; Fonari, A.; Brédas, J.-L.; Getmanenko, Y. A.; Timofeeva, T. V. *J. Mol. Struct.* **2015,** *1100,* 506–512. doi:10.1016/j.molstruc.2015.07.053
38. http://periodictable.com/Properties/A/VanDerWaalsRadius.v.html (accessed March 19, 2019).
39. Lukevics, E.; Arsenyan, P.; Belyakov, S.; Pudova, O. *Chem. Heterocycl. Compd.* **2002,** *38,* 763–777. doi:10.1023/a:1020607300418
40. Takimiya, K.; Shinamura, S.; Osaka, I.; Miyazaki, E. *Adv. Mater. (Weinheim, Ger.)* **2011,** *23,* 4347–4370. doi:10.1002/adma.201102007
41. Zade, S. S.; Bendikov, M. *Chem. – Eur. J.* **2008,** *14,* 6734–6741. doi:10.1002/chem.200701182
42. Zade, S. S.; Zamoshchik, N.; Bendikov, M. *Chem. – Eur. J.* **2009,** *15,* 8613–8624. doi:10.1002/chem.200900971
43. Zade, S. S.; Zamoshchik, N.; Bendikov, M. *Acc. Chem. Res.* **2011,** *44,* 14–24. doi:10.1021/ar1000555
44. Shabana, R.; Galal, A.; Mark, H. B., Jr.; Zimmer, H.; Gronowitz, S.; Hörnfeldt, A.-B. *Phosphorus, Sulfur Silicon Relat. Elem.* **1990,** *48,* 239–244. doi:10.1080/10426509008045904
45. Cardona, C. M.; Li, W.; Kaifer, A. E.; Stockdale, D.; Bazan, G. C. *Adv. Mater. (Weinheim, Ger.)* **2011,** *23,* 2367–2371. doi:10.1002/adma.201004554
46. Arbizzani, C.; Catellani, M.; Mastragostino, M.; Cerroni, M. G. *J. Electroanal. Chem.* **1997,** *423,* 23–28. doi:10.1016/s0022-0728(96)04879-6
47. Förtsch, S.; Bäuerle, P. *Polym. Chem.* **2017,** *8,* 3586–3595. doi:10.1039/c7py00764g
48. Funt, B. L.; Lowen, S. V. *Synth. Met.* **1985,** *11,* 129–137. doi:10.1016/0379-6779(85)90059-1
49. Krische, B.; Zagorska, M. *Synth. Met.* **1989,** *33,* 257–267. doi:10.1016/0379-6779(89)90472-4
50. Kolodziejczyk, B.; Mayevsky, D.; Winther-Jensen, B. *RSC Adv.* **2013,** *3,* 4568–4573. doi:10.1039/c3ra23120h
51. Ong, T.-T.; Ng, S.-C.; Chan, H. S. O. *Polymer* **2003,** *44,* 5597–5603. doi:10.1016/s0032-3861(03)00586-x
52. Audebert, P.; Miomandre, F. Electrchemistry and Conducting Polymers. In *Conjugated Polymers: Theory, Synthesis, Properties, and Characterization,* 3rd ed.; Skotheim, T. A.; Reynolds, J. R., Eds.; Handbook of Conducting Polymers; CRC Press: Boca Raton, Florida, USA, 2007; 18-1.
53. *SADABS. Program for Absorption Correction;* University of Göttingen: Germany, 1996.
54. Dolomanov, O. V.; Bourhis, L. J.; Gildea, R. J.; Howard, J. A. K.; Puschmann, H. *J. Appl. Crystallogr.* **2009,** *42,* 339–341. doi:10.1107/s0021889808042726
55. Salbeck, J. *J. Electroanal. Chem.* **1992,** *340,* 169–195. doi:10.1016/0022-0728(92)80297-h
56. *Gaussian 09,* Revision D.01; Gaussian, Inc.: Wallingford, CT, 2013.
57. Frey, J.; Bond, A. D.; Holmes, A. B. *Chem. Commun.* **2002,** 2424–2425. doi:10.1039/b207403f

License and Terms

BEILSTEIN JOURNAL OF ORGANIC CHEMISTRY

Synthesis, photophysical and electrochemical properties of pyridine, pyrazine and triazine-based (D–π–)$_2$A fluorescent dyes

Keiichi Imato, Toshiaki Enoki, Koji Uenaka and Yousuke Ooyama*

Full Research Paper

Open Access

Address:
Department of Applied Chemistry, Graduate School of Engineering, Hiroshima University, 1-4-1 Kagamiyama, Higashi-Hiroshima 739-8527, Japan

Email:
Yousuke Ooyama* - yooyama@hiroshima-u.ac.jp

* Corresponding author

Keywords:
D–π–A structure; fluorescent dyes; pyrazine; pyridine; triazine

Beilstein J. Org. Chem. **2019,** *15,* 1712–1721.
doi:10.3762/bjoc.15.167

Received: 14 May 2019
Accepted: 10 July 2019
Published: 22 July 2019

This article is part of the thematic issue "Dyes in modern organic chemistry".

Guest Editor: H. Ihmels

Abstract

The donor–acceptor–π-conjugated (D–π–)$_2$A fluorescent dyes **OUY-2**, **OUK-2** and **OUJ-2** with two (diphenylamino)carbazole thiophene units as D (electron-donating group)–π (π-conjugated bridge) moiety and a pyridine, pyrazine or triazine ring as electron-withdrawing group (electron-accepting group, A) have been designed and synthesized. The photophysical and electrochemical properties of the three dyes were investigated by photoabsorption and fluorescence spectroscopy, Lippert–Mataga plots, cyclic voltammetry and density functional theory calculations. The photoabsorption maximum ($\lambda_{max,abs}$) and the fluorescence maximum ($\lambda_{max,fl}$) for the intramolecular charge-transfer characteristic band of the (D–π–)$_2$A fluorescent dyes show bathochromic shifts in the order of **OUY-2** < **OUK-2** < **OUJ-2**. Moreover, the photoabsorption bands of the (D–π–)$_2$A fluorescent dyes are nearly independent of solvent polarity, while the fluorescence bands showed bathochromic shifts with increasing solvent polarity (i.e., positive fluorescence solvatochromism). The Lippert–Mataga plots for **OUY-2**, **OUK-2** and **OUJ-2** indicate that the $\Delta\mu$ (= $\mu_e - \mu_g$) value, which is the difference in the dipole moment of the dye between the excited (μ_e) and the ground (μ_g) states, increases in the order of **OUY-2** < **OUK-2** < **OUJ-2**. Therefore, the fact explains our findings that **OUJ-2** shows large bathochromic shifts of the fluorescence maxima in polar solvents, as well as the Stokes shift values of **OUJ-2** in polar solvents are much larger than those in non-polar solvents. The cyclic voltammetry of **OUY-2**, **OUK-2** and **OUJ-2** demonstrated that there is little difference in the HOMO energy level among the three dyes, but the LUMO energy levels decrease in the order of **OUY-2** > **OUK-2** > **OUJ-2**. Consequently, this work reveals that for the (D–π–)$_2$A fluorescent dyes **OUY-2**, **OUK-2** and **OUJ-2** the bathochromic shifts of $\lambda_{max,abs}$ and $\lambda_{max,fl}$ and the lowering of the LUMO energy level are dependent on the electron-withdrawing ability of the azine ring, which increases in the order of **OUY-2** < **OUK-2** < **OUJ-2**.

Introduction

Donor–π-conjugated–acceptor (D–π–A) dyes are constructed of an electron-donating group (D) such as a diphenyl or dialkylamino group and an electron-withdrawing group (electron-accepting group, A) such as a nitro, cyano, and carboxy group or an azine ring such as pyridine, pyrazine and triazine linked by π-conjugated bridges such as oligoenes and heterocycles. Thus, the D–π–A dyes exhibit intense photoabsorption and fluorescence emission properties based on the intramolecular charge transfer (ICT) excitation from the D moiety to the A moiety [1-4]. Moreover, the D–π–A structure possesses considerable structural characteristics: the increase in the electron-donating and electron-accepting abilities of the D and A moieties and the expansion of π conjugation, respectively, can lead to a decrease in the energy gap between the HOMO and LUMO because the highest occupied molecular orbital (HOMO) is localized over the π-conjugated system containing the D moiety, and the lowest unoccupied molecular orbital (LUMO) is localized over the A moiety. Thus, the photophysical and electrochemical properties based on the ICT characteristics of D–π–A dyes should be tuneable by not only the electron-donating ability of D and the electron-accepting ability of A, but also by the electronic characteristics of the π bridge. Consequently, the D–π–A dyes are of considerable practical concern as a useful fluorescence sensor for cation, anion and neural species [5-14], an efficient emitter for organic light emitting diodes (OLEDs) [15-24], and a promising photosensitizer for dye-sensitized solar cells (DSSCs) [25-34].

Thus, in this work, to gain insight into the photophysical and electrochemical properties of D–π–A fluorescent dyes with an azine ring as electron-withdrawing group, we have designed and synthesized the $(D–π–)_2A$ fluorescent dyes **OUY-2**, **OUK-2** and **OUJ-2** with two (diphenylamino)carbazole thiophene units as the D–π moiety and a pyridine, pyrazine or triazine ring as the A moiety (Figure 1), although we have already reported the synthesis of $(D–π–)_2A$ fluorescent dyes **OUY-2** [2] and **OUK-2** [3,4] and their partial photopysical and electrochemical properties. One advantage of $(D–π–)_2A$ fluorescent dyes over other D–π–A fluorescent dyes is their broad and intense photoabsorption spectral features. Herein, based on photoabsorption and fluorescence spectroscopy, Lippert–Mataga plots, cyclic voltammetry and density functional theory (DFT) calcu-

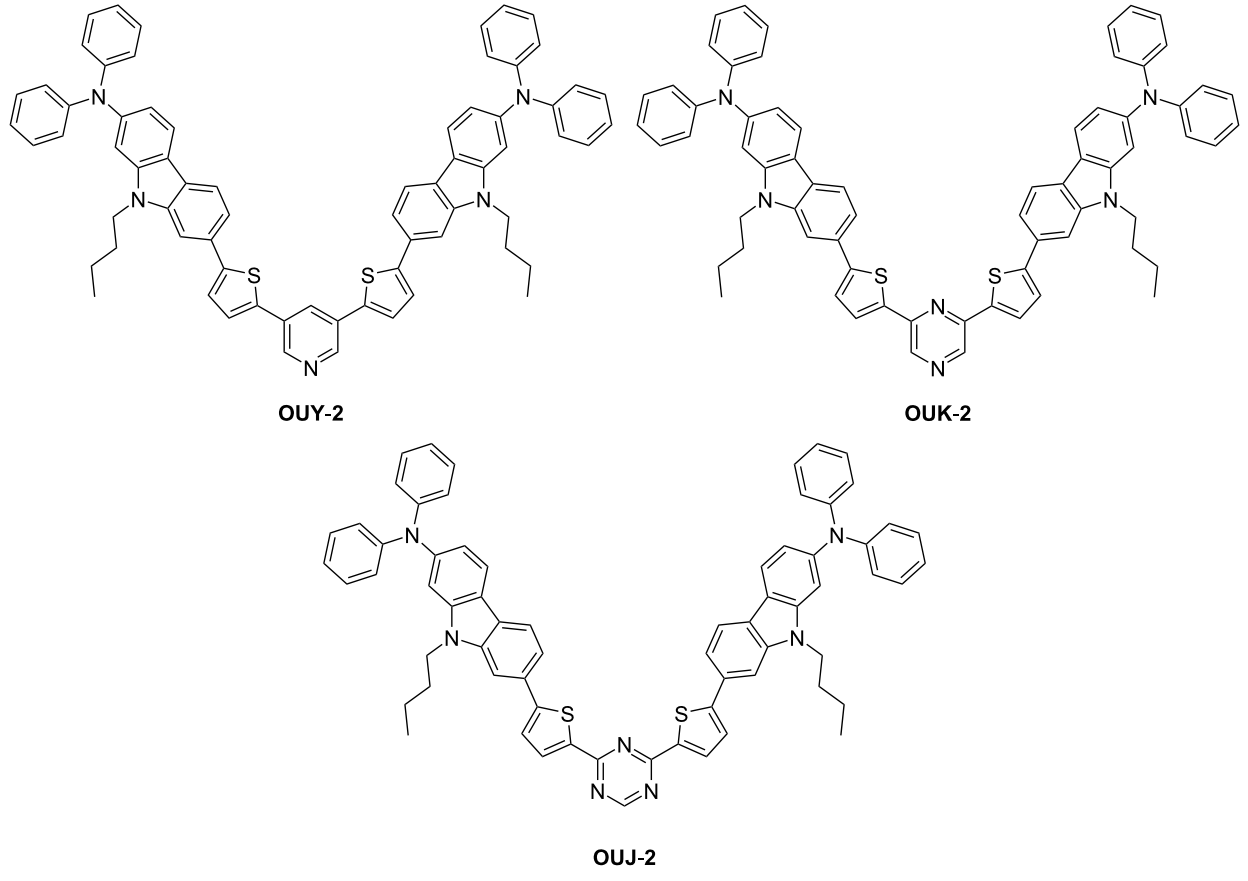

Figure 1: Chemical structures of the $(D–π–)_2A$ fluorescent dyes **OUY-2**, **OUK-2** and **OUJ-2**.

lations, we reveal the photophysical and electrochemical properties of the (D–π–)$_2$A fluorescent dyes **OUY-2**, **OUK-2** and **OUJ-2**.

Results and Discussion

Synthesis

The (D–π–)$_2$A fluorescent dyes **OUY-2** [2], **OUK-2** [3,4] and **OUJ-2** were prepared by Stille coupling of stannyl compound **1** [3] with 3,5-dibromopyridine, 2,6-diiodopyrazine, and 2,4-dichloro-1,3,5-triazine, respectively (Scheme 1; see Experimental section for the synthetic procedure of **OUJ-2**).

Optical properties

The photoabsorption and fluorescence spectra of **OUY-2**, **OUK-2** and **OUJ-2** in various solvents are shown in Figure 2, and their optical data are summarized in Table 1. **OUY-2**, **OUK-2** and **OUJ-2** in toluene as a non-polar solvent show the photoabsorption maximum ($\lambda_{max,abs}$) at 398 nm, 401 nm and 433 nm, respectively, which is assigned to the ICT excitation from the two (diphenylamino)carbazole thiophene units as D–π moiety to a pyridine, pyrazine or triazine ring as A moiety. For **OUK-2**, the shoulder band was observed at around 430 nm. Thus, the ICT-based photoabsorption band of the three dyes appears at a longer wavelength region in the order of **OUY-2** < **OUK-2** < **OUJ-2**, which is in agreement with the increase in the electron-withdrawing ability of the azine ring in the order of pyridyl group < pyrazyl group < triazyl group. The photoabsorption spectra of the three dyes are nearly independent of solvent polarity. This indicates that the electronic and structural characteristics of both the ground and Franck–Condon (FC) excited states do not differ much with a change in solvent polarity. The molar extinction coefficient (ε_{max}) for the ICT band is ca. 100000 M^{-1} cm^{-1} for **OUY-2**, 75000 M^{-1} cm^{-1} for **OUK-2** and 80000 M^{-1} cm^{-1} for **OUJ-2**. The corresponding fluorescence maximum ($\lambda_{max,fl}$) of the three dyes in toluene also appears at a longer wavelength region in the order of **OUY-2** (453 nm) < **OUK-2** (480 nm) < **OUJ-2** (509 nm). Interestingly, in contrast to the photoabsorption spectra, the fluorescence spectra are strongly dependent on the solvent polarity, that is, the three dyes showed a bathochromic shift of the fluorescence band with increasing solvent polarity from toluene to DMF (i.e., positive fluorescence solvatochromism). Thus, the Stokes shift (SS) values of the three dyes increase with increasing solvent polarity. Compared with **OUY-2**, **OUK-2** and **OUJ-2** exhibit significant fluorescence solvatochromic properties, that is, the two dyes show a significant decrease in the fluorescence quantum yield (Φ_f) in a polar solvent such as DMF (Φ_f = 0.59, 0.14 and 0.09 for **OUY-2**, **OUK-2** and **OUJ-2**, respectively), although in relatively low polar solvents **OUK-2** and **OUJ-2** exhibit a higher Φ_f value (0.48–0.65 and 0.72–0.86, respectively) than **OUY-2** (Φ_f = 0.38–0.58). For **OUK-2** and **OUJ-2**, the large bathochromic shifts of the fluorescence band with a significant decrease in the Φ_f value in polar solvents such as DMF might be arising from the twisted intramolecular charge transfer (TICT) excited state due to the twisting between the pyrazyl or triazyl group and the (diphenylamino)carbazole thiophene moiety, leading to non-radiative deactivation [1]. On the other hand, it is worth mentioning here

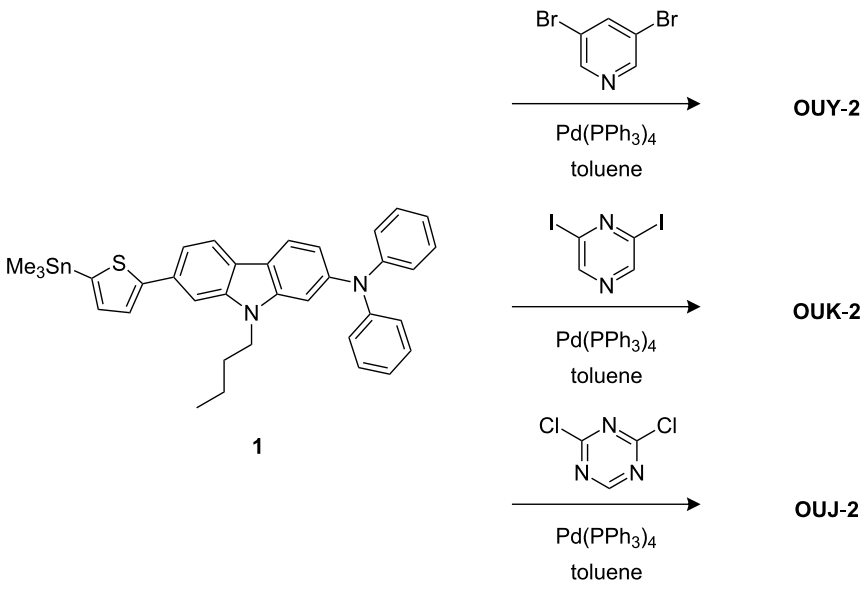

Scheme 1: Synthesis of **OUY-2**, **OUK-2** and **OUJ-2**.

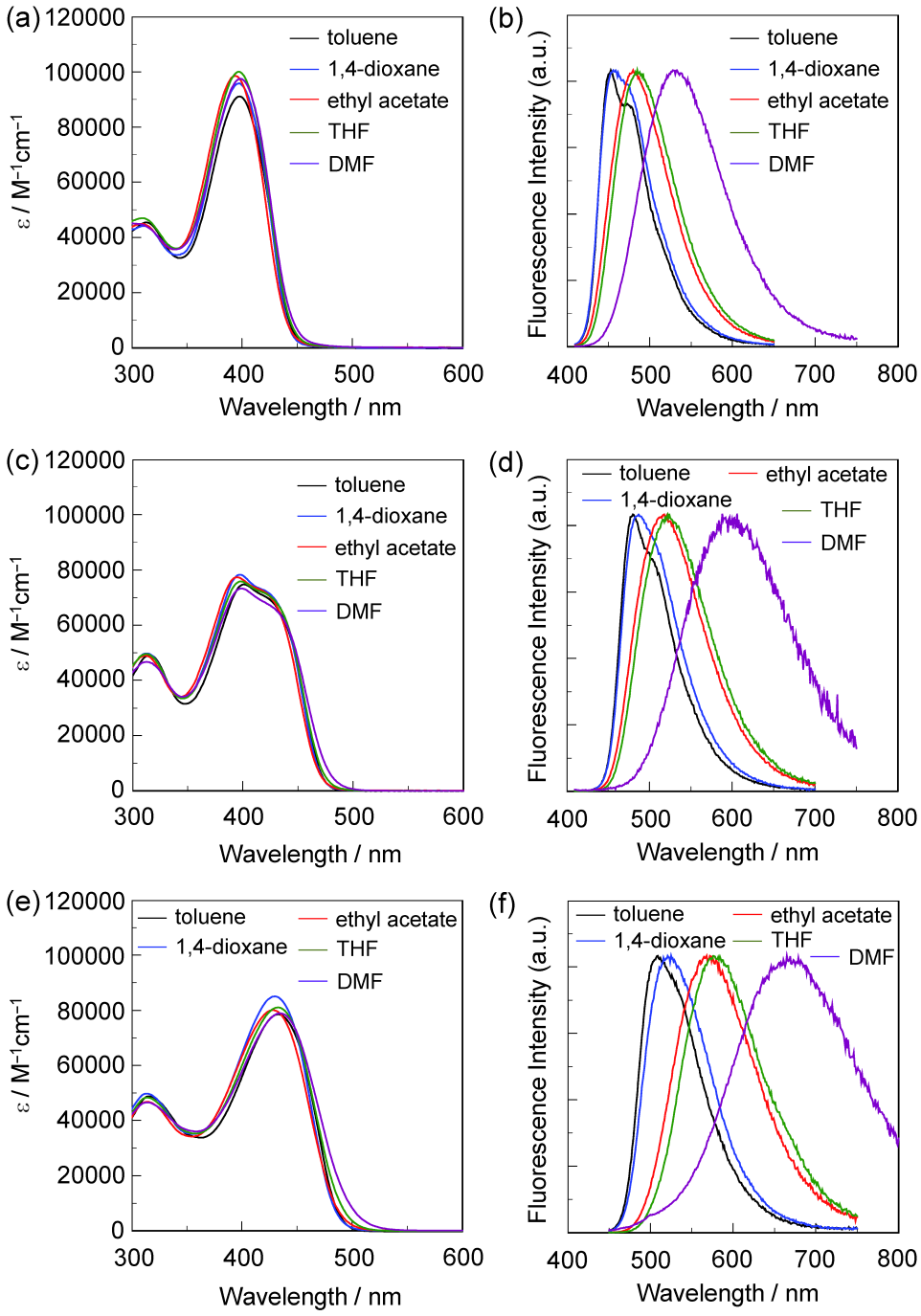

Figure 2: (a) Photoabsorption and (b) fluorescence (λ^{ex} = ca. 400 nm) spectra of **OUY-2** in various solvents. (c) Photoabsorption and (d) fluorescence (λ^{ex} = ca. 400 nm) spectra of **OUK-2** in various solvents. (e) Photoabsorption and (f) fluorescence (λ^{ex} = ca. 430 nm) spectra of **OUJ-2** in various solvents.

that the brightness values ($\varepsilon \times \Phi_f$) for **OUY-2**, **OUK-2** and **OUJ-2** in various solvents are fairly large (Table 1). Thus, the fact indicates that the $(D–\pi–)_2A$ fluorescent dyes have advantageous characteristics as emitters for OLEDs and fluorescence probes for biological imaging.

It is well accepted that the dipole–dipole interactions between the fluorescent dye and the solvent molecules are responsible for the solvent-dependent shifts in the fluorescence maxima [35-43]. Therefore, in order to understand the fluorescence solvatochromisms of **OUY-2**, **OUK-2** and **OUJ-2**, we have in-

Table 1: Optical data of **OUY-2**, **OUK-2** and **OUJ-2** in various solvents.

Dye	Solvent	$\lambda_{max,abs}$ [nm] (ε [$M^{-1}cm^{-1}$])	$\lambda_{max,fl}$ [nm] (Φ_f)[a]	Brightness [$M^{-1}cm^{-1}$]	Stokes shift [cm^{-1}]
OUY-2	toluene	398 (91100)	453 (0.38)	34600	3050
	1,4-dioxane	398 (95800)	455 (0.40)	38300	3147
	ethyl acetate	394 (98500)	480 (0.39)	38400	4547
	THF	397 (100000)	485 (0.58)	58000	4570
	DMF	399 (97500)	533 (0.59)	57500	6300
OUK-2	toluene	401 (74800)	480 (0.48)	35900	4104
	1,4-dioxane	397 (78300)	487 (0.62)	48500	4655
	ethyl acetate	398 (75800)	518 (0.55)	41700	5820
	THF	394 (77400)	524 (0.65)	50300	6296
	DMF	399 (73300)	588 (0.14)	10200	8055
OUJ-2	toluene	433 (78500)	509 (0.81)	63600	3448
	1,4-dioxane	430 (85100)	525 (0.86)	73200	4208
	ethyl acetate	428 (80100)	568 (0.72)	57700	5758
	THF	433 (81100)	576 (0.72)	58400	5733
	DMF	435 (78900)	665 (0.09)	7100	7950

[a]Fluorescence quantum yields (Φ_f) were determined by using a calibrated integrating sphere system (λ^{ex} = 400 nm for **OUY-2**, 400 nm for **OUK-2**, and 430 nm for **OUJ-2**, respectively).

vestigated the relationships between the solvent polarity-dependent shift of the fluorescence maximum and the dipole moment of dye molecule on the basis of the Lippert–Mataga equation (Equation 1) [44-46]:

$$v_{st} = \frac{1}{4\pi\varepsilon_0} \cdot \frac{2\Delta\mu^2}{hca^3} \Delta f + const. \quad (1)$$

where

$$\Delta f = \frac{\varepsilon - 1}{2\varepsilon + 1} - \frac{n^2 - 1}{2n^2 + 1} \quad (2)$$

Consequently, on the basis of Equation (1) and Equation (2), the change in the dipole moment, $\Delta\mu = \mu_e - \mu_g$, between the ground ($\mu_g$) and the excited ($\mu_e$) states can easily be evaluated from the slope of a plot of v_{st} against Δf (the Lippert–Mataga plot), where v_{st} is the Stokes shift (Table 1), ε_0 is the vacuum permittivity, h is Planck's constant, c is the velocity of light, a is the Onsager radius of the dye molecule (7.81 Å, 7.99 Å and 7.91 Å for **OUY-2**, **OUK-2** and **OUJ-2**, respectively, estimated from DFT calculation at the B3LYP/6-31G(d,p) level of theory [47]), Δf is the orientation polarizability, ε is the static dielectric constant, and n is the refractive index of the solvent. The Lippert–Mataga plots (Figure 3) for the three dyes show high linearity, indicating that for the three dyes the solvent-dependent shift in the fluorescence maximum is mainly attributed to the dipole–dipole interactions between the dye molecule and the solvent molecule. The slopes (m_{sl}) became steep in the order of **OUY-2** (10500 cm^{-1}) < **OUK-2** (12200 cm^{-1}) < **OUJ-2** (13700 cm^{-1}). The correlation coefficient (R^2) value for the calibration curve regarding the three dyes is 0.90 for **OUY-2**, 0.88 for **OUK-2**, and 0.89 for **OUJ-2**, which indicates good linearity. The Δμ values increase in the order of **OUY-2** (22 D) < **OUK-2** (25 D) < **OUJ-2** (26 D), which corresponds to the increase in the electron-withdrawing ability of the azine rings (pyridyl group < pyrazyl group < triazyl group). Consequently, the Lippert–Mataga plots explains our findings that **OUJ-2** shows large bathochromic shifts in its fluorescence maximum in polar solvents, as well as the SS values for **OUJ-2** in polar solvents are much larger than those in nonpolar solvents (Table 1).

In order to investigate the solid-state photophysical properties of **OUY-2**, **OUK-2** and **OUJ-2**, we have measured the solid-state fluorescence spectra of the solids (Figure 4). The $\lambda_{max,fl}$ of the as-recrystallized dyes appears at 550 nm for **OUY-2**, 592 nm for **OUK-2**, and 557 nm for **OUJ-2**, which showed a significant bathochromic shift by 97 nm, 112 nm, and 48 nm, respectively, compared with those in toluene. The solid-state Φ_f value is below 0.02 for **OUY-2** and **OUK-2** and 0.09 for **OUJ-2**, which are much lower than those in toluene. It is well known that D–π–A fluorescent dyes show bathochromic shifts of the $\lambda_{max,fl}$ and lower Φ_f values by changing from the solution state to the solid state. This fact is attributed to the delocalization of excitons or excimers due to the formation of intermolecular π–π interactions [48-51] between the dye molecules in the solid state, although we could not prepare single crystals of **OUY-2**, **OUK-2** and **OUJ-2** for the X-ray structural analysis.

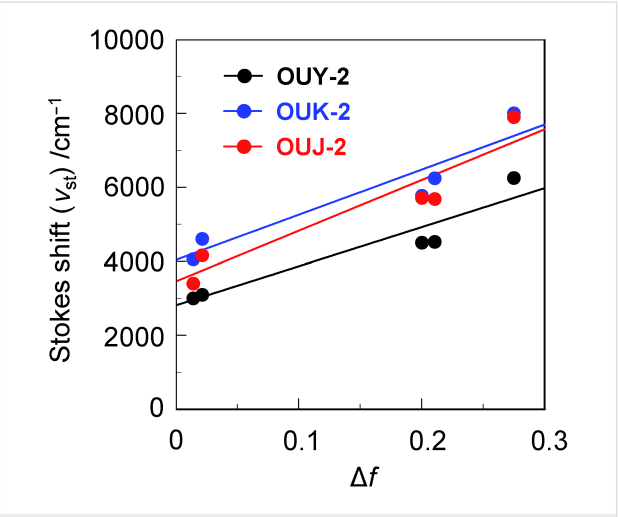

Figure 3: Correlation of the Stokes shift (ν_{st}) and the orientation polarizability (Δf) according to Equation 1 and Equation 2, respectively, for **OUY-2**, **OUK-2** and **OUJ-2**; solvent (ε, n, Δf): toluene (2.38, 1.4969, 0.0132), 1,4-dioxane (2.21, 1.4224, 0.0205), ethyl acetate (6.02, 1.3724, 0.199), THF (7.58, 1.4072, 0.2096) and DMF (36.71, 1.4305, 0.274) [4].

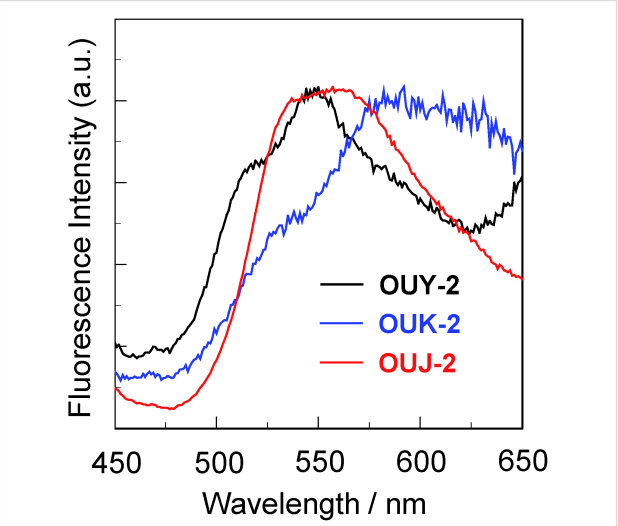

Figure 4: Fluorescence spectra of **OUY-2** (λ^{ex} = 370 nm), **OUK-2** (λ^{ex} = 370 nm) and **OUJ-2** (λ^{ex} = 380 nm) in the solid state.

Electrochemical properties

The electrochemical properties of **OUY-2**, **OUK-2** and **OUJ-2** were investigated by cyclic voltammetry (CV) in DMF containing 0.1 M tetrabutylammonium perchlorate (Bu_4NClO_4). The cyclic voltammograms of the three dyes are shown in Figure 5. The reversible oxidation waves (E_{pa}^{ox}) for the three dyes were observed at 0.42 V for **OUY-2** and **OUK-2** and 0.45 V for **OUJ-2**, vs ferrocene/ferrocenium (Fc/Fc^+) (Table 2). The corresponding reduction waves (E_{pc}^{red}) appeared at 0.35 V for **OUY-2** and **OUK-2** and 0.36 V for **OUJ-2**, thus indicating that the three dyes undergo an electrochemically stable oxidation–reduction process. The HOMO energy level ($-[E_{1/2}^{ox} + 4.8]$ eV) versus the vacuum level was estimated from the half-wave potential for the oxidation ($E_{1/2}^{ox}$ = 0.39 V for **OUY-2** and **OUK-2** and 0.40 V for **OUJ-2**). Therefore, the HOMO energy level was −5.19 eV for **OUY-2** and **OUK-2** and −5.20 eV for **OUJ-2**, respectively. This fact indicates that the three dyes have comparable HOMO energy levels. The LUMO energy level versus the vacuum level was evaluated from the $E_{1/2}^{ox}$ and an intersection of photoabsorption and fluorescence spectra (449 nm; 2.76 eV for **OUY-2**, 481 nm; 2.58 eV for **OUK-2**, 506 nm; 2.45 eV for **OUJ-2**) in DMF. Consequently, the LUMO energy level was obtained through equation = [HOMO + E_{0-0}] eV, where E_{0-0} transition energy is the intersection of the photoabsorption and fluorescence spectra corresponding to the optical energy gap between the HOMO and the LUMO. Thus, the LUMO energy level versus the vacuum level lowers in the order of **OUY-2** (−2.43 eV) > **OUK-2** (−2.61 eV) > **OUJ-2** (−2.75 eV). This result demonstrates that an increase of the electron-withdrawing ability of the azine ring lowers the LUMO energy level of the $(D–\pi–)_2A$ fluorescent dyes. Consequently, the fact revealed that the bathochromic shift of the ICT-based photoabsorption band in the order of **OUY-2** < **OUK-2** < **OUJ-2** is attributed to the stabilization of the LUMO energy level due to the increase in the electron-withdrawing ability of the azine ring in the order of pyridyl < pyrazyl < triazyl, resulting in a decrease in the energy gap between the HOMO and the LUMO.

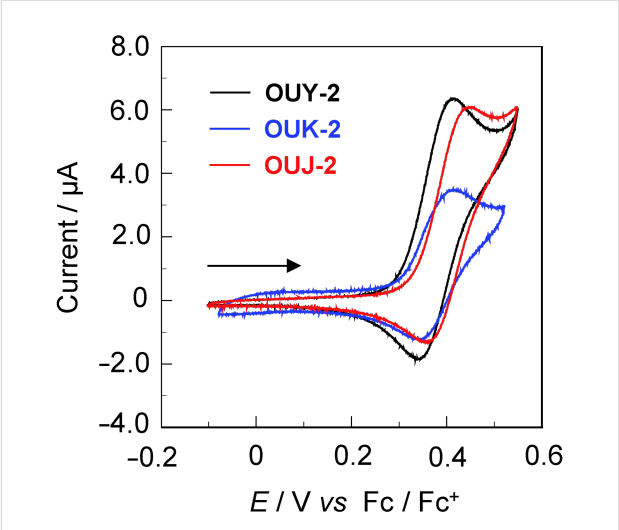

Figure 5: Cyclic voltammograms of **OUY-2**, **OUK-2** and **OUJ-2** in DMF containing 0.1 M Bu_4NClO_4. The arrow denotes the direction of the potential scan.

Theoretical calculations

In order to examine the HOMO and LUMO distributions of **OUY-2**, **OUK-2** and **OUJ-2**, the molecular structures and the

Table 2: Electrochemical data and HOMO and LUMO energy level of **OUY-2, OUK-2** and **OUJ-2**.

Dye	E_{pa}^{ox} [V][a]	E_{pc}^{red} [V][a]	$E_{1/2}^{ox}$ [V][a]	HOMO [eV][b]	LUMO [eV][c]	E_{0-0} [eV][d]
OUY-2	0.42	0.35	0.39	−5.19	−2.43	2.76 eV
OUK-2	0.42	0.35	0.39	−5.19	−2.61	2.58 eV
OUJ-2	0.45	0.36	0.40	−5.20	−2.75	2.45 eV

[a]The anodic peak (E_{pa}^{ox}), the cathodic peak (E_{pc}^{red}) and the half-wave ($E_{1/2}^{ox}$) potentials for oxidation vs Fc/Fc^+ were recorded in DMF/Bu_4NClO_4 (0.1 M) solution; [b]the HOMO energy level ($-[E^{ox}_{1/2} + 4.8]$ eV) versus the vacuum level was evaluated from the $E_{1/2}^{ox}$ for oxidation; [c]the LUMO energy level versus the vacuum level was evaluated from the HOMO and the optical energy gap (E_{0-0}), that is, the LUMO energy level was obtained through equation = [HOMO + E_{0-0}] eV; [d]the optical energy gap (E_{0-0}) was determined from the intersection of the photoabsorption and fluorescence spectra in DMF.

molecular orbitals of the three dyes were calculated using the DFT at the B3LYP/6-31G(d,p) level of theory [47]. The results of the DFT calculation for the three dyes indicated that the HOMO is mostly localized on the two (diphenylamino)carbazole moieties containing the thiophene ring and the LUMO is mostly localized on the thienylpyridine moiety for **OUY-2**, the thienylpyrazine moiety for **OUK-2** and the thienyltriazine moiety for **OUJ-2** (Figure 6). Accordingly, the DFT calculations reveal that the photoexcitation of **OUY-2**, **OUK-2** and **OUJ-2** induces the ICT from the two (diphenylamino)carbazole moieties to each azine ring. The HOMO energy level of the three dyes is remarkably similar to each other (−4.80 eV, −4.78 eV and −4.84 eV for **OUY-2**, **OUK-2** and **OUJ-2**, respectively), and the LUMO energy level is lowered in the order of **OUY-2** (−1.56 eV) > **OUK-2** (−1.76 eV) > **OUJ-2** (−1.98 eV), which are in good agreement with the experimental results from the photoabsorption and fluorescence spectral analyses (Figure 2) and the cyclic voltammetry (Figure 5). Thus, the experimental results and the DFT calculation strongly demonstrated that the bathochromic shift of the ICT-based photoabsorption band in the order of **OUY-2** < **OUK-2** < **OUJ-2** is attributed to a stabilization of the LUMO

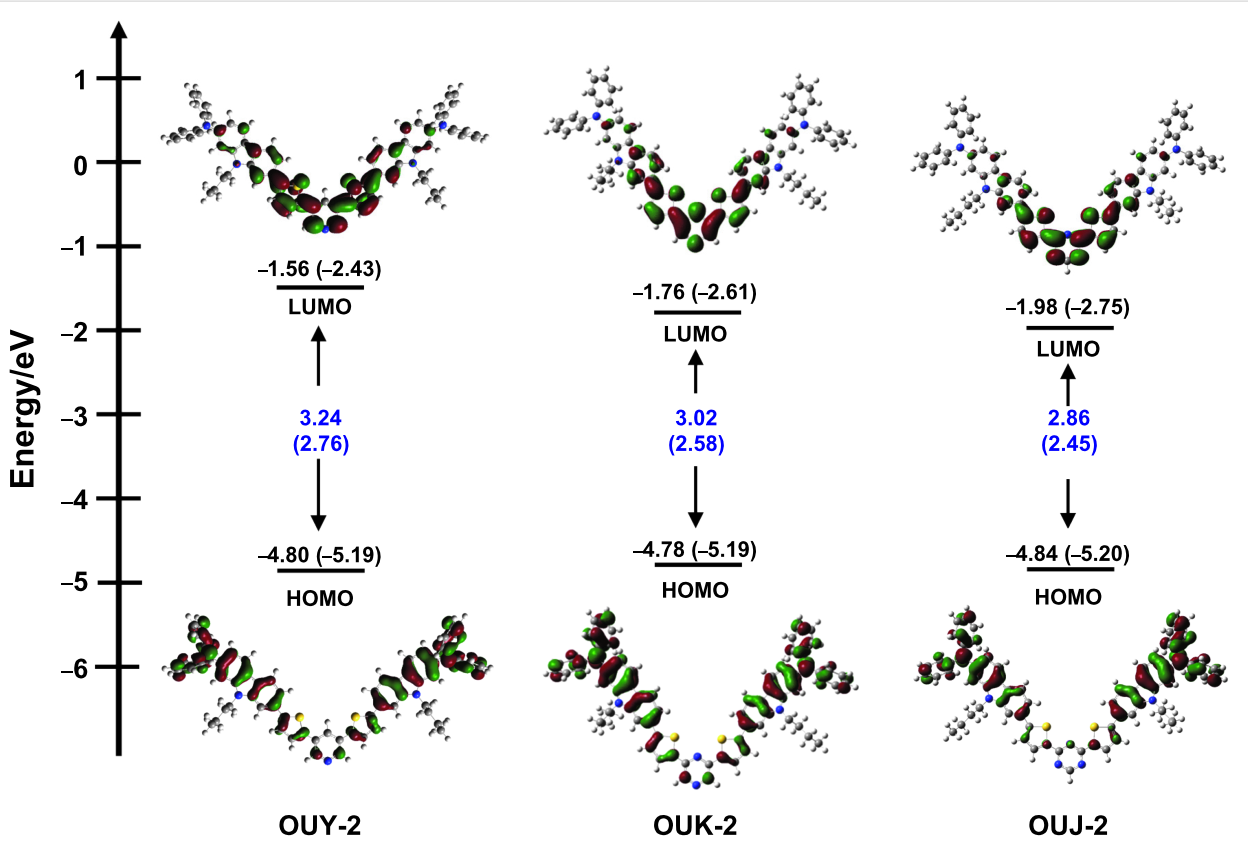

Figure 6: Energy level diagram, HOMO and LUMO of **OUY-2**, **OUK-2** and **OUJ-2**, derived from the DFT calculations at the B3LYP/6-31G(d,p) level of theory. Numbers in parentheses are the experimental values.

energy level due to the increase in the electron-withdrawing ability of the azine ring in the order of pyridyl < pyrazyl < triazyl.

Conclusion

To gain insight into the photophysical and electrochemical properties of D–π–A fluorescent dyes with azine rings as electron-withdrawing groups, we have designed and synthesized a new type of (D–π–)$_2$A fluorescent dyes **OUY-2**, **OUK-2** and **OUJ-2** with two (diphenylamino)carbazole thiophene units as the D (electron-donating group)–π (π-conjugated bridge) moiety and a pyridine, pyrazine or triazine ring as the electron-withdrawing group (electron-accepting group, A), and their photophysical and electrochemical properties were investigated. It was found that the intramolecular charge-transfer (ICT)-based photoabsorption and fluorescence bands of the three dyes appear at a longer wavelength region in the order of **OUY-2** < **OUK-2** < **OUJ-2**. This result is due to the increase in the electron-withdrawing ability of the azine ring in the order of pyridyl < pyrazyl < triazyl. Moreover, the (D–π–)$_2$A fluorescent dyes showed a large bathochromic shift of the fluorescence maxima with increasing solvent polarity (i.e., positive fluorescence solvatochromism). The Lippert–Mataga plots revealed that the difference in the dipole moment of the dye between the excited state and the ground state increases in the order of **OUY-2** < **OUK-2** < **OUJ-2**. Thus, the fact explains our findings that **OUJ-2** shows large bathochromic shifts of fluorescence maxima in polar solvents, as well as the Stokes shift values for **OUJ-2** in polar solvents are much larger than those in nonpolar solvents. Cyclic voltammetry and DFT calculations demonstrated that the HOMO energy levels of the three dyes are remarkably similar, but the LUMO energy level is lowered in the order of **OUY-2** > **OUK-2** > **OUJ-2**, showing that increasing the electron-withdrawing ability of the azine ring lowers the LUMO energy level of the (D–π–)$_2$A fluorescent dyes. Consequently, this work reveals that for the (D–π–)$_2$A fluorescent dyes **OUY-2**, **OUK-2** and **OUJ-2**, the bathochromic shift of photoabsorption and fluorescence maxima and the lowering of the LUMO energy levels are dependent on the electron-withdrawing ability of the azine ring which increases in the order of **OUY-2** < **OUK-2** < **OUJ-2**.

Experimental

General methods

Melting points were measured with a Yanaco micro melting point apparatus MP model. FTIR spectra were recorded on a Shimadzu IRAffinity-1 spectrometer by ATR method. High-resolution mass spectra were acquired on a Thermo Fisher Scientific LTQ Orbitrap XL. ^{1}H NMR and ^{13}C NMR spectra were recorded on a Varian-400 (400 MHz) FT NMR spectrometer. Photoabsorption spectra were measured with a Hitachi U-2910 spectrophotometer, and fluorescence spectra were measured with a Horiba FluoroMax-4 spectrofluorometer. The fluorescence quantum yields in solution were determined by a Horiba FluoroMax-4 spectrofluorometer by using a calibrated integrating sphere system. Cyclic voltammetry (CV) curves were recorded in DMF/Bu_4NClO_4 (0.1 M) solution with a three-electrode system consisting of Ag/Ag^+ as reference electrode, a Pt plate as working electrode, and Pt wire as counter electrode by using an electrochemical measurement system HZ-7000 (Hokuto Denko).

Synthesis

General synthetic procedure of (D–π–)$_2$A fluorescent dyes **OUY-2**, **OUK-2** and **OUJ-2**

OUY-2 [2], **OUK-2** [3] and **OUJ-2** were prepared by Stille coupling of stannyl compound **1** [3] with 3,5-dibromopyridine, 2,6-diiodopyrazine, and 2,4-dichloro-1,3,5-triazine, respectively, by using $Pd(PPh_3)_4$ as a catalyst in toluene at 110 °C under an argon atmosphere (Scheme 1).

Synthesis of OYJ-2: A solution of **1** [3] (0.60 g, 0.95 mmol), 2,4-dichloro-1,3,5-triazine (0.071 g, 0.48 mmol), and $Pd(PPh_3)_4$ (0.18 g, 0.16 mmol) in toluene (10 mL) was stirred for 48 h at 110 °C under an argon atmosphere. After concentrating under reduced pressure, the resulting residue was dissolved in dichloromethane and washed with water. The dichloromethane extract was evaporated under reduced pressure. The residue was chromatographed on silica gel (ethyl acetate/dichloromethane 1:4 as eluent) to give **OUJ-2** (0.38 g, yield 70%) as yellow solid; mp 267–269 °C; IR (ATR) ṽ: 1594, 1548, 1491 cm^{-1}; ^{1}H NMR (400 MHz, CD_2Cl_2) δ 0.89 (t, J = 7.3 Hz, 6H), 1.29–1.35 (m, 4H), 1.75–1.83 (m, 4H), 4.22 (t, J = 7.1 Hz, 4H), 6.96 (dd, J = 1.8 and 8.4 Hz, 2H), 7.02–7.06 (m, 4H), 7.13–7.16 (m, 10H), 7.26–7.30 (m, 8H), 7.57 (d, J = 4.0 Hz, 2H), 7.60–7.63 (dd, J = 8.1 and 1.5 Hz, 2H), 7.72 (s, 2H), 7.95 (d, J = 8.4 Hz, 2H), 8.04 (d, J = 8.1 Hz, 2H), 8.27 (d, J = 4.0 Hz, 2H), 9.00 (s, 1H) ppm; ^{13}C NMR (100 MHz, CD_2Cl_2) δ 14.04, 20.86, 31.47, 43.10, 105.17, 106.55, 117.52, 117.92, 118.47, 120.53, 121.40, 123.08, 123.94, 124.50, 124.79, 129.58, 130.62, 133.57, 139.41, 141.56, 142.95, 147.31, 148.55, 153.55, 167.62 ppm (one aromatic carbon signal was not observed due to overlapping resonances); HRMS–ESI (m/z): [M + H] $^+$ calcd. for $C_{67}H_{56}N_7S_2$, 1022.40331; found, 1022.40344.

Supporting Information

Supporting Information File 1

^{1}H and ^{13}C NMR spectra of **OUJ-2**.
[https://www.beilstein-journals.org/bjoc/content/supplementary/1860-5397-15-167-S1.pdf]

Acknowledgements

This work was supported by a Grant-in-Aid for Scientific Research on Innovative Areas “Soft Crystals” (No. 2903) (JSPS KAKENHI Grant No. 18H04520) and for Scientific Research (B) (JSPS KAKENHI Grant No. 19H02754), and by Shorai Foundation for Science and Technology.

ORCID® iDs

Yousuke Ooyama - https://orcid.org/0000-0002-0257-6930

Preprint

A non-peer-reviewed version of this article has been previously published as a preprint doi:10.3762/bxiv.2019.22.v1

References

1. Ooyama, Y.; Uenaka, K.; Ohshita, J. *RSC Adv.* **2015,** *5,* 21012–21018. doi:10.1039/c4ra16399k
2. Ooyama, Y.; Uenaka, K.; Ohshita, J. *Eur. J. Org. Chem.* **2015,** 3713–3720. doi:10.1002/ejoc.201500341
3. Ooyama, Y.; Uenaka, K.; Harima, Y.; Ohshita, J. *RSC Adv.* **2014,** *4,* 30225–30228. doi:10.1039/c4ra03999h
4. Enoki, T.; Ohshita, J.; Ooyama, Y. *Bull. Chem. Soc. Jpn.* **2018,** *91,* 1704–1709. doi:10.1246/bcsj.20180210
5. Guliyev, R.; Coskun, A.; Akkaya, E. U. *J. Am. Chem. Soc.* **2009,** *131,* 9007–9013. doi:10.1021/ja902584a
6. Woodford, C. R.; Frady, E. P.; Smith, R. S.; Morey, B.; Canzi, G.; Palida, S. F.; Araneda, R. C.; Kristan, W. B., Jr.; Kubiak, C. P.; Miller, E. W.; Tsien, R. Y. *J. Am. Chem. Soc.* **2015,** *137,* 1817–1824. doi:10.1021/ja510602z
7. Escudero, D. *Acc. Chem. Res.* **2016,** *49,* 1816–1824. doi:10.1021/acs.accounts.6b00299
8. Saha, M. L.; Yan, X.; Stang, P. J. *Acc. Chem. Res.* **2016,** *49,* 2527–2539. doi:10.1021/acs.accounts.6b00416
9. Mahendran, V.; Pasumpon, K.; Thimmarayaperumal, S.; Thilagar, P.; Shanmugam, S. *J. Org. Chem.* **2016,** *81,* 3597–3602. doi:10.1021/acs.joc.6b00267
10. Sandeep, A.; Praveen, V. K.; Kartha, K. K.; Karunakaran, V.; Ajayaghosh, A. *Chem. Sci.* **2016,** *7,* 4460–4467. doi:10.1039/c6sc00629a
11. Black, H. T.; Pelse, I.; Wolfe, R. M. W.; Reynolds, J. R. *Chem. Commun.* **2016,** *52,* 12877–12880. doi:10.1039/c6cc06443d
12. Ji, L.; Griesbeck, S.; Marder, T. B. *Chem. Sci.* **2017,** *8,* 846–863. doi:10.1039/c6sc04245g
13. Xu, Y.; Yu, S.; Chen, Q.; Chen, X.; Li, Y.; Yu, X.; Pu, L. *Chem. – Eur. J.* **2016,** *22,* 12061–12067. doi:10.1002/chem.201601540
14. Zhou, J.; Outlaw, V. K.; Townsend, C. A.; Bragg, A. E. *Chem. – Eur. J.* **2016,** *22,* 15212–15215. doi:10.1002/chem.201603284
15. Lin, S.-L.; Chan, L.-H.; Lee, R.-H.; Yen, M.-Y.; Kuo, W.-J.; Chen, C.-T.; Jeng, R.-J. *Adv. Mater. (Weinheim, Ger.)* **2008,** *20,* 3947–3952. doi:10.1002/adma.200801023
16. Park, I. S.; Komiyama, H.; Yasuda, T. *Chem. Sci.* **2017,** *8,* 953–960. doi:10.1039/c6sc03793c
17. Duan, C.; Li, J.; Han, C.; Ding, D.; Yang, H.; Wei, Y.; Xu, H. *Chem. Mater.* **2016,** *28,* 5667–5679. doi:10.1021/acs.chemmater.6b01691
18. Huang, J.-J.; Hung, Y.-H.; Ting, P.-L.; Tsai, Y.-N.; Gao, H.-J.; Chiu, T.-L.; Lee, J.-H.; Chen, C.-L.; Chou, P.-T.; Leung, M.-k. *Org. Lett.* **2016,** *18,* 672–675. doi:10.1021/acs.orglett.5b03631
19. Zhang, Q.; Li, J.; Shizu, K.; Huang, S.; Hirata, S.; Miyazaki, H.; Adachi, C. *J. Am. Chem. Soc.* **2012,** *134,* 14706–14709. doi:10.1021/ja306538w
20. Feuillastre, S.; Pauton, M.; Gao, L.; Desmarchelier, A.; Riives, A. J.; Prim, D.; Tondelier, D.; Geffroy, B.; Muller, G.; Clavier, G.; Pieters, G. *J. Am. Chem. Soc.* **2016,** *138,* 3990–3993. doi:10.1021/jacs.6b00850
21. Hirai, H.; Nakajima, K.; Nakatsuka, S.; Shiren, K.; Ni, J.; Nomura, S.; Ikuta, T.; Hatakeyama, T. *Angew. Chem., Int. Ed.* **2015,** *54,* 13581–13585. doi:10.1002/anie.201506335
22. Sasabe, H.; Hayasaka, Y.; Komatsu, R.; Nakao, K.; Kido, J. *Chem. – Eur. J.* **2017,** *23,* 114–119. doi:10.1002/chem.201604303
23. Yao, L.; Zhang, S.; Wang, R.; Li, W.; Shen, F.; Yang, B.; Ma, Y. *Angew. Chem., Int. Ed.* **2014,** *53,* 2119–2123. doi:10.1002/anie.201308486
24. Suzuki, K.; Kubo, S.; Shizu, K.; Fukushima, T.; Wakamiya, A.; Murata, Y.; Adachi, C.; Kaji, H. *Angew. Chem., Int. Ed.* **2015,** *54,* 15231–15235. doi:10.1002/anie.201508270
25. Mishra, A.; Fischer, M. K. R.; Bäuerle, P. *Angew. Chem., Int. Ed.* **2009,** *48,* 2474–2499. doi:10.1002/anie.200804709
26. Ooyama, Y.; Harima, Y. *Eur. J. Org. Chem.* **2009,** 2903–2934. doi:10.1002/ejoc.200900236
27. Li, X.; Zheng, Z.; Jiang, W.; Wu, W.; Wang, Z.; Tian, H. *Chem. Commun.* **2015,** *51,* 3590–3592. doi:10.1039/c4cc08539f
28. Kakiage, K.; Aoyama, Y.; Yano, T.; Oya, K.; Kyomen, T.; Hanaya, M. *Chem. Commun.* **2015,** *51,* 6315–6317. doi:10.1039/c5cc00464k
29. Wu, J.; Li, G.; Zhang, L.; Zhou, G.; Wang, Z.-S. *J. Mater. Chem. A* **2016,** *4,* 3342–3355. doi:10.1039/c5ta09763k
30. Gao, Y.; Li, X.; Hu, Y.; Fan, Y.; Yuan, J.; Robertson, N.; Hua, J.; Marder, S. R. *J. Mater. Chem. A* **2016,** *4,* 12865–12877. doi:10.1039/c6ta05588e
31. Yao, Z.; Zhang, M.; Li, R.; Yang, L.; Qiao, Y.; Wang, P. *Angew. Chem., Int. Ed.* **2015,** *54,* 5994–5998. doi:10.1002/anie.201501195
32. Brogdon, P.; Giordano, F.; Puneky, G. A.; Dass, A.; Zakeeruddin, S. M.; Nazeeruddin, M. K.; Grätzel, M.; Tschumper, G. S.; Delcamp, J. H. *Chem. – Eur. J.* **2016,** *22,* 694–703. doi:10.1002/chem.201503187
33. Ooyama, Y.; Inoue, S.; Nagano, T.; Kushimoto, K.; Ohshita, J.; Imae, I.; Komaguchi, K.; Harima, Y. *Angew. Chem., Int. Ed.* **2011,** *50,* 7429–7433. doi:10.1002/anie.201102552
34. Ooyama, Y.; Sato, T.; Harima, Y.; Ohshita, J. *J. Mater. Chem. A* **2014,** *2,* 3293–3296. doi:10.1039/c3ta15067d
35. Sumalekshmy, S.; Gopidas, K. R. *J. Phys. Chem. B* **2004,** *108,* 3705–3712. doi:10.1021/jp022549l
36. Sumalekshmy, S.; Gopidas, K. R. *New J. Chem.* **2005,** *29,* 325–331. doi:10.1039/b409411e
37. Sumalekshmy, S.; Gopidas, K. R. *Photochem. Photobiol. Sci.* **2005,** *4,* 539–546. doi:10.1039/b503251b
38. Dias, F. B.; Pollock, S.; Hedley, G.; Pålsson, L.-O.; Monkman, A.; Perepichka, I. I.; Perepichka, I. F.; Tavasli, M.; Bryce, M. R. *J. Phys. Chem. B* **2006,** *110,* 19329–19339. doi:10.1021/jp0643653
39. Zhao, G.-J.; Chen, R.-K.; Sun, M.-T.; Liu, J.-Y.; Li, G.-Y.; Gao, Y.-L.; Han, K.-L.; Yang, X.-C.; Sun, L. *Chem. – Eur. J.* **2008,** *14,* 6935–6947. doi:10.1002/chem.200701868
40. Aronica, C.; Venancio-Marques, A.; Chauvin, J.; Robert, V.; Lemercier, G. *Chem. – Eur. J.* **2009,** *15,* 5047–5055. doi:10.1002/chem.200802325

41. Butler, R. S.; Cohn, P.; Tenzel, P.; Abboud, K. A.; Castellano, R. K. *J. Am. Chem. Soc.* **2009,** *131,* 623–633. doi:10.1021/ja806348z
42. Ooyama, Y.; Ito, G.; Kushimoto, K.; Komaguchi, K.; Imae, I.; Harima, Y. *Org. Biomol. Chem.* **2010,** *8,* 2756–2770. doi:10.1039/c003526b
43. Enoki, T.; Matsuo, K.; Ohshita, J.; Ooyama, Y. *Phys. Chem. Chem. Phys.* **2017,** *19,* 3565–3574. doi:10.1039/c6cp08573c
44. Lippert, E. *Z. Naturforsch., A: Astrophys., Phys. Phys. Chem.* **1955,** *10,* 541–545. doi:10.1515/zna-1955-0707
45. Mataga, N.; Kaifu, Y.; Koizumi, M. *Bull. Chem. Soc. Jpn.* **1956,** *29,* 465–470. doi:10.1246/bcsj.29.465
46. Makitra, R. G. *Reichardt, C., Solvents and Solvent Effects in Organic Chemistry, Weinheim: Wiley-VCH, 2003, 630 p.;* Russian Journal of General Chemistry, Vol. 75; Springer Science and Business Media LLC, 2005; pp 664 ff. doi:10.1007/s11176-005-0294-y
47. Both the geometry optimization and energy calculation were performed by employing density functional theory (DFT), at the level of B3LYP/6-31G(d,p) on the Gaussian09 program package, Gaussian 09, *Revision A.02,* Gaussian, Inc., Wallingford, CT, 2009.
48. Langhals, H.; Potrawa, T.; Nöth, H.; Linti, G. *Angew. Chem., Int. Ed. Engl.* **1989,** *28,* 478–480. doi:10.1002/anie.198904781
49. Yeh, H.-C.; Wu, W.-C.; Wen, Y.-S.; Dai, D.-C.; Wang, J.-K.; Chen, C.-T. *J. Org. Chem.* **2004,** *69,* 6455–6462. doi:10.1021/jo049512c
50. Ooyama, Y.; Okamoto, T.; Yamaguchi, T.; Suzuki, T.; Hayashi, A.; Yoshida, K. *Chem. – Eur. J.* **2006,** *12,* 7827–7838. doi:10.1002/chem.200600094
51. Ooyama, Y.; Hagiwara, Y.; Oda, Y.; Fukuoka, H.; Ohshita, J. *RSC Adv.* **2014,** *4,* 1163–1167. doi:10.1039/c3ra45785k

License and Terms

BEILSTEIN JOURNAL OF ORGANIC CHEMISTRY

Functional panchromatic BODIPY dyes with near-infrared absorption: design, synthesis, characterization and use in dye-sensitized solar cells

Quentin Huaulmé[1], Cyril Aumaitre[1], Outi Vilhelmiina Kontkanen[2], David Beljonne[2], Alexandra Sutter[3], Gilles Ulrich[3], Renaud Demadrille[*1] and Nicolas Leclerc[*3]

Full Research Paper

Open Access

Address:
[1]CEA, Univ. Grenoble Alpes, CNRS, IRIG, SyMMES, F-38000 Grenoble, France, [2]Chimie des Matériaux Nouveaux & Centre d'Innovation et de Recherche en Matériaux Polymères Université de Mons - UMONS / Materia Nova Place du Parc, 20, B-7000 Mons, Belgium and [3]ICPEES – UMR7515, CNRS-Université de Strasbourg, 25 rue Becquerel, 67087 Strasbourg CEDEX 02, France

Email:
Renaud Demadrille[*] - renaud.demadrille@cea.fr; Nicolas Leclerc[*] - leclercn@unistra.fr

* Corresponding author

Keywords:
boron-dipyrromethene; BODIPY; dye-sensitized solar cells; near-infrared absorbers; organic dyes

Beilstein J. Org. Chem. **2019,** *15,* 1758–1768.
doi:10.3762/bjoc.15.169

Received: 12 April 2019
Accepted: 10 July 2019
Published: 24 July 2019

This article is part of the thematic issue "Dyes in modern organic chemistry".

Guest Editor: H. Ihmels

Abstract

We report two novel functional dyes based on a boron-dipyrromethene (BODIPY) core displaying a panchromatic absorption with an extension to the near-infrared (NIR) range. An innovative synthetic approach for preparing the 2,3,5,6-tetramethyl-BODIPY unit is disclosed, and a versatile way to further functionalize this unit has been developed. The optoelectronic properties of the two dyes were computed by density functional theory modelling (DFT) and characterized through UV–vis spectroscopy and cyclic voltammetry (CV) measurements. Finally, we report preliminary results obtained using these functional dyes as photosensitizers in dye-sensitized solar cells (DSSCs).

Introduction

The past two decades have witnessed tremendous efforts to develop alternative photovoltaic (PV) technologies. Among them, dye-sensitized solar cells (DSSCs) display numerous advantages compared to its fully organic counterpart, i.e., bulk heterojunction solar cells, or other hybrid PV technologies such as perovskite solar cells. DSSCs can display satisfactory power conversion efficiencies (PCE) in the range of 10 to 14% [1-3] but also a long-term stability when specific electrolytes based on ionic liquids are employed [4,5]. Besides, this technology enables the fabrication of solar panels that can be prepared

semi-transparent, colorful, and out of non-toxic constituents [6]. Historically, Ru(II)–polypyridyl complexes were the most used dyes as photosensitizers in DSSCs (N719 or N749 Black Dye) [7] but these molecules reveal low absorption coefficients over the visible range. Furthermore, they contain a rare and a relatively high-cost element (Ru) and their plausible toxicity restrains their development at the industrial level. For these reasons, in the last decade, metal-free organic dyes based on donor–(π-spacer)–acceptor structure have hence been extensively investigated and screened as sensitizers in DSSCs. Among the hundreds of dyes developed so far for this application, only few can show panchromatic absorption [8,9]. To improve the photogeneration of current, and hence the efficiency of DSSCs, the development of new dye molecules better matching the solar emission spectrum or exhibiting absorption in the near-infrared (NIR) range could be a fruitful strategy.

Several families of molecules displaying an infrared absorption have been investigated in the last decade, such as phthalocyanines [10,11], organic push–pull compounds [12], and boron-dipyrromethene [13] (BODIPY®). BODIPY dyes are one of the most extensively studied class of fluorophores due to their unique properties, including high absorption coefficients in the visible and NIR ranges, high fluorescence quantum yields, and high stability in various media. More importantly, they display a very versatile chemistry, allowing the fine tuning of all their physical and optical properties [14]. They hence have found applications in various fields, such as lasers dyes [15], (bio)-labeling [16,17], photodynamic therapy [18], or even bulk heterojunction solar cells [19,20] or DSSCs [21,22].

In this articl we report an innovative synthetic approach for synthesizing 2,3,5,6-tetramethyl-BODIPY compounds and a way to further functionalize such cores has been developed. The optoelectronic properties of the functional molecules were investigated using UV–vis spectroscopy, and we show that they can absorb light up to 900 nm in solution and 1000 nm in solid state, after grafting on anatase-TiO_2 mesoporous films. The cyclic voltammetry (CV) measurements indicate that the compounds have HOMO and LUMO energy levels suitable for an application in DSSCs, in rather good agreement with the values obtained from DFT calculations. Finally, we report preliminary results employing these molecules as photosensitizers in dye solar cells with iodine-based liquid electrolytes. We show that the limited performances of these new BODIPY derivatives arise from their deep LUMO energy level. In terms of energy, the latter lies close to the conduction band of the electron-transporting oxide, limiting therefore the driving force of electronic injection, and hence the overall efficiency of the resulting solar cell.

Results and Discussion

1. Design and DFT calculations

In many opto-electronic devices the light-absorption properties of the semiconductors are a critical parameter. This is particularly the case when solar energy conversion applications are targeted. For instance, in order to maximize the photocurrent density in a DSSC device, the sensitizer has to display high molar absorption coefficients, ideally along the entire visible range. Additionally, it must display appropriate positioning of frontier molecular orbitals (highest occupied molecular orbital/lowest unoccupied molecular orbital, HOMO/LUMO) energy levels with respect to the conduction band (CB) of the metal oxide and the redox potential of the electrolyte. Abundant literature on BODIPY derivatives allowed us to identify a chemical approach to fulfill those criteria, i.e., the introduction of an electron rich unit at the 3rd and 5th positions of the BODIPY core via a vinyl spacer [14,21,23,24]. Introduction of such units on those positions is known to lead to a larger bathochromic shift of the $S_0 \rightarrow S_1$ absorption band than the same substitution on its 2nd and 6th positions [25]. A thiophene-triphenylamine unit was selected among the reported electron-donating units, due to its reversible redox properties and high electron-donating strength (see Figure 1) [26]. In order to promote the delocalization from the electron-donating unit to the electron-withdrawing and anchoring group located on its 8 position, a 2,3,5,6-tetramethyl-BODIPY derivative has been designed (see Figure 1). Indeed, most of the BODIPY based materials, used in organic semiconducting applications, exhibit methyl groups in the 1,7-positions. However, such groups in these positions hinder sterically the position 8 of BODIPY cores and therefore lead to a severe twist of the aromatic unit grafted on. Removing these methyl groups is an effective way to reduce the dihedral angle between the meso substituent and the BODIPY core by lowering the steric hindrance between the two latter. It has been previously reported that a better molecular planarity usually originates a higher charge injection efficiency [27]. Furthermore, it has been reported that introduction of hydrophobic alkyl chains on a sensitizer is a way to improve the open-circuit voltage (V_{oc}), by reducing the electronic recombination rate at the electrolyte/semi-conducting oxide interface [28]. To probe the validity of this concept for a BODIPY derivative, we decided to synthetize the two molecular structures disclosed in Figure 1, namely **BOD-TTPA-alk** and **BOD-TTPA**.

To support our molecular design, and especially to have better insight on the electronic structure and optical properties of the dyes, we performed (time-dependent) density functional theory (TD-DFT) calculations on the four representative molecules displayed in Figure 2: Dyes (**1** and **3**) vs (**2** and **4**) differ by the position (2,6 or 1,7) of the methyl groups on the BODIPY core,

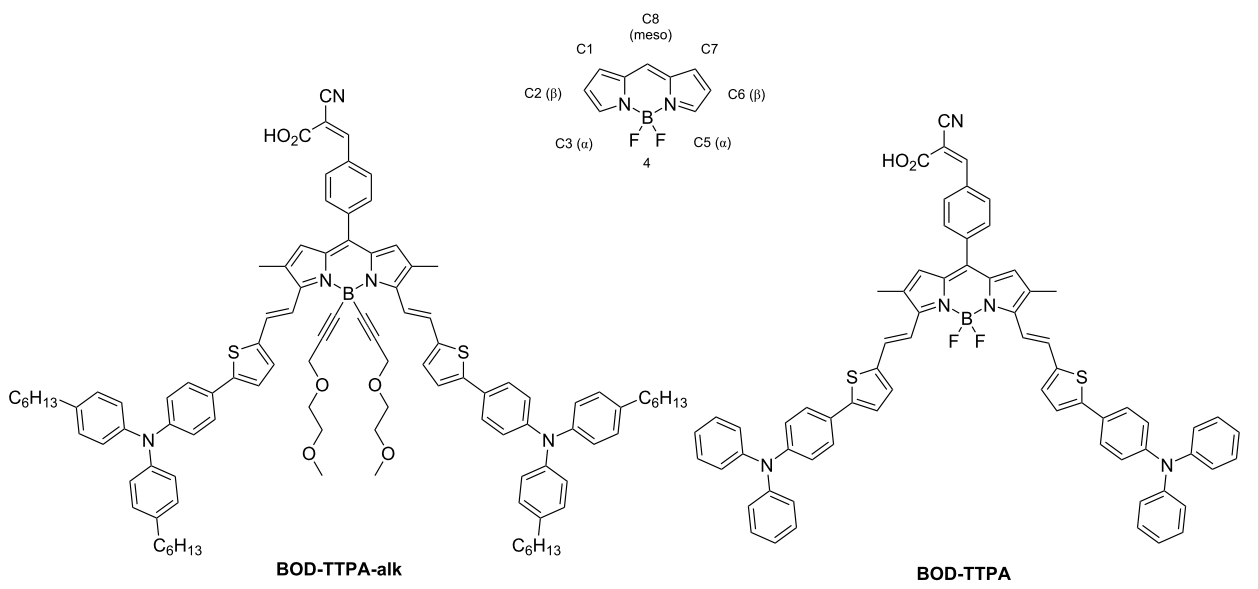

Figure 1: Molecular structures of the two target compounds **BOD-TTPA-alk** and **BOD-TTPA,** and the chemical structure of a BODIPY core displaying its positions numbering.

while dyes (**1** and **2**) vs (**3** and **4**) differ by the presence (or not) of a triphenylamine donor group on the thiophene ring. As we are dealing with charge-transfer electronic excitations, we have adopted a tuned range-separated CAM-B3LYP functional and the polarizable continuum model (PCM) to account for (implicit) solvent effects (in THF).

The one-electron energy diagram reported in Figure 2 shows that: (i) Grafting the triphenylamine donor moieties on the thiophene-vinylene bridge only slightly (by ca. 0.1 eV) lowers the ionization potential of the dyes, compare (**1**,**2**) to (**3**,**4**); this is explained by the fact that the HOMO molecular orbital mostly spreads on the BODIPY-vinylthiophene core of the molecules, with only slight contributions from the TPA units (ii) The position of the methyl groups has by far a larger impact on the electron affinity of the molecules, which is substantially increased when going from **2** to **1**, and from **4** to **3**. This is clearly not a direct electronic effect but rather results from the close to orthogonal orientation of the anchoring groups induced by steric effects in **2** and **4**. As a result, while the LUMO orbital largely extends through the BODIPY unit towards the cyanoacrylic acid anchors in the case of **1** and **3**, it is completely confined to the BODIPY-vinylthiophene core in **2** and **4**, explaining the deeper unoccupied levels in the former molecules.

Thus, our calculations suggest that, in case of an allowed HOMO–LUMO transition, **1** and **3** should show a bathochromically shifted optical absorption spectrum, thereby hopefully allowing for a more efficient sunlight absorption, yet also a reduced energy driving force for charge separation at the TiO_2 surface. To check this hypothesis, we performed TD-DFT simulations of the optical absorption spectra of the 4 representative dyes. The results reported in Figure 3 are fully consistent with the predictions from the one-electron picture. There is a substantial red shift of the lowest optical absorption band, from ≈750 nm in **2** to ≈850 nm in **1** by moving the methyl groups from (1,7) to (2,6) positions, in line with the increased electronic delocalization over the anchoring groups. An additional virtue of the placement of the methyl groups in positions (2,6) is to extend the absorption range of the dyes across the whole visible range. Very similar effects are observed for the TPA-free molecules, except for an overall blue shift of the main absorption bands resulting from the reduced size of the π-electronic system.

2. Synthesis

The synthesis of the target materials is schemed in Figure 4. To introduce the selected substitution pattern, 2,3-dimethylpyrrole **1** is first synthesized through a Trofimov reaction in a one-pot two-step reaction [29]. The condensation of the aforementioned pyrrole on *para*-iodobenzoyl chloride affords the corresponding dipyrromethenium chloride, which was then converted into its BODIPY analogue **2** through complexation by $BF_3{\cdot}OEt_2$ in basic media. Regioselective introduction of distyryl substituents is achieved via Knoevenagel-type condensation in the presence of piperidine using aldehyde derivatives **3** and **4** whose synthesis are described in Supporting Information File 1. This condensation reaction affords compounds **5** and **6** with a slight variation of their pendant alkyl chains. The stereoisomerism of

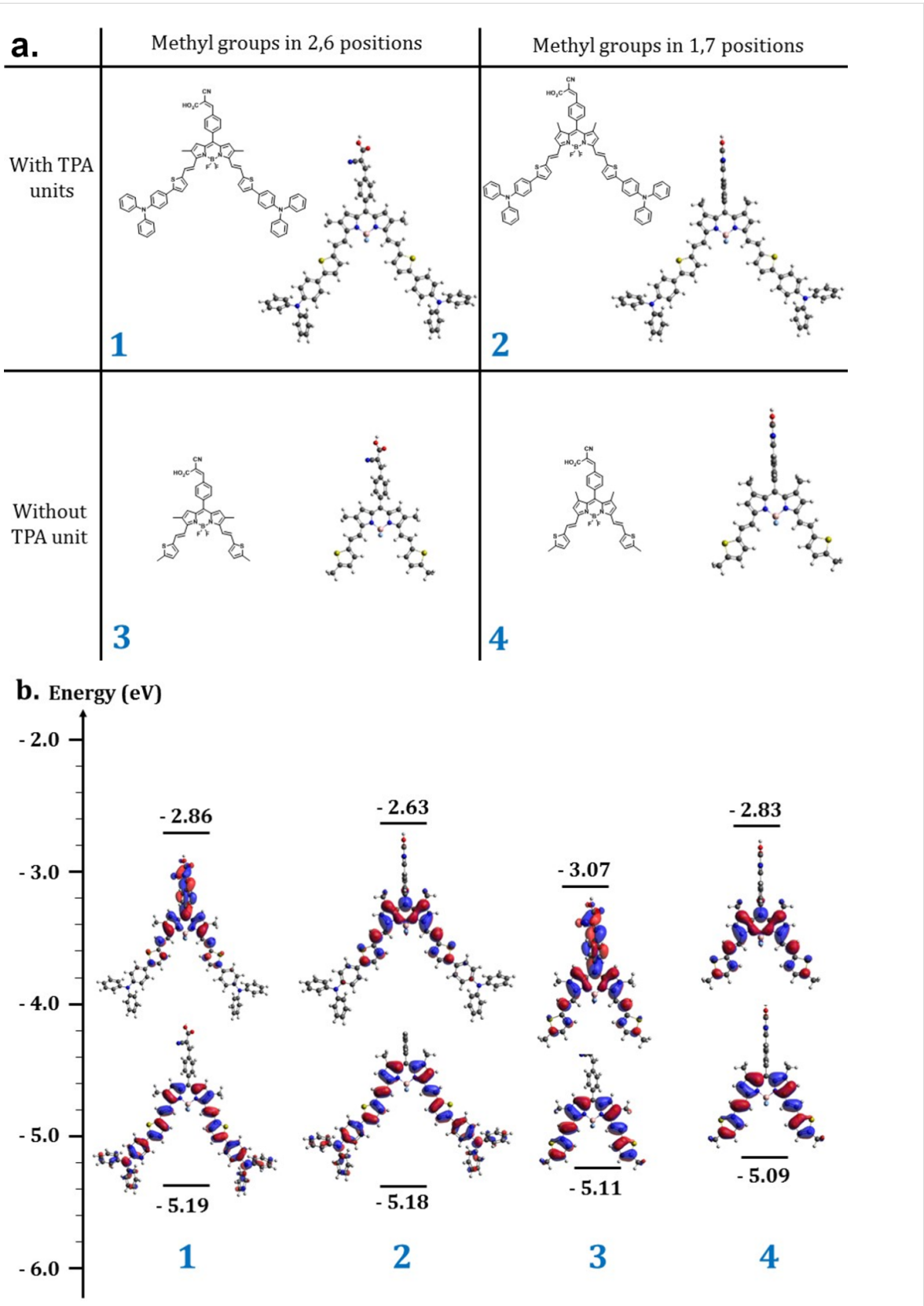

Figure 2: a) Geometrical optimization of four representative BODIPY-based materials for DSSCs application. b) Frontiers molecular orbitals repartition and their predicted energy values for the selected four representative BODIPY-based dyes.

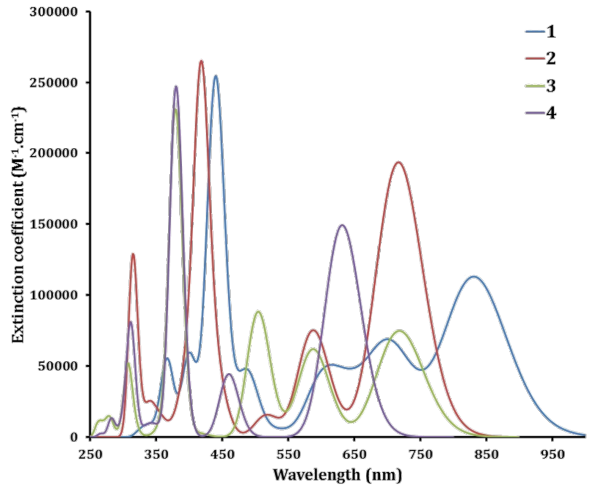

Figure 3: Predicted absorption spectra of the four dyes.

the resulting distyryl compound (*trans*) has been unambiguously attributed by ^{1}H NMR (see Figures **S9** and **S11** in Supporting Information File 1), whose spectra feature characteristic constant couplings of 16.2 and 16.1 Hz. It is worth mentioning that the fluorine substitution was performed on the boron center after introduction of the styryl residues, introduction prior to the Knoevenagel reaction is known to impede it [30]. The introduction of the aldehyde moiety is carried out through catalytic carbo-palladation reaction using molecular carbon monoxide in the presence of methyl formiate as hydrogen source in modest yield (35% and 19% for **8** and **10**, respectively) due to the formation of a relatively large amount of dehalogenation side-product. Finally, a Knoevenagel condensation in the presence of cyanoacetic acid and piperidine is performed to lead to the targeted compounds **BOD-TTPA-alk** and **BOD-TTPA**.

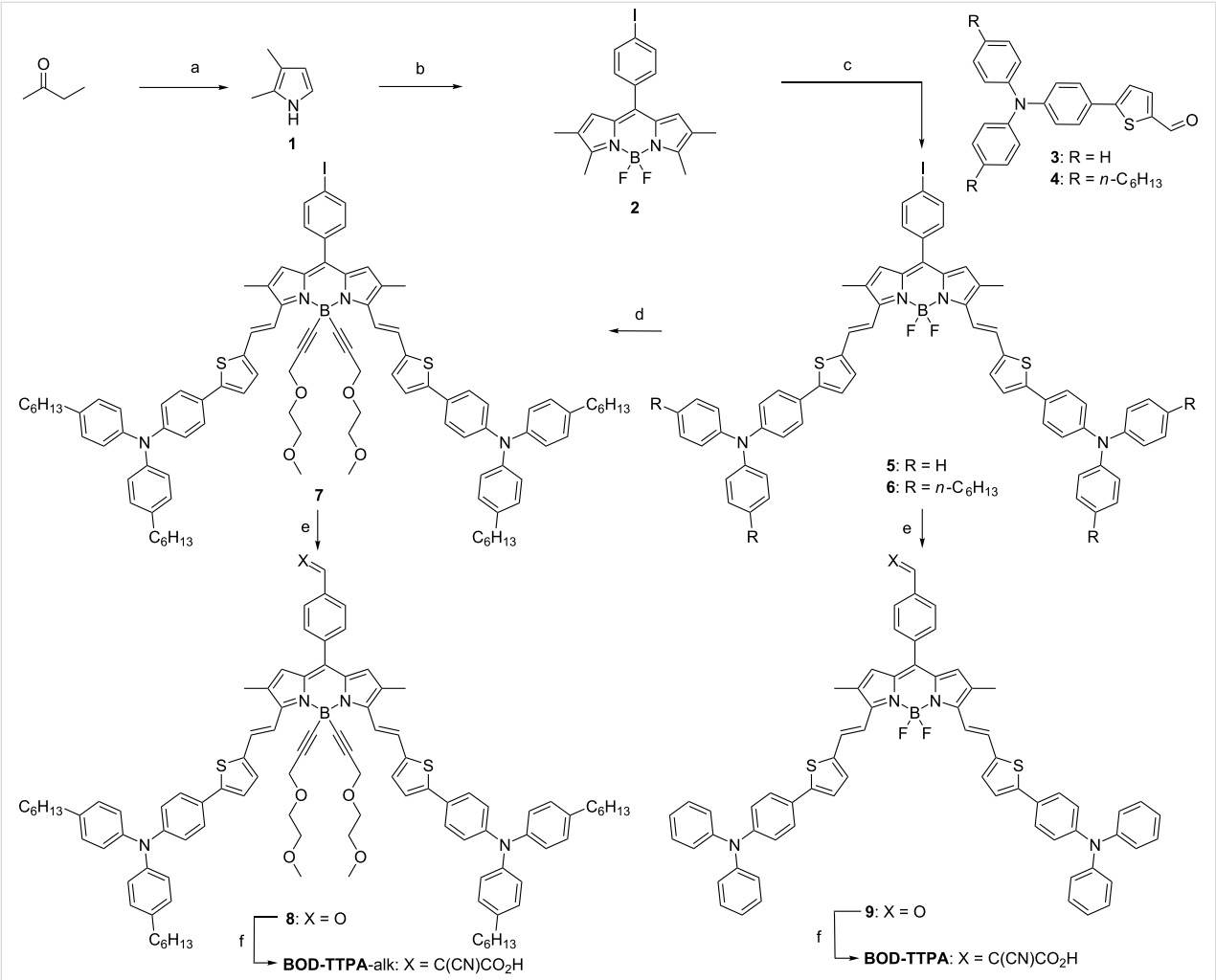

Figure 4: Synthetic scheme of the selected materials. a) hydroxylamine hydrochloride, $NaHCO_3$, DMSO, 60 °C then acetylene, KOH, DMSO, 110 °C, 24% over the two steps; b) 4-iodobenzoyl chloride, DCM, rt then DDQ, DCM, rt then NEt_3, $BF_3{\cdot}OEt_2$, 0 °C to rt, 35%; c) piperidine, cat. PTSA, toluene, 130 °C, **5**: 35%, **6**: 30%; d) (3-(2-methoxyethoxy)prop-1-yn-1-yl)magnesium bromide, THF, 60 °C, 85%; e) carbon monoxide, sodium formiate, $[Pd(PPh_3)_2Cl_2]$, anhydrous DMF, 100 °C, **8**: 19%, **9**: 35%; f) cyanoacetic acid, piperidine, MeCN, $CHCl_3$, 80 °C, **BOD-TTPA**: 34%, **BOD-TTPA-alk**: 26%.

3. Optical properties

The optical properties of compounds **BOD-TTPA-alk** and **BOD-TTPA** were first evaluated in diluted (≈10^{-6} M in THF) solution (see Figure 5). They both display two intense absorption bands. At lower energy, the absorption band displays a rather large and high extinction coefficient ($5{\cdot}10^{-4}$ $M^{-1}cm^{-1}$) band attributed to the $S_0 \rightarrow S_1$ transition of the BODIPY core, and still displays its characteristic shoulder at higher energy [14]. Another intense absorption band is located around 400 nm and is attributed to the $\pi \rightarrow \pi^*$ transition of the triphenylamine thiophene residues. It is worth noting that almost no difference is observed between those two materials, which is consistent with their identical electronic structure. As often with such distyryl-BODIPY derivatives [19,25], no clear cut-off of absorbance is observed in the whole part of the visible range, leading to a panchromatic absorption. The absorption is not limited to the visible domain, indeed the compound **BOD-TTPA-alk** and **BOD-TTPA** exhibit a λ_{max} in solution located at 771 nm and 768 nm, respectively, with an absorption edge close to 900 nm. The absorption in the NIR region is a peculiar property that is of course a considerable advantage for solar cell applications.

With the aim of investigating the behavior of those dyes once adsorbed on mesoporous TiO_2, sensitization has been performed on 2 µm thick TiO_2 mesoporous layer (see Figure 5b and c). To prevent dye aggregation on the surface of the semiconducting oxide, and to mimic the real conditions of use in solar cells, chenodeoxycholic acid (CDCA) was employed as co-sensitizer and hence added to the sensitization solution [31]. For the dyeing solutions the concentration of the dye was 1 mM and the concentration of CDCA was 10 mM in a chloroform/ethanol mixture (1:1 in volume). The absorbance spectra of the resulting sensitized TiO_2 layers are recorded and presented in Figure 5b.

For both dyes, grafting them on the surface clearly impacts the absorption bands attributed to the BODIPY part of the systems.

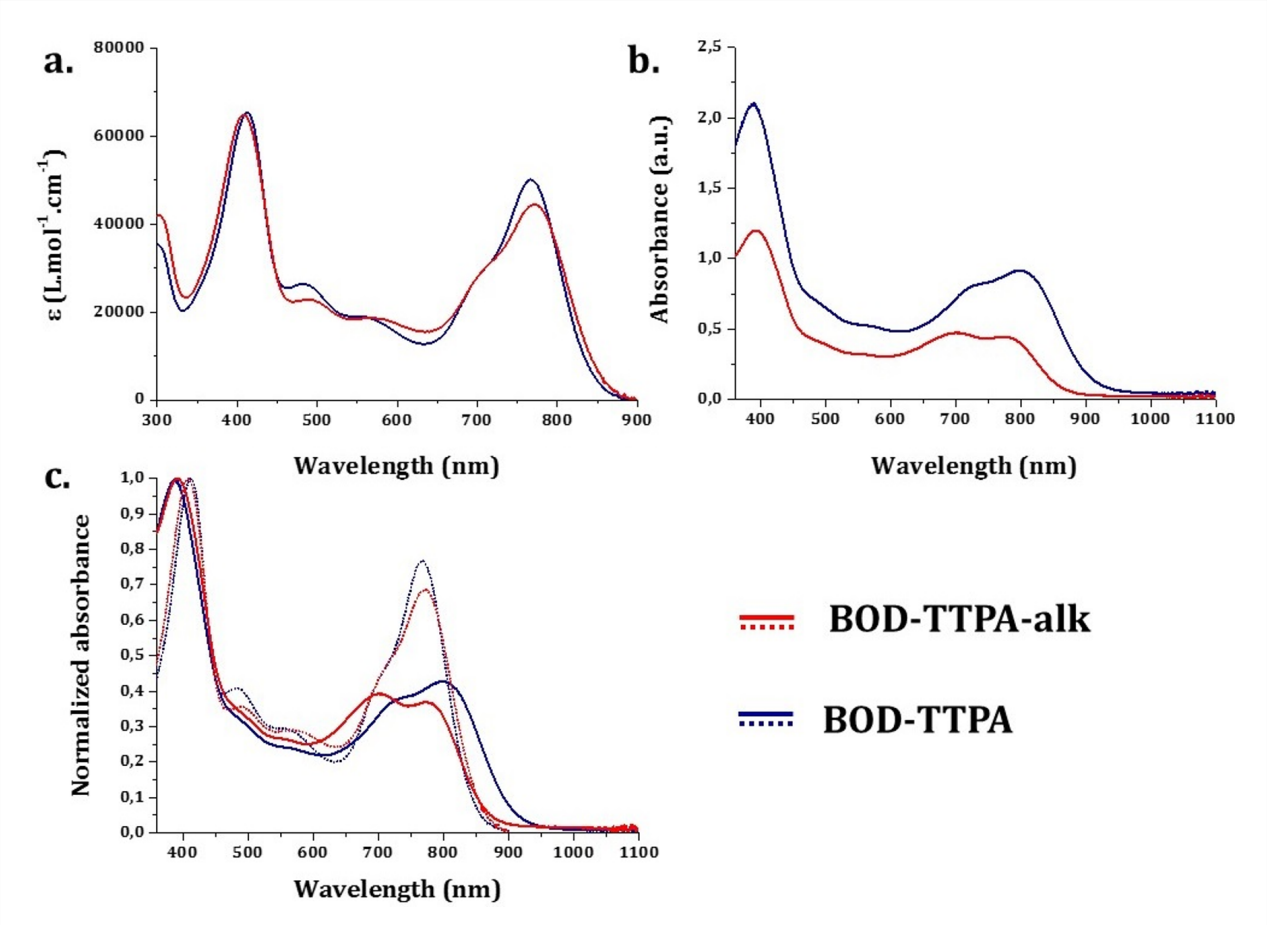

Figure 5: a) Absorption spectra of compounds **BOD-TTPA-alk** and **BOD-TTPA** (THF, ≈10^{-6} M, 25 °C). b) Absorbance spectra of 2 µm thick mesoporous TiO_2 sensitized in a solution of dye/CDCA (1:10, molar ratio). c) Normalized absorbance spectra of **BOD-TTPA-alk** (red traces) and **BOD-TTPA** (blue traces), both in diluted solution (aerated THF, ≈10^{-6} M, 25 °C – dashed lines) and once adsorbed on 2 µm thick mesoporous TiO_2 (solid lines).

The absorption coefficient of the lower energy absorption band, attributed to the $S_0 \rightarrow S_1$ transition, is reduced and a higher energy band around 700 nm increases in intensity. This last one is more likely attributed to a conformationally restricted form of the dye once adsorbed which shows an absorption value closed to mono-styryl species, thus reinforcing the panchromatic absorption of this dye. As long as **BOD-TTPA-alk** is concerned, no significant shift of the lower energy band is observed (see Table 1 and Figure 5a). This suggests no self-aggregation of the alkylated dye occurs on the oxide surface, which can be explained by the presence of the co-adsorbent CDCA, and of the multiple alkyl chain substitution of the TPA units. On the other hand, a bathochromic shift of the absorption profile of **BOD-TTPA** is observed from diluted solution to the anchored dye (see Figure 5a). Despite the same amount of CDCA in the dyeing solution (10 molar equivalents), this result suggests a higher tendency for π stacking interactions. Once anchored, **BOD-TTPA** exhibits consequently a broader absorption profile than its alkylated counterpart **BOD-TTPA-alk**.

Furthermore, the measured intensity of absorbance of the sensitized TiO_2 layer is much higher for **BOD-TPA** than **BOD-TTPA-alk** in spite of the fact that the dyeing was performed with solutions containing exactly the same concentration of the dyes. The thickness of the aforementioned TiO_2 layer being identical and the two dyes **BOD-TTPA-alk** and **BOD-TTPA** displaying very similar absorption coefficient (see Table 1), sensitization of mesoporous TiO_2 will be more effective for **BOD-TTPA** than **BOD-TTPA-alk**. This lower absorption originating from a lower grafting level may arise from the overall size of the molecule **BOD-TTPA-alk** that displays 4 alkyl chains and 2 ethylene glycol chains. The bigger size of **BOD-TTPA-alk** can eventually prevents its diffusion through all the pores of the TiO_2 layer or decreases the density of grafted molecules due to steric hindrance.

4. Electrochemical characterization

Cyclic voltammetry of both BODIPY dyes was carried out in deoxygenated DCM solutions containing tetrabutylammonium hexafluorophosphate as salt (see Figure S24 and S25 in Supporting Information File 1), to investigate their oxidation and reduction processes as well as to determine the energy levels of their highest occupied molecular orbital (HOMO) and lower unoccupied molecular orbital (LUMO). All the redox potentials were calibrated with respect to Ferrocene (Fc), assuming that $E(Fc/Fc^+)$ = 0.40 V with respect to SCE (see experimental details). The low solubility of the BOD-TTPA derivative makes this material much more difficult to characterize than its alkylated counterpart. However, both dyes exhibit similar first oxidation potentials about 0.6 V and 0.55 V for **BOD-TTPA** and **BOD-TTPA-alk**, respectively. Both processes are reversible. It worth noting that the **BOD-TTPA-alk** exhibits also a second reversible oxidation process at higher voltage of 0.8 V. Finally, for both dyes, a quasi-reversible reduction process could be observed at −0.6 V and −0.8 V for **BOD-TTPA** and **BOD-TTPA-alk**, respectively.

The HOMO and LUMO levels were determined by using the following equations (HOMO = E_{ox} + 4.4 eV) and (LUMO = E_{red} + 4.4 eV) where the onset potentials are in volts (vs SCE) and HOMO and LUMO are in electron volts [32]. We thus calculated HOMO and LUMO levels of −5.0 eV and −3.8 eV for **BOD-TTPA** against −4.95 eV and −3.6 eV for **BOD-TTPA-alk**. The small change of the HOMO energy levels is in line with the performed calculations (see section 1), where the HOMO molecular orbital is shown to be mostly spread on the BODIPY-vinylthiophene moieties of the dyes, with only slight contributions from the TPA units. The significant decrease in electronic affinity observed in **BOD-TTPA-alk** is likely due to the boron center alkylation. Similar effects have been already shown after fluorine substitution of BODIPY [33].

5. DSSCs fabrication and device performances

In order to investigate the photovoltaic performances of the two functional dyes **BOD-TTPA-alk** and **BOD-TTPA**, a set of DSSCs were fabricated following a procedure reported previously [4]. The $J(V)$ characteristics of the devices were recorded in dark and upon irradiation with a mask. For the measurements a solar simulator with AM 1.5G filter was used after calibration with a Silicon cell at 1000 W m^{-2}. For a direct comparison, we fabricated solar cells with the same photoelectrode composition consisting of a double layer TiO_2 (a 12 µm-thick transparent layer and a 4 µm-thick scattering layer) purchased

Table 1: Selected optical properties of compounds **BOD-TTPA-alk** and **BOD-TTPA**.

Compounds	$\lambda_{max}^{solution}$ (nm)	ε (L·mol^{-1}·cm^{-1}) at $\lambda_{max}^{solution}$	$\lambda_{onset}^{solution}$ (nm)	$\lambda_{max}^{TiO_2}$ (nm)	$\lambda_{onset}^{TiO_2}$ (cm)
BOD-TTPA-alk	409, 771	$6.49 \cdot 10^4$, $4.46 \cdot 10^4$	841	393, 700, 771	867
BOD-TTPA	411, 768	$6.52 \cdot 10^4$, $5.00 \cdot 10^4$	856	389, 801	907

from Solaronix. This thickness was selected on the basis of a previous study showing that thicker electrodes (typically above 12 µm) give rise to highest photocurrent density.

When dyes with low-lying LUMO energy levels are employed as sensitizers together with TiO_2 electrodes, the choice of the electrolyte is crucial. From CV experiments (see previous section) we found that the LUMO levels of the dyes are at −3.9 and −3.6 eV. In other words, they are located roughly 0.1–0.4 eV above the energy level of the conducting band of the oxide (which is around −4 eV). This alignment of the energy levels could be damaging to the electron injection process. Indeed, it is known that a minimum driving force of 0.15 eV (neglecting entropy changes during the light absorption) is required to efficiently inject photo excited electrons from the LUMO of the dyes in the CB of the oxide [34].

Usually iodine-based liquid electrolytes are comprising additives such as *tert*-butylpyridine (^{t}BP) which is known to shift the CB band of the oxide positively by creating a dipole effect at the surface of TiO_2. By suppressing this dipole effect, the CB of TiO_2 could be relocated deeper and this could facilitate the photo-injection process. Consequently, for preliminary investigations we prepared an electrolyte with a formulation close to the one of HI-30 commercialized by Solaronix. HI-30 electrolyte is known to be compatible with a large variety of organic dyes. We therefore designed a modified electrolyte inspired from HI-30 with the following composition: 0.5 M of butylmethylimidazolium iodide (BMII), 0.03 M of I_2 0.5 M of LiI, 0.1 M of guanidinium thiocyanate in a mixture of acetonitrile and 3-methoxyproprionitrile (85:15). Compared to classical electrolytes, in this formulation we removed ^{t}BP, hoping that the suppression of the interface dipole would shift the CB energy level of TiO_2 and, consequently, enhance injection process [35].

The *J*(V) curves of the devices containing compounds **BOD-TTPA-alk** and **BOD-TTPA** are reported in Figure 6. Selected photovoltaic parameters obtained from three different measurements for each dye are gathered in Table 2. **BOD-TTPA-alk** exhibits a maximum power conversion efficiency of 1.12% a short-circuit current (J_{sc}) of 4.70 mA·cm^{-2}, an open-circuit voltage (V_{oc}) of 0.37 V and a fill factor (FF) of 65%. On the other hand, **BOD-TTPA** displays a power conversion efficiency of 1.22%, along with a J_{sc} of 7.33 mA·cm^{-2}, a V_{oc} of 0.33 V and a FF of 51%. Despite being rather low compared to the performances of more conventional dyes, these results are quite consistent with previous reports on BODIPY sensitizers with absorption in the NIR region [36].

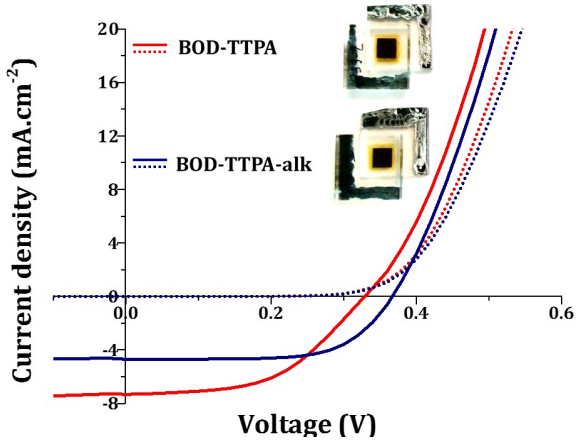

Figure 6: *J*(V) curves of the best performing DSSCs devices sensitized with compounds **BOD-TTPA-alk** (blue traces) and **BOD-TTPA** (red traces) in dark (dashed lines) and under AM1.5G conditions (solid lines). Light source: AM1.5G at 100 mW·cm^{-2}, electrolyte composition: 0.5 M of BMII, 0.03 M of I_2, 0.5 M of LiI, 0.1 M of guanidinium thiocyanate in a mixture of acetonitrile and 3-methoxyproprionitrile (85:15, v/v), electrodes: 12 µm mesoporous anatase TiO_2 + 4 µm TiO_2 scattering layer, dyeing bath: [Dye] = 0.2 mM, [CDCA] = 2 mM in $CHCl_3$/EtOH 1:1 (v/v)).

First, comparing the photovoltaic behavior of the two dyes one should note that the J_{sc} delivered by the solar cells are rather different (4.70 mA·cm^{-2} for **BOD-TTPA-alk** versus 7.33 mA·cm^{-2} for **BOD-TTPA**). The higher J_{sc} obtained with **BOD-TTPA** can be explained with the broader and more intense absorption in the NIR range once grafted on TiO_2 compared to its alkylated counterpart. Second, one can notice that the V_{oc} and FF recorded for devices sensitized with **BOD-TTPA-alk** are slightly higher compared to the ones prepared

Table 2: Photovoltaic parameters of compounds **BOD-TTPA-alk** and **BOD-TTPA** (light source: AM1.5G at 100 mW·cm^{-2}, electrolyte composition: 0.5 M of BMII, 0.03 M of I_2, 0.5 M of LiI, 0.1 M of guanidinium thiocyanate in a mixture of acetonitrile and 3-methoxyproprionitrile (85:15, v/v), electrodes: 12 µm mesoporous anatase TiO_2, + 4 µm TiO_2 scattering layer, dyeing bath: [Dye] = 0.2 mM, [CDCA] = 2 mM in $CHCl_3$/EtOH 1:1, v/v). Highest value and mean values over three measurements in parenthesis.

Dye	J_{sc} (mA·cm^{-2})	V_{oc} (V)	FF	PCE (%)
BOD-TTPA-alk	4.70 (4.64)	0.37 (0.37)	0.65 (0.64)	1.12 (1.12)
BOD-TTPA	7.33 (7.10)	0.33 (0.33)	0.51 (0.50)	1.22 (1.20)

out of **BOD-TTPA**. This could be explained by the presence of the alkyl chains on the TPA units that are known to prevent the redox mediator to interact with the TiO_2 surface thus reducing the probability to observe a recombination process between the photo-injected electrons and the iodide.

To confirm that the main factor limiting the device performances is the position of the LUMO level of these dyes with respect to the CB of the oxide, we investigated the effect of ^{t}BP content in the electrolyte. By adding ^{t}BP in the electrolyte one can tune the electronic properties, i.e., the CB energy level position of TiO_2 [31,37-39]. The effect is well-known, a negative dipole-related shift of the TiO_2 Fermi level occurs by ^{t}BP adsorption on the surface. As the LUMO levels of the dyes are estimated close to the CB Fermi level, the use of ^{t}BP should lead to a drop of the J_{sc} because of the reduction of the driving force for the injection. Simultaneously a rise of the V_{oc} is expected. A shift of CB energy level toward the vacuum level (i.e., away from the redox potential of the electrolyte) results in a higher open-circuit voltage (V_{oc}). Indeed, in DSSCs the V_{oc} is determined by the quasi-Fermi-level of the metal oxide semiconductor, which is correlated with its CB edge and electron density (see Figure 7).

Solar cells fabricated with various amount of ^{t}BP in the electrolyte were investigated (see Table S1 in Supporting Information File 1). It appears from Figure 7 that increasing the concentration of ^{t}BP implies, as expected, an increase of V_{oc}, from 328 mV to 460 mV for **BOD-TTPA-alk** and from 360 mV to 420 mV for **BOD-TTPA**. On the other hand, the J_{sc} values for **BOD-TTPA-alk** and **BOD-TTPA** all decrease from 7.33 to 0.88 mA·cm^{-2} and from 4.70 to 0.41 mA·cm^{-2}, respectively. This result unambiguously highlights that the shift of TiO_2 CB impedes the photo-injection of electrons [40]. This proves that the LUMO energy levels of the dyes **BOD-TTPA-alk** and **BOD-TTPA** are too close from the CB of the oxide. Despite a higher V_{oc}, the loss of J_{sc} is responsible for the overall decrease of the power conversion efficiencies.

Conclusion

We have designed, synthesized and characterized two novel functional BODIPY-based dyes showing intense panchromatic

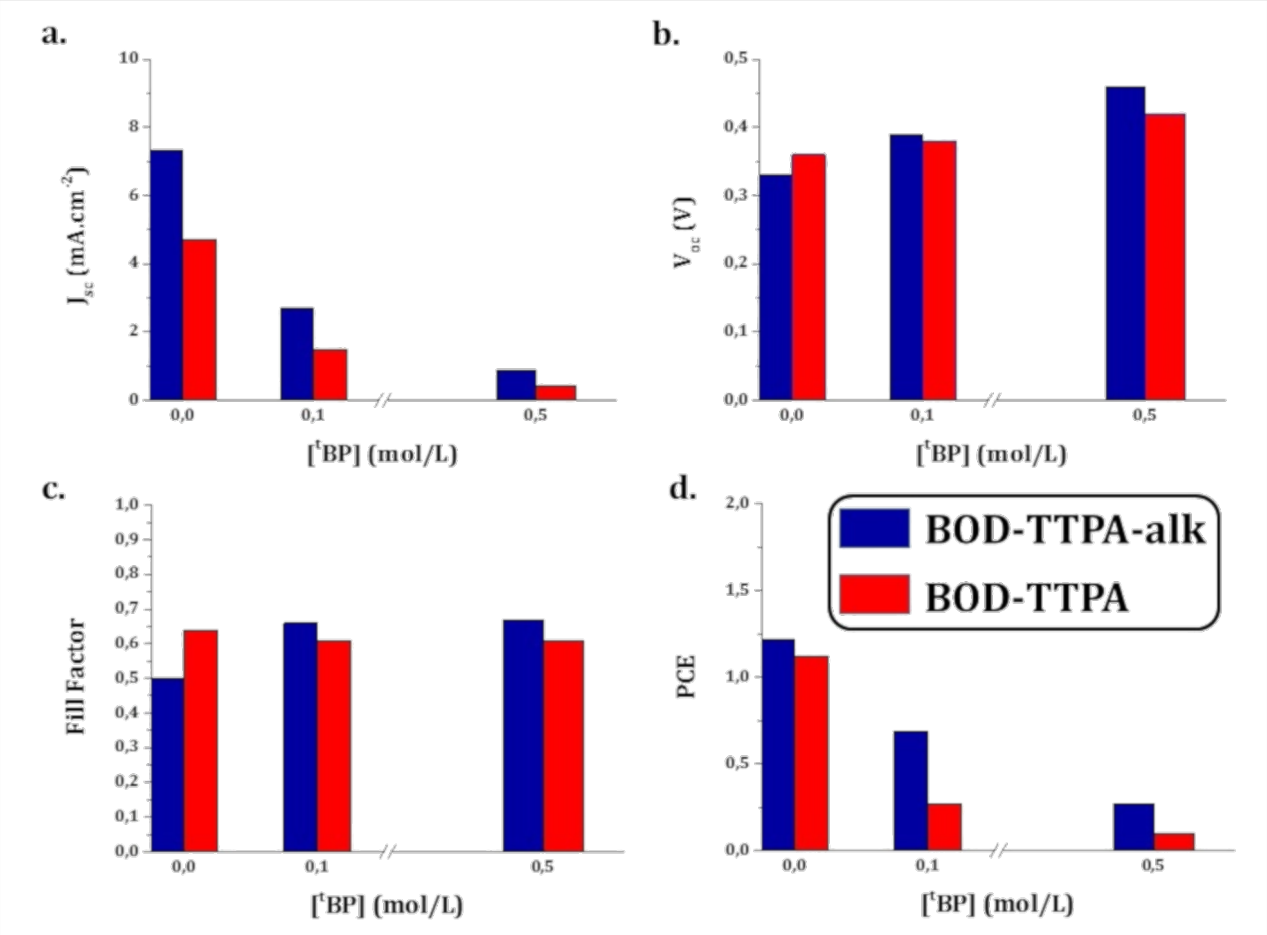

Figure 7: Photovoltaic parameters evolution with the increasing concentration of ^{t}BP in the electrolyte.

absorption that extends in the NIR region ($\varepsilon > 2{\cdot}10^4$ $M^{-1}{\cdot}cm^{-1}$ from 300 to more than 800 nm). The introduction of a cyanoacrylic anchoring function on these dyes allowed us to use them as photosensitizers of TiO_2 mesoporous electrodes in a DSSC device configuration. We demonstrate PCEs of 1.12% and 1.22%, respectively, for the dye bearing alkyl chains on the TPA unit and for the unsubstituted one. We identified that the limitation of their efficiency in solar cells originates from the unappropriated alignment of their LUMO energy levels with respect to the position of the CB of the metal oxide.

This work highlights that despite remarkable absorption properties, further structural optimization aiming at tuning the LUMO energy level position is necessary. This strategy is very likely to yield more efficient NIR sensitizers. Work following this conclusion is in progress.

Supporting Information

Supporting Information File 1

Experimental part and copies of NMR spectra.
[https://www.beilstein-journals.org/bjoc/content/supplementary/1860-5397-15-169-S1.pdf]

Acknowledgements

The authors acknowledge financial support from the French Research Agency ANR (grants ANR ANR-14-OHRI-0003 ODYCE). DB is a FNRS Research Director.

ORCID® iDs

Quentin Huaulmé - https://orcid.org/0000-0003-2888-9887
Outi Vilhelmiina Kontkanen - https://orcid.org/0000-0002-2892-2141
David Beljonne - https://orcid.org/0000-0001-5082-9990
Gilles Ulrich - https://orcid.org/0000-0002-6980-6091
Renaud Demadrille - https://orcid.org/0000-0002-7455-5709

References

1. Kakiage, K.; Aoyama, Y.; Yano, T.; Oya, K.; Fujisawa, J.-i.; Hanaya, M. *Chem. Commun.* **2015,** *51,* 15894–15897. doi:10.1039/c5cc06759f
2. Mathew, S.; Yella, A.; Gao, P.; Humphry-Baker, R.; Curchod, B. F. E.; Ashari-Astani, N.; Tavernelli, I.; Rothlisberger, U.; Nazeeruddin, M. K.; Grätzel, M. *Nat. Chem.* **2014,** *6,* 242–247. doi:10.1038/nchem.1861
3. Yao, Z.; Wu, H.; Li, Y.; Wang, J.; Zhang, J.; Zhang, M.; Guo, Y.; Wang, P. *Energy Environ. Sci.* **2015,** *8,* 3192–3197. doi:10.1039/c5ee02822a
4. Joly, D.; Pellejà, L.; Narbey, S.; Oswald, F.; Chiron, J.; Clifford, J. N.; Palomares, E.; Demadrille, R. *Sci. Rep.* **2014,** *4,* 4033. doi:10.1038/srep04033
5. Wang, P.; Yang, L.; Wu, H.; Cao, Y.; Zhang, J.; Xu, N.; Chen, S.; Decoppet, J.-D.; Zakeeruddin, S. M.; Grätzel, M. *Joule* **2018,** *2,* 2145–2153. doi:10.1016/j.joule.2018.07.023
6. Fakharuddin, A.; Jose, R.; Brown, T. M.; Fabregat-Santiago, F.; Bisquert, J. *Energy Environ. Sci.* **2014,** *7,* 3952–3981. doi:10.1039/c4ee01724b
7. Aghazada, S.; Nazeeruddin, M. K. *Inorganics* **2018,** *6,* 52. doi:10.3390/inorganics6020052
8. Kubo, Y.; Eguchi, D.; Matsumoto, A.; Nishiyabu, R.; Yakushiji, H.; Shigaki, K.; Kaneko, M. *J. Mater. Chem. A* **2014,** *2,* 5204–5211. doi:10.1039/c3ta15340a
9. Cid, J.-J.; Yum, J.-H.; Jang, S.-R.; Nazeeruddin, M. K.; Martínez-Ferrero, E.; Palomares, E.; Ko, J.; Grätzel, M.; Torres, T. *Angew. Chem., Int. Ed.* **2007,** *46,* 8358–8362. doi:10.1002/anie.200703106
10. García-Iglesias, M.; Yum, J.-H.; Humphry-Baker, R.; Zakeeruddin, S. M.; Péchy, P.; Vázquez, P.; Palomares, E.; Grätzel, M.; Nazeeruddin, M. K.; Torres, T. *Chem. Sci.* **2011,** *2,* 1145–1150. doi:10.1039/c0sc00602e
11. Martín-Gomis, L.; Fernández-Lázaro, F.; Sastre-Santos, Á. *J. Mater. Chem. A* **2014,** *2,* 15672–15682. doi:10.1039/c4ta01894j
12. Ji, J.-M.; Zhou, H.; Kim, H. K. *J. Mater. Chem. A* **2018,** *6,* 14518–14545. doi:10.1039/c8ta02281j
13. Singh, S. P.; Gayathri, T. *Eur. J. Org. Chem.* **2014,** 4689–4707. doi:10.1002/ejoc.201400093
14. Ulrich, G.; Ziessel, R.; Harriman, A. *Angew. Chem., Int. Ed.* **2008,** *47,* 1184–1201. doi:10.1002/anie.200702070
15. Zhang, D.; Martín, V.; García-Moreno, I.; Costela, A.; Pérez-Ojeda, M. E.; Xiao, Y. *Phys. Chem. Chem. Phys.* **2011,** *13,* 13026–13033. doi:10.1039/c1cp21038f
16. Cheng, M. H. Y.; Savoie, H.; Bryden, F.; Boyle, R. W. *Photochem. Photobiol. Sci.* **2017,** *16,* 1260–1267. doi:10.1039/c7pp00091j
17. Kowada, T.; Maeda, H.; Kikuchi, K. *Chem. Soc. Rev.* **2015,** *44,* 4953–4972. doi:10.1039/c5cs00030k
18. Huang, L.; Li, Z.; Zhao, Y.; Zhang, Y.; Wu, S.; Zhao, J.; Han, G. *J. Am. Chem. Soc.* **2016,** *138,* 14586–14591. doi:10.1021/jacs.6b05390
19. Bura, T.; Leclerc, N.; Fall, S.; Lévêque, P.; Heiser, T.; Retailleau, P.; Rihn, S.; Mirloup, A.; Ziessel, R. *J. Am. Chem. Soc.* **2012,** *134,* 17404–17407. doi:10.1021/ja3072513
20. Bessette, A.; Hanan, G. S. *Chem. Soc. Rev.* **2014,** *43,* 3342–3405. doi:10.1039/c3cs60411j
21. Klfout, H.; Stewart, A.; Elkhalifa, M.; He, H. *ACS Appl. Mater. Interfaces* **2017,** *9,* 39873–39889. doi:10.1021/acsami.7b07688
22. Qin, C.; Mirloup, A.; Leclerc, N.; Islam, A.; El-Shafei, A.; Han, L.; Ziessel, R. *Adv. Energy Mater.* **2014,** *4,* 1400085. doi:10.1002/aenm.201400085
23. Loudet, A.; Burgess, K. *Chem. Rev.* **2007,** *107,* 4891–4932. doi:10.1021/cr078381n
24. Aguiar, A.; Farinhas, J.; da Silva, W.; Ghica, M. E.; Brett, C. M. A.; Morgado, J.; Sobral, A. J. F. N. *Dyes Pigm.* **2019,** *168,* 103–110. doi:10.1016/j.dyepig.2019.04.031
25. Bulut, I.; Huaulmé, Q.; Mirloup, A.; Chávez, P.; Fall, S.; Hébraud, A.; Méry, S.; Heinrich, B.; Heiser, T.; Lévêque, P.; Leclerc, N. *ChemSusChem* **2017,** *10,* 1878–1882. doi:10.1002/cssc.201700465
26. Joly, D.; Pellejà, L.; Narbey, S.; Oswald, F.; Meyer, T.; Kervella, Y.; Maldivi, P.; Clifford, J. N.; Palomares, E.; Demadrille, R. *Energy Environ. Sci.* **2015,** *8,* 2010–2018. doi:10.1039/c5ee00444f
27. Zhang, F.; Wang, R.; Wang, Y.; Zhang, X.; Liu, B. *Phys. Chem. Chem. Phys.* **2019,** *21,* 6256–6264. doi:10.1039/c9cp00091g

28. Mishra, A.; Fischer, M. K. R.; Bäuerle, P. *Angew. Chem., Int. Ed.* **2009,** *48,* 2474–2499. doi:10.1002/anie.200804709
29. Poirel, A.; De Nicola, A.; Retailleau, P.; Ziessel, R. *J. Org. Chem.* **2012,** *77,* 7512–7525. doi:10.1021/jo301300b
30. Bura, T.; Retailleau, P.; Ziessel, R. *Angew. Chem., Int. Ed.* **2010,** *49,* 6659–6663. doi:10.1002/anie.201003206
31. Hara, K.; Dan-oh, Y.; Kasada, C.; Ohga, Y.; Shinpo, A.; Suga, S.; Sayama, K.; Arakawa, H. *Langmuir* **2004,** *20,* 4205–4210. doi:10.1021/la0357615
32. Kulkarni, A. P.; Tonzola, C. J.; Babel, A.; Jenekhe, S. A. *Chem. Mater.* **2004,** *16,* 4556–4573. doi:10.1021/cm049473l
33. Goze, C.; Ulrich, G.; Mallon, L. J.; Allen, B. D.; Harriman, A.; Ziessel, R. *J. Am. Chem. Soc.* **2006,** *128,* 10231–10239. doi:10.1021/ja062405a
34. Grätzel, M. *Acc. Chem. Res.* **2009,** *42,* 1788–1798. doi:10.1021/ar900141y
35. Rühle, S.; Greenshtein, M.; Chen, S.-G.; Merson, A.; Pizem, H.; Sukenik, C. S.; Cahen, D.; Zaban, A. *J. Phys. Chem. B* **2005,** *109,* 18907–18913. doi:10.1021/jp0514123
36. Erten-Ela, S.; Yilmaz, M. D.; Icli, B.; Dede, Y.; Icli, S.; Akkaya, E. U. *Org. Lett.* **2008,** *10,* 3299–3302. doi:10.1021/ol8010612
37. Koops, S. E.; O'Regan, B. C.; Barnes, P. R. F.; Durrant, J. R. *J. Am. Chem. Soc.* **2009,** *131,* 4808–4818. doi:10.1021/ja8091278
38. Yu, Q.; Wang, Y.; Yi, Z.; Zu, N.; Zhang, J.; Zhang, M.; Wang, P. *ACS Nano* **2010,** *4,* 6032–6038. doi:10.1021/nn101384e
39. Nazeeruddin, M. K.; Kay, A.; Rodicio, I.; Humphry-Baker, R.; Mueller, E.; Liska, P.; Vlachopoulos, N.; Graetzel, M. *J. Am. Chem. Soc.* **1993,** *115,* 6382–6390. doi:10.1021/ja00067a063
40. Wu, J.; Lan, Z.; Lin, J.; Huang, M.; Huang, Y.; Fan, L.; Luo, G. *Chem. Rev.* **2015,** *115,* 2136–2173. doi:10.1021/cr400675m

License and Terms

BEILSTEIN JOURNAL OF ORGANIC CHEMISTRY

A golden opportunity: benzofuranone modifications of aurones and their influence on optical properties, toxicity, and potential as dyes

Joza Schmitt and Scott T. Handy*

Full Research Paper

Open Access

Address:
Department of Chemistry, Middle Tennessee State University, Murfreesboro, TN 37132, USA

Email:
Scott T. Handy* - scott.handy@mtsu.edu

* Corresponding author

Keywords:
aurone; dyeing; dyes; substitution effect; toxicity; UV–vis spectrum

Beilstein J. Org. Chem. **2019,** *15,* 1781–1785.
doi:10.3762/bjoc.15.171

Received: 25 April 2019
Accepted: 12 July 2019
Published: 25 July 2019

This article is part of the thematic issue "Dyes in modern organic chemistry".

Guest Editor: H. Ihmels

Abstract

Aurones are a small subclass of the flavonoid family known primarily for their unusual structure and the golden yellow color they impart to the flowers of snapdragons and cosmos. Most studies of aurones focus on their range of biological activities, but relatively little has been reported with respect to their optical properties, unlike their aza and thio analogs. What little is known has focused entirely on the influence of the benzylidene portion. In this study, the influence of substitution in the benzofuranone ring on the UV–vis spectrum is explored, as well as an initial screening of their toxicity and a qualitative preliminary study of their potential to act as fabric dyes.

Introduction

Aurones are a fascinating minor sub-family of the flavonoid natural products [1,2]. While they feature the same C15 composition as other flavonoids, the skeleton is quite different, featuring a benzofuranone connected to an aromatic ring via an exocyclic alkene. This unusual skeleton has attracted a modest amount of synthetic attention and fairly recently significant biological focus. At the same time, aurones were first noted (and indeed their name is derived from) for their golden yellow color. The colors of flavonoids in general have been appreciated and used for virtually the entirety of recorded history and yet the application of aurones as dyes or pigments has not been reported or studied [3].

Even the optical properties of aurones have had very minimal study. The reports that have appeared have all focused on fluorescent properties and have also been largely limited in scope to the influence of the benzylidene portion. Most noteworthy is the report by Bane and co-workers examining the UV–vis and fluorescent properties of a series of amino-substituted aurones [4]. Subsequently, Liu and co-workers explored the same series of

aurones using computational methods to develop and validate the method for the rational design of new aurone fluorophores [5].

Two more recent studies have explored the influence of the benzofuranone portion of the aurone system. Salas examined a larger set of compounds featuring methoxy substitution at 4 or 5-position on the benzofuranone and methoxy moiety and one methoxy/bromo-substituted benzylidene group, but none in which the benzofuranone was unsubstituted (see Figure 1 for numbering) [6]. This meant that no comparison regarding the influence of substitution could realistically be made. They did observe that a methoxy group at the 5-position resulted in a shift to longer wavelength by roughly 20 nm compared to a methoxy substituent at the 4-position and a strong dependence upon solvent polarity. While this shift was quite reasonably attributed to the inductive effect of the oxygen, no other substitution was studied. Muñoz-Becerra and co-workers have also reported a computational study of amino aurone derivatives with variations in the benzofuranone portion of the molecule, though all substitution was strictly at the 4-position of the benzofuranone [7].

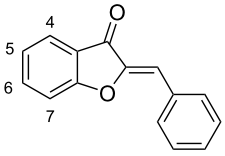

Figure 1: Aurone ring system and numbering.

As an extension of our on-going studies of the aurone ring system, we chose to study the potential for aurones to be used as dyes as well as a more extensive study of the impact of substitution in the benzofuranone portion of the molecule on its optical properties.

Results and Discussion

Synthesis

We have previously reported the synthesis of a significant number of new aurones by way of the common Knoevenagel condensation approach, mostly varying in the benzylidene portion. To explore benzofuranone variations using this method, different benzofuranone starting materials are required. Although not likely to be the most colorful, we elected for simplicity's sake to use *p*-tolualdehyde as the benzylidene precursor for all of the new aurones. The synthesis itself was performed via one of two methods (Figure 2). For all compounds without a free hydroxy group, the neutral alumina method of Varma combined with an aldehyde scavenging step was employed to afford pure products without the need for any chromatography in generally reasonable yields and excellent purity [8]. For hydroxy-substituted compounds, a more traditional base-mediated reaction was employed [9]. Product purification was not as easy in these cases and the product yield was sacrificed for the sake of high purity, so yields should not be considered optimized.

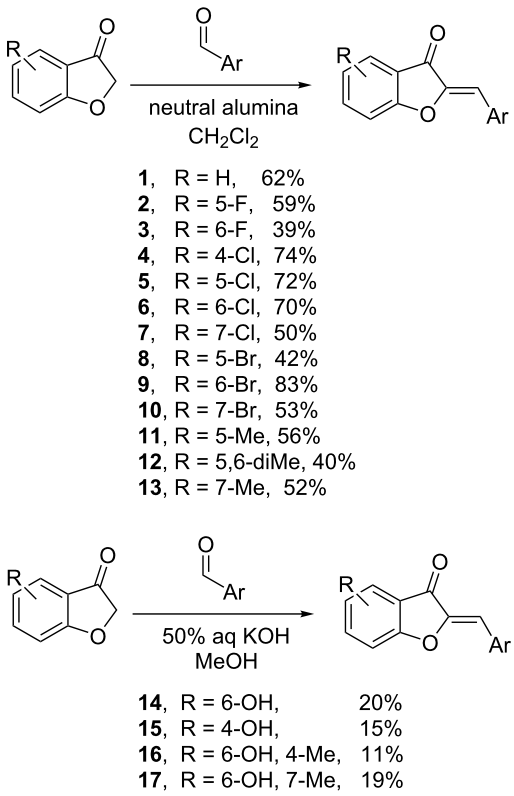

Figure 2: Aurone syntheses.

Spectral and toxicity studies

With the desired compounds in hand, their UV–visible spectra were recorded at concentrations between 29 and 44 μM in acetonitrile (Figure 3 and Table 1). While not all substituents were prepared at every position, some interesting trends were observed. Substitution at the 4-position whether halogen or hydroxy afforded essentially identical lambda maxima (390 nm), slighly red-shifted compared to the unsubstituted compound **1**. On the other hand, hydroxy groups at the 6-position result in a significant blue shift of this lambda max by roughly 40 nm to around 338 nm, presumably due to their donating effect and conjugation with the carbonyl oxygen. Halogen substituents at the 6-position generally had little effect, with the exception of the most electron-withdrawing fluorine, which resulted in a slight blue-shift of roughly 10 nm. Unexpectedly, any halogen at the 5-position had an effect nearly identical to that of halogen at the 4-position, resulting in a slight red-shift compared to the unsubstituted compound. On the other

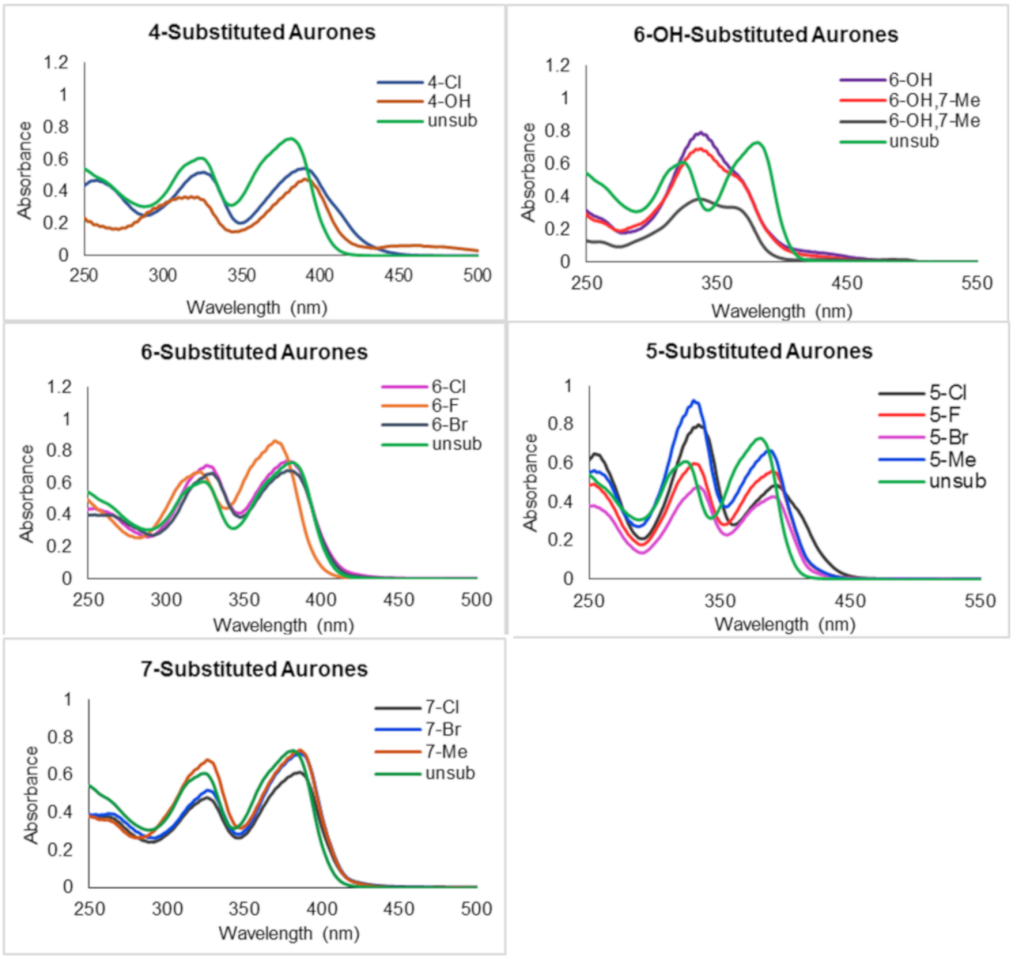

Figure 3: UV–vis spectral comparisons in acetonitrile.

hand, substitution at the 7-position had virtually no effect, which is to be expected due to the lack of direct conjugation with the carbonyl as well as the only modest electronic effects of alkyl, chlorine, and bromine. In general, the substituent effects are all fairly modest and result in fairly moderate changes in the extinction coefficient (although hydroxy substitution does definitely increase this value by roughly 50%).

While these results on the impact of the benzofuranone portion of aurones on their optical properties are interesting, if one were to think about using them as dyes, toxicity is also an important consideration. Generally, aurones are considered to be relatively non-toxic, although data reported in the literature shows considerable variability even in this respect. An initial screening of toxicity was conducted at a fairly high concentration (200 μM) on the present series of compounds using a standard HEP G2 inhibition assay (Table 1). Compared to a currently used yellow dye (tartrazine), the aurones are similar to more toxic. Within the aurone series, though, an interesting pair of trends can be observed. First, all hydroxylated aurones are comparatively more toxic, displaying >50% inhibition at 200 μM. Methyl groups are similarly mostly more toxic. For the halogens, however, location is fairly important, with the 6 or 7 position being much less toxic (similar to tartrazine) and dramatically better than the unsubstituted base compound **1**, with the unexpected exception of 7-bromo compound **10**. Whether this trend is general or not for aurone compounds is an interesting question for future study.

Preliminary dyeing efforts

As the initial inspiration for this work was the potential of aurones as textile dyes, two of the more interesting compounds, aurones **15** and **10** were used in a very preliminary attempt at fabric dyeing. Three processes were compared: pre-, simultaneous, and post-mordanting. As can be seen in Figure 4, dyeing did occur in all cases. With aurone **10**, simultaneous mordanting qualitatively appeared to be better, while with aurone **15** pre-mordanting was superior. Aurone **15** afforded more vibrant

Table 1: Toxicity and UV spectral data for aurones.

Compound	Substituent	λ_{max} (nm)[a]	ε (L mol^{-1} cm^{-1})	Hep G2 % inhibition[b]
1	H	382	20208	86.27 ± 1.09
2	5-F	394	17188	87.01 ± 0.56
3	6-F	370	24252	3.52 ± 3.39
4	4-Cl	390	17129	15.13 ± 5.75
5	5-Cl	394	16551	72.68 ± 2.77
6	6-Cl	378	23187	25.07 ± 18.77
7	7-Cl	386	17247	3.64 ± 3.64
8	5-Br	394	15112	59.35 ± 1.25
9	6-Br	378	22435	75.22 ± 3.84
10	7-Br	390	22250	5.85 ± 11.12
11	5-Me	390	15470	80.88 ± 1.38
12	5- and 6-Me	382	19522	24.95 ± 2.23
13	7-Me	386	18380	87.54 ± 1.61
14	6-OH	338	33050	66.79 ± 3.04
15	4-OH	390	22664	54.04 ± 4.65
16	6-OH, 4-Me	338	30445	67.76 ± 6.06
17	6-OH, 7-Me	336	will not dissolve completely	78.58 ± 7.11
tartrazine	N/A	N/A	N/A	6.81

[a]UV–vis spectra determined in CH_3CN. [b]Toxicity values determined at 200 μM concentration of compound.

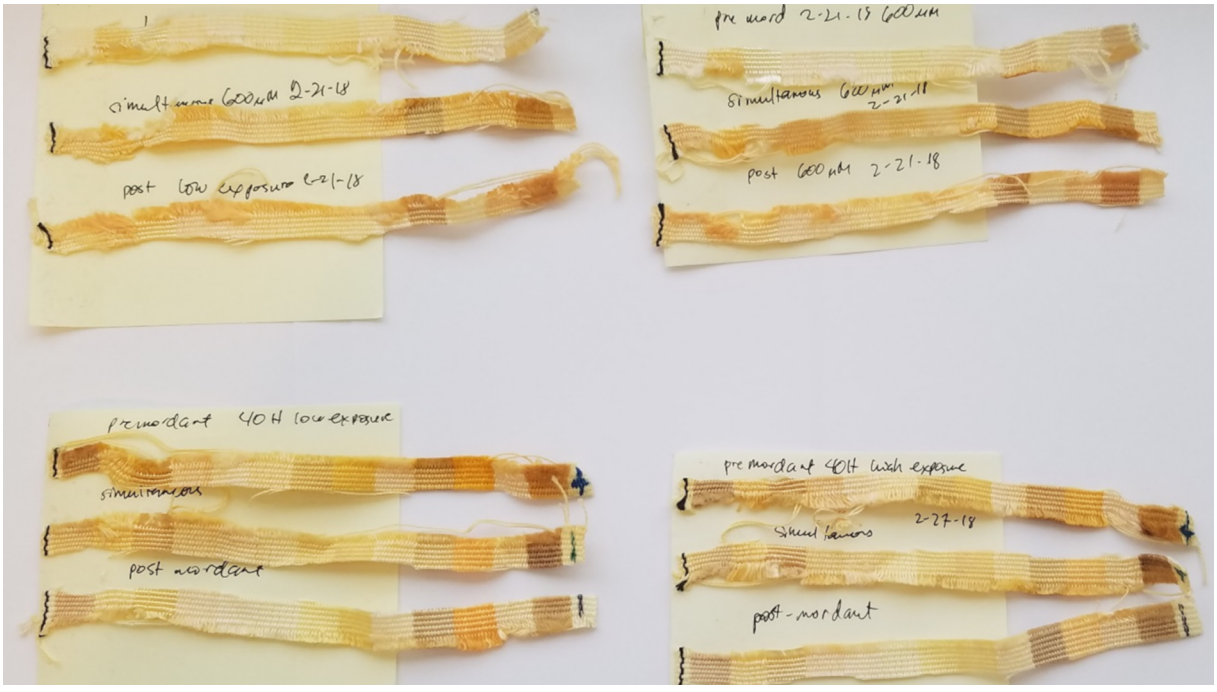

Figure 4: Fabric dying and photobleaching. The top two sets show dyed fabric strips with premordant, simultaneous, and post-mordant dying (top to bottom) using aurone **10** after dyeing (left) and after one week of sun exposure (right). The bottom two are similarly dyed fabric strips with premordant, simultaneous, and post-mordant dying (top to bottom) using aurone **15** after dyeing (left) and after one week of sun exposure (right). The fabric order on the strip is acetate, rayon, sef, arnel, cotton, creslan, dacron 54, dacron 64, nylon 6.6, orlon 75, silk, polypropylene, viscose rayon, and wool from left to right.

colors in general and also adhered to a wider range of fabrics. While several were natural fibers (silk and wool in particular), synthetics including polypropylene were also substrates. This feature is quite remarkable and has the potential to make aurone dyes useful in dyeing polypropylene, a substrate that is generally only dyed with any efficiency using an extrusion method. Of

equal interest was that a highly qualitative photobleaching study indicated a significant degree of stability of these aurone-based dyes, with simultaneous or pre-mordanting offering better stability. Clearly further studies of the generality of this observation as well as its longer term retention and photostability are required.

Conclusion

In conclusion, the benzofuranone portion of the aurone skeleton does have a definite impact on both the UV–vis spectral and cytotoxicity properties of aurones. Interestingly, the position of the substituent was often more important than the exact substituent (at least for the examples studied), with halogen or hydroxy at the 4-position are red-shifted by roughly 10 nm compared to the unsubstituted compound and any halogen or methyl at the 5-position likewise displays a similar shift. Only hydroxylation at the 6-position displays a significant blue shift by roughly 40 nm. With respect to toxicity, halogens were the least toxic substituents, displaying the lowest cytotoxicity when at the 6- or 7-positions. Hydroxylation or substitution at the 4-position invariably lead to higher cytotoxicity, though often times no worse than the unsubstituted benzofuranone system. Finally, preliminary dyeing studies showed the expected absorption on natural fibers, but also an unexpected affinity for polypropylene. Future studies of these and other aurones are underway and the results will be reported in due course.

Experimental

Full details of the synthesis and photochemical studies can be found in Supporting Information File 1 as well as copies of the spectra for all new compounds. Raw data for the toxicity and absorption studies can be found in Supporting Information File 2.

Supporting Information

Supporting Information File 1

Experimental methods and spectra for all new compounds.
[https://www.beilstein-journals.org/bjoc/content/supplementary/1860-5397-15-171-S1.pdf]

Supporting Information File 2

Absorption data and individual plots for all compounds.
[https://www.beilstein-journals.org/bjoc/content/supplementary/1860-5397-15-171-S2.xlsx]

Acknowledgements

The support of Middle Tennessee State University and the Department of Chemistry are gratefully acknowledged.

ORCID® iDs

Joza Schmitt - https://orcid.org/0000-0001-9244-4909
Scott T. Handy - https://orcid.org/0000-0003-4199-7292

References

1. Haudecoeur, R.; Boumendjel, A. *Curr. Med. Chem.* **2012,** *19,* 2861–2875. doi:10.2174/092986712800672085
2. Zwergel, C.; Gaascht, F.; Valente, S.; Diederich, M.; Bagrel, D.; Kirsch, G. *Nat. Prod. Commun.* **2012,** *7,* 389–394. doi:10.1177/1934578x1200700322
3. Yusuf, M.; Shabbir, M.; Mohammad, F. *Nat. Prod. Bioprospect.* **2017,** *7,* 123–145. doi:10.1007/s13659-017-0119-9
4. Shanker, N.; Dilek, O.; Mukherjee, K.; McGee, D. W.; Bane, S. L. *J. Fluoresc.* **2011,** *21,* 2173–2184. doi:10.1007/s10895-011-0919-y
5. Xue, Y.; Dou, Y.; An, L.; Zheng, Y.; Zhang, L.; Liu, Y. *RSC Adv.* **2016,** *6,* 7002–7010. doi:10.1039/c5ra25733f
6. Espinosa-Bustos, C.; Cortés-Arriagada, D.; Soto-Arriaza, M. A.; Robinson-Duggon, J.; Pizarro, N.; Cabrera, A. R.; Fuentealba, D.; Salas, C. O. *Photochem. Photobiol. Sci.* **2017,** *16,* 1268–1276. doi:10.1039/c7pp00078b
7. Muñoz-Becerra, K.; Villegas-Escobar, N.; Zúñiga-Loyola, C.; Cortés-Arriagada, D.; Toro-Labbé, A. *Mol. Phys.* **2019,** *117,* 1451–1458. doi:10.1080/00268976.2018.1559372
8. Varma, R. S.; Varma, M. *Tetrahedron Lett.* **1992,** *33,* 5937–5940. doi:10.1016/s0040-4039(00)61093-6
9. Lee, C.-Y.; Chew, E.-H.; Go, M.-L. *Eur. J. Med. Chem.* **2010,** *45,* 2957–2971. doi:10.1016/j.ejmech.2010.03.023

License and Terms

BEILSTEIN JOURNAL OF ORGANIC CHEMISTRY

Identification of optimal fluorescent probes for G-quadruplex nucleic acids through systematic exploration of mono- and distyryl dye libraries

Xiao Xie, Michela Zuffo, Marie-Paule Teulade-Fichou and Anton Granzhan*

Full Research Paper

Open Access

Address:
CNRS UMR9187, INSERM U1196, Institut Curie, Université Paris Sud, Université Paris Saclay, Bât. 110, Centre universitaire Paris Sud, F-91405 Orsay, France

Email:
Anton Granzhan* - anton.granzhan@curie.fr

* Corresponding author

Keywords:
fluorescent probes; G-quadruplex DNA; G-quadruplex RNA; nucleic acids; styryl dyes

Beilstein J. Org. Chem. **2019,** *15,* 1872–1889.
doi:10.3762/bjoc.15.183

Received: 10 May 2019
Accepted: 23 July 2019
Published: 06 August 2019

This article is part of the thematic issue "Dyes in modern organic chemistry".

Associate Editor: D. Spring

Abstract

A library of 52 distyryl and 9 mono-styryl cationic dyes was synthesized and investigated with respect to their optical properties, propensity to aggregation in aqueous medium, and capacity to serve as fluorescence "light-up" probes for G-quadruplex (G4) DNA and RNA structures. Among the 61 compounds, 57 dyes showed preferential enhancement of fluorescence intensity in the presence of one or another G4-DNA or RNA structure, while no dye displayed preferential response to double-stranded DNA or single-stranded RNA analytes employed at equivalent nucleotide concentration. Thus, preferential fluorimetric response towards G4 structures appears to be a common feature of mono- and distyryl dyes, including long-known mono-styryl dyes used as mitochondrial probes or protein stains. However, the magnitude of the G4-induced "light-up" effect varies drastically, as a function of both the molecular structure of the dyes and the nature or topology of G4 analytes. Although our results do not allow to formulate comprehensive structure–properties relationships, we identified several structural motifs, such as indole- or pyrrole-substituted distyryl dyes, as well as simple mono-stryryl dyes such as DASPMI [2-(4-(dimethylamino)styryl)-1-methylpyridinium iodide] or its 4-isomer, as optimal fluorescent light-up probes characterized by high fluorimetric response (I/I_0 of up to 550-fold), excellent selectivity with respect to double-stranded DNA or single-stranded RNA controls, high quantum yield in the presence of G4 analytes (up to 0.32), large Stokes shift (up to 150 nm) and, in certain cases, structural selectivity with respect to one or another G4 folding topology. These dyes can be considered as promising G4-responsive sensors for in vitro or imaging applications. As a possible application, we implemented a simple two-dye fluorimetric assay allowing rapid topological classification of G4-DNA structures.

Introduction

Development of fluorescent probes for G-quadruplex (G4) DNA and RNA is an active research area. In fact, these non-canonical nucleic acid structures appear to be biologically relevant, although a complete understanding of their roles is still missing [1-3]. At the same time, they represent versatile building blocks for artificial nano-architectures and nanodevices

[4,5]. In this context, small-molecule fluorescent probes find applications for in vitro detection of G4 structures and their differentiation from other DNA or RNA forms [6-10], topological characterization of G4 structures [11-14], real-time detection of G4 formation [15], and implementation of G4-based molecular devices [16,17] and biosensors [18-23]. Also, there have been promising reports on cellular imaging of G4-DNA [24-29] and G4-RNA [30-33] structures using small-molecule probes. A large number of fluorescent probes for G4-DNA and RNA have thus emerged in the last years, as summarized in several recent reviews on this subject [34-39]. Moreover, novel probes continue to be regularly reported. However, in most cases, the discovery of novel probes is based on serendipitous findings or limited variations of already established fluorogenic scaffolds. This provokes a flood of "one-molecule" papers that report on novel exciting probes, but do not compare their performance with that of already established ones [40-51]. Systematic approaches to the development of fluorescent probes are still rare and explore only a limited range of the chemical space [52-57]. This is a major hurdle to the establishment of solid structure–properties relationships. Therefore, the choice of the best probe for a particular application, as well as the development of novel probes with improved or tailored properties, still remain problematic tasks.

Along these lines, we have previously reported that cationic styryl-type dyes, such as distyrylpyridinium derivatives **1a** and **2a** (Figure 1) represent a promising starting point for the development of fluorescent probes selective for a variety of G4-DNA structures [58]. Another distyryl dye, namely coumarin derivative **1y** (**BCVP**), provides a bimodal (colorimetric and fluorimetric) output towards G4-DNA through the selective disruption of H-aggregates formed in buffered solution [59]. In the meantime, numerous other styryl derivatives were reported as efficient "light-up" probes for G4-DNA and RNA, validating the potential of this molecular scaffold (Figure 1) [22,33,60-63]. Nevertheless, the structural determinants for the desired properties of the probes (i.e., high selectivity for G4-DNA or G4-RNA with respect to double-stranded or single-stranded nucleic acids, high fluorimetric response and quantum yield, low background fluorescence) are still poorly understood, mostly due to the lack of comparative studies. To explore this aspect, we report the

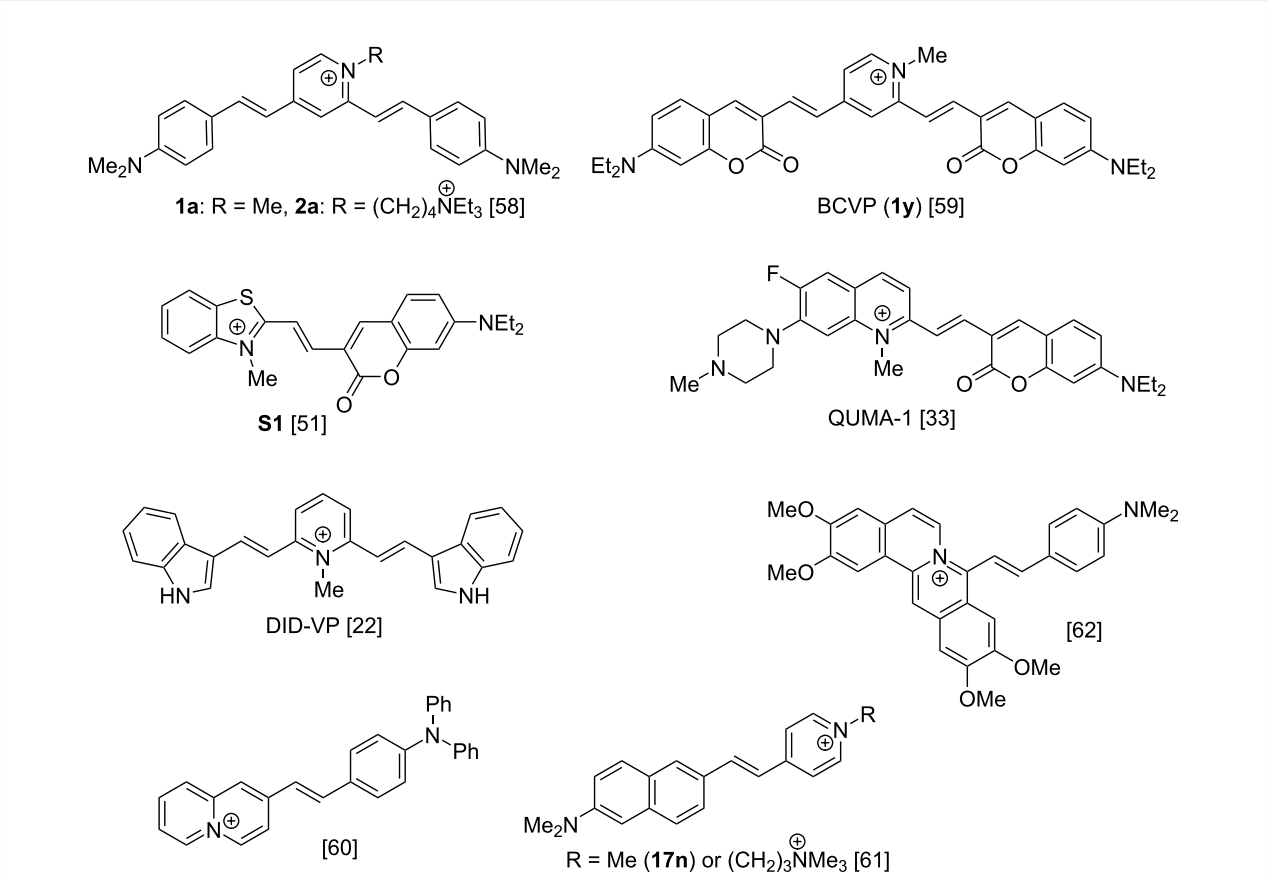

Figure 1: Some di- and mono-styryl dyes previously reported as fluorescent "light-up" probes for G4-DNA and RNA. Counter-ions are omitted for the sake of clarity.

synthesis and systematic study of a library of 61 di- and mono-styryl dyes, as potential "light-up" probes for G4 structures. The study aims at the improvement of photophysical properties of the dyes and the establishment of structure–properties relationships.

Results

Design and synthesis of the dye library

On the basis of the previously established distyryl scaffold, we designed 49 novel derivatives through systematic variation of the electron-donating lateral aromatic groups Ar (**a**–**Þ**), the cationic heterocyclic core Het^+ (**1**–**16**) and, in the case of 2,4-disubstituted derivatives (**1–6**), the substituent R (Figure 2). Among these, several distyryl dyes (**1o**, **1x, 7x** [64] and **10a** [65]) have been previously reported as fluorescent probes for detection of double-stranded DNA. Compounds **15a** and **16a** are homo-dimeric derivatives, featuring two distyryl moieties connected via a C_3 (**15a**) or a C_4 (**16a**) linker. In addition, we included 9 mono-styryl derivatives. Among these, compounds **17a** and **18a** are long-known [66,67]; however, to the best of our knowledge, they have not been studied as fluorescent probes for G4 structures so far. On the contrary, dye **17n** (Figure 1) was reported as a fluorescent probe for G4-DNA during the preparation of the present work earlier this year [61]. Of note, numerous mono-styryl dyes combining indole and quinolinium or pyridinium fragments have been described as bright, photostable stains for double-stranded DNA, although their interaction with G4 structures has not been assessed [68-70].

All dyes, except for distyryl derivative **6a** and mono-styryl derivative **19a**, were obtained through a piperidine-catalyzed Knoevenagel condensation of the corresponding heterocyclic precursors **I1–5** and **I7–16** with 1.5 molar equivalents (per styryl unit) of aromatic aldehydes ArCHO (Scheme 1A,B). The synthesis of precursors **I3–5** and **I15** is presented in Scheme 2 and detailed in Supporting Information File 1. Dyes **6a** and **19a**, which could not be obtained by this route, were synthesized through quaternization of the corresponding neutral styryl precursors with alkyl halides (Scheme 1C,D).

Most dyes of the library were prepared and handled as iodide salts. However, in the case of very lipophilic dyes, the solubility of iodide salts in the high-ionic-strength aqueous buffer required for native G4 structures was insufficient. In these cases, ion exchange to bromide (**1b**, **1ð**, **1u**, **6a**, **7b**, **7n**) or chloride (**1d**, **1k–1q**, **1t**, **1w**, **7ð**, as well as **8a–12a** and **14a–16a**) was performed using ion-exchange resins (cf. Supporting Information File 1 and Table 1), in order to achieve a satisfactory level of solubility in aqueous buffer (i.e., no visible precipitation at a dye concentration of 10 μM in K-100 buffer: 10 mM $LiAsO_2Me_2$, 100 mM KCl, pH 7.2). Dyes containing side-chain substituents (**2a–6a**) were obtained directly as bromide salts, sufficiently soluble in the aqueous buffer. All dyes were rigorously purified by recrystallization and their identity and purity were confirmed by ^1H and ^{13}C NMR, LC–MS and elemental analysis data.

Optical properties

The library of styryl dyes covers a broad spectral range, with absorption maxima ranging, in MeOH, from 407 nm (**1j**) to 605 nm (**1þ**), and molar extinction coefficients from around 45,000 to 60,000 cm^{-1} M^{-1} (Table 1). Several representative absorption spectra are shown in Figure 3. In aqueous buffer solutions (K-100: 10 mM $LiAsO_2Me_2$, 100 mM KCl, pH 7.2) and at dye concentration of 10 μM, the absorption bands of most dyes are blue-shifted by 10 to 30 nm and undergo a hypochromic effect, compared with organic solvents such as MeOH or DMSO. This behavior evidences a more or less significant aggregation propensity of dyes in aqueous medium, even though, in all tested cases, no visible precipitation occurred. In addition, some dyes (**1c**, **1ð**, **1Þ**, **9a**, **10a**) display even larger (>50 nm) blue shifts of their absorption bands (Figure 3B). This is a characteristic feature for the formation of H-aggregates, as already described for dye **1y** [59]. On the other hand, several dyes displayed new, strong absorption bands, red-shifted by ≈70 nm (**14p**) or more than 100 nm (**1d** and **12a**) in aqueous buffer solution, with respect to organic solvents. These could be ascribed to the formation of J-aggregates (Figure 3A and 3F). This phenomenon was already observed, although at a lower extent, with dye **1a** [58]. With respect to the molecular structure of dyes, it may be concluded that lipophilic substituents (**1c**, **1d**, **1ð**, **1y**, **1Þ**) and/or π-expanded heterocyclic cores (**9a**, **10a**, **12a**, **14p**) promote the dye aggregation, but the nature of the resulting aggregate (H vs J) is unpredictable. Conversely, small or hydrophilic substituents (**1e**, **1f**, **1h**, **1x**, **7e**, **7x**) or charged aminoalkyl chains (**3a**, **4a**) reduce the tendency of the dyes to self-aggregate, as suggested by the reduced hypochromism of their absorption bands in aqueous solutions. Of note, our assessment of the aggregation behavior of the dyes is only preliminary, as it was performed at a single concentration (10 μM) and fixed ionic strength of the medium (110 mM). A complete investigation of this phenomenon is outside the scope of the present work. Finally, as typically observed for styryl dyes, most of the library members displayed very weak fluorescence both in organic solvents (MeOH, DMSO) and in aqueous buffer, as assessed by visual inspection of the respective solutions.

In non-aggregating conditions, the influence of the molecular structure of the dyes on their absorption bands can be clearly observed. Thus, when Ar contains poor electron-donating sub-

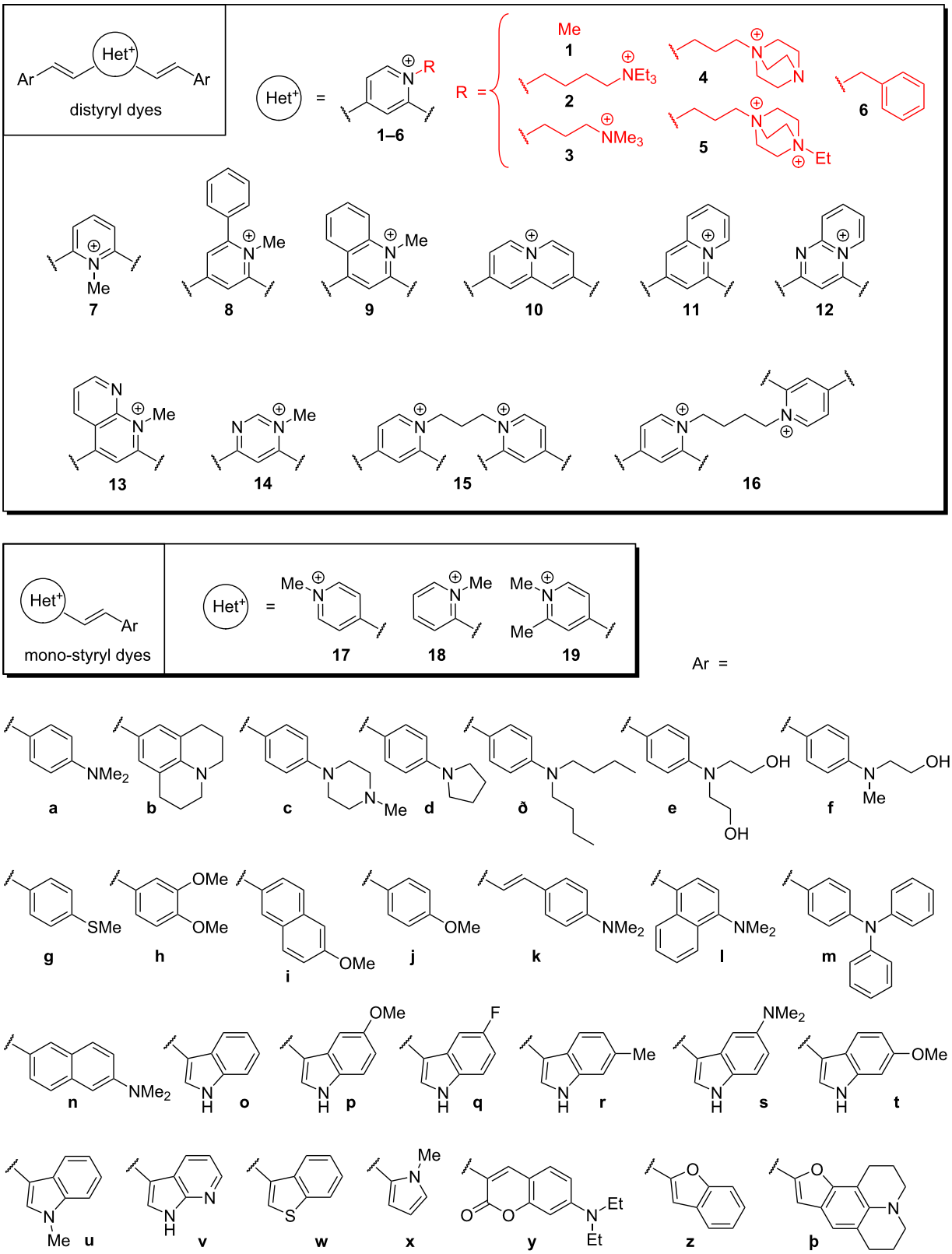

Figure 2: Design of a library of di- and mono-styryl dyes. Counter-ions are omitted for the sake of clarity.

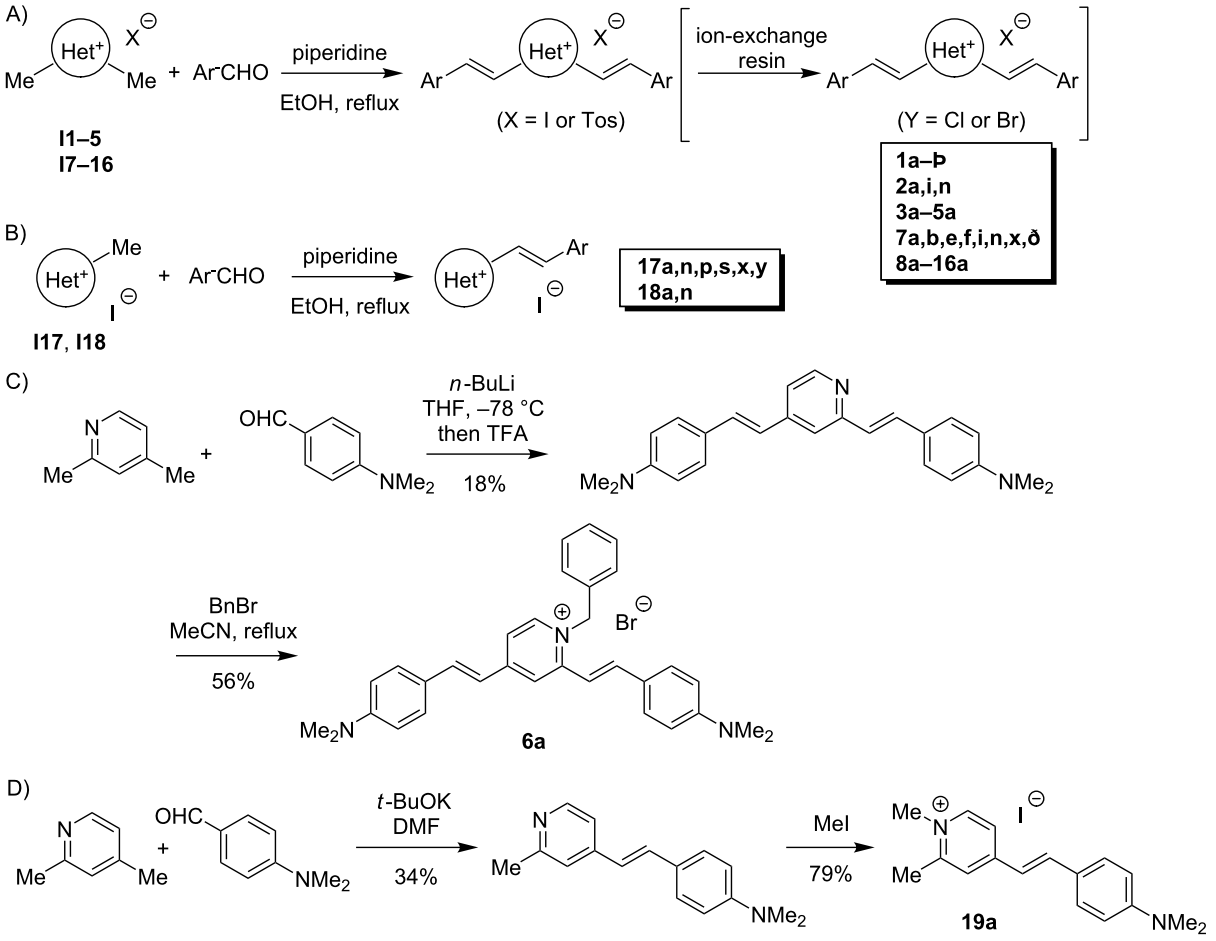

Scheme 1: A, B) General synthesis of A) distyryl and B) mono-styryl dyes via Knoevenagel condensation route. C) Synthesis of the dye **6a**. D) Synthesis of the dye **19a**.

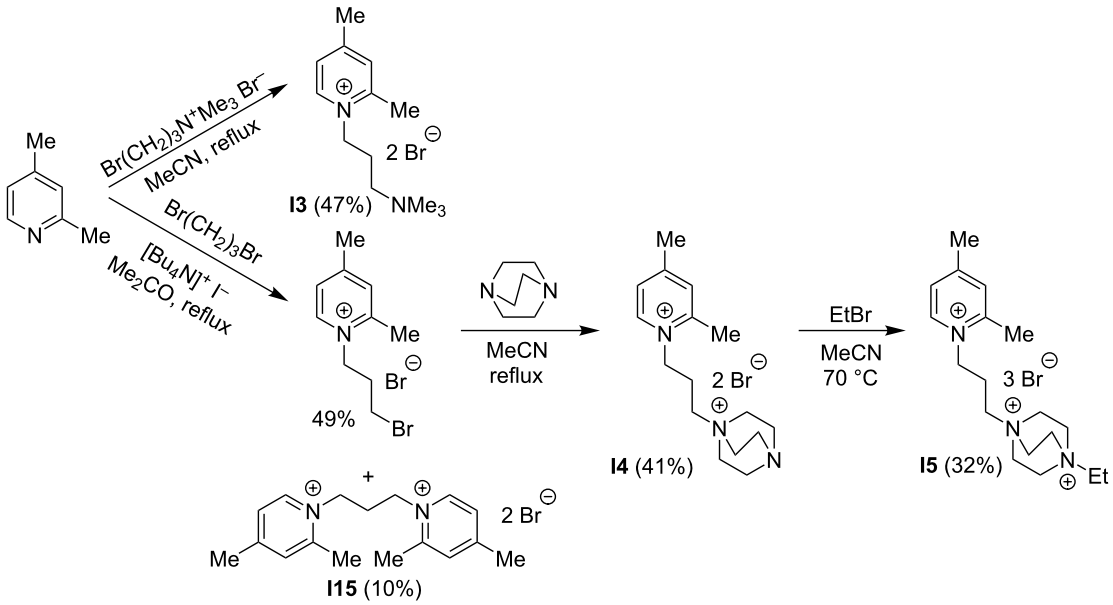

Scheme 2: Synthesis of **I3–5** and **I15**.

Table 1: Positions of maxima and intensity of long-wavelength absorption bands of dyes in MeOH and K-100 aqueous buffer.[a]

Dye	Anion	MeOH		Buffer K-100	
		λ_{max} [nm][b]	ε [10^3 cm^{-1} M^{-1}]	λ_{max} [nm][b]	ε [10^3 cm^{-1} M^{-1}]
distyryl dyes					
1a	I^-	507	61.7	476, 616 (sh) (J)	39.9, 1.4
1b	Br^-	551	61.4	510	28.7
1c	I^-	472	53.7	422 (H)	43.6
1d	Cl^-	521	67.7	620 (J), 531 (sh)	34.5, 27.5
1ð	Br^-	524	65.9	459 (H)	43.3
1e	I^-	508	63.7	486	53.6
1f	I^-	510	61.9	486	45.6
1g	I^-	418	50.4	404	40.6
1h	I^-	422	44.6	403	40.8
1i	I^-	425	54.7	414	23.2
1j	I^-	407	46.7	393	393
1k	Cl^-	533	66.4	510	26.3
1l	Cl^-	468	32.8	443	22.4
1m	Cl^-	493	61.0	479	38.3
1o	Cl^-	466, 409 (sh)	56.2, 32.6	458	27.0
1p	Cl^-	474	57.2	465	29.3
1q	Cl^-	457, 404 (sh)	55.3, 34.0	487	27.3
1r	I^-	473, 417 (sh)	56.9, 32.2	462	28.8
1s	I^-	482	33.4	456	24.6
1t	Cl^-	476	55.5	455	20.8
1u	Br^-	472, 418 (sh)	52.2, 31.6	459	31.0
1v	I^-	435, 391 (sh)	48.8, 33.6	413, 367	22.0, 19.9
1w	Cl^-	410	32.8	404	22.5
1x	I^-	473, 419 (sh)	50.9, 32.5	455	42.7
1y	I^-	527	95.3	580, 460 (H)	14.9, 44.0
1z	I^-	423	55.9	416	45.3
1Þ	I^-	605	62.6	542 (H)	30.4
2a	2 Br^-	516	62.9	483	43.1
2i	2 Br^-	430	53.2	411	32.8
2n	2 Br^-	508	56.9	475	28.3
3a	2 Br^-	523	65.1	493	44.9
4a	2 Br^-	524	57.4	493	48.1
5a	3 Br^-	528	64.5	495	43.3
6a	Br^-	520	64.7	491	25.0
7a	I^-	494	70.3	465	44.9
7b	Br^-	535	66.4	507	29.0
7ð	Cl^-	511	79.5	480	43.4
7e	I^-	497	73.5	475	60.2
7f	I^-	497	68.9	474	52.3
7i	I^-	420	62.5	400	20.1
7n	Br^-	489	64.0	480	21.2
7x	I^-	467	57.3	448	48.7
8a	Cl^-	512	62.1	476	38.6
9a	Cl^-	565, 497	56.6, 48.3	492 (H)	33.5
10a	Cl^-	516	87.0	463 (H)	28.7
11a	Cl^-	473	61.1	432	32.8
12a	Cl^-	551	56.7	659 (J), 471	42.8, 16.8
13a	Tos^-	597, 512	53.9, 42.0	570 (sh), 515	24.9, 27.0

Table 1: Positions of maxima and intensity of long-wavelength absorption bands of dyes in MeOH and K-100 aqueous buffer.[a] (continued)

14a	Cl^-	569, 471	82.3, 29.7	564	54.4
14p	Cl^-	523, 420	74.4, 20.5	590 (J)	67.5
15a	2 Cl^-	520	115.2	523	61.4
16a	2 Cl^-	510	111.7	490	69.1
mono-styryl dyes					
17a	I^-	475	47.1	448	31.5
17n	I^-	473	37.1	422	29.1
17p	I^-	444	42.3	422	35.5
17s	I^-	449	33.2	424	32.2
17x	I^-	440	35.1	424	24.3
17y	I^-	495	61.2	491	54.1
18a	I^-	461	42.1	435	28.4
18n	I^-	459	33.4	409	26.0
19a	I^-	466	45.9	438	31.2
other					
ThT[c]	Cl^-	415	28.1	410	24.7

[a]10 mM $LiAsMe_2O_2$, 100 mM KCl, pH 7.2. [b]sh: shoulder, H: H-aggregate band, J: J-aggregate band. [c]Thioflavin T.

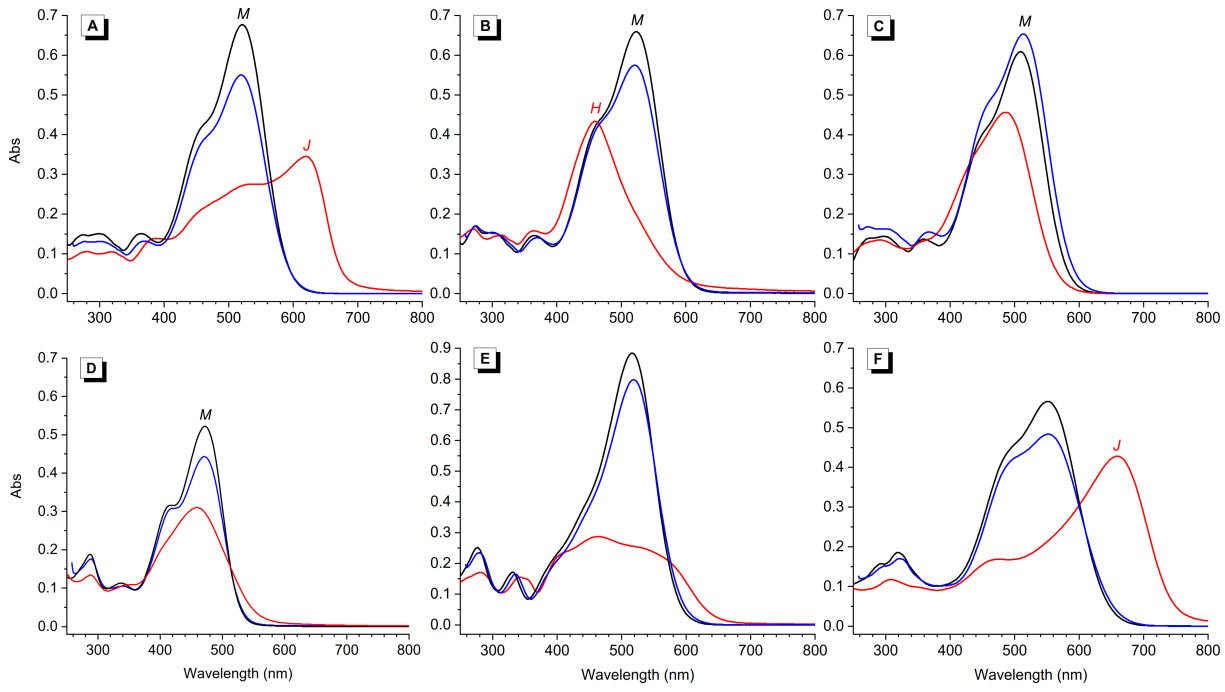

Figure 3: Representative absorption spectra of distyryl dyes: A) **1d**, B) **1ð**, C) **1f**, D) **1u,** E) **10a** and F) **12a** in DMSO (blue), MeOH (black) and K-100 aqueous buffer (red lines); *c* = 10 µM in all cases. Band assignment (when possible): M, monomer; H, H-aggregate; J, J-aggregate.

stituents (**1g–1j**), the absorption spectra of the dyes are blue-shifted with respect to the prototype dye **1a**. Conversely, strongly electron-donating (**1b**, **1d**) or π-extended (**1k**, **1Þ**) Ar units lead to bathochromic shifts of absorption bands (Table 1 and Figure 4A). The influence of the heterocyclic core is equally important: replacement of the 2,4-pyridinium unit in

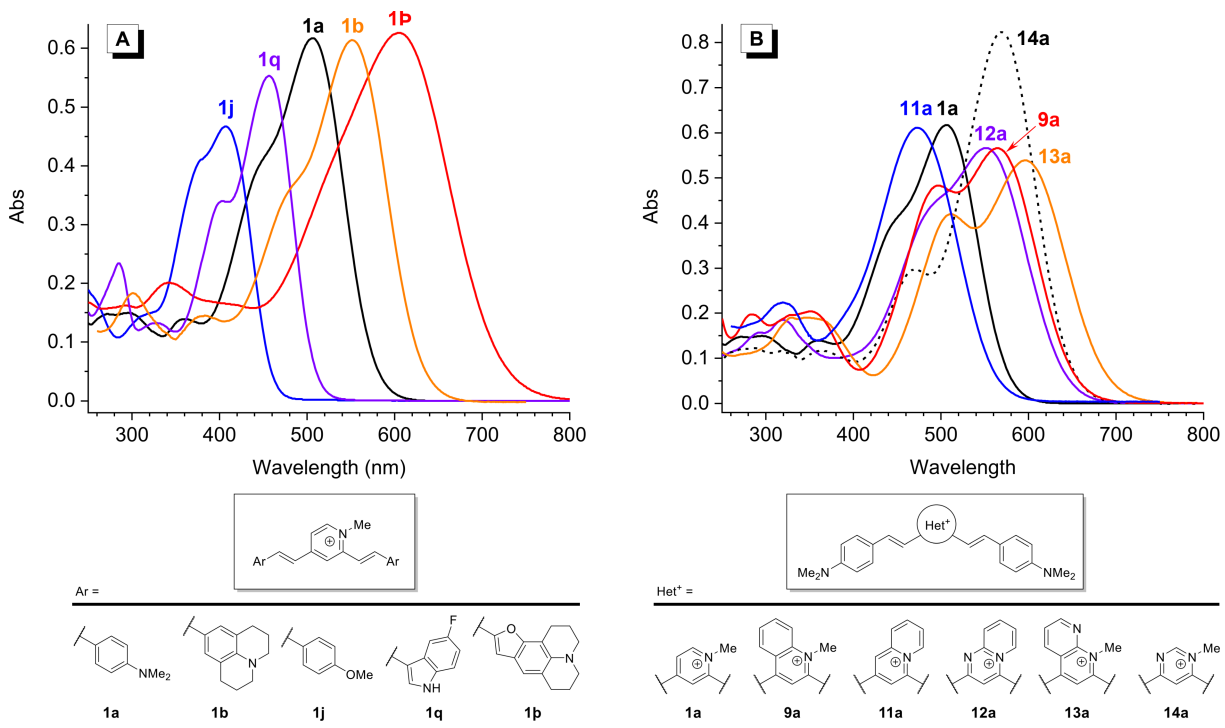

Figure 4: Representative absorption spectra of the distyryl dyes (c = 10 µM in MeOH) demonstrating the influence of the molecular structure on the optical properties. A) Variation of Ar groups. B) Variation of the Het^+ core.

dye **1a** with a 2,6-pyridinium (**7a**) or a 2,4-quinolizinium moiety (**11a**) leads to a blue shift of the absorption maximum, whereas all other heterocyclic units lead to significantly stronger (**10a**, **14a**) and/or red-shifted (**9a**, **12a**, **13a**) absorption bands (Table 1 and Figure 4B). On the other hand, the nature of the substituent R in the 2,4-pyridinium unit has only a minor influence on the optical properties, and the absorption bands of the dyes **2a–6a** are only slightly red-shifted (by 10–20 nm in MeOH) with respect to that of **1a**.

Fluorimetric response of dyes towards DNA and RNA structures

The fluorimetric response of the dye library was investigated against a set of 14 diverse nucleic acid structures (Table 2), including ten G4-DNA structures of different topologies (parallel G4: *c-kit2*, *25CEB*, *c-kit87up*, *c-myc, c-src1*; parallel dimer G4: *c-myb;* hybrid G4: *22AG*, *46AG*; antiparallel G4: *TBA*, *HRAS*), two G4-RNA structures (*TERRA* and *NRAS*), as well as genomic double-stranded DNA (calf thymus DNA, *ct DNA*) and RNA from calf liver (*cl RNA*). Screened samples contained fixed concentrations of dyes (2.5 µM) and nucleic acids (5 µM). Corrections to the concentration of nucleic acids were made to take into account the peculiarities of some of the samples. In particular, *46AG* was tested at 2.5 µM, to account for its dimeric G4 nature, and *ct DNA* and *cl RNA* were tested at 110 µM nucleotide concentration, which is equivalent to the total nucleotide concentration in a 5 µM sample of a 22 nt oligonucleotide. All samples were prepared in a K^+-rich buffer solution (K-100, see Table 1 footnote). Thioflavin T (ThT), which is widely used for detection of G4 structures, was included for comparison. The fluorescence intensity was measured using a microplate reader. In order to screen a large panel of dyes against a number of analytes, the measurements were performed at fixed excitation and emission wavelengths, selected with a set of filters and adapted to the absorption and emission characteristics of each dye (Supporting Information File 1, Table S1).

The results of the screening, presented as relative enhancement of fluorescence intensity in the presence of nucleic acids (I/I_0, where I is the fluorescence intensity of the dye in the presence of two equivalents of nucleic acid and I_0 is the fluorescence of the dye alone), are shown in the form of a heat-map in Figure 5 (for numeric values cf. Supporting Information, Table S1). In addition, group-average data, i.e., average fluorescence response of each dye towards 12 G4 (DNA and RNA) analytes vs average response to non-G4 (*ct DNA* and *cl RNA*) controls, are presented in Figure 6. This plot facilitates the identification of the most promising probes, disregarding the differences in response of dyes with respect to individual analytes within each group. The inspection of these data leads to a number of interesting observations. 1) Most dyes of the library display signifi-

Table 2: Nucleic acid samples used in the first screening round.

Acronym	Sequence (5′ → 3′)	Topology	Number of G-tetrads	Ref.
G4-DNA				
c-kit2	GGGCGGGCGCGAGGGAGGGG	parallel	3	[71]
25CEB	AGGGTGGGTGTAAGTGTGGGTGGGT	parallel with a long loop	3	[72]
c-kit87up	AGGGAGGGCGCTGGGAGGAGGG	parallel with a snap-back loop	3	[73]
c-myc	TGAGGGTGGGTAGGGTGGGTAA	parallel	3	[74]
c-src1	GGGCGGCGGGCTGGGCGGGG	parallel	3	[75,76]
c-myb	GGAGGAGGAGGA	parallel (dimer)	2	[77]
22AG	A$(GGGTTA)_3$GGG	hybrid (mixture of isoforms)	3	[78]
46AG	A$(GGGTTA)_7$GGG	hybrid (dimeric G4)[a]	2 × 3	[79]
HRAS	TCGGGTTGCGGGCGCAGGGCACGGGCG	antiparallel	3	[80]
TBA	GGTTGGTGTGGTTGG	antiparallel	2	[81]
G4-RNA				
TERRA	r(AGGGUUAGGGUUAGGGUUAGGGU)	parallel	3	[82]
NRAS	r(GGGAGGGGCGGGUCUGGG)	parallel	3	[83]
controls				
ct DNA	calf thymus DNA	double-stranded DNA	N/A	
cl RNA	calf liver RNA	single-stranded RNA	N/A	

[a]Used at half of the oligonucleotide concentration with respect to other G4 samples.

cant fluorescence enhancement ($I/I_0 > 10$) in the presence of at least one DNA or RNA target. Only 9 of 61 styryl dyes (**1j**–**m**, **1w**, **1z**, **1þ**, **7n** and **7ð**) displayed weak or no fluorescence enhancement with all nucleic acid analytes. 2) Most remarkably, the fluorescence of all dyes, with the exception of a few most "unresponsive" ones (**1j**, **1l, 1z**, and **7ð**), is preferentially enhanced in the presence of G4-DNA or G4-RNA structures, although to a varying extent. In fact, among the 61 tested dyes, none showed preferential response to double-stranded DNA (ct DNA) or single-stranded RNA (cl RNA) controls. 3) Compared to the prototype dye **1a**, modifications of the core (Het^+) unit (**7a–14a**) within the distyryl scaffold do not produce significant variations in the fluorimetric response of the dyes. The same holds true for the homo-distyryl compounds **15a** and **16a**, which do not outperform dye **1a**. 4) Likewise, in the 2,4-pyridinium series of dyes, introduction of an aminoalkyl (**3a**) or benzyl substituent (**6a**) does not significantly improve the performance of the probes, as was already described for the dye **2a** [58]. Instead, introduction of a DABCO fragment (bringing two additional positive charges) in **4a** and **5a** leads to higher fluorimetric response of the probes to G4-DNA (e.g., for **5a**, $I/I_0 = 330$ with *22AG*), although accompanied by a concomitant loss of selectivity with respect to ds DNA ($I/I_0 = 25$ for **5a**). 5) In contrast, modification of Ar units strongly influences the fluorimetric response of the dyes. In particular, dyes containing indole residues (**1o–s**, **1u** and **1v**; red dots in Figure 6) show particularly large fluorescence enhancement in the presence of most G4-DNA and G4-RNA targets (**1p**: up to 550-fold with *22AG*) and thus represent a significant improvement with respect to dye **1a** ($I/I_0 < 170$, with all analytes) and ThT ($I/I_0 \leq 200$, with all analytes). Distyryl dyes containing pyrrole residues (**1x**, **7x**: blue dots in Figure 6) also demonstrate outstanding fluorescence enhancement in the presence of G4-DNA analytes (**1x**: up to 690-fold with *TERRA*; **7x**: up to 220-fold with *c-kit2*). However, in the case for **1x**, a marked loss of selectivity with respect to non-G4 analytes can be observed ($I/I_0 = 40$ in the presence of *ct DNA* and 60 in the presence *cl RNA*; cf. Figure 6). Conversely, as mentioned above, the dyes containing benzothiophene (**1w**) or benzofuran (**1z**, **1þ**) residues perform poorly as fluorescent probes. 6) Strongly aggregating dyes (i.e., **1d**, **1ð**, **10a** and **12a**) generally do not show higher light-up effects than weakly aggregating analogues **1a** or **1e**. As a remarkable exception, dye **1d** shows strong and highly selective response towards the dimeric G4-DNA *46AG* ($I/I_0 = 350$), which can be attributed to higher-affinity binding of the dye at the interface between two G4 units, leading to efficient disaggregation. 7) Finally, several mono-styryl dyes, especially **17a**, **17p**, **18a** and **19a** also display significant fluorescence enhancements in the presence of G4 structures (e.g., **17a**: up to 340-fold, **18a**: up to 300-fold, both in the presence of *c-myc*), even

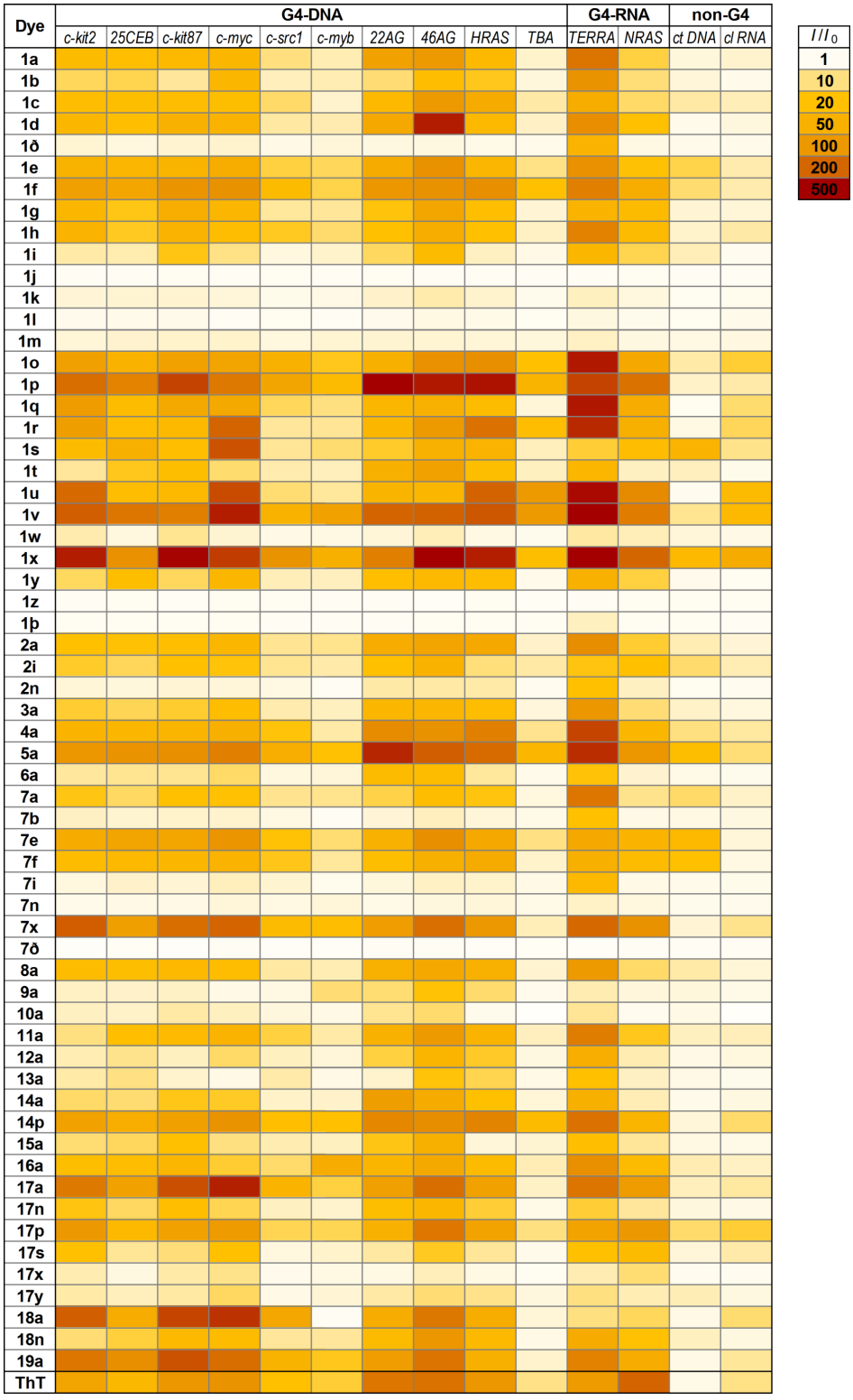

Figure 5: Heat map of the relative emission intensity enhancement (I/I_0) of styryl dyes and thioflavin T (ThT) (c = 2.5 μM in K-100 buffer) in the presence of 2 molar equiv of G4-DNA (46AG: 1 molar equivalent), G4-RNA, or ct DNA and cl RNA controls used at equivalent nucleotide concentration. Darker cells indicate higher I/I_0 values (see legend). For the numeric data, excitation and emission wavelengths see Supporting Information File 1, Table S1.

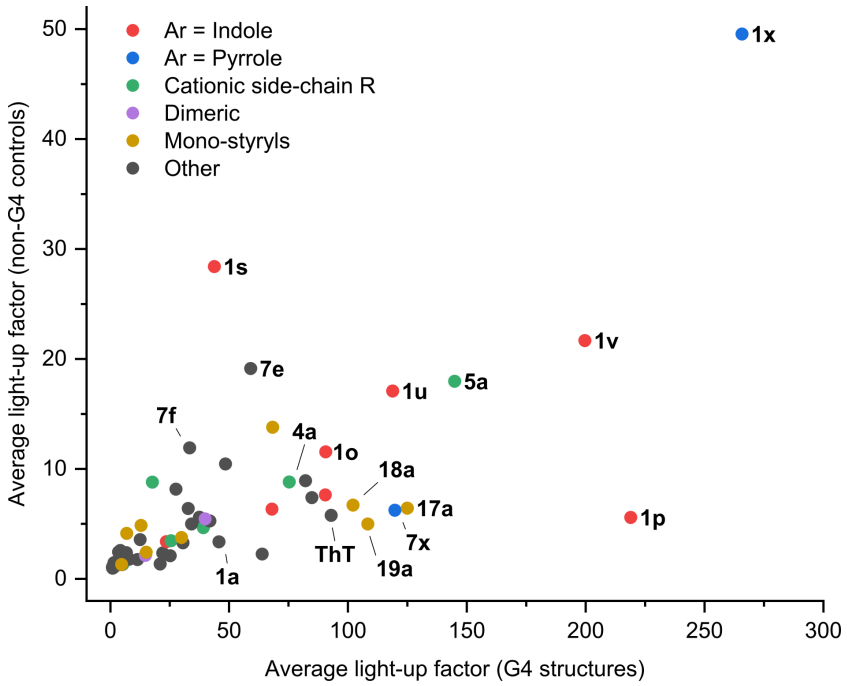

Figure 6: Analysis of the light-up response matrix of the dyes. The average light-up factor of each dye with respect to non-G4 targets (*ct DNA* and *cl RNA*) is plotted against the corresponding average light-up factor obtained with 12 G4 targets. The grouping of dyes is arbitrary and serves to highlight some of the structural motifs. Of note, *x* and *y* axes display different scales.

higher than those of the distyryl analogues **1a** and **7a**, and good selectivity with respect to double-stranded DNA.

A number of patterns could also be revealed with respect to the differential response of the probes towards various G4 targets. 1) Remarkably, G4-RNA *TERRA* systematically induces the highest fluorimetric response of most probes from the distyryl series, but not from the mono-styryl one. 2) In contrast, *TBA* and *c-myb* (i.e., both two-quartet quadruplexes) are poorly detected by most dyes (including ThT), in agreement with what was observed with other probes [6,14,57]. Nonetheless, several indole-containing dyes enable sensitive detection of these targets (with I/I_0 up to 100, **1u** and **1v**), with an excellent selectivity with respect to double-stranded DNA. 3) Several dyes display preferential response towards one or another topological group of analytes. The first group (dyes **1a**, **1d**, **1p**, **1x**) is selective towards hybrid (*22AG*, *46AG*) and antiparallel (*HRAS*) G4-DNA, whereas the second group (dyes **1s**, **1u**, **1v**, **17a** and **18a**) shows fluorimetric selectivity for parallel G4-DNA forms (*c-kit2*, *c-kit87up*, *c-myc*). To verify the preferences of the dyes with respect to the conformation of the G4 analytes, we analysed the data matrix presented in Figure 5 using principal component analysis (PCA). *TBA* and *c-myb,* which had proven mostly unresponsive, were excluded from the analysis. The response pattern of each dye is represented as a dot in the plot of the two first principal components (PC1 vs PC2, Figure 7). In this plot, PC1 (*x* axis) correlates with the overall light-up intensity observed for each dye with the tested targets. On the contrary, PC2 (*y* axis) correlates with the intra-G4 selectivity of each compound, with compounds selective for hybrid and antiparallel G4s locating in the lower part of the plot and compounds selective for parallel G4s locating in the upper part. Interestingly, the loading vectors for parallel G4-RNA (*NRAS* and *TERRA*) fall in between those of parallel and hybrid/antiparallel DNA G4s, suggesting an impact of the ribose backbone on the interaction. As can be inferred from the dot distribution in the plot, the mono-styryl motif and the pyrrole substituent within the distyryl motif (**1x**, **7x**) clearly promote the selectivity for the parallel G4 structures. On the other side, the effect of the indole motif is less clear, with most of the dyes not displaying any well-defined preference, except for **1p**. This latter compound displays a marked selectivity for hybrid and antiparallel topologies, and in particular for the *22AG* target.

Topological classification of G4-DNA by dual-dye analysis

On the basis of screening results, two dyes, namely **1p** and **18a**, were selected to build a fluorimetric test for conformational classification of DNA oligonucleotides. As discussed above, they present complementary preferences with respect to the analyte groups, with **1p** preferentially responding to hybrid and **18a** to parallel G4-DNA structures. Moreover, both dyes

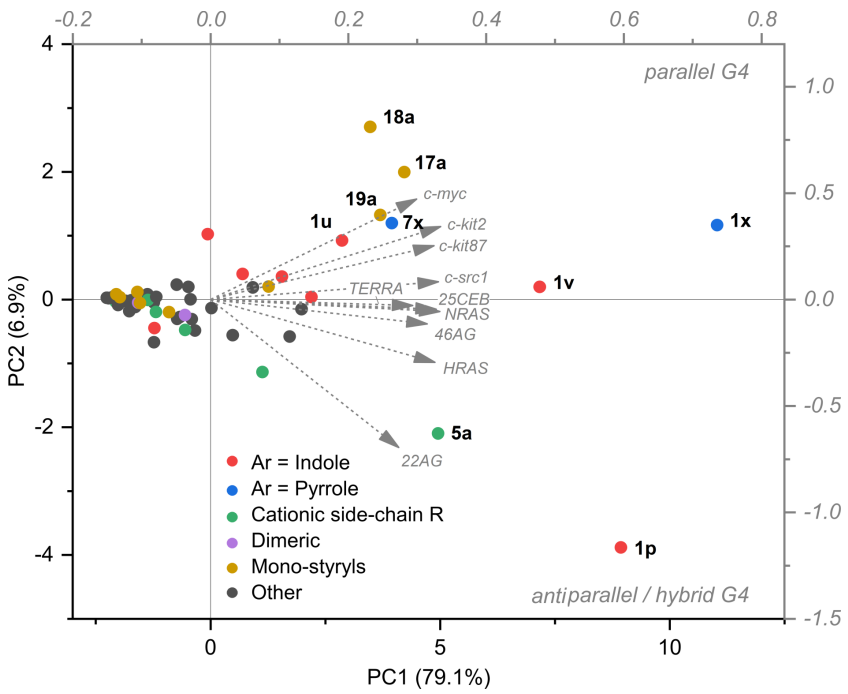

Figure 7: PC1 vs PC2 plot obtained from the principal component analysis of the light-up data matrix for all dyes (*ct DNA* and *cl RNA* were excluded, as well as TBA and *c-myb* due to their low light-up factors). Color coding highlights the distribution of the dyes sharing similar structural motifs.

showed excellent light-up response and selectivity for G4 targets over controls. The concomitant analysis of the response of both dyes should thus allow the sensitive discrimination of different G4 topologies. The response of two dyes was tested against a panel of 33 DNA analytes (Supporting Information File 1, Table S2), comprising some of the previously tested oligonucleotides (*c-myc*, *25CEB*, *22AG*, *46AG*, *TBA*, *ct DNA*). Altogether, the panel of analytes comprehended five conformational groups of roughly equal size, representing the three G4 topologies (parallel, antiparallel and hybrid) as well as single and double strands. RNA targets were excluded from this experiment, even though G4-RNA TERRA triggered the highest fluorescence responses for many dyes. On one side, the interest of G4-RNA topology investigation is limited. In fact, to date, they have never been shown to adopt a structure other than parallel one [84,85]. On the other side, PCA proved that the response of the dyes to RNA targets differs from that to parallel G4-DNA, which might complicate data interpretation.

Emission intensities of both dyes were measured for the new DNA panel in the conditions previously utilized for the screening (2.5 μM dye, 5 μM DNA oligonucleotide, K-100 buffer). The data points corresponding to the oligonucleotides in the set are displayed in a 2D scatter plot (Figure 8), featuring normalized emission intensities of **1p** and **18a** dyes as *x* and *y* axes, respectively. Notably, the oligonucleotides appeared to be grouped in clusters broadly mirroring their conformations. Specifically, parallel G4s cluster in the upper left part of the plot (red dots), as a result of high fluorescence response with **18a** and moderate-to-low response with **1p**. Hybrid G4s (green dots) produce moderate light-up values for **18a** and high ones for **1p**, thus clustering on the right side of the plot. Finally, antiparallel G4s (blue dots) locate in the lower left part of the plot, corresponding to almost null emission enhancement by **18a** and low one by **1a**. Despite the low response to antiparallel G4 structures, these can be still clearly distinguished from double- and single-stranded controls (pink and black dots), to which none of the two dyes proves responsive. A few G4 structures located relatively far from the areas occupied by the respective groups. This is the case of *G4CT*, *Bcl2Mid* and, at least partially, *UpsB-Q3*. In the case of *G4CT*, previous studies report the existence of an equilibrium between a monomolecular antiparallel form and a bimolecular parallel one, affected by K^+ and oligonucleotide concentration [86]. As already suggested, this oligonucleotide is probably present as a mixture of conformations in our working conditions [14]. It is thus likely that the parallel one strongly influences the position of the data in the plot, being better stained by dye **18a**. For both *Bcl2Mid* and *UpsB-Q3*, CD spectra are partially different from those obtained with typical hybrid G4s, normally related to the telomeric sequence [14]. This might indicate the presence of peculiar structural elements that might as well play a role in deter-

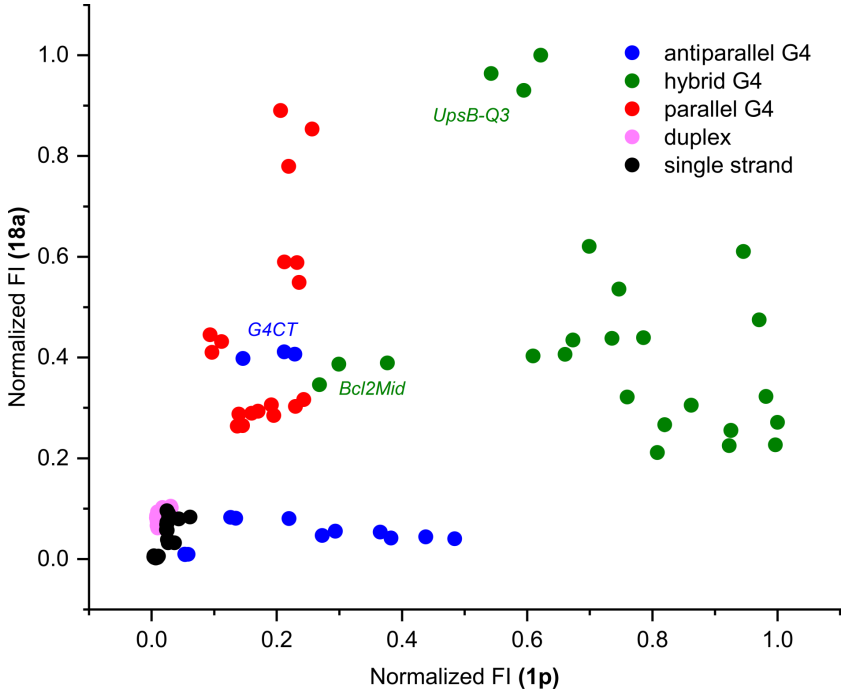

Figure 8: Dual-dye conformational analysis of an extended panel of 33 DNA oligonucleotides. This is performed on normalized datasets (data referring to each of the two dyes are normalized separately), plotting the resulting fluorescence of compound **18a** against that of compound **1p**. Data for each target are presented as independent triplicates.

mining the probes response. On the overall, the combination of the two probes proved quite efficacious at both (1) distinguishing G4 forming DNA sequences from controls, comprehending randomly generated single strands with varying content of guanine and a wealth of duplex structures, and (2) discriminating G4 structures based on their topology, with the exception of a few notable cases presenting structural peculiarities.

Quantum yield and brightness of the probes

Four highly responsive and G4-selective dyes, namely **1p**, **1u**, **17a** and **18a** (Figure 9), were chosen for fluorescence quantum yield and brightness measurements, in order to assess their potential for imaging applications. The quantum yield of dyes was measured in the 1.2–3 μM concentration range, in the absence or in the presence of an excess of two G4-DNA analytes, namely *c-myc* (parallel G4) or *22AG* (hybrid G4), and

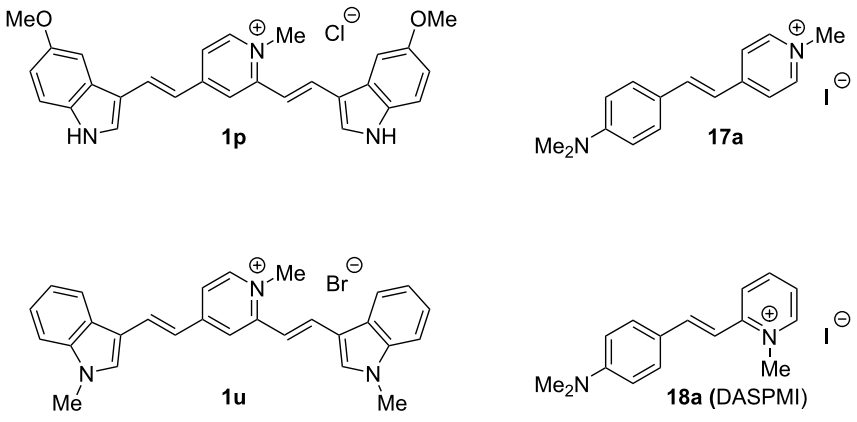

Figure 9: Selected probes featuring high fluorimetric response towards G4 structures.

brightness data were obtained from the multiplication of the corresponding quantum yield by the molar absorptivity coefficient at absorption maxima (ε_{max}) values, for dyes alone and dye–G4 complexes. The obtained data are presented in Table 3. The images of dyes in the absence and in the presence of selected DNA samples are shown in Figure 10.

All dyes display moderate to good quantum yields and brightnesses upon complexation with both G4 analytes. In more detail, distyryl dyes **1p** and **1u** prove more performant in this sense, displaying higher quantum yield and brightness (Φ = 0.12 to 0.32, B = (4.0–11.4) × 10^3 cm^{-1} M^{-1}) than mono-styryl dyes (Φ = 0.040–0.085, B = (1.1–2.3) × 10^3 cm^{-1} M^{-1}). It must

Table 3: Optical parameters (absorption and emission maxima, Stokes shift, molar absorptivity coefficient at the absorption maximum, fluorescence quantum yield and brightness) of dyes **1p**, **1u**, **17a** and **18a** in the absence of DNA or in the presence of G4-DNA structures (*c-myc* and *22AG*).

Properties	Conditions[a]	1p	1u	17a	18a
λ_{max} (abs) [nm][b]	*c-myc*	501	504	463	450
	22AG	508	497	455	447
λ_{max} (em) [nm][c]	*c-myc*	571	560	611	584
	22AG	570	560	606	582
$\Delta\lambda$ [nm][d]	*c-myc*	70	56	148	134
	22AG	62	63	151	135
ε_{max} [10^3 cm^{-1} M^{-1}][e]	no DNA	29.3	31.0	31.5	28.4
	c-myc	32.6	35.7	26.8	24.3
	22AG	30.6	29.2	28.6	26.6
Φ[f]	no DNA	0.0041	0.0114	0.0015	0.0056
	c-myc	0.124	0.319	0.085	0.079
	22AG	0.227	0.293	0.047	0.040
B [10^3, cm^{-1} M^{-1}][g]	no DNA	0.12	0.35	0.047	0.16
	c-myc	4.04	11.4	2.27	1.92
	22AG	6.95	8.56	1.34	1.06

[a]Whenever indicated: in the presence of 6 μM of the respective G4-DNA. [b]Absorption maximum in K-100 buffer, in the concentration range of 1.2–3 μM. [c]Fluorescence emission maximum (λ_{ex} = 500 nm). [d]Stokes shift. [e]Molar absorptivity coefficient at the absorbance maximum for the dye alone or the dye-G4 complex. [f]Fluorescence quantum yield (integration range: 510–800 nm, reference: rhodamine 6G in EtOH). [g]Brightness ($B = \varepsilon_{max} \times \Phi$).

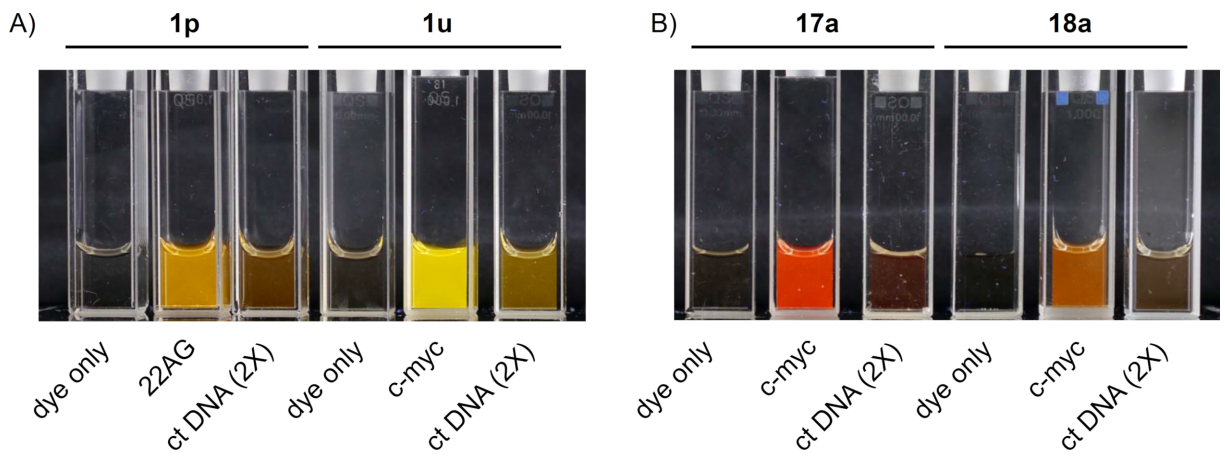

Figure 10: Photographs of solutions of A) distyryl dyes **1p** and **1u**; B) mono-styryl dyes **17a** and **18a**, in the absence or in the presence of G4 (*22AG* or *c-myc*, 10 μM) or ds DNA (ct DNA, 250 μM bp) upon bottom illumination with UV light (λ = 312 nm); in all cases, c(dye) = 5 μM in K-100 buffer.

be noted that the increase of fluorescence quantum yields observed in the presence of G4-DNA (Φ/Φ_0) is significantly lower (up to five-fold) than the corresponding light-up factor measured at a single wavelength (Table S1, Supporting Information File 1). This is typically due to red shifts of absorption and emission spectra of dyes in the presence of nucleic acids, leading to the overestimation of the light-up effect. Nevertheless, single-wavelength light-up factors are of primordial importance for imaging applications, which are performed with a single set of excitation of emission filters. As can be inferred from the data in Table 3, Φ values mirror the selectivity patterns already observed in the screening experiments. In fact, dye **1p** in the presence of hybrid G4 (*22AG*) is roughly twice as fluorescent as its complex with *c-myc* (Φ = 0.227 and 0.124, respectively). On the other side, complexes of **1u**, **17a** and **18a** with *c-myc* are more fluorescent than those with *22AG*. Among these, **1u** certainly forms the brightest and most fluorescent complexes (Φ = 0.32 and 0.29; B = 11.4 and 8.6×10^3 cm^{-1} M^{-1} for *c-myc* and *22AG*, respectively). However, the differences observed between the two G4 analytes are narrow, with respect to those observed with the other dyes.

The analysis of absorption spectra also allowed us to quantify the red-shift effect observed for all dyes upon complexation to G4 structures, which is more pronounced for distyryl dyes **1p** and **1u** (36–45 nm, cf. Table 1 and Table 3) than for monostyryl dyes **17a** and **18a** (7–15 nm, cf. Table 1 and Table 3). Moreover, comparison of the absorption maxima with the corresponding emission ones enabled us to calculate the Stokes shifts for the samples. Of note, all compounds display remarkable shifts, ranging from 56 to 151 nm, although these are more pronounced for distyryl dyes (142 nm on average) than for monostyryl ones (63 nm on average). The combination of the absorption maxima redshift and these high Stokes shifts contributes to make the selected styryl dyes excellent tools for optical imaging.

Discussion

Despite the wealth of scaffolds already reported for the fluorimetric detection of G4 structures, the published studies usually lack a systematic investigation of the factors governing their interaction with DNA and sensing capabilities. In fact, although it is known in broad terms that some molecular features (e.g., size and shape of the aromatic scaffold, charge, redox potential) influence the interaction of dyes with G4-DNA, a thorough assessment of such phenomena by comparative studies is lacking in most reports. In this work, we address this gap within the family of styryl dyes, trying to establish how to construct an optimized dye for G4 sensing. In particular, we studied the optical properties and the fluorimetric response of 61 in-house synthesized compounds against a set of G4-DNA and G4-RNA analytes, as well as the respective non-G4 controls. The data were analyzed aiming at the identification of structural motifs or physical properties (such as aggregation in aqueous medium) of dyes which could govern their fluorimetric response towards one or another group of analytes. Most remarkably, our results demonstrated that a large majority of the dyes (57 out of 61) undergo preferential fluorescence enhancement in the presence of G4 structures, compared with double-stranded (DNA) and single-stranded (RNA) controls (the remaining four dyes did not undergo a fluorescence enhancement with any of the analytes). Can it be considered as a general rule? Considering the significant structural diversity of our library and the related works [41,49], this is highly probable, with regard to mono- and distyryl scaffolds. This implies that styryl-based fluorescent probes initially developed for detection or visualization of DNA, RNA, or other analytes, either in vitro or in cellular imaging applications, must be reassessed in view of their potential strong bias for G4 motifs. Indeed, a remarkable "light-up" effect of SYPRO Orange, a widely used protein stain belonging to the mono-styryl dye family, in the presence of G4-DNA has been reported earlier this year [49]. Moreover, mono-styryls **17a** and **18a** (the latter also known as DASPMI) are long-known and widely used as mitochondrial stains [87,88] and groove-binding fluorescent probes for double-stranded DNA [89,90]. Herein, we report that the fluorescence enhancement of these dyes induced by parallel G4 structures is dramatically higher compared to ds DNA.

Although the preferential response to G4 structures seems to be an inherent feature of the styryl scaffold, the magnitude of the "light-up" effect drastically varies within the series. Our results clearly point to several structural motifs that appear advantageous for high fluorimetric response and high quantum yield of the probes. First of all, indole substituents, including core-substituted indoles, emerge as the most efficient in this sense, as demonstrated by several distyryls (**1o–v**) with superior properties with respect to the prototype compound **1a**. A similar effect of indole substituents was already observed in the family of mono-styryl dyes developed for detection of double-stranded DNA [68,70,91]. Moreover, pyrrole-substituted distyryls (**1x** and **7x**) also display very high fluorimetric response (up to I/I_0 = 690, for **1x**–TERRA complex), albeit at the expense of somewhat lower selectivity with respect to ds DNA and ss RNA. It may be suggested that electron-rich heterocyclic substituents (indole and pyrrole) act by lowering the reduction potential of dyes, rendering the photoinduced electron-transfer reaction with guanine residues in DNA energetically disfavored and resulting in higher fluorescence quantum yields. However, in the absence of redox potential data, this assump-

tion could not be experimentally verified. Finally, we showed that the mono-styryl design can yield probes with interesting properties, such as high light-up factors (up to 340, for **17a**–*c-myc* complex) and a clear-cut selectivity for parallel-stranded G4 motifs. Interestingly, in the mono-styryl family, dyes containing indole (**17p**, **17s**) or pyrrole (**17x**) substituents did not perform better than the simplest styryl derivatives, i.e., **17a** and **18a**. This fact demonstrates that our data are still insufficient to formulate generalized structure–properties relationships.

Conclusion

To summarize, a systematic analysis enabled us to select the optimal probes within the styryl dye family (i.e., those displaying high quantum yield and brightness, excellent light-up factor, and remarkable selectivity for a certain G4 class). A comparison with literature data demonstrates that dyes **1p** and **1u** largely outperform, in terms of brightness and quadruplex-vs-duplex selectivity, the widely used fluorescent probes, such as thioflavin T (ThT, Φ = 0.25, in the presence of *22AG*/K^+ conditions) and thiazole orange (TO, Φ = 0.19 in the presence of *22AG*/K^+ conditions) [92], and approach the brightest G4-DNA probes developed so far, such as trialryimidazole IZCM-7 (Φ = 0.52, in the presence of *c-myc*) [52] and the NIR-emitting squaraine dye CAS-C1 (Φ of up to 0.74 with parallel G4-DNA) [93]. Applications of these dyes can be multiple. As an example, we proposed herein the implementation of a simple two-dye array to classify G4-DNA structures based on their topology. Applications in the design of G4-based logic gates could also be envisaged. Taking into account the favorable optical properties, in particular high brightness and large Stokes shift, the same probes could be utilized to proceed to cellular imagining of G4 structures, certainly with caution regarding the inherent propensity of cationic dyes to accumulate in mitochondria. At the same time, our work establishes an approach to optimize the structure of renowned scaffolds and achieve maximal performances in G4 sensing.

Supporting Information

Supporting Information File 1

Experimental details and supplementary Tables S1 and S2.
[https://www.beilstein-journals.org/bjoc/content/supplementary/1860-5397-15-183-S1.pdf]

Acknowledgements

The authors thank Ms. Anne Cucchiarini (Institut Curie) for HPLC analysis and Mr. Élie Benchimol for help in the synthesis of the dyes. This work was supported by Institut Curie (post-doctoral fellowship to M.Z.).

ORCID® iDs

Michela Zuffo - https://orcid.org/0000-0003-3556-2196
Marie-Paule Teulade-Fichou - https://orcid.org/0000-0002-2053-7513
Anton Granzhan - https://orcid.org/0000-0002-0424-0461

References

1. Rhodes, D.; Lipps, H. J. *Nucleic Acids Res.* **2015,** *43,* 8627–8637. doi:10.1093/nar/gkv862
2. Tian, T.; Chen, Y.-Q.; Wang, S.-R.; Zhou, X. *Chem* **2018,** *4,* 1314–1344. doi:10.1016/j.chempr.2018.02.014
3. Mukherjee, A. K.; Sharma, S.; Chowdhury, S. *Trends Genet.* **2019,** *35,* 129–144. doi:10.1016/j.tig.2018.11.001
4. Yatsunyk, L. A.; Mendoza, O.; Mergny, J.-L. *Acc. Chem. Res.* **2014,** *47,* 1836–1844. doi:10.1021/ar500063x
5. Mergny, J.-L.; Sen, D. *Chem. Rev.* **2019,** *119,* 6290–6325. doi:10.1021/acs.chemrev.8b00629
6. Renaud de la Faverie, A.; Guédin, A.; Bedrat, A.; Yatsunyk, L. A.; Mergny, J.-L. *Nucleic Acids Res.* **2014,** *42,* e65. doi:10.1093/nar/gku111
7. Xu, S.; Li, Q.; Xiang, J.; Yang, Q.; Sun, H.; Guan, A.; Wang, L.; Liu, Y.; Yu, L.; Shi, Y.; Chen, H.; Tang, Y. *Sci. Rep.* **2016,** *6,* 24793. doi:10.1038/srep24793
8. Kim, M.; Kreig, A.; Lee, C.-Y.; Rube, H. T.; Calvert, J.; Song, J. S.; Myong, S. *Nucleic Acids Res.* **2016,** *44,* 4807–4817. doi:10.1093/nar/gkw272
9. Hu, M.-H.; Chen, S.-B.; Wang, Y.-Q.; Zeng, Y.-M.; Ou, T.-M.; Li, D.; Gu, L.-Q.; Huang, Z.-S.; Tan, J.-H. *Biosens. Bioelectron.* **2016,** *83,* 77–84. doi:10.1016/j.bios.2016.04.029
10. Chang, T.; Li, W.; Ding, Z.; Cheng, S.; Liang, K.; Liu, X.; Bing, T.; Shangguan, D. *Anal. Chem. (Washington, DC, U. S.)* **2017,** *89,* 8162–8169. doi:10.1021/acs.analchem.7b01992
11. Sabharwal, N. C.; Savikhin, V.; Turek-Herman, J. R.; Nicoludis, J. M.; Szalai, V. A.; Yatsunyk, L. A. *FEBS J.* **2014,** *281,* 1726–1737. doi:10.1111/febs.12734
12. Zhao, D.; Dong, X.; Jiang, N.; Zhang, D.; Liu, C. *Nucleic Acids Res.* **2014,** *42,* 11612–11621. doi:10.1093/nar/gku833
13. Kreig, A.; Calvert, J.; Sanoica, J.; Cullum, E.; Tipanna, R.; Myong, S. *Nucleic Acids Res.* **2015,** *43,* 7961–7970. doi:10.1093/nar/gkv749
14. Zuffo, M.; Xie, X.; Granzhan, A. *Chem. – Eur. J.* **2019,** *25,* 1812–1818. doi:10.1002/chem.201805422
15. Endoh, T.; Rode, A. B.; Takahashi, S.; Kataoka, Y.; Kuwahara, M.; Sugimoto, N. *Anal. Chem. (Washington, DC, U. S.)* **2016,** *88,* 1984–1989. doi:10.1021/acs.analchem.5b04396
16. He, H.-Z.; Chan, D. S.-H.; Leung, C.-H.; Ma, D.-L. *Nucleic Acids Res.* **2013,** *41,* 4345–4359. doi:10.1093/nar/gkt108
17. Chen, H.; Sun, H.; Zhang, X.; Sun, X.; Shi, Y.; Xu, S.; Tang, Y. *New J. Chem.* **2016,** *40,* 1940–1943. doi:10.1039/c5nj02652k
18. Ma, D.-L.; Chan, D. S.-H.; Man, B. Y.-W.; Leung, C.-H. *Chem. – Asian J.* **2011,** *6,* 986–1003. doi:10.1002/asia.201000870
19. Yeasmin Khusbu, F.; Zhou, X.; Chen, H.; Ma, C.; Wang, K. *TrAC, Trends Anal. Chem.* **2018,** *109,* 1–18. doi:10.1016/j.trac.2018.09.013
20. Sun, X.; Li, Q.; Xiang, J.; Wang, L.; Zhang, X.; Lan, L.; Xu, S.; Yang, F.; Tang, Y. *Analyst* **2017,** *142,* 3352–3355. doi:10.1039/c7an01062a
21. Chen, H.; Zhang, X.; Sun, H.; Sun, X.; Shi, Y.; Xu, S.; Tang, Y. *Analyst* **2015,** *140,* 7170–7174. doi:10.1039/c5an01507c
22. Lu, Y.-J.; Hu, D.-P.; Deng, Q.; Wang, Z.-Y.; Huang, B.-H.; Fang, Y.-X.; Zhang, K.; Wong, W.-L. *Analyst* **2015,** *140,* 5998–6004. doi:10.1039/c5an01158b

23. Sun, H.; Yu, L.; Chen, H.; Xiang, J.; Zhang, X.; Shi, Y.; Yang, Q.; Guan, A.; Li, Q.; Tang, Y. *Talanta* **2015,** *136,* 210–214. doi:10.1016/j.talanta.2015.01.027
24. Tseng, T.-Y.; Wang, Z.-F.; Chien, C.-H.; Chang, T.-C. *Nucleic Acids Res.* **2013,** *41,* 10605–10618. doi:10.1093/nar/gkt814
25. Shivalingam, A.; Izquierdo, M. A.; Le Marois, A.; Vyšniauskas, A.; Suhling, K.; Kuimova, M. K.; Vilar, R. *Nat. Commun.* **2015,** *6,* 8178. doi:10.1038/ncomms9178
26. Huang, W.-C.; Tseng, T.-Y.; Chen, Y.-T.; Chang, C.-C.; Wang, Z.-F.; Wang, C.-L.; Hsu, T.-N.; Li, P.-T.; Chen, C.-T.; Lin, J.-J.; Lou, P.-J.; Chang, T.-C. *Nucleic Acids Res.* **2015,** *43,* 10102–10113. doi:10.1093/nar/gkv1061
27. Zhang, S.; Sun, H.; Wang, L.; Liu, Y.; Chen, H.; Li, Q.; Guan, A.; Liu, M.; Tang, Y. *Nucleic Acids Res.* **2018,** *46,* 7522–7532. doi:10.1093/nar/gky665
28. Doria, F.; Nadai, M.; Zuffo, M.; Perrone, R.; Freccero, M.; Richter, S. N. *Chem. Commun.* **2017,** *53,* 2268–2271. doi:10.1039/c6cc08492c
29. Yang, C.; Hu, R.; Li, Q.; Li, S.; Xiang, J.; Guo, X.; Wang, S.; Zeng, Y.; Li, Y.; Yang, G. *ACS Omega* **2018,** *3,* 10487–10492. doi:10.1021/acsomega.8b01190
30. Xu, S.; Li, Q.; Xiang, J.; Yang, Q.; Sun, H.; Guan, A.; Wang, L.; Liu, Y.; Yu, L.; Shi, Y.; Chen, H.; Tang, Y. *Nucleic Acids Res.* **2015,** *43,* 9575–9586. doi:10.1093/nar/gkv1040
31. Laguerre, A.; Hukezalie, K.; Winckler, P.; Katranji, F.; Chanteloup, G.; Pirrotta, M.; Perrier-Cornet, J.-M.; Wong, J. M. Y.; Monchaud, D. *J. Am. Chem. Soc.* **2015,** *137,* 8521–8525. doi:10.1021/jacs.5b03413
32. Chen, S.-B.; Hu, M.-H.; Liu, G.-C.; Wang, J.; Ou, T.-M.; Gu, L.-Q.; Huang, Z.-S.; Tan, J.-H. *J. Am. Chem. Soc.* **2016,** *138,* 10382–10385. doi:10.1021/jacs.6b04799
33. Chen, X.-C.; Chen, S.-B.; Dai, J.; Yuan, J.-H.; Ou, T.-M.; Huang, Z.-S.; Tan, J.-H. *Angew. Chem., Int. Ed.* **2018,** *57,* 4702–4706. doi:10.1002/anie.201801999
34. Ma, D.-L.; Shiu-Hin Chan, D.; Yang, H.; He, H.-Z.; Leung, C.-H. *Curr. Pharm. Des.* **2012,** *18,* 2058–2075. doi:10.2174/138161212799958314
35. Largy, E.; Granzhan, A.; Hamon, F.; Verga, D.; Teulade-Fichou, M.-P. *Top. Curr. Chem.* **2012,** 111–177. doi:10.1007/128_2012_346
36. Vummidi, B. R.; Alzeer, J.; Luedtke, N. W. *ChemBioChem* **2013,** *14,* 540–558. doi:10.1002/cbic.201200612
37. Ma, D.-L.; Zhang, Z.; Wang, M.; Lu, L.; Zhong, H.-J.; Leung, C.-H. *Chem. Biol.* **2015,** *22,* 812–828. doi:10.1016/j.chembiol.2015.06.016
38. Suseela, Y. V.; Narayanaswamy, N.; Pratihar, S.; Govindaraju, T. *Chem. Soc. Rev.* **2018,** *47,* 1098–1131. doi:10.1039/c7cs00774d
39. Chilka, P.; Desai, N.; Datta, B. *Molecules* **2019,** *24,* 752. doi:10.3390/molecules24040752
40. Chen, X.; Wang, J.; Jiang, G.; Zu, G.; Liu, M.; Zhou, L.; Pei, R. *RSC Adv.* **2016,** *6,* 70117–70123. doi:10.1039/c6ra11152a
41. Wang, M.-Q.; Xu, J.; Zhang, L.; Liao, Y.; Wei, H.; Yin, Y.-Y.; Liu, Q.; Zhang, Y. *Bioorg. Med. Chem.* **2019,** *27,* 552–559. doi:10.1016/j.bmc.2018.12.037
42. Guan, A.-j.; Zhang, X.-F.; Sun, X.; Li, Q.; Xiang, J.-F.; Wang, L.-X.; Lan, L.; Yang, F.-M.; Xu, S.-J.; Guo, X.-M.; Tang, Y.-L. *Sci. Rep.* **2018,** *8,* 2666. doi:10.1038/s41598-018-20960-7
43. Yan, J.-w.; Tian, Y.-g.; Tan, J.-h.; Huang, Z.-s. *Analyst* **2015,** *140,* 7146–7149. doi:10.1039/c5an01573a
44. Lin, D.; Fei, X.; Gu, Y.; Wang, C.; Tang, Y.; Li, R.; Zhou, J. *Analyst* **2015,** *140,* 5772–5780. doi:10.1039/c5an00866b
45. Ihmels, H.; Thomas, L. *Org. Biomol. Chem.* **2013,** *11,* 480–487. doi:10.1039/c2ob26779a
46. Chen, Y.; Yan, S.; Yuan, L.; Zhou, Y.; Song, Y.; Xiao, H.; Weng, X.; Zhou, X. *Org. Chem. Front.* **2014,** *1,* 267–270. doi:10.1039/c3qo00048f
47. Wang, Y.-Q.; Hu, M.-H.; Guo, R.-J.; Chen, S.-B.; Huang, Z.-S.; Tan, J.-H. *Sens. Actuators, B* **2018,** *266,* 187–194. doi:10.1016/j.snb.2018.03.125
48. Chen, S.-B.; Wu, W.-B.; Hu, M.-H.; Ou, T.-M.; Gu, L.-Q.; Tan, J.-H.; Huang, Z.-S. *Chem. Commun.* **2014,** *50,* 12173–12176. doi:10.1039/c4cc05394j
49. Deore, P. S.; Manderville, R. A. *New J. Chem.* **2019,** *43,* 4994–4997. doi:10.1039/c9nj00188c
50. Wu, S.; Wang, L.; Zhang, N.; Liu, Y.; Zheng, W.; Chang, A.; Wang, F.; Li, S.; Shangguan, D. *Chem. – Eur. J.* **2016,** *22,* 6037–6047. doi:10.1002/chem.201505170
51. Jiang, G.; Chen, X.; Xu, L.; Cao, Y.; Hong, S.; Liu, M.; Cao, W.; Pei, R. *ChemistrySelect* **2017,** *2,* 2783–2788. doi:10.1002/slct.201601889
52. Hu, M.-H.; Chen, S.-B.; Guo, R.-J.; Ou, T.-M.; Huang, Z.-S.; Tan, J.-H. *Analyst* **2015,** *140,* 4616–4625. doi:10.1039/c5an00761e
53. Lu, Y.-J.; Wang, Z.-Y.; Hu, D.-P.; Deng, Q.; Huang, B.-H.; Fang, Y.-X.; Zhang, K.; Wong, W.-L.; Chow, C.-F. *Dyes Pigm.* **2015,** *122,* 94–102. doi:10.1016/j.dyepig.2015.06.018
54. Zhang, L.; Er, J. C.; Li, X.; Heng, J. J.; Samanta, A.; Chang, Y.-T.; Lee, C.-L. K. *Chem. Commun.* **2015,** *51,* 7386–7389. doi:10.1039/c5cc01601k
55. Tera, M.; Hirokawa, T.; Okabe, S.; Sugahara, K.; Seimiya, H.; Shimamoto, K. *Chem. – Eur. J.* **2015,** *21,* 14519–14528. doi:10.1002/chem.201501693
56. Zuffo, M.; Guédin, A.; Leriche, E.-D.; Doria, F.; Pirota, V.; Gabelica, V.; Mergny, J.-L.; Freccero, M. *Nucleic Acids Res.* **2018,** *46,* e115. doi:10.1093/nar/gky607
57. Xie, X.; Reznichenko, O.; Chaput, L.; Martin, P.; Teulade-Fichou, M.-P.; Granzhan, A. *Chem. – Eur. J.* **2018,** *24,* 12638–12651. doi:10.1002/chem.201801701
58. Xie, X.; Choi, B.; Largy, E.; Guillot, R.; Granzhan, A.; Teulade-Fichou, M.-P. *Chem. – Eur. J.* **2013,** *19,* 1214–1226. doi:10.1002/chem.201203710
59. Xie, X.; Renvoisé, A.; Granzhan, A.; Teulade-Fichou, M.-P. *New J. Chem.* **2015,** *39,* 5931–5935. doi:10.1039/c5nj01325a
60. Das, A. K.; Ihmels, H.; Kölsch, S. *Photochem. Photobiol. Sci.* **2019,** *18,* 1373–1381. doi:10.1039/c9pp00096h
61. Kumari, B.; Yadav, A.; Pany, S. P.; Pradeepkumar, P. I.; Kanvah, S. *J. Photochem. Photobiol., B* **2019,** *190,* 128–136. doi:10.1016/j.jphotobiol.2018.10.007
62. Pithan, P. M.; Decker, D.; Druzhinin, S. I.; Ihmels, H.; Schönherr, H.; Voß, Y. *RSC Adv.* **2017,** *7,* 10660–10667. doi:10.1039/c6ra27684a
63. Wang, M.-Q.; Liu, X.-N.; Guo, Z.-J.; Feng, C.; Rui, M. *New J. Chem.* **2018,** *42,* 4933–4939. doi:10.1039/c8nj00203g
64. Su, J.-J.; Wang, L.-Y.; Zhang, X.-H.; Fu, Y.-L.; Huang, Y.; Wei, Y.-S. *J. Braz. Chem. Soc.* **2011,** *22,* 73–79. doi:10.1590/s0103-50532011000100009
65. Maçôas, E.; Marcelo, G.; Pinto, S.; Cañeque, T.; Cuadro, A. M.; Vaquero, J. J.; Martinho, J. M. G. *Chem. Commun.* **2011,** *47,* 7374–7376. doi:10.1039/c1cc12163d
66. Crippa, G. B.; Verdi, T. *Ann. Chim. Appl.* **1936,** *26,* 418–423.
67. Clemo, G. R.; Swan, G. A. *J. Chem. Soc.* **1938,** 1454–1455. doi:10.1039/jr9380001454
68. Bohländer, P. R.; Wagenknecht, H.-A. *Org. Biomol. Chem.* **2013,** *11,* 7458–7462. doi:10.1039/c3ob41717d
69. Bohländer, P. R.; Wagenknecht, H.-A. *Eur. J. Org. Chem.* **2014,** 7547–7551. doi:10.1002/ejoc.201403119

70. Bohländer, P. R.; Wagenknecht, H.-A. *Methods Appl. Fluoresc.* **2015,** *3,* 044003. doi:10.1088/2050-6120/3/4/044003
71. Kuryavyi, V.; Phan, A. T.; Patel, D. J. *Nucleic Acids Res.* **2010,** *38,* 6757–6773. doi:10.1093/nar/gkq558
72. Amrane, S.; Adrian, M.; Heddi, B.; Serero, A.; Nicolas, A.; Mergny, J.; Phan, A. T. *J. Am. Chem. Soc.* **2012,** *134,* 5807–5816. doi:10.1021/ja208993r
73. Phan, A. T.; Kuryavyi, V.; Burge, S.; Neidle, S.; Patel, D. J. *J. Am. Chem. Soc.* **2007,** *129,* 4386–4392. doi:10.1021/ja068739h
74. Ambrus, A.; Chen, D.; Dai, J.; Jones, R. A.; Yang, D. *Biochemistry* **2005,** *44,* 2048–2058. doi:10.1021/bi048242p
75. Rodriguez, R.; Miller, K. M.; Forment, J. V.; Bradshaw, C. R.; Nikan, M.; Britton, S.; Oelschlaegel, T.; Xhemalce, B.; Balasubramanian, S.; Jackson, S. P. *Nat. Chem. Biol.* **2012,** *8,* 301–310. doi:10.1038/nchembio.780
76. Murat, P.; Gormally, M. V.; Sanders, D.; Di Antonio, M.; Balasubramanian, S. *Chem. Commun.* **2013,** *49,* 8453–8455. doi:10.1039/c3cc44737e
77. Matsugami, A.; Ouhashi, K.; Kanagawa, M.; Liu, H.; Kanagawa, S.; Uesugi, S.; Katahira, M. *J. Mol. Biol.* **2001,** *313,* 255–269. doi:10.1006/jmbi.2001.5047
78. Renčiuk, D.; Kejnovská, I.; Školáková, P.; Bednářová, K.; Motlová, J.; Vorlíčková, M. *Nucleic Acids Res.* **2009,** *37,* 6625–6634. doi:10.1093/nar/gkp701
79. Yue, D. J. E.; Lim, K. W.; Phan, A. T. *J. Am. Chem. Soc.* **2011,** *133,* 11462–11465. doi:10.1021/ja204197d
80. Membrino, A.; Cogoi, S.; Pedersen, E. B.; Xodo, L. E. *PLoS One* **2011,** *6,* e24421. doi:10.1371/journal.pone.0024421
81. Schultze, P.; Macaya, R. F.; Feigon, J. *J. Mol. Biol.* **1994,** *235,* 1532–1547. doi:10.1006/jmbi.1994.1105
82. Martadinata, H.; Phan, A. T. *Biochemistry* **2013,** *52,* 2176–2183. doi:10.1021/bi301606u
83. Kumari, S.; Bugaut, A.; Huppert, J. L.; Balasubramanian, S. *Nat. Chem. Biol.* **2007,** *3,* 218–221. doi:10.1038/nchembio864
84. Fay, M. M.; Lyons, S. M.; Ivanov, P. *J. Mol. Biol.* **2017,** *429,* 2127–2147. doi:10.1016/j.jmb.2017.05.017
85. Małgowska, M.; Czajczynska, K.; Gudanis, D.; Tworak, A.; Gdaniec, Z. *Acta Biochim. Pol.* **2016,** *63,* 609–621. doi:10.18388/abp.2016_1335
86. Rehm, C.; Holder, I. T.; Groß, A.; Wojciechowski, F.; Urban, M.; Sinn, M.; Drescher, M.; Hartig, J. S. *Chem. Sci.* **2014,** *5,* 2809–2818. doi:10.1039/c4sc00440j
87. Bereiter-Hahn, J. *Biochim. Biophys. Acta, Bioenerg.* **1976,** *423,* 1–14. doi:10.1016/0005-2728(76)90096-7
88. Ramadass, R.; Bereiter-Hahn, J. *Biophys. J.* **2008,** *95,* 4068–4076. doi:10.1529/biophysj.108.135079
89. Kumar, C. V.; Turner, R. S.; Asuncion, E. H. *J. Photochem. Photobiol., A* **1993,** *74,* 231–238. doi:10.1016/1010-6030(93)80121-o
90. Sahoo, D.; Bhattacharya, P.; Chakravorti, S. *J. Phys. Chem. B* **2010,** *114,* 2044–2050. doi:10.1021/jp910766q
91. Schwechheimer, C.; Rönicke, F.; Schepers, U.; Wagenknecht, H.-A. *Chem. Sci.* **2018,** *9,* 6557–6563. doi:10.1039/c8sc01574k
92. Mohanty, J.; Barooah, N.; Dhamodharan, V.; Harikrishna, S.; Pradeepkumar, P. I.; Bhasikuttan, A. C. *J. Am. Chem. Soc.* **2013,** *135,* 367–376. doi:10.1021/ja309588h
93. Grande, V.; Shen, C.-A.; Deiana, M.; Dudek, M.; Olesiak-Banska, J.; Matczyszyn, K.; Würthner, F. *Chem. Sci.* **2018,** *9,* 8375–8381. doi:10.1039/c8sc02882f

License and Terms

BEILSTEIN JOURNAL OF ORGANIC CHEMISTRY

Tautomerism as primary signaling mechanism in metal sensing: the case of amide group

Vera Deneva*[1], Georgi Dobrikov[1], Aurelien Crochet[2], Daniela Nedeltcheva[1], Katharina M. Fromm[2] and Liudmil Antonov*[1]

Full Research Paper

Open Access

Address:
[1]Institute of Organic Chemistry with Centre of Phytochemistry, Bulgarian Academy of Sciences, Sofia 1113, Bulgaria and [2]University of Fribourg, Department of Chemistry, Chemin du Musée 9, CH-1700 Fribourg, Switzerland

Email:
Vera Deneva* - vdeneva@orgchm.bas.bg; Liudmil Antonov* - lantonov@orgchm.bas.bg

* Corresponding author

Keywords:
amide group; azo dye; molecular sensor; sidearm; tautomerism

Beilstein J. Org. Chem. **2019,** *15,* 1898–1906.
doi:10.3762/bjoc.15.185

Received: 17 May 2019
Accepted: 01 August 2019
Published: 08 August 2019

This article is part of the thematic issue "Dyes in modern organic chemistry".

Guest Editor: H. Ihmels

Abstract

The concept for sensing systems using the tautomerism as elementary signaling process has been further developed by synthesizing a ligand containing 4-(phenyldiazenyl)naphthalene-1-ol as a tautomeric block and an amide group as metal capturing antenna. Although it has been expected that the intramolecular hydrogen bonding (between the tautomeric hydroxy group and the nitrogen atom from the amide group) could stabilize the pure enol form in some solvents, the keto tautomer is also observed. This is a result from the formation of intramolecular associates in some solvents. Strong bathochromic and hyperchromic effects in the visible spectra accompany the 1:1 formation of complexes with some alkaline earth metal ions.

Introduction

The design of new organic sensing systems is an undividable part of the development of coordination chemistry [1]. Particularly chromophore ligands have been successfully utilized for colorimetric detection of the majority of metal ions as complex [2]. Some of them are used as standard tools in chelatometric titrations [3]. The design of specific ligands for alkali metal determination is still a challenge. In the case of alkaline earth metal ions, the reagents with reasonable selectivity are still not commonly accepted since they compete with transitional metal ions [4]. The discovery of crown ethers [5] and 3D-based ligands [6] unquestionably helped the development of natural ligand-supported metal investigations.

The ion recognition is based on the existence of two molecular states (ligand and complex) with different optical properties and a structure that allows fast transfer from the ligand to the complex upon addition of the desired metal ion [7]. The tautomeric proton exchange has the same properties when the equilibrium is switched from one to the other tautomer. The tautomerism can be controlled by metal ion addition, when an ionophore unit

is implemented in the tautomeric backbone. The conceptual idea to achieve the pure enol tautomer through intramolecular hydrogen bonding with the ionophore [7,8] is shown in Scheme 1. The complex formation ejects the tautomeric proton and stabilizes the keto tautomer.

Several successful tautomeric ligands, based on 4-(phenyldiazenyl)naphthalen-1-ol (**1**) [8] (**2** and **3**, Scheme 2) as a tautomeric unit have been developed by us. We found that compounds **2** and **3** exist in the neutral state solely as enol tautomers due to intramolecular hydrogen bonding involving the tautomeric hydroxy group and that the complexation shifts the equilibrium to the **K** form. Although **3** exhibits a 3D structure and as a result, shows high stability constants upon complexation, the selectivity is rather low, which can be attributed to the crown ether complexation features in general. Developing the system further, leads to modification of the ionophore part by replacing the crown ether with other ionophores, such as done in the case of **4** and **5**. The quantum-chemical calculations for **4** and **5** have demonstrated that the stable enol tautomers exist as intramolecular C=O···HO bonded system, while in the **K** forms the ionophore part does not participate in hydrogen bonding and can be considered as a basic 2-alkyl substitution [9]. Consequently, the stabilization between the **E** and **K** forms is a result of the competition between the strength of the hydrogen bonding in the enol tautomer and the effect of simple alkyl substitution in the keto form skeleton. The calculations also suggest that the efficient switching towards the enol form can be achieved only when R' = NMe_2 (Scheme 2).

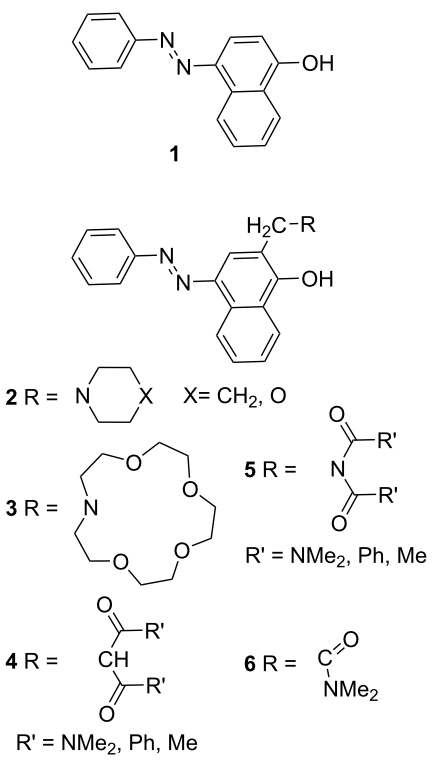

Scheme 2: 4-(Phenyldiazenyl)naphthalen-1-ol (**1**) and tautomeric ligands based on it.

Theoretical modelling of structures **4** and **5** have also shown that only one of the carbonyl groups from the ionophore unit really participates in the capturing of the metal ion upon complexation. Therefore, the aim of the current article is to estimate theoretically and experimentally, the tautomeric state and complexation abilities of compound **6**, where only one carbonyl group in the ionophore part is present (Scheme 2). It is expected that the enol tautomer stabilization would be achieved in the neutral state as a result of the strong intramolecular hydrogen bonding between the tautomeric OH group and the carbonyl group in the ionophore part. The complex formation, depending on the size and charge of the metal ion, should shift the tautomeric equilibrium towards the keto tautomer and should provide stabilization of the complex. To the best of our knowledge, such a system has not been synthesized and studied up to now.

Results and Discussion

Compound **1** is a well-studied tautomeric structure featuring a moderate energy gap between the enol and the keto tautomeric forms [10]. For this reason, the tautomeric equilibrium can be easily affected by changing the solvent. However, the

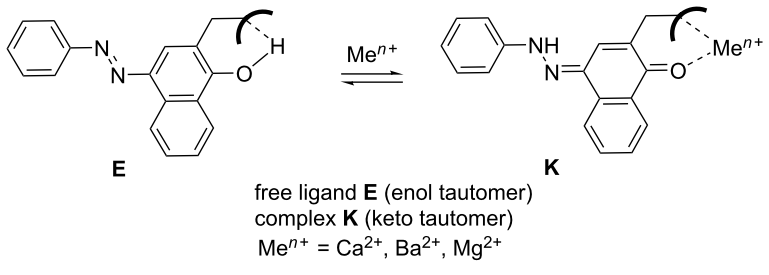

Scheme 1: Conceptual idea for tautomeric metal sensing.

tautomeric equilibrium has not been switched fully to either of the tautomers in solution. For instance, the experimentally determined ΔG values at room temperature range from 1.42 kcal/mol, which corresponds to around 8% (in cyclohexane) or 10% (in methylcyclohexane/toluene) of the **K** tautomer [11,12], to −0.71 kcal/mol in chloroform [8], where this tautomer dominates. The ΔG value of 0.33 kcal/mol in acetonitrile, determined experimentally [8], have been used to validate the level of theory used in the current study. As seen from Table S1 (Supporting Information File 1) the best result has been achieved by using M06-2X/6-31++G** functional and basis set, which predicts the relative energy of the tautomers (ΔE value, defined as $E_{\mathbf{K}} - E_{\mathbf{E}}$) of 0.33 kcal/mol, perfectly matching the experiment.

In the case of **6** the calculations yield a ΔE value of 3.14 kcal/mol in acetonitrile, which leads to the expectation that the tautomeric equilibrium should be fully shifted to **6E**. The corresponding most stable structure of the enol form is shown in Figure 1, where hydrogen bonding between the tautomeric OH group and the sidearm carbonyl group can be seen.

The tautomeric equilibrium in **1** is strongly solvent-dependent as mentioned above and which can also be seen from Figure 2a. For instance, through intermolecular hydrogen bonding with the carbonyl oxygen atom from the tautomeric backbone, chloroform stabilizes the keto tautomer, absorbing at ≈480 nm, while in acetonitrile the enol form is also presented with a maximum at ≈410 nm.

A comparison between the absorption spectra of **1** and **6** shows that the tautomeric equilibrium in **6** is also surprisingly solvent dependent. As shown on Figure 2b, the tautomeric equilibrium in **6** is shifted, but not fully, towards the **K** form in acetonitrile and chloroform and towards the **E** form in dichloromethane and

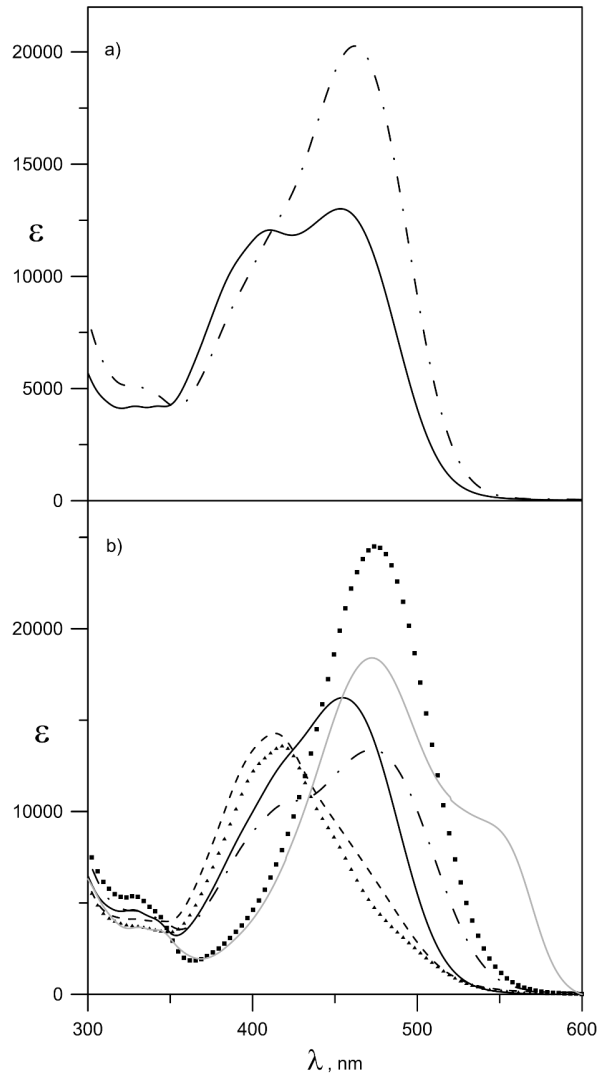

Figure 2: Absorption spectra of compounds **1** (a) and **6** (b) in acetonitrile (—), chloroform (– · –), dichloromethane (---), ethanol (■■■), toluene (▲▲▲) and dimethylformamide (grey solid line).

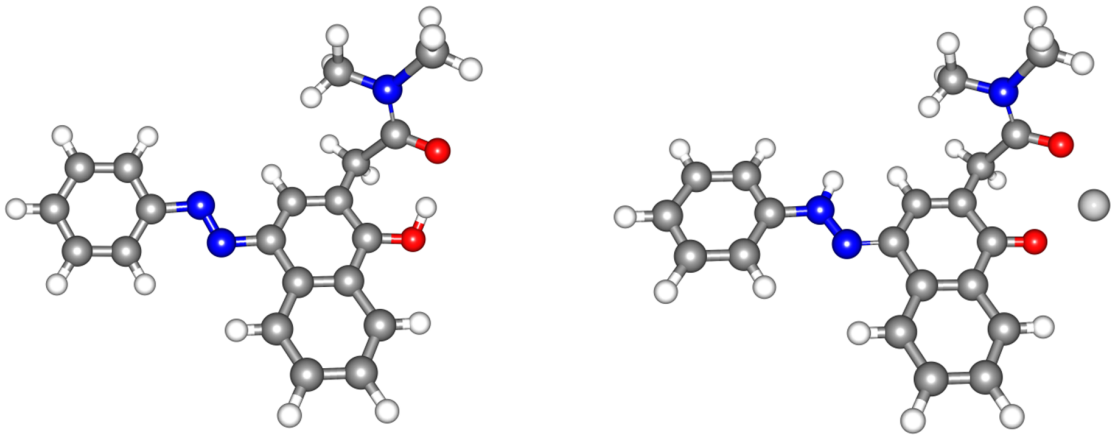

Figure 1: The most stable tautomeric form of **6** in neutral state (left) and upon complexation with $Mg(ClO_4)_2$ (right).

toluene. In ethanol and dimethylformamide, the maximum of the enol form visually disappears (the new maximum around 550 nm in the spectrum in dimethylformamide belongs to the deprotonated form, see Figure 4 below). A careful study of the spectra shown in Figure 2b leads to the conclusion that in all solvents the absorption maximum of the enol tautomer is in the range of 415–420 nm, while the maximum of the keto form in acetonitrile (455 nm) is substantially blue shifted compared to the other solvents (≈480 nm in ethanol, dimethylformamide and chloroform).

Having in mind the theoretical predictions discussed above, the existence of the keto tautomer in solution is surprising. This behavior might mean that either the enol stabilizing intramolecular H-bonding is not strong enough and can be broken by the solvent or there are intermolecular interactions not taken into account by the calculations. The former could be the reason in some of the solvents, which have the capacity to stabilize **6K** as proton acceptor (dimethylformamide), proton donor (chloroform) or both (ethanol). The latter could be the reason for the keto tautomer stabilization in acetonitrile.

The explanation for the sudden stabilization of **6K** was found by X-ray measurements of its crystal, obtained in acetonitrile. The crystal structure of **6**, shown in Figure 3, clearly indicates that the **K** form is stabilized through the formation of linear intermolecular associates. It can be seen that a hydrogen bond is formed between the nitrogen proton of one keto tautomer and the carbonyl group of another neighboring molecule. Probably, the process of associate formation is facilitated by the position of the chromophore part in the isolated **K** form (Figure 3, left). Obviously, the formation of the seven-membered hydrogen-bonding ring in **6E** cannot compete with the flexibility of the system in the case of the intermolecular association. Compared to another tautomeric C=O containing ionophore, recently developed [13], it seems that the existence of a carbonyl group leads in some cases to stabilization of the keto tautomer through formation of associates.

This kind of aggregation reflects to the spectrum of **6** in acetonitrile. The formed aggregate (see Figure S1, Supporting Information File 1) has a H-type structure (also called “sandwich” type) [14] with parallel assignment of the monomer molecules, consequently, its absorption maximum should be blue shifted compared to the monomeric species. If we assume that in ethanol or in dimethylformamide only the monomeric keto form is present, the blue shift of the absorption in acetonitrile indicates that the keto form here exists exclusively as H-aggregates as in the crystal structure.

The absorption spectra of **6** in acetonitrile upon addition of $Mg(ClO_4)_2$ are shown in Figure 4. A clear isosbestic point can be seen in the area where the enol tautomer does not absorb, indicating that the tautomeric equilibrium is shifted towards the keto tautomer (in form of the complex) as a result of the general equilibrium scheme below:

$$\mathbf{6E} \rightleftharpoons \mathbf{6K} \overset{Me^{2+}}{\rightleftharpoons} \mathbf{6K}{:}Me^{2+}$$

The complexation provides a substantial red shift (from 455 to 513 nm) compared to the neutral ligand with increased intensi-

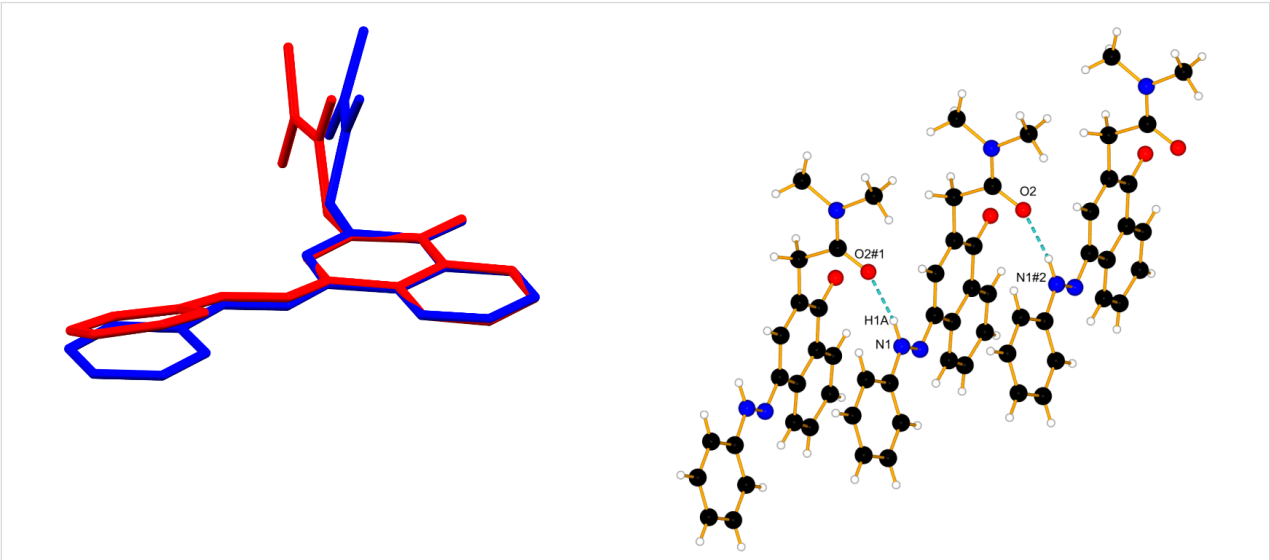

Figure 3: Left: Theoretically predicted structure of **6K** (blue), overlaid with the X-ray structure (red). Right: X-ray structure of **6**, #1: x − 1, y, z; #2: x + 1, y, z; H bonds are drawn as blue dashed lines.

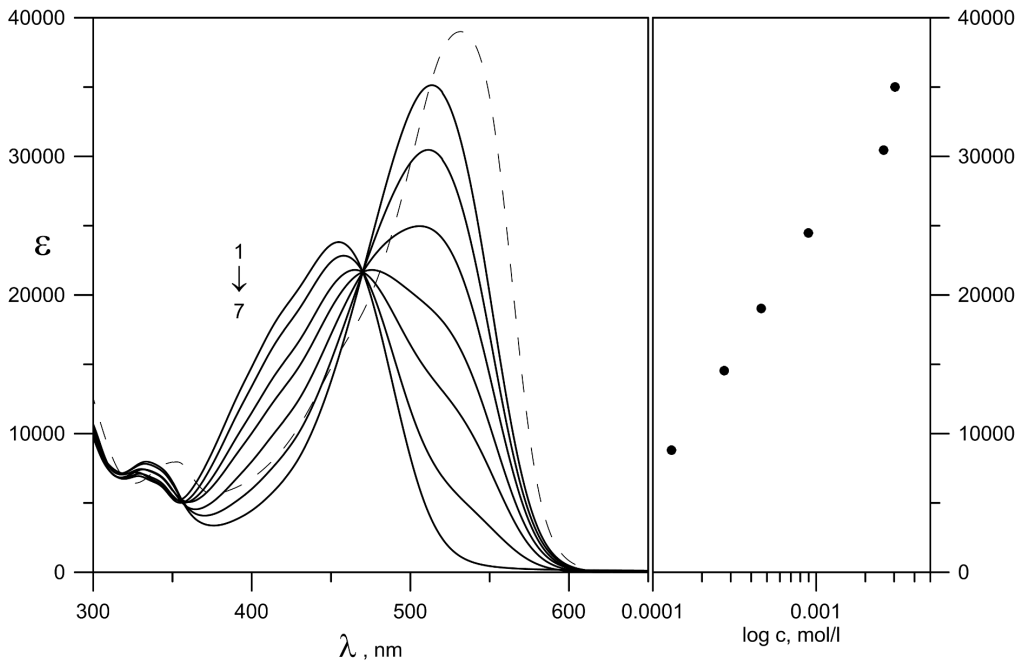

Figure 4: Left: Absorption spectra of **6** with stepwise addition of $Mg(ClO_4)_2$ in acetonitrile (1 – neutral ligand; 7 – complex $C_{Mg(ClO4)2} = 1.23 \times 10^{-3}$ M. The spectrum of the deprotonated form of **6** is drawn with dashes. Right: Molar absorptivity at 513 nm as a function of the concentration of the salt in a logarithmic scale.

ty of the new maximum at 513 nm. The comparison between the spectra of the complex and the deprotonated ligand, shown in Figure 4, indicates that the complex formation is not related to deprotonation. These results coincide with the results obtained for compound **3** [15].

The complexation abilities of **6** towards some alkaline-earth metal ions were studied and the obtained spectra of the complexes are given in Figure 5. As seen the λ_{max} values of the complex changes with the change of the type of the metal ion. We assume the formation of a 1:1 complex (the Job's plots are shown on Figure S2, Supporting Information File 1) as shown in Figure 1, which leads to a substantial red spectral shift and allows the recognition of each metal ion based on the complex peak position.

The estimated stability constants and the absorption maxima of the complexes are summarized in Table 1. The complex formation causes a substantial red shift, which varies with the metal ion. It is worth mentioning that complexation with any alkaline metal was not observed. As seen, **6** shows strong complexation with Ba^{2+}, which fits well with the size of the cavity formed between the two carbonyl groups of the keto form of the ligand, while the corresponding stability constants with Ca^{2+} and Mg^{2+} are very similar. However, as shown in Figure 5 and Table 1, the difference in the spectral maxima of the complexes allows detection of each of the studied cations.

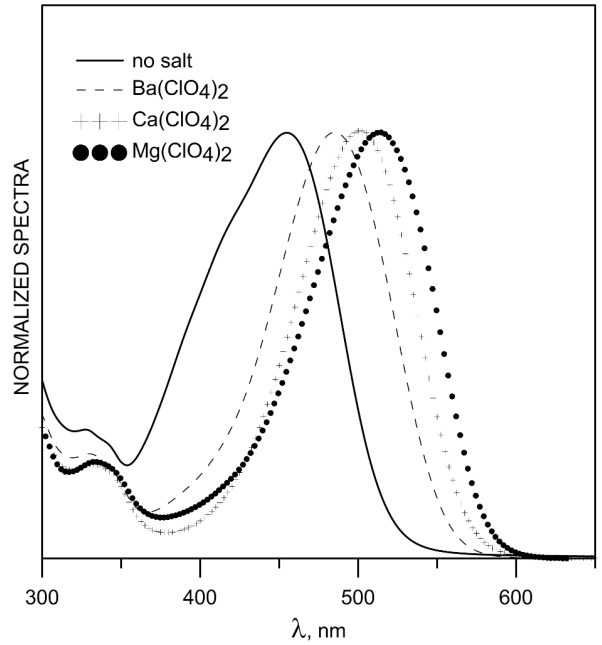

Figure 5: Normalized spectra of the free ligand **6** ($c = 5 \times 10^{-5}$ M) and its complexes obtained with $Ba(ClO_4)_2$, $Ca(ClO_4)_2$ and $Mg(ClO_4)_2$.

Conclusion

In the current study, we modeled theoretically and experimentally the tautomerism and complexation abilities of a new tautomeric ligand, based on 4-(phenyldiazenyl)naphthalen-1-ol.

Table 1: Absorption maxima of the complexes with different alkaline-earth metal ions and stability constants of the complexes of **6** in acetonitrile.

Metal ion	log β	λ_{max} complex [nm]
Ba^{2+}	3.2 ± 0.10	485
Ca^{2+}	2.8 ± 0.04	501
Mg^{2+}	2.6 ± 0.05	513

According to the theoretical calculations the enol form stabilization could be achieved through a strong intramolecular hydrogen bond formed between the tautomeric hydroxy group and the carbonyl group from the tautomeric backbone. However, intermolecular association plays a role in some solvents as shown by the experimental results. The calculations predict that the complexation with alkali earth metal ions could lead to a full shift of the tautomeric equilibrium towards the keto tautomer, which was finally observed in solution. The formed 1:1 complexes showed large bathochromic and hyperchromic shifts in the visible spectra.

Experimental

Organic synthesis

The synthetic route to compound **6** is shown in Scheme 3.

Preparation of compound **c**

The starting intermediate **b** was prepared according to the described procedure [16] from commercially available ketone **a**.

2-(1-Hydroxynaphthalen-2-yl)-*N*,*N*-dimethylacetamide (**c**)

Compound **b** (1.22 g, 6.03 mmol) was suspended in 20 mL dry dichloromethane and cooled to 0 ºC. Consequently, to this suspension were added dry diisopropylethylamine (6.3 mL, 36.20 mmol), TBTU (3.87 g, 12.07 mmol) and 2.0 M solution of dimethylamine in dry THF (6.0 mL, 12.07 mmol). The reaction mixture was stirred for 7 days at rt (reaction monitoring by TLC – dichloromethane/petroleum ether 5:2). The reaction mixture was washed successively with aq citric acid and water, dried over Na_2SO_4, filtered and evaporated under vacuum. The crude product was purified by column chromatography – 75 g silica gel, phase dichloromethane/petroleum ether 5:2 – to give 0.59 g (43%) of pure **c** as beige crystals. Mp 87–88 °C; ^{1}H NMR (600.11 MHz, $CDCl_3$, 293 K) δ 8.36 (m, 1H, H-9), 7.74 (m, 1H, H-6), 7.45 (m, 2H, H-7, H-8), 7.33 (d, *J* = 8.3 Hz, 1H, H-4), 7.13 (d, *J* = 8.3 Hz, 1H, H-3), 3.87 (s, 2H, H-11), 3.23 (s, 3H, N-CH_3), 2.98 (s, 3H, N-CH_3); ^{13}C NMR (150.90 MHz, $CDCl_3$, 293 K) δ 173.44 (1C, *C*=O), 153.26 (1C, C-1), 134.02 (2C, C-5, C-10), 128.09 (1C, C-3), 127.05 (1C, C-6), 126.18 (1C, C-7), 125.13 (1C, C-8), 122.74 (1C, C-9), 119.30 (1C, C-4), 113.11 (1C, C-2), 38.48 (1C, N-*C*H_3), 36.89 (1C, C-11), 35.95 (1C, N-*C*H_3); anal. calcd for $C_{14}H_{15}NO_2$ (229.11): C, 73.34; H, 6.59; N, 6.11; found: C, 73.25; H, 6.68; N, 6.03%.

Preparation of compound **6**

(*E*)-2-(1-Hydroxy-4-(phenyldiazenyl)naphthalen-2-yl)-*N*,*N*-dimethylacetamide

Preparation of phenyldiazonium salt solution: Aniline (0.90 mL, 10.00 mmol) was dissolved in a mixture of concentrated hydrochloric acid (5 mL) and distilled water (20 mL). A solution of sodium nitrite (0.83 g, 12.00 mmol) in distilled water (5 mL) was prepared in a test tube. The sodium nitrite solution was added dropwise to the acidic solution of the amine over 5 min at 0 °C. The mixture was stirred at 0 °C for 40 min. Compound **c** (0.59 g, 2.57 mmol) was dissolved in an aqueous solution of

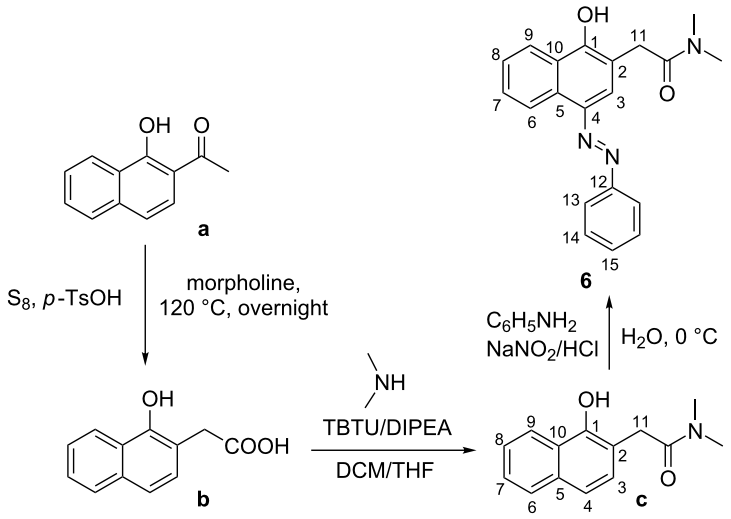

Scheme 3: Synthetic route of **6**.

NaOH (1.03 g, 25.73 mmol in 10 mL distilled water) and cooled to 0 °C. The above prepared phenyldiazonium salt solution (6.43 mL, 2.57 mmol) was added dropwise to the solution of **c** at 0 °C. The resultant deep red mixture was stirred for 1 h at 0 °C. The crude product **6** was precipitated by addition of 20% hydrochloric acid, filtered and washed with distilled water. For further purification the crude product was dissolved in 5 mL dichloromethane and purified by column chromatography – 75 g silica gel, phase dichloromethane/methyl *tert*-butyl ether 10:1. After column chromatography, the product was additionally washed with petroleum ether and dried in vacuum to give 0.720 g (84%) of pure **6** as bright red crystals. Mp 152–153 °C; ^{1}H NMR* (600.11 MHz, DMSO-d_6 with 1.5 equiv excess of NaOH, 293 K) δ 11.51 (br s, 1H, O*H*), 8.50 (br d, *J* = 8.5 Hz, 1H, H-9), 8.10 (br s, 1H, H-3), 8.07 (br d, *J* = 8.0 Hz, 1H, H-6), 7.68 (m, 1H, H-8), 7.59 (m, 2H, H-13), 7.50 (m, 1H, H-7), 7.42 (m, 2H, H-14), 7.10 (m, 1H, H-15), 3.64 (s, 2H, H-11), 3.12 (s, 3H, N-CH_3), 2.85 (s, 3H, N-CH_3); ^{13}C NMR* (150.90 MHz, DMSO-d_6 with 1.5 equiv excess of NaOH, 293 K) δ 169.84 (1C, *C*=O), 135.31 (2C, C-5, C-10), 130.94 (br s, 1C, C-8), 129.41 (2C, C-14), 128.63 (br s, 1C), 126.71 (br s, 1C, C-7), 125.06 (1C, C-6), 123.67 (br s, 1C, C-15), 122.46 (1C, C-9), 115.98 (br s, 2C, C-13), 112.36 (1C, C-2), 37.16 (1C, N-*C*H$_3$), 35.07 (1C, N-*C*H$_3$), 34.70 (1C, C-11); anal. calcd for $C_{20}H_{19}N_3O_2$ (333.39): C, 72.05; H, 5.74; N, 12.60; found, C, 72.12; H, 5.70; N, 12.67%; HRMS (rel. int.) *m*/*z*: 333.14649 (−2.05527 ppm).

*Due to tautomerism, the NMR spectra in most of the solvents (DMSO-d_6, $CDCl_3$, acetone-d_6, acetonitrile-d_3 etc.) are not informative. In all cases a complicated mixture of tautomers and lack of signals was observed. Therefore, the NMR spectra were recorded in strong basic media, in order to obtain a single tautomeric skeleton. Nevertheless, some signals in the ^{13}C NMR spectra do still not appear even after 1024 scans.

Theoretical calculations

Quantum-chemical calculations were performed using the Gaussian 09 D.01 program suite [17]. The M06-2X functional [18,19] was used with the 6-31++G** basis set for the calculations. This fitted hybrid meta-GGA functional with 54% HF exchange was especially developed to describe main-group thermochemistry and noncovalent interactions. It shows very good results in predicting the position of the tautomeric equilibria for compounds with intramolecular hydrogen bonds as well as describing the ground and excited state proton transfer mechanism [20-25].

The solvent effect was described using the Polarizable Continuum Model (the integral equation formalism variant, IEFPCM, as implemented in Gaussian 09) [26]. All ground state structures were optimized without restrictions, using tight optimization criteria and an ultrafine grid in the computation of two-electron integrals and their derivatives. The true minima were verified by performing frequency calculations in the corresponding environment. The TD-DFT method [27-29], carried out with the same functional and basis set, was used for predicting vertical transitions.

Spectral measurements

The NMR spectra were recorded on a Bruker Avance II+ 600 spectrometer. In case of $CDCl_3$ tetramethylsilane was used as internal standard. In case of DMSO-d_6, the spectra were calibrated to the residual solvent peaks (for DMSO-d_6: δ = 2.50 for ^{1}H). ^{13}C NMR spectra were calibrated in all cases to the residual solvent peaks (for $CDCl_3$ δ = 77.00, for DMSO-d_6 δ = 39.52). The following additional NMR techniques were used for all compounds: DEPT 135, COSY, HSQC and HMBC. Mass spectra (MS) were recorded on a Thermo Scientific High Resolution Magnetic Sector MS DFS spectrometer. UV–vis spectral measurements were performed on a Jasco V-570 UV–vis–NIR spectrophotometer, equipped with a thermostatic cell holder (using Huber MPC-K6 thermostat with 1 °C precision) in spectral grade solvents at 20 °C. The complexation was studied in acetonitrile. AR grade $Mg(ClO_4)_2$ (Fluka), $Ca(ClO_4)_2{\cdot}4H_2O$ (Aldrich) and $Ba(ClO_4)_2{\cdot}xH_2O$ (Fluka) were vacuum dried at 90 °C for 3 days. Due to the red shift upon complexation, the estimation of the stability constants was performed at the maximum of the complex using the final complex spectrum (Figure 5). Deprotonation was made with trimethylamine (Aldrich).

X-ray crystallographic measurements

Experimental

Single crystals of **6** were crystallized from acetonitrile by slow evaporation. A suitable crystal was selected and was mounted on a loop in oil on a Stoe IPDS2T diffractometer. The crystallographic data of the single crystal were collected with Cu Kα_1 radiation (λ = 1.54186 Å). The crystal was kept at 250(2) K during data collection by an Oxford Cryosystem open-flow cryostat. Using Olex2 [30], the structure was solved with the ShelXT [31] structure solution program using Intrinsic Phasing and refined with the ShelXL [31] refinement package using Least Squares minimization.

Crystal structure determination of 6

Crystal data for $C_{20}H_{19}N_3O_2$ (*M* =333.38 g/mol): monoclinic, space group $P2_1/c$ (no. 14), *a* = 5.5438(8) Å, *b* = 17.850(2) Å, *c* = 17.184(3) Å, β = 91.719(12)°, *V* = 1699.7(4) Å^3, *Z* = 4, *T* = 250(2) K, μ(Cu Kα) = 0.691 mm^{-1}, d_{calc} = 1.303 g/cm^3, 14285 reflections measured (7.142° ≤ 2Θ ≤ 135.89°), 2929 unique (R_{int} = 0.0894, R_{sigma} = 0.0584) which were used in all

calculations. The final R_1 was 0.0627 ($I > 2\sigma(I)$) and wR_2 was 0.1642 (all data). The CIF file can be obtained from the Cambridge Crystallographic Data Centre: CCDC-1914884 (**6**).

Supporting Information

Supporting Information File 1

Additional experimental and calculated data.
[https://www.beilstein-journals.org/bjoc/content/supplementary/1860-5397-15-185-S1.pdf]

Acknowledgements

The financial support from Bulgarian National Science Fund (Grant Number DFNI DM09/6 and DCOST 01/05/2017) is gratefully acknowledged. The authors thank the referees for the valuable comments and suggestions leading to a substantial improvement of the paper.

ORCID® iDs

Vera Deneva - https://orcid.org/0000-0002-1285-9037
Georgi Dobrikov - https://orcid.org/0000-0003-0437-2162
Aurelien Crochet - https://orcid.org/0000-0002-4763-2764
Katharina M. Fromm - https://orcid.org/0000-0002-1168-0123
Liudmil Antonov - https://orcid.org/0000-0003-0520-1517

Preprint

A non-peer-reviewed version of this article has been previously published as a preprint doi:10.3762/bxiv.2019.23.v1

References

1. Lawrance, G. A. *Introduction to Coordination Chemistry;* John Wiley & Sons, Ltd.: Chichester, UK, 2010. doi:10.1002/9780470687123
2. Lee, B. *Opt. Fiber Technol.* **2003,** *9,* 57–79. doi:10.1016/s1068-5200(02)00527-8
3. Hildebrand, G. P.; Reilley, C. N. *Anal. Chem. (Washington, DC, U. S.)* **1957,** *29,* 258–264. doi:10.1021/ac60122a025
4. Vögtle, F.; Weber, E., Eds. *Host Guest Complex Chemistry / Macrocycles;* Springer: Berlin, Heidelberg, Germany, 1985. doi:10.1007/978-3-642-70108-5
5. Pedersen, C. J. *Science* **1988,** *241,* 536–540. doi:10.1126/science.241.4865.536
6. Gokel, G. W.; Dishong, D. M.; Diamond, C. J. *J. Chem. Soc., Chem. Commun.* **1980,** 1053–1054. doi:10.1039/c39800001053
7. Nedeltcheva-Antonova, D.; Antonov, L. Controlled Tautomerism: Is It Possible?. In *Tautomerism: Concepts and Applications in Science and Technology;* Antonov, L., Ed.; Wiley-VCH: Weinheim, Germany, 2016; pp 273–294. doi:10.1002/9783527695713.ch12
8. Antonov, L.; Deneva, V.; Simeonov, S.; Kurteva, V.; Nedeltcheva, D.; Wirz, J. *Angew. Chem., Int. Ed.* **2009,** *48,* 7875–7878. doi:10.1002/anie.200903301
9. Deneva, V.; Antonov, L. *Mol. Phys.* **2019,** *117,* 1613–1620. doi:10.1080/00268976.2018.1562127
10. Antonov, L.; Kurteva, V.; Crochet, A.; Mirolo, L.; Fromm, K. M.; Angelova, S. *Dyes Pigm.* **2012,** *92,* 714–723. doi:10.1016/j.dyepig.2011.06.026
11. Antonov, L. *Molecules* **2019,** *24,* No. 2252. doi:10.3390/molecules24122252
12. Joshi, H.; Kamounah, F. S.; van der Zwan, G.; Gooijer, C.; Antonov, L. *J. Chem. Soc., Perkin Trans. 2* **2001,** 2303–2308. doi:10.1039/b106241g
13. Kurteva, V. B.; Antonov, L. M.; Nedeltcheva, D. V.; Crochet, A.; Fromm, K. M.; Nikolova, R. P.; Shivachev, B. L.; Nikiforova, M. S. *Dyes Pigm.* **2012,** *92,* 1266–1277. doi:10.1016/j.dyepig.2011.07.013
14. Antonov, L.; Gergov, G.; Petrov, V.; Kubista, M.; Nygren, J. *Talanta* **1999,** *49,* 99–106. doi:10.1016/s0039-9140(98)00348-8
15. Antonov, L. M.; Kurteva, V. B.; Simeonov, S. P.; Deneva, V. V.; Crochet, A.; Fromm, K. M. *Tetrahedron* **2010,** *66,* 4292–4297. doi:10.1016/j.tet.2010.04.049
16. Neyyappadath, R. M.; Cordes, D. B.; Slawin, A. M. Z.; Smith, A. D. *Chem. Commun.* **2017,** *53,* 2555–2558. doi:10.1039/c6cc10178j
17. *Gaussian 09,* Revision D.01; Gaussian, Inc.: Wallingford, CT, USA, 2013.
18. Zhao, Y.; Truhlar, D. G. *Acc. Chem. Res.* **2008,** *41,* 157–167. doi:10.1021/ar700111a
19. Zhao, Y.; Truhlar, D. G. *Theor. Chem. Acc.* **2008,** *120,* 215–241. doi:10.1007/s00214-007-0310-x
20. Kawauchi, S.; Antonov, L. *J. Phys. Org. Chem.* **2013,** *26,* 643–652. doi:10.1002/poc.3143
21. Manolova, Y.; Kurteva, V.; Antonov, L.; Marciniak, H.; Lochbrunner, S.; Crochet, A.; Fromm, K. M.; Kamounah, F. S.; Hansen, P. E. *Phys. Chem. Chem. Phys.* **2015,** *17,* 10238–10249. doi:10.1039/c5cp00870k
22. Manolova, Y.; Marciniak, H.; Tschierlei, S.; Fennel, F.; Kamounah, F. S.; Lochbrunner, S.; Antonov, L. *Phys. Chem. Chem. Phys.* **2017,** *19,* 7316–7325. doi:10.1039/c7cp00220c
23. Hristova, S.; Dobrikov, G.; Kamounah, F. S.; Kawauchi, S.; Hansen, P. E.; Deneva, V.; Nedeltcheva, D.; Antonov, L. *RSC Adv.* **2015,** *5,* 102495–102507. doi:10.1039/c5ra20057a
24. Marciniak, H.; Hristova, S.; Deneva, V.; Kamounah, F. S.; Hansen, P. E.; Lochbrunner, S.; Antonov, L. *Phys. Chem. Chem. Phys.* **2017,** *19,* 26621–26629. doi:10.1039/c7cp04476c
25. Hristova, S.; Deneva, V.; Pittelkow, M.; Crochet, A.; Kamounah, F. S.; Fromm, K. M.; Hansen, P. E.; Antonov, L. *Dyes Pigm.* **2018,** *156,* 91–99. doi:10.1016/j.dyepig.2018.03.070
26. Tomasi, J.; Mennucci, B.; Cammi, R. *Chem. Rev.* **2005,** *105,* 2999–3094. doi:10.1021/cr9904009
27. Improta, R. UV-Visible Absorption and Emission Energies in Condensed Phase by PCM/TD-DFT Methods. In *Computational Strategies for Spectroscopy;* Barone, V., Ed.; John Wiley & Sons, Inc.: oboken, NJ, USA, 2011; pp 37–75. doi:10.1002/9781118008720.ch1
28. Adamo, C.; Jacquemin, D. *Chem. Soc. Rev.* **2013,** *42,* 845–856. doi:10.1039/c2cs35394f
29. Antonov, L.; Kawauchi, S.; Okuno, Y. *Bulg. Chem. Commun.* **2014,** *46,* 228–237.
30. Dolomanov, O. V.; Bourhis, L. J.; Gildea, R. J.; Howard, J. A. K.; Puschmann, H. *J. Appl. Crystallogr.* **2009,** *42,* 339–341. doi:10.1107/s0021889808042726
31. Sheldrick, G. M. *Acta Crystallogr., Sect. A: Found. Adv.* **2015,** *71,* 3–8. doi:10.1107/s2053273314026370

BEILSTEIN JOURNAL OF ORGANIC CHEMISTRY

Naphthalene diimides with improved solubility for visible light photoredox catalysis

Barbara Reiß and Hans-Achim Wagenknecht*

Full Research Paper

Open Access

Address:
Institute of Organic Chemistry, Karlsruhe Institute of Technology (KIT), Fritz-Haber-Weg 6, 76131 Karlsruhe, Germany

Email:
Hans-Achim Wagenknecht* - Wagenknecht@kit.edu

* Corresponding author

Keywords:
chromophore; dyes; electrochemistry; photochemistry; photoredox catalysis

Beilstein J. Org. Chem. **2019,** *15,* 2043–2051.
doi:10.3762/bjoc.15.201

Received: 20 May 2019
Accepted: 12 August 2019
Published: 27 August 2019

This article is part of the thematic issue "Dyes in modern organic chemistry".

Guest Editor: H. Ihmels

Abstract

Five core-substituted naphthalene diimides bearing two dialkylamino groups were synthesized as potential visible light photoredox catalysts and characterized by methods of optical spectroscopy and electrochemistry in comparison with one unsubstituted naphthalene diimide as reference. The core-substituted naphthalene diimides differ by the alkyl groups at the imide nitrogens and at the nitrogens of the two substituents at the core in order to enhance their solubility in DMF and thereby enhance their photoredox catalytic potential. The 1-ethylpropyl group as rather short and branched alkyl substituent at the imide nitrogen and the *n*-propyl group as short and unbranched one at the core amines yielded the best solubilities. The electron-donating diaminoalkyl substituents together with the electron-deficient aromatic core of the naphthalene diimides increase the charge-transfer character of their photoexcited states and thus shift their absorption into the visible light (500–650 nm). The excited state reduction potential was estimated to be approximately +1.0 V (vs SCE) which is sufficient to photocatalyze typical organic reactions. The photoredox catalytic activity in the visible light range was tested by the α-alkylation of 1-octanal as benchmark reaction. Irradiations were performed with LEDs in the visible light range between 520 nm and 640 nm. The irradiation by visible light together with the use of an organic dye instead of a transition metal complex as photoredox catalyst improve the sustainability and make photoredox catalysis "greener".

Introduction

Photocatalysis couples the physical process of light absorption to an organic-chemical reaction by means of time, space and energetics. In order to apply visible light for photocatalysis despite its rather low energy this coupling requires to be mediated by a sensitizing species – a photocatalyst. If the interacting mode between the sensitizer and the reactant is via charge transfer, it is named photoredox catalysis. This research field has been established over the past decade [1-20]. In principle, it

is a sustainable method for catalysis because sunlight is an essentially unlimited and thereby "green" natural light source and LEDs – conveniently used for irradiation experiments in the laboratory – are cheap and energy-saving artificial sources for irradiations. The current "working horse" for photoredox catalysis is mainly $[Ru(bpy)_3]^{2+}$ [21], due to its strong MLCT (metal-to-ligand charge transfer) absorption, the excellent yield of its triplet state and the long lifetime, the versatile redox behavior (Ru^{3+} vs Ru^{+}) in quenching processes and the chemical and photochemical robustness. Despite their positive photoredox catalytic behavior, transition metal complexes have disadvantages, including high costs due to limited availability, toxicity [22,23] and polluting properties [24]. This thwarts the principally "green" concept of photoredox catalysis. In order to avoid transition metals and enhance the sustainability further, organic compounds, mainly eosin Y [25], rhodamine 6G [26], 9-mesityl-10-methylacridinium perchlorate [27], 1,2,3,5-tetrakis(carbazol-9-yl)-4,6-dicyanobenzenes [28] and *N*-phenylphenothiazines [29] were applied as important alternative photoredox catalysts [30,31]. These studies conclusively showed that there is no universal photoredox catalyst for different organic transformations. Instead, each photoredox catalyst has its own reactivity profile and scope. In order to apply organic dyes in advanced photoredox catalysts in a versatile way, it is crucial that modifications can be easily incorporated into the core structure in order to tune optical and redox properties. Naphthalene diimides (NDIs) as the smallest possible rylene dyes are such an important class of organic dyes. In contrast to their bigger homologs perylene diimides which were rarely used for photoredox catalysis [32-34], NDIs have a lower tendency to self-aggregate due to their smaller aromatic surface and thus are slightly better soluble in organic solvents [35-38]. NDIs are intensively applied as functional dyes [39,40], for artificial photosynthesis [41,42], for molecular architectures by self-assembly [43,44], as molecular sensors [45-47] and for organic electronics [48,49], but yet nearly completely unexplored for photoredox catalysis. Core-unsubstituted NDIs are colorless compounds with high extinction coefficients at the border between UV-A and visible light. Their fluorescence quantum yields are rather low and fluorescence lifetimes are rather short due to ISC into the triplet state [50,51]. NDIs are reversibly reducible and their stable radical anions absorb in the visible to NIR light range [37]. The aromatic core of NDIs can be easily modified by substituents in order to tune their optical and redox properties as mentioned above [39,40,52]. The common synthetic approach for core-substituted NDIs (cNDIs) makes tailor-made dyes rather easily accessible. With respect to these unique properties, NDIs should also be explored for photoredox catalysis. We present herein the synthesis and characterization of NDI **1** as unsubstituted chromophore reference and cNDIs **2**–**6** as potential visible light photoredox catalysts. The cNDIs **2**–**6** differ by the alkyl groups at the imide nitrogens and at the nitrogens of the two core substituents at the core in order to enhance their solubility. In general, NDIs are electron-poor chromophores. The diamino substituents of cNDIs **2**–**6** are expected to increase the charge-transfer character of their photoexcited states in order to shift their absorption into the visible light and to improve their photoredox catalytic power. The photoredox catalytic activity was representatively tested by the MacMillan benchmark reaction [53]. For this type of photoredox catalytic reaction, solubility of cNDIs in DMF is a crucial prerequisite.

Results and Discussion

Synthesis of cNDIs **2**–**6** and their solubility

The commercially available precursor for all NDIs is 1,4,5,8-naphthalenetetracarboxylic acid anhydride (**7**) and the synthesis of cNDIs follows a modular approach. Core-unsubstituted NDIs are typically prepared by condensation of **7** with 2–3 equivalents of the respective amine. The corresponding reaction of **7** with *n*-octylamine in DMF gave the reference NDI **1** in 90% yield (Scheme 1) [54]. The synthetic module for cNDIs with two substituents at the core is the 2,6-dibromo anhydride derivative **8** that can be synthesized from **7** by elementary bromine, dibromoisocyanuric acid, or 1,3-dibromo-5,5-dimethylhydantoine (DBH) in concentrated sulfuric acid, or oleum in good yields [55-57]. The regioselective introduction of just two substituents can be controlled by stoichiometry. Accordingly, the 2,6-dibromo derivative **8** was prepared by 1.5 equivalents DBH and further used as crude product because it cannot be purified due to its very poor solubility. The subsequent condensation with *n*-octylamine, 1,4-dimethylpentylamine and 1-ethylpropylamine in refluxing CH_2Cl_2 gave the cNDIs **9**–**11** in 42%, 14% and 24% yields, respectively. Finally, the two bromo groups in cNDIs **9**–**11** were substituted by *n*-propylamine as nucleophile in refluxing CH_2Cl_2 to the cNDIs **2**, **3** and **6** in 80%, 87% and 58% yields, respectively. The two cNDIs **4** and **5** carrying the same alkyl groups at the imide nitrogens and at the nitrogens of the core substituents were directly synthesized (in one step) by 1-propylbutylamine or 1-ethylpropylamine using pressure reaction vials. The yields were rather low, 14% for **4** and 25% for **5**, but they should be regarded with respect to the fact that the additional time-consuming isolations of the respective dibromo-cNDI intermediates were omitted. After purification by column chromatography, all five cNDIs **2**–**6** were resolved in benzene and lyophilized under reduced pressure.

In general, NDIs are well soluble in CH_2Cl_2. As mentioned in the introduction, solubility of cNDIs as potential photoredox catalysts in DMF or in mixtures of DMF with CH_2Cl_2 is a crucial prerequisite for their photoredox catalytic suitability. The solubility was determined by preparing saturated solutions

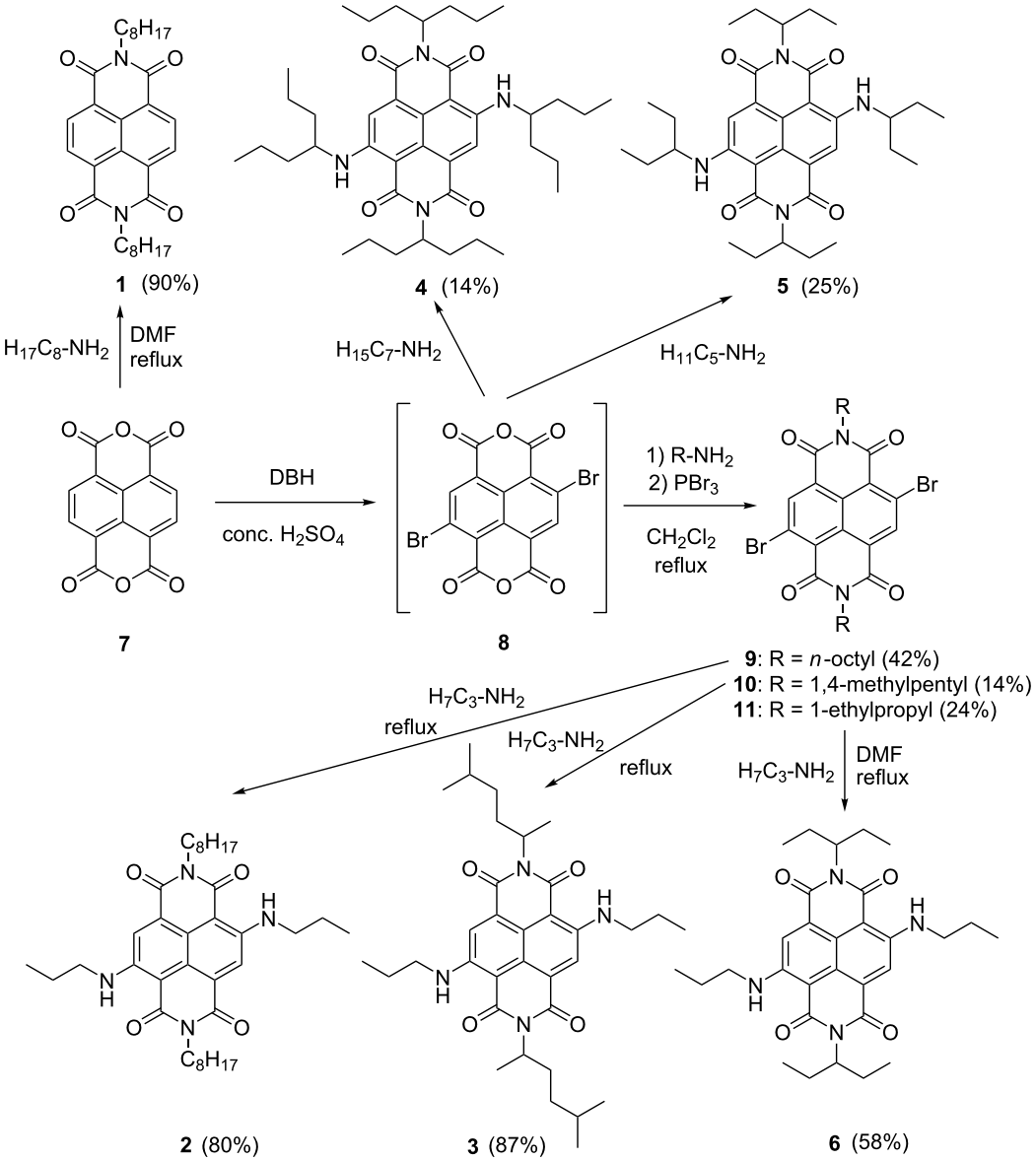

Scheme 1: Synthesis of reference NDI **1** and cNDIs **2**–**6**; bottom: image of saturated solutions of cNDIs **2**–**6** in DMF.

of the respective NDI **1** or cNDIs **2**–**6** at 22 °C in pure DMF. The absorbance was measured after filtration of the solution and after redilution if the optical density in the cuvette with 1 cm path length exceeded 1. The reference NDI **1** with the two *n*-octyl substituents at the imide nitrogens showed a maximum concentration (c_{max}) of 2.5 mM. Saturated samples in DMF gave the first impression of cNDIs **2**–**6** (see bottom image in Scheme 1), and merely by visible inspection, the solubility of the cNDIs follows the order from **2** to **6**. In fact, c_{max} of **2** is far below 1 mM and difficult to determine by this simple method.

At the far end, the best and measurable solubilities showed cNDIs **5** and **6** with c_{max} of 0.6 mM and 2.7 mM, respectively. The 1-ethylpropyl groups as rather short and branched alkyl substituents at the imide nitrogens and the *n*-propyl groups as short and unbranched ones at the core amines gave the best combination to improve the solubility. This qualifies cNDI **6** as the best soluble potential visible light photoredox catalyst.

Characterization of NDI **1**, cNDI **2** and cNDI **6**

The synthesized reference NDI **1** and the new cNDI **6** as potential photoredox catalyst were characterized in DMF and CH_2Cl_2 by means of optical spectroscopy and electrochemistry. The UV–vis absorbance of the core-unsubstituted NDI **1** in CH_2Cl_2 show characteristic bands in the range between 300 nm and 400 nm with the maximum at 380 nm (Figure 1). The absorbance of NDI **1** in DMF is very similar to that in CH_2Cl_2, only the extinction is slightly reduced. The charge transfer character of the excited state of cNDI **6** should yield an absorbance in the visible range for photoredox catalysis. In fact, the absorbance of the new cNDI **6** in CH_2Cl_2 shows considerably red-shifted bands in the range between 500 nm and 650 nm with the maximum at 612 nm. The absorbance of **6** in DMF is very similar to that in CH_2Cl_2. The similarities of the UV–vis absorbance of the cNDIs **2** and **6** in CH_2Cl_2 exemplarily evidences that length and branching of the alkyl substituents both at the imide nitrogens and at the core amino groups have only little influence on the optical properties but significantly modulate the solubility in DMF. This result agrees with other cNDIs in literature [47,48,58]. NDI **1** shows weak fluorescence in CH_2Cl_2 with a maximum at 384 nm and a quantum yield of 7%. The Stokes' shift is small (413 cm^{-1}). Based on these values, the excitation energy E_{00} for the singlet state which is an important prerequisite for photoredox catalysis with **1** can be estimated to be 3.25 eV. In DMF, the fluorescence of **1** is completely quenched. This is due to a photoinduced charge transfer between NDI **1** and DMF. DMF has an oxidation potential of 0.38 V vs SCE [59]. Together with the reduction potential of E_{red} = 0.69 V and E_{00} = 3.25 eV for NDI **1** (vide infra), this electron transfer is clearly exergonic ($\Delta G = E_{ox} - E_{red} - E_{00}$ = −2.2 eV). NDI **6** shows a strong and broad fluorescence in CH_2Cl_2 with a maximum at 640 nm and a quantum yield of 48%. The Stokes' shift is rather large (715 cm^{-1}). The excitation energy E_{00} of cNDI **6** in the singlet state is approximately 1.98 eV and is significantly smaller than that of NDI **1** due to the visible light excitation which delivers less energy to the excited state.

The redox potentials of the reference NDI **1** and the cNDI **2** (due to the better solubility) were determined in comparison by cyclic voltammetry in CH_2Cl_2 and in the presence of 0.1 M *n*-Bu_4PF_6 as conducting salt (see Supporting Information File 1). The cyclic voltagram of NDI **1** shows two reversible reductions and one irreversible oxidation with $E \approx 0.85$ V vs SCE. The two potentials in the negative potential range can be assigned to the formation of the radical anion $\mathbf{1}^{\bullet-}$, $E_{½}(\mathbf{1}/\mathbf{1}^{\bullet-})$ = −0.69 V, and the dianion $\mathbf{1}^{2-}$, $E_{½}(\mathbf{1}^{\bullet-}/\mathbf{1}^{2-})$ = 1.10 V (Table 1). These values agree well with literature results [48,49,54]. In comparison, the reductions of cNDI **2** to the radical anion $\mathbf{2}^{\bullet-}$ were observed at $E_{½}(\mathbf{2}/\mathbf{2}^{\bullet-})$ = −1.06 V and to the dianion $\mathbf{2}^{2-}$ at $E_{½}(\mathbf{2}^{\bullet-}/\mathbf{2}^{2-})$ = −1.50 V and show the electronic effect of the two *n*-propylamino substituents. Additionally, two reversible oxidations were observed at $E_{½}(\mathbf{2}^{\bullet+}/\mathbf{2})$ = +0.99 V and $E_{½}(\mathbf{2}^{2+}/\mathbf{2}^{\bullet+})$ = +1.40 V which can be assigned to the electron-donating effect of the *n*-propylamino groups. The key values for the photoredox catalytic activity (vide infra) are the excited state potential for the reduction, $E^*_{red}(\mathbf{2}^*/\mathbf{2}^{\bullet-})$ = +0.92 V, and for the oxidation $E^*_{ox}(\mathbf{2}^{\bullet+}/\mathbf{2}^*)$ = −0.99 V. According to the categories for strength of chemical redox agents [60], cNDI **2** in the excited state is a strong oxidant and a mild reductant. We assume based on literature-known cNDIs that the different alkyl groups of the other cNDIs **3**–**6** have no or only very little influence on the electrochemical properties in comparison with those of cNDI **2** [48,49]. Hence, the photoredox properties of the new cNDI **2**–**6** are comparable to those of eosin Y and rhodamine 6G as other organic photoredox catalysts.

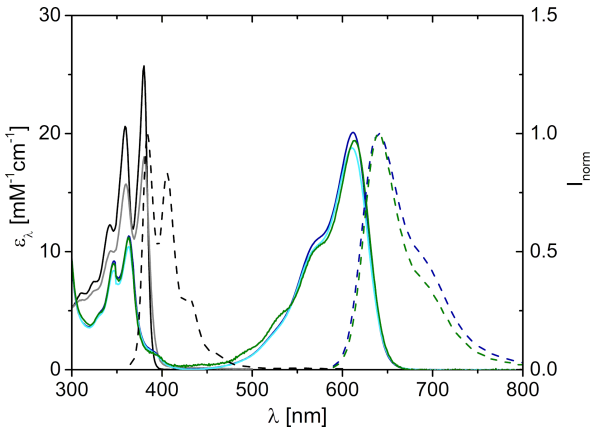

Figure 1: Optical properties of NDI **1** and cNDIs **2** and **6**: UV–vis absorbance in CH_2Cl_2 and in DMF (normal lines), normalized fluorescence in CH_2Cl_2 (dashed lines); **1** in CH_2Cl_2 (black), **1** in DMF (gray), **2** in CH_2Cl_2 (green), **6** in CH_2Cl_2 (dark blue), **6** in DMF (light blue), I_{exc} = 350 nm for **1**, λ_{exc} = 600 nm for **2** and **6**.

Photoredox catalysis with NDI **1** and cNDI **6**

The α-alkylation of 1-octanal (**12**) by diethyl 2-bromomalonate (**13**) yielding product **14** (Scheme 2) is one of the benchmark reactions for photoredox catalysis because it combines photoredox catalysis with organocatalysis [53]. Initially, $[Ru(bpy)_3]Cl_2$ was applied by MacMillan et al. as photoredox catalyst together with the chiral imidazolidinone **15** as organo-

Table 1: Optical and electrochemical properties of NDI **1** and cNDI **2** (in CH_2Cl_2) in comparison to other organic photoredox catalyst **X**, in particular eosin Y (EY), rhodamine 6G (Rh6G) and 9-mesityl-10-methylacridinium perchlorate (MesAcr) 1,2,3,5-tetrakis(carbazol-9-yl)-4,6-dicyanobenzenes (4CzIPN) and *N*-phenylphenothiazine (Ptz).

X	λ [nm]	E_{00}[a] [eV]	$E_{½}$(**X**/**X**$^{\bullet-}$) [V]	E^*_{red}(**X***/**X**$^{\bullet-}$)[a] [V]	$E_{½}$(**X**$^{\bullet+}$/**X**) [V]	E^*_{ox}(**X**$^{\bullet+}$/**X***)[a] [V]
1	380	3.25	−0.69	+2.56	–	–
2	612	1.98	−1.06	+0.92	+0.99	−0.99
EY [61]	539[b]	2.31	−1.08[c]	+1.23	+0.76[c]	−1.58
Rh6G [62]	530[d]	2.32	−1.14	+1.18	+1.23	−1.09
MesAcr [63]	425	2.67[e]	−0.49	+2.08[e]	–	–
Ptz [29]	320	3.25	–	–	+0.75	−2.50
4CzIPN [28]	≈370[b]	2.67	−1.24[b]	+1.43	+1.49[b]	−1.18

All potentials were converted from the ferrocene scale to the SCE scale [64]. [a]For singlet state. [b]In MeCN. [c]In MeOH. [d]In EtOH. [e]CT state.

catalyst to achieve enantioselectivity. Several proposal for the mechanism are found in literature ranging from a closed photoredox catalytic cycle [53,61] to a chain propagation mechanism with photoredox initiation [65]. We evaluated the reference NDI **1** and the cNDI **6** as new photoredox catalysts using this benchmark reaction. The samples were degassed by the freeze-pump-thaw method, the catalysis was performed under inert gas conditions (Argon), and the chemical conversions and yields were determined by ^{1}H NMR spectroscopy (see Supporting Information File 1). The enantiomeric excess of the product **14** was determined after conversion with (2S,4S)-(+)-pentanediol into diastereomers and by integration of the corresponding signals in the ^{1}H NMR spectrum. In all experiments with NDI **1** the enantiomeric excess exceeded a value of 78%; in all experiments with cNDI **6** the enantiomeric excess was higher than 81%. This parameter is omitted for clarity in the following paragraphs because enantioselectivity is not a matter of discussion in this work.

The photoredox catalysis with NDI **1** was performed by LEDs with 387 nm maximum emission wavelength and an irradiation time of 18 h. In order to ensure solubility of all components, a solvent mixture of DMF/CH_2Cl_2 = 1:1 was used. 20 mol % of organocatalyst **15** were applied. 2,6-Lutidine was added as base to trap protons that are potentially formed during the reaction and to ensure enamine formation with the organocatalyst **15**. Under these conditions, a moderate conversion of **13** (65%) and a low yield of product **14** (25%) were obtained (Table 2). In pure CH_2Cl_2 as solvent there was only a small conversion, but no product **14** detectable. Only the debrominated diethyl malonate was identified as side product. This makes conclusively clear that the solvent DMF is needed for this type of photoredox reaction. The control reaction without light did not show conversion at all. Control reactions with light, but without NDI **1** showed, however, a low conversion of 24% and a low yield of 18%. This is due to the UV-A absorption of the enamine that is formed as intermediate between 1-octanal (**12**) and the organocatalyst **15**. Similar photochemical reactions by direct excitation of the emanine intermediate were described by Melchiorre et al. [66]. In pure DMF this effect is even stronger and increases the conversion to 80% and the yield to 58% even in the absence of NDI **1**. Obviously, photoredox catalytically driven conversion by NDI **1** competes with the direct excitation of the intermediate enamine. This is the reason why lowering

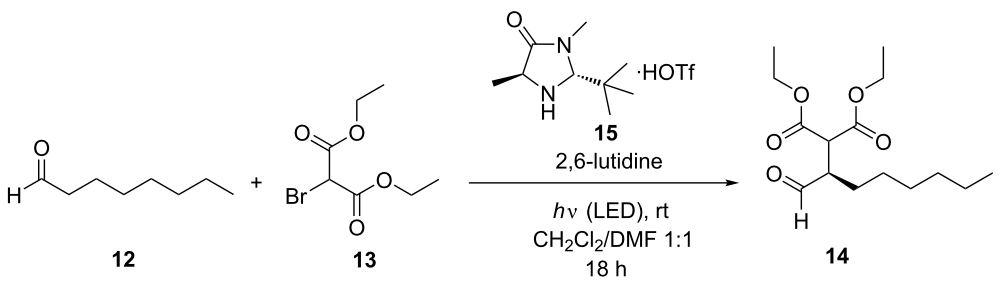

Scheme 2: Photocatalytic α-alkylation of octanal (**12**): 500 mM **12**, 250 mM **13**, 50 mM (20 mol %) organocatalyst **15**, 500 mM 2,6-lutidine, NDI **1** or cNDI **2**–**6** as photoredox catalyst in 1.3 mL solvent, stirring, irradiation by LED, see Table 2.

Table 2: Photoredox catalytic conversions of diethyl 2-bromomalonate (**13**) with 1-octanal (**12**) and yields of product **14** by different photoredox catalysts (**X**).

Entry	X	mol %	LED	solvent	Conversion (%) of **13**	Yield (%) of **14**
1	**1**	5	387	DMF/CH_2Cl_2 1:1	65	25
2[a]	**1**	5	387	DMF/CH_2Cl_2 1:1	87	45
3	**1**	2.5	387	DMF/CH_2Cl_2 1:1	67	32
4	**1**	1.25	387	DMF/CH_2Cl_2 1:1	67	30
5[a]	**1**	1.25	387	DMF/CH_2Cl_2 1:1	99	60
6	–	–	387	DMF/CH_2Cl_2 1:1	24	18
7	**1**	5	387	CH_2Cl_2	30	n.d.
8	**1**	5	387	DMF	69	44
9	–	–	387	DMF	80	58
10	**6**	0.1	520	DMF/CH_2Cl_2 1:1	77	69
11	**6**	0.1	597	DMF/CH_2Cl_2 1:1	46	43
12	**6**	0.1	637	DMF/CH_2Cl_2 1:1	n.d.	n.d.

[a]40 mol % **15**.

the concentration of the photoredox catalyst **1** from 5 mol % over 2.5 mol % to 1.25 mol % did not reduce conversions and yields, but increasing the amount of organocatalyst **15** from 20 mol % to 40 mol % finally improved the conversion to 99% and the yield to 60% Table 2, entry 5).

These photoredox catalytic experiments with NDI **1** made obvious that the excitation must be shifted from the UV-A range into the visible range in order to achieve selective excitation of the photoredox catalyst and not a mixture of different photomechanisms. cNDI **6** with its absorbance between 500 nm and 650 nm and a maximum at 612 nm fullfills this requirement. The corresponding photoredox catalytic experiment with cNDI **6** and the 597 nm LED as irradiation source gives a conversion of 46% and a product yield of 43%. The emission of this LED overlays well with the absorbance of cNDI **6** (Figure 2). As expected, the photoredox catalytic reaction with cNDI **6** is much "cleaner" than with NDI **1** and the substrate conversion differs only slightly from the product yield. Taken together, cNDI **6** is a suitable visible light photoredox catalyst for this reaction although its excited state potential (comparable to $E^*_{red}(\mathbf{2}^*/\mathbf{2}^{\bullet-})$ = +1.92 V) is much lower than that of NDI **1** ($E^*_{red}(\mathbf{1}^*/\mathbf{1}^{\bullet-})$ = +2.56 V) but obviously still sufficiently high. However, irradiations at different wavelengths gave surprising results: (i) If the 637 nm LED is applied for irradiation, there is no conversion of substrate **13** detectable although the emission of this LED also overlays well with the absorbance of cNDI **6**. (ii) If the 520 nm LED was applied the conversion increased to 77% and the yield to 69%, although excitation of only the side absorption band of cNDI **6** is realized in this experiment. Obviously, there is a strong difference between the absorbance of cNDI **6** and its photoredox catalytic activity profile with respect to the irradiation wavelength which was further studied by more detailed kinetic measurements.

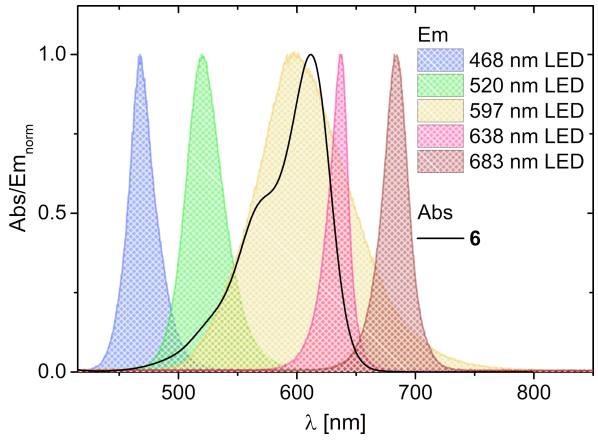

Figure 2: Normalized absorbance of cNDI **6** in comparison to normalized emission of the 468 nm, 520 nm, 597 nm, 638 nm and 683 nm LEDs.

Time-dependent product analysis was performed during the photoredox catalytic conversions using different LEDs for irradiations at 468 nm, 520 nm, 597 nm, 638 nm and 683 nm (see LED emissions in Figure 2, results in Figure 3). These experiments were performed in pure DMF, which further accelerates the photoredox catalytic conversion due to the better solubility of the cNDI **6**. The product formation is almost finished after 4 h of irradiation. The most productive excitation provides the 520 nm LED with a product yield of 82% although the emission of this LED overlays only partially with the absorbance of cNDI **6**. The emissions of the 597 nm and 638 nm LEDs do

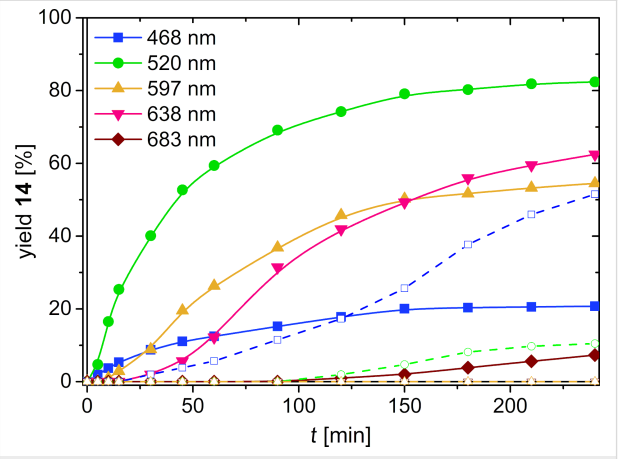

Figure 3: Kinetic analysis of yields of product **14** in the presence (solid lines) and in the absence (dashed lines) of cNDI **6**: 500 mM **12**, 250 mM **13**, 50 mM organocatalyst **15**, 500 mM 2,6-lutidine in 1.3 mL DMF, stirring, irradiation by LEDs.

overlay better but show lower yields of 55% and 62%, respectively, in photoredox catalysis. The lag phases of more than 30 min in the latter experiments indicate that indeed the enamine formation plays a crucial role. According to the mechanism suggested by Yoon et al. the photoredox catalytic cycle is initiated by the oxidation of the enamine [65]. Control experiments were performed without cNDI **6** as photoredox catalyst to elucidate product formation by direct excitation of the intermediate enamine, as discussed above. In fact, by irradiation at 468 nm there is a significant amount of product formed without cNDI **6** (52% yield) that even exceeds the product formation in the presence of cNDI **6** (21% yield). By irradiation at 520 nm there is only a small amount (10% yield) of product **14** formed without cNDI **6**, but only after longer irradiation times (approximately after 2 h). Irradiations at 597 nm and 638 nm are completely unproductive without the cNDI **6** as photoredox catalyst. It is obvious that the absorbance of cNDI **6** differs from the photoredox catalytic activity profile. This activity profile shows highest values at 520 nm whereas the absorbance has the maximum at 612 nm. The observed spectral sensitivity of the photoredox catalytic product formation cannot be easily explained. One possible reason could be the different luminous flux of the applied high-power LEDs. Given that Kasha's rule is also applicable for photochemical reactions and not only fluorescence this result is probably a "non-Kasha" photophysical dynamic behavior which can be found also for other photochemical reactions in the literature [67], but needs further investigations by time-resolved spectroscopy. The irradiations at 638 nm and 597 nm overlap with the emission range of cNDI **6** so that an inner filter effect cannot be excluded. Taken together, it makes clear that tuning of optical and electrochemical properties of potential photoredox catalysts have to be combined with their elucidation of their photophysical dynamic behavior.

Conclusion

The cNDIs **2**–**6** were synthesized as potential photoredox catalysts that differ by the alkyl groups at the imide nitrogen and at the two amino substituents at the core in order to improve their solubility. Especially the cNDI **6** showed a good solubility in DMF that is comparable to the unsubstituted NDI **1** and suitable for photoredox catalysis in solvent mixtures with DMF. Due to the charge-transfer character in the excited state the absorbances of cNDIs **2** and **6** are shifted into the visible range with a broad band between 500 nm and 650 nm. The reduction potential to form the radical anion of such a cNDI is significantly shifted to a more negative potential of $E_{½}(\mathbf{2}/\mathbf{2}^{\bullet-})$ = 1.06 V. Together with E_{00} = 1.98 eV an excited state potential of $E^*_{red}(\mathbf{2}^*/\mathbf{2}^{\bullet-})$ = +0.92 V was estimated for the singlet state which renders such cNDIs to be suitable to photocatalyze organic reactions. The photoredox catalytic activities of NDI **1** and cNDI **6** in comparison were successfully evaluated for the MacMillan benchmark reaction. This photoredox catalytic reaction in the presence of cNDI **6** was much "cleaner" than with NDI **1** since the conversions differed only slightly from the product yields. Irradiations were performed with LEDs in the visible light range between 520 nm and 640 nm. The substrate conversion and product yields were significantly higher by LED irradiation into the absorbance shoulder at 520 nm which implies a non-Kasha-type photodynamic behavior. This makes clear that future photoredox catalysts must not only by tuned by their optical and electrochemical properties but also by their photophysical dynamics. To the best of our knowledge this is the first report on the usage of cNDIs as photoredox catalysts. The irradiation by visible light from LEDs as energy-saving light sources together with the use of an organic dye instead of a transition metal complex as photoredox catalyst improve the sustainability and make photoredox catalysis "greener".

Experimental

All experimental details are described in the Supporting Information File 1.

Supporting Information

Supporting Information File 1

Synthetic protocols, copies of ^{1}H and ^{13}C NMR spectra, mass spectra, and cyclic voltammetry data.
[https://www.beilstein-journals.org/bjoc/content/supplementary/1860-5397-15-201-S1.pdf]

Acknowledgements

Financial support by the Deutsche Forschungsgemeinschaft (Wa 1386/16-1) and KIT is gratefully acknowledged. BR thanks the GRK 1626 "Chemical photocatalysis" (funded by the

Deutsche Forschungsgemeinschaft) for participation in their qualification program.

ORCID® iDs

Hans-Achim Wagenknecht - https://orcid.org/0000-0003-4849-2887

References

1. Shaw, M. H.; Twilton, J.; MacMillan, D. W. C. *J. Org. Chem.* **2016,** *81,* 6898–6926. doi:10.1021/acs.joc.6b01449
2. Marzo, L.; Pagire, S. K.; Reiser, O.; König, B. *Angew. Chem., Int. Ed.* **2018,** *57,* 10034–10072. doi:10.1002/anie.201709766
3. Romero, N. A.; Nicewicz, D. A. *Chem. Rev.* **2016,** *116,* 10075–10166. doi:10.1021/acs.chemrev.6b00057
4. Skubi, K. L.; Blum, T. R.; Yoon, T. P. *Chem. Rev.* **2016,** *116,* 10035–10074. doi:10.1021/acs.chemrev.6b00018
5. Staveness, D.; Bosque, I.; Stephenson, C. R. J. *Acc. Chem. Res.* **2016,** *49,* 2295–2306. doi:10.1021/acs.accounts.6b00270
6. Buzzetti, L.; Crisenza, G. E. M.; Melchiorre, P. *Angew. Chem., Int. Ed.* **2019,** *58,* 3730–3747. doi:10.1002/anie.201809984
7. Meggers, E. *Chem. Commun.* **2015,** *51,* 3290–3301. doi:10.1039/c4cc09268f
8. Zou, Y.-Q.; Hörmann, F. M.; Bach, T. *Chem. Soc. Rev.* **2018,** *47,* 278–290. doi:10.1039/c7cs00509a
9. Arias-Rotondo, D. M.; McCusker, J. K. *Chem. Soc. Rev.* **2016,** *45,* 5803–5820. doi:10.1039/c6cs00526h
10. Oelgemöller, M.; Hoffmann, N. *Org. Biomol. Chem.* **2016,** *14,* 7392–7442. doi:10.1039/c6ob00842a
11. Fukuzumi, S.; Ohkubo, K. *Org. Biomol. Chem.* **2014,** *12,* 6059–6071. doi:10.1039/c4ob00843j
12. Ravelli, D.; Fagnoni, M.; Albini, A. *Chem. Soc. Rev.* **2013,** *42,* 97–113. doi:10.1039/c2cs35250h
13. Zeitler, K.; Neumann, M. Synergistic Visible Light Photoredox Catalysis. In *Chemical Photocatalysis;* König, B., Ed.; De Gruyter: Berlin, 2013; pp 151–168. doi:10.1515/9783110269246
14. Pannwitz, A.; Wenger, O. S. *Chem. Commun.* **2019,** *55,* 4004–4014. doi:10.1039/c9cc00821g
15. Majek, M.; Jacobi von Wangelin, A. *Acc. Chem. Res.* **2016,** *49,* 2316–2327. doi:10.1021/acs.accounts.6b00293
16. Hopkinson, M. N.; Tlahuext-Aca, A.; Glorius, F. *Acc. Chem. Res.* **2016,** *49,* 2261–2272. doi:10.1021/acs.accounts.6b00351
17. Zhou, Q.-Q.; Zou, Y.-Q.; Lu, L.-Q.; Xiao, W.-J. *Angew. Chem., Int. Ed.* **2019,** *58,* 1586–1604. doi:10.1002/anie.201803102
18. Wang, C.-S.; Dixneuf, P. H.; Soulé, J.-F. *Chem. Rev.* **2018,** *118,* 7532–7585. doi:10.1021/acs.chemrev.8b00077
19. Parasram, M.; Gevorgyan, V. *Chem. Soc. Rev.* **2017,** *46,* 6227–6240. doi:10.1039/c7cs00226b
20. Reckenthäler, M.; Griesbeck, A. G. *Adv. Synth. Catal.* **2013,** *355,* 2727–2744. doi:10.1002/adsc.201300751
21. Tucker, J. W.; Stephenson, C. R. J. *J. Org. Chem.* **2012,** *77,* 1617–1622. doi:10.1021/jo202538x
22. Kruszyna, H.; Kruszyna, R.; Hurst, J.; Smith, R. P. *J. Toxicol. Environ. Health* **1980,** *6,* 757–773. doi:10.1080/15287398009529895
23. Brabec, V.; Nováková, O. *Drug Resist. Updates* **2006,** *9,* 111–122. doi:10.1016/j.drup.2006.05.002
24. Nriagu, J. O. *Science* **1996,** *272,* 223. doi:10.1126/science.272.5259.223
25. Hari, D. P.; König, B. *Chem. Commun.* **2014,** *50,* 6688–6699. doi:10.1039/c4cc00751d
26. Ghosh, I.; Marzo, L.; Das, A.; Shaikh, R.; König, B. *Acc. Chem. Res.* **2016,** *49,* 1566–1577. doi:10.1021/acs.accounts.6b00229
27. McManus, J. B.; Nicewicz, D. A. *J. Am. Chem. Soc.* **2017,** *139,* 2880–2883. doi:10.1021/jacs.6b12708
28. Speckmeier, E.; Fischer, T. G.; Zeitler, K. *J. Am. Chem. Soc.* **2018,** *140,* 15353–15365. doi:10.1021/jacs.8b08933
29. Speck, F.; Rombach, D.; Wagenknecht, H.-A. *Beilstein J. Org. Chem.* **2019,** *15,* 52–59. doi:10.3762/bjoc.15.5
30. Nicewicz, D. A.; Nguyen, T. M. *ACS Catal.* **2014,** *4,* 355–360. doi:10.1021/cs400956a
31. Sideri, I. K.; Voutyritsa, E.; Kokotos, C. G. *Org. Biomol. Chem.* **2018,** *16,* 4596–4614. doi:10.1039/c8ob00725j
32. Ghosh, I.; Ghosh, T.; Bardagi, J. I.; König, B. *Science* **2014,** *346,* 725–728. doi:10.1126/science.1258232
33. Weiser, M.; Hermann, S.; Penner, A.; Wagenknecht, H.-A. *Beilstein J. Org. Chem.* **2015,** *11,* 568–575. doi:10.3762/bjoc.11.62
34. Gong, H.-X.; Cao, Z.; Li, M.-H.; Liao, S.-H.; Lin, M.-J. *Org. Chem. Front.* **2018,** *5,* 2296–2302. doi:10.1039/c8qo00445e
35. Weil, T.; Vosch, T.; Hofkens, J.; Peneva, K.; Müllen, K. *Angew. Chem., Int. Ed.* **2010,** *49,* 9068–9093. doi:10.1002/anie.200902532
36. Würthner, F.; Ahmed, S.; Thalacker, C.; Debaerdemaeker, T. *Chem. – Eur. J.* **2002,** *8,* 4742–4750. doi:10.1002/1521-3765(20021018)8:20<4742::aid-chem4742>3.0.co;2-l
37. Röger, C.; Ahmed, S.; Würthner, F. *Synthesis* **2007,** 1872–1876. doi:10.1055/s-2007-983718
38. Andric, G.; Boas, J. F.; Bond, A. M.; Fallon, G. D.; Ghiggino, K. P.; Hogan, C. F.; Hutchison, J. A.; Lee, M. A.-P.; Langford, S. J.; Pilbrow, J. R.; Troup, G. J.; Woodward, C. P. *Aust. J. Chem.* **2004,** *57,* 1011–1019. doi:10.1071/ch04130
39. Al Kobaisi, M.; Bhosale, S. V.; Latham, K.; Raynor, A. M.; Bhosale, S. V. *Chem. Rev.* **2016,** *116,* 11685–11796. doi:10.1021/acs.chemrev.6b00160
40. Suraru, S.-L.; Würthner, F. *Angew. Chem., Int. Ed.* **2014,** *53,* 7428–7448. doi:10.1002/anie.201309746
41. Wiederrecht, G. P.; Niemczyk, M. P.; Svec, W. A.; Wasielewski, M. R. *J. Am. Chem. Soc.* **1996,** *118,* 81–88. doi:10.1021/ja953159y
42. Hasharoni, K.; Levanon, H.; Greenfield, S. R.; Gosztola, D. J.; Svec, W. A.; Wasielewski, M. R. *J. Am. Chem. Soc.* **1996,** *118,* 10228–10235. doi:10.1021/ja961919e
43. Molla, M. R.; Ghosh, S. *Chem. – Eur. J.* **2012,** *18,* 9860–9869. doi:10.1002/chem.201201299
44. Pandeeswar, M.; Avinash, M. B.; Govindaraju, T. *Chem. – Eur. J.* **2012,** *18,* 4818–4822. doi:10.1002/chem.201200197
45. Guha, S.; Saha, S. *J. Am. Chem. Soc.* **2010,** *132,* 17674–17677. doi:10.1021/ja107382x
46. Doria, F.; Nadai, M.; Sattin, G.; Pasotti, L.; Richter, S. N.; Freccero, M. *Org. Biomol. Chem.* **2012,** *10,* 3830–3840. doi:10.1039/c2ob07006e
47. Doria, F.; Folini, M.; Grande, V.; Cimino-Reale, G.; Zaffaroni, N.; Freccero, M. *Org. Biomol. Chem.* **2015,** *13,* 570–576. doi:10.1039/c4ob02054e
48. Nowak-Król, A.; Shoyama, K.; Stolte, M.; Würthner, F. *Chem. Commun.* **2018,** *54,* 13763–13772. doi:10.1039/c8cc07640e
49. Sakai, N.; Mareda, J.; Vauthey, E.; Matile, S. *Chem. Commun.* **2010,** *46,* 4225–4237. doi:10.1039/c0cc00078g
50. Alp, S.; Erten, Ş.; Karapire, C.; Köz, B.; Doroshenko, A. O.; İçli, S. *J. Photochem. Photobiol., A* **2000,** *135,* 103–110. doi:10.1016/s1010-6030(00)00306-3

51. Barros, T. C.; Brochsztain, S.; Toscano, V. G.; Filho, P. B.; Politi, M. J. *J. Photochem. Photobiol., A* **1997,** *111,* 97–104. doi:10.1016/s1010-6030(97)00205-0
52. Kishore, R. S. K.; Kel, O.; Banerji, N.; Emery, D.; Bollot, G.; Mareda, J.; Gomez-Casado, A.; Jonkheijm, P.; Huskens, J.; Maroni, P.; Borkovec, M.; Vauthey, E.; Sakai, N.; Matile, S. *J. Am. Chem. Soc.* **2009,** *131,* 11106–11116. doi:10.1021/ja9030648
53. Nicewicz, D. A.; MacMillan, D. W. C. *Science* **2008,** *322,* 77–80. doi:10.1126/science.1161976
54. Hasharoni, K.; Levanon, H.; Greenfield, S. R.; Gosztola, D. J.; Svec, W. A.; Wasielewski, M. R. *J. Am. Chem. Soc.* **1995,** *117,* 8055–8056. doi:10.1021/ja00135a040
55. Gao, X.; Qiu, W.; Yang, X.; Liu, Y.; Wang, Y.; Zhang, H.; Qi, T.; Liu, Y.; Lu, K.; Du, C.; Shuai, Z.; Yu, G.; Zhu, D. *Org. Lett.* **2007,** *9,* 3917–3920. doi:10.1021/ol701539z
56. Kishore, R. S. K.; Ravikumar, V.; Bernardinelli, G.; Sakai, N.; Matile, S. *J. Org. Chem.* **2008,** *73,* 738–740. doi:10.1021/jo702392q
57. Sasikumar, M.; Suseela, Y. V.; Govindaraju, T. *Asian J. Org. Chem.* **2013,** *2,* 779–785. doi:10.1002/ajoc.201300088
58. Demmig, S.; Langhals, H. *Chem. Ber.* **1988,** *121,* 225–230. doi:10.1002/cber.19881210205
59. Wasmus, S.; Vielstich, W. *Electrochim. Acta* **1993,** *38,* 185–189. doi:10.1016/0013-4686(93)85127-k
60. Connelly, N. G.; Geiger, W. E. *Chem. Rev.* **1996,** *96,* 877–910. doi:10.1021/cr940053x
61. Neumann, M.; Füldner, S.; König, B.; Zeitler, K. *Angew. Chem., Int. Ed.* **2011,** *50,* 951–954. doi:10.1002/anie.201002992
62. Ghosh, I.; König, B. *Angew. Chem., Int. Ed.* **2016,** *55,* 7676–7679. doi:10.1002/anie.201602349
63. Romero, N. A.; Nicewicz, D. A. *J. Am. Chem. Soc.* **2014,** *136,* 17024–17035. doi:10.1021/ja506228u
64. Pavlishchuk, V. V.; Addison, A. W. *Inorg. Chim. Acta* **2000,** *298,* 97–102. doi:10.1016/s0020-1693(99)00407-7
65. Cismesia, M. A.; Yoon, T. P. *Chem. Sci.* **2015,** *6,* 5426–5434. doi:10.1039/c5sc02185e
66. Silvi, M.; Arceo, E.; Jurberg, I. D.; Cassani, C.; Melchiorre, P. *J. Am. Chem. Soc.* **2015,** *137,* 6120–6123. doi:10.1021/jacs.5b01662
67. Demchenko, A. P.; Tomin, V. I.; Chou, P.-T. *Chem. Rev.* **2017,** *117,* 13353–13381. doi:10.1021/acs.chemrev.7b00110

License and Terms

BEILSTEIN JOURNAL OF ORGANIC CHEMISTRY

Synthesis and properties of sulfur-functionalized triarylmethylium, acridinium and triangulenium dyes

Marco Santella, Eduardo Della Pia, Jakob Kryger Sørensen and Bo W. Laursen*

Full Research Paper

Open Access

Address:
Nano-Science Center and Department of Chemistry, University of Copenhagen, Universitetsparken 5, 2100 Copenhagen Ø, Denmark

Email:
Bo W. Laursen* - bwl@nano.ku.dk

* Corresponding author

Keywords:
acridinium dyes; aromatic nucleophilic substitution; fluorescent dyes; sulfur-functionalized dyes; triangulenium dyes; triarylmethylium

Beilstein J. Org. Chem. **2019,** *15,* 2133–2141.
doi:10.3762/bjoc.15.210

Received: 28 June 2019
Accepted: 23 August 2019
Published: 09 September 2019

This article is part of the thematic issue "Dyes in modern organic chemistry".

Guest Editor: H. Ihmels

Abstract

Triangulenium dyes functionalized with one, two or three ethylthiol functionalities were synthesized and their optical properties were studied. The sulfur functionalities were introduced by aromatic nucleophilic substitution of methoxy groups in triarylmethylium cations with ethanethiol followed by partial or full ring closure of the *ortho* positions with nitrogen or oxygen bridges leading to sulfur-functionalized acridinium, xanthenium or triangulenium dyes. For all the dye classes the sulfur functionalities are found to lead to intensely absorbing dyes in the visible range (470 to 515 nm), quite similar to known analogous dye systems with dialkylamino donor groups in place of the ethylthiol substituents. For the triangulenium derivatives significant fluorescence was observed ($\Phi_f = 0.1$ to $\Phi_f = 0.3$).

Introduction

The design, synthesis and studies of organic fluorescent dyes have witnessed a revival in recent years, in particular due to their applications in imaging and biomedical assays and analytical techniques [1-5]. The desire to detect minute amounts of dye, ideally single molecules [6,7], in complex biological environments with high levels of autofluorescence, constantly challenges chemists to develop new dyes with improved or special properties. In the design of simple dyes parameters such as molar absorption coefficients (ε), absorption/emission wavelengths [8,9], fluorescence quantum yields (Φ_{fl}) [10,11], and fluorescence lifetime (τ_{fl}) [12,13] are key photophysical properties to consider and optimize for any given application.

We have for quite some time been interested in the synthesis, properties and applications of dyes from the triangulenium family (Figure 1) [14,15]. The triangulenium dyes can be divided into two main categories: 1) triangulenium dyes with donor substituents at the corners of the triangulenium ring

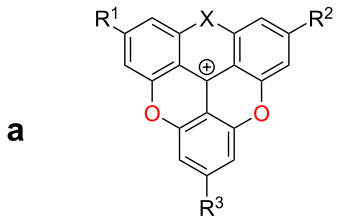

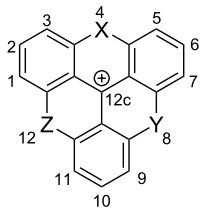

X = O, $R^1 = R^2 = R^3 = NR_2$	A_3-TOTA
X = O, $R^1 = R^2 = NR_2$, R^3 = H	A_2-TOTA
X = O, $R^1 = NR_2$, $R^2 = R^3$ = H	A_1-TOTA
X = NR, $R^1 = R^2 = R^3 = NR_2$	A_3-ADOTA
X = O, $R^1 = R^2 = R^3$ = OH	H-TOTA

X = Y = Z = O	TOTA
X = NR, Y = Z = O	ADOTA
X = Y = NR, Z = O	DAOTA
X = Y = Z = NR	TATA
X = S, Y = Z = O	DOTTA
X = S, Y = NR, Z = O	AOTTA

Figure 1: Structures of some representative triangulenium dyes. a) Rhodamine/fluorescine-like derivatives with donor groups in *para*-positions (2, 6, and 10) to the formal cation center (12c). b) Derivatives without donor groups.

system (position 2, 6 and 10, Figure 1a) [16-18], and 2) triangulenium dyes without such groups (Figure 1b) [19-21]. Dyes in the first category have intense absorption ($\varepsilon \approx 50{,}000–130{,}000\ M^{-1}{\cdot}cm^{-1}$), high fluorescence quantum yields ($\Phi_{fl} > 50\%$) and fluorescence lifetimes of 3–4 ns. All properties that agree well with their structural resemblance to rhodamines and fluoresceines, and triangulenium dyes such as A_3-TOTA$^+$ and H-TOTA$^+$ (Figure 1a) can be viewed as extended symmetric versions of these prominent dyes [16,22]. The second class of triangulenium dyes, without appended donor groups, are characterized by much less intense transitions ($\varepsilon \approx 5{,}000–20{,}000\ M^{-1}{\cdot}cm^{-1}$), which for some derivatives leads to unusually long fluorescence lifetimes ($\tau_{fl} \approx 20$ ns) [23,24]. This long fluorescence lifetime has been a key point of interest since it enables time-gated detection for suppression of autofluorescence [25,26] and provides attractive advantages in fluorescence polarization assays [13,27,28].

A common characteristic feature of triangulenium dye synthesis is the use of methoxy-substituted triarylmethylium salts as simple precursors allowing both introduction of dialkylamino donor groups and formation of the heterocyclic triangulenium ring systems. These characteristic types of aromatic nucleophilic substitution (S_NAr) reactions are exemplified by the synthesis of A_3-ADOTA$^+$ (Figure 2) [17]. Starting from the readily available tris(2,4,6-trimethoxyphenyl)methylium salt $(TMP)_3C^+$ [18,29], stepwise replacement of the *para*-methoxy groups by dialkylamines provides access to a wide variety of symmetric and asymmetric triarylmethylium dyes [18,30,31]. Replacement of two *o*-methoxy groups by one primary amine gives acridinium-type ring systems (Figure 2, step 2) and is a key reaction for the formation of the unsubstituted triangulenium dyes shown in Figure 1b [19,20]. Finally, formation of oxygen bridges in the triangulenium system (Figure 2, step 3) involves demethylation conditions and intramolecular S_NAr replacement of *ortho*-methoxy groups [18,32].

The S_NAr approach to the synthesis of triangulenium dyes [14,18,19] has been extremely successful and expanded the family greatly from the single derivative (TOTA$^+$, Figure 1b)

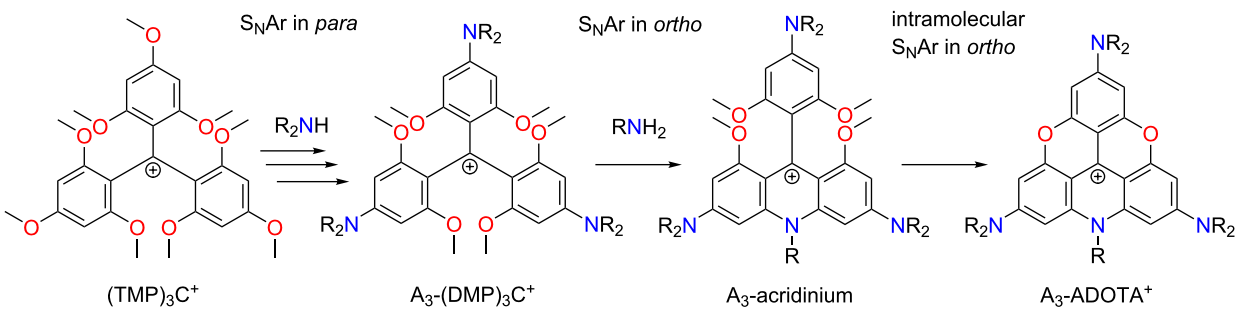

Figure 2: Examples of various types of S_NAr reactions typical in triangulenium synthesis, exemplified with the synthesis of A_3-ADOTA$^+$: step 1, replacement of *p*-methoxy groups with dialkylamines. Step 2, replacement of *o*-methoxy groups with a primary amine followed by intramolecular S_NAr reaction. Step 3, intramolecular S_NAr replacement of methoxy groups by hydroxy groups formed under ether-cleavage conditions.

first synthesized by Martin and Smith in 1964 [32], and also includes the family of helicenium dyes [33-35]. However, the introduction of groups other than nitrogen and oxygen has so far not been performed by the S_NAr approach. Thus in the preparation of the sulfur-bridged triangulenium ions DOTTA$^+$ and AOTTA$^+$ (Figure 1b) Lacour and co-workers reported unsuccessful attempts of S_NAr reactions with sulfur nucleophiles in *ortho*-position of $(TMP)_3C^+$ and had to assemble the thioxanthenium part of the triangulenium ring system independently by other means [36]. Similarly, we had to use a stepwise buildup of the triangulenium systems to introduce saturated [37] and unsaturated [38] carbon bridges.

Here we report for the first time the introduction of sulfur functionalities into triangulenium dyes by S_NAr reaction with ethylthiol nucleophiles in the *para*-positions accessing several new families of xanthenium, acridinium and triangulenium dyes with thioether donor groups.

Results and Discussion

Firstly, a series of triarylmethylium salts with variable number of *para*-methoxy substituents was synthesized. The easily achievable cations $(TMP)_3C^+$, $(DMP)(TMP)_2C^+$ and $(DMP)_2(TMP)C^+$ (Scheme 1) were prepared by their respective literature procedures [18,31]. To investigate the reactivity of these carbenium systems in S_NAr reactions with sulfur-based nucleophiles, simple alkylthiols were chosen, with the ethyl and *tert*-butyl thiols being the primary choice. S_NAr reactions with the two thiols were tested under identical reaction conditions (Scheme 1).

These conditions consisted of heating the reaction components in refluxing acetonitrile in the presence of collidine as base. For all three carbenium salts examinations showed that only ethanethiol lead to substitution. The progress of the reaction was conveniently followed by MALDI–TOF mass spectrometry. In case of the reactions with *tert*-butylthiolate, neither detection of the target molecule nor any of the intermediates were observed. This lack of reactivity is likely explained by the *tert*-butylthiolate nucleophile being too bulky to undergo reaction. In the successful reactions, which had occurred with ethanethiol, a high selectivity was observed for *para*-substitutions, giving S_x-$(DMP)_3C^+$ **1**, **2**, and **3** in reasonable yields of 20–50% after column chromatography purification. It is important to note that the gradual introduction of thioethers into the carbenium systems did not significantly influence the overall reactivity of the system towards subsequent nucleophilic aromatic substitution. When the reaction was followed by MALDI–TOFMS spectrometry it was thus possible to observe simultaneously the presence of the target compound and all of the intermediates involved in the reaction. This behavior is contrary to the reaction pattern observed when using dialkylamines as nucleophiles, where the strong electron-donating effect of the introduced amines stabilize the carbenium ion products and thus significantly reduces the reactivity of the remaining methoxy groups for further substitutions [18,39]. This observation is in agreement with the much stronger cation stabilization of the dialkylamino group compared to the methoxy group. The ability of the alkylthio group to stabilize carbenium ions, given by the Hammet σ_p^+ value [40], on the other hand is quite similar to the methoxy group or even a little lower [41], and does thus not slow down the multistep S_NAr reactions.

The new *ortho*-methoxytriarylcarbenium ions with one, two and three *para*-SEt groups (**1**–**3**) are potential precursors for a wide variety of new triangulenium, xanthenium, and acridinium dyes. To elucidate some of these possibilities we first investigated transformations of the symmetric derivative **1**. Treatment with primary alkylamines, *n*-propylamine and *n*-octylamine, yielded exclusively the acridinium products **4a**,**b** (Scheme 2). This *ortho* S_NAr transformation is similar to what is reported for the $(DMP)_3C^+$ system [19,20,42] lacking *para*-substituents and for

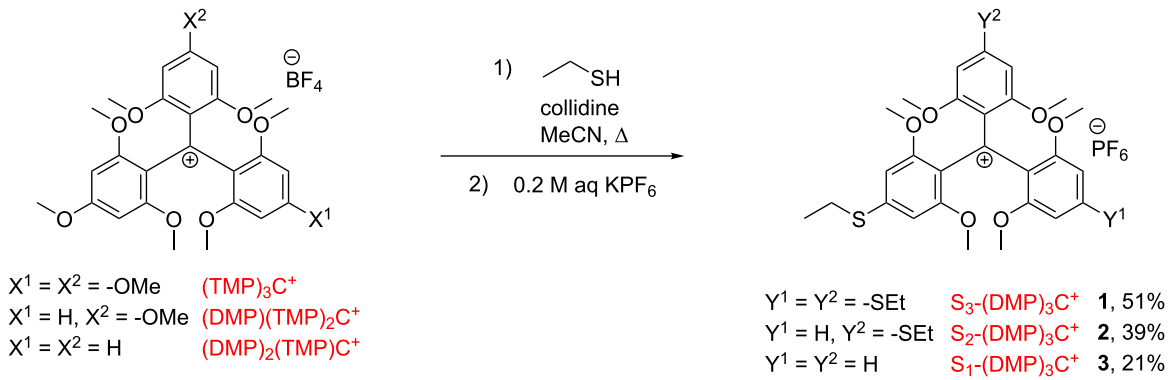

Scheme 1: Synthesis of three novel S_X-$(DMP)_3C^+$ PF_6^- ethylsulfanyl-substituted triarylmethylium salts.

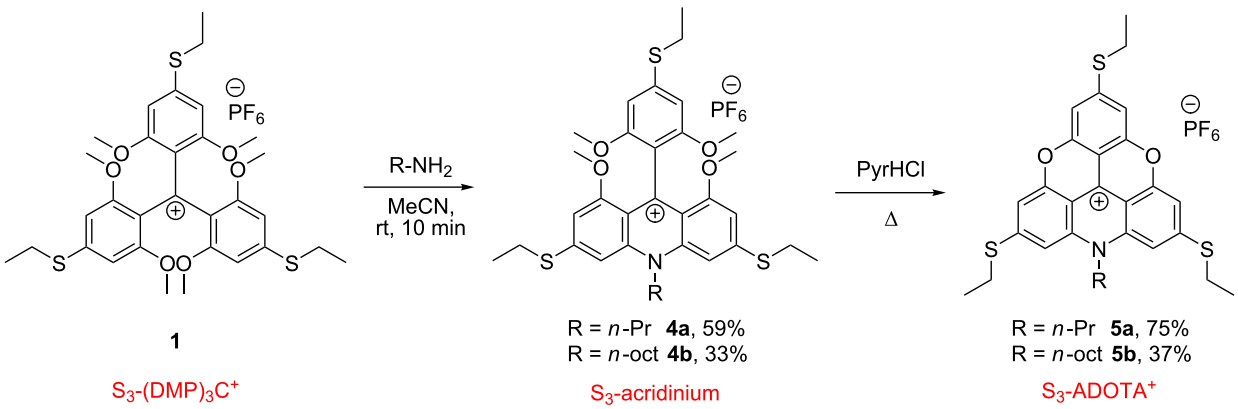

Scheme 2: Synthetic route for the synthesis of S_3-ADOTA$^+$.

the *para*-amino-substituted analogue [17] (step 2 in Figure 1). It was found that the reactivity in S_NAr reactions of **1** with primary amines was high and the acridinium compounds **4a**,**b** were obtained in few minutes after the addition of 2 equiv of the corresponding primary amine at room temperature. Further ring closure to two oxygen bridges in acridinium compounds **4a** and **4b** to the corresponding triangulenium dyes S_3-ADOTA$^+$ (**5a**,**b**) was achieved by heating in molten pyridine hydrochloride (Scheme 2).

It is noteworthy that the ethylthio ether linkages remained intact upon treatment with molten PyrHCl, which was found to result in complicated mixtures of dealkylated byproducts when these conditions were applied on dialkylamino-substituted carbenium systems [18].

The direct ring closure of **1** in PyrHCl yielded in a similar manner the sulfur-functionalized trioxatriangulenium system S_3-TOTA$^+$ (**6**) as shown in Scheme 3. Mono ring closure was achieved under milder ether cleaving conditions with aqueous HBr in acetic acid, leading to the ethylthio-substituted xanthenium system **7** in 43% yield (Scheme 3).

By applying similar molten pyridine hydrochloride conditions to the mono- and disubstituted thioether carbenium salts (**2** and **3**), it was possible to isolate the derivatives S_2-TOTA$^+$ (**8**) and S_1-TOTA$^+$ (**9**), respectively as their hexafluorophosphate salts (Scheme 4). The two S_x-TOTA$^+$ derivatives were obtained with good yield after purification by column chromatography and subsequent recrystallization.

To conclude, the successful introduction of -SEt groups by the S_NAr approach, and subsequent nitrogen and oxygen ring-closure reactions provides access to several new families of carbenium dyes, all with the unusual -SR donor group: thus **1**–**3** represent new triarylmethylium dyes, **4a** and **4b** sulfur analogues of aminoacridinium dyes (acridine orange-like structures), **7** a fluorescein-like xanthenium dye, **5a** and **5b** are sulfur-substituted ADOTA$^+$ dyes, and finally the three sulfur-substituted TOTA$^+$ dyes **6**, **8** and **9**.

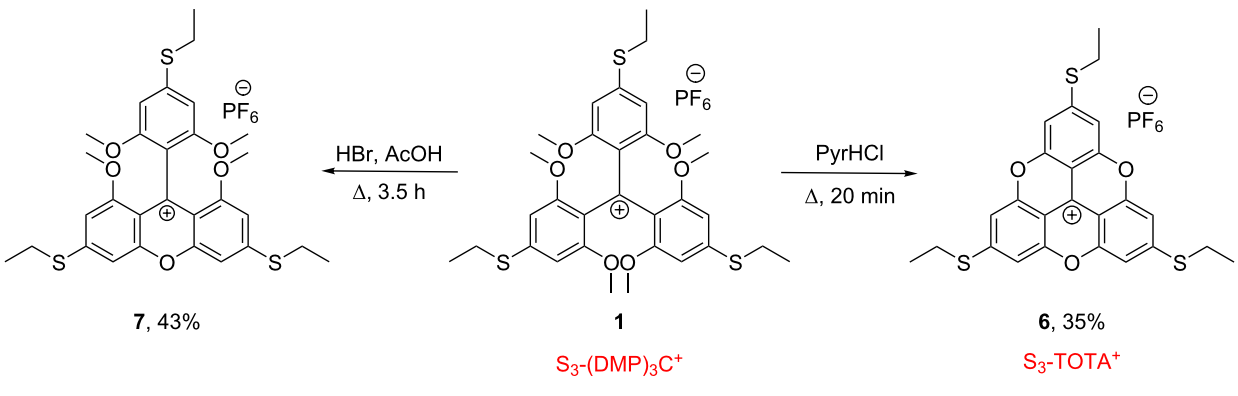

Scheme 3: Synthesis of S_3-TOTA$^+$ PF_6^- (**6**) and the mono ring closed xanthenium **7**.

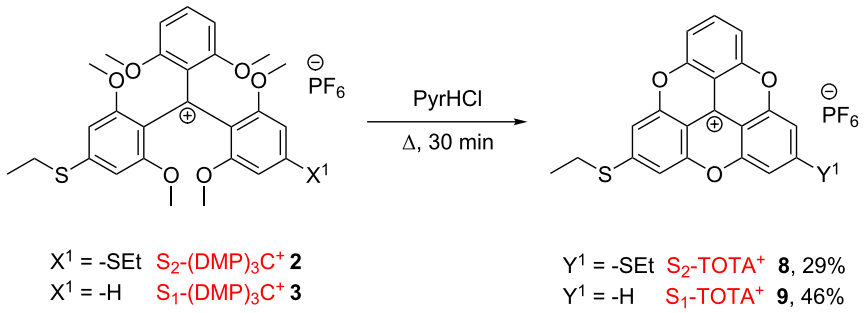

Scheme 4: Synthesis of S_2-TOTA$^+$ PF_6^- (**8**) and S_1-TOTA$^+$ PF_6^- (**9**).

Now the relevant questions are: how do the -SR donor groups influence transition energies and intensities? And how do they affect fluorescence quantum yields in these new dye systems? To the extent possible we will compare the new sulfur-functionalized dyes to known analogues with -OR or -NR_2 donor groups in the same positions.

The sulfur-substituted triarylmethylium dyes **1, 2** and **3** display broad absorption bands in the 500–700 nm region (Figure 3), that in shape and relative transition energy are quite similar to the analogues with similar numbers of *para*-methoxy or diethylamino groups [31], as shown by comparison of maximum absorption wavelength ($\lambda_{max,abs}$) and molar absorptivity (ε) in Table 1. It is noticed that the -SEt donor group in these *ortho*-hexamethoxytriarylmethylium dyes provides transition energies and intensities very similar to those of commonly used dialkylamino-donor groups, but significantly red-shifted relative to the methoxy-substituted analogues.

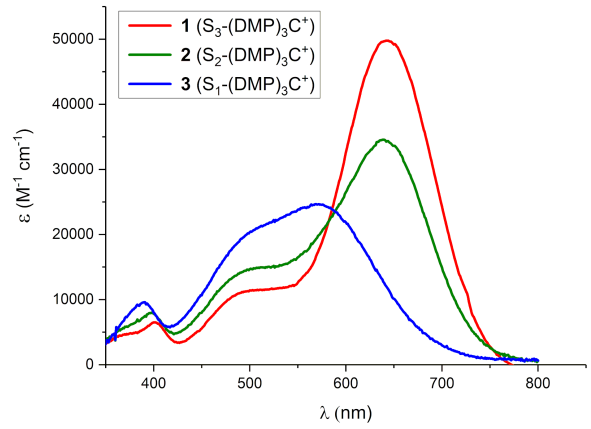

Figure 3: UV–vis spectra in MeCN: S_3-(DMP)$_3$C$^+$ (**1**, red), S_2-(DMP)$_3$C$^+$ (**2**, green), and S_1-(DMP)$_3$C$^+$ (**3**, blue).

Absorption spectra of the partially ring-closed acridinium and xanthenium compounds, with three *para*-SEt groups, **4a** and **7**, respectively, are shown in Figure 4. For these compounds the spectra are dominated by strong transitions assigned to the 3,6-diethylthio-acridinium and -xanthenium ring systems peaking at 457 nm (ε = 47000 $M^{-1}{\cdot}cm^{-1}$) and at 520 nm (ε = 60000 $M^{-1}{\cdot}cm^{-1}$), respectively (see Supporting Information File 1, Table S1 for additional data in more solvents). The energy and intensity of these transitions are quite similar to those found in dialkylamino analogues, that are 3,6-diaminoacridines and rhodamines [43,44]. The weak tails on the red side of these bands are tentatively assigned to internal charge-transfer transitions from the perpendicularly [19,42] arranged ethylthio(dimethoxy)phenyl group to the xanthenium/acridinium systems polarized along the *y*-axes (Figure 4, inset). This bichromophoric behavior has been studied in detail for the dialkylamino-substituted xanthenium/rhodamine system [45,46], and is also the likely reason for these compounds being non-fluorescent.

Table 1: Summary of absorption data of triarylmethylium ions in MeCN.

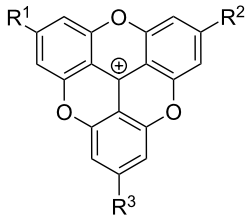

	$\lambda_{max.abs.}$ (ε, $M^{-1}{\cdot}cm^{-1}$)		
donor groups R^1, R^2, R^3	-SEt	-OMe[a]	-NEt_2[a]
one donor $R^2 = R^3 = H$	576 nm (24600)	491 nm (14100)	457 nm (16900)
two donors $R^3 = H$	639 nm (34600)	580 nm (18400)	637 nm (40400)
three donors	642 nm (49800)	577 nm (23400)	634 nm (49400)

[a]Data from [43,44].

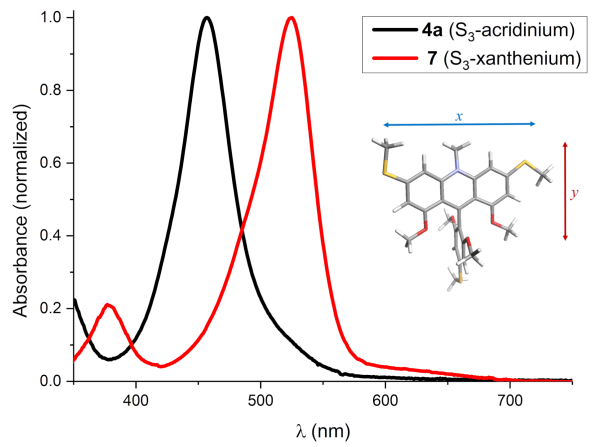

Figure 4: UV–vis spectra in MeCN: S_3-acridinium (**4a**, black) and S_3-xanthenium (**7**, red). Inset: The 3D structure of **4a** with indication of the principle axes of the electronic transitions.

The three sulfur-substituted trioxatriangulenium dyes **6**, **8**, and **9** all display a first absorption band around 480 nm (Figure 5), with increasing intensity as the number of -SEt groups on the $TOTA^+$ core increases. This behavior resembles the trend observed for the analogue series of amino-substituted TOTA's (Table 2) [18,31]. In the two low-symmetry derivatives **8** and **9** transitions to the S_2 excited states are observed at around 400 nm, while the D_{3h} symmetric S_3-$TOTA^+$ shows only one, though broad, absorption band corresponding to merging of the S_1 and S_2 transitions into one, arising from the degenerated HOMO in the symmetric dye. The influence of solvent and counter ions on such degenerate states have been studied in detail for the A_3-TOTA system [22,47] and related triarylmethylium dyes such as crystal violet [48,49].

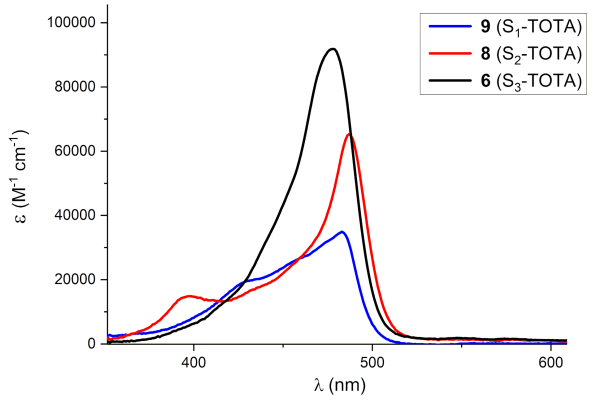

Figure 5: UV–vis spectra in CH_2Cl_2: S_1-$TOTA^+$ (**9**, blue line), S_2-$TOTA^+$ (**8**, red line), and S_3-$TOTA^+$ (**6**, black line).

When three -SEt groups are placed on the asymmetric azadioxatriangulenium core, as in S_3-$ADOTA^+$ (**5a**), the presence of two

Table 2: Summary of absorption data of substituted TOTA dyes in CH_2Cl_2.

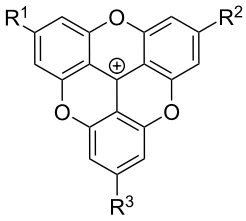

	$\lambda_{max,abs}$ (ε, $M^{-1}\cdot cm^{-1}$)	
Donor groups R^1, R^2, R^3	-SEt	$-NEt_2$
one donor $R^2 = R^3 = H$	S_1-$TOTA^+$ (**9**) 483 nm (35000)	A_1-$TOTA^{+a}$ 507 nm (41700)
two donors $R^3 = H$	S_2-$TOTA^+$ (**8**) 487 nm (65200)	A_2-$TOTA^{+a}$ 513 nm (59700)
three donors	S_3-$TOTA^+$ (**6**) 478 nm (91900)	A_3-$TOTA^{+b}$ 471 nm (132900)

[a]Data from [31]; [b]data from [18].

electronic transitions becomes very clear, with two well-resolved peaks in the absorption spectrum (Figure 6). The transition at 442 nm is assigned to the $S_0 \rightarrow S_2$ transition and nearly coincides with the main transition observed in the S_3-acridinium (**4a**) precursor before ring closure (Figure 4), indicating that this, the most intense transition belongs to the same chromophore, now part of the triangulenium ring system. The $S_0 \rightarrow S_1$ transition in **5a** is found at 507 nm, where the open form only had a very weak shoulder in its absorption spectrum (Figure 4). The ring closure of **4a** into the fully planar triangulenium system **5a** leads to a significant increase in the orbital overlap and thus also in the intensity of the $S_0 \rightarrow S_1$ transition. This assignment is supported by calculations of the orbitals involved in the first two electronic transitions (Figure 6), which confirm their localization in different parts of the $ADOTA^+$ system. The much more allowed $S_0 \rightarrow S_1$ transition is also in agreement with the observation that **5a** (and **5b**) display intense fluorescence (Figure 6).

Table 3 summarizes the spectral and photophysical properties on the triangulenium dyes showing any applicable fluorescence. Beside S_3-$ADOTA^+$ (**5a**) that are the double and triple -SEt-substituted TOTAs **6** and **8**, for which the fluorescence spectra are shown in Figure 7, with fluorescence quantum yields of 16% and 12%, respectively. From the measured fluorescence lifetimes and quantum yields (Table 3) it is possible to calculate the radiative lifetimes (τ_0), which are found to be in qualita-

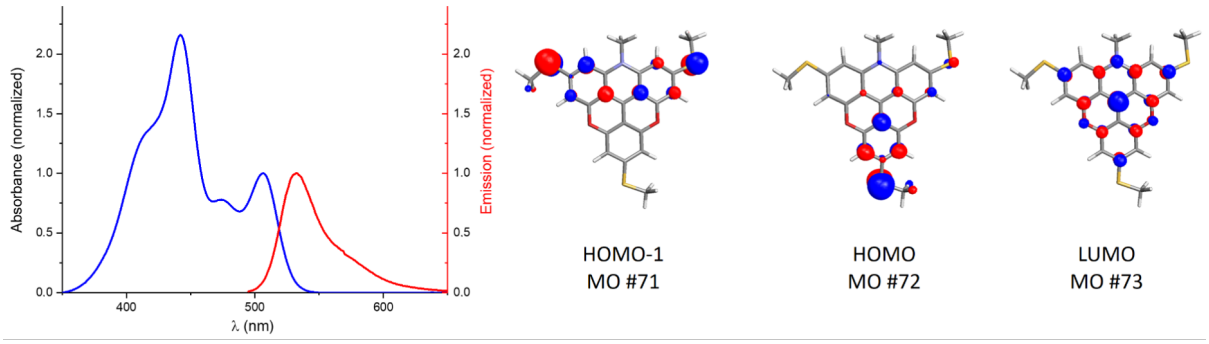

Figure 6: UV–vis absorption and fluorescence spectra (λ_{ex} = 485 nm) of **5a** in CH_2Cl_2 solution. Calculated molecular orbital contour plots (semi-empirical method AM1).

Table 3: Summary of optical properties of the fluorescent derivatives.

Compound	Solvent	$\lambda_{max,abs}$ (nm)	ε ($M^{-1}\cdot cm^{-1}$)	$\lambda_{max,fl}$ (nm)	Φ_f[a]	τ (ns)	τ_0[b] (ns)
5a (S_3-ADOTA)	CH_2Cl_2	442 507	76700 35400	532	0.28	3.9	13.9
6 (S_3-TOTA)	CH_2Cl_2	478	91850	505	0.16	0.7	4.4
8 (S_2-TOTA)	CH_2Cl_2	487	65200	509	0.12	0.7	5.8

[a]Measured relative to fluorescein in 0.1 M aqueous NaOH (Φ = 0.96); [b]radiative lifetime $\tau_0 = \Phi_f/\tau$.

tive agreement with the molar absorption coefficients (ε) for the corresponding transitions, as expected from the Strickler–Berg relation [50].

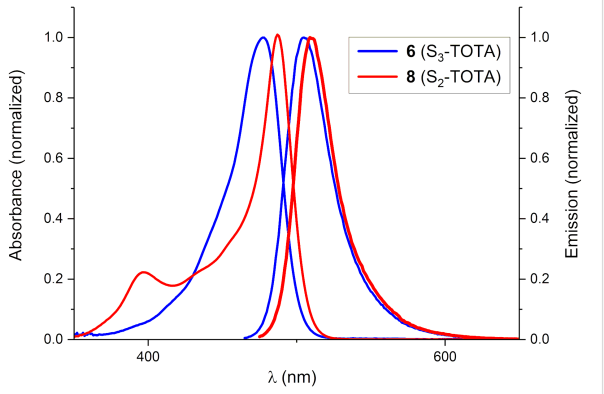

Figure 7: Normalized absorption and fluorescence spectra of **6** (S_3-TOTA$^+$), λ_{ex} = 460 nm, and **8** (S_2-TOTA$^+$), λ_{ex} = 470 nm, in CH_2Cl_2 solution.

While the spectral properties of the new -SEt-substituted dyes are surprisingly similar to the -NEt_2-substituted analogues across the various dye families they are obviously less bright fluorophores. Thus, the dialkylamino-substituted analogue of **5a** (A_3-ADOTA$^+$) has a reported quantum yield as high as 64% in acetonitrile [17], on par with A_3-TOTA$^+$ and A_2-TOTA$^+$ which display quantum yields from 50–100% depending on the solvent [31]. A similar reduction in fluorescence efficiency was observed by Kotaskova et al. for fluorescein derivatives with one alkylthio group in the 3 position replacing an -OH/-O^- group [51]. The origin of reduced fluorescence quantum yields in dyes with alkylthio donor groups in their chromophores is not clear at this point. It may result from enhanced internal conversion or intersystem crossing to the triplet state. Further photophysical work will have to settle this issue and thereby suggest structural improvements and/or the best applications of these dyes.

Conclusion

The effective introduction of alkylthiol groups into the *para*-positions of triarylmethylium ions via S_NAr reactions was demonstrated. These new thioether-substituted triarylmethylium ions provide access to a broad range of new heterocyclic carbenium dyes of the xanthenium, acridinium and triangulenium type via further S_NAr reactions with primary amines and ring-closure reactions. The introduction of thioether donor groups in these dye classes is unprecedented, but is found to yield spectral properties quite similar to analogous dyes with dialkylamino groups. The synthesized thioether-substituted triangulenium derivatives are fluorescent, though with lower quantum yields (Φ_f = 0.1 to Φ_f = 0.3) than the corresponding dialkylamino-substituted analogues.

Supporting Information

Supporting Information File 1

Experimental details, full synthetic procedures, spectroscopic characterization and NMR spectra of new compounds, as well as additional UV–vis and fluorescence spectra.
[https://www.beilstein-journals.org/bjoc/content/supplementary/1860-5397-15-210-S1.pdf]

Acknowledgements

The work was supported by the Danish Council of Independent Research (DFF-6111-00483).

ORCID® iDs

Bo W. Laursen - https://orcid.org/0000-0002-1120-3191

References

1. Lavis, L. D.; Raines, R. T. *ACS Chem. Biol.* **2008,** *3,* 142–155. doi:10.1021/cb700248m
2. Grimm, J. B.; Muthusamy, A. K.; Liang, Y.; Brown, T. A.; Lemon, W. C.; Patel, R.; Lu, R.; Macklin, J. J.; Keller, P. J.; Ji, N.; Lavis, L. D. *Nat. Methods* **2017,** *14,* 987–994. doi:10.1038/nmeth.4403
3. Butkevich, A. N.; Lukinavičius, G.; D'Este, E.; Hell, S. W. *J. Am. Chem. Soc.* **2017,** *139,* 12378–12381. doi:10.1021/jacs.7b06412
4. Kolmakov, K.; Hebisch, E.; Wolfram, T.; Nordwig, L. A.; Wurm, C. A.; Ta, H.; Westphal, V.; Belov, V. N.; Hell, S. W. *Chem. – Eur. J.* **2015,** *21,* 13344–13356. doi:10.1002/chem.201501394
5. Haugland, R. P. *The Molecular Probes Handbook,* 11th ed.; Thermofischer Scientific, 2010.
6. Moerner, W. E.; Orrit, M. *Science* **1999,** *283,* 1670–1676. doi:10.1126/science.283.5408.1670
7. Grimm, J. B.; English, B. P.; Chen, J.; Slaughter, J. P.; Zhang, Z.; Revyakin, A.; Patel, R.; Macklin, J. J.; Normanno, D.; Singer, R. H.; Lionnet, T.; Lavis, L. D. *Nat. Methods* **2015,** *12,* 244–250. doi:10.1038/nmeth.3256
8. Lei, Z.; Li, X.; Luo, X.; He, H.; Zheng, J.; Qian, X.; Yang, Y. *Angew. Chem., Int. Ed.* **2017,** *56,* 2979–2983. doi:10.1002/anie.201612301
9. Staudinger, C.; Borisov, S. M. *Methods Appl. Fluoresc.* **2015,** *3,* 042005. doi:10.1088/2050-6120/3/4/042005
10. Panchuk-Voloshina, N.; Haugland, R. P.; Bishop-Stewart, J.; Bhalgat, M. K.; Millard, P. J.; Mao, F.; Leung, W.-Y.; Haugland, R. P. *J. Histochem. Cytochem.* **1999,** *47,* 1179–1188. doi:10.1177/002215549904700910
11. Song, X.; Johnson, A.; Foley, J. *J. Am. Chem. Soc.* **2008,** *130,* 17652–17653. doi:10.1021/ja8075617
12. Berezin, M. Y.; Achilefu, S. *Chem. Rev.* **2010,** *110,* 2641–2684. doi:10.1021/cr900343z
13. Meyer-Almes, F.-J. *Methods Appl. Fluoresc.* **2017,** *5,* 042002. doi:10.1088/2050-6120/aa7c7a
14. Bosson, J.; Gouin, J.; Lacour, J. *Chem. Soc. Rev.* **2014,** *43,* 2824–2840. doi:10.1039/c3cs60461f
15. Stępień, M.; Gońka, E.; Żyła, M.; Sprutta, N. *Chem. Rev.* **2017,** *117,* 3479–3716. doi:10.1021/acs.chemrev.6b00076
16. Westerlund, F.; Hildebrandt, C. B.; Sørensen, T. J.; Laursen, B. W. *Chem. – Eur. J.* **2010,** *16,* 2992–2996. doi:10.1002/chem.200902965
17. Laursen, B. W.; Sørensen, T. J. *J. Org. Chem.* **2009,** *74,* 3183–3185. doi:10.1021/jo9002486
18. Laursen, B. W.; Krebs, F. C.; Nielsen, M. F.; Bechgaard, K.; Christensen, J. B.; Harrit, N. *J. Am. Chem. Soc.* **1998,** *120,* 12255–12263. doi:10.1021/ja982550r
19. Laursen, B. W.; Krebs, F. C. *Chem. – Eur. J.* **2001,** *7,* 1773–1783. doi:10.1002/1521-3765(20010417)7:8<1773::aid-chem17730>3.0.co;2-f
20. Laursen, B. W.; Krebs, F. C. *Angew. Chem., Int. Ed.* **2000,** *39,* 3432–3434. doi:10.1002/1521-3773(20001002)39:19<3432::aid-anie3432>3.0.co;2-s
21. Hammershøj, P.; Sørensen, T. J.; Han, B.-H.; Laursen, B. W. *J. Org. Chem.* **2012,** *77,* 5606–5612. doi:10.1021/jo3007732
22. Laursen, B. W.; Reynisson, J.; Mikkelsen, K. V.; Bechgaard, K.; Harrit, N. *Photochem. Photobiol. Sci.* **2005,** *4,* 568–576. doi:10.1039/b501584g
23. Bogh, S. A.; Simmermacher, M.; Westberg, M.; Bregnhøj, M.; Rosenberg, M.; De Vico, L.; Veiga, M.; Laursen, B. W.; Ogilby, P. R.; Sauer, S. P. A.; Sørensen, T. J. *ACS Omega* **2017,** *2,* 193–203. doi:10.1021/acsomega.6b00211
24. Bogh, S. A.; Bora, I.; Rosenberg, M.; Thyrhaug, E.; Laursen, B. W.; Sørensen, T. J. *Methods Appl. Fluoresc.* **2015,** *3,* 045001. doi:10.1088/2050-6120/3/4/045001
25. Rich, R. M.; Stankowska, D. L.; Maliwal, B. P.; Sørensen, T. J.; Laursen, B. W.; Krishnamoorthy, R. R.; Gryczynski, Z.; Borejdo, J.; Gryczynski, I.; Fudala, R. *Anal. Bioanal. Chem.* **2013,** *405,* 2065–2075. doi:10.1007/s00216-012-6623-1
26. Rich, R. M.; Mummert, M.; Gryczynski, Z.; Borejdo, J.; Sørensen, T. J.; Laursen, B. W.; Foldes-Papp, Z.; Gryczynski, I.; Fudala, R. *Anal. Bioanal. Chem.* **2013,** *405,* 4887–4894. doi:10.1007/s00216-013-6879-0
27. Hall, M. D.; Yasgar, A.; Peryea, T.; Braisted, J. C.; Jadhav, A.; Simeonov, A.; Coussens, N. P. *Methods Appl. Fluoresc.* **2016,** *4,* 022001. doi:10.1088/2050-6120/4/2/022001
28. Sørensen, T. J.; Thyrhaug, E.; Szabelski, M.; Luchowski, R.; Gryczynski, I.; Gryczynski, Z.; Laursen, B. W. *Methods Appl. Fluoresc.* **2013,** *1,* 025001. doi:10.1088/2050-6120/1/2/025001
29. Wada, M.; Konishi, H.; Kirishima, K.; Takeuchi, H.; Natsume, S.; Erabi, T. *Bull. Chem. Soc. Jpn.* **1997,** *70,* 2737–2741. doi:10.1246/bcsj.70.2737
30. Laursen, B. W.; Nørgaard, K.; Reitzel, N.; Simonsen, J. B.; Nielsen, C. B.; Als-Nielsen, J.; Bjørnholm, T.; Sølling, T. I.; Nielsen, M. M.; Bunk, O.; Kjaer, K.; Tchebotareva, N.; Watson, M. D.; Müllen, K.; Piris, J. *Langmuir* **2004,** *20,* 4139–4146. doi:10.1021/la049944i
31. Sørensen, T. J.; Laursen, B. W. *J. Org. Chem.* **2010,** *75,* 6182–6190. doi:10.1021/jo1009917
32. Martin, J. C.; Smith, R. G. *J. Am. Chem. Soc.* **1964,** *86,* 2252–2256. doi:10.1021/ja01065a030
33. Laleu, B.; Mobian, P.; Herse, C.; Laursen, B. W.; Hopfgartner, G.; Bernardinelli, G.; Lacour, J. *Angew. Chem., Int. Ed.* **2005,** *44,* 1879–1883. doi:10.1002/anie.200462321
34. Herse, C.; Bas, D.; Krebs, F. C.; Bürgi, T.; Weber, J.; Wesolowski, T.; Laursen, B. W.; Lacour, J. *Angew. Chem., Int. Ed.* **2003,** *42,* 3162–3166. doi:10.1002/anie.200351443

35. Bosson, J.; Labrador, G. M.; Pascal, S.; Miannay, F.-A.; Yushchenko, O.; Li, H.; Bouffier, L.; Sojic, N.; Tovar, R. C.; Muller, G.; Jacquemin, D.; Laurent, A. D.; Le Guennic, B.; Vauthey, E.; Lacour, J. *Chem. – Eur. J.* **2016,** *22,* 18394–18403. doi:10.1002/chem.201603591
36. Nicolas, C.; Bernardinelli, G.; Lacour, J. *J. Phys. Org. Chem.* **2010,** *23,* 1049–1056. doi:10.1002/poc.1753
37. Rosenberg, M.; Rostgaard, K. R.; Liao, Z.; Madsen, A. Ø.; Martinez, K. L.; Vosch, T.; Laursen, B. W. *Chem. Sci.* **2018,** *9,* 3122–3130. doi:10.1039/c8sc00089a
38. Rosenberg, M.; Santella, M.; Bogh, S. A.; Muñoz, A. V.; Andersen, H. O. B.; Hammerich, O.; Bora, I.; Lincke, K.; Laursen, B. W. *J. Org. Chem.* **2019,** *84,* 2556–2567. doi:10.1021/acs.joc.8b02978
39. Simonsen, J. B.; Kjær, K.; Howes, P.; Nørgaard, K.; Bjørnholm, T.; Harrit, N.; Laursen, B. W. *Langmuir* **2009,** *25,* 3584–3592. doi:10.1021/la803733s
40. Hansch, C.; Leo, A.; Taft, R. W. *Chem. Rev.* **1991,** *91,* 165–195. doi:10.1021/cr00002a004
41. Brown, H. C.; Okamoto, Y. *J. Am. Chem. Soc.* **1958,** *80,* 4979–4987. doi:10.1021/ja01551a055
42. Laleu, B.; Herse, C.; Laursen, B. W.; Bernardinelli, G.; Lacour, J. *J. Org. Chem.* **2003,** *68,* 6304–6308. doi:10.1021/jo0345998
43. Drexhage, K. H. Structure and Properties of Laser Dyes. In *Dye Lasers;* Schäfer, F. P., Ed.; *Topics in Applied Physics*, Vol. 1; Springer: Berlin, Heidelberg, Germany, 1973; pp 144–193. doi:10.1007/978-3-662-11579-4_4
44. Griffiths, J. *Colour and Constitution of Organic Molecules;* Academic Press: London, 1976.
45. Sørensen, T. J.; Kilså, K.; Laursen, B. W. *Chem. – Eur. J.* **2015,** *21,* 8521–8529. doi:10.1002/chem.201500355
46. Sørensen, T. J.; Shi, D.; Laursen, B. W. *Chem. – Eur. J.* **2016,** *22,* 7046–7049. doi:10.1002/chem.201600496
47. Westerlund, F.; Elm, J.; Lykkebo, J.; Carlsson, N.; Thyrhaug, E.; Åkerman, B.; Sørensen, T. J.; Mikkelsen, K. V.; Laursen, B. W. *Photochem. Photobiol. Sci.* **2011,** *10,* 1963–1973. doi:10.1039/c1pp05253e
48. Lueck, H. B.; McHale, J. L.; Edwards, W. D. *J. Am. Chem. Soc.* **1992,** *114,* 2342–2348. doi:10.1021/ja00033a007
49. Lewis, L. M.; Indig, G. L. *Dyes Pigm.* **2000,** *46,* 145–154. doi:10.1016/s0143-7208(00)00049-8
50. Strickler, S. J.; Berg, R. A. *J. Chem. Phys.* **1962,** *37,* 814–822. doi:10.1063/1.1733166
51. Kotaskova, M.; Osman Oglou, O.; Helm, M. *Org. Biomol. Chem.* **2014,** *12,* 3816–3820. doi:10.1039/c4ob00533c

License and Terms

BEILSTEIN JOURNAL OF ORGANIC CHEMISTRY

Fluorescent phosphorus dendrimers excited by two photons: synthesis, two-photon absorption properties and biological uses

Anne-Marie Caminade[*1,2], Artem Zibarov[1,2], Eduardo Cueto Diaz[3], Aurélien Hameau[1,2], Maxime Klausen[3], Kathleen Moineau-Chane Ching[1,2], Jean-Pierre Majoral[1,2], Jean-Baptiste Verlhac[3], Olivier Mongin[4] and Mireille Blanchard-Desce[3]

Review

Open Access

Address:
[1]Laboratoire de Chimie de Coordination (LCC), CNRS, 205 Route de Narbonne, BP 44099, 31077 Toulouse Cedex 4, France, [2]LCC-CNRS, Université de Toulouse, CNRS, Toulouse, France, [3]Univ. Bordeaux, ISM (CNRS-UMR5255), Bat A12, 351 Cours de la Libération, 33400 Talence, France and [4]Univ. Rennes, CNRS, ISCR (Institut des Sciences Chimiques de Rennes), UMR 6226, F-35000 Rennes, France

Email:
Anne-Marie Caminade[*] - anne-marie.caminade@lcc-toulouse.fr

* Corresponding author

Keywords:
bioimaging; dendrimer; fluorescence; phosphorus; two-photon absorption

Beilstein J. Org. Chem. **2019,** *15,* 2287–2303.
doi:10.3762/bjoc.15.221

Received: 29 May 2019
Accepted: 15 August 2019
Published: 24 September 2019

This article is part of the thematic issue "Dyes in modern organic chemistry".

Guest Editor: H. Ihmels

Abstract

Different types of two-photon absorbing (TPA) fluorophores have been synthesized and specifically functionalized to be incorporated in the structure of phosphorus dendrimers (highly branched macromolecules). The TPA fluorophores were included in the periphery as terminal functions, in the core, or in the branches of the dendrimer structures, respectively. Also the functionalization in two compartments (core and surface, or branches and surface) was achieved. The consequences of the location of the fluorophores on the fluorescence and TPA properties have been studied. Several of these TPA fluorescent dendrimers have water-solubilizing functions as terminal groups, and fluorophores at the core or in the branches. They have been used as fluorescent tools in biology for different purposes, such as tracers for imaging blood vessels of living animals, for determining the phenotype of cells, for deciphering the mechanism of action of anticancer compounds, and for safer photodynamic therapy.

Introduction

Natural luminescence phenomena such as the bioluminescence of fireflies or of certain marine microorganisms, or the phosphorescence of certain minerals after being exposed to sun light, have fascinated Men for a long time. An important part of luminescence phenomena is due to the influence of light (generally visible or ultra-violet light) on matter, such as for instance a

molecule, which can emit light at a wavelength different from that absorbed. The classical Jablonski diagram (Figure 1, left part) represents electronic states of a molecule, and the transitions between these electronic states, depending on the energy. When a molecule absorbs light (a quantum of energy), it goes from a fundamental state (S_0) to an excited state (S_1). Depending on the type of molecules, two main ways can be taken to go back to the ground state: either a nonradiative decay of the energy absorbed, or the emission of fluorescence at a longer, less energetic wavelength. A third possibility (not shown in the Figure) concerns an intersystem conversion towards a triplet state (T_1), from which there will be emission of phosphorescence, having generally a lifetime longer than that of fluorescence. This classical one-photon excited fluorescence has led to the design of numerous types of chemical entities since the XIX century. For instance, fluorescein, which is a widely used fluorescent tracer for many applications, was synthesized for the first time in 1871 [1].

Besides this classical type of one-photon-induced fluorescence, a theoretical work by M. Göppert-Mayer in 1931 [2] predicted the possibility of the simultaneous absorption of two photons (of same or different energy), but this phenomenon was not observable until the advent of lasers. Two-photon excited (TPE) fluorescence is a third-order nonlinear optical process, which was first experimentally observed only in 1961 [3]. It provides intrinsic spatial selectivity in three dimensions, and can be induced at a frequency of half the actual energy gap, thus at longer wavelengths (typically 700–1300 nm), but the fluorescence generally occurs at the same wavelength than when excited with one photon, as illustrated in Figure 1 (right part). These properties have induced widespread popularity of TPE (also named TPA, for two-photon absorption) in the biology community, with on one side, the advent of two-photon excitation fluorescence microscopy [4], even for research clinical uses [5], and on the other side with the discovery of the TPA properties of quantum dots (inorganic nanocrystals [6]), widely used for imaging live cells, for in vivo imaging and diagnostics [7]. Even if the properties of quantum dots have been compared with those of classical organic fluorophores [8], organic fluorophores having giant TPA properties are far less common [9], although there are noticeable exceptions [10] for specifically engineered fluorophores [11]. The main reason is that a single organic fluorophore having TPA properties cannot be as brilliant as a quantum dot, mostly based on its smaller size (or number of delocalized electrons).

In view of this problem of brilliance, came the idea to gather several organic fluorophores (having TPA properties) in a single molecule. Dendrimers are highly branched macromolecules, which possess many properties [12] due, in particular, to a large number of terminal functions, easily modifiable. A schematized structure of a dendrimer is depicted in Figure 2, showing in particular the generations, i.e., the number of layers, both for the full structure, and for a linear representation of the same dendrimer, which will be mainly used in this review.

Many different types of fluorescent dendrimers (with hundreds of publications), having one or several classical fluorophores in their structure, have been already synthesized [13]. Besides,

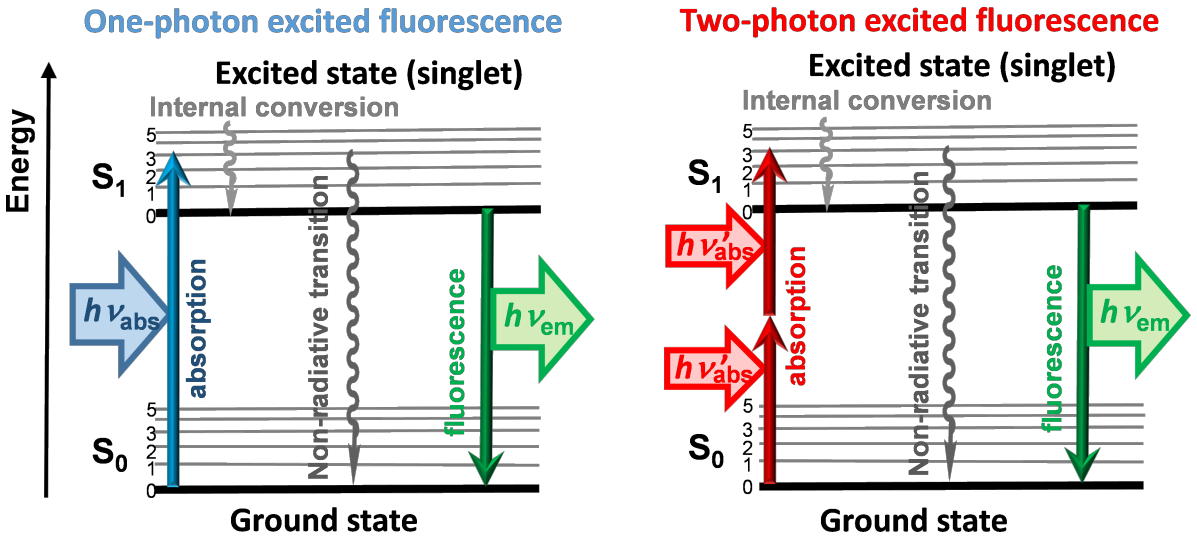

Figure 1: Jablonski-type diagram displaying the classical one-photon excited fluorescence (left), and the less-classical two-photon excited fluorescence (right).

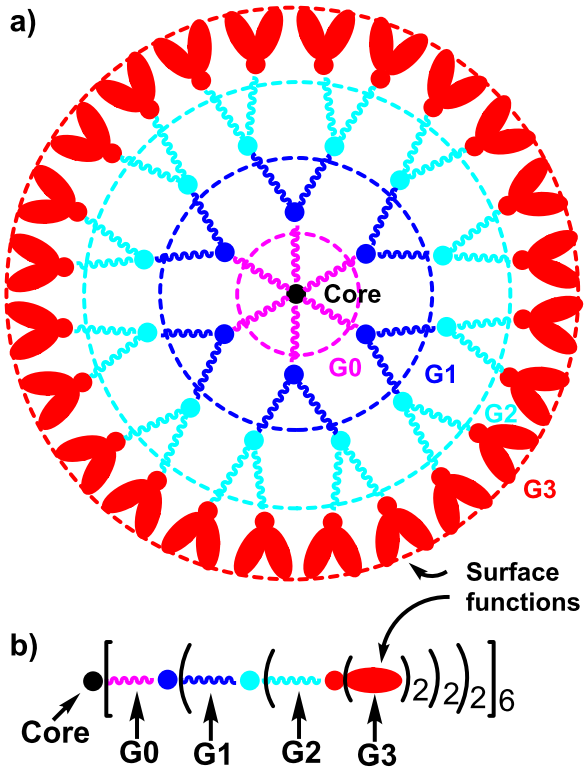

Figure 2: Two ways to represent schematized structures of dendrimers, showing the different generations (layers); a) full structure; b) linear structure with parentheses at each generation; multiplying the numbers associated with the parentheses gives the number of terminal functions (48 in the case of the third generation).

some types of dendrimers have shown non-traditional intrinsic luminescence, i.e., luminescence in the absence of known fluorophores [14]. Dendrimers functionalized with fluorophores having two-photon absorption properties have been synthesized far less frequently than those bearing classical fluorophores, even if the first examples were proposed in 2000 [15] and 2001 [16]. Among them, conjugated fluorescent dendrimers have been shown to lead to large TPA responses, with coherent coupling contributing to cooperative enhancement of TPA responses [17-21]. Phosphorus-containing dendrimers [22], mainly of the phosphorhydrazone type [23], stand out among all the other types of dendrimers by their properties [24], in particular in biology [25,26] and their highly modular structure [27]. Indeed, different types of modifications, on the terminal functions [28,29], at the core [30] or linked to the core [31], and in the branches [32] have been achieved. In this review, we will gather the syntheses, fluorescence properties, and some biological properties of phosphorhydrazone dendrimers bearing in some part of their structure organic fluorophores especially engineered to demonstrate TPA properties and maintain fluorescence upon confinement within the dendrimeric backbone. The presentation will be organized depending on the location of the fluorophores, either as terminal functions, at the core, in the branches, or at two different locations in the structure of the dendrimers, and will report at the end the biological properties.

Review

The synthesis of phosphorhydrazone dendrimers necessitates two steps to build one generation. Starting from a core having P–Cl functions, such as the hexachlorocyclotriphosphazene $N_3P_3Cl_6$ [33], the first step is the nucleophilic substitution with 4-hydroxybenzaldehyde in basic conditions. The second step comprises the condensation reaction of the aldehyde terminal functions with the phosphorhydrazide $H_2NNMeP(S)Cl_2$. This reaction affords the first generation (G1) dendrimer, having 12 P–Cl functions, whereas the core had only 6 P–Cl functions. Starting from this first generation, the two-step process can be repeated, as was done from the core, and the second generation is obtained (Scheme 1). The repetition of this two-step process has been carried out up to the eighth generation from the $N_3P_3Cl_6$ core [34], and up to the twelfth generation from the $(S)PCl_3$ core [35]. Thus, to incorporate the TPA fluorophores on the surface, it should have one function being able to react with P–Cl (or aldehyde) functions. For the incorporation of a TPA fluorophore at the core, it should have two identical functions able to react with two $N_3P_3Cl_6$. To incorporate TPA fluorophores in the branches, these should have two different functions, one able to react with P–Cl functions, the other one being able to react with the NH_2 group of the phosphorhydrazide, i.e., to replace 4-hydroxybenzaldehyde.

TPA fluorophores on the surface of dendrimers

The easiest way to modify the $P(S)Cl_2$ terminal functions of the phosphorhydrazone dendrimers consists in using phenols [36], and all the TPA fluorophores on the surface of dendrimers were linked in this way. The very first example of phosphorhydrazone dendrimers functionalized with TPA fluorophores used a blue-emitting quadrupolar fluorophore based on a fluorene core [37-41] and functionalized by a phenol on one side. The synthesis was carried out from generation 1 (12 fluorophores) to generation 4 (96 fluorophores) (Scheme 2). The measurement of the two-photon absorption cross-section, which is a marker of the efficiency of the TPA, displayed a linear increase with the number of fluorophores (Table 1), indicative of an additive behavior. In contrast, the fluorescence properties are only weakly affected. In particular, fluorescence quenching is prevented thanks to the design of the fluorophore [42]. It should be noted that the largest dendrimers, in particular generation 4, display very large two-photon absorption cross-sections (σ_2 up to 55,900 GM), which are comparable to those measured for the best quantum dots [43]. Thus these “organic nanodots” are fluo-

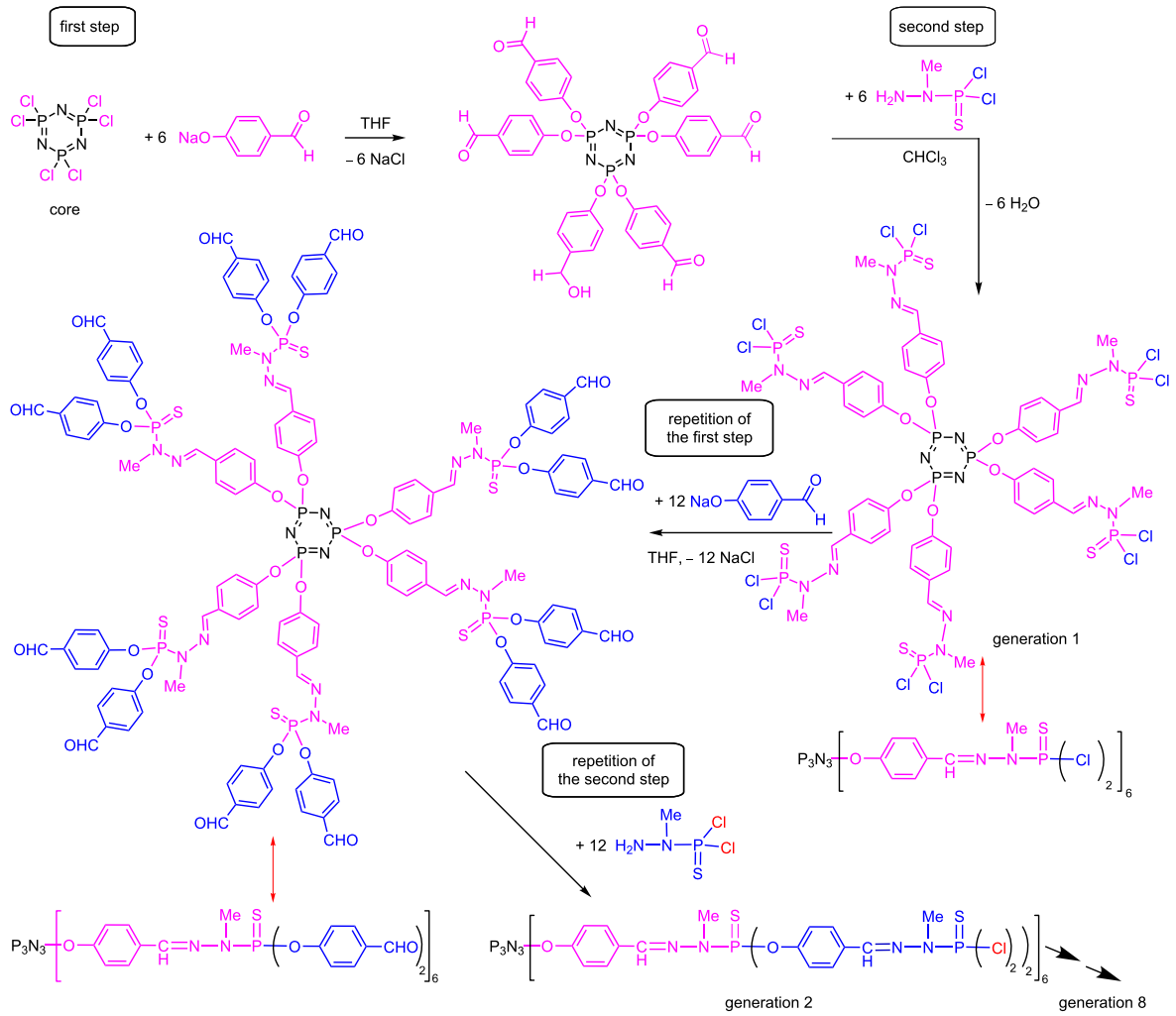

Scheme 1: Synthesis of phosphorhydrazone dendrimers, from the core to generation 2. Generation 1 dendrimers with $P(S)Cl_2$ or aldehyde terminal functions are represented both as the full structure and in the linear form with parentheses.

Table 1: Photophysical properties of the types of dendrimers shown in Scheme 2 (measured in toluene).

generation	monomer	1	2	3	4
number of fluorophores	1	12	24	48	96
$\lambda_{abs,max}$/nm	386	385	386	386	386
$\lambda_{em,max}$/nm	420	423	426	441	445
Φ_f	0.83	0.75	0.71	0.62	0.48
$\lambda_{TPA,max}$/nm	702	701	701	701	705
σ_2^{max} at $\lambda_{TPA,max}$/GM[a]	765	8,880	17,700	29,800	55,900

[a]GM for Göppert-Mayer, 1 GM = 10^{-50} cm^4 s $photon^{-1}$.

rescent markers competitive and complementary to quantum dots. This work allowed access to a variety of dendrimers with different emissive colors, by tuning the structure of the quadrupolar fluorophores grafted [44], and not depending on the size, contrarily to quantum dots.

Besides the blue-emitting TPA fluorophore shown in Scheme 2, a related green-emitting fluorophore functionalized by a phenol has been synthesized and grafted to the surface of the second generation dendrimer (Figure 3). A very high TPA cross-section of 35,000 GM was obtained at 740 nm for this dendrimer bear-

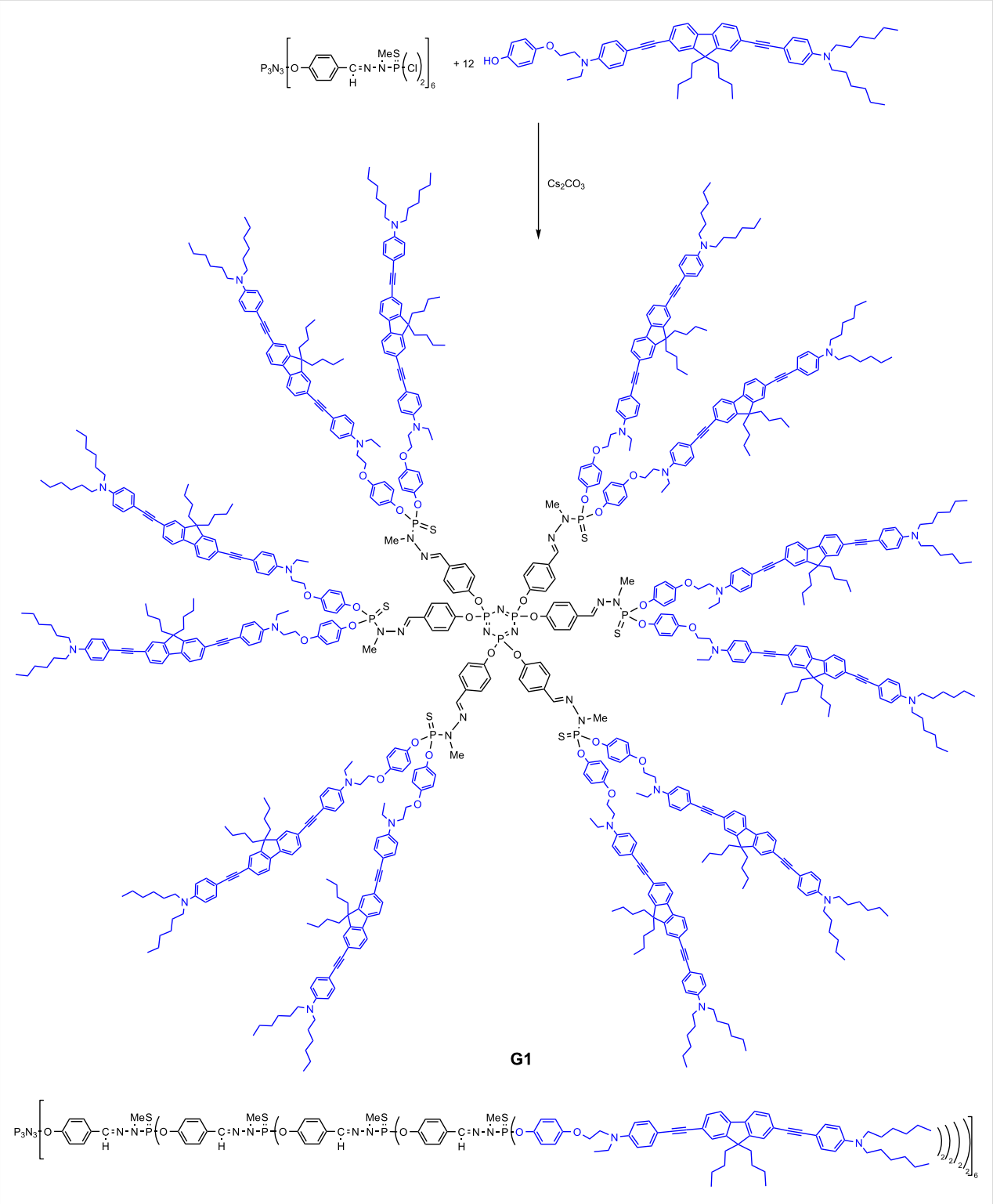

Scheme 2: Full structure of the generation 1 dendrimer bearing 12 blue-emitting TPA fluorophores on the surface, and linear structure of the generation 4 dendrimer bearing 96 TPA fluorophores on the surface.

ing 24 fluorophores, compared to 1,400 GM for the corresponding monomer and 780 GM for the quantum dot QD518 (CdSe) [45].

In both previous cases, an essential additive effect was observed, depending on the number of fluorophores grafted to the dendrimers. However, an influence of the structure of the

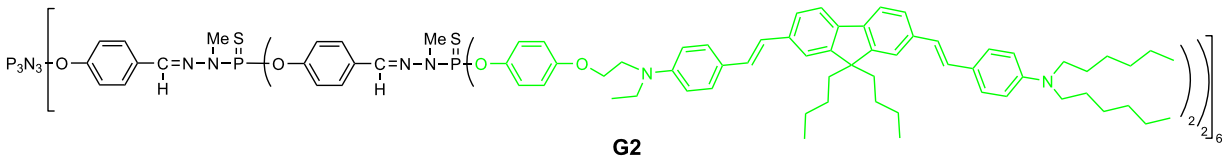

Figure 3: Linear structure of the generation 2 dendrimer bearing 24 green-emitting TPA fluorophores on the surface.

dendrimer can be observed in some cases, this effect being either positive or negative. Such effect is named the "dendritic (or dendrimer) effect", and is frequently observed for catalytic dendrimers, but also for some bioactive dendrimers [46].

A negative dendrimer effect has been observed for dioxaborine derivatives grafted on the surface of phosphorhydrazone dendrimers. In this case, a β-diketone functionalized by a phenol was first grafted on the surface of the dendrimer [47], then BF_3 was added to obtain the dioxaborines (Scheme 3). Monomer, dimer, and all generations of the dendrimer from zero (6 terminal groups) to four (96 terminal groups) have been synthesized. Dioxaborine derivatives are known as highly fluorescent tracers [48], and also as two-photon probes [49]. Deceptively, the fluorescence of the dendritic dioxaborines is quenched and dramatically decreased compared to the emission of the isolated monomeric fluorophore, presumably due to interactions between the terminal groups of the dendrimers [50].

However, interaction between the terminal groups could be beneficial in some particular cases. Indeed, a cooperative two-photon absorption enhancement has been observed in multichromophoric compounds, thanks to through-space interactions. Modelling suggested that changing the relative orientation/distance of the chromophores would allow cooperative TPA enhancement to be achieved [51]. Thus, multistilbazole molecular structures of different topologies and number of dipolar chromophores, including small dendrimers have been designed to study this possibility. All multichromophoric compounds performed better than the model chromophore. An amplification factor of up to 2.5 per chromophoric subunit was obtained for the $\sigma_2{}^{max}/\varepsilon^{max}$ response (Figure 4). Interestingly, the response of the dimers increases from the *para*- to the *meta*-position of the stilbazole units, and analogously, the second-generation dendrimer G2 leads to a higher ratio than the first-generation dendrimer, which corresponds in both cases to an increasing proximity of the chromophoric subunits [52].

A second series of compounds concerned derivatives of Nile Red functionalized by a phenol, also grafted to the first and second generation dendrimers (Figure 5). An enhancement of the TPA responses per chromophoric units was observed, but it is less pronounced than for the previous series. Indeed, an increase of TPA of only 20% is obtained for the dimer and 33% for the G1 dendrimer, but a 15% decrease of the TPA response was measured for the G2 dendrimer [53]. In addition, in that case, also the fluorescence quantum yield was found to decrease dramatically with an increasing number of fluorophores.

TPA fluorophore as core of dendrimers

None of the previous examples of dendrimers bearing as terminal functions compounds having TPA properties is soluble in water, and thus they cannot be used for biological purposes. Furthermore, many fluorophores are sensitive to the presence of water, which induces in many cases a quenching of the fluorescence [54]. Thus, it could be interesting to use the dendritic structure, which is relatively hydrophobic in the case of phosphorhydrazone dendrimers, to protect the fluorophore, and thus to use the fluorophore as core of the dendrimers. To increase the protective effect, a symmetrical TPA fluorophore functio-

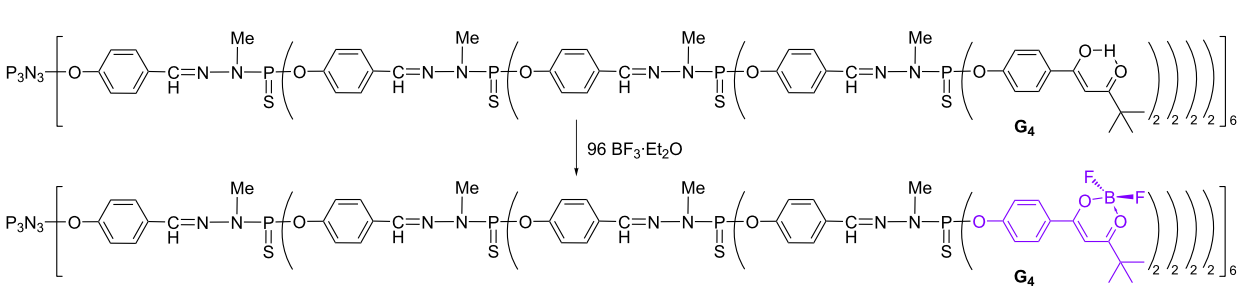

Scheme 3: Synthesis of the dioxaborine-functionalized dendrimer of generation 4.

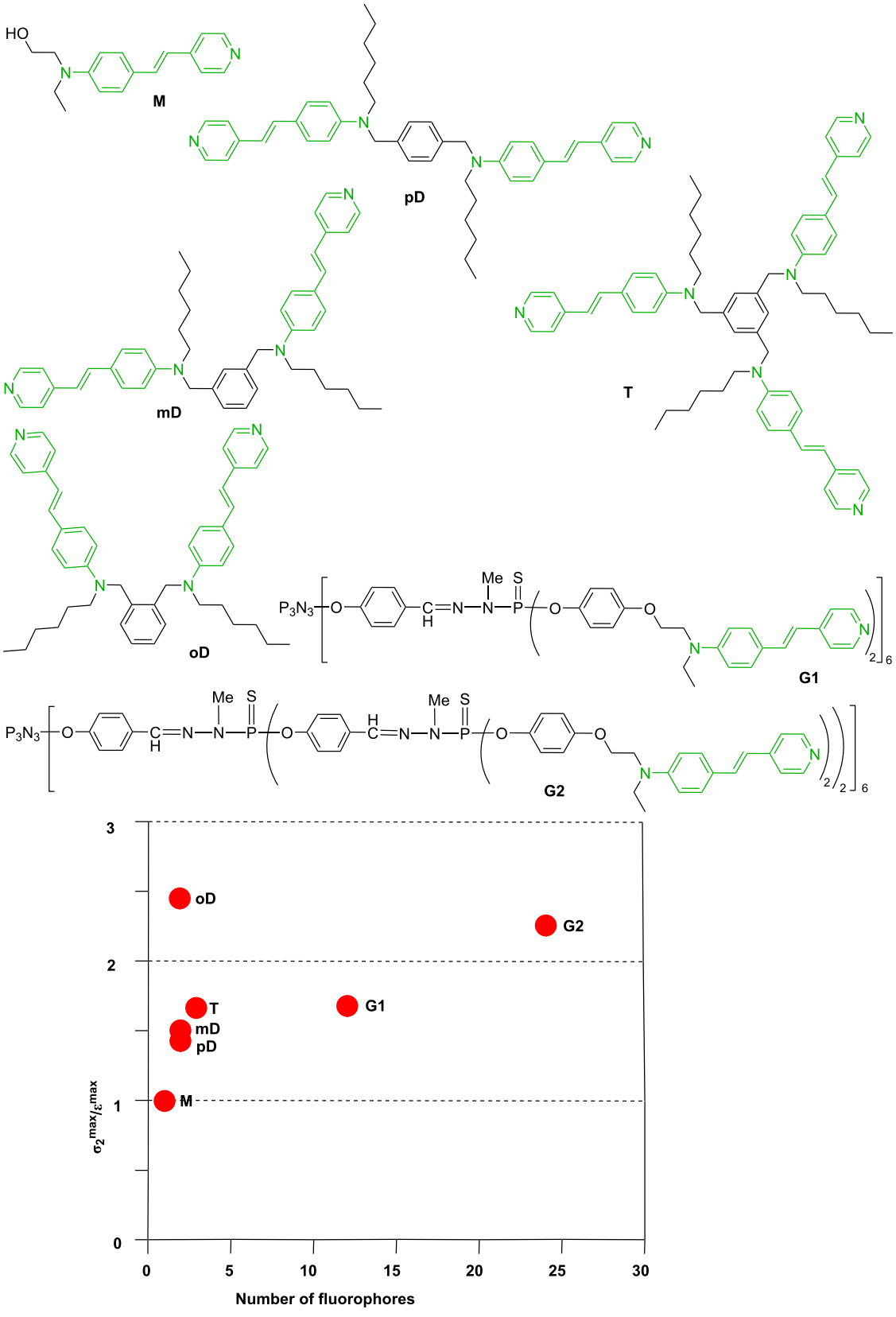

Figure 4: Diverse structures of multistilbazole compounds, and graph of the $\sigma_2^{max}/\varepsilon^{max}$ response, depending on the number of fluorophores.

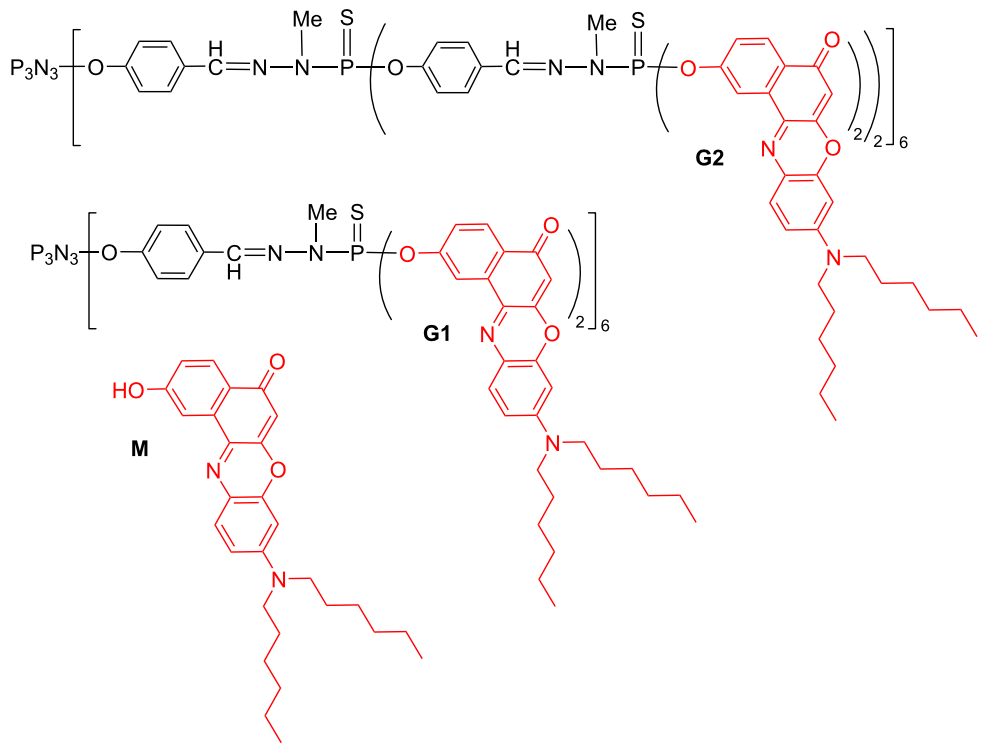

Figure 5: Nile Red derivatives: monomer (M) and two generations of dendrimers.

nalized by two phenols was reacted with two equivalents of $N_3P_3Cl_6$, to afford a core from which 10 branches emanate, instead of 6 as in the previous cases. The growing of the branches was carried out as outlined in Scheme 1, and diethylethylene diamine was grafted in the last step, to ensure the solubility in water [55] of the "dumbbell-like" dendritic structure (Scheme 4). Measurement of the TPA properties showed that the monomeric fluorophore displayed much lower

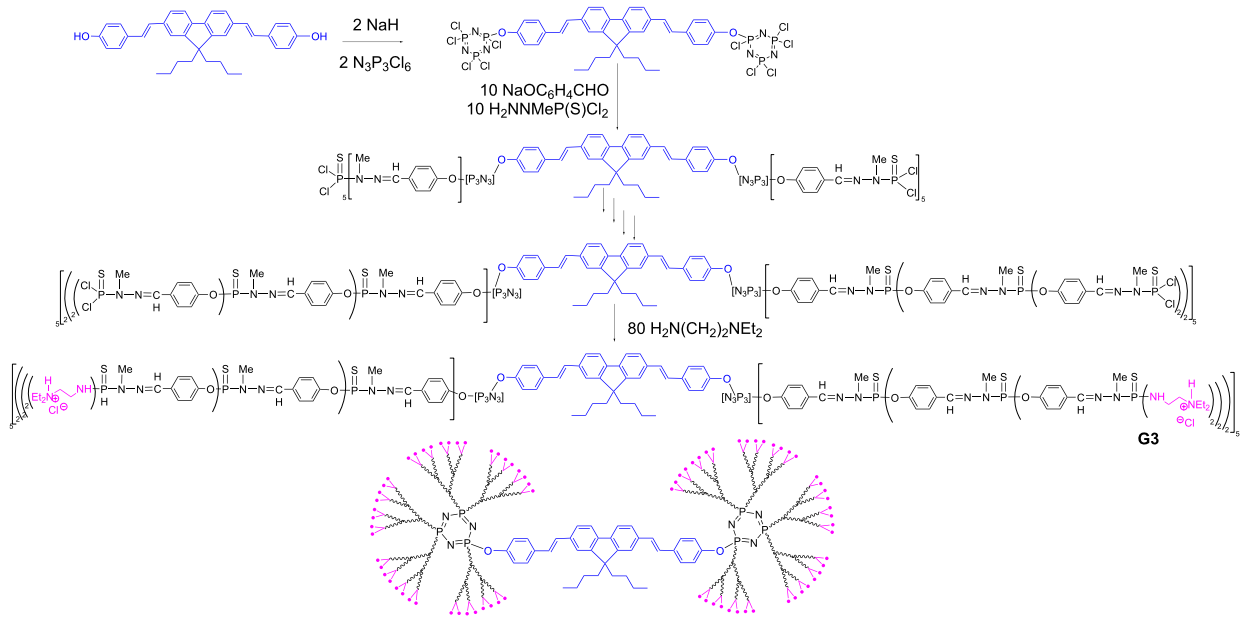

Scheme 4: Dumbbell-like dendrimers (third generation) having one TPA fluorophore at the core, and ammonium terminal functions.

TPA properties in water (σ_2 = 8 GM, to be compared with 155 GM in ethanol). On the contrary, the fluorophore included as core in all the water-soluble dumbbell-like dendrimers retains a similar TPA response as that of the model monomer in ethanol, as shown by σ_2 values of 104 GM for G1, 119 for G2, and 127 for G3, in water [56].

The same type of synthetic method was applied to another TPA fluorophore functionalized by two phenols, but having a longer linker between the fluorophore and the phenol (Scheme 5). Studies of both the dumbbell-like dendrimers of this new series with $P(S)Cl_2$ and ammonium terminal functions revealed that the branches are less protective towards the solvents than in the previous case. Indeed, the type of solvent has a large influence on the λ_{max} of the fluorescence for the dendrimer with $P(S)Cl_2$ terminal functions, which ranges from 443 nm in AcOEt to 501 nm in DMSO. Furthermore, the quantum yield (Φ_f) of the dendrimer with ammonium terminal groups was 0.42 in DMSO (to be compared with 0.78 for the corresponding fluorescent monomer of the core), and only 0.075 in water. On the contrary, the TPA response of the fluorophore at the core of the dendrimer is not much affected by the presence of water. Indeed, the TPA response of this dendrimer in water, in the NIR range (700–980 nm) is comparable to that of the corresponding monomeric fluorophore in DMSO [57]. This further confirms that the dendritic architecture provides an "organic-like" environment which preserves the TPA response. Yet, the difference in the structure of the core fluorophore promotes processes which significantly diminish the fluorescence of this dendrimer in water.

TPA fluorophores in the branches of dendrimers

Integrating TPA fluorophores as elements of the internal branches of dendrimers has two advantages, compared to the previous cases: i) the possibility to have water-solubilizing functions as terminal functions, suitable for biological uses (as in the case of TPA fluorophore as core), and ii) a relatively large number of TPA fluorophores included in the structure, which should increase the brilliance, as in the case of TPA fluorophores on the surface. However, there is also an inconvenience, which is the necessity to equip the fluorophore with two different functions, both being compatible with the synthetic process of the dendrimers. In the case of phosphorhydrazone dendrimers, the choice consisted in replacing 4-hydroxybenzaldehyde at one layer of the internal structure by a TPA fluorophore having a phenol on one side and a benzaldehyde on the other side. A detailed synthetic process for one of these bifunctionalized fluorophores is illustrated in Scheme 6. It is a multistep process, as 12 steps are needed to get this highly sophisticated fluorophore [58].

In general, the fluorophores are incorporated at the level of the first generation of the dendrimers. Twelve green-emitting TPA fluorophores were grafted, then reaction with the phosphorhydrazide $H_2NNMeP(S)Cl_2$ afforded the second generation of the dendrimer, with 12 $P(S)Cl_2$ terminal functions. These functions were modified in different ways to induce the solubility in water. In one case, phenol PEG (poly(ethylene glycol) was grafted together with pyridine imine phenol, affording dendrimers stochastically functionalized on the surface, but all having precisely 12 fluorophores in the internal structure [59]. Another way to induce solubility in water consists in having positively charged terminal functions [60], in particular ammonium groups. Thus, diethylethylenediamine was directly grafted to the $P(S)Cl_2$ terminal functions [61] (Scheme 7). The photophysical properties, in particular the TPA response of these dendrimers having green TPA fluorophores in the branches have not been determined yet; they have been synthesized for biological purposes that will be explained later.

The same type of synthetic process has been applied to another type of bifunctionalized fluorophore and the dendrimer was also functionalized with water-solubilizing functions. In the first case the synthesis was carried out up to the second generation, then 24 phenol-PEG were grafted. In the second case, the synthesis was carried out up to the third generation, which was functionalized with 48 ammonium groups (Figure 6). Photophysical studies of both compounds indicated that the fluorophores are more protected by the PEG groups of the second

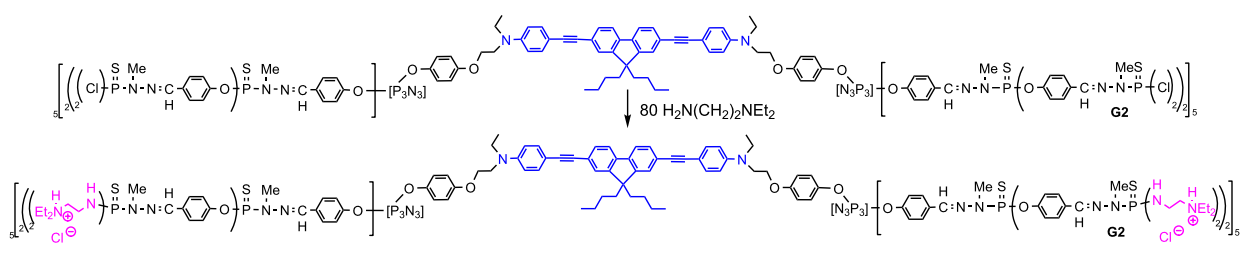

Scheme 5: Another example of dumbbell-like dendrimers having one TPA fluorophore at the core, and $P(S)Cl_2$ or ammonium terminal functions.

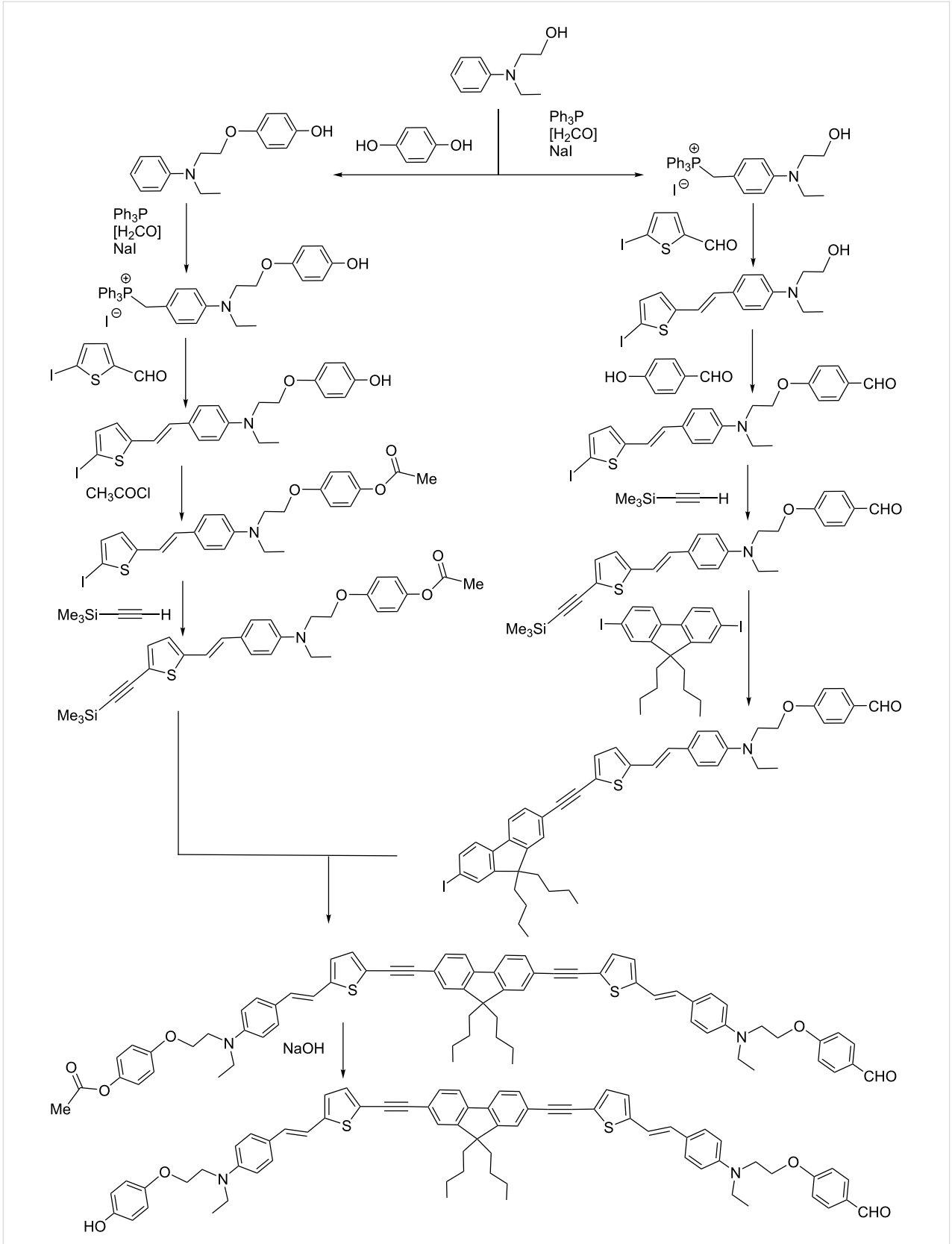

Scheme 6: The 12 steps needed to synthesize a sophisticated TPA fluorophore, to be used as branches of dendrimers, in replacement of hydroxybenzaldehyde.

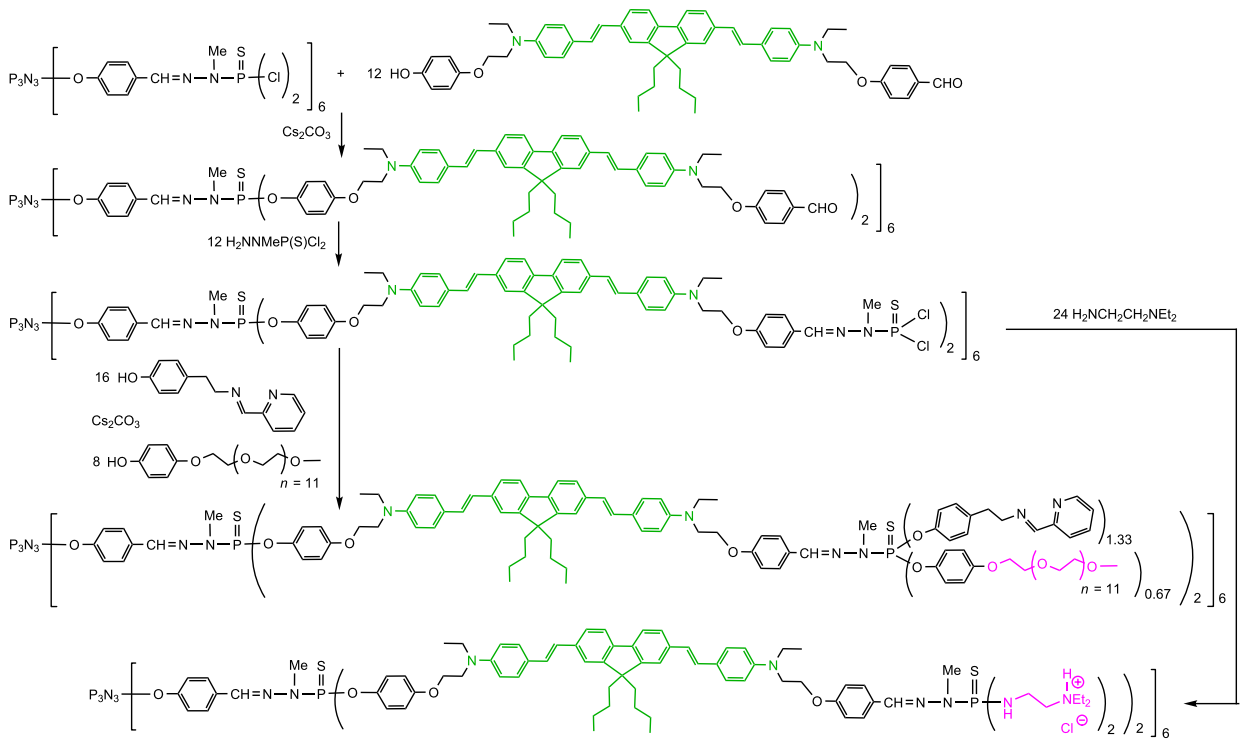

Scheme 7: Synthesis of dendrimers having TPA fluorophores as branches and water-solubilizing functions on the surface.

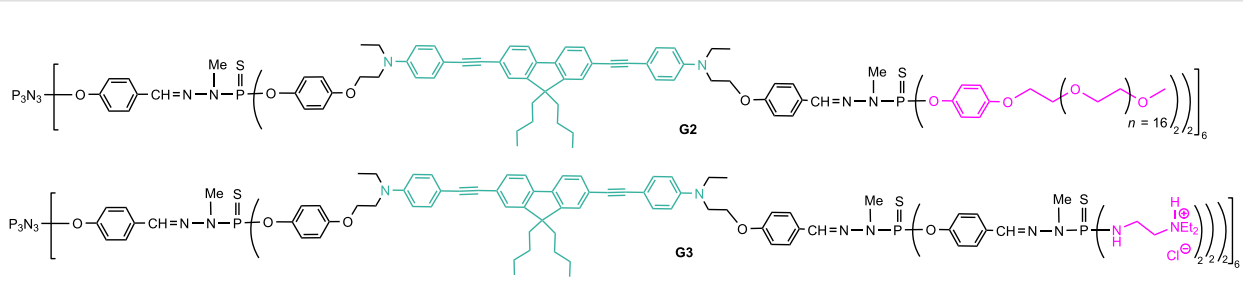

Figure 6: Other types of dendrimers having TPA fluorophores as branches and water-solubilizing functions on the surface.

generation G2 than by the ammonium groups of the third generation G3 as indicated by the quantum yields Φ_f = 0.24 (G3 ammonium) and 0.39 (G2 PEG). However, the TPA cross-section measurements gave σ_2^{max} = 13,600 GM for G3 ammonium, and 8,400 GM for G2 PEG. Thus, both compounds exhibit similar performances, the lower quantum yield being counter-balanced by a higher TPA cross-section, and vice versa [45].

TPA fluorophores at two levels of the dendrimer's structure

Having in hand the methods to introduce TPA fluorophores either on the surface, at the core, or in the branches of the dendrimers, it seems possible to have them at two different levels, for instance the core and the surface, or at the branches and the surface.

In the first example, the core used in Scheme 4 and the terminal functions shown in Scheme 2 were incorporated in dendrimers of different generations (0, 1, and 2), to detect the influence of the distance between the two types of fluorophores and also of a different geometry compared to the symmetrical dendrimers, on their properties (Figure 7). The structure of the dumbbell-like dendrimers has a detrimental influence on the quantum yield, when compared with the symmetrical dendrimers having almost the same number of fluorophores (Table 2). However, the G2 dumbbell-like dendrimer

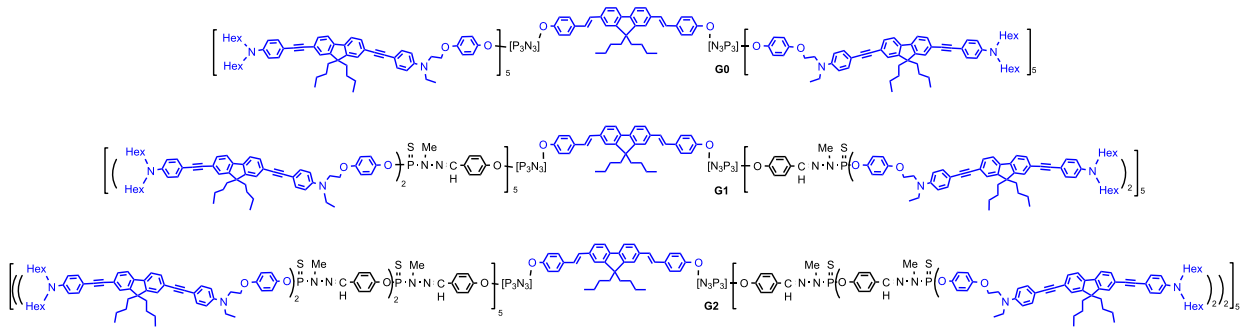

Figure 7: Generations 0, 1, and 2 of dumbbell-like dendrimers having one fluorophore at the core and either 10, 20 or 40 fluorophores on the surface.

Table 2: Comparison of the photophysical properties (in toluene) of the spherical dendrimers shown in Scheme 2, with that of the dumbbell-like dendrimers shown in Figure 7.

generation	0	1	1	2	2	3
structure	dumbbell-like	spherical	dumbbell-like	spherical	dumbbell-like	spherical
number of fluorophores	11	12	21	24	41	48
$\lambda_{abs,max}$/nm	382	385	382	385	384	386
$\lambda_{em,max}$/nm	443	423	444	426	445	441
Φ_f	0.44	0.75	0.11	0.71	0.26	0.62
σ_2^{max} (GM)	7,100	8,800	14,300	17,700	32,800	29,800

(41 fluorophores) has a higher TPA cross-section than the spherical dendrimer G3 (48 fluorophores). This change might be attributed to changes in the topology, relative orientation, and packing of the fluorophores [62].

Another example of fluorophores at two levels concerned the branches and the surface, as depicted in Figure 8. The fluorophore of the branches is the one shown in Figure 6, and the fluorophore of the surface is the one shown in Scheme 2 and Figure 7. This double layer dendrimer, having 18 (6 + 12) fluorophores in its structure, has a TPA cross-section (8,500 GM), which is comparable with that of the first generation dendrimer having only 12 fluorophores on the surface (8,880 GM). It appears that the higher degree of confinement in the double layer dendrimer has a detrimental influence on the TPA properties [63].

Biological properties of dendrimers having TPA properties

Most of the water-soluble fluorescent dendrimers shown in the previous paragraphs have been synthesized for diverse biological purposes. The first type of use concerned in vivo imaging with some of the dumbbell-like dendrimers. The second generation of the dendrimer shown in Figure 9 was injected to a rat and the two-photon imaging of the vessels of the living rat olfactory bulb could be obtained [56]. The other dumbbell-like dendrimer shown in Scheme 5 was used for imaging in 3D the blood vessels of the tail of a living Xenopus tadpole [63].

The dendrimer bearing ammonium terminal functions shown in Scheme 7 has been used as fluorescent marker for bone marrow-derived macrophages. It also allowed to determine the phenotype status of these macrophages at different time points

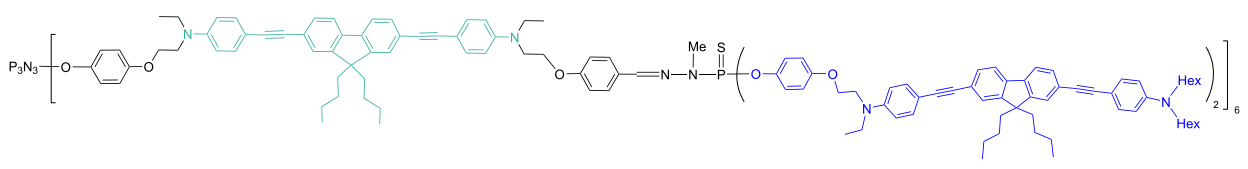

Figure 8: Double layer fluorescent dendrimer.

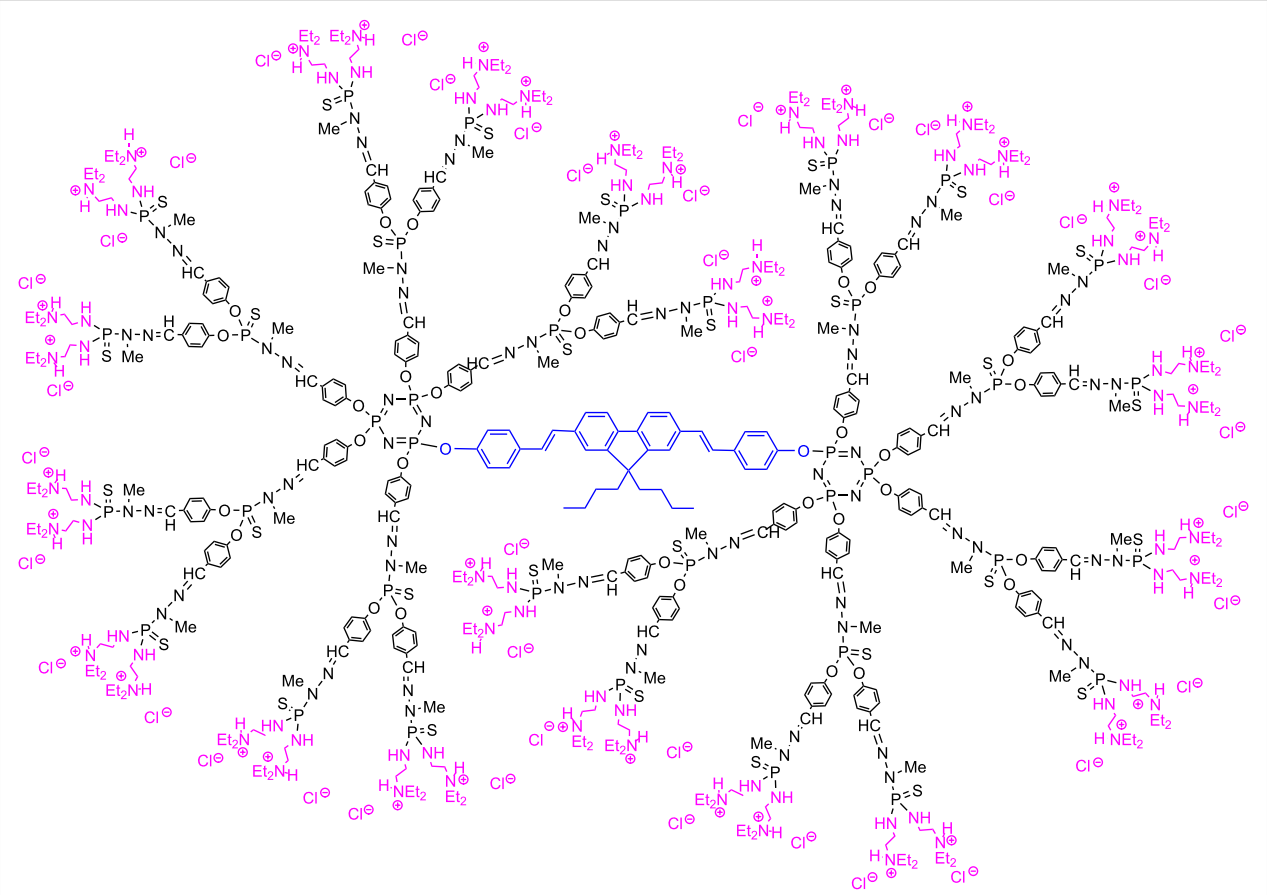

Figure 9: Dumbbell-like dendrimer used for two-photon imaging of the blood vessels of a living rat olfactory bulb.

after spinal cord injury. This dendrimer has potential uses as a drug/siRNA carrier and phenotype-specific cell tracer, i.e., for enhanced cell therapies combined with monitoring of cell fate and function [61].

Dendrimers with pyridine imine terminal functions and their copper complexes have an interesting antiproliferative capacity towards a range of human cancer cell lines, inducing early apoptosis, followed by secondary necrosis [64]. The fluorescent analog having pyridine imine and PEG terminal functions shown in Scheme 7 has been synthesized with the aim of deciphering the mechanism of action of these dendrimers, in particular for monitoring the intracellular penetration. This fluorescent dendrimer avidly binds to the cell membrane during the first 10 min of exposure and after 24 h, it has penetrated the cell, probably by endocytosis, and went in the intracellular space in a high proportion [59]. Besides the copper complexes, the gold complexes of these dendrimers display higher antiproliferative activities, in particular against both KB and HL-60 tumor cell lines (oral epidermoid carcinoma and human leukaemia, respectively), showing IC_{50}s (the quantity of a compound necessary to kill 50% of the cells) in the low nanomolar range. The corresponding fluorescent gold complex (Figure 10), keeps in a high level the anti-proliferative activities against KB and HL60: IC_{50}s of 60−70 nM and 40−50 nM against KB and HL60, respectively [65]. In these cases, the fluorescence of the

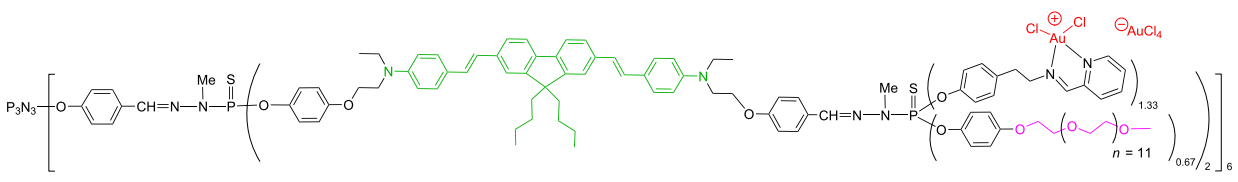

Figure 10: Fluorescent gold complex having high antiproliferative activities against different tumor cell lines.

dendrimer was not induced by TPA but classically by one photon.

The last example of biological uses concerns a second generation dendrimer built with the fluorophore shown in Scheme 6 at the level of the first generation and having triethylene glycol chains as terminal functions (Figure 11). This dendrimer retains some fluorescence as well as very high TPA cross-sections in a broad range of the NIR (near infra-red) biological spectral window. Furthermore, it displays significant singlet oxygen production, thus this dendrimer combines unique properties for bioimaging and anticancer therapy. Indeed, photodynamic therapy is used in oncology for the treatment of certain types of tumors. It is based on the activation by light of photosensitizers, able to generate singlet oxygen and/or other reactive oxygen species (ROS), to induce the destruction of the targeted tissues [66]. The dendrimer shown in Figure 11 was tested in vitro on human breast cancer cells MCF-7. One-photon absorption induced fluorescence demonstrated that this dendrimer is efficiently internalized after 3 h of incubation, more after 24 h, and was non-toxic at 50 μg mL^{-1} without irradiation. Two-photon irradiation was performed with a confocal microscope; cells were irradiated at 760 nm (in the near IR) by three scans of 1.57 s each at an average power of 80 mW. The percentage of living cells was determined two days after irradiation. 78% cell death was obtained under two-photon irradiation of MCF-7 cells incubated with this dendrimer. It was verified that no cell death was observed in similar irradiation conditions in the absence of the dendrimers, thus revealing the photosensitizing activity of this dendrimer. Importantly, no cell death was observed when the cells were exposed to daylight for 4 h, indicating that this dendrimer is non-toxic under daylight illumination conditions, while promoting cell death upon suitable two-photon irradiation in the NIR [58]. Thus, this dendrimer overcomes one of the common drawbacks of photodynamic therapy medical treatment, which requires patients to avoid daylight after photosensitizer injection.

Conclusion

The modularity of the synthesis of phosphorhydrazone dendrimers enables the incorporation of TPA fluorophores everywhere in their structure. Classically, the TPA fluorophores can be used as terminal functions of the dendrimers. Less classically, they can be used as core of the dendrimers, leading to dumbbell-like dendrimers, or be incorporated in the branches of the dendrimers. Playing with the specific functionalization of the TPA fluorophores enabled the synthesis of dendrimers having TPA fluorophores at two levels, such as core and surface, or branches and surface (Figure 12). Studies of the TPA properties demonstrated that some of these dendrimers outperform the TPA cross-section response of quantum dots, while having a much lower intrinsic toxicity, as being composed or organic matter instead of heavy metals. The grafting of water-solubilizing functions on the surface of the dendrimers incorporating TPA fluorophores inside their struc-

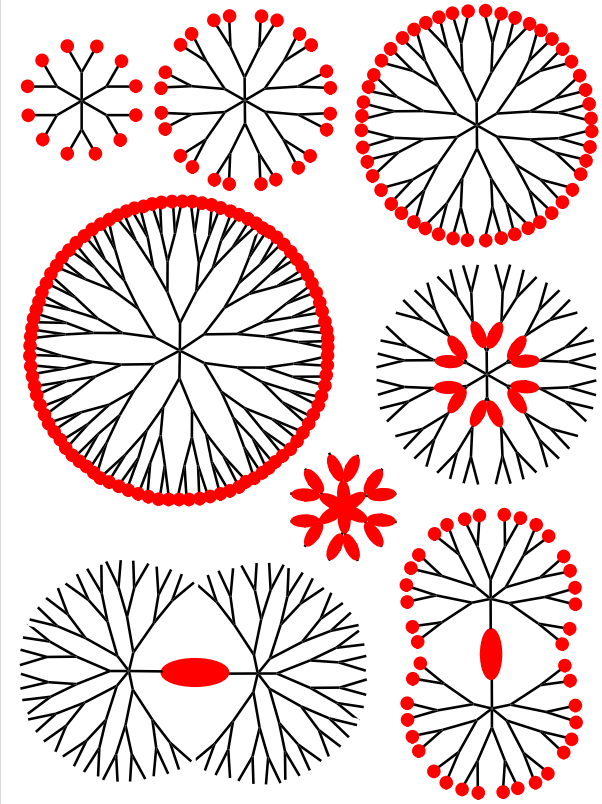

Figure 12: Schematization of the different types of TPA fluorescent phosphorus dendrimers and dendritic structures that have been already synthesized.

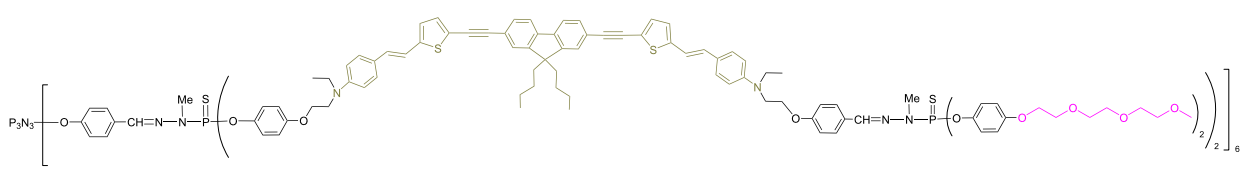

Figure 11: A fluorescent water-soluble dendrimer, applicable for two-photon photodynamic therapy and imaging.

ture has led to interesting properties in biology. Indeed, some of these dendrimers have been used in vivo as tracers for imaging blood vessels of rats and tadpoles, others have been used for determining phenotype of cells, for deciphering mechanism of action of anticancer compounds, and recently for safer photodynamic therapy.

In view of the results already obtained, there is no doubt that other biological properties of these fully organic "nanodots" can be foreseen, thanks to their low toxicity, large color modularity, and high TPA response.

Acknowledgements

We thank the ANR-2017 SLOW2 for financial support, and for a grant to AZ and MK. Part of this work has been supported by a funding from the European Community's Seventh Framework Program under TOPBIO project-grant agreement no. 264362. We also thank the CNRS.

ORCID® iDs

Anne-Marie Caminade - https://orcid.org/0000-0001-8487-3578
Artem Zibarov - https://orcid.org/0000-0002-2837-3728
Kathleen Moineau-Chane Ching - https://orcid.org/0000-0001-9478-347X
Jean-Pierre Majoral - https://orcid.org/0000-0002-0971-817X
Olivier Mongin - https://orcid.org/0000-0002-7743-9623
Mireille Blanchard-Desce - https://orcid.org/0000-0002-1572-9545

References

1. Baeyer, A. *Ber. Dtsch. Chem. Ges.* **1871,** *4,* 555–558. doi:10.1002/cber.18710040209
2. Göppert-Mayer, M. *Ann. Phys. (Berlin, Ger.)* **1931,** *401,* 273–294. doi:10.1002/andp.19314010303
3. Kaiser, W.; Garrett, C. G. B. *Phys. Rev. Lett.* **1961,** *7,* 229–231. doi:10.1103/physrevlett.7.229
4. Oheim, M.; Michael, D. J.; Geisbauer, M.; Madsen, D.; Chow, R. H. *Adv. Drug Delivery Rev.* **2006,** *58,* 788–808. doi:10.1016/j.addr.2006.07.005
5. Perry, S. W.; Burke, R. M.; Brown, E. B. *Ann. Biomed. Eng.* **2012,** *40,* 277–291. doi:10.1007/s10439-012-0512-9
6. Xu, G.; Zeng, S.; Zhang, B.; Swihart, M. T.; Yong, K.-T.; Prasad, P. N. *Chem. Rev.* **2016,** *116,* 12234–12327. doi:10.1021/acs.chemrev.6b00290
7. Michalet, X.; Pinaud, F. F.; Bentolila, L. A.; Tsay, J. M.; Doose, S.; Li, J. J.; Sundaresan, G.; Wu, A. M.; Gambhir, S. S.; Weiss, S. *Science* **2005,** *307,* 538–544. doi:10.1126/science.1104274
8. Resch-Genger, U.; Grabolle, M.; Cavaliere-Jaricot, S.; Nitschke, R.; Nann, T. *Nat. Methods* **2008,** *5,* 763–775. doi:10.1038/nmeth.1248
9. Kim, H. M.; Cho, B. R. *Chem. Rev.* **2015,** *115,* 5014–5055. doi:10.1021/cr5004425
10. Terenziani, F.; Katan, C.; Badaeva, E.; Tretiak, S.; Blanchard-Desce, M. *Adv. Mater. (Weinheim, Ger.)* **2008,** *20,* 4641–4678. doi:10.1002/adma.200800402
11. Pawlicki, M.; Collins, H. A.; Denning, R. G.; Anderson, H. L. *Angew. Chem., Int. Ed.* **2009,** *48,* 3244–3266. doi:10.1002/anie.200805257
12. Caminade, A.-M.; Turrin, C.-O.; Laurent, R.; Ouali, A.; Delavaux-Nicot, B., Eds. *Dendrimers: Towards Catalytic, Material and Biomedical Uses;* John Wiley & Sons Ltd.: Chichester, UK, 2011. doi:10.1002/9781119976530
13. Caminade, A.-M.; Hameau, A.; Majoral, J.-P. *Chem. – Eur. J.* **2009,** *15,* 9270–9285. doi:10.1002/chem.200901597
14. Tomalia, D. A.; Klajnert-Maculewicz, B.; Johnson, K. A.-M.; Brinkman, H. F.; Janaszewska, A.; Hedstrand, D. M. *Prog. Polym. Sci.* **2019,** *90,* 35–117. doi:10.1016/j.progpolymsci.2018.09.004
15. Adronov, A.; Fréchet, J. M. J.; He, G. S.; Kim, K.-S.; Chung, S.-J.; Swiatkiewicz, J.; Prasad, P. N. *Chem. Mater.* **2000,** *12,* 2838–2841. doi:10.1021/cm000586o
16. Drobizhev, M.; Karotki, A.; Rebane, A.; Spangler, C. W. *Opt. Lett.* **2001,** *26,* 1081–1083. doi:10.1364/ol.26.001081
17. Drobizhev, M.; Karotki, A.; Dzenis, Y.; Rebane, A.; Suo, Z.; Spangler, C. W. *J. Phys. Chem. B* **2003,** *107,* 7540–7543. doi:10.1021/jp034986l
18. Mongin, O.; Brunel, J.; Porrès, L.; Blanchard-Desce, M. *Tetrahedron Lett.* **2003,** *44,* 2813–2816. doi:10.1016/s0040-4039(03)00455-6
19. Varnavski, O.; Yan, X.; Mongin, O.; Blanchard-Desce, M.; Goodson, T. *J. Phys. Chem. C* **2007,** *111,* 149–162. doi:10.1021/jp0640068
20. Yao, D.; Hugues, V.; Blanchard-Desce, M.; Mongin, O.; Paul-Roth, C. O.; Paul, F. *New J. Chem.* **2015,** *39,* 7730–7733. doi:10.1039/c5nj01381j
21. Yao, D.; Zhang, X.; Triadon, A.; Richy, N.; Mongin, O.; Blanchard-Desce, M.; Paul, F.; Paul-Roth, C. O. *Chem. – Eur. J.* **2017,** *23,* 2635–2647. doi:10.1002/chem.201604654
22. Majoral, J.-P.; Caminade, A.-M. *Dendrimers* **1998,** 79–124. doi:10.1007/3-540-69779-9_3
23. Launay, N.; Caminade, A.-M.; Lahana, R.; Majoral, J.-P. *Angew. Chem., Int. Ed. Engl.* **1994,** *33,* 1589–1592. doi:10.1002/anie.199415891
24. Caminade, A.-M. *Chem. Soc. Rev.* **2016,** *45,* 5174–5186. doi:10.1039/c6cs00074f
25. Caminade, A.-M.; Turrin, C.-O.; Majoral, J.-P. *New J. Chem.* **2010,** *34,* 1512–1524. doi:10.1039/c0nj00116c
26. Caminade, A.-M. *Chem. Commun.* **2017,** *53,* 9830–9838. doi:10.1039/c7cc04949h
27. Galliot, C.; Larré, C.; Caminade, A.-M.; Majoral, J.-P. *Science* **1997,** *277,* 1981–1984. doi:10.1126/science.277.5334.1981
28. Slany, M.; Caminade, A.-M.; Majoral, J. P. *Tetrahedron Lett.* **1996,** *37,* 9053–9056. doi:10.1016/s0040-4039(96)02123-5
29. Caminade, A.-M.; Laurent, R.; Chaudret, B.; Majoral, J. P. *Coord. Chem. Rev.* **1998,** *178-180,* 793–821. doi:10.1016/s0010-8545(98)00057-5
30. Leclaire, J.; Dagiral, R.; Fery-Forgues, S.; Coppel, Y.; Donnadieu, B.; Caminade, A.-M.; Majoral, J.-P. *J. Am. Chem. Soc.* **2005,** *127,* 15762–15770. doi:10.1021/ja054797b
31. Hameau, A.; Fuchs, S.; Laurent, R.; Majoral, J.-P.; Caminade, A.-M. *Beilstein J. Org. Chem.* **2011,** *7,* 1577–1583. doi:10.3762/bjoc.7.186
32. Caminade, A.-M.; Fruchon, S.; Turrin, C.-O.; Poupot, M.; Ouali, A.; Maraval, A.; Garzoni, M.; Maly, M.; Furer, V.; Kovalenko, V.; Majoral, J.-P.; Pavan, G. M.; Poupot, R. *Nat. Commun.* **2015,** *6,* 7722. doi:10.1038/ncomms8722
33. Caminade, A.-M.; Ouali, A.; Hameau, A.; Laurent, R.; Rebout, C.; Delavaux-Nicot, B.; Turrin, C.-O.; Moineau Chane-Ching, K.; Majoral, J.-P. *Pure Appl. Chem.* **2016,** *88,* 919–929. doi:10.1515/pac-2016-0711

34. Launay, N.; Caminade, A.-M.; Majoral, J. P. *J. Organomet. Chem.* **1997,** *529,* 51–58. doi:10.1016/s0022-328x(96)06293-6
35. Lartigue, M.-L.; Donnadieu, B.; Galliot, C.; Caminade, A.-M.; Majoral, J.-P.; Fayet, J.-P. *Macromolecules* **1997,** *30,* 7335–7337. doi:10.1021/ma970570s
36. Majoral, J.-P.; Caminade, A.-M. *Eur. J. Inorg. Chem.* **2019,** 1457–1475. doi:10.1002/ejic.201801184
37. Mongin, O.; Porrès, L.; Moreaux, L.; Mertz, J.; Blanchard-Desce, M. *Org. Lett.* **2002,** *4,* 719–722. doi:10.1021/ol017150e
38. Silly, M. G.; Porrès, L.; Mongin, O.; Chollet, P.-A.; Blanchard-Desce, M. *Chem. Phys. Lett.* **2003,** *379,* 74–80. doi:10.1016/j.cplett.2003.08.017
39. Werts, M. H. V.; Gmouh, S.; Mongin, O.; Pons, T.; Blanchard-Desce, M. *J. Am. Chem. Soc.* **2004,** *126,* 16294–16295. doi:10.1021/ja0446606
40. Parent, M.; Mongin, O.; Kamada, K.; Katan, C.; Blanchard-Desce, M. *Chem. Commun.* **2005,** 2029–2031. doi:10.1039/b419491h
41. Charlot, M.; Izard, N.; Mongin, O.; Riehl, D.; Blanchard-Desce, M. *Chem. Phys. Lett.* **2006,** *417,* 297–302. doi:10.1016/j.cplett.2005.10.033
42. Mongin, O.; Krishna, T. R.; Werts, M. H. V.; Caminade, A.-M.; Majoral, J.-P.; Blanchard-Desce, M. *Chem. Commun.* **2006,** 915–917. doi:10.1039/b517270e
43. Larson, D. R.; Zipfel, W. R.; Williams, R. M.; Clark, S. W.; Bruchez, M. P.; Wise, F. W.; Webb, W. W. *Science* **2003,** *300,* 1434–1436. doi:10.1126/science.1083780
44. Mongin, O.; Porrès, L.; Charlot, M.; Katan, C.; Blanchard-Desce, M. *Chem. – Eur. J.* **2007,** *13,* 1481–1498. doi:10.1002/chem.200600689
45. Mongin, O.; Rouxel, C.; Vabre, J.-M.; Mir, Y.; Pla-Quintana, A.; Wei, Y.; Caminade, A.-M.; Majoral, J.-P.; Blanchard-Desce, M. *Proc. SPIE* **2009**. doi:10.1117/12.826699
46. Caminade, A.-M.; Ouali, A.; Laurent, R.; Turrin, C.-O.; Majoral, J.-P. *Chem. Soc. Rev.* **2015,** *44,* 3890–3899. doi:10.1039/c4cs00261j
47. Keller, M.; Ianchuk, M.; Ladeira, S.; Taillefer, M.; Caminade, A.-M.; Majoral, J.-P.; Ouali, A. *Eur. J. Org. Chem.* **2012,** 1056–1062. doi:10.1002/ejoc.201101521
48. Collot, M.; Fam, T. K.; Ashokkumar, P.; Faklaris, O.; Galli, T.; Danglot, L.; Klymchenko, A. S. *J. Am. Chem. Soc.* **2018,** *140,* 5401–5411. doi:10.1021/jacs.7b12817
49. Cogné-Laage, E.; Allemand, J.-F.; Ruel, O.; Baudin, J.-B.; Croquette, V.; Blanchard-Desce, M.; Jullien, L. *Chem. – Eur. J.* **2004,** *10,* 1445–1455. doi:10.1002/chem.200305321
50. Rouxel, C.; Mongin, O.; Hameau, A.; Ouali, A.; Blanchard-Desce, M.; Majoral, J.-P.; Caminade, A.-M. *Can. J. Chem.* **2017,** *95,* 948–953. doi:10.1139/cjc-2017-0135
51. Terenziani, F.; Morone, M.; Gmouh, S.; Blanchard-Desce, M. *ChemPhysChem* **2006,** *7,* 685–696. doi:10.1002/cphc.200500536
52. Terenziani, F.; Parthasarathy, V.; Pla-Quintana, A.; Maishal, T.; Caminade, A.-M.; Majoral, J.-P.; Blanchard-Desce, M. *Angew. Chem., Int. Ed.* **2009,** *48,* 8691–8694. doi:10.1002/anie.200903519
53. Robin, A.-C.; Parthasarathy, V.; Pla-Quintana, A.; Mongin, O.; Terenziani, F.; Caminade, A.-M.; Majoral, J.-P.; Blanchard-Desce, M. *Proc. SPIE* **2010**. doi:10.1117/12.860768
54. Kazmierczak-Baranska, J.; Pietkiewicz, A.; Janicka, M.; Wei, Y.; Turrin, C.-O.; Majoral, J.-P.; Nawrot, B.; Caminade, A.-M. *Nucleosides, Nucleotides Nucleic Acids* **2010,** *29,* 155–167. doi:10.1080/15257771003708462
55. Loup, C.; Zanta, M.-A.; Caminade, A.-M.; Majoral, J.-P.; Meunier, B. *Chem. – Eur. J.* **1999,** *5,* 3644–3650. doi:10.1002/(sici)1521-3765(19991203)5:12<3644::aid-chem3644>3.0.co;2-i
56. Krishna, T. R.; Parent, M.; Werts, M. H. V.; Moreaux, L.; Gmouh, S.; Charpak, S.; Caminade, A.-M.; Majoral, J.-P.; Blanchard-Desce, M. *Angew. Chem., Int. Ed.* **2006,** *45,* 4645–4648. doi:10.1002/anie.200601246
57. Rouxel, C.; Charlot, M.; Mongin, O.; Krishna, T. R.; Caminade, A.-M.; Majoral, J.-P.; Blanchard-Desce, M. *Chem. – Eur. J.* **2012,** *18,* 16450–16462. doi:10.1002/chem.201202832
58. Sourdon, A.; Gary-Bobo, M.; Maynadier, M.; Garcia, M.; Majoral, J.-P.; Caminade, A.-M.; Mongin, O.; Blanchard-Desce, M. *Chem. – Eur. J.* **2019,** *25,* 3637–3649. doi:10.1002/chem.201805617
59. Mignani, S.; El Brahmi, N.; Eloy, L.; Poupon, J.; Nicolas, V.; Steinmetz, A.; El Kazzouli, S.; Bousmina, M. M.; Blanchard-Desce, M.; Caminade, A.-M.; Majoral, J.-P.; Cresteil, T. *Eur. J. Med. Chem.* **2017,** *132,* 142–156. doi:10.1016/j.ejmech.2017.03.035
60. Caminade, A.-M.; Majoral, J.-P. *New J. Chem.* **2013,** *37,* 3358. doi:10.1039/c3nj00583f
61. Shakhbazau, A.; Mishra, M.; Chu, T.-H.; Brideau, C.; Cummins, K.; Tsutsui, S.; Shcharbin, D.; Majoral, J.-P.; Mignani, S.; Blanchard-Desce, M.; Bryszewska, M.; Yong, V. W.; Stys, P. K.; van Minnen, J. *Macromol. Biosci.* **2015,** *15,* 1523–1534. doi:10.1002/mabi.201500150
62. Mongin, O.; Pla-Quintana, A.; Terenziani, F.; Drouin, D.; Le Droumaguet, C.; Caminade, A.-M.; Majoral, J.-P.; Blanchard-Desce, M. *New J. Chem.* **2007,** *31,* 1354–1367. doi:10.1039/b702452p
63. Mongin, O.; Rouxel, C.; Robin, A.-C.; Pla-Quintana, A.; Rama Krishna, T.; Recher, G.; Tiaho, F.; Caminade, A.-M.; Majoral, J.-P.; Blanchard-Desce, M. *Proc. SPIE* **2008**. doi:10.1117/12.797873
64. El Brahmi, N.; El Kazzouli, S.; Mignani, S. M.; Essassi, E. M.; Aubert, G.; Laurent, R.; Caminade, A.-M.; Bousmina, M. M.; Cresteil, T.; Majoral, J.-P. *Mol. Pharmaceutics* **2013,** *10,* 1459–1464. doi:10.1021/mp4000184
65. Mignani, S. M.; El Brahmi, N.; El Kazzouli, S.; Laurent, R.; Ladeira, S.; Caminade, A.-M.; Pedziwiatr-Werbicka, E.; Szewczyk, E. M.; Bryszewska, M.; Bousmina, M. M.; Cresteil, T.; Majoral, J.-P. *Mol. Pharmaceutics* **2017,** *14,* 4087–4097. doi:10.1021/acs.molpharmaceut.7b00771
66. Lovell, J. F.; Liu, T. W. B.; Chen, J.; Zheng, G. *Chem. Rev.* **2010,** *110,* 2839–2857. doi:10.1021/cr900236h

BEILSTEIN JOURNAL OF ORGANIC CHEMISTRY

Synthesis of a dihalogenated pyridinyl silicon rhodamine for mitochondrial imaging by a halogen dance rearrangement

Jessica Matthias[1,2], Thines Kanagasundaram[3,4], Klaus Kopka[3,5] and Carsten S. Kramer[*3]

Full Research Paper

Open Access

Address:
[1]Max Planck Institute for Medical Research, Department of Optical Nanoscopy, Jahnstraße 29, 69120 Heidelberg, Germany, [2]Helmholtz International Graduate School, German Cancer Research Center (DKFZ), Im Neuenheimer Feld 223, 69120 Heidelberg, Germany, [3]Division of Radiopharmaceutical Chemistry, German Cancer Research Center (DKFZ), Im Neuenheimer Feld 223, 69120 Heidelberg, Germany, [4]Institute of Inorganic Chemistry, Im Neuenheimer Feld 270, 69120 Heidelberg, Germany and [5]German Cancer Consortium (DKTK), Heidelberg, Germany

Email:
Carsten S. Kramer* - c.kramer@dkfz-heidelberg.de

* Corresponding author

Keywords:
halogen-dance reaction; mitochondrial probe; near-infrared (NIR) dyes; one-pot reaction; silicon rhodamines

Beilstein J. Org. Chem. **2019,** *15,* 2333–2343.
doi:10.3762/bjoc.15.226

Received: 31 May 2019
Accepted: 05 September 2019
Published: 01 October 2019

This article is part of the thematic issue "Dyes in modern organic chemistry".

Guest Editor: H. Ihmels

Abstract

Background: Since their first synthesis, silicon xanthenes and the subsequently developed silicon rhodamines (SiR) gained a lot of attention as attractive fluorescence dyes offering a broad field of application. We aimed for the synthesis of a fluorinable pyridinyl silicon rhodamine for the use in multimodal (PET/OI) medical imaging of mitochondria in cancerous cells.

Results: A dihalogenated fluorinatable pyridinyl rhodamine could be successfully synthesized with the high yield of 85% by application of a halogen dance (HD) rearrangement. The near-infrared dye shows a quantum yield of 0.34, comparable to other organelle targeting SiR derivatives and absorbs at 665 nm (ε_{max} = 34 000 $M^{-1}cm^{-1}$) and emits at 681 nm (τ = 1.9 ns). Using colocalization experiments with MitoTracker® Green FM, we could prove the intrinsic targeting ability to mitochondria in two human cell lines (Pearson coefficient >0.8). The dye is suitable for live cell STED nanoscopy imaging and shows a nontoxic profile which makes it an appropriate candidate for medical imaging.

Conclusions: We present a biocompatible, nontoxic, small molecule near-infrared dye with the option of subsequent radiolabelling and excellent optical properties for medical and bioimaging. As a compound with intrinsic mitochondria targeting ability, the radiolabelled analogue can be applied in multimodal (PET/OI) imaging of mitochondria for diagnostic and therapeutic use in, e.g., cancer patients.

Introduction

Since their first synthesis by Fu and co-workers in 2008 [1], silicon xanthenes and the subsequently developed silicon rhodamines (SiR) have drawn a lot of attention as attractive fluorescence dyes offering a broad field of application. Their excellent spectral (absorption and emission bands in the near-infrared region), photophysical (bright and photostable) and biochemical (biocompatible, biological stable and cell membrane permeable) properties make them useful tools in live cell super-resolution microscopy [2-9], as direct probes for various biomolecules [10-13] or as sensors for metal ions [14-18], pH [16], voltage [19] or metabolites [20-23]. Several attempts were made, partially supported by DFT calculations, to correlate the dyes' structural features with their optical properties and control the latter by rational dye design [15,24-26]. These investigations led to new silicon rhodamine dyes with enhanced and fine-tuned properties (quantum yield, lifetime, brightness, absorption and emission maxima). A recent review compared the photophysical properties of numerous silicon rhodamines leading to further insights into the correlation of the dyes' chemical structure with their fluorogenic behavior [27]. Regarding the quantum yield, Hanaoka et al. have shown that introduction of methyl, methoxy or dimethylamine groups into the benzene moiety of silicon rhodamines could tune the HOMO energy level [15]. Depending on the oxidation potential and the HOMO energy level of the benzene moiety, the quantum yield was greatly altered but absorption and emission bands remained unchanged. Thus, the quantum yield shows a direct connection to the negative value of the HOMO energy level and/or the oxidation potential [15], but it is also influenced by other factors. Nonradiative quenching (e.g., bond rotation) can effectively contribute to depopulation of the fluorophore's excited state [28], yielding a lower quantum yield. However, the rational trends for both radiative and nonradiative decays still remain difficult to predict despite theoretical and experimental efforts of the past years [29]. Here we initially assume that, in analogy to BODIPY fluorophores [30], restricted rotation around the xanthene aryl bond should lead to an improved quantum yield.

In Scheme 1 we compile silicon rhodamines with high quantum yields as well as their structural analogues with lower quantum yields. Silicon fluoresceins were excluded from this compilation, although "2-COOH DCTM" [31], "2-COOH DFTM" [31], and "Maryland red" [32] are representatives with quantum yields up to 0.67. As described previously, azetidine substituents at the xanthene moiety of **5**, **7**, and **9** lead to an improved quantum yield and to a red shift in comparison to the *N*,*N*-dimethylaniline analogues **1**, **3**, and **4** (Table 1, entry 1 vs 5, 3 vs 7, and 4 vs 9). In contrast, the 4-fluoroazetidine moiety in **10** ("JF_{635}") causes a hypsochromic shift without affecting the high quantum yield compared to the azetidine analogue **9** ("JF_{646}") (Table 1, entry 9 vs 10). Comparing the phenyl substituted rhodamine **2** with its 2'-methyl substituted analogue **3**, restricted rotation around the xanthene–benzene bond leads to a drastic improvement of the quantum yield from 0.10 to 0.31 (Table 1, entry 2 vs 3). Accordingly, rhodamines like **3**, **4**, **11**, or **12** bearing 2'-substituents with A-values between a proton and a methyl group (such as F and Cl) show quantum yields from 0.19 (for F) [23] to 0.30 (for Cl) [23]. This observation leads us to the hypothesis that the quantum yield correlates positively with the bulkiness of the phenylic 2'-substituent, which restricts the rotation around the xanthene–benzene bond more strongly the larger it is.

Remarkably, dyes **1**, **5** and **6** already possess moderate to high quantum yields without any benzene moiety (Table 1, entries 1,

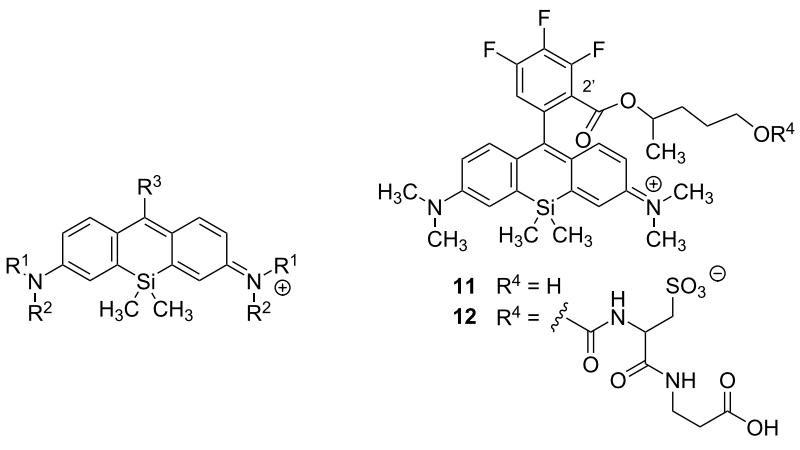

Scheme 1: Comparison of optical properties of different silicon rhodamines.

Table 1: Comparison of optical properties of different silicon rhodamines.

Entry	NR^1R^2	R^3		λ_{abs}	λ_{em}	Φ	Ref
1	$N(CH_3)_2$	H	**1** (SiP)	634	648	0.42[a,b]	[15]
2	$N(CH_3)_2$	Ph	**2**	646	667	0.10[b,c]	[33]
3	$N(CH_3)_2$	2-CH_3-Ph	**3**	646	660	0.31[a,b]	[15]
4	$N(CH_3)_2$	2-COOH-Ph	**4**	643	662	0.41[d,e]	[24]
5	azetidine	H	**5**	636	649	0.62[d,e]	[32]
6	azetidine	COOH	**6**	641	657	0.26[d,e]	[32]
7	azetidine	2-CH_3-Ph	**7**	649	663	0.47[d,e]	[32]
8	azetidine	2-CH_3-6-CH_3-Ph	**8**	651	664	0.51[d,e]	[32]
9	azetidine	2-COOH-Ph	**9** (JF_{646})	646	664	0.54[d,e]	[24]
10	3-fluoroazetidine	2-COOH-Ph	**10** (JF_{635})	635	652	0.56[d,e]	[25]
11			**11**	662	680	0.66[f,g,h]	[34]
12			**12**	663	680	0.70[f,h]	[34]
13	$N(CH_3)_2$	pyridin-4-yl	**13**	655	680	0.12[c,e]	[35]
14	azetidine	3-methylpyridin-4-yl	**14**	656	670	0.48[d,e]	

[a]In PBS buffer at pH 7.4; [b]cresyl violet in methanol was used as reference dye; [c]in PBS buffer; [d]in HEPES buffer at pH 7.3; [e]quantum yield was determined by absolute measurement; [f]in water; [g]the corresponding isopropyl ester showed a quantum yield of 0.60; [h]quantum yield determined in water with the reference dye Atto AZ 237.

5 and 6). The fluorophores **11** and **12** exhibit values of 0.66 and 0.70 and have, to the best of our knowledge, the highest quantum yields known amongst silicon rhodamines (Scheme 1, Table 1, entries 11 and 12). One reason might be the bulkiness of the ester group in 2'-position, an isopropyl ester derivative; another one might be the effects of the fluorine atoms and the ester group on the HOMO energy level of the benzene moiety.

Since our group is interested in PET-active near-infrared (NIR) dyes for bimodal medical imaging (PET/optical imaging (OI)), we wanted to develop the pyridinyl-substituted silicon rhodamine **15**, in which the 2-halopyridine moiety can easily be radiofluorinated to the PET-active dye **16** (Scheme 2, for examples on radiolabelling of 2-halopyridines see [36-38] and references therein). While the PET modality is highly interesting for precise medical imaging of diseases, the fluorescence modality can be utilized for medical interventions, such as fluorescence-guided surgery or sentinel lymph node detection or for histopathological analyses of biopsy material.

To date, only two pyridinyl-substituted silicon rhodamines have been published. Dye **13** (Scheme 1, Table 1, entry 13) shows good water solubility, has a quantum yield of 0.12 and offers

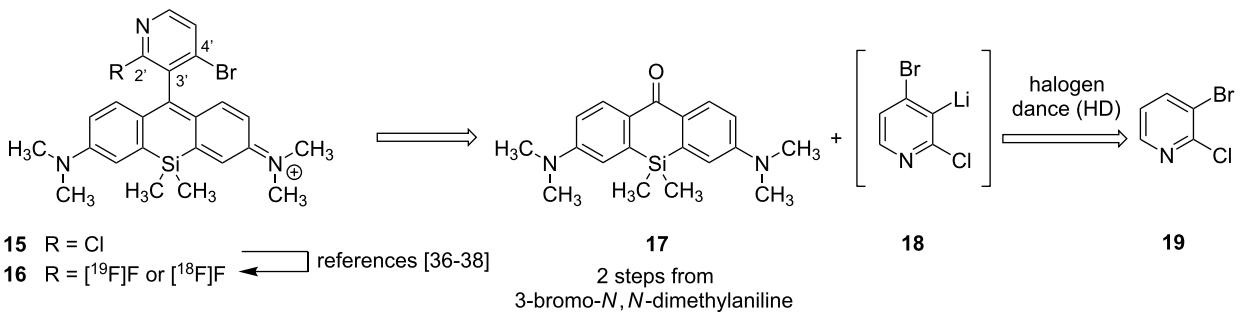

Scheme 2: Retrosynthetic analysis of the proposed small molecule bimodal probe [^{18}F]**16** for both optical and PET imaging of cancer cells with up-regulated mitochondrial activity.

intrinsic targeting ability to lysosomes [35]. Pyridine silicon rhodamine **14** (Table 1, entry 14) has an improved quantum yield of 0.48 [32], presumably due to the restricted rotation of the xanthene pyridine bond.

The 2-chloropyridinyl moiety in **15** is not only attractive because of its option for convenient fluorination, but also since its intrinsic targeting ability to acidic cellular compartments (such as the lysosomal-selective fluorophore **13**). We assumed that our proposed bimodal fluorophore would show a better selectivity for mitochondria because of its more lipophilic nature (clogP for **15** 3.712, for **16** 3.142) compared to **13** (clogP 2.136). Medical imaging of mitochondrial activity is highly interesting for various indications, ranging from neurodegenerative and metabolic diseases to ischemic injuries, necrosis, therapy response and cancer [39-43]. Because many cancer cells have a higher mitochondrial membrane potential than nontransformed cells [41,44,45], we believe that our imaging agent will achieve a reasonable tumor-to-background ratio.

Lipophilic cations such as the phosphonium cation or rhodamines are known to accumulate selectively within the mitochondria, driven by the mitochondrial plasma membrane potential [39,40]. Thereby, the high lipophilicity facilitates the diffusion through the lipid bilayers of the cell and mitochondrial membranes. Recently, a silicon rhodamine for selective mitochondrial staining was developed by conjugation of the SiR core with ten different amines varying in lipophilicity [46]. The authors showed that the optimal range of clogP values for mitochondrial targeting ranges from 5.50 to 6.33.

As mentioned above, the pyridinyl-substituted silicon rhodamines **13** and **14** are dyes with spectral properties in the near-infrared region. Dye **14** possess the higher quantum yield not only due to the azetidine substituents at the xanthene moiety, but also because of the restricted bond rotation owing to the 3'-methyl (pyridine numbering) group. Since the smaller 2'-fluorine substituent in **16** should lead to a decrease in quantum yield compared to **15**, we aimed for a molecule with an additional bulky 4'-substituent such as bromine. The bromine should not only alter the HOMO energy level of **16** in a favourable way, it can also be used for further functionalization. Until now, no silicon rhodamines are known that bear two phenylic halogen substituents (Cl/Cl, Cl/Br, Br/Br nor combinations with F) at the positions adjacent to the xanthene benzene bond. The same holds true for the oxygen counterparts with a dihalogenated pyridinyl motif. In fact, only two pyridinyl silicon rhodamines (**13** and **14**) are known so far, although halogenated pyridines are highly interesting for further functionalization or vector conjugation by nucleophilic aromatic substitution. For the implementation of the dihalogenated pyridine motif into the silicon rhodamine scaffold, we considered using a halogen dance (HD) reaction of 3-bromo-2-chloropyridine (**19**) to **18** followed by a condensation with silicon xanthone **17**, which is accessible in two steps from 3-bromo-*N*,*N*-dimethylaniline. The rearrangement of halo pyridine **19**, initiated by a halogen metal exchange with *n*-BuLi, was initially published and investigated by Mallet et al. who also investigated and termed the mechanism "homotransmetallation" [47]. The HD rearrangement reaction in general is an excellent method for the construction of highly substituted carbo- and heterocyclic systems (e.g., tetrasubstituted pyridines [48]) with substitution patterns difficult to obtain otherwise [49-51].

Results and Discussion

Approaches to synthesize the pyridinyl silicon rhodamine **15**

Table 2 and Scheme 3 summarize the experimental results towards the synthesis of the radiofluorinatable near-infrared dye **15**. To initiate the HD reaction, 3-bromo-2-chloropyridine (**19**) had first to be lithiated. After 30 min at −78 °C, the silicon xanthone **17** was added at the same temperature and the reaction mixture was subsequently warmed up to room temperature and stirred for varying time periods. By using *t*-BuLi as a lithiation reagent, the desired dye **15** was obtained at just 14% yield as a deep blue solid (Scheme 3, Table 2, entry 1). Owing to the mechanism of the homotransmetallation, the HD rearrangement of **19** is conducted with substoichiometric amounts of the lithiating agent (usually 0.5 equiv *n*-BuLi for 1 equiv **19**) [47,49]. Thus, we tried the reaction with 0.9 equiv of *t*-BuLi (Table 2, entry 2) and 0.5 equiv of *n*-BuLi (Table 2, entry 3), but the desired product was again obtained in poor yields with lots of unreacted starting material **17**. According to the mechanism of the halogen–metal exchange with *t*-BuLi, one equivalent of the base is used for the lithiation, while a second equivalent base eliminates hydrogen bromide from the resulting

Table 2: Optimization of the HD rearrangement of **19** and subsequent reaction with xanthone **17** to the silicon rhodamine dye **15**.

Entry	Equiv of lithiation reagent	Equiv of **19**	Yield **15**
1	20 *t*-BuLi	10	14%[a]
2	9 *t*-BuLi	10	14%[b], 28%[b,c]
3	5 *n*-BuLi	10	11%[d]
4	40 *t*-BuLi	20	85%[e]

[a]1.5 h reaction time after addition of 1 equiv of xanthone **17**; [b]24 h reaction time; [c]yield based on recovered starting material of xanthone **17**; [d]5 h reaction time, [e]4 h reaction time.

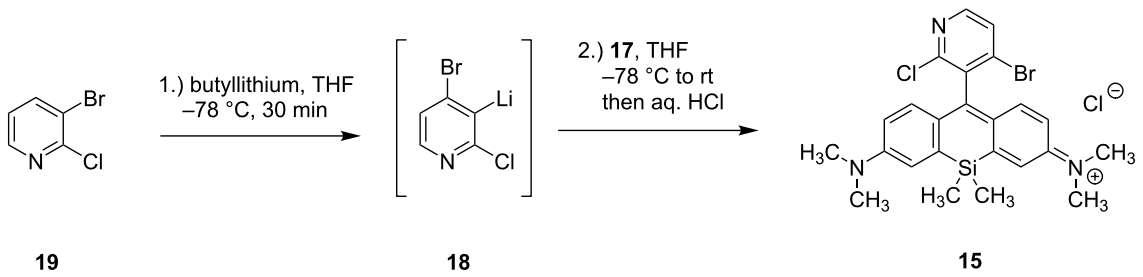

19 18 15

Scheme 3: Optimization of the HD rearrangement of **19** and subsequent reaction with xanthone **17** to the silicon rhodamine dye **15**.

t-BuBr. Therefore, entries 2 and 3 (Table 2) represent the use of approx. 0.5 equiv base for 1 equiv of **19**. After lithiation of **19**, the metallated intermediate (2-chloropyridin-3-yl)lithium reacts again with starting material **19** resulting, after several steps (the so called halogen dance), in the lithiated pyridine intermediate **18** that can add to the silicon xanthone **17**. Low temperatures for the HD reaction are required when more equivalents of the base are used to maintain a coexistence of **19** and its lithiated analogue. Using high excess of **19** could force the reaction to completeness leading to the dihalogenated pyridinyl silicon rhodamine in 85% yield without any monohalogenated byproduct and no necessity of HPLC purification.

Although **15** can be coupled or further functionalized at the bromine via a nucleophilic substitution, we explored also if the ester analogue *tert*-butyl 5-bromo-6-chloronicotinate could undergo a HD reaction with subsequent xanthone addition. The reaction did not lead to any product, neither with *n*-BuLi nor with *t*-BuLi. However, it is noteworthy that no HD reactions of nicotinic acids can be found in the literature. In fact, if 2,3-dihalogenated pyridines are used for the HD rearrangement as starting materials, only methyl groups are tolerated as carbon substituents.

Optical properties of the pyridinyl silicon rhodamine **15**

The dihalogenated pyridinyl SiR **15** has an absorption peak at 665 nm (ε_{max} = 34 000 $M^{-1}cm^{-1}$) and an emission peak at 681 nm (τ = 1.9 ns, Figure S3a, Table S2a, Supporting Information File 1) (measured in PBS buffer pH 7.4). It shows a red-shift of approx. 10 nm in absorption and emission compared to the azetidine-substituted pyridinyl dye **14** and a 10 nm red-shifted absorption with unchanged emission compared to pyridinyl dye **13** (Figure 1a). The quantum yield is with 0.34 (measured in PBS buffer pH 7.4, Figure S2a, Table S1a, Supporting Information File 1), remarkably higher than the value of pyridinyl dye **13**. This fact could be explained with rotation restriction around the pyridinyl–xanthene bond and/or with beneficial effects of the halogens on the HOMO energy level. Nevertheless, the pyridinyl SiR **14** performs better due to the addition contributions of the azetidine rings.

Next, we examined the targeting ability to mitochondria of the dihalogenated dye **15** by colocalization experiments with the commercially available mitochondria staining reagent MitoTracker® Green FM (Figure 1a,b and Figure S4a,b, Supporting Information File 2). To determine the Pearson coefficient for colocalization of SiR **15** with MitoTracker® Green FM, HeLa cells (human cervical cancer cells) and U2OS cells (human bone osteosarcoma epithelial cells) were co-stained with these dyes. The Pearson coefficients are reasonably high and similar for both cell lines (HeLa cells: 0.85 ± 0.05 (N = 20), U2OS cells: 0.81 ± 0.05 (N = 27)) supporting the application of SiR **15** as a specific NIR mito tracker probe. Pearson coefficients for selective mitochondria staining >0.8 correlate with much higher lipophilicity (clogP over 4.95). Especially SiR-Mito 8 offers a comparable quantum yield to dye **15** (ε and therefore brightness not available) combined with a Pearson coefficient ≥0.9 [46]. However, dye **15** has the benefit of further red-shifted absorption and emission properties as well as a photostability that allows for STED (stimulated emission depletion) nanoscopy [52,53].

As the 2-chloropyridinyl moiety in SiR dye **15** targets acidic cellular compartments in general, we additionally investigated potential lysosomal colocalization. Co-staining HeLa and U2OS cells with SiR dye **15** and the commercially available lysosomal staining reagent LysoTracker™ Green DND-26 showed absence of any lysosomal targeting ability and confirmed specific mitochondrial staining (Figure S4c,d, Supporting Information File 1).

Medical imaging agents are highly interesting especially if they can address multiple questions or can be applied for different purposes simultaneously, because they must undergo an expensive regulatory process before they attain approval for the

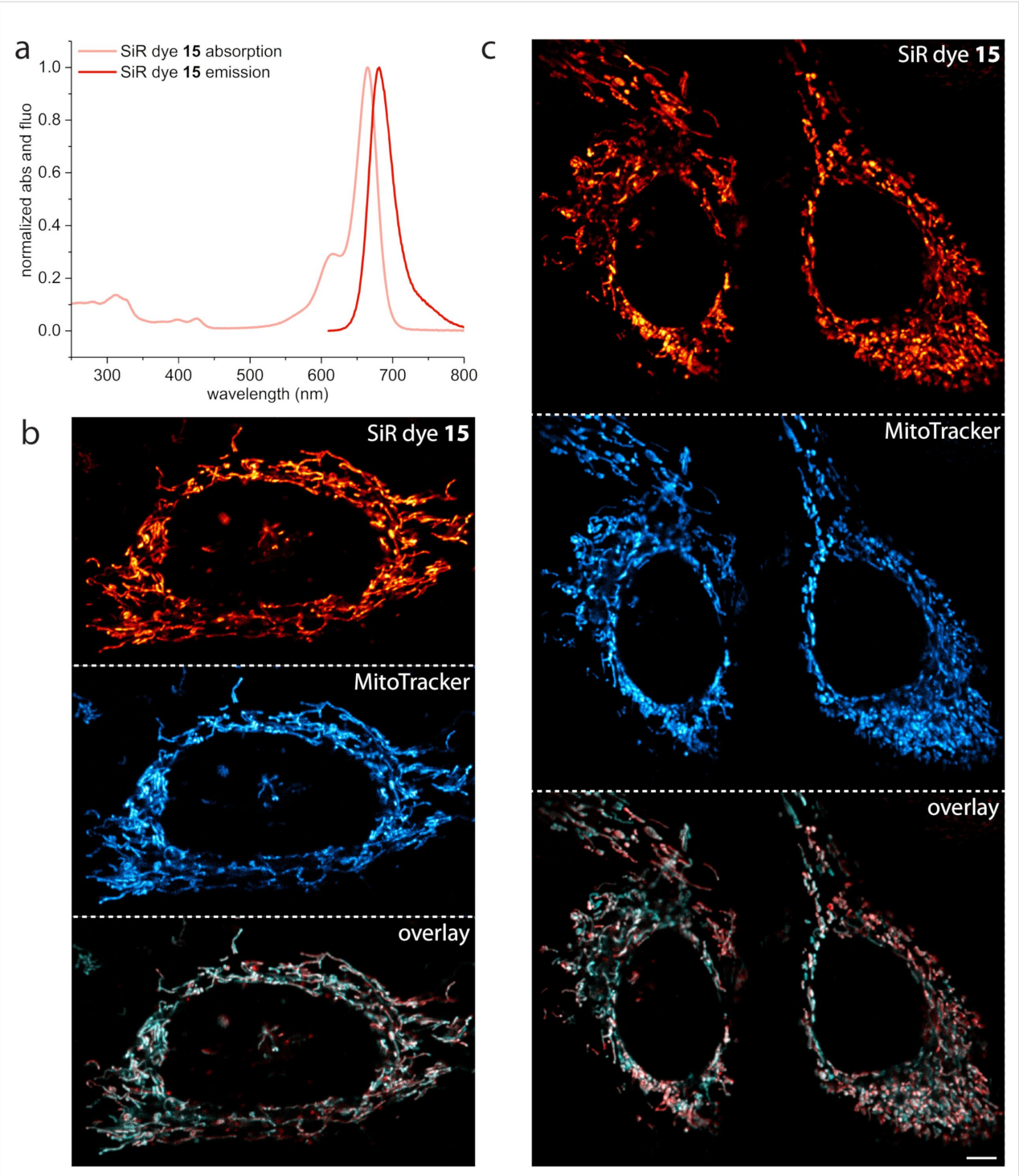

Figure 1: (a) Absorption and fluorescence emission spectra of dye **15** measured in PBS buffer pH 7.4. (b, c) Colocalization experiment of dye **15** (red) and MitoTracker® Green FM (cyan) in living HeLa (b) and U2OS (c) cells supporting the application of dye **15** as a specific NIR mito tracker probe. Both cell lines were incubated for 0.5 h with 1 µM of dye **15** and 100 nM of MitoTracker® Green FM, washed and imaged with excitation at 470 nm (380 µW) and 652 nm (7.5 µW). Confocal images are color shift and background corrected, scale bar 5 µm.

market. Therefore, we are interested also in purposes other than PET imaging or macroscopic fluorescence imaging. Histopathological examinations of biopsy material on subcellular level need high image quality. Thus, the option to use our proposed bimodal dye in STED nanoscopy would be advantageous. For example, Giedt et al. could show that analysis of mitochondrial

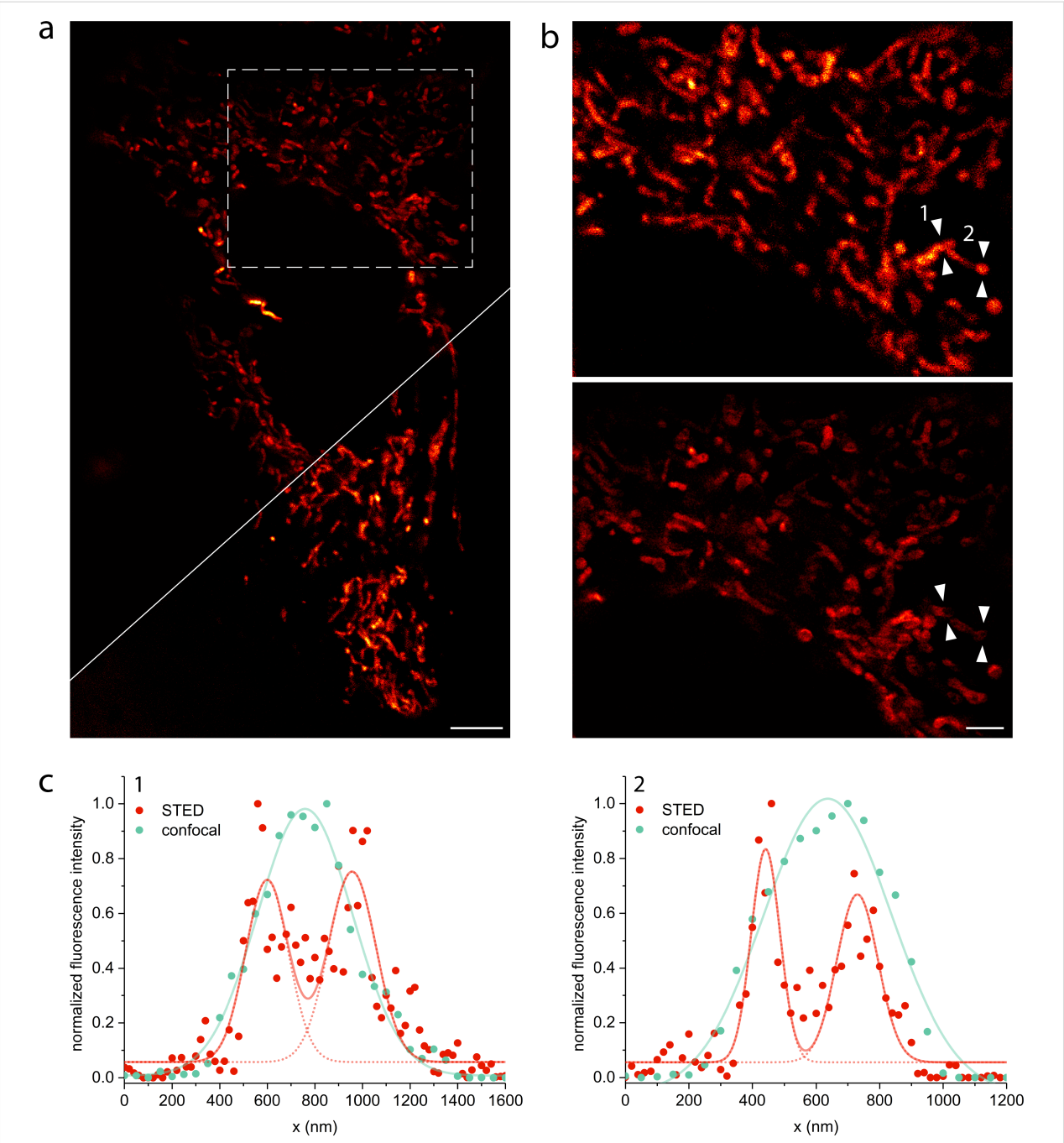

Figure 2: STED and confocal images of the mitochondrial network in living HeLa cells stained with 1 µM SiR dye **15** for 1 h. (a) STED image (excitation at 652 nm with 15 µW, depletion at 775 nm with 40 mW) with the corresponding confocal data (excitation at 652 nm with 7.5 µW) in the bottom right corner. STED image is background subtracted and linearly deconvolved (Lorentzian PSF), confocal image is only background subtracted, scale bar 5 µm. (b) Magnified view of the region marked in (a) in confocal (top) and STED mode (bottom), scale bar 2 µm. (c) Line profiles marked in (b) proving the gain in spatial resolution of STED (red) compared to confocal (cyan). Line profiles were taken from only background corrected (not deconvolved) data (Figure S8, Supporting Information File 1), counts were averaged over five pixels, normalized and fitted to a single (confocal) or double (STED) Gaussian function. To avoid photobleaching, the STED power was set as low as possible but as high as necessary to resolve the tubular structure of mitochondria resulting in full width half maxima (FWHM) of 219 ± 15 nm (1, left), 306 ± 21 nm (1, right), 114 ± 7 nm (2, left) and 200 ± 9 (2, right). The peak to peak distances are 363 nm (1) and 294 nm (2). The FWHM of the confocal fits are 470 ± 15 nm (1) and 474 ± 25 nm (2).

morphology can be used as a biomarker for cancer phenotype assignment and for drug response analysis [54]. For STED imaging, HeLa cells were stained for 1 h with 1 µM of dye **15**, washed and imaged live. Figure 2 and Figure S5, Supporting Information File 1, compare STED images with their corresponding confocal images. By resolving the tubular structure of

mitochondria, we prove successful application of our mitochondria-selective pyridinyl SiR **15** in STED nanoscopy.

Toxicity of the pyridinyl silicon rhodamine **15**

Although for PET examinations only nano- or picomolar amounts of the radiopharmaceutical compound are needed, medical applications of fluorescence dyes (e.g., fluorescence-guided interventions) require larger amounts of material. Therefore, cytotoxicity testing is necessary for our proposed bimodal imaging agent **16** and its precursor **15**. For toxicity assessment, the frequency and duration of cell division with and without incubation with dye **15** was analyzed via time-lapse holographic imaging (Figure 3). U2OS cells were incubated with 1 µM dye **15** in medium for 1 h and, after washing with dye free medium, continually imaged over a period of 14.5 h using a holographic incubator microscope. The analysis of the data revealed that the frequency and duration of cell division of the cells incubated with dye **15** show no difference to the untreated control (frequency of cell division with SiR dye **15**: 0.30 ± 0.05 divisions per cell, without dye: 0.32 ± 0.06 divisions per cell, for division duration see Figure S7, Supporting Information File 1). These results are supported by cell count and confluency analysis (Figure S9, Supporting Information File 1). In summary, we conclude that dye **15** does not show any significant cytotoxicity in this human cell line. Comparable experiments with HeLa cells strengthen these results (data not shown).

Conclusion

We have proven the feasibility of synthesizing a pyridinyl silicon rhodamine dye with two halogen atoms adjacent to the xanthene–pyridine bond by application of a halogen dance rearrangement. By our optimized procedure, we have obtained the dye **15** at high yield and without the necessity of HPLC purification. The chlorine atom in 2'-position can potentially be used to introduce the PET radionuclide fluorine-18 while the bromine atom serves as a constraint against rotation around the xanthene–pyridine bond as well as a leverage point for further linkage. The quantum yield is reasonably high (0.34). However, despite the improved molecule rigidity and thus presumably less nonradiative decay, dye **15** does not outperform the quantum yield of monosubstituted pyridine SiR **14**. Additional experiments (supported by DFT calculations) on the orbital effects of both halogens and the nitrogen position in the pyridine ring are needed to explain these effects with confidence.

In addition, our SiR dye **15** displays photophysical properties (extinction coefficient, quantum yield, lifetime) in the same range, but rather at the lower end, compared to other near-infrared silicon rhodamine derivatives with similar spectral properties [3,4,7]. However, it is in line with the group of SiR derivatives directly targeting certain cellular structures or organelles [7,55-57] and extends this list with a NIR mito tracker® probe.

Just like the recently published squaraine variant dye MitoESq-635 [58], our SiR dye **15** offers the option of imaging mitochondria in living cells using STED nanoscopy without the necessity of an additional tagging step. In contrast to MitoESq-635, our SiR dye **15** selectively stains mitochondria without background from unspecific membrane staining. However, higher photostability and a lower saturation intensity for STED result in a better performance in time-lapse live cell STED imaging of MitoESq-635. Taken together, our SiR dye **15** is a valid compromise between MitoESq-635 and SiR-Mito 8 offering nontoxic, specific mitochondrial staining in live cell STED imaging.

In summary, we present a biocompatible, nontoxic, small molecule near-infrared dye with the option of subsequent radiolabelling and excellent optical properties for biomedical imaging. As a compound with intrinsic mitochondria targeting ability, the radiolabelled analogue can find application in multimodal (PET/OI) imaging of mitochondria for diagnostic and therapeutic use in, e.g., cancer patients. (Radio)fluorination of dye **15** is the subject of ongoing research and will be presented elsewhere.

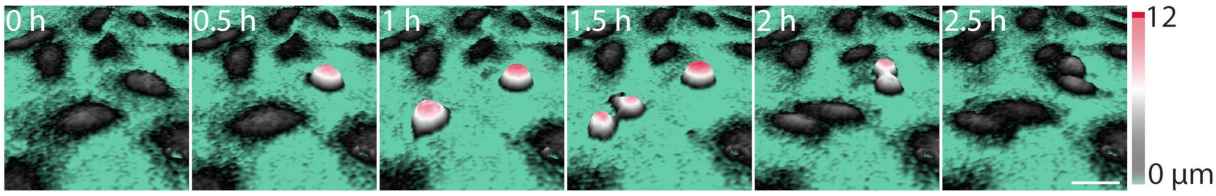

Figure 3: Exemplary holographic image sequence of two cell divisions of U2OS cells treated with 1 µM of dye **15**. Dividing cells round up and can be distinguished from non-dividing cells by height. After incubation with 1 µM dye **15** for 1 h, the cells were washed and then holographically imaged using a HoloMonitor® M4 time-lapse cytometer. Cell proliferation was followed for 14.5 h (30 min between images) and corresponding time-lapse movies are available in Supporting Information Files 2–5, scale bar 50 µm.

Supporting Information

Synthesis of dye **15**, its optical characterization and detailed information on microscopy experiments, including videos showing undisturbed cell proliferation in U2OS cells incubated with 1 µM of dye **15** for 1 h compared to untreated U2OS cells are given.

Supporting Information File 1

Experimental and analytical data, spectra, live cell imaging and assessment of cytotoxicity.
[https://www.beilstein-journals.org/bjoc/content/supplementary/1860-5397-15-226-S1.pdf]

Supporting Information File 2

Independent experiment assessing cell division of U2OS cells after treatment with 1 µM SiR dye **15**.
[https://www.beilstein-journals.org/bjoc/content/supplementary/1860-5397-15-226-S2.avi]

Supporting Information File 3

Independent experiment assessing cell division of U2OS cells after treatment with 1 µM SiR dye **15**.
[https://www.beilstein-journals.org/bjoc/content/supplementary/1860-5397-15-226-S3.avi]

Supporting Information File 4

Independent control experiment assessing undisturbed cell division of U2OS cells.
[https://www.beilstein-journals.org/bjoc/content/supplementary/1860-5397-15-226-S4.avi]

Supporting Information File 5

Independent control experiment assessing undisturbed cell division of U2OS cells.
[https://www.beilstein-journals.org/bjoc/content/supplementary/1860-5397-15-226-S5.avi]

Acknowledgements

We are very grateful to the Wilhelm Sander Stiftung for a grant on bimodal tumor tracers (2018.024.1). We thank Yvonne Remde for support with synthesis, Dr. Mariano Bossi for support with spectroscopic characterization, Dr. Rifka Vlijm for support with image analysis and Dr. Johann Engelhardt for construction of and support with the microscope setup.

ORCID® iDs

Jessica Matthias - https://orcid.org/0000-0001-6560-2174
Thines Kanagasundaram - https://orcid.org/0000-0001-8265-8591
Klaus Kopka - https://orcid.org/0000-0003-4846-1271
Carsten S. Kramer - https://orcid.org/0000-0001-9932-423X

References

1. Fu, M.; Xiao, Y.; Qian, X.; Zhao, D.; Xu, Y. *Chem. Commun.* **2008,** 1780–1782. doi:10.1039/b718544h
2. Thompson, A. D.; Omar, M. H.; Rivera-Molina, F.; Xi, Z.; Koleske, A. J.; Toomre, D. K.; Schepartz, A. *Angew. Chem., Int. Ed.* **2017,** *56,* 10408–10412. doi:10.1002/anie.201704783
3. Butkevich, A. N.; Ta, H.; Ratz, M.; Stoldt, S.; Jakobs, S.; Belov, V. N.; Hell, S. W. *ACS Chem. Biol.* **2018,** *13,* 475–480. doi:10.1021/acschembio.7b00616
4. Butkevich, A. N.; Mitronova, G. Y.; Sidenstein, S. C.; Klocke, J. L.; Kamin, D.; Meineke, D. N. H.; D'Este, E.; Kraemer, P.-T.; Danzl, J. G.; Belov, V. N.; Hell, S. W. *Angew. Chem., Int. Ed.* **2016,** *55,* 3290–3294. doi:10.1002/anie.201511018
5. Kozma, E.; Estrada Girona, G.; Paci, G.; Lemke, E. A.; Kele, P. *Chem. Commun.* **2017,** *53,* 6696–6699. doi:10.1039/c7cc02212c
6. Grimm, J. B.; Klein, T.; Kopek, B. G.; Shtengel, G.; Hess, H. F.; Sauer, M.; Lavis, L. D. *Angew. Chem., Int. Ed.* **2016,** *55,* 1723–1727. doi:10.1002/anie.201509649
7. Lukinavičius, G.; Reymond, L.; Umezawa, K.; Sallin, O.; D'Este, E.; Göttfert, F.; Ta, H.; Hell, S. W.; Urano, Y.; Johnsson, K. *J. Am. Chem. Soc.* **2016,** *138,* 9365–9368. doi:10.1021/jacs.6b04782
8. Takakura, H.; Zhang, Y.; Erdmann, R. S.; Thompson, A. D.; Lin, Y.; McNellis, B.; Rivera-Molina, F.; Uno, S.-n.; Kamiya, M.; Urano, Y.; Rothman, J. E.; Bewersdorf, J.; Schepartz, A.; Toomre, D. *Nat. Biotechnol.* **2017,** *35,* 773–780. doi:10.1038/nbt.3876
9. Lukinavičius, G.; Umezawa, K.; Olivier, N.; Honigmann, A.; Yang, G.; Plass, T.; Mueller, V.; Reymond, L.; Corrêa, I. R., Jr.; Luo, Z.-G.; Schultz, C.; Lemke, E. A.; Heppenstall, P.; Eggeling, C.; Manley, S.; Johnsson, K. *Nat. Chem.* **2013,** *5,* 132–139. doi:10.1038/nchem.1546
10. Shieh, P.; Siegrist, M. S.; Cullen, A. J.; Bertozzi, C. R. *Proc. Natl. Acad. Sci. U. S. A.* **2014,** *111,* 5456–5461. doi:10.1073/pnas.1322727111
11. Iwatate, R. J.; Kamiya, M.; Umezawa, K.; Kashima, H.; Nakadate, M.; Kojima, R.; Urano, Y. *Bioconjugate Chem.* **2018,** *29,* 241–244. doi:10.1021/acs.bioconjchem.7b00776
12. Kim, E.; Yang, K. S.; Kohler, R. H.; Dubach, J. M.; Mikula, H.; Weissleder, R. *Bioconjugate Chem.* **2015,** *26,* 1513–1518. doi:10.1021/acs.bioconjchem.5b00152
13. Hanaoka, K.; Kagami, Y.; Piao, W.; Myochin, T.; Numasawa, K.; Kuriki, Y.; Ikeno, T.; Ueno, T.; Komatsu, T.; Terai, T.; Nagano, T.; Urano, Y. *Chem. Commun.* **2018,** *54,* 6939–6942. doi:10.1039/c8cc02451k
14. Du, M.; Huo, B.; Liu, J.; Li, M.; Fang, L.; Yang, Y. *Anal. Chim. Acta* **2018,** *1030,* 172–182. doi:10.1016/j.aca.2018.05.013
15. Koide, Y.; Urano, Y.; Hanaoka, K.; Terai, T.; Nagano, T. *ACS Chem. Biol.* **2011,** *6,* 600–608. doi:10.1021/cb1002416
16. Wang, T.; Zhao, Q.-J.; Hu, H.-G.; Yu, S.-C.; Liu, X.; Liu, L.; Wu, Q.-Y. *Chem. Commun.* **2012,** *48,* 8781–8783. doi:10.1039/c2cc34159j
17. Wang, B.; Cui, X.; Zhang, Z.; Chai, X.; Ding, H.; Wu, Q.; Guo, Z.; Wang, T. *Org. Biomol. Chem.* **2016,** *14,* 6720–6728. doi:10.1039/c6ob00894a
18. Egawa, T.; Hanaoka, K.; Koide, Y.; Ujita, S.; Takahashi, N.; Ikegaya, Y.; Matsuki, N.; Terai, T.; Ueno, T.; Komatsu, T.; Nagano, T. *J. Am. Chem. Soc.* **2011,** *133,* 14157–14159. doi:10.1021/ja205809h
19. Huang, Y.-L.; Walker, A. S.; Miller, E. W. *J. Am. Chem. Soc.* **2015,** *137,* 10767–10776. doi:10.1021/jacs.5b06644

20. Zhang, H.; Liu, J.; Liu, C.; Yu, P.; Sun, M.; Yan, X.; Guo, J.-P.; Guo, W. *Biomaterials* **2017,** *133,* 60–69. doi:10.1016/j.biomaterials.2017.04.023
21. Huo, Y.; Miao, J.; Han, L.; Li, Y.; Li, Z.; Shi, Y.; Guo, W. *Chem. Sci.* **2017,** *8,* 6857–6864. doi:10.1039/c7sc02608k
22. Koide, Y.; Urano, Y.; Hanaoka, K.; Terai, T.; Nagano, T. *J. Am. Chem. Soc.* **2011,** *133,* 5680–5682. doi:10.1021/ja111470n
23. Umezawa, K.; Yoshida, M.; Kamiya, M.; Yamasoba, T.; Urano, Y. *Nat. Chem.* **2017,** *9,* 279–286. doi:10.1038/nchem.2648
24. Grimm, J. B.; English, B. P.; Chen, J.; Slaughter, J. P.; Zhang, Z.; Revyakin, A.; Patel, R.; Macklin, J. J.; Normanno, D.; Singer, R. H.; Lionnet, T.; Lavis, L. D. *Nat. Methods* **2015,** *12,* 244–250. doi:10.1038/nmeth.3256
25. Grimm, J. B.; Muthusamy, A. K.; Liang, Y.; Brown, T. A.; Lemon, W. C.; Patel, R.; Lu, R.; Macklin, J. J.; Keller, P. J.; Ji, N.; Lavis, L. D. *Nat. Methods* **2017,** *14,* 987–994. doi:10.1038/nmeth.4403
26. Chi, W.; Qiao, Q.; Lee, R.; Liu, W.; Teo, Y. S.; Gu, D.; Lang, M. J.; Chang, Y.-T.; Xu, Z.; Liu, X. *Angew. Chem., Int. Ed.* **2019,** *58,* 7073–7077. doi:10.1002/anie.201902766
27. Ikeno, T.; Nagano, T.; Hanaoka, K. *Chem. – Asian J.* **2017,** *12,* 1435–1446. doi:10.1002/asia.201700385
28. Lavis, L. D.; Raines, R. T. *ACS Chem. Biol.* **2008,** *3,* 142–155. doi:10.1021/cb700248m
29. Savarese, M.; Aliberti, A.; De Santo, I.; Battista, E.; Causa, F.; Netti, P. A.; Rega, N. *J. Phys. Chem. A* **2012,** *116,* 7491–7497. doi:10.1021/jp3021485
30. Zhao, N.; Xuan, S.; Fronczek, F. R.; Smith, K. M.; Vicente, M. G. H. *J. Org. Chem.* **2017,** *82,* 3880–3885. doi:10.1021/acs.joc.6b02981
31. Hirabayashi, K.; Hanaoka, K.; Takayanagi, T.; Toki, Y.; Egawa, T.; Kamiya, M.; Komatsu, T.; Ueno, T.; Terai, T.; Yoshida, K.; Uchiyama, M.; Nagano, T.; Urano, Y. *Anal. Chem. (Washington, DC, U. S.)* **2015,** *87,* 9061–9069. doi:10.1021/acs.analchem.5b02331
32. Grimm, J. B.; Brown, T. A.; Tkachuk, A. N.; Lavis, L. D. *ACS Cent. Sci.* **2017,** *3,* 975–985. doi:10.1021/acscentsci.7b00247
33. Fischer, C.; Sparr, C. *Angew. Chem., Int. Ed.* **2018,** *57,* 2436–2440. doi:10.1002/anie.201711296
34. Kolmakov, K.; Hebisch, E.; Wolfram, T.; Nordwig, L. A.; Wurm, C. A.; Ta, H.; Westphal, V.; Belov, V. N.; Hell, S. W. *Chem. – Eur. J.* **2015,** *21,* 13344–13356. doi:10.1002/chem.201501394
35. Zhang, H.; Li, K.; Li, L.-L.; Yu, K.-K.; Liu, X.-Y.; Li, M.-Y.; Wang, N.; Liu, Y.-H.; Yu, X.-Q. *Chin. Chem. Lett.* **2019,** *5,* 1063–1066. doi:10.1016/j.cclet.2019.03.017
36. Dolci, L.; Dolle, F.; Jubeau, S.; Vaufrey, F.; Crouzel, C. *J. Labelled Compd. Radiopharm.* **1999,** *42,* 975–985. doi:10.1002/(sici)1099-1344(199910)42:10<975::aid-jlcr256>3.0.co;2-e
37. Olberg, D. E.; Arukwe, J. M.; Grace, D.; Hjelstuen, O. K.; Solbakken, M.; Kindberg, G. M.; Cuthbertson, A. *J. Med. Chem.* **2010,** *53,* 1732–1740. doi:10.1021/jm9015813
38. Naumiec, G. R.; Cai, L.; Lu, S.; Pike, V. W. *Eur. J. Org. Chem.* **2017,** 6593–6603. doi:10.1002/ejoc.201700970
39. Zielonka, J.; Joseph, J.; Sikora, A.; Hardy, M.; Ouari, O.; Vasquez-Vivar, J.; Cheng, G.; Lopez, M.; Kalyanaraman, B. *Chem. Rev.* **2017,** *117,* 10043–10120. doi:10.1021/acs.chemrev.7b00042
40. Murphy, M. P. *Biochim. Biophys. Acta, Bioenerg.* **2008,** *1777,* 1028–1031. doi:10.1016/j.bbabio.2008.03.029
41. Murphy, M. P.; Smith, R. A. J. *Adv. Drug Delivery Rev.* **2000,** *41,* 235–250. doi:10.1016/s0169-409x(99)00069-1
42. Murayama, C.; Kawaguchi, A. T.; Kamijo, A.; Naito, K.; Kanazawa, M.; Tsukada, H. *PLoS One* **2017,** *12,* e0170911. doi:10.1371/journal.pone.0170911
43. Li, J.; Lu, J.; Zhou, Y. *BioMed Res. Int.* **2017,** No. 5246853. doi:10.1155/2017/5246853
44. Rideout, D. C.; Calogeropoulou, T.; Jaworski, J. S.; Dagnino, R., Jr.; McCarthy, M. R. *Anticancer Drug Des.* **1989,** *4,* 265–280.
45. Murphy, M. P. *Trends Biotechnol.* **1997,** *15,* 326–330. doi:10.1016/s0167-7799(97)01068-8
46. Sung, J.; Rho, J. G.; Jeon, G. G.; Chu, Y.; Min, J. S.; Lee, S.; Kim, J. H.; Kim, W.; Kim, E. *Bioconjugate Chem.* **2019,** *30,* 210–217. doi:10.1021/acs.bioconjchem.8b00845
47. Mallet, M.; Quéguiner, G. *Tetrahedron* **1979,** *35,* 1625–1631. doi:10.1016/0040-4020(79)80026-5
48. Miller, R. E.; Rantanen, T.; Ogilvie, K. A.; Groth, U.; Snieckus, V. *Org. Lett.* **2010,** *12,* 2198–2201. doi:10.1021/ol100493v
49. Schnürch, M.; Spina, M.; Khan, A. F.; Mihovilovic, M. D.; Stanetty, P. *Chem. Soc. Rev.* **2007,** *36,* 1046–1057. doi:10.1039/b607701n
50. Schlosser, M. *Angew. Chem., Int. Ed.* **2005,** *44,* 376–393. doi:10.1002/anie.200300645
51. Erb, W.; Mongin, F. *Tetrahedron* **2016,** *72,* 4973–4988. doi:10.1016/j.tet.2016.06.078
52. Hell, S. W.; Wichmann, J. *Opt. Lett.* **1994,** *19,* 780–782. doi:10.1364/ol.19.000780
53. Hell, S. W. *Science* **2007,** *316,* 1153–1158. doi:10.1126/science.1137395
54. Giedt, R. J.; Fumene Feruglio, P.; Pathania, D.; Yang, K. S.; Kilcoyne, A.; Vinegoni, C.; Mitchison, T. J.; Weissleder, R. *Sci. Rep.* **2016,** *6,* No. 32985. doi:10.1038/srep32985
55. Erdmann, R. S.; Takakura, H.; Thompson, A. D.; Rivera-Molina, F.; Allgeyer, E. S.; Bewersdorf, J.; Toomre, D.; Schepartz, A. *Angew. Chem., Int. Ed.* **2014,** *53,* 10242–10246. doi:10.1002/anie.201403349
56. Lukinavičius, G.; Blaukopf, C.; Pershagen, E.; Schena, A.; Reymond, L.; Derivery, E.; Gonzalez-Gaitan, M.; D'Este, E.; Hell, S. W.; Wolfram Gerlich, D.; Johnsson, K. *Nat. Commun.* **2015,** *6,* 8497. doi:10.1038/ncomms9497
57. Lukinavičius, G.; Reymond, L.; D'Este, E.; Masharina, A.; Göttfert, F.; Ta, H.; Güther, A.; Fournier, M.; Rizzo, S.; Waldmann, H.; Blaukopf, C.; Sommer, C.; Gerlich, D. W.; Arndt, H.-D.; Hell, S. W.; Johnsson, K. *Nat. Methods* **2014,** *11,* 731–733. doi:10.1038/nmeth.2972
58. Yang, X.; Yang, Z.; He, Y.; Shan, C.; Yan, W.; Wu, Z.; Chai, P.; Teng, J.; Qu, J.; Xi, P. *bioRxiv* **2019,** 646117. doi:10.1101/646117

BEILSTEIN JOURNAL OF ORGANIC CHEMISTRY

Mono- and bithiophene-substituted diarylethene photoswitches with emissive open or closed forms

A. Lennart Schleper[1,2], Mariano L. Bossi[3], Vladimir N. Belov[*1] and Stefan W. Hell[1,3]

Full Research Paper

Open Access

Address:
[1]Department of NanoBiophotonics, Max Planck Institute for Biophysical Chemistry, 37077 Göttingen, Germany, [2]Department of Organic Chemistry, Heidelberg University, Im Neuenheimer Feld 270, 69120 Heidelberg, Germany and [3]Department of Optical Nanoscopy, Max Planck Institute for Medical Research, Jahnstrasse 29, 69120 Heidelberg, Germany

Email:
Vladimir N. Belov[*] - vbelov@mpibpc.mpg.de

* Corresponding author

Keywords:
diarylethenes; dyes; fluorescence; organic synthesis; photochromism; photoswitching

Beilstein J. Org. Chem. **2019,** *15,* 2344–2354.
doi:10.3762/bjoc.15.227

Received: 31 May 2019
Accepted: 10 September 2019
Published: 01 October 2019

This article is part of the thematic issue "Dyes in modern organic chemistry".

Guest Editor: H. Ihmels

Abstract

We present a new series of photochromic 1,2-bis(2-ethylbenzo[*b*]thiophen-3-yl)perfluorocyclopentenes with an oxidized benzothiophene core (O) or a nonoxidized one, decorated with mono- (Th_1) and bithiophene (Th_2) units attached to positions 6 and 6′ (Sy = symmetric) or only to position 6 (As = asymmetric). "Oxidized" compounds have highly fluorescent closed forms emitting in the visible region (yellow to red). The dyes with nonoxidized benzothiophenes possess fluorescent open forms with rather low emission efficiency. The photoswitching kinetics was studied at several wavelengths with UV and visible light. New diarylethenes underwent ring-closure reactions by irradiation with UV light (365 nm, 405 nm), and the reversible ring-opening by irradiation with visible light (470 nm, 530 nm). The on-switching of fluorescence due to the ring-closure reaction was observed also with visible light of 470 nm (to an extent of 10% for compound **SyOTh$_1$**) and attributed to the Urbach tail effect. Due to a high degree of fluorescence modulation (>270), good fatigue resistance and large fluorescence quantum yield, compound **SyOTh$_1$** emerged as a candidate for single-molecule based super-resolution fluorescence microscopy.

Introduction

Reversibly photoswitchable diarylethenes (DAEs) with highly fluorescent "closed" forms combine photochromic and fluorescent entities in one molecule [1] and contain a perfluorocyclopentene bridge linking two 2-alkyl-1-benzothiophene-1,1-oxide residues with a C=C bond via C-3 and C-3′ atoms [2,3]. The "open" form of the DAE core (see graphical abstract and Table 1) is only weakly fluorescent ($\varphi_{Fl} \approx 0.01$) [4]. In general, diarylethenes with fluorescent open forms are rare, while photoswitchable compounds with highly fluorescent "open" *and* "closed" forms represent a yet unknown and unique class of ratiometric fluorophores.

Recently, we demonstrated that asymmetric DAEs with oxidized 2-ethylbenzo[*b*]thiophene-3-yl units have high cyclo-

reversion quantum yields (a desirable feature for super-resolution RESOLFT microscopy), large Stokes shifts and acceptable absorptivity [5]. Yet unknown asymmetric "thiophenylated" DAEs may have unique properties. Oligothiophenes are highly fluorescent [6,7], and therefore, we reasoned that their incorporation into DAEs with oxidized 2-alkylbenzo[*b*]thiophene units might produce fluorescent open forms in addition to the intrinsic fluorescence of the closed forms. In particular, we expected that the prolonged conjugation path, even at "one side" of the molecule (in asymmetric compounds) would enable switching with focusable light of 375 nm and above. To test this hypothesis, we designed a series of DAEs with mono- and bithiophene substituents attached to positions 6 and 6′ of an oxidized or a nonoxidized 2-alkylbenzo[*b*]thiophene core. The structures of "thiophenylated" DAEs **AsTh$_1$**, **AsTh$_2$**, **SyTh$_1$**, **SyTh$_2$**, **AsOTh$_1$**, **AsOTh$_2$**, **SyOTh$_1$**, and **SyOTh$_2$** prepared and studied in this work are given in Figure 1.

Methyl esters of the thiophene carboxylic acids were chosen as model building blocks, because they possess optical properties similar to the free acids. The future promising candidates which were expected to emerge in the course of synthesis and screening could be eventually transformed to the corresponding carboxylic acids possessing higher solubility in aqueous buffers and reactive groups required for bioconjugation.

Results and Discussion

Synthetic procedures

To enable a facile synthesis of oxidized and nonoxidized 1,2-bis(2-ethylbenzo[*b*]thiophen-3-yl)perfluorocylopentenes

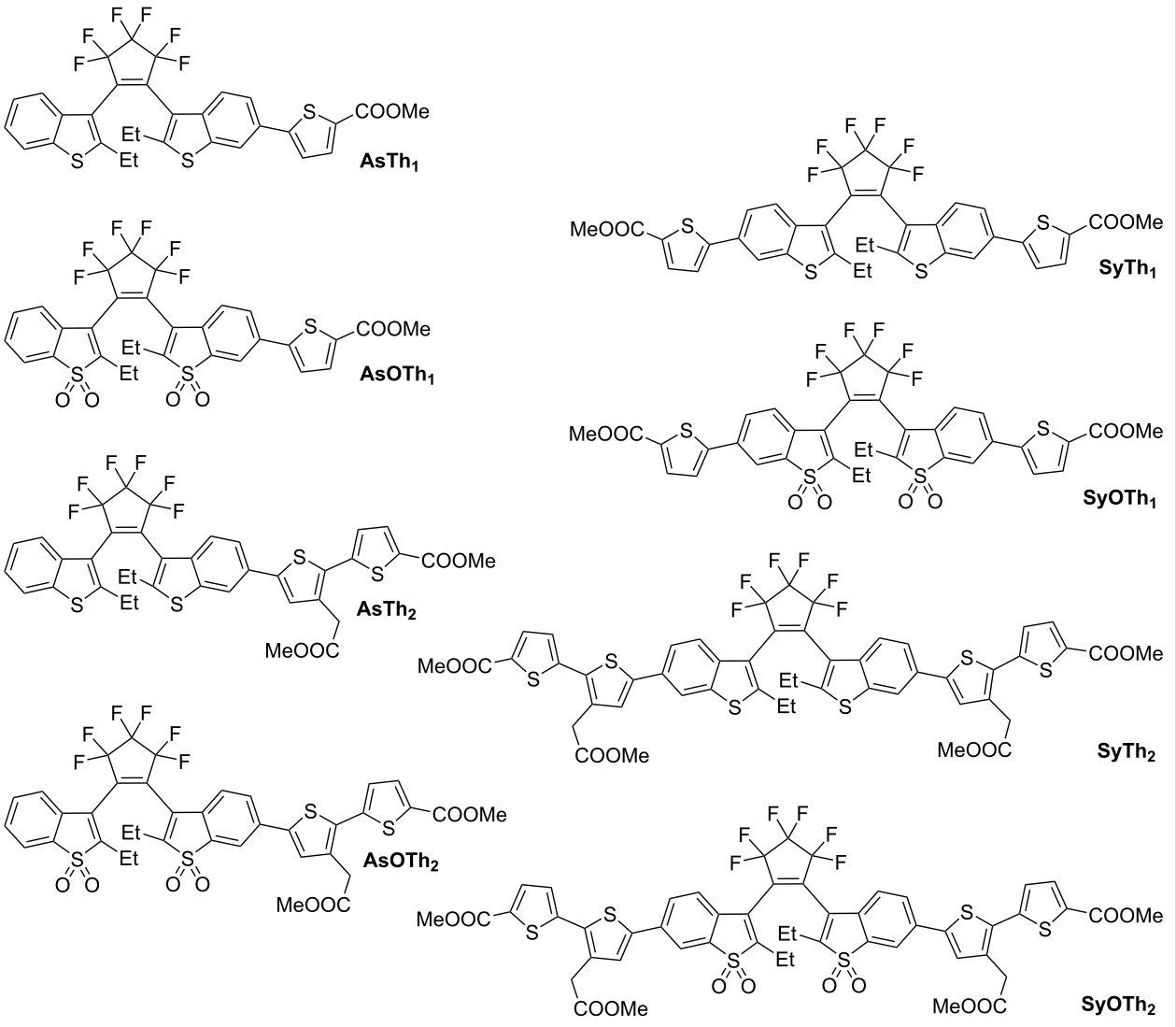

Figure 1: Structures of "thiophenylated" DAEs prepared and studied in this work.

decorated with thiophene units, mono- and diiodinated core structures **4**, **5**, **7**, and **8** (Scheme 1), as well as mono- and bithiopheneboronic esters **9** and **12** (Scheme 2) were prepared.

The transformations leading to diarylethene cores **3** and **6** were carried out on a 10–100 mmol scale (Scheme 1). The iodination at positions 6 and 6' of benzo[*b*]thiophene residues has been reported [5,8]. Following those protocols, diiodides **5** and

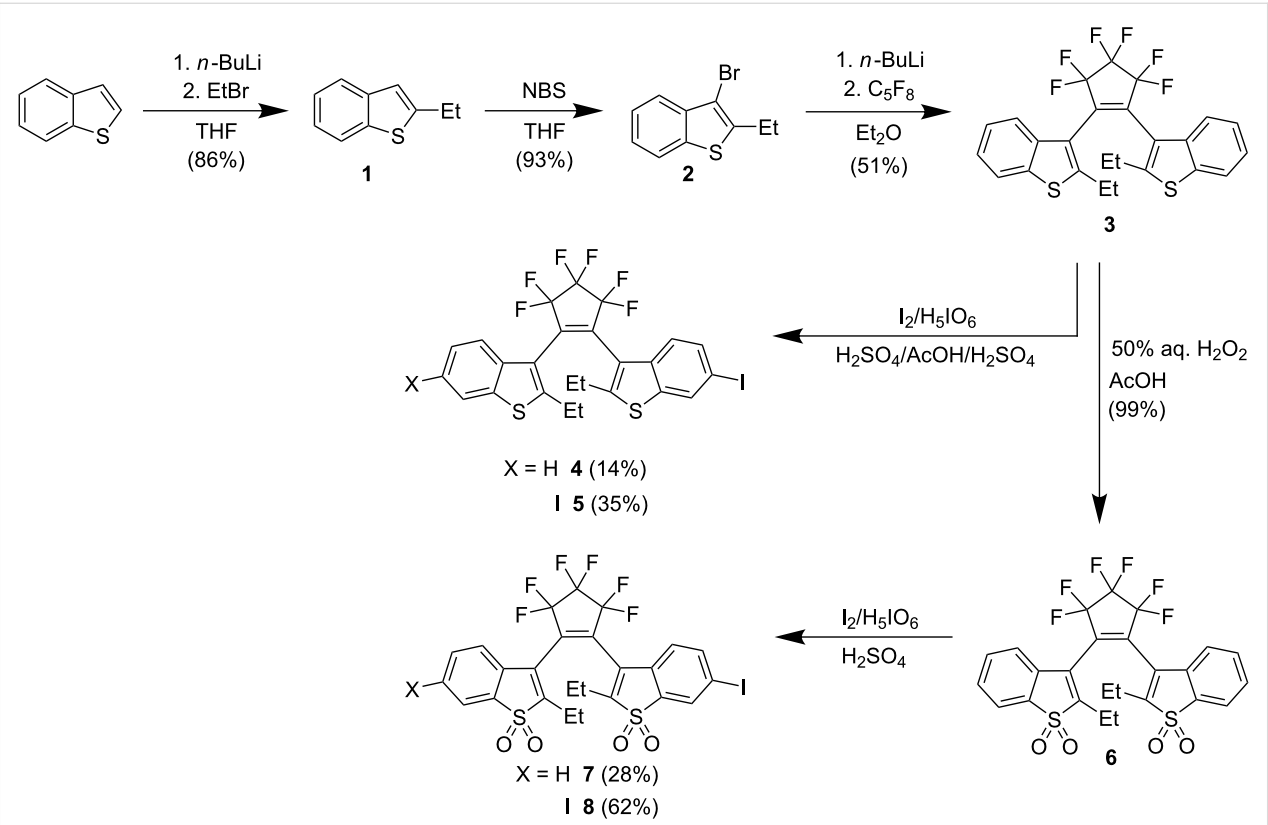

Scheme 1: Synthesis routes towards mono- and diiodinated core structures **4**, **5**, **7**, and **8**.

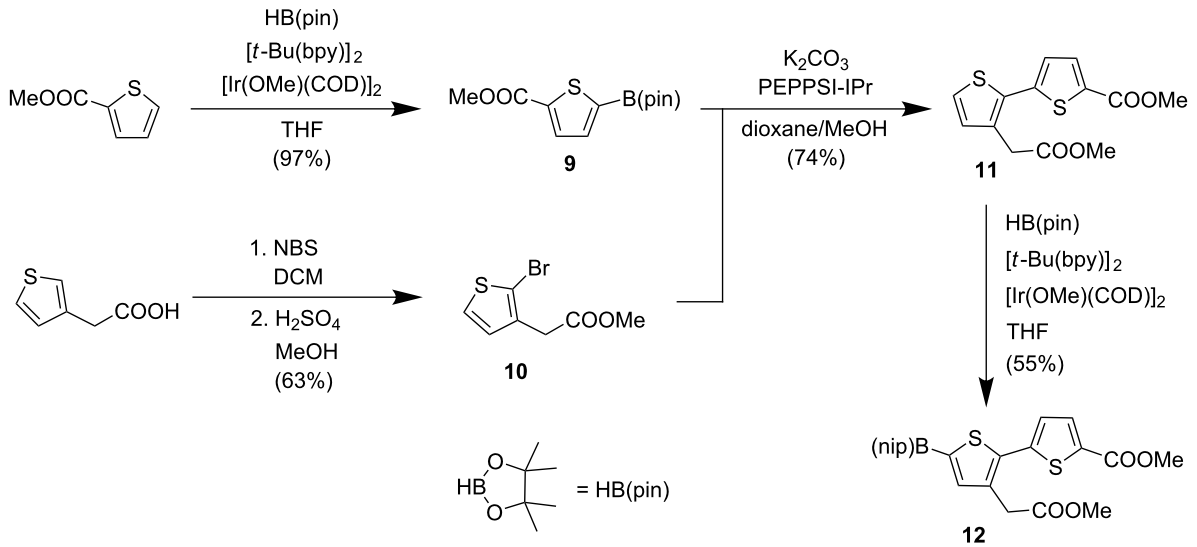

Scheme 2: Synthesis of thiophene- and bithiopheneboronic esters **9** and **12** (bpy – 4,4'-di-*tert*-butyl-2,2'-dipyridine; COD – cycloocta-1,5-diene; NBS – *N*-bromosuccinimide, DCM – dichloromethane).

8 were obtained in fairly good yields by treatment of **3** with elemental iodine and periodic acid in aqueous acetic acid with addition of sulfuric acid, and by treatment of **6** with elemental iodine and periodic acid in concentrated sulfuric acid, respectively. The conditions for monoiodination of **6** have been published recently [5]. We observed that the reproducible monoiodination of DAE **3** to form compound **4** was possible under similar conditions and in low yield (14%) by using smaller amounts of periodic acid (0.34 equiv) and iodine (0.68 equiv) than the amounts of these reagents used for diiodination (see Experimental for details). The progress of the reaction leading to monoiodide **4** was monitored by HPLC. Despite incomplete conversion, the formation of diiodide **5** could not be fully suppressed. The R_f values of **3** (TLC [SiO_2, hexane]: $R_f = 0.17$), monoiodide **4** ($R_f = 0.19$), and diiodide **5** ($R_f = 0.20$) were very similar, and DAE **4** could not be isolated by column chromatography on regular silica gel. Instead, monoiodide **4** was obtained in 14% yield as colorless solid after preparative HPLC on a reversed phase (C18) column and lyophilization. The constitution and structure of **4** was confirmed by HRMS, ^{1}H and ^{19}F NMR spectroscopy (see Figure S1 in Supporting Information File 1). These results show that "desymmetrization" of DAEs still represents a real synthetic challenge. Diiodides **5** and **8** provide the possibility [9,10] to obtain symmetric DAEs, and monoiodides **4** and **7** allow for a short and straightforward approach towards asymmetric DAEs.

The thiophene- and bithiopheneboronic esters **9** and **12** were prepared as shown in Scheme 2. C–H activation of methyl thiophene-2-carboxylate in position 5 was achieved by using a bis(1,5-cyclooctadiene)di-μ-methoxydiiridium(I) catalyst with 4,4'-di-*tert*-butyl-2,2'-dipyridyl as ligands. The reaction with pinacolborane (HB(pin)) gave ester **9** in 97% yield [11]. Another ester (**10**) was synthesized by bromination of 3-thiopheneacetic acid with NBS (applying an ultrasound bath) followed by esterification of the crude product with methanol in the presence of sulfuric acid [12]. Other regioisomeric bromides were also formed, but they were separated by column chromatography on the next step. Bithiophene **11** was prepared in 74% yield by using a Suzuki–Miyaura coupling (catalyzed by PEPPSI-IPr) between boronic ester **9** and bromide **10** [13,14]. Boronation of bithiophene **11** was achieved under conditions similar to the preparation of thiophene **9** and afforded ester **12** in 55% yield (79% crude yield with 70% purity). However, in this case, larger amounts of catalyst and pinacolborane were required for good conversions.

Finally, the photoswitchable DAEs **AsTh$_1$**, **SyTh$_1$**, **AsTh$_2$**, **SyTh$_2$**, **AsOTh$_1$**, **SyOTh$_1$**, **AsOTh$_2$**, and **SyOTh$_2$** (Figure 1) were obtained using a standard procedure for a Suzuki–Miyaura coupling of iodides **4**, **5**, **7**, and **8** with boronic acid esters **9** and **12** (see Scheme 3). Throughout the text, abbreviations "As" and "Sy" denote asymmetric and symmetric substitution patterns, respectively; "O" indicates oxidized benzothiophene units, and "Th_1"/ "Th_2" specify the number of thiophene units in the side chain. The coupling products were isolated via preparative HPLC in yields ranging from 21% to 75%. While in all cases the open forms of the diarylethenes were isolated, small amounts of **SyOTh$_1$** in its closed form (formed by handling in the lab not fully protected from light) were detected by HPLC (Figure S33 in Supporting Information File 1). The constitution, structures, and purities of the final products were confirmed by HRMS, ^{1}H and ^{19}F NMR spectroscopy, as well as analytical HPLC.

Saponification of the ester groups was performed only for nonoxidized benzothiophenes, as shown for compound **SyTh$_2$** in Scheme 4. Diarylethenes with "oxidized" benzothiophene units and perfluorocyclopentene rings react with aqueous or alcoholic solutions of strong bases [5,10,15]. Under these conditions, substitution of fluorine and/or the addition of nucleophiles to the electron-poor double bond take place. Therefore, *tert*-butyl protection is required for carboxylates present in diarylethenes with "oxidized" benzothiophene units and perfluorocyclopentene rings. Photoswitches containing the free carboxylic acid residues benefit from solubility in aqueous buffers and the presence of a reactive group required for further modifications. The methyl groups were cleaved using 1 M aq NaOH, and the product **SyTh$_2$-H** was isolated by preparative HPLC in 84% yield (see Scheme 4). As shown in Figure S2 (see Supporting Information File 1), tetraester **SyTh$_2$** displayed six ^{1}H NMR signals between 3.70 and 4.00 ppm, belonging to two inequivalent methyl ester groups and the methylene group of the parallel and antiparallel isomers. After the reaction, four of the six signals vanished, and only two methylene signals (two isomers) were detected, confirming cleavage of the methyl esters.

Photophysical properties

The absorption and emission properties as well as the photochromic properties of eight "thiophenylated" DAEs were studied in acetonitrile solutions (Table 1). The properties of the OFs (open forms) were obtained from diluted solutions at a known concentration prior to irradiation. Solutions were irradiated in a home-made setup [5] with 355 nm light until the photostationary state ($PSS_{365\ nm}$). Figure 2 shows changes of absorption and emission spectra in the course of the switching process for compound **SyTh$_2$**. Irradiated solutions in the $PSS_{365\ nm}$ were analyzed by HPLC at the isosbestic point. Conversion to the CF (closed form) α_{PSS} = [CF]/([CF] + [OF]) was calculated from the proportion of the area corresponding to the CF ($area_{CF}$/[$area_{CF}$ + $area_{OF}$]). The absorption spectrum of the

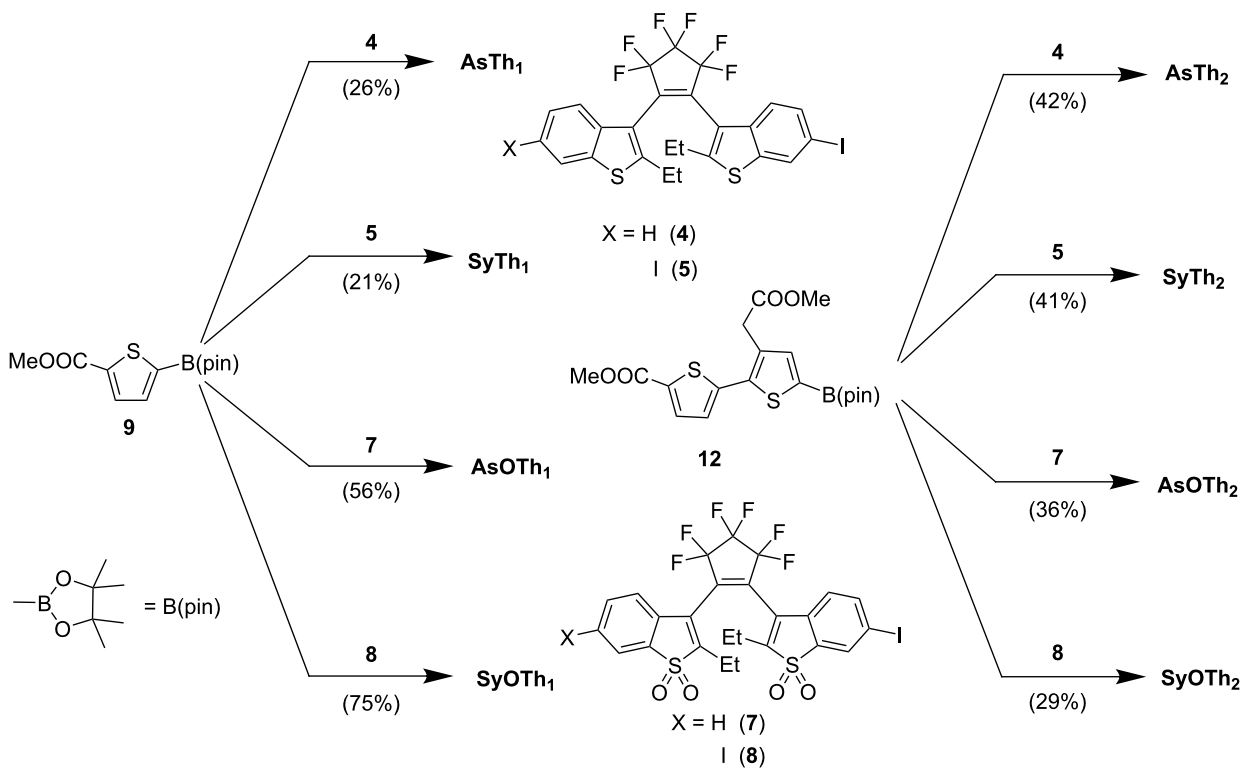

Scheme 3: Photoswitchable diarylethenes **AsTh$_1$**, **SyTh$_1$**, **AsTh$_2$**, **SyTh$_2$**, **AsOTh$_1$**, **SyOTh$_1$**, **AsOTh$_2$**, and **SyOTh$_2$** synthesized via a Suzuki–Miyaura coupling. Conditions: 60 °C, argon atmosphere, an emulsion of the starting compounds, $Pd_2(dba)_3$, $P(Cy)_3$ stock solution, and aqueous K_2CO_3 in THF (see Supporting Information File 1 for details).

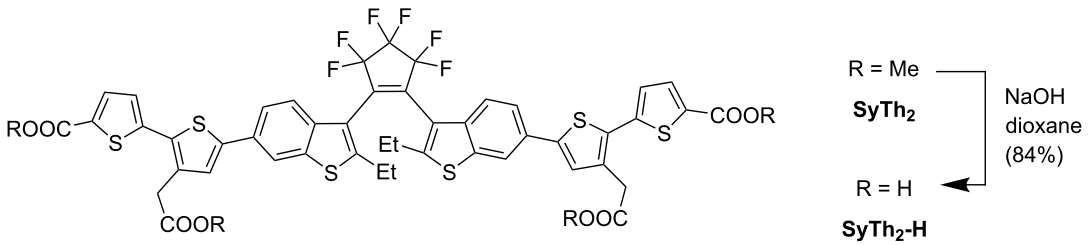

Scheme 4: Saponification of methyl ester groups in tetraester **SyTh$_2$** leading to tetracarboxylic acid **SyTh$_2$-H**.

CF was calculated from the absorption spectrum at the $PSS_{365\ nm}$ and the absorption spectrum of the OF, using the obtained conversion. The obtained spectra for all CF's matched, within experimental errors, the absorption recorded on the diode array detector of the HPLC, at the center of the elution peak of the corresponding isomer (see for example, Figures S26 and S38 in Supporting Information File 1). Emission properties of the CF's were obtained from solutions at the $PSS_{365\ nm}$, with excitation at a wavelength at which the OF's do not absorb (only the CF absorbs). The data on switching kinetics is given in Table 2 and discussed in the next section.

We first analyzed the absorption spectra of the open forms (see Figure 3A) in more detail. Addition of thiophene rings to the core structures **3** and **6** induced a red-shift in the OF (Table 1) [4,16]. Their absorption maxima were located between 327 nm and 385 nm, and present interesting correlations. First, the positions of the main absorption bands of the corresponding symmetric and asymmetric DAEs were very similar. The symmetric DAEs have higher absorption coefficients than their asymmetric counterparts (by a factor of 1.3–3.2). Considering the very similar band positions, this indicates that in the OF each benzothiophene unit (with aligning thiophene group(s)) contrib-

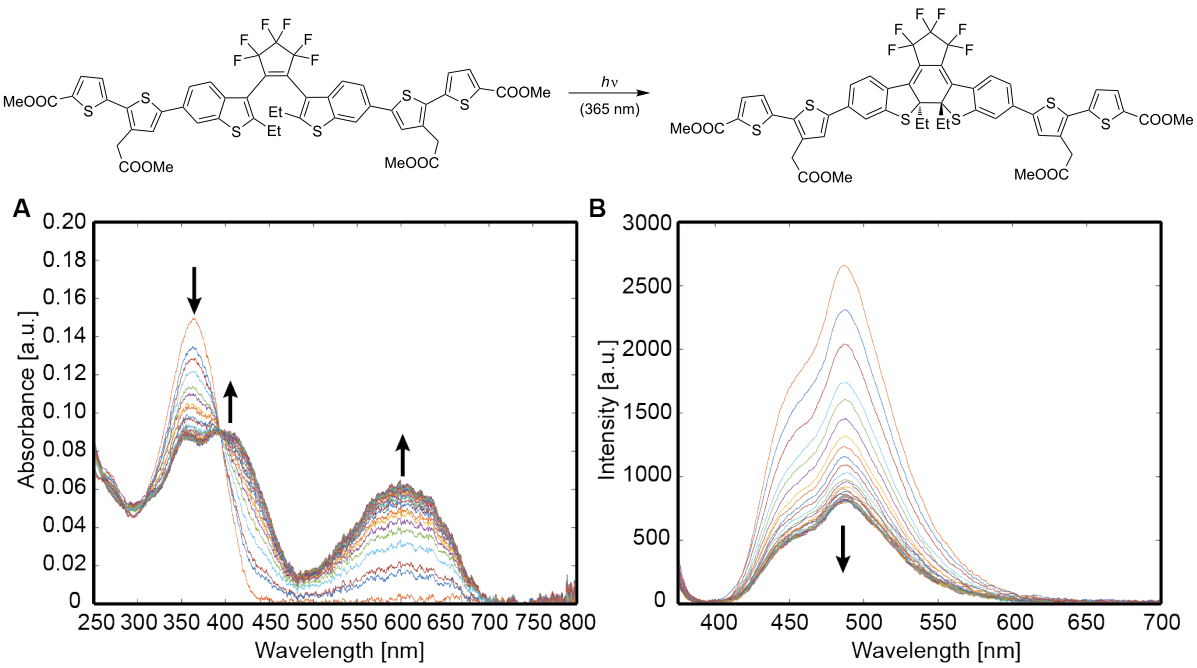

Figure 2: Absorption (A) and emission (B) spectra of **SyTh$_2$** in acetonitrile in the course of the cyclization reaction (irradiation at 365 nm). Emission was not fully depleted due to incomplete conversion in the photostationary state (PSS, α = 71%).

Table 1: Optical properties of the photochromic DAEs (in acetonitrile solution).

	Absorption					Emission						Stokes shift [nm] (cm^{-1})
	OF[a]		CF[a]		Separation[b]	OF			CF			
	λ_{abs} [nm]	$\varepsilon/10^3$ [$M^{-1}cm^{-1}$]	λ_{abs} [nm]	$\varepsilon/10^3$ [$M^{-1}cm^{-1}$]	[nm] (cm^{-1})	λ_{em}[c] (λ_{ex}) [nm]	φ_{Fl}[d]	τ_{Fl}[e] [ns]	λ_{em}[c] (λ_{ex}) [nm]	φ_{Fl}[d]	τ_{Fl}[e] [ns]	
AsTh$_1$	327	25.8	562	13.5	235 (12800)	410 (320)	0.01	0.20	–	–	–	83 (6190)
SyTh$_1$	328	50.6	584	21.3	256 (13400)	410 (340)	0.01	0.23	–	–	–	82 (6100)
AsTh$_2$	363	20.0	566	12.1	203 (9880)	462 (360)	0.09	0.24	–	–	–	99 (5900)
SyTh$_2$	363	63.1	591	32.5	228 (10600)	469 (410)	0.08	0.24	–	–	–	106 (6230)
AsOTh$_1$	356	15.5	447	37.1	91 (5720)	–	–	–	550 (460)	0.36	1.63	103 (4190)
SyOTh$_1$	355	31.4	478	53.5	123 (7250)	–	–	–	560 (470)	0.48	1.91	82 (3060)
AsOTh$_2$	385	36.4	480	58.6	95 (5140)	–	–	–	656 (460)	0.16	1.28	176 (5590)
SyOTh$_2$	384	47.9	524	63.8	140 (6960)	–	–	–	670 (530)	0.18	1.16	146 (4160)
3[f] [16]	258	16.5	536	9.6	278 (20100)	–	–	–	–	–	–	–
6 [4]	310	5.3	412	23.7	102 (7990)	464	0.01	0.26[g] 5.04[h]	509	0.06	0.51	154[i] (10700)[i] 97[j] (4630)[j]

[a]Wavelength and extinction coefficient at the absorption maxima. [b]Separation between absorption maxima of OF and CF. [c]Position of the emission maxima (excitation wavelength). [d]Fluorescence quantum yield. [e]Fluorescence lifetime. [f]In hexane solution. [g]Parallel isomer. [h]Antiparallel isomer. [i]OF (open form). [j]CF (closed form).

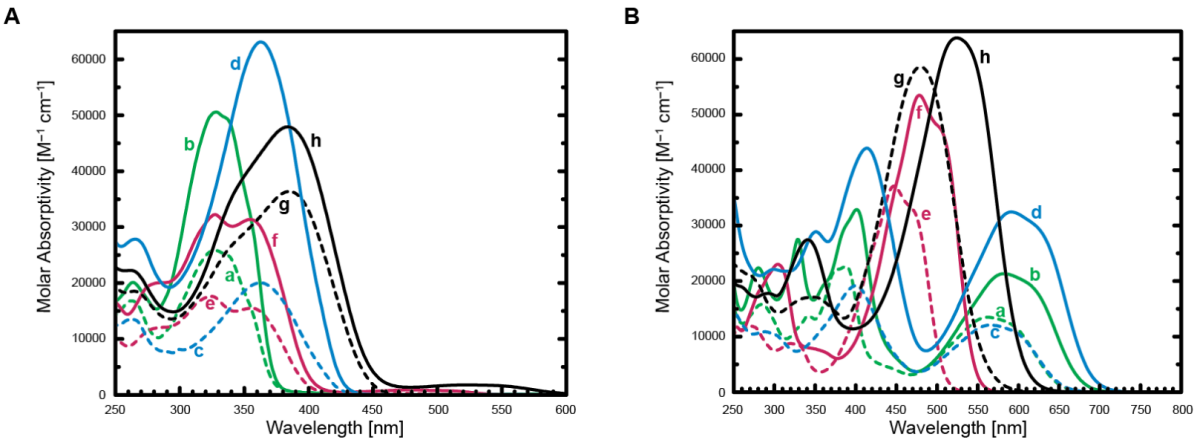

Figure 3: Absorption spectra of the OFs (A) and CFs (B) of **AsTh$_1$** (a), **SyTh$_1$** (b), **AsTh$_2$** (c), **SyTh$_2$** (d), **AsOTh$_1$** (e), **SyOTh$_1$** (f), **AsOTh$_2$** (g), and **SyOTh$_2$** (h). The absorption of the OFs in (A) above 460 nm is due to the presence of low amounts of the corresponding CFs (formed during manipulation of the solids and/or preparation of the solutions).

utes into absorption independently. It was confirmed that asymmetric compounds with "compact" structures can be transformed to the closed form with the same light as bulkier analogs (the latter featuring slower ring-opening reactions; see Table 2). Second, a bithiophene residue induces a red-shift of 30–35 nm in the absorption of the OF with respect to a monothiophene ring. The oxidized DAEs (OF) absorbed at higher wavelengths than the corresponding nonoxidized analogs (by ca. 20–30 nm), and a splitting of the band is observed with a shoulder appearing at the blue edge. In general, substitution in the OF with a bithiophene side chain induced a slightly larger red-shift than oxidation of benzothiophene units.

The absorption maxima of the CFs were located between 447 nm and 591 nm; they present remarkably larger differences than the corresponding OFs (see Figure 3B). Compared with the parent compounds **3** and **6** [4,16], the CFs of all new DAEs displayed, again, red-shifted absorption bands. Unlike for the OFs (Figure 3A), oxidation produces a strong blue shift of the absorption bands of the CF (compare the curves a–d and e–h in Figure 3B). This shift is stepwise reduced from 124 nm in the unsubstituted compounds (**3**→**6**), to 65 nm in the presence of four thiophene residues (**SyTh$_2$**→**SyOTh$_2$**). It is worth noting that for asymmetric compounds (**AsTh$_2$**→**AsOTh$_2$**), the shift (20 nm) is smaller than for symmetric DAEs having the same total number of thiophene rings (**SyTh$_1$**→**SyOTh$_1$**). All CFs showed several absorption bands, while nonoxidized DAEs have two distinct absorption bands in the visible range. The data in Figure 3 indicate that, contrary to the OF, both benzo[*b*]thiophene moieties (with side rings) interact and determine the location of the absorption band in the CF. If we compare the absorption spectra of **SyOTh$_1$** and **AsOTh$_2$**, we see that the most red-shifted bands have very similar positions. This is a remarkable feature, as both compounds consist of the same parts: two oxidized benzothiophenes and, in total, two thiophenes as substituents. It appears that the sequence of the building blocks is less important than their nature and quantity. The same regularity holds true (with less precision) for the most red-shifted absorption bands of **SyTh$_1$** and **AsTh$_2$** (CFs have 18 nm difference in band positions); both DAEs consisting of same building blocks, again!

If we consider the positions of the absorption bands of the OF and CF of each oxidized DAE, we observe that they are separated "only" by 90–140 nm. On the other hand, in nonoxidized DAEs, these bands are separated by 200–260 nm. This large difference is justified by the fact that the oxidation red-shifts the band positions of the OF, and blue-shifts the band positions of the CF. A conversion of the separation between the absorption bands from wavelengths to wavenumbers allows the evaluation of the relative energy gaps between the HOMO and LUMO. We can see that the energy gap between HOMO and LUMO in nonoxidized DAEs is decreased to a higher extent upon cyclization than in oxidized DAEs. Furthermore, we noted that asymmetric DAEs have a smaller separation between absorption maxima of OF and CF than their symmetric counterparts. We observed that nonoxidized DAEs exhibited a higher extinction coefficient in the OF than in the CF (by a factor of 1.7–2.4); oxidized DAEs revealed an opposite trend (higher absorption in the CF by a factor of 1.3–2.4).

New DAEs have very different emission properties (see Figure 4 and Table 1). the oxidized DAEs strongly emit in their CFs, and the nonoxidized DAEs emit in their OFs, but rather weakly. Interestingly, unsubstituted DAEs **3** and **6** (Scheme 1) were either nonemissive at all (**3**), or very poorly emissive in

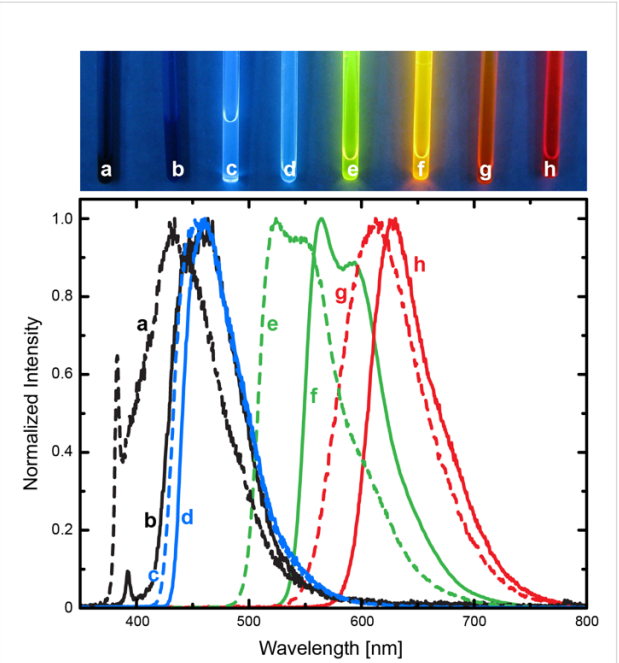

Figure 4: Solutions of compounds **AsTh$_1$** (a), **SyTh$_1$** (b), **AsTh$_2$** (c), **SyTh$_2$** (d), **AsOTh$_1$** (e), **SyOTh$_1$** (f), **AsOTh$_2$** (g), and **SyOTh$_2$** (h) in $CDCl_3$ as mixtures of OFs and CFs under irradiation with 366 nm (top), and the corresponding emission spectra in MeCN (bottom). Emission of the compounds covers the range from UV to the blue and red regions. Sharp peaks at ca. 390 nm (a and b) are Raman bands of the solvent.

both forms (**6**) [4,16]. The new DAEs – when nonoxidized – possessed blue emission with maxima between 410 nm and 470 nm. In this case, the difference in emission between asymmetric and symmetric substitution patterns was negligible. This feature can be explained by the fact that due to the twisted conformation of the open form, the emission transition involves the isolated benzothiophene unit (including the side ring). As expected, in MeCN quantum yields of nonoxidized compounds with a bithiophene side chain were higher (ca. 8% compared to 1% for a monothiophene derivative), but still moderate. Fluorescence lifetimes were short (0.2 ns), in accordance with moderate quantum yields.

The oxidized compounds were strongly fluorescent in their closed forms, with emission maxima in the range between 550 nm and 670 nm. The difference between the positions of emission bands of the structurally related symmetric and asymmetric compounds was small, compared to the change caused by an additional thiophene ring to the benzothiophene core. Oxidized DAEs with monothiophene units as side chains exhibited higher fluorescence quantum yields than the structurally related DAEs with bithiophenes (>35% compared to <20%). Longer fluorescent lifetimes (1.3–1.9 ns) of the oxidized DAEs (CFs) correspond to the better fluorescence quantum yields. They exceeded lifetimes measured for the fluorescence of the unsubstituted DAE **6** by a factor of 4, and the fluorescence quantum yield of the CF of **6** was surpassed by the oxidized DAEs with thiophene side rings by a factor of 3–8 [4]. The open forms of the substituted oxidized compounds were nonemissive.

The Stokes shift of the OFs of nonoxidized DAEs was always ca. 6000 cm^{-1}, independent of the substitution pattern. For comparison, this value was much lower than the Stokes shift of the OF of compound **6** (10,700 cm^{-1}) [4]. The Stokes shift of the CFs of oxidized DAEs varied between 3000 cm^{-1} and 5600 cm^{-1}, which is comparable with the Stokes shift observed for the CF of **6** (4600 cm^{-1}) [4]. In the case of oxidized DAEs, asymmetric compounds possessed higher Stokes shifts by ca. 1000 cm^{-1} than symmetric DAEs. Only compound **AsOTh$_2$** has a higher Stokes shift than the CF of unsubstituted DAE **6**.

Two important observations were made in this part of the work. First, the OFs of oxidized DAEs absorb at higher wavelengths, and their CFs absorb at lower wavelengths than the corresponding isomers of the nonoxidized counterparts. Second, the CFs of nonoxidized DAEs were found to be nonemissive. This important property will be taken into account in the design of the future photoswitchable compounds with ratiometric fluorescence modulation.

Switching kinetics

Table 2 contains an overview of the most important parameters related to the switching kinetics.

All compounds, except **AsOTh$_2$** and **SyOTh$_2$**, were reversibly switchable between open and closed forms by irradiation with 365 nm (cyclization) and 470 nm (cycloreversion) light. For compounds **AsOTh$_2$** and **SyOTh$_2$**, irreversible photobleaching was the main reaction path observed after irradiation with visible (470–530 nm) light (see Figures S55 and S61 in Supporting Information File 1). Considering the trend for other DAEs [1,5,9,10], we expect the cycloreversion quantum yields of compounds **AsOTh$_2$** and **SyOTh$_2$** to be $<10^{-6}$–10^{-7}, which means that the bleaching quantum yields are on the order of $>10^{-5}$–10^{-6}. The nonoxidized DAEs were also switchable by irradiation of the OF at 530 nm. In general, nonoxidized DAEs switched faster in both directions than the oxidized DAEs (by 1–4 orders of magnitude). Furthermore, the nonoxidized compounds (apart from **SyTh$_1$**) revealed higher cycloreversion quantum yields ($\varphi_{CF\rightarrow OF}$) than cyclization quantum yields ($\varphi_{OF\rightarrow CF}$); the oxidized compounds showed an opposite trend. As a result, the degree of conversion in the photostationary state found for nonoxidized compounds was moderate <70% (ca. 30% for asymmetric and 70% for symmetric dyes), but the

Table 2: Switching kinetics of the photochromic compounds (in acetonitrile solution).

	α[a] [%]	$\varphi_{OF\rightarrow CF}$[b]	$\varphi_{CF\rightarrow OF}$[c]	$\varphi_{on\text{-}switching}/\varphi_{off\text{-}switching}$	N_{ph}[d]
AsTh$_1$	36	0.13	0.14	1.1[e]	<1
SyTh$_1$	71	0.16	0.07	0.4[e]	<1
AsTh$_2$	28	0.03	0.15	5.0[e]	3
SyTh$_2$	71	0.04	0.06	1.5[e]	2
AsOTh$_1$	>98	$9.0 \cdot 10^{-2}$	$1.6 \cdot 10^{-3}$	56[f]	225
SyOTh$_1$	>98	$2.4 \cdot 10^{-2}$	$8.8 \cdot 10^{-5}$	273[f]	5230
AsOTh$_2$	>98	$7.6 \cdot 10^{-5}$	–[g]	–	–
SyOTh$_2$	>99	$1.9 \cdot 10^{-4}$	–[g]	–	–
3[h] [16]	53[i]	0.39[i]	0.35[j]	–	–
6 [4]	31	0.24[i]	0.25[k]	–	–

[a]Conversion into the CF in the PSS (365 nm). [b]Irradiation at 365 nm. [c]Irradiation at 530 nm. [d]The number of average emitted photons before off-switching is proportional to the ratio of fluorescence quantum yield and off-switching quantum yield; the off-switching quantum yield is $\varphi_{OF\rightarrow CF}$ for nonoxidized and $\varphi_{CF\rightarrow OF}$ for oxidized compounds. [e]Ratio of cycloreversion and cyclization. [f]Ratio of cyclization and cycloreversion. [g]Irreversible bleaching overcame the cycloreversion reaction. [h]In hexane. [i]Irradiation at 313 nm. [j]Irradiation at 517 nm. [k]Irradiation at 405 nm.

oxidized analogs show complete conversions (>98%). Interestingly, decoration of the core structures **3** and **6** (Scheme 1) with thiophene rings lowered the switching quantum yields by several orders of magnitude. It became obvious that the rate of cyclization and cycloreversion reactions decreased when the conjugation path became longer (transition from the unsubstituted core to monothiophene and then to bithiophene derivatives). In all cases, asymmetric substitution allowed faster cycloreversion than symmetric substitution, which is a positive effect regarding potential application of these dyes as reversible fluorescent markers in RESOLFT microscopy [5].

Two processes – fluorescence and off-switching – compete for the depopulation of the same excited state [10]. Hence, the ratio of fluorescence quantum yield and off-switching quantum yield is proportional to the number of emitted photons (N_{ph}) per cycle or per incursion into the fluorescent state (i.e., before off-switching takes place). Due to its high fluorescence quantum yield (φ_{fl}) and low cycloreversion quantum yield ($\varphi_{CF\rightarrow OF}$), compound **SyOTh$_1$** is expected to emit more than 5200 photons per cycle on average. Furthermore, compound **SyOTh$_1$** proved to be highly fatigue resistant. As shown in Figure 5, it endured >160 switching cycles in acetonitrile solution while losing only ca. 15% of its absorption. The extrapolation of the change in absorption yielded about 340 switching cycles, until a 50% signal loss occurs. Thus, this compound is a good candidate for a marker applicable in STORM/PALM and MINFLUX super-resolution techniques [17,18]. It even showed superior switching kinetics (regarding the ratio of fluorescence quantum yield and cycloreversion quantum yield) compared to DAEs which were already applied in super-resolution microscopy [10,15]. The nonoxidized analog of **SyOTh$_1$**, compound **SyTh$_1$**, showed even higher fatigue resistance. In acetonitrile solution, extrapolation of the first 160 switching cycles predicted that >3500 switching cycles may be expected before a 50% signal loss will occur. The high fatigue resistance of compound **SyTh$_1$** indicated that nonoxidized DAEs may, in general, be more photostable than oxidized DAEs. However, due to poor emission, **SyTh$_1$** was not considered as a fluorescence marker. Another promising compound for applications in super-resolution microscopy was DAE **AsOTh$_1$**. A high emission efficiency and a relatively fast cycloreversion, makes it a good candidate for a photoswitch applicable in RESOLFT microscopy.

Urbach tail effect

Under irradiation with visible light, most DAEs show complete conversion into the OF, because OFs do not absorb at wavelengths corresponding to the absorption band of the CF. However, compound **SyOTh$_1$** presented a remarkably "low" value of $\alpha_{CF\rightarrow OF}$ [470 nm] = 0.9 in MeCN. A similar behavior has been recently reported and ascribed to the so-called Urbach tail effect [19,20], i.e., the ring-closing photoreaction is induced by absorbing very weak hot bands of the OF, in the visible range. Neither nonoxidized DAEs, nor the asymmetric compound **AsOTh$_1$** show this effect at observable levels; the other oxidized compounds are "irreversible". To further investigate this phenomenon, **SyOTh$_1$** was irradiated with visible light of even longer wavelength (530 nm). Remarkably, conversion from the CF to the OF was practically complete (Figure 6). Thus, this photochromic DAE can be switched "on" with 470 nm light to an extent of 10%, and switched "off" with 530 nm light. In Figure 6C we present ten switching cycles performed with visible light, alternating between blue and green irradiation (no UV light was used for switching!). The emission signal (not shown) presents the same on/off behavior.

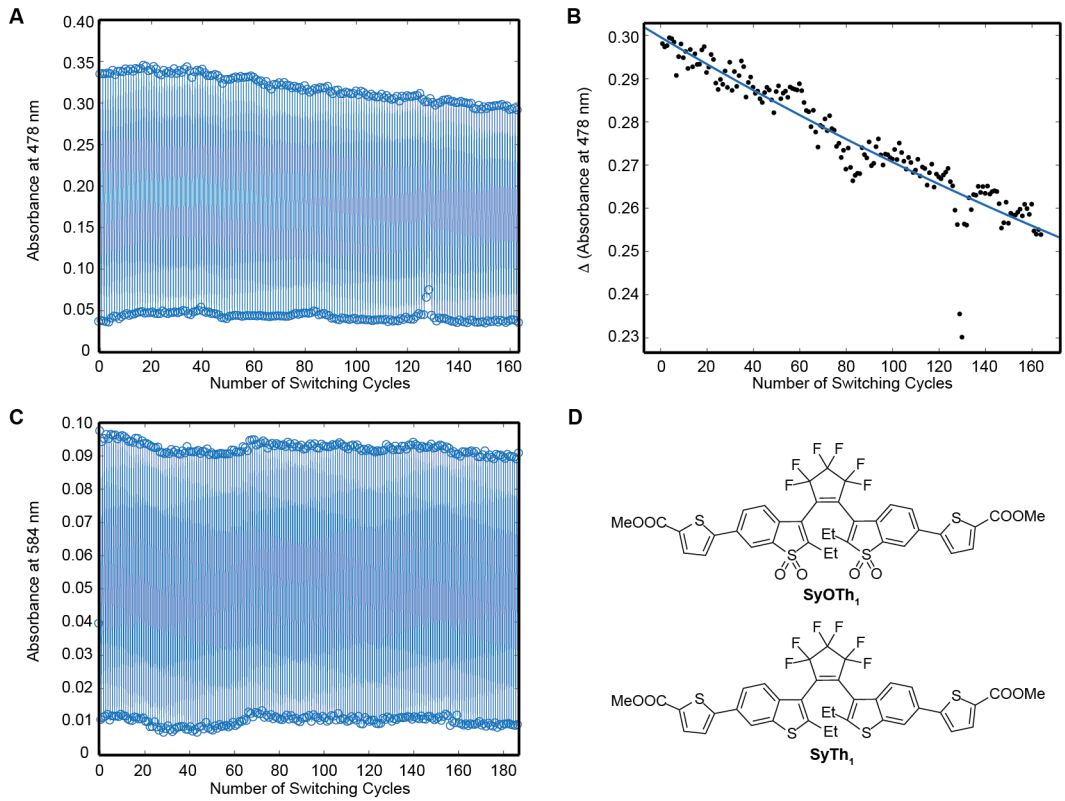

Figure 5: Fatigue resistances of compounds **SyOTh$_1$** (A and B) and **SyTh$_1$** (C). Parts A and C show the absorbance at certain wavelengths after cyclization (top values) and cycloreversion (bottom values). Part B shows the change in absorbance at 478 nm for each full switching cycle (CF–OF–CF) for compound **SyOTh$_1$**. Dots: the measured values; blue line: an exponential fit. Part D shows the structures of both compounds.

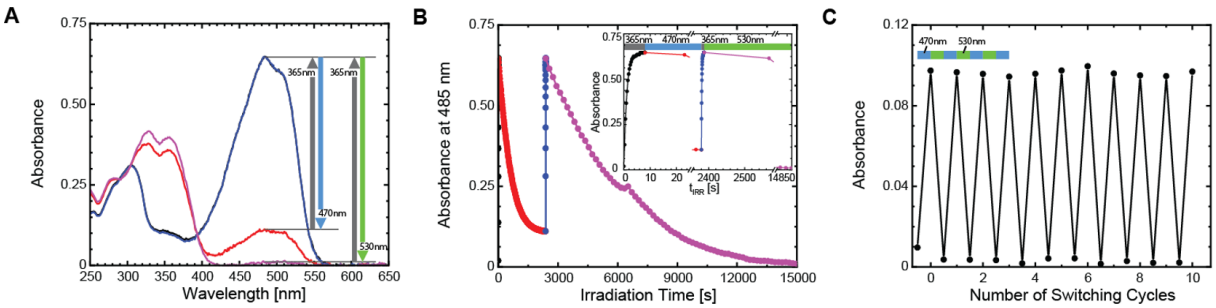

Figure 6: (A) Absorption spectra of compound **SyOTh$_1$** in MeCN at the photostationary states under irradiation with 365 nm light (blue/black lines), 470 nm light (red line), and 530 nm light (purple line). Part B, irradiation kinetics (same color code). Part C, ten complete *on*/*off* switching cycles performed with visible light.

Conclusion

We prepared eight 1,2-bis[(2-ethylbenzo[*b*]thiophene)-3-yl]perfluorocyclopentenes with oxidized and nonoxidized cores and decorated them with mono- and bithiophene rings in symmetric and asymmetric fashions. By studying the optical properties of the new compounds, we found that DAEs with nonoxidized benzothiophene units possess fluorescent open forms with low emission efficiencies. The new DAEs are relatively fast switches, and, in particular, the nonoxidized DAEs exhibited high cycloreversion quantum yields. Due to a high on/off ratio of >270, good fatigue resistance and large fluorescence quantum yield, compound **SyOTh$_1$** may be an excellent marker for single-molecule based super-resolution fluorescence microscopy, e.g., MINFLUX and STORM. In addition, **SyOTh$_1$** presents a remarkable *on*-switching of 10% of its maximal fluorescence signal with 470 nm light, and the ring-closure reaction was fully reversible by irradiation with longer wavelengths. This offers the possibility of reversible switching a DAE only with visible,

avoiding harmful (cytotoxic) UV irradiation. In view of the forthcoming solubilizing strategies applicable to fluorescent DAEs and intended for the crucial improvement of their fatigue resistance in aqueous solutions [21], the switching core of compound **AsOTh$_1$** is expected to provide a promising marker for RESOLFT microscopy (after attaching the reactive group).

Supporting Information

Supporting Information File 1

Experimental part and additional spectra of synthesized compounds.
[https://www.beilstein-journals.org/bjoc/content/supplementary/1860-5397-15-227-S1.pdf]

Acknowledgements

Jürgen Bienert, Jens Schimpfhauser, Jan Seikowki (Facility für synthetische Chemie, Max-Planck-Institut für biophysikalische Chemie, Göttingen), Dr. Holm Frauendorf, and the central analytics' team (Institut für organische und biomolekulare Chemie der Georg-August Universität Göttingen) are cordially acknowledged for recording NMR and mass spectra. ALS was supported by a Cusanuswerk scholarship.

ORCID® iDs

Mariano L. Bossi - https://orcid.org/0000-0001-6755-8074
Vladimir N. Belov - https://orcid.org/0000-0002-7741-4653

References

1. Irie, M.; Fukaminato, T.; Matsuda, K.; Kobatake, S. *Chem. Rev.* **2014,** *114,* 12174–12277. doi:10.1021/cr500249p
2. Jeong, Y.-C.; Yang, S. I.; Ahn, K.-H.; Kim, E. *Chem. Commun.* **2005,** 2503–2505. doi:10.1039/b501324k
3. Jeong, Y.-C.; Yang, S. I.; Kim, E.; Ahn, K.-H. *Tetrahedron* **2006,** *62,* 5855–5861. doi:10.1016/j.tet.2006.04.029
4. Barrez, E.; Laurent, G.; Pavageau, C.; Sliwa, M.; Métivier, R. *Phys. Chem. Chem. Phys.* **2018,** *20,* 2470–2479. doi:10.1039/c7cp06541h
5. Uno, K.; Bossi, M. L.; Konen, T.; Belov, V. N.; Irie, M.; Hell, S. W. *Adv. Opt. Mater.* **2019,** *7,* 1801746. doi:10.1002/adom.201801746
6. Åslund, A.; Herland, A.; Hammarström, P.; Nilsson, K. P. R.; Jonsson, B.-H.; Inganäs, O.; Konradsson, P. *Bioconjugate Chem.* **2007,** *18,* 1860–1868. doi:10.1021/bc700180g
7. Becker, R. S.; Seixas de Melo, J.; Maçanita, A. L.; Elisei, F. *J. Phys. Chem.* **1996,** *100,* 18683–18695. doi:10.1021/jp960852e
8. Krayushkin, M. M.; Bogacheva, A. M.; Levchenko, K. S.; Kobeleva, O. I.; Valova, T. M.; Barachevskii, V. A.; Pozzo, J.-L.; Struchkova, M. I.; Shmelin, P. S.; Kalik, M. A.; Baryshnikova, T. K.; Charushin, V. N. *Mendeleev Commun.* **2013,** *23,* 78–80. doi:10.1016/j.mencom.2013.03.007
9. Uno, K.; Niikura, H.; Morimoto, M.; Ishibashi, Y.; Miyasaka, H.; Irie, M. *J. Am. Chem. Soc.* **2011,** *133,* 13558–13564. doi:10.1021/ja204583e
10. Roubinet, B.; Weber, M.; Shojaei, H.; Bates, M.; Bossi, M. L.; Belov, V. N.; Irie, M.; Hell, S. W. *J. Am. Chem. Soc.* **2017,** *139,* 6611–6620. doi:10.1021/jacs.7b00274
11. Chotana, G. A.; Kallepalli, V. A.; Maleczka, R. E., Jr.; Smith, M. R., III. *Tetrahedron* **2008,** *64,* 6103–6114. doi:10.1016/j.tet.2008.02.111
12. Palamà, I.; Di Maria, F.; Viola, I.; Fabiano, E.; Gigli, G.; Bettini, C.; Barbarella, G. *J. Am. Chem. Soc.* **2011,** *133,* 17777–17785. doi:10.1021/ja2065522
13. Klingstedt, T.; Shirani, H.; Mahler, J.; Wegenast-Braun, B. M.; Nyström, S.; Goedert, M.; Jucker, M.; Nilsson, K. P. R. *Chem. – Eur. J.* **2015,** *21,* 9072–9082. doi:10.1002/chem.201500556
14. Simon, R. A.; Shirani, H.; Åslund, K. O. A.; Bäck, M.; Haroutunian, V.; Gandy, S.; Nilsson, K. P. R. *Chem. – Eur. J.* **2014,** *20,* 12537–12543. doi:10.1002/chem.201402890
15. Roubinet, B.; Bossi, M. L.; Alt, P.; Leutenegger, M.; Shojaei, H.; Schnorrenberg, S.; Nizamov, S.; Irie, M.; Belov, V. N.; Hell, S. W. *Angew. Chem., Int. Ed.* **2016,** *55,* 15429–15433. doi:10.1002/anie.201607940
Angew. Chem., **2016,** *128,* 15655–15659. doi:10.1002/ange.201607940
16. Yamaguchi, T.; Irie, M. *J. Photochem. Photobiol., A* **2006,** *178,* 162–169. doi:10.1016/j.jphotochem.2005.10.043
17. Henriques, R.; Griffiths, C.; Hesper Rego, E.; Mhlanga, M. M. *Biopolymers* **2011,** *95,* 322–331. doi:10.1002/bip.21586
18. Balzarotti, F.; Eilers, Y.; Gwosch, K. C.; Gynnå, A. H.; Westphal, V.; Stefani, F. D.; Elf, J.; Hell, S. W. *Science* **2017,** *355,* 606–612. doi:10.1126/science.aak9913
19. Kashihara, R.; Morimoto, M.; Ito, S.; Miyasaka, H.; Irie, M. *J. Am. Chem. Soc.* **2017,** *139,* 16498–16501. doi:10.1021/jacs.7b10697
20. Arai, Y.; Ito, S.; Fujita, H.; Yoneda, Y.; Kaji, T.; Takei, S.; Kashihara, R.; Morimoto, M.; Irie, M.; Miyasaka, H. *Chem. Commun.* **2017,** *53,* 4066–4069. doi:10.1039/c6cc10073b
21. Uno, K.; Bossi, M. L.; Irie, M.; Belov, V. N.; Hell, S. W. *J. Am. Chem. Soc.* **2019,** *141*. doi:10.1021/jacs.9b08748

License and Terms

BEILSTEIN JOURNAL OF ORGANIC CHEMISTRY

Probing of local polarity in poly(methyl methacrylate) with the charge transfer transition in Nile red

Aydan Yadigarli, Qimeng Song, Sergey I. Druzhinin* and Holger Schönherr*

Full Research Paper

Open Access

Address:
Physical Chemistry I and Research Center of Micro and Nanochemistry and Engineering (Cμ), Department of Chemistry and Biology, University of Siegen, Adolf-Reichwein-Str. 2, 57076, Siegen, Germany

Email:
Sergey I. Druzhinin* - druzhinin@chemie.uni-siegen.de;
Holger Schönherr* - schoenherr@chemie.uni-siegen.de

* Corresponding author

Keywords:
charge transfer; dipole moment; fluorescence; inhomogeneous broadening; oxazine dye; polarity probe; polymer permittivity

Beilstein J. Org. Chem. **2019,** *15,* 2552–2562.
doi:10.3762/bjoc.15.248

Received: 12 July 2019
Accepted: 25 September 2019
Published: 25 October 2019

This article is part of the thematic issue "Dyes in modern organic chemistry" and is dedicated to Prof. Dr. Günther von Bünau.

Guest Editor: H. Ihmels

Abstract

The permittivity of polymers and its spatial distribution play a crucial role in the behavior of thin films, such as those used, e.g., as sensor coatings. In an attempt to develop a conclusive approach to determine these quantities, the polarity of the model polymer poly(methyl methacrylate) (PMMA) in 600 nm thin films on a glass support was probed by the energy of the charge transfer transition in the oxazine dye Nile red (NR) at 25 °C. The absorption and fluorescence spectra of NR were observed to shift to the red with increasing solvent polarity, because of the intramolecular charge transfer character of the optical transition. New types of solvatochromic plots of emission frequency against absorption frequency and vice versa afforded the Onsager radius-free estimation of the ground and excited states dipole moment ratio. With this approach the values of these dipole moments of 11.97 D and 18.30–19.16 D, respectively, were obtained for NR. An effective local dielectric constant of 5.9–8.3 for PMMA thin films was calculated from the solvatochromic plot and the fluorescence maximum of NR observed in the PMMA films. The fluorescence band of NR in the rigid PMMA films shifted to the red by 130 cm^{-1} with increasing excitation wavelength from 470 to 540 nm, while in a series of liquids the position of the emission maximum of NR remained constant within same range of the excitation wavelength. It is concluded that the fluorescence spectrum of NR in PMMA undergoes inhomogeneous broadening due to different surroundings of NR molecules in the ground state and slow sub-glass transition (T_g) relaxations in PMMA.

Introduction

The chain and segment mobility as well as the permittivity of polymers possess an enormous impact on the properties of polymers and polymer thin films. For ultrathin films, in which the film thickness is in the order of the radius of gyration, special effects of confinement have been observed. Prominent examples are the properties of substrate-supported ultrathin polymer

films, in which the values of the glass transition temperature (T_g) and segmental mobilities were found to be altered. Likewise, this holds for transport properties, including polymer nanocapsule membrane permeability [1], enzyme-triggered bacterial sensors [2-5] and intelligent self-controlled drug delivery systems [4,6-10], as well as dynamics of polymers at interfaces [11].

To be able to understand local properties of polymers, in particular in nanoenvironments of polymeric vesicles (polymersomes), comprising a hydrophilic corona and a hydrophobic wall [1,12], or in substrate-supported ultrathin films [13], the analysis of the photophysical properties of tracer dye molecules was found to be beneficial. In time-resolved fluorescence measurements and dye diffusion studies, the nanoenvironments in polymersomes could be assigned [1,12], solute transport be characterized [1] and segment mobilities inferred [13], respectively. For other purposes the oxazine tracer dye Nile red (NR, Figure 1) served as a local probe to enable the study of degradation of enzyme labile polymersomes [14]. The same dye has been reported as probe for local permittivity in polymers, in particular, the spatial distribution of the dielectric constant measured for thin PMMA films was described using NR as a reported dye [15].

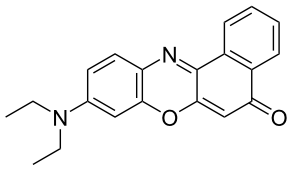

Figure 1: Molecular structure of Nile red (NR).

Because NR is (i) a photostable dye, (ii) possesses convenient optical properties, such as excitation with visible light, and fluorescence, which does not overlay with absorption of many biomolecules, and (iii) exhibits fluorescence, which is strongly influenced by the polarity of the environment, it has been employed as a polarity probe in biological applications [16-19] and materials/nanoscience [15,20-23]. For instance, the spatial distribution of the dielectric constant for thin PMMA films was mapped by analyzing the position of the fluorescence of NR employed as a reporter dye [15]. Besides polarity, the Young's modulus of the polymer matrix was found to be related to the fluorescence lifetimes (τ_f) of NR [21]. Furthermore, the spectral position of NR fluorescence was used to detect a lipid droplet in monkey aortic smooth muscle cells [16], for visualizing different proteins, such as lactoglobulin, casein and albumin [17]. In fluorescence lifetime imaging microscopy τ_f as a viable contrast parameter was employed to image lipid droplets in living HeLa cells stained with NR [19]. Recently, the phase of the microcapsules and their energy release were analyzed by monitoring the color of NR fluorescence in an energy storage microsystem [22].

Although NR solvent effects are a useful tool in biology and technology, an adequate description and characterization of the phenomenon is still far from accurate. Fortunately, a contribution of solute to the large amplitude motion of the diethylamino group (twisting) in intramolecular charge transfer excited state of NR, postulated in references [21,24,25] was later associated with an artefact [26]. However, the characteristics of NR in solvents and in matrices, such as the polarity of NR in the ground and excited states, as one can see in detail below, remains still rather controversial.

Here we aim at the development of a conclusive approach to determine the permittivity of polymers and its spatial distribution as they play a crucial role in the behavior of thin films, as alluded to above. Poly(methyl methacrylate) (PMMA) in submicrometer thin films on a glass support served as a model system.

The relaxation processes in bulk PMMA are well established and have been well characterized by dielectric [27-29] and dynamic mechanical analyses [30-32], NMR spectroscopy [33], and fluorescence spectroscopy [28]. For PMMA, the α-relaxation as slowest relaxation is observed at the glass transition (T_g = 95–110 °C) [34]. It corresponds to long-range conformational changes of the polymer backbone. This relaxation is frozen in the current experiments. However, the secondary β-, γ-, and δ-relaxations, which correspond to the side chain motions of the ester group and rotations of the methyl groups attached to the main as well as to the side chains, possess characteristic relaxation temperatures T_β = 10–40 °C, T_γ = −100 to −170 °C, and T_δ = −180 °C [28,31]. In PMMA, the dynamics of the ester group (β-relaxation) can furthermore be coupled with the α-relaxation [29].

Results and Discussion

For the development of a quantitative understanding of the polar probe NR in various nanoenvironments it is imperative to obtain a consistent description of the charge transfer at the electronic transition. For this purpose, the best choice is to study NR in dipolar solvents free from specific interactions with this solute. Finally, the polarity of the polymer matrix that does not possess comparable solute–solvent interactions will be probed with NR.

Dipole moments

With increasing solvent polarity, the maxima in the fluorescence spectra of NR in liquid solvents at 25 °C were observed

to gradually shift to the red, from 17660 cm^{-1} in nonpolar *n*-hexane to 16090 cm^{-1} in polar acetonitrile, showing no indication of dual fluorescence (Figure 2a). This behavior for NR [35] is similar to donor–acceptor-substituted stilbenes [36,37], benzenes [38,39] and aminocoumarins [35,40,41]. This effect is caused by solvent relaxation around dipolar solutes that possess in the lowest excited state a substantially higher dipole moment (μ_e) than that in the ground state (μ_g).

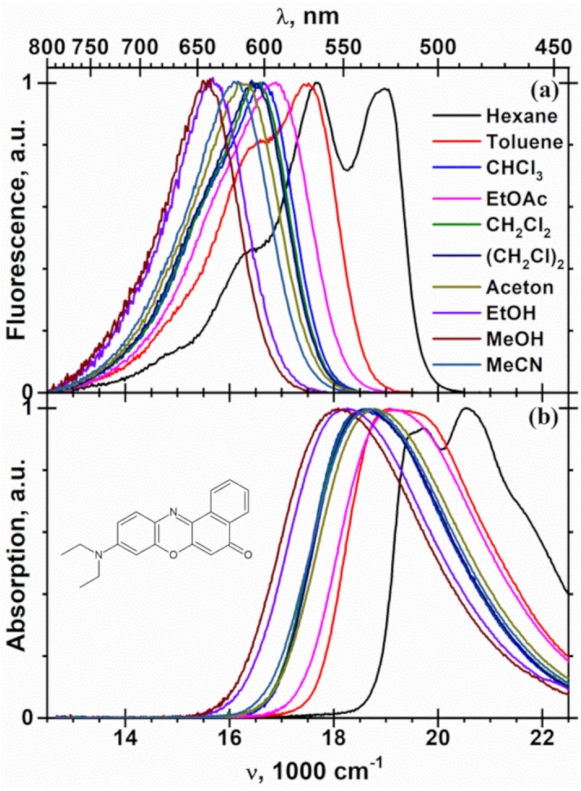

Figure 2: Fluorescence (a) and absorption (b) spectra of NR in solvents of different polarity at 25 °C. The solvent marks are hexane for *n*-hexane, $CHCl_3$ for chloroform, EtOAc for ethyl acetate, CH_2Cl_2 for dichloromethane, $(CH_2Cl)_2$ for 1,2-dichloroethane, EtOH for ethanol, MeOH for methanol and MeCN for acetonitrile.

To calculate the value of μ_e, the frequencies of emission (ν_f) and absorption (ν_a) are plotted [39,42] in Figure 3a against the Lippert solvent polarity function $f(\varepsilon) - f(n^2)$ [43], where ε is the dielectric constant and *n* is the refractive index of the solvent, $f(x) = (x - 1)/(2x + 1)$.

$$\nu_f = -\frac{2\mu_e(\mu_e - \mu_g)}{hc\rho^3}(f(\varepsilon) - f(n^2)) + \nu_{0f} \quad (1)$$

$$\nu_a = -\frac{2\mu_g(\mu_e - \mu_g)}{hc\rho^3}(f(\varepsilon) - f(n^2)) + \nu_{0a} \quad (2)$$

Here ν_{0f} and ν_{0a} are the frequencies at zero value of the polarity function, ρ is the Onsager cavity radius, *h* is Planck's constant, and *c* is the speed of light. The experimentally determined positions of the maxima in the absorption and fluorescence spectra of NR as well as the solvent polarity properties are listed in Table 1.

The data points for the dipolar aprotic solvents acetonitrile, acetone and ethyl acetate and the nonpolar *n*-hexane, shown by filled circles in Figure 3a, lie along a straight line. From its slope of −7210 cm^{-1} and μ_g = 11.97 D the value of μ_e = 18.30 D is calculated. The fluorescence spectra of NR in the protic solvents ethanol and methanol are substantially shifted to the red (Figure 2a), although they possess similar $f(\varepsilon) - f(n^2)$ values

Table 1: Absorption (ν_a) and fluorescence (ν_f) maxima of NR, fluorescence maxima (ν_{fs}) of the intramolecular charge transfer state of 4-(diisopropylamino)benzonitrile (DIABN) in different solvents, solvent dielectric constants (ε), refractive indexes (*n*) and Lippert polarity functions at 25 °C.

N	Solvent	ε[a]	n[b]	$f(\varepsilon) - f(n^2)$[c]	ν_a, cm^{-1}	ν_f, cm^{-1}	ν_{fs}[d], cm^{-1}
1	hexane	1.88	1.372	0.000	20130[d]	17660[d]	25720
2	toluene	2.37	1.494	0.013	19010	17470	23840
3	$CHCl_3$[e]	4.89	1.442	0.152	18520	16630	
4	EtOAc[f]	5.99	1.370	0.200	19140	16840	22260
5	CH_2Cl_2[g]	8.87	1.421	0.218	18570	16510	21770
6	$(CH_2Cl)_2$[h]	10.36	1.443	0.221	18590	16460	21650
7	acetone	20.56	1.356	0.285	18780	16270	
8	ethanol	24.60	1.360	0.289	18220	15670	20310
9	methanol	32.32	1.327	0.309	18100	15540	19860
10	MeCN[i]	36.65	1.342	0.306	18680	16090	20490

[a]Dielectric constants from ref [49]. [b]Refractive indexes from ref [50]. [c]Lippert polarity function $f(\varepsilon) - f(n^2)$. [d]Half-sum of wavenumbers for the maxima of the first and second vibronic peaks in the spectrum possessing practically equal intensities, see Figure 1. [e]Chloroform. [f]Ethyl acetate. [g]Dichloromethane. [h]1,2-Dichloroethane. [i]Acetonitrile.

compared to those for acetone and acetonitrile, respectively (Table 1). This effect is reminiscent of the anomalous fluorescence red shift of fluorophores in alcohols [44]. The additional red shift of NR in protic solvents, such as alcohols and probably chloroform, is associated with the hydrogen-bond formation with the carbonyl group of the dye [45]. The fluorescence maxima of NR in highly polarizable toluene and in chlorinated solvents lie also clearly below the straight line in Figure 3a. This is tentatively attributed to the different inductive solute–solvent interactions, which are neglected in Equation 1. Such additional red shift in the case of halogenated solvents has been explained before by the formation of exciplexes [46-48].

In polar solvents the absorption band of NR is shifted to the red, from 19670 cm^{-1} in *n*-hexane down to 18680 cm^{-1} in acetonitrile (Figure 3a), in the same direction as its fluorescence spectrum. A somewhat smaller magnitude of the shift of 990 cm^{-1} compared to that observed in the fluorescence spectrum (1570 cm^{-1}) indicates a higher dipole moment in the excited state ($\mu_e > \mu_g$) and a larger negative slope in Equation 1 $\sim\mu_e(\mu_e - \mu_e)$ than in Equation 2 $\sim\mu_g(\mu_e - \mu_g)$. This solvatochromic plot with its slope of −4730 cm^{-1} resembles plot according to Equation 1 in Figure 3a, namely the points for dipolar acetonitrile, acetone, ethyl acetate and nonpolar *n*-hexane fit to a straight line (2), NR in other solvents exhibits again a stronger red shift due to specific and inductive solute–solvent interactions.

In order to eliminate any scaling effect of the Onsager radius on the relation between μ_g and μ_e, Equation 2 can be rearranged to obtain the polarity function

$$f(\varepsilon) - f(n^2) = \frac{hc\rho^3}{2\mu_g(\mu_e - \mu_g)}(\nu_{0a} - \nu_a). \qquad (3)$$

Substitution of Equation 3 in Equation 1, assuming equal ρ values of the same molecule for the absorption and emission transitions, gives the following simple Onsager radius-independent linear relation between emission and absorption frequencies.

$$\nu_f = \frac{\mu_e}{\mu_g}\nu_a + \nu_{0f} - \frac{\mu_e}{\mu_g}\nu_{0a} \qquad (4)$$

In Figure 3b the fluorescence maxima of NR are plotted versus the absorption maxima. The solvent is indicated by its number according to Table 1. Data for solvents that possess similar refractive indices (n = 1.342−1.347) fit to Equation 4 with a slope 1.529, indicating a substantial (53%) increase of the dipole moment upon excitation of NR. A clear deviation is observed for protic solvents and highly polarizable solvents (with n = 1.421−1.494) due to the different efficiency of hydrogen bond formation and contributions of inductive solute–solvent interactions in the ground and excited states.

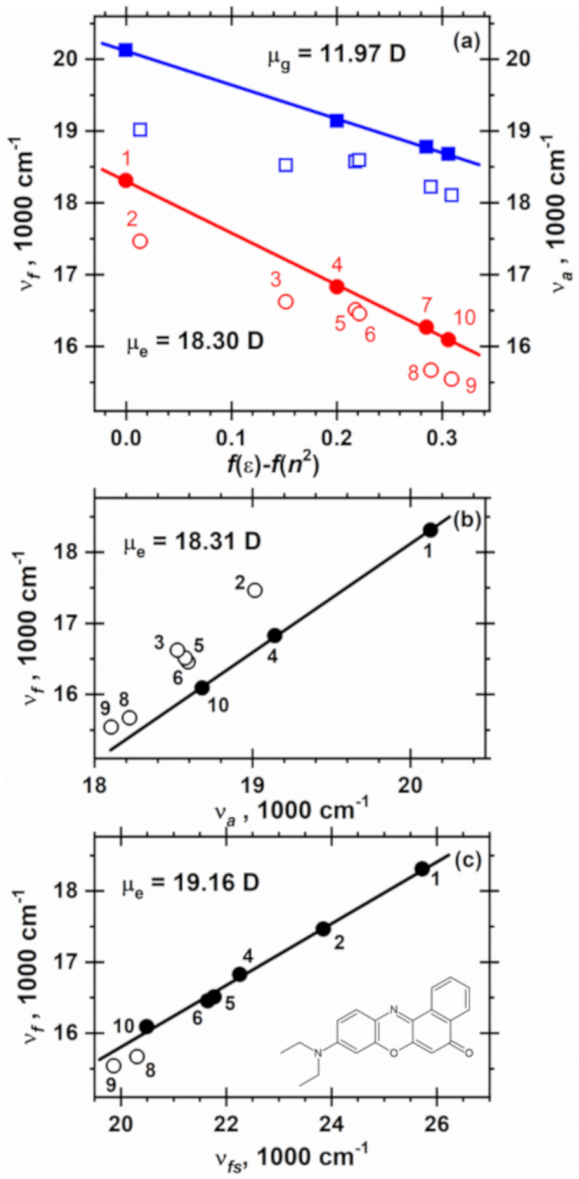

Figure 3: Solvatochromic plot of the absorption (ν_a) and fluorescence (ν_f) maxima of NR in a series of solvents at 25 °C (a) against the Lippert solvent polarity function $f(\varepsilon) - f(n^2)$, (b) against absorption maximum ν_a and (c) against the fluorescence maximum (ν_{fs}) of the intramolecular charge-transfer band of 4-(diisopropylamino)benzonitrile (DIABN). In panel (a) the data for ν_a and ν_f are shown with blue squares and red circles, respectively. From the slopes of the straight lines fitted through the filled circles and squares according to Equation 1 and Equation 2 in (a), Equation 4 in (b) and Equation 10 in (c) the ground (μ_g) and excited state dipole moments (μ_e) of NR are calculated, see Table 2. The solvents are indicated by the numbers in the first column of Table 1.

The slopes of the two linear relations Equation 1 $\alpha = -2\mu_e(\mu_e - \mu_g)/hc\rho^3$ and Equation 4 $\beta_a = \mu_g/\mu$ allow one to calculate both ground and excited states dipole moments as

$$\mu_g = \sqrt{-\frac{\alpha hc\rho^3}{2\beta_a(\beta_a - 1)}} \quad (5)$$

$$\mu_e = \sqrt{-\frac{\alpha\beta_a hc\rho^3}{2(\beta_a - 1)}} \quad (6)$$

From $\alpha = -7210$ cm^{-1} (Figure 3a) and the $\beta_a = 1.529$ (Figure 3b), one obtains $\mu_g = 11.97 \pm 0.36$ D and $\mu_e = 18.30 \pm 0.61$ D, see Table 2.

Using a similar method [60,61], in which it is not necessary to assume the radius ρ, the ratio of the slopes of the solvatochromic plots for fluorescence (Equation 1) and absorption (Eqution 2) also yields a value for β_a. Although closely matching values of β_a are expected for both the ratio method and from the direct correlation according to Equation 4, when the same set of solvents is employed in Equations 1, 2 and 4, the resulting values of β_a could be erroneous, if *different* sets of solvents were used in Equation 1 and Equation 2.

Alike to Equation 4, the excited state dipole moment can be determined from a plot of the fluorescence maxima of the studied fluorophore versus the fluorescence maxima of a standard fluorophore with known ground and excited dipole moments μ_{gs} and μ_{es} [38,39]. Application of Equation 1 to the spectra of the standard fluorophore and rearrangement in order to express solvent polarity function yields

$$f(\varepsilon) - f(n^2) = \frac{hc{\rho_s}^3}{2\mu_{es}(\mu_{es} - \mu_{gs})}(\nu_{0fs} - \nu_{fs}). \quad (7)$$

Then substitution of the solvent polarity function again into Equation 1 for the studied fluorophore gives a linear correlation (Equation 8) of ν_f and ν_{fs}

$$\nu_f = \frac{\mu_e(\mu_e - \mu_g){\rho_s}^3}{\mu_{es}(\mu_{es} - \mu_{gs})\rho^3}\nu_{fs} + \nu_{0f} - \frac{\mu_e(\mu_e - \mu_g){\rho_s}^3}{\mu_{es}(\mu_{es} - \mu_{gs})\rho^3}\nu_{0fs}. \quad (8)$$

The subscript *s* indicates values related to the above mentioned standard. In Equation 8 the effect of the very important parameter, the Onsager radius, on the resulting dipole moment also decreases, because the ratio ${\rho_s}^3/\rho^3$ should be practically independent from the method how these radii are estimated.

In Figure 2c the fluorescence maximum data are plotted versus that of the intramolecular charge transfer state of 4-(diisopropylamino)benzonitrile (DIABN). Data for all solvents except for the alcohols are fitted well to the linear Equation 8 with a positive slope $\beta_f = 0.434$. The value

$$\mu_e = \frac{\mu_g}{2} + \sqrt{\frac{{\mu_g}^2}{4} + \beta_f\mu_{es}(\mu_{es} - \mu_{gs})\frac{\rho^3}{{\rho_s}^3}} \quad (9)$$

of 19.16 ± 0.19 D agrees well with that determined from the solvatochromic expressions (Equations 1, 2 and 4), see Table 2.

Substitution of the polarity function (Equation 7), calculated with the reference fluorophore in Equation 2, gives the following relations between absorption maxima of NR and emission maxima of the dipole moment standard:

Table 2: Ground (μ_g) and excited (μ_e) state dipole moments of NR.

Equation	Slope, cm^{-1}	μ_g[a], D	ρ, pm	μ_e[b], D
1	−7210 ± 110	11.97± 0.35	545	18.30 ± 0.53
2	−4730 ± 100	11.97± 0.35	545	18.31 ± 0.47
4	1.529[c] ± 0.023[c]	11.97± 0.35	545	18.30 ± 0.61
8	0.434[c] ± 0.015[c]	11.97± 0.35 6.78[d]	545 468[d]	19.16 ± 0.19 18[d]
2[e]	−6000 ± 420	11.97± 0.35	545	20.00 ± 0.51
10[e]	0.366[c] ± 0.019[c]	11.97± 0.35 6.78[d]	545 468[d]	21.68 ± 0.51 18[d]

[a]Other reported values (in Debye units D) are 7 [47,51,52], 7 [53,54] (for phenoxazone 9, the *N*,*N*-dimethylamino analogue of NR), 7.51 [55], 7.97 [55], 8.2 [56,57], 8.4 [44], 8.9 [44], 14 [48]. [b]Other values (in D) 6.9 [52], 7.7 [51], 8.5 [51], 10.0 [57], 10.2 [56], 10.4 [58], 10.5 [58], 10.77 [55], 12.48 [55], 13.15 [55], 13.4 [44], 14.13 [55], 14.4 [44], 14.5 [47], 17 [47], 18 [48], 18 [53,54] (for phenoxazone 9, the *N*,*N*-dimethylamino analogue of NR), 18.5 [48], and 18.6 [51,52]. [c]Dimensionless. [d]Values for DIABN [38,39]. [e]Absorption maxima from [59].

$$\nu_a = \frac{\mu_g(\mu_e - \mu_g)\rho_s^3}{\mu_{es}(\mu_{es} - \mu_{gs})\rho^3}\nu_{fs} + \nu_{0a} - \frac{\mu_g(\mu_e - \mu_g)\rho_s^3}{\mu_{es}(\mu_{es} - \mu_{gs})\rho^3}\nu_{0fs}. \quad (10)$$

With the slope of the linear function (10)

$$\beta_f = \frac{\mu_g(\mu_e - \mu_g)\rho_s^3}{\mu_{es}(\mu_{es} - \mu_{gs})\rho^3}. \quad (11)$$

The excited state dipole moment can be evaluated as

$$\mu_e = \mu_g + \beta_f \frac{\mu_{es}(\mu_{es} - \mu_{gs})\rho^3}{\mu_g \rho_s^3}. \quad (12)$$

The published values of the dipole moments [44,47,48,51-56] of NR, summarized in the footnote of Table 2, are almost uniformly dispersed in the wide range from 7 to 14 D for μ_g and from 6.9 to 19.6 D for μ_e, respectively. All data demonstrate an increasing of dipole moment at the excitation $\mu_e - \mu_g$ between 1.8 and 11.6 D [44,51,56,62,63], also with μ_g = 7 D and μ_e = 6.9 ± 2.1 D [52] it is still correct within the experimental uncertainty. Thus, the values of NR μ_g = 11.97 D and $\mu_e - \mu_g$ from 6.34 to 7.20 D obtained here (Table 2) agree with the published data. The excited state dipole moment μ_e from 18.30 to 19.16 D and the slightly higher μ_e = 20–22 D (Figure S1, Supporting Information File 1, Table 2) calculated from the published absorption maxima of NR [59] using Equation 2 and Equation 10 is on the upper bound of the published μ_e values.

From a theoretical point of view, the very broad distribution of dipole moments published in the literature [44,47,48,51-58] might be caused because (i) various experimental approaches were used, including solvatochromic, thermochromic and dielectric friction techniques, and (ii) different theoretical models of solvatochromic effects were employed, some of them take inductive solute–solvent interactions and solute polarizability into account, others neglect them, and (iii) different definitions of the molecular dipole moment in solvent-free conditions in vacuum or in solvents with zero polarity function $f(\varepsilon) - f(n^2)$ were used. Most of these divergences can be compensated by an appropriate selection of the solvent set. For example, the effect of inductive solute–solvent interactions on ν_a or ν_f becomes practically invariant, when the refractive index is constant in a series of solvents. From an experimental point of view, the broad distribution of reported dipole moments could also be the result of an imprecise correction of emission spectra for the spectral response or their imprecise presentation on the wavenumber scale. The major challenge appears to be the lack of independently determined parameters of the NR ground state dipole moment and/or its cavity radius, which are both important.

Two values of the Onsager radius, 410 pm [51,52,55,57,58] and 500 pm [44,47,57,62], were used in [44,47,48,51-56,62,63] to evaluate μ_e or $\mu_e - \mu_g$. The first value is the van der Waals radius $\rho = (3V/4\pi)^{1/3}$, where the van der Waals volume V is the sum of atomic increments [64]. The second value was chosen arbitrarily as a typical value. In addition, both these values of ρ were not verified with respect to their applicability for use in solvatochromy of NR.

In the present paper, we used $\rho = \rho_0(M/M_0)^{1/3}$, where M is the molar mass of the fluorophore and the lower index '0' marks the corresponding quantity related to *N*,*N*-dimethylaminobenzonitrile (DMABN). The Onsager radius of DMABN was tailored to ρ_0 = 420 pm [39] in order to get μ_e = 17 D for the charge transfer excited state of DMABN from the solvatochromic plot (Equation 1). The corresponding dipole moments were determined with cavity radius free techniques: μ_g = 6.60 D [39] by dielectric spectroscopy and μ_e = 17 D [65] by time-resolved microwave conductivity. For the secondary standard DIABN ρ_s = 468 pm is calculated from ρ_0, μ_{gs} = 6.78 was measured by dielectric spectroscopy and μ_{gs} = 18 D was determined from the solvatochromic plot (Equation 8) relative to the wavenumber maxima of the excited state charge transfer emission spectra of DMABN [38,39]. For NR a cavity radius of ρ = 545 pm is calculated based on ρ_0 and M.

When the literature values of the absorption maxima of NR [59], ρ = 545 pm and μ_g = 11.97 D are fitted with Equation 2 and Equation 10, values that are close to the values of μ_e = 20–22 D reported here are obtained (Table 2). Because the cavity radius for NR is adapted for solvatochromy in our work, reliable values of the ground state and excited state dipole moments of NR can indeed be calculated.

The crucial importance of the correct value for the Onsager radius is demonstrated by fitting data from Table 1 with Equation 2 and Equation 5 for a van der Waals radius ρ = 410 [51,52,55,57,58]. This fit yields μ_g = 7.81 D instead of 11.97 D (Table 2) and μ_e = 11.94 D instead of 18.30 D (Table 2). These values are close to μ_g = 8.2 D and μ_e = 14.4 D from reference [56], where both dipole moments were determined by similar analysis of absorption and fluorescence spectra of NR. Thus, the large dispersion of reported NR dipole moments [44,47,48,51-56,62,63] is mainly caused by insufficient precision of the value for the cavity radius of NR.

Polymer polarity probed with NR

The fluorescence spectra of NR in low and high molar mass PMMA films (Figure 4, Figure S2, Supporting Information File 1) were found to be close to spectra acquired in ethyl acetate (Figure 2a), which may be used as a model for the polymer repeat unit. The broad structureless fluorescence maximum at ≈600 nm for NR in PMMA reported in references [62,66] might be caused by remaining traces of solvent from PMMA solution (toluene) [66] in close vicinity to NR molecules, similar to results for NR in poly(vinylidene fluoride) films cast from dimethyl sulfoxide [15]. This notion is supported by fluorescence maxima (λ_f) of NR in PMMA at the excitation wavelength λ_e = 500 nm, which are in the range of 571 < λ_f < 579 nm, depending on the polymer molar mass and casting solvents. For ethyl acetate, the fluorescence of NR occurs at longer wavelength λ_f = 588 nm, which does not agree with the results in reference [66].

When λ_e increases, the fluorescence spectrum of NR in the polymer matrix shifts linearly to the red by 130 cm^{-1} from 17100 at λ_e = 470 nm to 16970 cm^{-1} at λ_e = 540 nm, mainly in the blue part of the spectrum and at the maximum (Figure 4, Figure 5 and Figure S2, Supporting Information File 1). In contrast to PMMA, neither the shape of the fluorescence spectrum of NR nor the position of its maximum depend on λ_e in liquid solutions, such as in the polymer repeat unit model ethyl acetate, and in solvents used for preparation of spin-coated PMMA films, such as chloroform, dichloromethane and 1,2-dichloroethane (Figure 5, Figure 6 and Figures S3, S4 and S5, Supporting Information File 1). These facts and the blue shifted fluorescence of NR in PMMA in comparison to mentioned above solutions (Figure 5) demonstrate that the local polarity in PMMA and/or its dynamics are different than in similar liquid solutions. The fluorescence maxima of NR at λ_e = 500 nm, the slopes $d\nu_f/d\lambda_e$ of the fluorescence spectrum drift with the excitation wavelength and the thicknesses of spin-coated PMMA films are collected in Table 3. On the one hand, such independence of the fluorescence spectra of NR in liquid solution supports the high purity of the NR used and its high stability also in the chlorinated solvents, cf. with a lack of a red edge effect for 4-fluoro-*N*,*N*-dimethylaniline [67]. On the other hand, when the relaxation time of the molecules or segments (τ_r) of the polymer matrix is much longer than the NR fluorescence decay time τ_f = 3.87 ns [62] in PMMA and of ≈5 ns [62] in the liquid solvents used, the orientational relaxation of the molecules or segments around in the excited NR is not complete. Consequently, the fluorescence of NR in polymers originating from a not solvent-relaxed excited state possesses higher energy. The corresponding matrix polarity is characterized by an effective dielectric constant $\varepsilon(2\pi/\tau_f)$ between ε, the zero frequency, and $\varepsilon_\infty = n^2$, the optical frequency permittivity of the medium.

$$\varepsilon\left(\frac{2\pi}{\tau_f}\right) = \varepsilon_\infty + \frac{\varepsilon - \varepsilon_\infty}{1 + \left(\frac{\tau_r}{\tau_f}\right)^2} \tag{13}$$

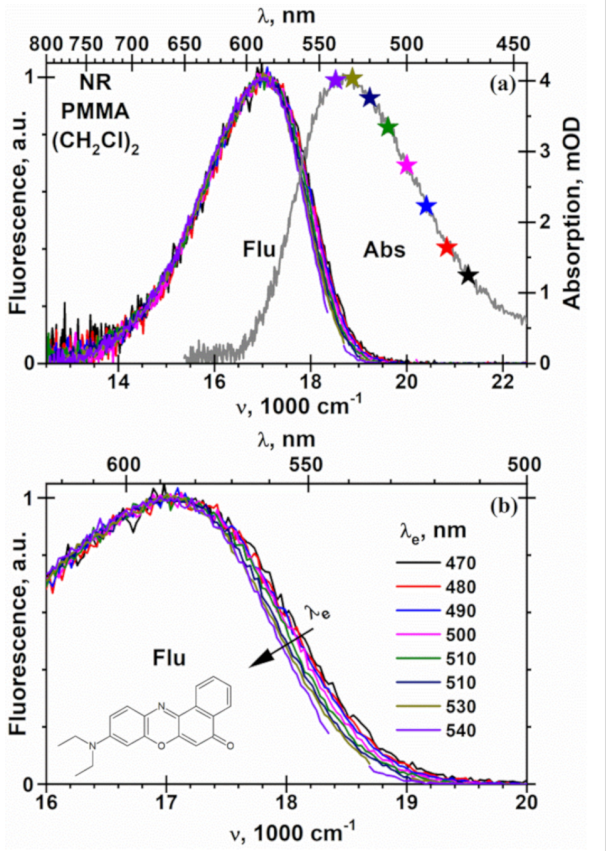

Figure 4: Absorption (a) and fluorescence (a, b) spectra of NR in PMMA (350 kg/mol) film 500 nm thin at different excitation wavelength (λ_e). The film was prepared by spin-coating of PMMA solution in 1,2-dichloroethane ($(CH_2Cl)_2$) on the 20 × 20 × 0.15 mm^3 glass doped with NR. The concentration of NR in the PMMA film of 2.1 mM was calculated from the optical density (panel (a)) and thickness of PMMA film with the molar extinction coefficient NR in 1,4-dioxane of 38000 $M^{-1}{\cdot}cm^{-1}$ [68]. The λ_e values are indicated with stars on the absorption spectrum in panel (a). The regions λ_e ± 5 nm in the fluorescence spectra (a, b) are not shown due to overlap with strong scattering excitation light.

In a similar manner, the dipolar units are dispersed around NR molecules in the ground state. The observable absorption spectrum is a superposition of the spectra of such partial solvates of NR. According to Equation 2 the absorption of stronger solvated NR molecules is shifted to the red. The more NR is irradiated in the red, the higher is the contribution of stronger solvated NR molecules that are excited. A response time τ_r of seconds for a polarization dynamics was estimated for PMMA

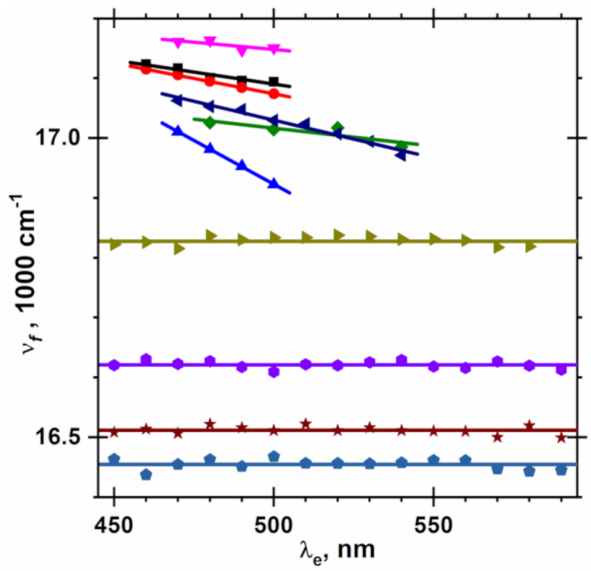

Figure 5: Dependence of the fluorescence maximum (ν_f) of NR on the excitation wavelength (λ_e) in rigid PMMA matrix (six data sets on the top) and in fluid solutions (four data sets on the bottom) at 25 °C. The details of the preparation of the submicron PMMA films are listed in Table 3. The straight lines for NR in the PMMA matrices and horizontal lines for NR fluid solutions at λ_e = 500 nm are shown from top to bottom in the following series: PMMAH from CH_2Cl_2, PMMAL from CH_2Cl_2, $CHCl_3$ and $(CH_2Cl)_2$, PMMAH from $CHCl_3$ and $(CH_2Cl)_2$, ethyl acetate, $CHCl_3$, CH_2Cl_2, and $(CH_2Cl)_2$, respectively.

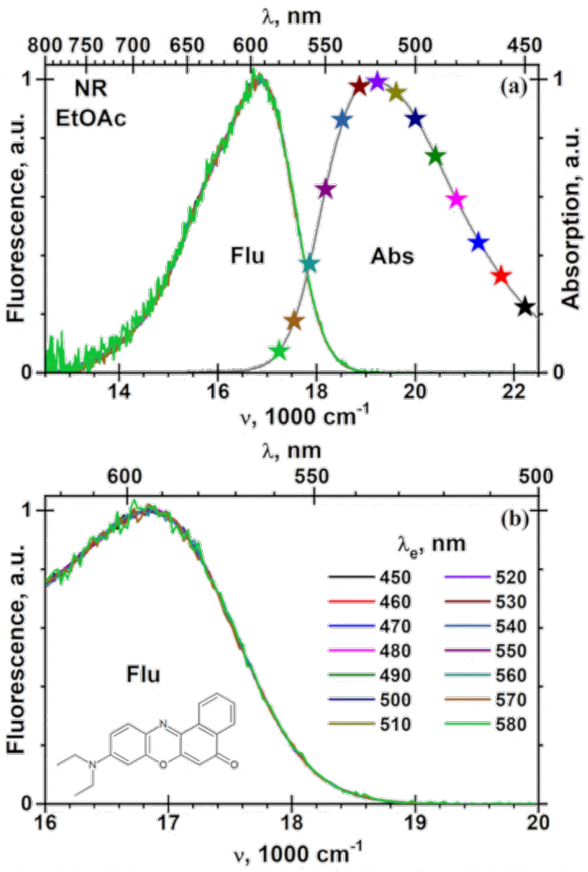

Figure 6: Absorption (a) and fluorescence (a, b) spectra of NR in ethyl acetate (EtOAc) at different excitation wavelength (λ_e) at 25 °C. The λ_e values are indicated with the stars on the absorption spectrum in panel (a).

films in an external electric field [69]. Although short $\tau_f << \tau_r$ in the region of $2\pi/\tau_f \approx 1$ GHz prevent a substantial rearrange of the solvation shell around the NR molecules in the excited state, solvated molecules absorbing more in the red also fluoresce in the red tail of the spectrum. Such inhomogeneous broadening of absorption and fluorescence spectra can explain the observable drift in the fluorescence spectra of NR in PMMA to the red for long wavelength excitation (Figure 4 and Figure S2, Supporting Information File 1).

The value of νf decreases in the series of the spin-coating solvents dichloromethane, chloroform and 1,2-dichloroethane. The absolute value of the red drift rate $d\nu_f/d\lambda_e$ gradually grows up in

Table 3: Fluorescence maxima (ν_f) of NR at the excitation wavelength (λ_e) of 500 nm in PMMA spin-coated film of thickness (d), ν_f drift rate ($d\nu_f/d\lambda_e$), Lippert solvent polarity function and dielectric constant (ε) of the PMMA films at 25 °C.

PMMA[a]	Solvent	ν_f, cm^{-1}	$-d\nu_f/d\lambda_e$ μm^{-2}	d, nm	$f(\varepsilon) - f(n^2)$[b]	ε[c]
PMMA-L	CH_2Cl_2[d]	17120	8	400	0.167 ± 0.004	6.4 ± 0.3
	$CHCl_3$[e]	17070	10	480	0.170 ± 0.004	6.6 ± 0.3
	$(CH_2Cl)_2$[f]	16920	29	380	0.191 ± 0.005	8.3 ± 0.5
PMMA-H	CH_2Cl_2[d]	17150	5	960	0.159 ± 0.004	5.9 ± 0.2
	$CHCl_3$[e]	17020	6	480	0.178 ± 0.005	7.2 ± 0.4
	$(CH_2Cl)_2$[f]	17040	13	500	0.176 ± 0.005	7.0 ± 0.3

[a]Average molar masses are 33 kg/mol (PMMA-L) and 350 kg/mol (PMMA-H). [b]Estimated from Equation 9 for NR using slope from Table 2 and intercept ν_{0f} = 18300 ± 26 cm^{-1} for the straight line (Equation 1) in Figure 3a. [c]Calculated from PMMA Lippert solvent polarity function $f(\varepsilon) - f(n^2)$ and n = 1.490 [70]. [d]Dichloromethane. [e]Chloroform. [f]1,2-Dichloroethane.

the same series. This cast solvent effect of 200 and 130 cm^{-1} with low and high PMMA molar mass is more pronounced than the influence of PMMA molar mass in the same solvent, which were 30, 50 and 120 cm^{-1} for dichloromethane, chloroform and 1,2-dichloroethane, respectively. These results for ν_f and $-d\nu_f/d\lambda_e$ can be rationalized by correlating them with the boiling points of these solvents of 34.6 °C, 62.2 °C and 83.5 °C, respectively. Due to fast solvent evaporation of the most volatile solvent, i.e., dichloromethane, the polymer units are less ordered or dense around the NR molecules. For the least volatile solvent, i.e., 1,2-dichloroethane, a more ordered surrounding of the NR molecules in the ground state leads to a red shift of the fluorescence spectra. The observation might also be explained by a smaller residual amount of solvent for the volatile dichloromethane than for 1,2-dichloroethane and a corresponding plasticizing effect.

The effective Lippert polarity function is determined from the linear Equation 1 by using ν_f of NR in PMMA measured at λ_e = 500 nm, where an overlap of the fluorescence spectra with scattered excitation light is minimal (Figure 4 and Figure S2, Supporting Information File 1). In parallel to ν_f, the polarity function, having values between 0.159 and 0.191 close to that of the model solvent ethyl acetate (0.200, Table 3), depends more sensitively on the spin-coating solvent than on the molar mass of the PMMA. Based on the magnitudes of the refractive index of PMMA, n = 1.490 [70], 1.491 [71] at 578.1 nm and 1.4868 [72] at 600 nm, the effective local dielectric constants are estimated as 5.9–8.3, which agrees with published data [70,73,74]. The value of $\varepsilon(2\pi/\tau_f)$ in Equation 13 clearly exceeds the high frequency permittivity of PMMA (n^2 = 2.22), indicating substantial mobility of the local environment of NR in the PMMA matrix. For bulk PMMA, dielectric spectroscopy measurements gave values for ε = 3.7 [70], 4.99 [73] and 8 [74] for PMMA films. In reference [15] the local polarity of PMMA film probe by NR was found ε = 3.64. This value is probably underestimated, because in contrast to the present study λ_f of NR was estimated not from the spectrum, but from the ratio of integrated fluorescence intensities above and below ≈600 nm. In the following analysis ε was evaluated directly from a double-exponential fit of $\varepsilon(\lambda_f)$ without any correction for n, which would have been necessary.

Conclusion

New types of relative solvatochromic plots, in which the position of the emission maximum is plotted versus the position of absorption maximum or vice versa, allow one to estimate the ratio of the ground and excited state dipole moments. The values obtained are practically independent from the magnitude of the Onsager cavity radius. The absorption and fluorescence spectra of NR shift to the red with increasing solvent polarity, because of the intramolecular charge transfer character of the optical transition. From the plots of the maxima of the fluorescence and absorption wavenumber spectra in dipolar solvents, which possess negligible specific solute–solvent interactions, versus the Lippert solvent polarity function, and from this fluorescence frequency against corresponding absorption frequency and from the fluorescence maxima of DIABN with known dipole moments, consistent values of the ground and excited state dipole moments of 11.97 D and 18.30–19.16 D were calculated for NR using an Onsager radius of 545 pm. The local environment of NR as local polarity probe molecule in PMMA films demonstrates a local mobility that is higher than that expected from the permittivity of bulk PMMA. The local dielectric constant of 5.9–8.3 implies that beside electronic and atomic polarization (rearrangement of atomic bonds and valence angles) a certain dipolar orientation degree of freedom take place in PMMA within the lifetime of excited state of NR. The restriction of the orientational relaxation causes an inhomogeneous broadening of the fluorescence spectrum of NR and its excitation wavelength dependence. The inhomogeneity depends stronger on the condition of PMMA film preparation than on the PMMA molar mass.

Experimental

General. NR was purchased from Carl Roth (Germany) and was used as received. Poly(methyl methacrylate) (PMMA) with an average molar mass of 350 kg/mol and 33 kg/mol was used (Aldrich, USA). Uvasol acetone, *n*-hexane and methanol (Merck, Germany), absolute ethanol and chloroform (VWR, Germany), 1,2-dichloroethane (Carl Roth, Germany), toluene, dichloromethane, acetonitrile and ethyl acetate (Fisher Scientific, Germany) were used without further purification. The solvents were checked for the lack of fluorescence when excited with 450–600 nm. Polymer films with or without NR were prepared by spin-casting of 3 wt % polymer solutions in 1,2-dichloroethane, dichloromethane or chloroform on silicon wafers (for ellipsometry) and on 20 × 20 × 0.15 mm^3 Metzler glass coverslip (for optical measurement) at 1000 rpm for 25 seconds using a homebuilt spin-coater. NR stock solutions in the same solvent were added to the polymer solution to get NR-labeled PMMA films. After the spin-coating the samples were kept in the fume hood overnight for evaporation of the solvents.

Measurements Absorption and fluorescence spectra were measured at 25 °C by Cary 50 and Cary Eclipse (Varian, Australia) spectrometers, respectively. The fluorescence spectra were corrected for the spectral response. The thickness of the PMMA films were measured with an alpha-SE ellipsometric (J.A. Woollam Co., USA) according to published protocols [2,3].

Supporting Information

Supporting Information File 1

Solvatochromic plots and fluorescence spectra of NR.
[https://www.beilstein-journals.org/bjoc/content/supplementary/1860-5397-15-248-S1.pdf]

Acknowledgements

This work was supported by the University of Siegen.

ORCID® iDs

Sergey I. Druzhinin - https://orcid.org/0000-0002-6545-8819
Holger Schönherr - https://orcid.org/0000-0002-5836-5569

References

1. Handschuh-Wang, S.; Wesner, D.; Wang, T.; Lu, P.; Tücking, K.-S.; Haas, S.; Druzhinin, S. I.; Jiang, X.; Schönherr, H. *Macromol. Chem. Phys.* **2017,** *218,* 1600454. doi:10.1002/macp.201600454
2. Sadat Ebrahimi, M. M.; Schönherr, H. *Langmuir* **2014,** *30,* 7842–7850. doi:10.1021/la501482u
3. Sadat Ebrahimi, M.-M.; Voss, Y.; Schönherr, H. *ACS Appl. Mater. Interfaces* **2015,** *7,* 20190–20199. doi:10.1021/acsami.5b05746
4. Zhou, J.; Yao, D.; Qian, Z.; Hou, S.; Li, L.; Jenkins, A. T. A.; Fan, Y. *Biomaterials* **2018,** *161,* 11–23. doi:10.1016/j.biomaterials.2018.01.024
5. Milo, S.; Thet, N. T.; Liu, D.; Nzakizwanayo, J.; Jones, B. V.; Jenkins, A. T. A. *Biosens. Bioelectron.* **2016,** *81,* 166–172. doi:10.1016/j.bios.2016.02.059
6. Kumar, A.; Montemagno, C.; Choi, H.-J. *Sci. Rep.* **2017,** *7,* 3059. doi:10.1038/s41598-017-03259-x
7. Mura, S.; Nicolas, J.; Couvreur, P. *Nat. Mater.* **2013,** *12,* 991–1003. doi:10.1038/nmat3776
8. Karimi, M.; Ghasemi, A.; Sahandi Zangabad, P.; Rahighi, R.; Moosavi Basri, S. M.; Mirshekari, H.; Amiri, M.; Shafaei Pishabad, Z.; Aslani, A.; Bozorgomid, M.; Ghosh, D.; Beyzavi, A.; Vaseghi, A.; Aref, A. R.; Haghani, L.; Bahrami, S.; Hamblin, M. R. *Chem. Soc. Rev.* **2016,** *45,* 1457–1501. doi:10.1039/c5cs00798d
9. Alvarez-Lorenzo, C.; Bromberg, L.; Concheiro, A. *Photochem. Photobiol.* **2009,** *85,* 848–860. doi:10.1111/j.1751-1097.2008.00530.x
10. Müller, S.; Cavallaro, A.; Vasilev, K.; Voelcker, N. H.; Schönherr, H. *Macromol. Chem. Phys.* **2016,** *217,* 2243–2251. doi:10.1002/macp.201600099
11. Voß, Y.; Wassel, E.; Jiang, S.; Song, Q.; Druzhinin, S. I.; Schönherr, H. *Macromol. Biosci.* **2017,** *17,* 1600337. doi:10.1002/mabi.201600337
12. Tücking, K.-S.; Handschuh-Wang, S.; Schönherr, H. *Aust. J. Chem.* **2014,** *67,* 578–584. doi:10.1071/ch13527
13. Frank, B.; Gast, A. P.; Russell, T. P.; Brown, H. R.; Hawker, C. *Macromolecules* **1996,** *29,* 6531–6534. doi:10.1021/ma960749n
14. Haas, S.; Hain, N.; Raoufi, M.; Handschuh-Wang, S.; Wang, T.; Jiang, X.; Schönherr, H. *Biomacromolecules* **2015,** *16,* 832–841. doi:10.1021/bm501729h
15. Hess, C. M.; Riley, E. A.; Palos-Chávez, J.; Reid, P. J. *J. Phys. Chem. B* **2013,** *117,* 7106–7112. doi:10.1021/jp4008398
16. Greenspan, P.; Mayer, E. P.; Fowler, S. D. *J. Cell Biol.* **1985,** *100,* 965. doi:10.1083/jcb.100.3.965
17. Sackett, D. L.; Wolff, J. *Anal. Biochem.* **1987,** *167,* 228–234. doi:10.1016/0003-2697(87)90157-6
18. Kucherak, O. A.; Oncul, S.; Darwich, Z.; Yushchenko, D. A.; Arntz, Y.; Didier, P.; Mély, Y.; Klymchenko, A. S. *J. Am. Chem. Soc.* **2010,** *132,* 4907–4916. doi:10.1021/ja100351w
19. Levitt, J. A.; Chung, P.-H.; Suhling, K. *J. Biomed. Opt.* **2015,** *20,* 096002. doi:10.1117/1.jbo.20.9.096002
20. Synak, A.; Bojarski, P.; Grobelna, B.; Gryczyński, I.; Fudala, R.; Mońka, M. *Opt. Mater.* **2018,** *78,* 82–87. doi:10.1016/j.optmat.2018.02.009
21. Jee, A.-Y.; Park, S.; Kwon, H.; Lee, M. *Chem. Phys. Lett.* **2009,** *477,* 112–115. doi:10.1016/j.cplett.2009.06.088
22. Zhang, Y.; Zhang, Z.; Ding, Y.; Pikramenou, Z.; Li, Y. *ACS Appl. Mater. Interfaces* **2019,** *11,* 8693–8698. doi:10.1021/acsami.8b17679
23. Chiang, C.-L.; Wu, M.-F.; Dai, D.-C.; Wen, Y.-S.; Wang, J.-K.; Chen, C.-T. *Adv. Funct. Mater.* **2005,** *15,* 231–238. doi:10.1002/adfm.200400102
24. Camargo Dias, L., Jr.; Custodio, R.; Pessine, F. B. T. *Chem. Phys. Lett.* **1999,** *302,* 505–510. doi:10.1016/s0009-2614(99)00145-1
25. Yablon, D. G.; Schilowitz, A. M. *Appl. Spectrosc.* **2004,** *58,* 843–847. doi:10.1366/0003702041389328
26. Zuehlsdorff, T. J.; Haynes, P. D.; Payne, M. C.; Hine, N. D. M. *J. Chem. Phys.* **2017,** *146,* 124504. doi:10.1063/1.4979196
27. Crider, P. S.; Majewski, M. R.; Zhang, J.; Oukris, H.; Israeloff, N. E. *Appl. Phys. Lett.* **2007,** *91,* 013102. doi:10.1063/1.2753539
28. Ardi, M. S.; Dick, W.; Kubát, J. *Colloid Polym. Sci.* **1993,** *271,* 739–747. doi:10.1007/bf00660090
29. Bergman, R.; Alvarez, F.; Alegría, A.; Colmenero, J. *J. Chem. Phys.* **1998,** *109,* 7546–7555. doi:10.1063/1.477376
30. Sane, S. B.; Knauss, W. G. *Mech. Time-Depend. Mater.* **2001,** *5,* 293–324. doi:10.1023/a:1012517421899
31. Sane, S. B.; Knauss, W. G. *Mech. Time-Depend. Mater.* **2001,** *5,* 325–343. doi:10.1023/a:1012586719210
32. de Deus, J. F.; Souza, G. P.; Corradini, W. A.; Atvars, T. D. Z.; Akcelrud, L. *Macromolecules* **2004,** *37,* 6938–6944. doi:10.1021/ma049941c
33. Schmidt-Rohr, K.; Kulik, A. S.; Beckham, H. W.; Ohlemacher, A.; Pawelzik, U.; Boeffel, C.; Spiess, H. W. *Macromolecules* **1994,** *27,* 4733–4745. doi:10.1021/ma00095a014
34. McCrum, N. G.; Read, B. E.; Williams, G. *Anelastic and Dielectric Effects in Polymeric Solids;* John Wiley & Sons: London, 1967.
35. Moog, R. S.; Kim, D. D.; Oberle, J. J.; Ostrowski, S. G. *J. Phys. Chem. A* **2004,** *108,* 9294–9301. doi:10.1021/jp0486088
36. Ernsting, N. P.; Breffke, J.; Vorobyev, D. Y.; Duncan, D. A.; Pfeffer, I. *Phys. Chem. Chem. Phys.* **2008,** *10,* 2043–2049. doi:10.1039/b717541h
37. Druzhinin, S. I.; Galievsky, V. A.; Yoshihara, T.; Zachariasse, K. A. *J. Phys. Chem. A* **2006,** *110,* 12760–12768. doi:10.1021/jp0652547
38. Zachariasse, K. A.; Druzhinin, S. I.; Bosch, W.; Machinek, R. *J. Am. Chem. Soc.* **2004,** *126,* 1705–1715. doi:10.1021/ja037544w
39. Galievsky, V. A.; Druzhinin, S. I.; Demeter, A.; Jiang, Y.-B.; Kovalenko, S. A.; Pérez Lustres, L.; Venugopal, K.; Ernsting, N. P.; Allonas, X.; Noltemeyer, M.; Machinek, R.; Zachariasse, K. A. *ChemPhysChem* **2005,** *6,* 2307–2323. doi:10.1002/cphc.200500267
40. Zhang, X.-X.; Liang, M.; Ernsting, N. P.; Maroncelli, M. *J. Phys. Chem. B* **2013,** *117,* 4291–4304. doi:10.1021/jp305430a

41. Andreatta, D.; Sen, S.; Pérez Lustres, J. L.; Kovalenko, S. A.; Ernsting, N. P.; Murphy, C. J.; Coleman, R. S.; Berg, M. A. *J. Am. Chem. Soc.* **2006,** *128,* 6885–6892. doi:10.1021/ja0582105
42. Baumann, W.; Bischof, H.; Fröhling, J.-C.; Brittinger, C.; Rettig, W.; Rotkiewicz, K. *J. Photochem. Photobiol., A* **1992,** *64,* 49–72. doi:10.1016/1010-6030(92)85093-a
43. Lippert, E. *Z. Naturforsch., A: Astrophys., Phys. Phys. Chem.* **1955,** *10,* 541–545. doi:10.1515/zna-1955-0707
44. Golini, C. M.; Williams, B. W.; Foresman, J. B. *J. Fluoresc.* **1998,** *8,* 395–404. doi:10.1023/a:1020584801600
45. Klymchenko, A. S.; Duportail, G.; Demchenko, A. P.; Mély, Y. *Biophys. J.* **2004,** *86,* 2929–2941. doi:10.1016/s0006-3495(04)74344-1
46. Ghoneim, N.; Suppan, P. *J. Lumin.* **1989,** *44,* 83–86. doi:10.1016/0022-2313(89)90024-0
47. Ghoneim, N. *Spectrochim. Acta, Part A* **2000,** *56,* 1003–1010. doi:10.1016/s1386-1425(99)00199-7
48. Renge, I. *J. Photochem. Photobiol., A* **2018,** *353,* 433–444. doi:10.1016/j.jphotochem.2017.11.048
49. Static Dielectric Constants of Pure Liquids and Binary Liquid Mixtures. In *Landolt-Börnstein. Numerical Data and Functional Relationships in Science and Technology - Group IV Physical Chemistry;* Madelung, O., Ed.; Springer: Berlin, 1991; Vol. 6. doi:10.1007/b44266
50. Optical Constants. Refractive Indices of Organic Liquids. In *Landolt-Börnstein. Numerical Data and Functional Relationships in Science and Technology - Group III Condensed Matter;* Lechner, M. D., Ed.; Springer: Berlin, 1996; Vol. 38B. doi:10.1007/b85533
51. Dutt, G. B.; Doraiswamy, S.; Periasamy, N.; Venkataraman, B. *J. Chem. Phys.* **1990,** *93,* 8498–8513. doi:10.1063/1.459288
52. Dutt, G. B.; Doraiswamy, S.; Periasamy, N. *J. Chem. Phys.* **1991,** *94,* 5360–5368. doi:10.1063/1.460521
53. Reiser, D.; Laubereau, A. *Ber. Bunsen-Ges.* **1982,** *86,* 1106–1114. doi:10.1002/bbpc.198200048
54. Reiser, D.; Laubereau, A. *Chem. Phys. Lett.* **1982,** *92,* 297–301. doi:10.1016/0009-2614(82)80280-7
55. Ghanadzadeh Gilani, A.; Moghadam, M.; Zakerhamidi, M. S. *Dyes Pigm.* **2012,** *92,* 1052–1057. doi:10.1016/j.dyepig.2011.07.018
56. Kawski, A.; Bojarski, P.; Kukliński, B. *Chem. Phys. Lett.* **2008,** *463,* 410–412. doi:10.1016/j.cplett.2008.08.088
57. Kawski, A.; Bojarski, P. *Chem. Phys.* **2010,** *375,* 52–57. doi:10.1016/j.chemphys.2010.07.018
58. Kawski, A.; Kukliński, B.; Bojarski, P. *Chem. Phys.* **2009,** *359,* 58–64. doi:10.1016/j.chemphys.2009.03.006
59. Deye, J. F.; Berger, T. A.; Anderson, A. G. *Anal. Chem. (Washington, DC, U. S.)* **1990,** *62,* 615–622. doi:10.1021/ac00205a015
60. Suppan, P. *Chem. Phys. Lett.* **1983,** *94,* 272–275. doi:10.1016/0009-2614(83)87086-9
61. Suppan, P. *J. Photochem. Photobiol., A* **1990,** *50,* 293–330. doi:10.1016/1010-6030(90)87021-3
62. Dutta, A. K.; Kamada, K.; Ohta, K. *J. Photochem. Photobiol., A* **1996,** *93,* 57–64. doi:10.1016/1010-6030(95)04140-0
63. Sarkar, N.; Das, K.; Nath, D. N.; Bhattacharyya, K. *Langmuir* **1994,** *10,* 326–329. doi:10.1021/la00013a048
64. Edward, J. T. *J. Chem. Educ.* **1970,** *47,* 261. doi:10.1021/ed047p261
65. Schuddeboom, W.; Jonker, S. A.; Warman, J. M.; Leinhos, U.; Kuehnle, W.; Zachariasse, K. A. *J. Phys. Chem.* **1992,** *96,* 10809–10819. doi:10.1021/j100205a041
66. Samsonova, L. G.; Selivanov, N. I.; Kopylova, T. N. *Opt. Spectrosc.* **2014,** *116,* 72–76. doi:10.1134/s0030400x14010196
67. Zachariasse, K. A.; Demeter, A.; Druzhinin, S. I. *J. Phys. Chem. A* **2017,** *121,* 1223–1232. doi:10.1021/acs.jpca.6b12142
68. Taniguchi, M.; Lindsey, J. S. *Photochem. Photobiol.* **2018,** *94,* 290–327. doi:10.1111/php.12860
69. Chen, R.; Zhang, G.; Gao, Y.; Xiao, L.; Jia, S. *Appl. Phys. Lett.* **2012,** *100,* 203118. doi:10.1063/1.4717049
70. Van Krevelen, D. W.; Te Nijenhuis, K. *Magnetic Properties;* Properties of Polymers; Elsevier: Amsterdam, Netherlands, 2009; pp 287–318. doi:10.1016/B978-0-08-054819-7.00010-8
71. Sultanova, N.; Kasarova, S.; Nikolov, I. *Acta Phys. Pol., A* **2009,** *116,* 585–587. doi:10.12693/aphyspola.116.585
72. Tsuda, S.; Yamaguchi, S.; Kanamori, Y.; Yugami, H. *Opt. Express* **2018,** *26,* 6899–6915. doi:10.1364/oe.26.006899
73. Clayton, L. M.; Sikder, A. K.; Kumar, A.; Cinke, M.; Meyyappan, M.; Gerasimov, T. G.; Harmon, J. P. *Adv. Funct. Mater.* **2005,** *15,* 101–106. doi:10.1002/adfm.200305106
74. Nasr, G. M.; Ahmed, R. M. *Mod. Phys. Lett. B* **2010,** *24,* 911–919. doi:10.1142/s0217984910022962

License and Terms

BEILSTEIN JOURNAL OF ORGANIC CHEMISTRY

A new approach to silicon rhodamines by Suzuki–Miyaura coupling – scope and limitations

Thines Kanagasundaram[1,2], Antje Timmermann[1,2], Carsten S. Kramer[*1,§] and Klaus Kopka[1,3,§]

Full Research Paper

Open Access

Address:
[1]Division of Radiopharmaceutical Chemistry, German Cancer Research Center (DKFZ), Im Neuenheimer Feld 280, 69120 Heidelberg, Germany, [2]Institute of Inorganic Chemistry, Im Neuenheimer Feld 270, 69120 Heidelberg, Germany and [3]German Cancer Consortium (DKTK), Heidelberg, Germany

Email:
Carsten S. Kramer[*] - c.kramer@dkfz-heidelberg.de

* Corresponding author
§ KK and CSK contributed equally to this work and share senior authorship.

Keywords:
cross coupling; fluorescent dyes; near-infrared (NIR) dyes; silicon rhodamines; Suzuki–Miyaura coupling

Beilstein J. Org. Chem. **2019,** *15,* 2569–2576.
doi:10.3762/bjoc.15.250

Received: 31 May 2019
Accepted: 02 October 2019
Published: 29 October 2019

This article is part of the thematic issue "Dyes in modern organic chemistry".

Guest Editor: H. Ihmels

Abstract

Background: Silicon rhodamines are of particular interest because of their advantageous dye properties (fluorescence- and biostability, quantum efficiency, tolerance to photobleaching). Therefore, silicon rhodamines find frequent application in STED (stimulated emission depletion) microscopy, as sensor molecules for, e.g., ions and as fluorophores for the optical imaging of tumors. Different strategies were already employed for their synthesis. Because of just three known literature examples in which Suzuki–Miyaura cross couplings gave access to silicon rhodamines in poor to moderate yields, we wanted to improve these first valuable experimental results.

Results: The preparation of the xanthene triflate was enhanced and several boron sources were screened to find the optimal coupling partner. After optimization of the palladium catalyst, different substituted boroxines were assessed to explore the scope of the Pd-catalyzed cross-coupling reaction.

Conclusions: A number of silicon rhodamines were synthesized under the optimized conditions in up to 91% yield without the necessity of HPLC purification. Moreover, silicon rhodamines functionalized with free acid moieties are directly accessible in contrast to previously described methods.

Introduction

Silicon rhodamines are versatile fluorescent dyes that found extensive use in super-resolution microscopy [1-8] and as probes for targeting various biomolecules [9-12] or sensors for metal ions [13-17], pH [15], voltage [18] or metabolites [19-22]. Since our group is interested in synthesizing new tumor tracers for intraoperative imaging of cancerous lesions, we were interested in silicon rhodamines due to their fluorescence properties in the biological window (650 nm to 1350 nm). While clinically approved fluorescence dyes like ICG (indocyanine green, M_w = 775 g/mol) have a high molecular weight and could therefore alter pharmacokinetic or -dynamic properties of the tumor tracers, silicon rhodamines are relatively small and already examined as fluorophores for the optical imaging of tumors. Using silicon rhodamine SiR700 a more enhanced tumor-to-background ratio in optical imaging could be achieved compared to the cyanine based dyes Cy5.5 and Alexa Fluor® 680 [23]. Moreover, silicon rhodamines demonstrated in in vivo imaging experiments excellent fluorescence properties and biostabilities [23] as well as exhibited high quantum efficiencies with high tolerance to photobleaching [24]. A silicon rhodamine antibody conjugate could also be successfully applied for optical imaging of a xenograft tumor (human malignant meningioma) in a mouse model [24]. Again, in direct comparison with the cyanine dye Cy5.5, the silicon rhodamine conjugate showed no fading indicating that silicon rhodamine dyes are more suitable for long time observation than cyanine-based fluorophores [24].

Different synthetic approaches were established to form the silicon rhodamine framework **1** (Scheme 1). While the group of Wu used a copper(II) bromide-catalyzed solvent-free condensation of a diarylsilane **2** with various benzaldehydes **3** [25], Sparr and Fischer added the double Grignard reagent **4** to methyl esters **5** [26]. A similar approach was established by Lavis, herein electrophiles (anhydrides or esters) were added to lithium or magnesium organyls **4** [27]. Johnsson and co-workers

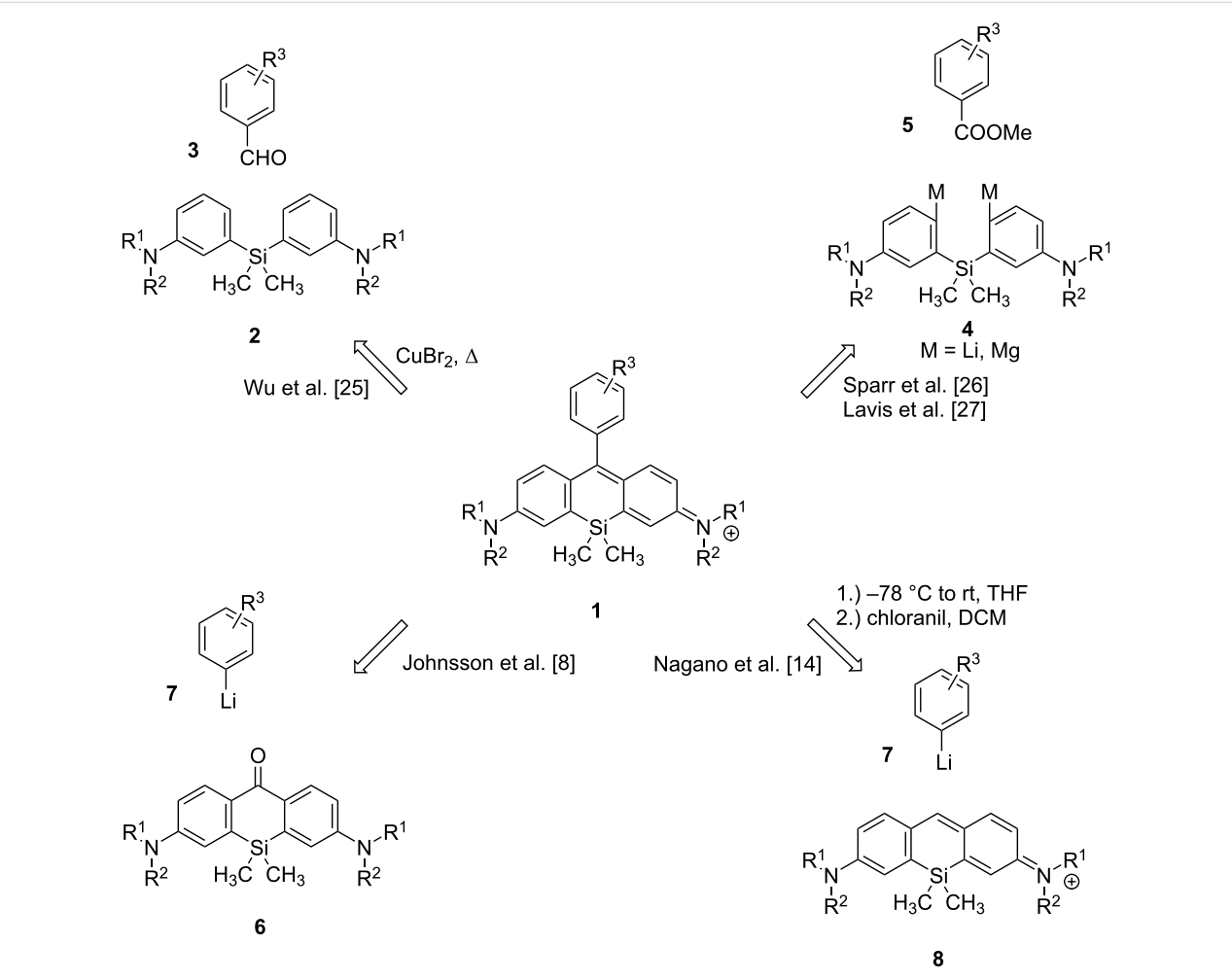

Scheme 1: Different synthetic approaches to silicon rhodamine dyes.

could establish dye formation by addition of aryllithium **7** to the silicon xanthone **6** [8]. A related strategy, adding lithium compound **7** to a preformed tricyclic system **8**, was used by Nagano et al. to synthesize the Ge and Sn rhodamine analogues [14].

In a recent publication, Urano et al. synthesized the rhodamines **13**–**15** by coupling the triflate of xanthone **12** with boroxines **9b**–**11b** (Scheme 2) [22,28]. Hereby, the boroxines **9b**–**11b** were accessible by thermal dehydration of the corresponding boronic acids **9a**–**11a**. With this procedure product **13** was obtained in only 6% yield, which is presumably due to a competing coupling reaction of the boroxine moiety of **9b** with the chlorine atom of **9b** or sterical reasons (the chlorine in 2'-position might lead to repulsion during the cross-coupling reaction). The reaction of the triflate with cyano-substituted phenylboroxines **10b** and **11b** led to silicon rhodamine dyes **14** and **15** in poor yields of 23 and 19%, respectively. The reaction conditions applied for the cross coupling of the triflate were similar to those published by Calitree and Detty for the coupling of the triflates derived from the O, S, Se, and Te-xanthones **16** with various phenylboroxines (bearing nitro, carboxylic acid, methyl and methoxy substituents) [29]. Here yields of 53–79% were obtained (for O and S analogues; 85–99% yields based on recovered starting material (brsm)). Since the yields reported by Urano for the Si-analogous Suzuki reactions were much lower (6–23%) [22], we wanted to examine if the aforementioned substrates were outliers and a cross-coupling reaction could be a valuable approach to silicon

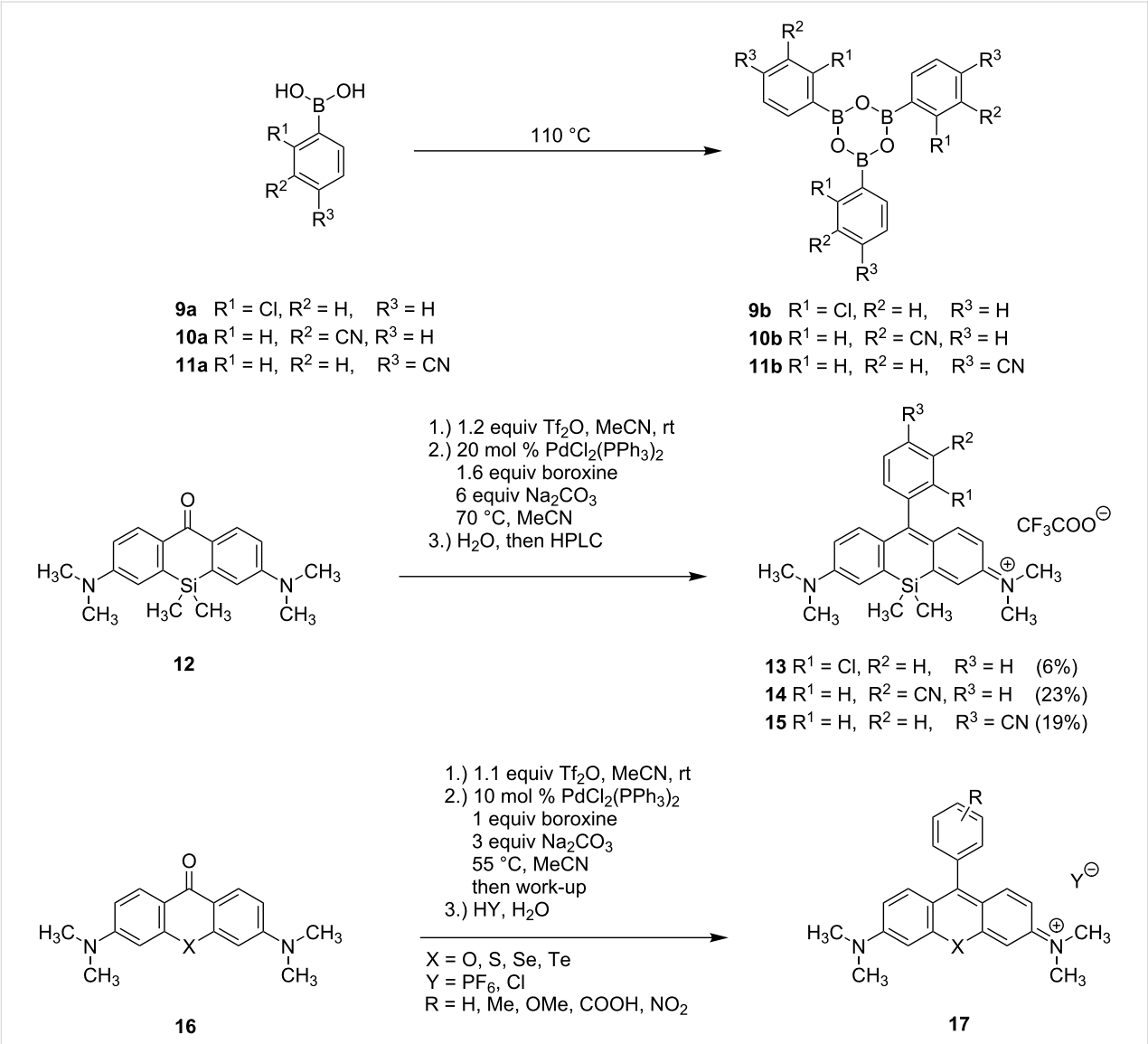

Scheme 2: Previous work from Calitree [29] and Urano [22,28] on the Suzuki–Miyaura coupling of triflates, derived from xanthones **12** and **16**, with boroxines.

rhodamines. Thus, we aimed at the optimization of coupling conditions as well as evaluation of the best boron compounds for coupling. Since carboxylic acid-substituted dyes like compound **17** (X = Si, R = COOH) can be easily coupled to tumor binding vectors, we wanted to investigate if these dyes are also accessible by Suzuki–Miyaura coupling.

Results and Discussion

Optimization of reaction conditions

At first we investigated the effects of different catalysts and boron compounds on the synthesis of silicon rhodamine **22** via Suzuki–Miyaura cross coupling (Scheme 3, Table 1). Triflate **21** was obtained without further purification from **12** by addition of triflic anhydride in dry acetonitrile. Boroxine **18b** was formed by heating of boronic acid (**18a**) at 110 °C because it was shown by Calitree and Detty that free boronic acid leads to the destruction of the triflate, resulting in the corresponding xanthone [29]. Applying standard conditions on xanthone **12** by treatment with triflic anhydride in dry acetonitrile and subsequent addition of base, catalyst and boroxine **18b** yielded the desired fluorophore **22** in 41% yield together with unreacted xanthone **12** (Table 1, entry 1). Since the initial triflate forma-

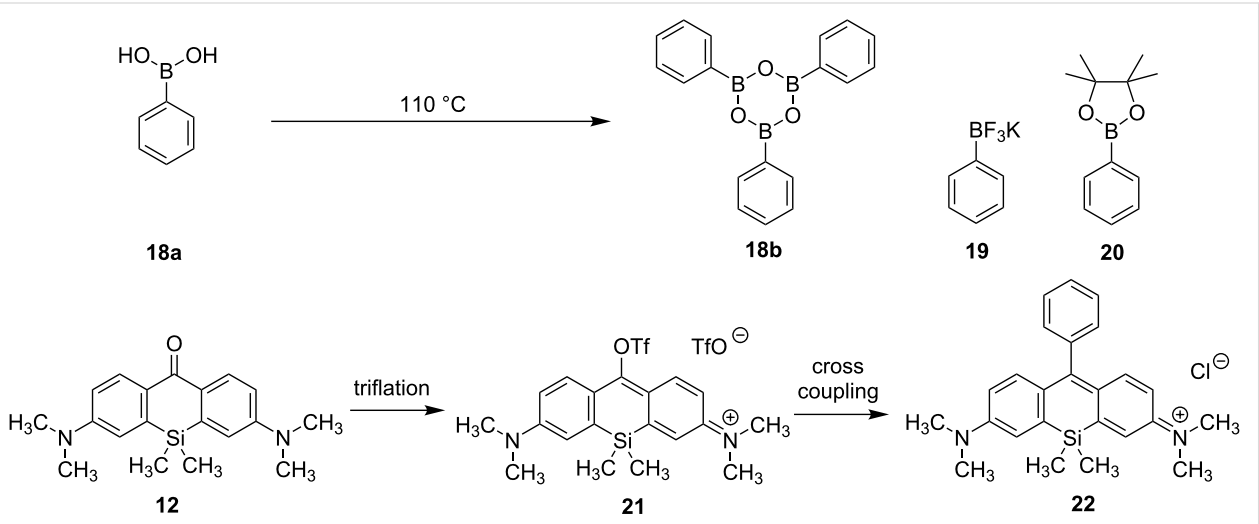

Scheme 3: Optimization of cross-coupling conditions of triflate **21**, derived from Si-xanthone **12**, with boron species **18b**, **19** and **20** (see Table 1).

Table 1: Optimization of cross-coupling conditions of triflate **21**, derived from Si-xanthone **12**, with boron species **18b**, **19** and **20**.

Entry	Triflation	Cross coupling			Yield (**22**)
		Catalyst (10 mol %)	Boron species (1 equiv)	Conditions	
1	1.1 equiv Tf_2O, MeCN, rt, 20 min	$PdCl_2(PPh_3)_2$	**18b**	3 equiv Na_2CO_3, MeCN, 70 °C, overnight	41%[a]
2	1 equiv Comins' reagent (5-Cl-2-pyridyl-NTf_2), MeCN, rt, 1 h	–	–	–	–
3	1.1 equiv Tf_2O, DCM, rt, 20 min, then evaporation	$PdCl_2(PPh_3)_2$	**18b**	3 equiv Na_2CO_3, MeCN, 70 °C, overnight	49%[a], 80%[a,b]
4	1.1 equiv Tf_2O, DCM, rt, 20 min, then evaporation	$Pd(PPh_3)_4$	**18b**	3 equiv Na_2CO_3, MeCN, 70 °C, overnight	39%[a], 82%[a,b]
5	1.1 equiv Tf_2O, DCM, rt, 20 min, then evaporation	$PdCl_2(PPh_3)_2$	**18b**	3 equiv Cs_2CO_3, MeCN, 70 °C, overnight	n.r.
6	1.1 equiv Tf_2O, DCM, rt, 20 min, then evaporation	$PdCl_2(PPh_3)_2$	**19**	3 equiv Na_2CO_3, MeCN, 70 °C, overnight	48%[a]
7	1.1 equiv Tf_2O, DCM, rt, 20 min, then evaporation	$PdCl_2(PPh_3)_2$	**20**	3 equiv Na_2CO_3, MeCN, 70 °C, overnight	n.r.
8	1.1 equiv Tf_2O, DCM, rt, 20 min, then evaporation	$PdCl_2(dppf)$	**18b**	3 equiv Na_2CO_3, MeCN, 70 °C, overnight	67%, 73%[b]

[a]Corrected yield, contamination with $[PPh_4]^+$. [b]Based on recovered starting material (brsm) **12**.

tion to **21** was unreliable and often incomplete, leading to lower yields, Comins reagent was investigated as an alternative triflation reagent. Notably, the use of Comins reagent showed no transformation from the yellow xanthone **12** to the deep blue triflate **21** at all (Table 1, entry 2). Exchange of anhydrous acetonitrile by anhydrous dichloromethane, which was removed in vacuo prior to coupling, provided triflate **21** as a blue salt without xanthone residues, hereby the yield could be slightly enhanced but still the conditions of the coupling reaction led to some back reaction of **21** to **12** (Table 1, entry 3). While the use of $PdCl_2(PPh_3)_2$ was successful in the synthesis of chalcogenorhodamine dyes [29], the usage of that catalyst gave just low yields when applied in the synthesis of the silicon analogues (Scheme 2) [22]. Although $Pd(PPh_3)_4$ was not found to be an effective catalyst for the synthesis of rhodamine and rosamine dyes as well as for their selenium or tellurium analogous [29], the usage of that Pd(0) catalyst showed yields comparable with those obtained with $PdCl_2(PPh_3)_2$ (Table 1, entry 4). The exchange of sodium carbonate with cesium carbonate resulted in no reaction at all (Table 1, entry 5). Whereby usage of potassium phenyltrifluoroborate (**19**) resulted in a yield comparable to boroxine **18b** (Table 1, entry 6), usage of pinacol ester **20** showed no reaction in the cross-coupling reaction (Table 1, entry 7). Although described optimizations of the reaction conditions could lead to the silicon rhodamine **22** in moderate yields, an inseparable impurity of the cationic fluorophore was detected. After identifying this impurity as the tetraphenylphosphonium cation, we exchanged the triphenylphosphine ligand of the catalyst with dppf (1,1'-bis(diphenylphosphino)ferrocene). Remarkably, not only the yield was increased with $PdCl_2$(dppf) from 49% to 67%, even the dye **22** was obtained with high purity after column chromatography without the necessity of further HPLC purification (Table 1, entry 8).

Exploration of substrate scope

Next we explored the substrate scope of the Suzuki–Miyaura coupling by screening commercially available boronic acids (Scheme 4, Table 2). Hereby, $PdCl_2$(dppf) was also tested in order to suppress the formation of the inseparable phosphonium cation species. At first, we investigated the use of 3-boronobenzoic acid (**23a**) that should lead to a rhodamine suitable for coupling to a tumor vector, but boroxine **23b** was converted to **23c** with $PdCl_2(PPh_3)_2$ in poor yields (Scheme 4 and Table 2, entry 1). However, $PdCl_2$(dppf) performed better and led to the acid-substituted silicon rhodamine **23c** in a moderate yield of 31% (56% brsm) (Table 2, entry 2). The moderate yield might be explained with the destruction of the triflate by the acid moiety of **23c**. In order to prevent the destruction of the initially formed triflate **21**, 4-boronobenzaldehyde (**24a**)

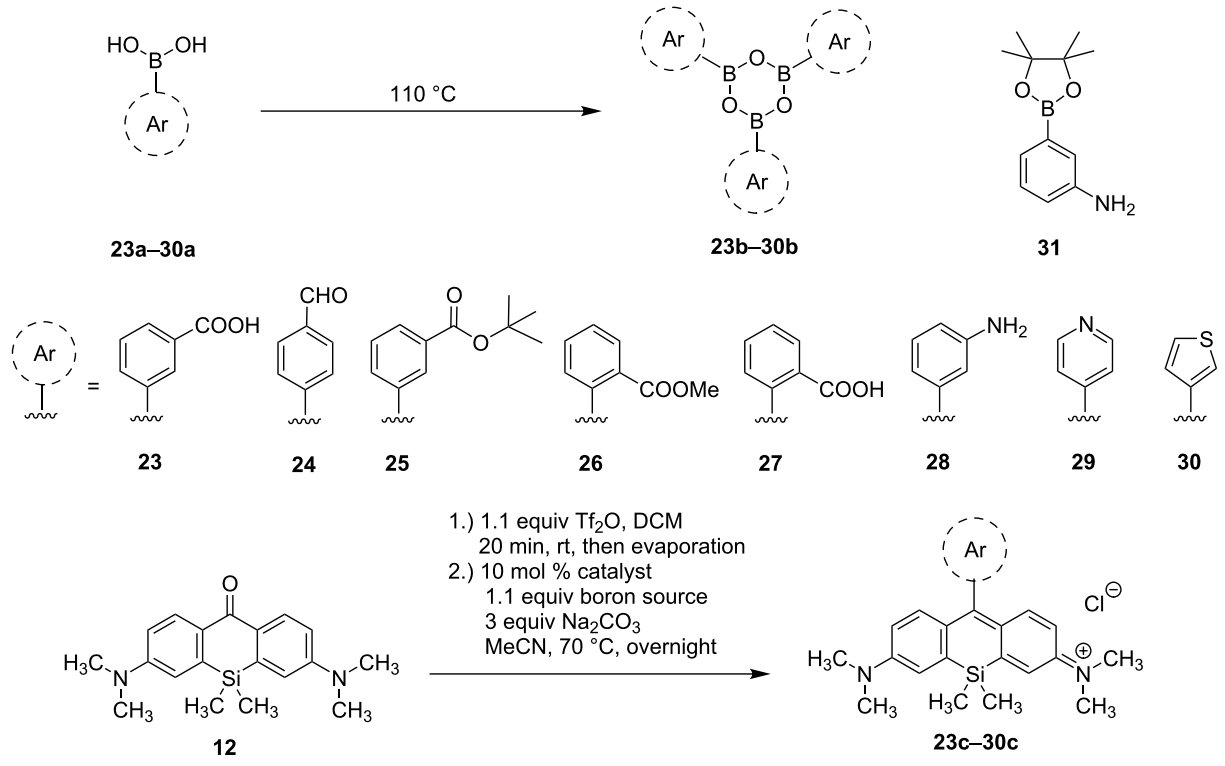

Scheme 4: Coupling reactions of silicon xanthone **12** with different boron species (**23b**–**30b**, **31**).

Table 2: Coupling reactions of silicon xanthone **12** with different boron species (**23b**–**30b**, **31**).

Entry	Boron source	Catalyst	Yield
1	**23b**	$PdCl_2(PPh_3)_2$	5%[a], 46%[a,b] (**23c**)
2	**23b**	$PdCl_2$(dppf)	31%, 56%[b] (**23c**)
3	**24b**	$PdCl_2(PPh_3)_2$	traces (**24c**)
4	**25b**	$PdCl_2(PPh_3)_2$	43%[a], 62%[a,b] (**25c**)
5	**25b**	$PdCl_2$(dppf)	53%, 66%[b] (**25c**)
6	**26b**	$PdCl_2(PPh_3)_2$	n.r.
7	**27b**	$PdCl_2(PPh_3)_2$	n.r.
8	**28b**	$PdCl_2(PPh_3)_2$	n.r.
9	**31**	$PdCl_2(PPh_3)_2$	n.r.
10	**29b**	$PdCl_2(PPh_3)_2$	n.r.
11	**30b**	$PdCl_2(PPh_3)_2$	37%[a], 56%[a,b] (**30c**)
12	**30b**	$PdCl_2$(dppf)	91% (**30c**)

[a]Corrected yield, contamination with $[PPh_3Ar]^+$. [b]Based on recovered starting material (brsm) **12**.

was intended as a coupling substrate but yielded silicon rhodamine **24c** only in traces (Table 2, entry 3). Usage of the *tert*-butyl-protected boronobenzoic acid **25a**, or its boroxine counterpart **25b**, respectively, gave fluorophore **25c** suitable for later coupling reactions in reasonable yields of 43% and 53%, depending on the catalyst used (Table 2, entries 4 and 5). Again, the reaction catalyzed by $PdCl_2$(dppf) resulted in an enhanced yield compared to catalysis with $PdCl_2(PPh_3)_2$. Next we aimed at the synthesis of a silicon rhodamine bearing an acid function in 2'-position. With a less bulky methyl ester in the 2'-position of the phenylboroxine, the transmetalation and the new bond formation through reductive elimination should be less hindered, but remarkably, no reaction was observed either with the methyl ester **26b** or the free acid **27b** (Table 2, entries 6 and 7). Next we explored if amino-substituted silicon rhodamine **28c** is accessible via Pd-catalysis. The resulting rhodamine **28c** could be a possible substrate for the conversion into an azide and follow-up click reactions with alkyne-substituted tumor vectors. While heating of amine **28a** to the corresponding boroxine **28b** lead to formation of a brown solid (presumably due to degradation), the reaction of triflate **21** with the pinacol ester **31** showed no product formation at all (Table 2, entries 8 and 9). Since we were able to investigate the functional group tolerance of the coupling reaction, we shifted our focus towards heterocyclic boronic acids as substrates. Since 4'-pyridinyl- [27,30] and 3'-thienyl- [27,31-33] substituted silicon rhodamines are already known, we investigated the synthesis of these dyes by Suzuki–Miyaura cross coupling. Firstly, pyridinylboronic acid **29a** was used as a substrate after heating at 110 °C, but no conversion was observed presumably due to the formation of an internal salt (protonated pyridine ring and deprotonated boronic acid) and ensuing difficult formation of boroxine **29b** (Table 2, entry 10). Switching to the neutral heterocyclic boronic acid **30a**, the corresponding thienyl-substituted silicon rhodamine **30c** could be obtained in 37% (56% brsm) yield with the $PdCl_2(PPh_3)_2$ catalyst. Remarkably, the yield could be clearly enhanced by catalysis with $PdCl_2$(dppf) and the thienyl-substituted fluorophore **30c** could subsequently be synthesized in 91% yield.

Table 3 compares the reaction outcome of the silicon rhodamine synthesis via Suzuki coupling with other employed methods: synthesis of the phenyl-substituted silicon rhodamine **22** by Suzuki cross coupling affords the product in a similar yield compared to the addition of phenyllithium to xanthone **12** or the attack of the double metallated bis-aniline **4** ($R^1 = R^2$ = Me, M = Mg) to the benzoic acid methyl ester [26]. However, the cross coupling of triflate **21** with boroxine **25b** led to the ester-substituted rhodamine **25c** in a reasonable yield of 53% (66%

Table 3: Comparison of common methods for silicon rhodamine synthesis.

Method → / Fluorophore ↓	Addition of lithium organyl to **12**[a]	Suzuki–Miyaura cross coupling	Attack of **4** ($R^1 = R^2$ = Me, M = Mg) to **5** (R^3 = H)
phenyl-substituted SiR (**22**)	72%	67%, 73%[b]	72% [26]
tert-butylbenzoic acid-substituted SiR (**25c**)	7%	53%, 66%[b]	–
thienyl-substituted SiR (**30c**)	77%	91%	–

[a]Conditions: 7 equiv aryl bromide, 14 equiv *t*-BuLi, THF, −78 °C, 30 min, then 1 equiv **12** at −78 °C to rt, overnight, then aq HCl, work-up, purification with DCM/MeOH 99:1 to 9:1. [b]Based on recovered starting material (brsm) **12**.

brsm) while the addition of the lithiated *tert*-butyl 3-bromobenzoate gave the fluorophore **25c** in only 7% yield. Finally, the cross-coupling reaction of **12** and **30b** to rhodamine **30c** clearly outperforms the addition of lithiated 2-bromothiophene to xanthone **12** since 2-bromothiophene might also undergo lithiation in 5-position in competition to the halogen metal exchange (in general multiple halogenated aryls are problematic nucleophiles for these addition reactions).

Conclusion

Since just three literature examples are known to date in which Suzuki–Miyaura cross-coupling reactions gave access to silicon rhodamines in poor to moderate yields (Scheme 2), we wanted to improve these first valuable experimental results. In general, the amount of re-isolated starting material **12** could be significantly reduced when acetonitrile was exchanged with dichloromethane in the triflation reaction to provide triflate **21** neat and more reliable. Screening of different boron species and catalysts showed that, like in the syntheses of O, S, Se, and Te-rhodamines, boroxines were a suitable source, but also potassium trifluoroborates can be taken into consideration for the reaction design, whereas pinacol esters didn't show any reactivity. While $PdCl_2(PPh_3)_2$ was a sufficient catalyst for the cross coupling, application of $PdCl_2$(dppf) led to clearly enhanced yields: overall the Suzuki–Miyaura cross-coupling reaction gave access to silicon rhodamines with neutral (hetero)aromatic xanthene substituents (phenyl: 67%, respectively 73% brsm; thienyl: 91%) (even though the term 'dihydrosilaanthracene' is correct to name the Si-anthracene moiety, the term 'Si-xanthene' is widely used in the literature (see e.g. [30]); also the term Si-xanthone (for derivatives of **12**) is established instead of 9-silaanthracen-10(9*H*)-one). The conditions tolerated also the use of the unprotected acid functionality of the boroxine **23b** (**23c**, 31%, respectively 56% brsm), while application of basic boronic acids failed (**28**, **29**), presumably due to unsuccessful boroxine formation. The main advantage of the cross coupling is the access to acid-functionalized fluorophores like **23c** that can be immediately coupled to a molecule of interest (e.g., tumor binding vectors) whereas previously published methodologies need, e.g., an ester, orthoester or oxazoline protecting group for the acid. But also the *tert*-butyl ester-functionalized boroxine **25** is suitable for the cross coupling. With the current catalytic system, coupling of 2-substituted boroxines (**26**, **27**) remains challenging, but optimizing the catalytic system with ligands suitable for coupling of multisubstituted aryls is under current investigation. In conclusion, several silicon rhodamines could be synthesized under the optimized conditions, without the necessity of HPLC purification, in up to 91% yield whereby the free acids are directly accessible in contrast to the three hitherto described methods.

Supporting Information

Supporting Information File 1

Experimental procedures and NMR spectra of all synthesized compounds as well as photochromic characterization data (fluorescence spectra, quantum yield) of thienyl-substituted silicon rhodamine **30c**.
[https://www.beilstein-journals.org/bjoc/content/supplementary/1860-5397-15-250-S1.pdf]

Acknowledgements

We are very grateful to the Wilhelm Sander Stiftung for a grant on bi-modal tumor tracers (2018.024.1). We thank Yvonne Remde for synthetic support. We are thankful to Jessica Matthias (group of Stefan Hell, MPI for Medical Research Heidelberg) for measurement of the UV–vis spectrum of **30c**.

ORCID® iDs

Thines Kanagasundaram - https://orcid.org/0000-0001-8265-8591
Antje Timmermann - https://orcid.org/0000-0002-9557-9320
Carsten S. Kramer - https://orcid.org/0000-0001-9932-423X
Klaus Kopka - https://orcid.org/0000-0003-4846-1271

References

1. Thompson, A. D.; Omar, M. H.; Rivera-Molina, F.; Xi, Z.; Koleske, A. J.; Toomre, D. K.; Schepartz, A. *Angew. Chem., Int. Ed.* **2017,** *56,* 10408–10412. doi:10.1002/anie.201704783
2. Butkevich, A. N.; Ta, H.; Ratz, M.; Stoldt, S.; Jakobs, S.; Belov, V. N.; Hell, S. W. *ACS Chem. Biol.* **2018,** *13,* 475–480. doi:10.1021/acschembio.7b00616
3. Butkevich, A. N.; Mitronova, G. Y.; Sidenstein, S. C.; Klocke, J. L.; Kamin, D.; Meineke, D. N. H.; D'Este, E.; Kraemer, P.-T.; Danzl, J. G.; Belov, V. N.; Hell, S. W. *Angew. Chem., Int. Ed.* **2016,** *55,* 3290–3294. doi:10.1002/anie.201511018
4. Kozma, E.; Estrada Girona, G.; Paci, G.; Lemke, E. A.; Kele, P. *Chem. Commun.* **2017,** *53,* 6696–6699. doi:10.1039/c7cc02212c
5. Grimm, J. B.; Klein, T.; Kopek, B. G.; Shtengel, G.; Hess, H. F.; Sauer, M.; Lavis, L. D. *Angew. Chem., Int. Ed.* **2016,** *55,* 1723–1727. doi:10.1002/anie.201509649
6. Lukinavičius, G.; Reymond, L.; Umezawa, K.; Sallin, O.; D'Este, E.; Göttfert, F.; Ta, H.; Hell, S. W.; Urano, Y.; Johnsson, K. *J. Am. Chem. Soc.* **2016,** *138,* 9365–9368. doi:10.1021/jacs.6b04782
7. Takakura, H.; Zhang, Y.; Erdmann, R. S.; Thompson, A. D.; Lin, Y.; McNellis, B.; Rivera-Molina, F.; Uno, S.-n.; Kamiya, M.; Urano, Y.; Rothman, J. E.; Bewersdorf, J.; Schepartz, A.; Toomre, D. *Nat. Biotechnol.* **2017,** *35,* 773–780. doi:10.1038/nbt.3876
8. Lukinavičius, G.; Umezawa, K.; Olivier, N.; Honigmann, A.; Yang, G.; Plass, T.; Mueller, V.; Reymond, L.; Corrêa, I. R., Jr.; Luo, Z.-G.; Schultz, C.; Lemke, E. A.; Heppenstall, P.; Eggeling, C.; Manley, S.; Johnsson, K. *Nat. Chem.* **2013,** *5,* 132–139. doi:10.1038/nchem.1546
9. Shieh, P.; Siegrist, M. S.; Cullen, A. J.; Bertozzi, C. R. *Proc. Natl. Acad. Sci. U. S. A.* **2014,** *111,* 5456–5461. doi:10.1073/pnas.1322727111

10. Iwatate, R. J.; Kamiya, M.; Umezawa, K.; Kashima, H.; Nakadate, M.; Kojima, R.; Urano, Y. *Bioconjugate Chem.* **2018,** *29,* 241–244. doi:10.1021/acs.bioconjchem.7b00776
11. Kim, E.; Yang, K. S.; Kohler, R. H.; Dubach, J. M.; Mikula, H.; Weissleder, R. *Bioconjugate Chem.* **2015,** *26,* 1513–1518. doi:10.1021/acs.bioconjchem.5b00152
12. Hanaoka, K.; Kagami, Y.; Piao, W.; Myochin, T.; Numasawa, K.; Kuriki, Y.; Ikeno, T.; Ueno, T.; Komatsu, T.; Terai, T.; Nagano, T.; Urano, Y. *Chem. Commun.* **2018,** *54,* 6939–6942. doi:10.1039/c8cc02451k
13. Du, M.; Huo, B.; Liu, J.; Li, M.; Fang, L.; Yang, Y. *Anal. Chim. Acta* **2018,** *1030,* 172–182. doi:10.1016/j.aca.2018.05.013
14. Koide, Y.; Urano, Y.; Hanaoka, K.; Terai, T.; Nagano, T. *ACS Chem. Biol.* **2011,** *6,* 600–608. doi:10.1021/cb1002416
15. Wang, T.; Zhao, Q.-J.; Hu, H.-G.; Yu, S.-C.; Liu, X.; Liu, L.; Wu, Q.-Y. *Chem. Commun.* **2012,** *48,* 8781. doi:10.1039/c2cc34159j
16. Wang, B.; Cui, X.; Zhang, Z.; Chai, X.; Ding, H.; Wu, Q.; Guo, Z.; Wang, T. *Org. Biomol. Chem.* **2016,** *14,* 6720–6728. doi:10.1039/c6ob00894a
17. Egawa, T.; Hanaoka, K.; Koide, Y.; Ujita, S.; Takahashi, N.; Ikegaya, Y.; Matsuki, N.; Terai, T.; Ueno, T.; Komatsu, T.; Nagano, T. *J. Am. Chem. Soc.* **2011,** *133,* 14157–14159. doi:10.1021/ja205809h
18. Huang, Y.-L.; Walker, A. S.; Miller, E. W. *J. Am. Chem. Soc.* **2015,** *137,* 10767–10776. doi:10.1021/jacs.5b06644
19. Zhang, H.; Liu, J.; Liu, C.; Yu, P.; Sun, M.; Yan, X.; Guo, J.-P.; Guo, W. *Biomaterials* **2017,** *133,* 60–69. doi:10.1016/j.biomaterials.2017.04.023
20. Huo, Y.; Miao, J.; Han, L.; Li, Y.; Li, Z.; Shi, Y.; Guo, W. *Chem. Sci.* **2017,** *8,* 6857–6864. doi:10.1039/c7sc02608k
21. Koide, Y.; Urano, Y.; Hanaoka, K.; Terai, T.; Nagano, T. *J. Am. Chem. Soc.* **2011,** *133,* 5680–5682. doi:10.1021/ja111470n
22. Umezawa, K.; Yoshida, M.; Kamiya, M.; Yamasoba, T.; Urano, Y. *Nat. Chem.* **2017,** *9,* 279–286. doi:10.1038/nchem.2648
23. McCann, T. E.; Kosaka, N.; Koide, Y.; Mitsunaga, M.; Choyke, P. L.; Nagano, T.; Urano, Y.; Kobayashi, H. *Bioconjugate Chem.* **2011,** *22,* 2531–2538. doi:10.1021/bc2003617
24. Koide, Y.; Urano, Y.; Hanaoka, K.; Piao, W.; Kusakabe, M.; Saito, N.; Terai, T.; Okabe, T.; Nagano, T. *J. Am. Chem. Soc.* **2012,** *134,* 5029–5031. doi:10.1021/ja210375e
25. Wang, B.; Chai, X.; Zhu, W.; Wang, T.; Wu, Q. *Chem. Commun.* **2014,** *50,* 14374–14377. doi:10.1039/c4cc06178k
26. Fischer, C.; Sparr, C. *Angew. Chem., Int. Ed.* **2018,** *57,* 2436–2440. doi:10.1002/anie.201711296
27. Grimm, J. B.; Brown, T. A.; Tkachuk, A. N.; Lavis, L. D. *ACS Cent. Sci.* **2017,** *3,* 975–985. doi:10.1021/acscentsci.7b00247
28. Urano, Y.; Kamiya, M.; Umezawa, K.; Yoshida, M. Glutathione-detecting fluorescent probe. U.S. Pat. Appl. US2017/0045525 A1, Feb 16, 2017.
29. Calitree, B. D.; Detty, M. R. *Synlett* **2010,** 89–92. doi:10.1055/s-0029-1218535
30. Zhang, H.; Li, K.; Li, L.-L.; Yu, K.-K.; Liu, X.-Y.; Li, M.-Y.; Wang, N.; Liu, Y.-H.; Yu, X.-Q. *Chin. Chem. Lett.* **2019,** *30,* 1063–1066. doi:10.1016/j.cclet.2019.03.017
31. Groves, K.; Bruff, R. Substituted silaxanthenium red to near-infrared fluorochromes for in vitro and in vivo imaging and detection. WO Pat. Appl. WO2014/144793 A1, Sept 18, 2014.
32. Gamsey, S.; Bernat, V.; Kutyavin, A.; Clary, J. W.; Pradhan, S. Near-IR Glucose Sensors. U. S..Pat. Appl. US20180179233 A1, June 28, 2018.
33. Urano, Y.; Kamiya, M.; Tachibana, R. Preparation of spiro compounds as red fluorescent probes for use in detection of peptdase activity. WO Pat. Appl. WO 2018151260 A1, Aug 23, 2018.

License and Terms

BEILSTEIN JOURNAL OF ORGANIC CHEMISTRY

Arylisoquinoline-derived organoboron dyes with a triaryl skeleton show dual fluorescence

Vânia F. Pais[1], Tristan Neumann[1], Ignacio Vayá[2], M. Consuelo Jiménez[2], Abel Ros[*3,4] and Uwe Pischel[*1]

Full Research Paper

Open Access

Address:
[1]CIQSO – Centre for Research in Sustainable Chemistry and Department of Chemistry, University of Huelva, Campus de El Carmen s/n, 21071 Huelva, Spain, [2]Department of Chemistry/Institute of Chemical Technology UPV-CSIC, Universitat Politècnica de València, Camino de Vera s/n, 46022 Valencia, Spain, [3]Institute for Chemical Research (CSIC-US) and Innovation Center in Advanced Chemistry (ORFEO–CINQA), C/ Américo Vespucio 49, 41092 Seville, Spain and [4]Department of Organic Chemistry, University of Seville, C/ Prof. García González 1, 41012 Seville, Spain

Email:
Abel Ros[*] - abel.ros@iiq.csic.es; Uwe Pischel[*] - uwe.pischel@diq.uhu.es

* Corresponding author

Keywords:
anions; dyes; fluorescence; laser-flash photolysis; organoboron

Beilstein J. Org. Chem. **2019,** *15,* 2612–2622.
doi:10.3762/bjoc.15.254

Received: 05 July 2019
Accepted: 14 October 2019
Published: 04 November 2019

This article is part of the thematic issue "Dyes in modern organic chemistry".

Guest Editor: H. Ihmels

Abstract

Four new dyes that derive from borylated arylisoquinolines were prepared, containing a third aryl residue (naphthyl, 4-methoxy-naphthyl, pyrenyl or anthryl) that is linked via an additional stereogenic axis. The triaryl cores were synthesized by Suzuki couplings and then transformed into boronic acid esters by employing an Ir(I)-catalyzed reaction. The chromophores show dual emission behavior, where the long-wavelength emission band can reach maxima close to 600 nm in polar solvents. The fluorescence quantum yields of the dyes are generally in the range of 0.2–0.4, reaching in some cases values as high as 0.5–0.6. Laser-flash photolysis provided evidence for the existence of excited triplet states. The dyes form fluoroboronate complexes with fluoride anions, leading to the observation of the quenching of the long-wavelength emission band and ratiometric response by the build-up of a hypsochromically shifted emission signal.

Introduction

Boron-containing tri- and tetra-coordinated chromophores have attracted considerable interest due to their often peculiar and highly advantageous photophysical properties that include spectrally tunable and highly intense fluorescence [1,2]. On the one hand, those compounds that contain the boron atom in a valence-saturated situation corresponding to sp^3 hybridization

(such as Bodipy dyes [3,4], N,C-chelate organoboron dyes [5-9], BASHY dyes [10,11] or Boranils [12,13]) often feature quite rigid structures which contribute to high fluorescence quantum yields. These dyes have been applied for example in optoelectronics [14-16], sensing [17-20], and bioimaging [6,20-26]. On the other hand, boron with sp^2 hybridization, such as in triarylboranes, offers the possibility to modulate fluorescence properties by the addition of Lewis bases (e.g., fluoride ions [27-31]) or by exploring the electron-accepting properties of the boron, including charge-transfer and photoinduced electron-transfer phenomena or two-photon absorption [32-36].

As part of our research program we have developed arylisoquinolines that integrate a boronic acid ester [37-39] or a $BMes_2$ unit [6,40]. The presence of the boron-substituent confers interesting photophysical properties to these dyes such as intramolecular charge-transfer processes and tunable red-shifted emission bands. Generally, the so far investigated borylated arylisoquinoline dyes show principally fluorescence quenching (on-off switching) on the formation of the corresponding fluoroboronate complexes [37].

Herein, we extended our previously reported arylisoquinoline-derived organoboron dye platform with an additional axially linked aryl residue (see structures **16**–**19** in Figure 1) in the expectation to modulate the fluorescence properties and fluoride response of these dyes. The additional aryl residues allow the verification of the effect of aromatic conjugation (naphthyl, anthryl, pyrenyl) and electron-donor strength (naphthyl versus 4-methoxynaphthyl) on the photophysical properties. Beside the observation of interesting dual emission properties for these dyes, some showed a pronounced ratiometric fluorescence response on fluoride ion addition.

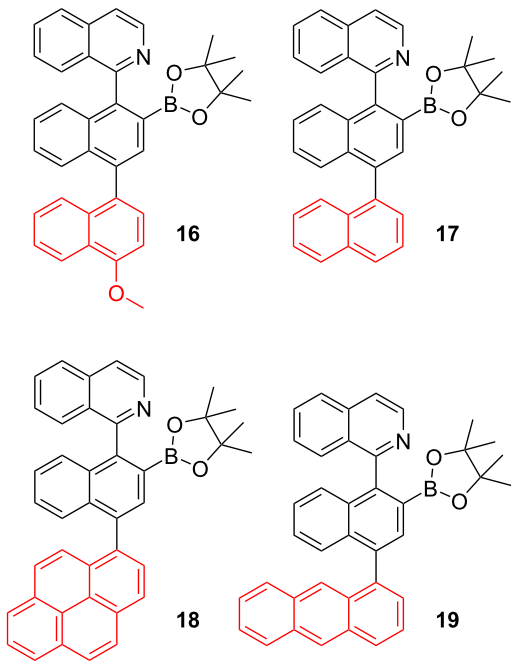

Figure 1: Structures of the dyes **16**–**19**.

Results and Discussion

Synthesis of the borylated dyes 16–19

For the synthesis of the triaryl systems **12**–**15**, precursors of the organoboron dyes **16**–**19**, the construction of two stereogenic axes was required. Therefore, a synthetic route based on consecutive cross-coupling reactions was planned. Starting from 1-bromo-4-methoxynaphthalene (**1**), the Pd-catalyzed Suzuki coupling reaction with commercial boronic acids afforded the naphthyl and pyrenyl derived methyl ethers **2** and **3** in 78% and 87% yield, respectively (Scheme 1). For the synthe-

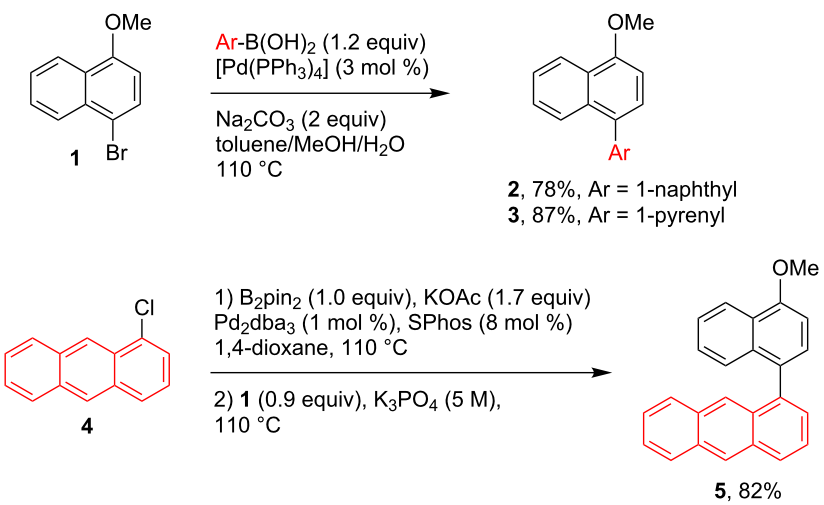

Scheme 1: Synthesis of the precursors **2**, **3**, and **5**.

sis of the anthryl derivative **5** a Pd-catalyzed one-pot reaction consisting of a borylation and Suzuki coupling was applied. Thus, starting from 1-chloroanthracene (**4**) and using SPhos/Pd_2dba_3 (8:1) as the catalyst, a full conversion to the Miyaura-type borylated intermediate was achieved (TLC analysis) after 5 hours at 110 ºC. The addition of 1-bromo-4-methoxynaphthalene (**1**, 0.9 equiv) and K_3PO_4, and stirring overnight at 110 ºC, afforded the biaryl methyl ether **5** in an 82% yield (Scheme 1). Similarly, Buchwald´s methodology [41] was applied in the synthesis of **7,** which was obtained in 70% yield after tetrahydropyran (THP) group deprotection in MeOH/CH_2Cl_2 using $TsOH{\cdot}H_2O$ as the catalyst (Scheme 2). In a conventional triflation (Tf_2O, DMAP cat.), **7** was converted into **8** with a yield of 86%. For the synthesis the triflates **9**–**11** a one-pot demethylation–triflation sequence was followed (Scheme 2). The treatment of biaryl methyl ethers **2**, **3** or **5** with BBr_3 (1.1 equiv) in anhydrous CH_2Cl_2 (0 ºC→rt) allowed the transformation into the alcohol intermediates, which were treated with triflic anhydride (Tf_2O) in dry dichloromethane to afford **9**–**11** in 59–79% yield.

With the triflates **8**–**11** at hand, these were transformed into the triaryl systems **12**–**15** following a similar Pd-catalyzed one-pot borylation-Suzuki coupling strategy as mentioned above, using 1-chloroisoquinoline as the coupling partner (Scheme 3). The desired compounds **12**–**15** were obtained in 44–70% yield. The ^{1}H NMR spectra, recorded at 25 °C, showed the coexistence of the *syn* and *anti* atropisomers because of the slow rotation around the chiral axis at this temperature. Free rotation around the C–C bond was observed at 80 °C and hence, variable-temperature ^{1}H NMR studies showed coalescence of the signals to give an average spectrum (see Supporting Information File 1).

The synthesis of the borylated dyes **16**–**19** was carried out following a methodology that was previously reported by some of us [42] and that is based on the Ir-catalyzed nitrogen-directed *ortho*-borylation of arylisoquinolines [37,38]. Despite of the presence of many aromatic C–H bonds which could be borylated, the choice of a suitable pyridine-hydrazone ligand [42] allowed to perform the borylation reactions at 55 °C, showing complete regioselectivity in the C–H borylation. This procedure afforded the dyes **16**–**19** in good to very good yields of 51–83% (Scheme 3). The introduction of the Bpin moiety hinders the free rotation around axis A (Scheme 3) of the compounds **16**–**19**; therefore, complex mixtures of the *syn*/*anti* atropoisomers (0.45:0.55; *syn*:*anti*) were observed in NMR spectroscopy. To facilitate the C–C bond rotation around axis B (Scheme 3) and simplify the NMR spectra, the measurements were undertaken at 80 °C in C_6D_6 using a screw-cap NMR tube. Although significant changes were registered, a complete coalescence of the signals was not observed. The chiral HPLC analysis (see HPLC traces in Supporting Information File 1) demonstrated the high purity of compounds **16**–**19**. The sharp peaks and separation times higher than 2 minutes are in accordance with a high rotation barrier. All compounds were identified by their ^{1}H and ^{13}C NMR spectra. The sp^2 character of the boron was confirmed by ^{11}B NMR spectroscopy, revealing a typical resonance signal at 31–32 ppm [43]. Hence, the iso-

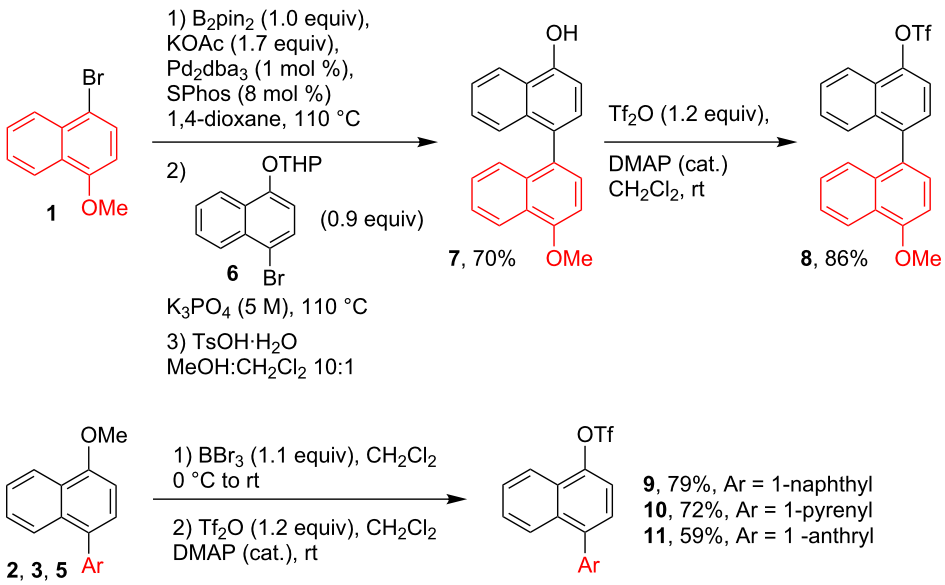

Scheme 2: Synthesis of the precursor triflates **8**–**11**.

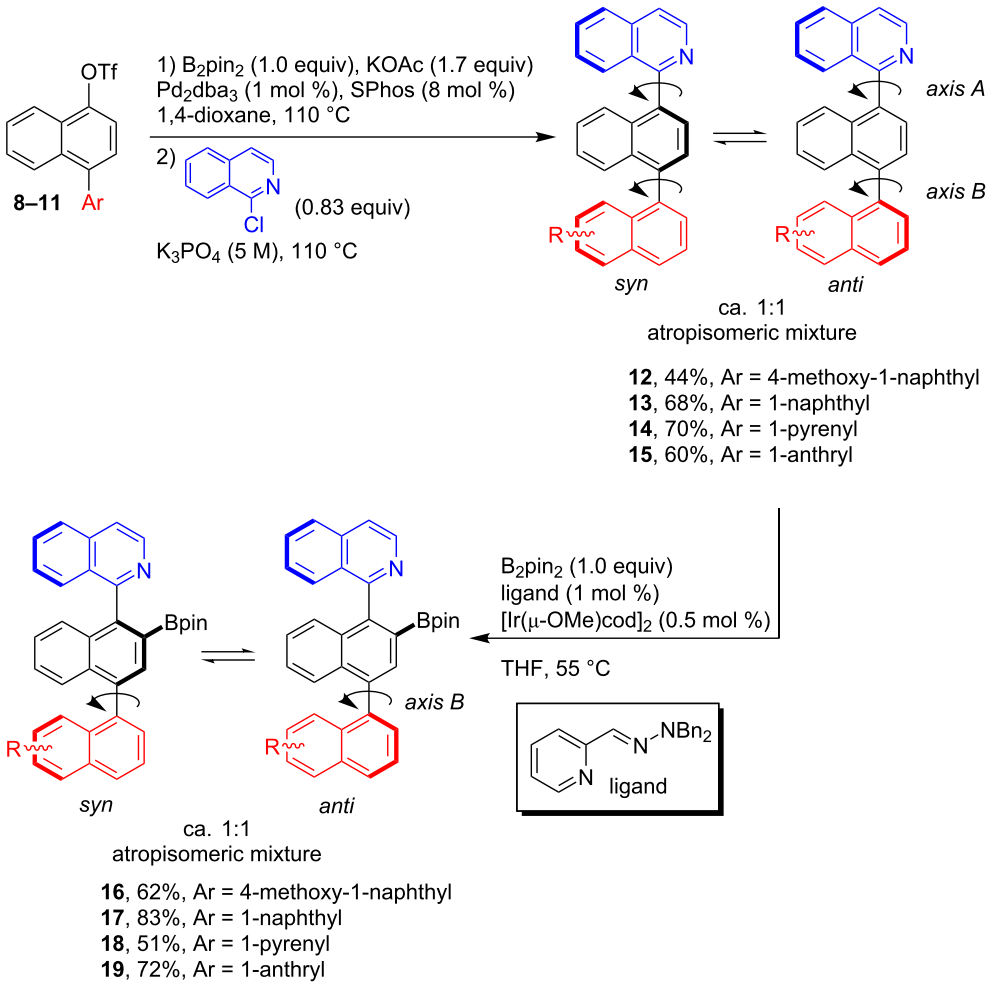

Scheme 3: Synthesis of **12**–**15** and the organoboron dyes **16**–**19**.

quinoline nitrogen does not engage in the formation of an intramolecular Lewis pair, akin to related borylated arylisoquinolines [37,38].

UV–vis absorption and fluorescence properties

The absorption and fluorescence properties of the herein investigated dyes **16**–**19** in air-equilibrated solutions, using three solvents (dichloromethane, acetonitrile, dimethyl sulfoxide), are summarized in Table 1. A first inspection of these data showed that the UV–vis absorption spectra feature the typical bands corresponding to their aromatic moieties (see Figure 2 for the spectra in acetonitrile). For example, for the dyes **18** and **19** π–π* transition bands in the wavelength range of 330–400 nm with characteristic vibronic fine structure were observed. Further, the dyes have a sharp peak at 322 nm that is assigned to the isoquinoline chromophore. The only exception is dye **18** where this peak is hidden under a strong absorption band corresponding to the pyrenyl moiety.

Most interesting are the fluorescence properties of the dyes (see spectra in Figure 2), which revealed a dual emission phenomenon (see ratio I_{LW}/I_{SW} of the intensities I of the long-wavelength (LW) and short-wavelength (SW) emission band; Table 1). The monitoring of the emission corresponding to both bands yields identical excitation spectra which also coincide with the absorption spectra of the dyes. This underpins the authenticity of the emission signals. The appearance of the LW emission for all investigated dyes can be clearly linked to the presence of the boron-containing substituent. This follows from the observation that the corresponding arylisoquinolines without boron substitution feature only one blue-shifted emission band that is very similar to the SW band of the borylated dye, e.g., the non-borylated analogues of the dyes **17**, **18**, and **19** fea-

Table 1: UV–vis and fluorescence properties of the dyes **16**–**19** in various solvents.

	$\lambda_{abs,max}$ (nm) [ε ($M^{-1}cm^{-1}$)]	$\lambda_{fluo,max}$ (nm) SW/LW	I_{LW}/I_{SW}	Φ_{fluo}	τ_{fluo} (ns) SW/LW
CH_2Cl_2					
16	303 [10800]	429/555	7.1	0.59	0.43/6.11
17	296 [11500]	397/512	7.1	0.17	0.16/3.96
18	345 [36900]	431/549	4.6	0.48	0.91/4.02
19	365 [6900]	409/551	2.3	0.30	0.57/5.22
CH_3CN (0.4 vol % DMF as co-solvent)					
16	302 [10100]	437/565	15.7	0.48	0.40/6.03
17	294 [16000]	400/514	11.2	0.14	0.13/3.26
18	343 [33000]	435/565	3.0	0.35	0.39/4.74
19	363 [13300]	408/582	2.4	0.15	0.32/4.83
$(CH_3)_2SO$					
16	304 [10500]	451/577	3.7	0.41	0.72/4.91
17	296 [17400]	402/519	5.3	0.20	0.22/3.63
18	346 [29700]	444/569	1.8	0.47	0.55/4.81
19	366 [6500]	413/592	1.0	0.22	0.60/4.70

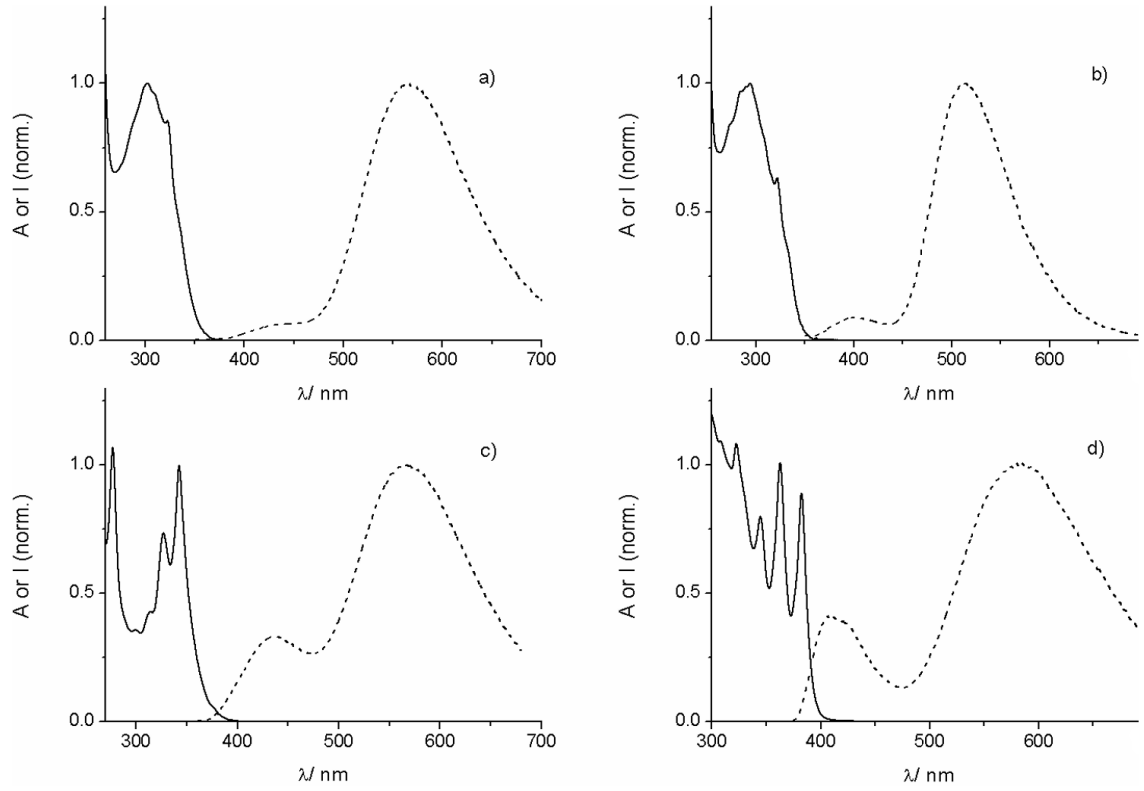

Figure 2: UV–vis absorption (solid line) and fluorescence (dashed line) spectra of a) **16**, b) **17**, c) **18**, and d) **19** in air-equilibrated acetonitrile (containing 0.4 vol % DMF as co-solvent).

ture a single emission band with a maximum at 401, 442, and 420 nm, in acetonitrile, respectively. These are tentatively assigned to π–π* transitions of the variable aryl moiety. Interestingly, in tetrahydrofuran, containing oxygen as donor atom, only the SW emission band is seen, i.e., $\lambda_{fluo,max}$ = 409 nm (**16**), 402 nm (**17**), 426 nm (**18**), 425 nm (**19**). This points to the interpretation that the SW emission has its origin in a Lewis adduct between the boron center as acceptor and the solvent as donor. The maxima of the rather broad LW bands of the dyes are observed between 510 and 590 nm in acetonitrile, corresponding to maximal apparent Stokes shifts of ca. 190–270 nm. As demonstrated previously for other borylated arylisoquinoline dyes [37,38], the emission energy of the LW band is tightly linked with the redox potential of the aryl residue. Having in mind that the borylated naphthyl is present in all four dyes it is instructive to compare the oxidation potentials (E_{ox}) of the additional aryl residues. This leads to the following order: naphthyl (E_{ox} = 1.70 V vs SCE in acetonitrile) > 4-methoxynaphthyl (1.38 V) > pyrenyl (1.16 V) > anthryl (1.09 V) [44]. On the one hand, the dye with the easiest oxidizable aromatic residue (dye **19**) has the most red-shifted emission maximum, being at 582 nm in acetonitrile. On the other hand, dye **17** with a naphthyl, that is harder to oxidize, shows the most blue-shifted LW emission (maximum at 514 nm in acetonitrile). The LW emission maxima of other dyes (**16** and **18**) are situated in between. These trends support that for the herein investigated dyes intramolecular charge-transfer (ICT) phenomena might play a role in the observation of the LW emission features. According to our previous observations the electron-acceptor moiety is likely constituted by the isoquinolinyl moiety [37,38], while the donor is related to the electronically variable aryl residue. Comparing the emission maxima of the dyes in the less polar dichloromethane with those in the highly polar dimethyl sulfoxide, additional trends can be seen. Thus, dye **17** shows only a slight bathochromic shift of the emission maximum on changing to the polar solvent (Δλ = +7 nm). However, dye **19** features a solvatofluorochromic effect of Δλ = +41 nm under the same conditions. The dyes **16** and **18** show somewhat smaller bathochromic shifts on increasing the solvent polarity (Δλ = +20–22 nm).

Regarding the fluorescence quantum yields (Φ_{fluo}) of the dyes, the highest values were determined for the compounds **16** and **18**, being in the range of 0.35–0.59 in the investigated solvents. The dyes **17** and **19** show smaller values for Φ_{fluo} (ca. 0.15–0.30). The fluorescence lifetime of the SW emission was measured as 300–900 ps, being in some cases very close to the resolution limit of our time-correlated single-photon-counting setup. The LW emission showed considerably longer lifetimes in the 3–6 ns range. The photophysical behavior of the dyes is tentatively summarized in Scheme 4.

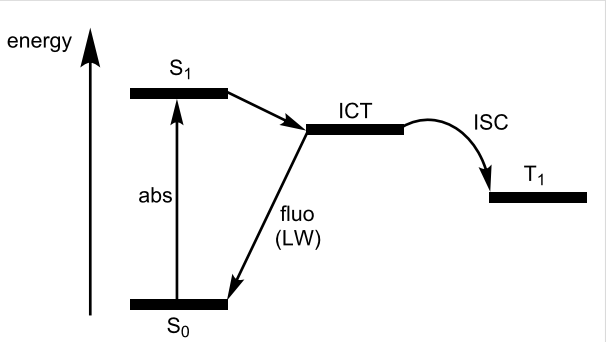

Scheme 4: Jablonski diagram representing the photophysical processes in the dyes **16**–**19**.

Laser-flash photolysis

The photophysical characterization of the dyes **16**–**19** was completed by nanosecond laser-flash photolysis experiments in acetonitrile [45]. The laser excitation (λ_{exc} = 308 nm) of the dyes **16** and **17** in nitrogen-purged solution yielded transient absorption spectra with a broad band at λ_{max} = 610 and 600 nm, respectively (see Figure 3 for dye **17**). These transients showed lifetimes in the microsecond range (τ_T = 4.2 μs (**16**) and 4.4 μs (**17**)), were efficiently quenched by oxygen (bimolecular quenching constant k_q ca. 1.1–1.2 × 10^9 $M^{-1}s^{-1}$), and led to the energy-transfer triplet-sensitization of β-carotene (observation of the triplet–triplet absorption band at 520 nm). The experimental results corroborate the assignment of the transients to excited triplet states of **16** and **17**. Noteworthy, the dyes **18** and **19** are characterized by distinct transient absorption spectra (excitation at λ_{exc} = 355 nm) with signals at shorter wavelengths. Based on the microsecond lifetime (τ_T = 3.1 μs (**18**) and 2.4 μs (**19**)), oxygen quenching (k_q ca. 2.9-3.1 × 10^9 $M^{-1}s^{-1}$), and

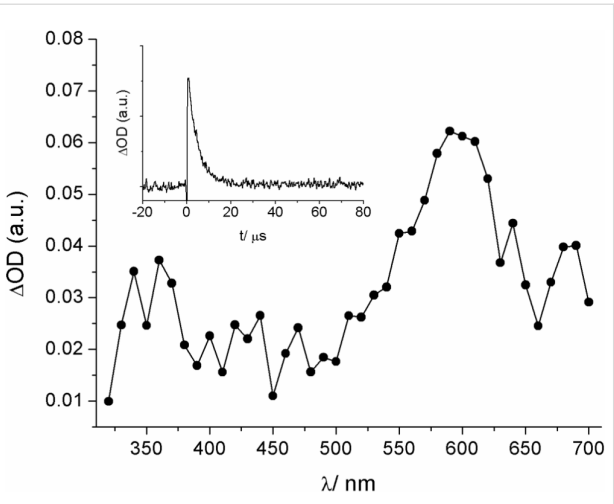

Figure 3: Transient absorption spectrum (600 ns delay) of dye **17** in nitrogen-purged acetonitrile on excitation at 308 nm. The inset shows the corresponding kinetics at 600 nm.

β-carotene triplet sensitization experiments the signals at 410 nm (dye **18**) and 430 nm (dye **19**) were assigned to excited triplet states as well. An additional signal at 470 nm for dye **18** is insensitive to oxygen and was tentatively attributed to the formation of a pyrene-based radical cation, resulting from photoionization [46].

Interaction with fluoride anions

The presence of the boronic acid ester moiety does not only contribute to significant changes in the fluorescence properties but constitutes also a potential binding motif for Lewis bases. In this context it is well established that the electron-deficient trivalent boron can bind anions, such as fluoride or cyanide, through interaction with the vacant $2p_\pi$ orbital [30]. In Figure 4 the fluorescence responses of the dyes **16**–**19** on the addition of tetra-*n*-butylammonium fluoride (Bu_4NF) in acetonitrile are depicted. The dyes **16** and **17** show a strong fluorescence quenching of their LW bands, while the SW bands experience a slight increase. However, the situation for the dyes **18** and **19** is dramatically different. Here the LW band is substituted by a strong blue-shifted emission. This leads to a clear ratiometric behavior and a large dynamic response. The blue-shifted emission for the fluoroboronate Lewis adduct is in accordance with the observations made for donor solvents such as tetrahydrofuran (see above). As for the dyes **16** and **17**, also for **18** and **19** isoemissive points were noted. These observations corroborate the uniformity of the reaction with fluoride anions. The UV–vis absorption spectra show much smaller changes as compared to the fluorescence (not shown). However, also here isosbestic points were observed. The formation of the fluoroboronate complexes was corroborated by the detection of the corresponding mass peaks (see Supporting Information File 1). In addition, ^{11}B NMR spectra, for the example of dye **17**, reveal that the boron changes from sp^2 to sp^3 hybridization on addition of 1 equiv F^-; i.e., the ^{11}B NMR signal shifts from 31.5 ppm to 7.0 ppm (see Supporting Information File 1). This is in line with the formation of the fluoroboronate complex, instead of unwanted processes such as protodeboronation which could be potentially caused by acid traces in Bu_4NF. Noteworthy, the addition of other anions, such as bromide, iodide, or cyanide did not result in significant changes of the optical spectra of the dyes.

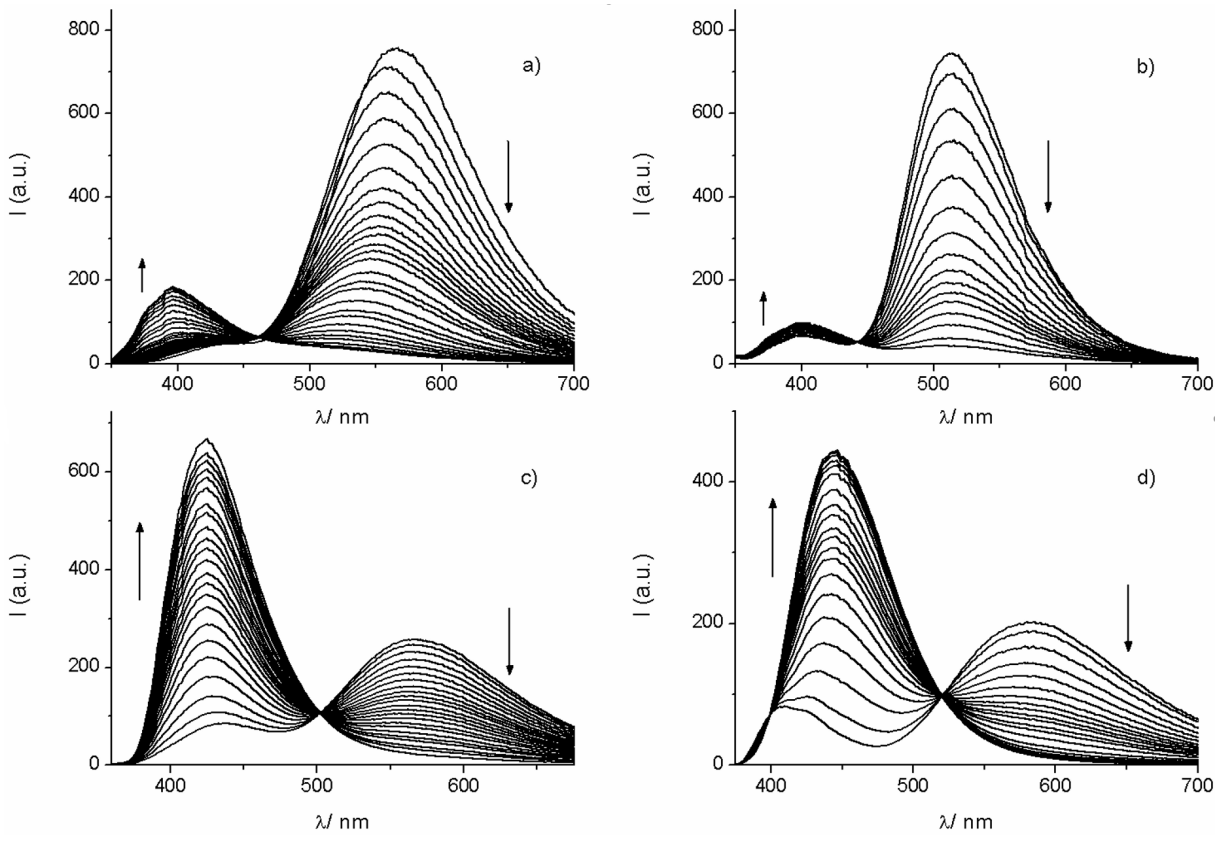

Figure 4: Fluorescence titrations of the dyes (ca. 4–11 μM) with Bu_4NF in acetonitrile. a) **16** (up to 156 equiv F^-), b) **17** (up to 40 equiv F^-), c) **18** (up to 152 equiv F^-), d) **19** (up to 100 equiv F^-).

Fluorescence titrations yielded the formation constants for the respective 1:1 fluoroboronate complexes. The values are in the order of 10^4 M^{-1} (1.6×10^4 M^{-1} (**16**); 4.8×10^4 M^{-1} (**17**); 2.6×10^4 M^{-1} (**18**); 2.0×10^4 M^{-1} (**19**)), which are very comparable to the constants that were obtained for related borylated arylisoquinoline dyes [37].

Conclusion

The family of borylated arylisoquinoline dyes was extended by members that contain additional aryl substituents, leading to compounds with two stereogenic axes. The dyes show pronounced dual emission patterns with long-wavelength maxima close to 600 nm in polar solvents such as acetonitrile or dimethyl sulfoxide. The emission maxima of the long-wavelength band vary systematically with the electron-donor strength of the additional aryl residue (naphthyl, 4-methoxynaphthyl, pyrenyl, anthryl). This provides some hint that intramolecular charge-transfer phenomena are likely involved. Laser-flash photolysis studies provided insights into the existence of excited triplet states. The addition of fluoride anions led to pronounced fluorescence quenching effects, as the result of the formation of fluoroboronate complexes. In the case of the pyrenyl- and anthryl-substituted dyes a clear ratiometric behavior was noted. No quenching was seen for the addition of cyanide ions or bromide and chloride. This makes the new dyes selective fluorescent receptors for fluoride anions.

Experimental

General methods and materials

^{1}H NMR spectra were recorded at 400 MHz or 500 MHz and ^{13}C NMR spectra were recorded at 100 MHz or 125 MHz. Chloroform-*d* ($CDCl_3$), acetone-d_6 ($(CD_3)_2CO$) and benzene-d_6 (C_6D_6) were used as solvents and the solvent peak was employed as reference. ^{11}B NMR spectra were recorded with complete proton decoupling at 160 MHz, using $BF_3{\cdot}Et_2O$ (0.00 ppm for ^{11}B NMR) as standard.

All chemical reactions were carried out in oven-dried Schlenk tubes under an argon atmosphere. Toluene, 1,4-dioxane, and methanol were purchased from Carlo Erba and were used as received. Anhydrous THF was obtained using Grubbs-type solvent drying columns. $[Pd(PPh_3)_4]$, $Pd_2(dba)_3$, SPhos ligand, 1-chloroisoquinoline, and pinacolborane (HBpin) were supplied by Aldrich, $[Ir(\mu\text{-OMe})(cod)]_2$ was from Strem Chemicals, and bis(pinacolate)diboron (B_2pin_2) was purchased from Frontier Scientific. All reagents were used as received. 1-Bromo-4-methoxynaphthalene (**1**) [47], 1-chloroanthracene (**4**) [48], and 1-(tetrahydropyran-2'-yloxy)-4-bromonaphthalene (**6**) [49] were synthesized according to literature procedures. The solvents for the photophysical measurements were purchased from Aldrich (acetonitrile) or Scharlau (dichloromethane, dimethyl sulfoxide) and were of spectroscopic quality.

UV–vis absorption and corrected fluorescence spectra were measured with standard equipment (Shimadzu UV-1603 and Varian Cary Eclipse), using quartz cuvettes of 1 cm optical path length. The fluorescence quantum yields were determined with quinine sulfate as standard reference (Φ_{fluo} = 0.55 in 0.05 M H_2SO_4) [50,51]. The lifetimes were measured by time-correlated single-photon counting (Edinburgh instruments FLS 920).

Laser-flash photolysis experiments were performed using a XeCl excimer laser (λ_{exc} = 308 nm; 17 ns fwhm; 20 mJ/pulse). Alternatively, a Q-switched Nd:YAG laser (Quantel Brilliant, 355 nm, 5 ns fwhm, 15 mJ/pulse) was coupled to a mLFP-111 Luzchem miniaturized equipment. The concentration of **16**–**19** was kept in the range of 20–30 μM in acetonitrile. The solutions were air-equilibrated or bubbled for 30 min with N_2 or O_2 before acquisition. All the experiments were carried out at room temperature.

The detailed procedures for the synthesis of the precursors can be found in Supporting Information File 1. Below the borylation of the precursors **12**–**15** to yield the dyes **16**–**19** is described and the NMR characterization data of the dyes are given.

General procedure for the Ir-catalyzed borylation – synthesis of the dyes **16**–**19**

Following the described procedure [42], a dried Schlenk tube was loaded with the substrate (**12**–**15**) and B_2Pin_2 (1 equiv). After three vacuum–argon cycles, 1 mL catalyst stock solution per 0.5 mmol substrate and pinacolborane (HBPin, 5 mol %) was added. The reaction mixture was stirred at 55 °C until quantitative consumption of the starting material. The mixture was cooled to room temperature, concentrated to dryness, and the crude product was purified by column chromatography (*n*-hexane/EtOAc mixtures).

Note: The catalyst stock solution (25 mL) was prepared by dissolving 2-pyridinecarboxaldehyde *N*,*N*-dibenzylhydrazone (37.6 mg, 0.125 mmol) and $[Ir(\mu\text{-OMe})(cod)]_2$ (41 mg, 0.063 mmol) in dry THF. Sonication for one hour was used to facilitate dissolution. The resulting red-brown solution was kept under argon.

1-(4'-Methoxy-3-(4,4,5,5-tetramethyl-1,3,2-dioxaborolan-2-yl)-[1,1'-binaphthalen]-4-yl)isoquinoline (**16**)

Following the above described general procedure for the Ir-catalyzed borylation starting from **12** (85 mg, 0.21 mmol) and after

flash chromatography on silica gel (toluene/EtOAc 7:1), **16** was obtained as a light-yellow foam (70 mg, 62% yield). NMR spectra recorded at 25 °C showed a ca. 0.45:0.55 diastereomeric mixture of atropisomers. To simplify the spectra the measurements were undertaken at 80 °C. ^{1}H NMR (400 MHz, C_6D_6, 80 °C) δ 8.80 (d, *J* = 5.6 Hz, 0.5H), 8.78 (d, *J* = 5.6 Hz, 0.5H), 8.60 (d, *J* = 8.0 Hz, 0.5H), 8.58 (d, *J* = 8.0 Hz, 0.5H), 8.46 (s, 0.5H), 8.44 (s, 0.5H), 7.70–7.47 (m, 5H), 7.34–7.26 (m, 2H), 7.10–6.99 (m, 4H), 6.62 (d, *J* = 7.2 Hz, 0.5H), 6.61 (d, *J* = 7.6 Hz, 0.5H), 3.61 (s, 3H), 0.80 (s, 6H), 0.69 (s, 3H), 0.65 (s, 3H) ppm, two proton signals were hidden under the C_6D_6 peak; ^{13}C NMR (100 MHz, C_6D_6, 80 °C) δ 162.8, 156.1, 145.7, 145.6, 143.1, 138.9, 136.6, 135.5, 134.9 (br s), 133.5, 133.4, 131.9, 130.6, 129.5, 128.6, 127.4, 127.1, 126.8, 126.6, 126.2, 125.5, 125.4, 122.8, 122.5, 120.1, 119.7, 119.6, 104.4, 104.1, 83.4, 55.4, 24.6 ppm, *C*–B not observed; ^{11}B NMR (128 MHz, C_6D_6) δ 32.0 ppm (br s); HRESIMS *m*/*z*: $[M + Na]^+$ calcd. for $C_{36}H_{32}BNNaO_3$, 560.2367; found, 560.2370.

1-(3-(4,4,5,5-Tetramethyl-1,3,2-dioxaborolan-2-yl)-[1,1'-binaphthalen]-4-yl)isoquinoline (**17**)

Following the above described general procedure for the Ir-catalyzed borylation starting from **13** (95 mg, 0.25 mmol) and after flash chromatography on silica gel (*n*-hexane/EtOAc 4:1), **17** was obtained as light-yellow foam (105 mg, 83% yield). NMR spectra recorded at 25 °C showed a ca. 0.45:0.55 diastereomeric mixture of atropisomers. To simplify the spectra the measurements were undertaken at 80 °C. ^{1}H NMR (500 MHz, C_6D_6, 80 °C) δ 8.77 (br s, 1H), 8.38 (s, 0.55H) 8.36 (s, 0.45H), 7.81–7.77 (m, 3H), 7.68–7.53 (m, 4.55H), 7.49 (d, *J* = 5.5 Hz, 1H), 7.39 (br s, 1.45H), 7.30 (br s, 1H), 7.25 (br s, 1H), 7.11–7.02 (m, 4H), 0.81 (s, 6H), 0.70 (s, 3H), 0.68 (s, 3H) ppm; ^{13}C NMR (100 MHz, C_6D_6, 80 °C) δ 162.6, 145.7, 143.0, 139.5, 138.6, 136.5, 135.0, 134.4, 133.9, 133.3, 133.0, 130.5, 129.5, 128.7, 128.5, 127.9, 127.5, 127.1, 127.1, 126.7, 126.6, 126.3, 126.2, 126.1, 126.0, 125.8, 125.5, 119.6, 83.4, 24.5 ppm, *C*–B not observed; ^{11}B NMR (128 MHz, C_6D_6) δ 31.3 ppm (br s); HREIMS *m*/*z*: $[M]^+$ calcd. for $C_{35}H_{30}BNO_2$, 507.2370; found, 507.2375.

1-(4-(Pyren-1-yl)-2-(4,4,5,5-tetramethyl-1,3,2-dioxaborolan-2-yl)naphthalen-1-yl)isoquinoline (**18**)

Following the above described general procedure for the Ir-catalyzed borylation starting from **14** (114 mg, 0.25 mmol) and after flash chromatography on silica gel (*n*-hexane/EtOAc 5:1), **18** was obtained as a light-yellow foam (74 mg, 51% yield). NMR spectra recorded at 25 °C showed a ca. 0.45:0.55 diastereomeric mixture of atropisomers. To simplify the spectra the measurements were undertaken at 80 °C. ^{1}H NMR (500 MHz, C_6D_6, 80 °C) δ 8.87 (d, *J* = 5.5 Hz, 0.55H), 8.85 (d, *J* = 5.5 Hz, 0.55H), 8.62 (s, 0.55H), 8.59 (s, 0.45H), 8.12 (d, *J* = 7.6 Hz, 0.55H), 8.08 (d, *J* = 9.1 Hz, 0.45H), 8.01–7.98 (m, 2H), 7.94–7.93 (m, 2H), 7.91–7.82 (m, 2H), 7.80–7.71 (m, 3H), 7.68–7.58 (m, 3H), 7.47 (d, *J* = 5.5 Hz, 1H), 7.26 (d, *J* = 8.1 Hz, 0.45H), 7.29 (d, *J* = 8.3 Hz, 0.55H), 7.12 (d, *J* = 7.4 Hz, 0.55H), 7.09 (d, *J* = 6.9 Hz, 0.45H), 7.06–7.00 (m, 3H), 0.79 (s, 6H), 0.65 (s, 2.7H), 0.62 (s, 3.3H) ppm; ^{13}C NMR (100 MHz, C_6D_6, 80 °C) δ 162.7, 145.9, 143.3, 139.0, 136.8, 136.8, 136.6, 135.3, 133.7, 133.4, 132.2, 131.9, 131.9, 131.6, 130.7, 130.6, 129.6, 129.3, 127.3, 126.8, 126.6, 126.5, 126.4, 126.4, 126.2, 125.8–125.7, 125.5–125.3, 124.8, 119.6, 83.5, 24.5 ppm, *C*–B not observed; ^{11}B NMR (128 MHz, C_6D_6) δ 32.0 ppm (br s); HREIMS $[M]^+$ calcd. for $C_{41}H_{32}BNO_2$, 581.2526; found, 581.2530.

1-(4-(Anthracen-1-yl)-2-(4,4,5,5-tetramethyl-1,3,2-dioxaborolan-2-yl)naphthalen-1-yl)isoquinoline (**19**)

Following the above described general procedure for the Ir-catalyzed borylation starting from **15** (84 mg, 0.21 mmol) and after flash chromatography on silica gel (toluene/EtOAc 20:1), **19** was obtained as a yellow foam (100 mg, 72% yield). NMR spectra recorded at 25 °C showed a ca. 0.44:0.56 diastereomeric mixture of atropisomers. To simplify the spectra the measurements were undertaken at 80 °C. ^{1}H NMR (500 MHz, C_6D_6, 80 °C) δ 8.81 (d, *J* = 5.6 Hz, 0.55H), 8.79 (d, *J* = 5.6 Hz, 0.45H) 8.54 (s, 0.55H), 8.49 (s, 0.45H), 8.44 (s, 0.45H), 8.33 (s, 1H), 8.26 (s, 0.55H), 8.00–7.93 (m, 1.45H), 7.81 (t, *J* = 8.6 Hz, 1H), 7.71–7.59 (m, 4H), 7.49 (d, *J* = 5.6 Hz, 1H), 7.41–7.27 (m, 3H), 7.19–7.10 (m, 1.55H), 7.05–6.97 (m, 4H), 0.80 (s, 2.7H), 0.79 (s, 3.3H), 0.69 (s, 2.7H), 0.64 (s, 3.3H) ppm; ^{13}C NMR (125 MHz, C_6D_6, 80 °C) δ 162.6, 145.9, 145.9, 143.1, 143.0, 139.6, 139.4, 138.8, 136.5, 135.2, 135.1, 133.3, 133.2, 132.6, 132.5, 132.5, 132.4, 132.3, 132.2, 130.5, 130.4, 129.5, 129.5, 129.3, 129.2, 128.6, 128.5, 128.5, 128.3, 128.1, 127.9, 127.5, 127.3, 127.2, 127.2, 127.1, 126.9, 126.8, 126.8, 126.7, 126.7, 126.5, 126.3, 126.3, 126.1, 125.8, 125.6, 125.4, 125.2, 125.2, 119.6, 83.4, 24.5, 24.4 ppm, *C*–B not observed; ^{11}B NMR (160 MHz, C_6D_6) δ 31.5 ppm (br s); HREIMS *m*/*z*: $[M]^+$ calcd. for $C_{39}H_{32}BNO_2$, 557.2526; found, 557.2508.

Supporting Information

Supporting Information File 1

Additional synthetic procedures for **2**, **3**, **5**, and **7**–**15**, ^{1}H and ^{13}C NMR spectra of the dyes **16**–**19** and their precursors, ESIMS spectra and ^{11}B NMR spectroscopy of fluoroboronate complexes, HPLC traces for the dyes **16**–**19**.

[https://www.beilstein-journals.org/bjoc/content/supplementary/1860-5397-15-254-S1.pdf]

Acknowledgements

Funding by the Spanish Ministry of Economy, Industry, and Competitiveness (CTQ2014-54729-C2-1-P for U.P., CTQ2013-48164-C2-1-P and CTQ2013-48164-C2-2-P for A.R., Ramón y Cajal contracts RYC-2013-12585 for A.R. and RYC-2015-17737 for I.V.), the Spanish Ministry of Science, Innovation, and Universities (CTQ2017-89832-P for U.P., CTQ2016-78875-P for M.C.J., and CTQ2017-89416-R for I.V.), the European Research and Development Fund, and the Andalusian Government (2012/FQM-2140 for U.P., 2009/FQM-4537 and 2012/FQM-1078 for A.R) is gratefully acknowledged.

ORCID® iDs

Ignacio Vayá - https://orcid.org/0000-0003-1682-9342
Abel Ros - https://orcid.org/0000-0002-3455-5675
Uwe Pischel - https://orcid.org/0000-0001-8893-9829

References

1. Frath, D.; Massue, J.; Ulrich, G.; Ziessel, R. *Angew. Chem.* **2014,** *126,* 2322–2342. doi:10.1002/ange.201305554
Angew. Chem., Int. Ed. **2014,** *53,* 2290–2310. doi:10.1002/anie.201305554
2. Ji, L.; Griesbeck, S.; Marder, T. B. *Chem. Sci.* **2017,** *8,* 846–863. doi:10.1039/c6sc04245g
3. Loudet, A.; Burgess, K. *Chem. Rev.* **2007,** *107,* 4891–4932. doi:10.1021/cr078381n
4. Ulrich, G.; Ziessel, R.; Harriman, A. *Angew. Chem.* **2008,** *120,* 1202–1219. doi:10.1002/ange.200702070
Angew. Chem., Int. Ed. **2008,** *47*, 1184–1201. doi:10.1002/anie.200702070
5. Amarne, H.; Baik, C.; Murphy, S. K.; Wang, S. *Chem. – Eur. J.* **2010,** *16,* 4750–4761. doi:10.1002/chem.200903582
6. Pais, V. F.; Alcaide, M. M.; López-Rodríguez, R.; Collado, D.; Nájera, F.; Pérez-Inestrosa, E.; Álvarez, E.; Lassaletta, J. M.; Fernández, R.; Ros, A.; Pischel, U. *Chem. – Eur. J.* **2015,** *21,* 15369–15376. doi:10.1002/chem.201501626
7. Shaikh, A. C.; Ranade, D. S.; Thorat, S.; Maity, A.; Kulkarni, P. P.; Gonnade, R. G.; Munshi, P.; Patil, N. T. *Chem. Commun.* **2015,** *51,* 16115–16118. doi:10.1039/c5cc06351e
8. Liu, K.; Lalancette, R. A.; Jäkle, F. *J. Am. Chem. Soc.* **2017,** *139,* 18170–18173. doi:10.1021/jacs.7b11062
9. Vanga, M.; Lalancette, R. A.; Jäkle, F. *Chem. – Eur. J.* **2019,** *25,* 10133–10140. doi:10.1002/chem.201901231
10. Santos, F. M. F.; Rosa, J. N.; Candeias, N. R.; Parente Carvalho, C.; Matos, A. I.; Ventura, A. E.; Florindo, H. F.; Silva, L. C.; Pischel, U.; Gois, P. M. P. *Chem. – Eur. J.* **2016,** *22,* 1631–1637. doi:10.1002/chem.201503943
11. Alcaide, M. M.; Santos, F. M. F.; Pais, V. F.; Carvalho, J. I.; Collado, D.; Pérez-Inestrosa, E.; Arteaga, J. F.; Boscá, F.; Gois, P. M. P.; Pischel, U. *J. Org. Chem.* **2017,** *82,* 7151–7158. doi:10.1021/acs.joc.7b00601
12. Frath, D.; Azizi, S.; Ulrich, G.; Retailleau, P.; Ziessel, R. *Org. Lett.* **2011,** *13,* 3414–3417. doi:10.1021/ol2011665
13. Urban, M.; Durka, K.; Jankowski, P.; Serwatowski, J.; Luliński, S. *J. Org. Chem.* **2017,** *82,* 8234–8241. doi:10.1021/acs.joc.7b01001
14. Wakamiya, A.; Taniguchi, T.; Yamaguchi, S. *Angew. Chem.* **2006,** *118,* 3242–3245. doi:10.1002/ange.200504391
Angew. Chem., Int. Ed. **2006,** *45,* 3170–3173. doi:10.1002/anie.200504391
15. Rao, Y.-L.; Wang, S. *Inorg. Chem.* **2011,** *50,* 12263–12274. doi:10.1021/ic200658v
16. Li, D.; Zhang, H.; Wang, Y. *Chem. Soc. Rev.* **2013,** *42,* 8416–8433. doi:10.1039/c3cs60170f
17. Coskun, A.; Akkaya, E. U. *J. Am. Chem. Soc.* **2006,** *128,* 14474–14475. doi:10.1021/ja066144g
18. Bozdemir, O. A.; Guliyev, R.; Buyukcakir, O.; Selcuk, S.; Kolemen, S.; Gulseren, G.; Nalbantoglu, T.; Boyaci, H.; Akkaya, E. U. *J. Am. Chem. Soc.* **2010,** *132,* 8029–8036. doi:10.1021/ja1008163
19. Niu, L.-Y.; Guan, Y.-S.; Chen, Y.-Z.; Wu, L.-Z.; Tung, C.-H.; Yang, Q.-Z. *J. Am. Chem. Soc.* **2012,** *134,* 18928–18931. doi:10.1021/ja309079f
20. Zhang, X.; Xiao, Y.; Qi, J.; Qu, J.; Kim, B.; Yue, X.; Belfield, K. D. *J. Org. Chem.* **2013,** *78,* 9153–9160. doi:10.1021/jo401379g
21. Zheng, Q.; Xu, G.; Prasad, P. N. *Chem. – Eur. J.* **2008,** *14,* 5812–5819. doi:10.1002/chem.200800309
22. Han, J.; Loudet, A.; Barhoumi, R.; Burghardt, R. C.; Burgess, K. *J. Am. Chem. Soc.* **2009,** *131,* 1642–1643. doi:10.1021/ja8073374
23. Kowada, T.; Maeda, H.; Kikuchi, K. *Chem. Soc. Rev.* **2015,** *44,* 4953–4972. doi:10.1039/c5cs00030k
24. Kolemen, S.; Işık, M.; Kim, G. M.; Kim, D.; Geng, H.; Buyuktemiz, M.; Karatas, T.; Zhang, X.-F.; Dede, Y.; Yoon, J.; Akkaya, E. U. *Angew. Chem.* **2015,** *127,* 5430–5434. doi:10.1002/ange.201411962
Angew. Chem., Int. Ed. **2015,** *54,* 5340–5344. doi:10.1002/anie.201411962
25. Bachollet, S. P. J. T.; Volz, D.; Fiser, B.; Münch, S.; Rönicke, F.; Carrillo, J.; Adams, H.; Schepers, U.; Gómez-Bengoa, E.; Bräse, S.; Harrity, J. P. A. *Chem. – Eur. J.* **2016,** *22,* 12430–12438. doi:10.1002/chem.201601915
26. Frath, D.; Didier, P.; Mély, Y.; Massue, J.; Ulrich, G. *ChemPhotoChem* **2017,** *1,* 109–112. doi:10.1002/cptc.201700012
27. Kubo, Y.; Yamamoto, M.; Ikeda, M.; Takeuchi, M.; Shinkai, S.; Yamaguchi, S.; Tamao, K. *Angew. Chem.* **2003,** *115,* 2082–2086. doi:10.1002/ange.200250788
Angew. Chem., Int. Ed. **2003,** *42*, 2036–2040. doi:10.1002/anie.200250788
28. Melaimi, M.; Gabbaï, F. P. *J. Am. Chem. Soc.* **2005,** *127,* 9680–9681. doi:10.1021/ja053058s
29. Hudnall, T. W.; Kim, Y.-M.; Bebbington, M. W. P.; Bourissou, D.; Gabbaï, F. P. *J. Am. Chem. Soc.* **2008,** *130,* 10890–10891. doi:10.1021/ja804492y
30. Wade, C. R.; Broomsgrove, A. E. J.; Aldridge, S.; Gabbaï, F. P. *Chem. Rev.* **2010,** *110,* 3958–3984. doi:10.1021/cr900401a
31. Hudson, Z. M.; Liu, X.-Y.; Wang, S. *Org. Lett.* **2011,** *13,* 300–303. doi:10.1021/ol102749y
32. Bai, D.-R.; Liu, X.-Y.; Wang, S. *Chem. – Eur. J.* **2007,** *13,* 5713–5723. doi:10.1002/chem.200700364
33. Pron, A.; Zhou, G.; Norouzi-Arasi, H.; Baumgarten, M.; Müllen, K. *Org. Lett.* **2009,** *11,* 3550–3553. doi:10.1021/ol9012487
34. Pan, H.; Fu, G.-L.; Zhao, Y.-H.; Zhao, C.-H. *Org. Lett.* **2011,** *13,* 4830–4833. doi:10.1021/ol201909r
35. Bonn, A. G.; Wenger, O. S. *J. Org. Chem.* **2015,** *80,* 4097–4107. doi:10.1021/acs.joc.5b00416

36. Griesbeck, S.; Zhang, Z.; Gutmann, M.; Lühmann, T.; Edkins, R. M.; Clermont, G.; Lazar, A. N.; Haehnel, M.; Edkins, K.; Eichhorn, A.; Blanchard-Desce, M.; Meinel, L.; Marder, T. B. *Chem. – Eur. J.* **2016,** *22,* 14701–14706. doi:10.1002/chem.201602639
37. Pais, V. F.; El-Sheshtawy, H. S.; Fernández, R.; Lassaletta, J. M.; Ros, A.; Pischel, U. *Chem. – Eur. J.* **2013,** *19,* 6650–6661. doi:10.1002/chem.201203887
38. Pais, V. F.; Lineros, M.; López-Rodríguez, R.; El-Sheshtawy, H. S.; Fernández, R.; Lassaletta, J. M.; Ros, A.; Pischel, U. *J. Org. Chem.* **2013,** *78,* 7949–7961. doi:10.1021/jo401147t
39. Pais, V. F.; Lassaletta, J. M.; Fernández, R.; El-Sheshtawy, H. S.; Ros, A.; Pischel, U. *Chem. – Eur. J.* **2014,** *20,* 7638–7645. doi:10.1002/chem.201402027
40. Domínguez, Z.; López-Rodríguez, R.; Álvarez, E.; Abbate, S.; Longhi, G.; Pischel, U.; Ros, A. *Chem. – Eur. J.* **2018,** *24,* 12660–12668. doi:10.1002/chem.201801908
41. Billingsley, K. L.; Barder, T. E.; Buchwald, S. L. *Angew. Chem.* **2007,** *119,* 5455–5459. doi:10.1002/ange.200701551
Angew. Chem., Int. Ed. **2007,** *46,* 5359–5363. doi:10.1002/anie.200701551
42. Ros, A.; Estepa, B.; López-Rodríguez, R.; Álvarez, E.; Fernández, R.; Lassaletta, J. M. *Angew. Chem.* **2011,** *123,* 11928–11932. doi:10.1002/ange.201104544
Angew. Chem., Int. Ed. **2011,** *50,* 11724–11728. doi:10.1002/anie.201104544
43. Zhu, L.; Shabbir, S. H.; Gray, M.; Lynch, V. M.; Sorey, S.; Anslyn, E. V. *J. Am. Chem. Soc.* **2006,** *128,* 1222–1232. doi:10.1021/ja055817c
44. Montalti, M.; Credi, A.; Prodi, L.; Gandolfi, M. T. *Handbook of Photochemistry,* 3rd ed.; Taylor & Francis: Boca Raton, FL, 2006. doi:10.1201/9781420015195
45. Boscá, F.; Cuquerella, M. C.; Pais, V. F.; Ros, A.; Pischel, U. *ChemPhotoChem* **2018,** *2,* 34–41. doi:10.1002/cptc.201700176
46. Hara, M.; Tojo, S.; Kawai, K.; Majima, T. *Phys. Chem. Chem. Phys.* **2004,** *6,* 3215–3220. doi:10.1039/b403409k
47. Carreño, M. C.; García-Ruano, J. L.; Sanz, G.; Toledo, M. A.; Urbano, A. *J. Org. Chem.* **1995,** *60,* 5328–5331. doi:10.1021/jo00121a064
48. Moursounidis, J.; Wege, D. *Aust. J. Chem.* **1988,** *41,* 235–249. doi:10.1071/ch9880235
49. Weimar, M.; Dürner, G.; Bats, J. W.; Göbel, M. W. *J. Org. Chem.* **2010,** *75,* 2718–2721. doi:10.1021/jo100053j
50. Melhuish, W. H. *J. Phys. Chem.* **1960,** *64,* 762–764. doi:10.1021/j100835a014
51. Melhuish, W. H. *J. Phys. Chem.* **1961,** *65,* 229–235. doi:10.1021/j100820a009

License and Terms

BEILSTEIN JOURNAL OF ORGANIC CHEMISTRY

Plasma membrane imaging with a fluorescent benzothiadiazole derivative

Pedro H. P. R. Carvalho[1,2], Jose R. Correa[1], Karen L. R. Paiva[1], Daniel F. S. Machado[1], Jackson D. Scholten[2] and Brenno A. D. Neto[*1,2]

Letter

Open Access

Address:
[1]Laboratory of Medicinal and Technological Chemistry, University of Brasília, Chemistry Institute (IQ-UnB), Campus Universitário Darcy Ribeiro, Brasília, Distrito Federal, 70904-970, Brazil and [2]Laboratory of Molecular Catalysis, Institute of Chemistry, Graduate Program (PPGQ), Universidade Federal do Rio Grande do Sul, Porto Alegre, RS, 91501-970, Brazil

Email:
Brenno A. D. Neto[*] - brenno.ipi@gmail.com

* Corresponding author

Keywords:
benzothiadiazole; bioprobe; cell imaging; fluorescence; mitochondria; molecular architecture; plasma membrane

Beilstein J. Org. Chem. **2019,** *15,* 2644–2654.
doi:10.3762/bjoc.15.257

Received: 31 May 2019
Accepted: 15 October 2019
Published: 06 November 2019

This article is part of the thematic issue "Dyes in modern organic chemistry".

Guest Editor: H. Ihmels

Abstract

This work describes a novel fluorescent 2,1,3-benzothiadiazole derivative designed to act as a water-soluble and selective bioprobe for plasma membrane imaging. The new compound was efficiently synthesized in a two-step procedure with good yields. The photophysical properties were evaluated and the dye proved to have an excellent photostability in several solvents. DFT calculations were found in agreement with the experimental data and helped to understand the stabilizing intramolecular charge-transfer process from the first excited state. The new fluorescent derivative could be applied as selective bioprobe in several cell lines and displayed plasma-membrane affinity during the imaging experiments for all tested models.

Introduction

The selective staining of plasma membranes is of paramount importance to study cellular processes and events associated with this dynamic cellular component. After more than one century of the idea considering cell plasma membranes as lipid bilayers [1], the importance to understand the functions, processes and events associated with plasma membranes is still vital. We are only beginning to understand many of the processes and functions related to this component responsible for the boundaries of the cells [2-4]. Various details have emerged due to the development of new sensitive molecular probes capable of staining organelles and cell components selectively, however, many open questions remain.

Plasma membranes are the natural barrier between the extracellular environment and the cytoplasm, thus playing a pivotal role in cellular uptaking processes, trafficking and signaling [5]. Many models aim at describing the membranes' behavior in several solvents and aqueous solutions [6]. However, the direct

imaging and observation of plasma membranes in live cells is still one of the most promising strategies to investigate their roles, functions and to relate them with specific cellular responses [7].

The selective imaging of plasma membranes allows the tracking of the cell morphology, the cell status, cellular division step, signal transduction, apoptosis and even necrosis [8-10]. The monitoring of plasma membranes, their biophysical properties, endocytosis/exocytosis of several types of molecules, as well as their dynamic changes, may be performed by using fluorogenic organic dyes or derivatives thereof [11-15].

The design and synthesis of small organic fluorescence imaging probes capable of selectively stain plasma membranes has been proven, however, often as a challenging task. The development of small organic probes, in general, has been hindered by the requirement of multistep syntheses to obtain the fluorophore and by poor performances related to most of them. Therefore, many studies are still based on the use of WGA [16] (wheat germ agglutinin) or membrane proteins bearing fluorescent protein tags [11]. Water solubility is another issue that has to be considered. For the development of new fluorogenic dyes for plasma membrane imaging there are two desirable features of the product to be considered: solubility in aqueous media and affinity for membranes. However, based on the available reports these properties seem to be antagonistic. Breakthrough works have, however, described the successful design and application of water-soluble plasma membrane probes [17,18].

We have been developing a new class of selective bioprobes based on the derivatization of the 2,1,3-benzothiadiazole (BTD) core (Figure 1) [19-22]. After we disclosed the use of these BTD derivatives as a new class of selective fluorescence imaging probes, many contributions [23-37] appeared successfully applying fluorescent BTDs in bioimaging experiments (see examples in Figure 1).

Based on our interest in the development of new bioimaging agents [38-40], we disclose herein the design, synthesis, properties and application of a new fluorogenic BTD derivative as a water-soluble selective plasma membrane probe for bioimaging experiments.

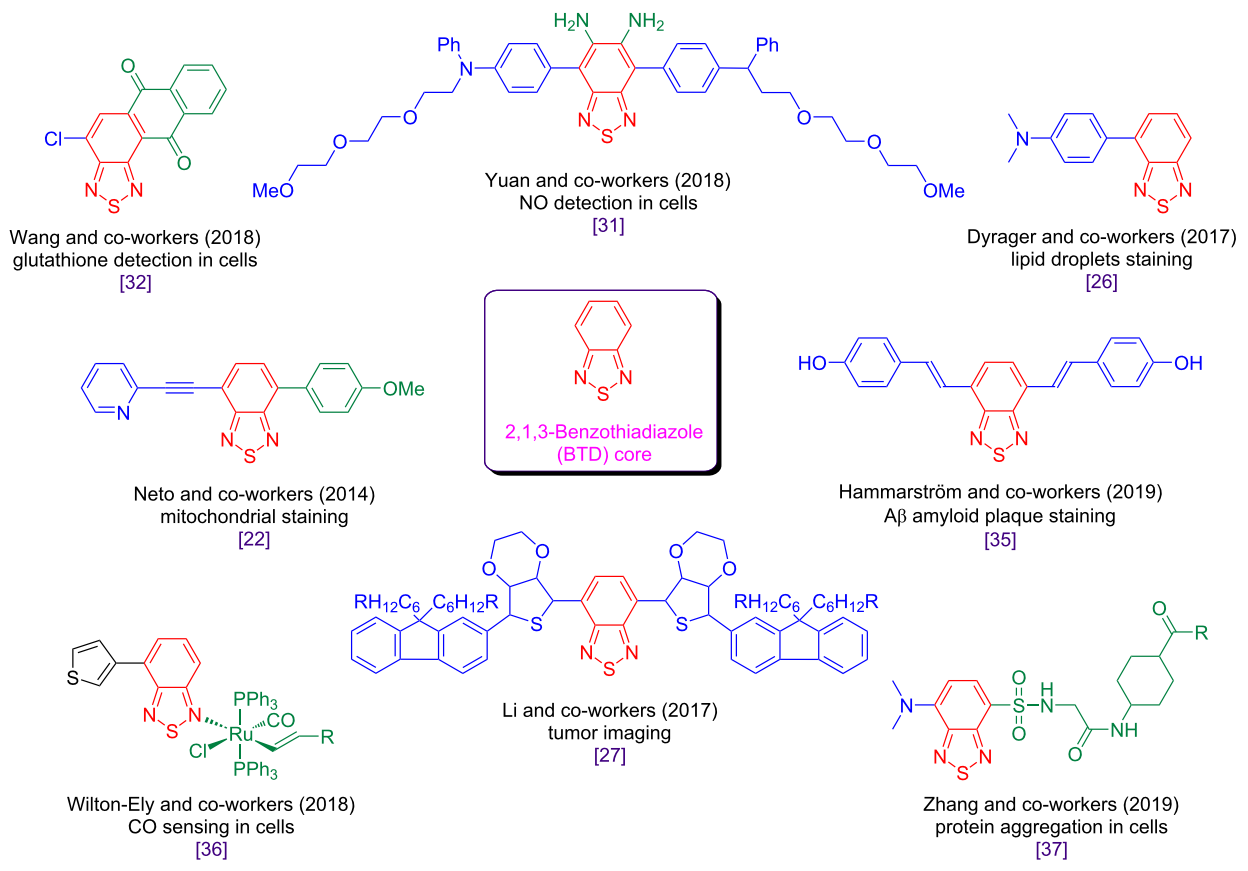

Figure 1: The 2,1,3-benzothiadiazole (BTD) core and its derivatives that are successfully applied in bioimaging experiments.

Results and Discussion

The new water-soluble fluorescent BTD derivative (named BTD-4APTEG) was planned and synthesized as shown in Scheme 1. The new fluorescent structure is accessible in a two-step procedure from the commercially available 4-bromo-2,1,3-benzothiadiazole (BTD-Br) and 4-aminopyridine (4AP), as we have recently described [41]. The Buchwald–Hartwig amination protocol afforded the fluorescent BTD-4AP in 80% yield after purification [41]. The new derivative was then synthesized by a direct alkylation reaction which afforded the desired compound BTD-4APTEG in 65% yield after purification (see details in the Experimental section).

The structure of BTD-4APTEG bears a lipophilic anchor to improve its affinity towards the lipidic bilayer of the plasma membrane. In fact, the lipophilic character of similar small BTD derivatives demonstrated improved affinity for lipid-based structures, as we [42,43] and others [26,29] have shown. The intramolecular H-bond is in addition responsible for the rigidity of the structure and enables a better conjugation with the 4AP substituent at the C4 carbon of the BTD heterocyclic core. The ionic nature of the structure in combination with a hydrophilic anion ($MeSO_3^-$, methanesulfonate) and the presence of the hydrophilic domain (triethylene glycol monomethyl ether) make the dye a water-soluble BTD derivative. The photophysical properties of the new compound BTDE-4APTEG have been investigated and the results are summarized in Table 1 and presented in Figure 2.

All absorption maxima were observed in the UV region close to 375 nm and with reasonable molar extinction coefficients. Large Stokes shifts were noted in all tested solvents (134–173 nm), thus pointing to efficient stabilizations through intramolecular charge-transfer (ICT) processes from the excited states. The largest Stokes shift was noted in the aqueous solution, indicating the dye's stability in this solvent. The solvatochromic analyses of ETN vs Stokes shifts using the values provided by Richardt [44] were found in accordance with the

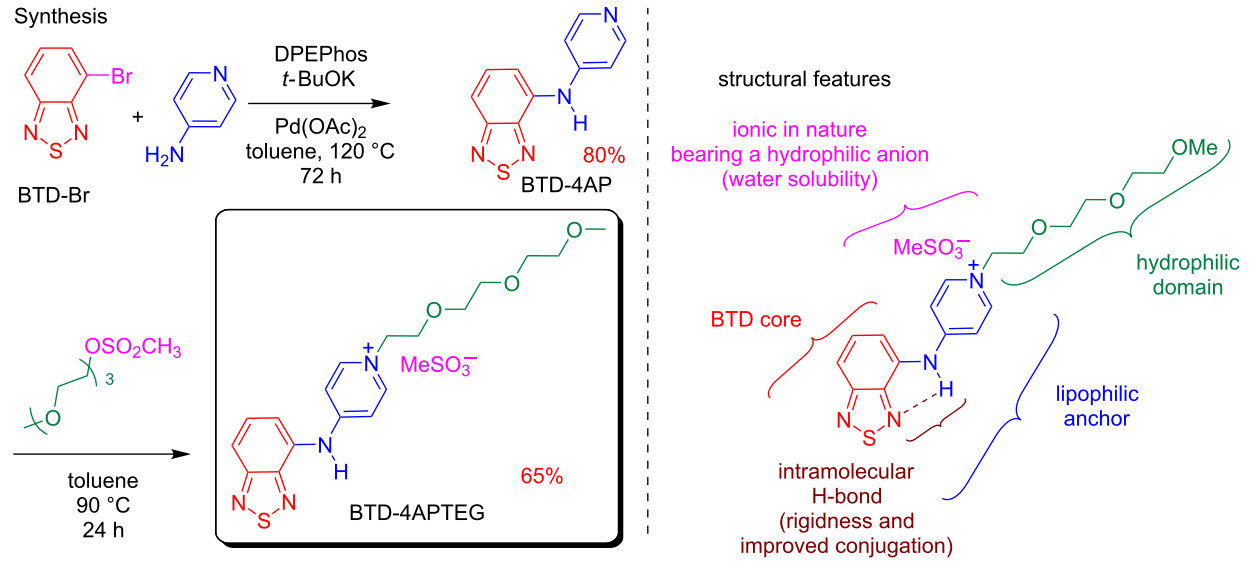

Scheme 1: Synthesis of the plasma membrane BTD probe (BTD-4APTEG) and its structural features.

Table 1: UV–vis and fluorescence emission data (in different solvents at 10 μM for all analyses) for the synthesized compound.

Compound	Solvent	$\lambda_{max,abs}$ (nm)	log ε	$\lambda_{max,em}$ (nm)	Stokes shift (nm/cm^{-1})
BTD-4APTEG	CH_2Cl_2	368	3.0	512	144/7643
	DMSO	375	2.9	525	150/7619
	MeCN	363	2.9	518	155/8243
	MeOH	362	2.9	523	161/8504
	toluene	383	2.2	517	134/6767
	water	370	2.9	543	173/8611

$\Phi_{toluene}$ 0.002, Φ_{MeCN} 0.02, Φ_{water} 0.01, Φ_{DCM} 0.02, Φ_{MeOH} 0.03, Φ_{DMSO} 0.02.

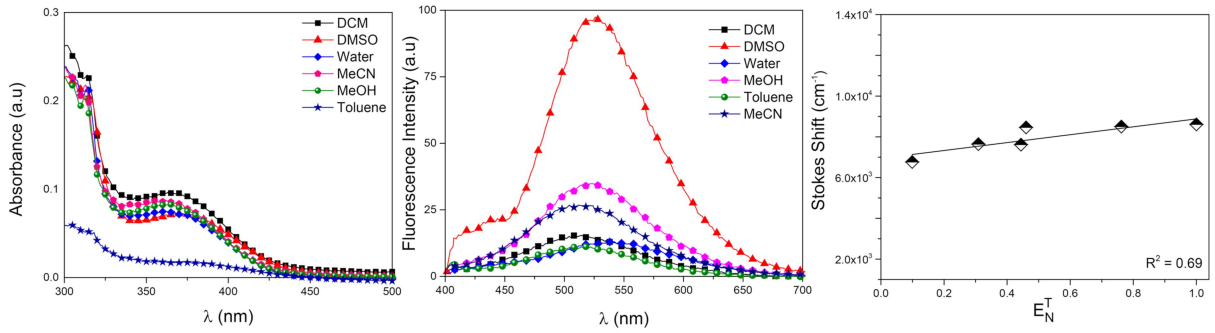

Figure 2: (Left) UV–vis, (center) fluorescence emission and (right) solvatochromic effect (Stokes shift in wavenumbers versus solvent polarity in ETN) of the synthesized BTD-4APTEG (10 μM for all analyses).

ICT proposition and the calculated linear correlation from the plots [45] corroborated this proposition. The photostability of the new compound was measured in aqueous media as a preclude of the bioimaging experiments and proved to be stable under constant light irradiation for more than 4 hours (see Figure S4 in Supporting Information File 1).

Theoretical calculations were then performed for a better comprehension of the photophysical data obtained for BTD-4APTEG by means of the time-dependent density functional theory (TD-DFT). In practice, when applying DFT calculations, there is no "universal" exchange correlation functional (XCF), thus the performance of different XCFs in simulating the absorption spectra of BTD-4APTEG had to be assessed. We aimed at describing the maxima absorption peak position associated with the π–π* transitions, as expected for this type of 4,7-disubstituted BTDs [46-50].

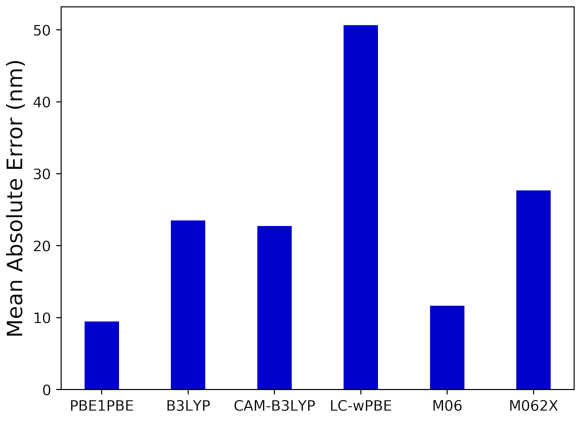

Figure 3: Mean absolute error (MAE) comparing both the experimental and the estimated TD-DFT λ_{max} positions in different solvents for BTD-4APTEG. The computed λ_{max} value corresponds to the largest wavelength band associated with the $S_0 \rightarrow S_1$ electronic excitation.

In Figure 3 the mean absolute error (MAE) between the theoretical and experimental absorption maxima (λ_{max}) in different solvents is shown. The results showed the hybrid XCF, PBE1PBE yielded the best overall performance across all studied solvents with an absolute deviation below 10 nm. PBE1PBE was therefore selected as the most suitable XCF (amongst the six investigated XCFs) for studying the photophysical properties of BTD-4APTEG.

The structure geometry was fully optimized in acetonitrile, dichloromethane, DMSO, methanol and water (Figure 4A). It turned out that the optimized geometries were not affected by the implicit solvation model affording root mean squared deviations of atomic positions of about 10^{-4} Å. The obtained CAM-B3LYP/6-311+G(d) geometries showed that the BTD core of the BTD-4APTEG is twisted by nearly 30° with respect to the NH fragment (see Figure S5 in Supporting Information File 1). Although this torsion diminishes the strength of the H-bond and conjugation, the effect is not strong enough to affect the emissive properties of the designed structure, as noted for the calculated properties of the designed structure (Figure 4).

The UV–vis absorption spectra of BTD-4APTEG calculated at the PBE1PBE/6-311+G(2d,p)//CAM-B3LYP/6-311+G(d) are shown in Figure 4B and solvent effects were also accounted using the IEF-PCM formalism [51]. The theoretical absorption bands showed an excellent agreement with those obtained experimentally in both terms the peak positions as well as their relative intensities.

The π–π* band is entirely described by a HOMO–LUMO vertical transition as visualized in Figure 4C. The LUMO orbital is strictly distributed over the BTD core in the BTD-4APTEG molecule, which is the net result of its electron density withdrawal character. The HOMO orbital distributes over the BTD basic scaffold and the vicinal ring but does not involve participation of the side chain of the chromophore. The electron density difference between the ground S_0 and first excited

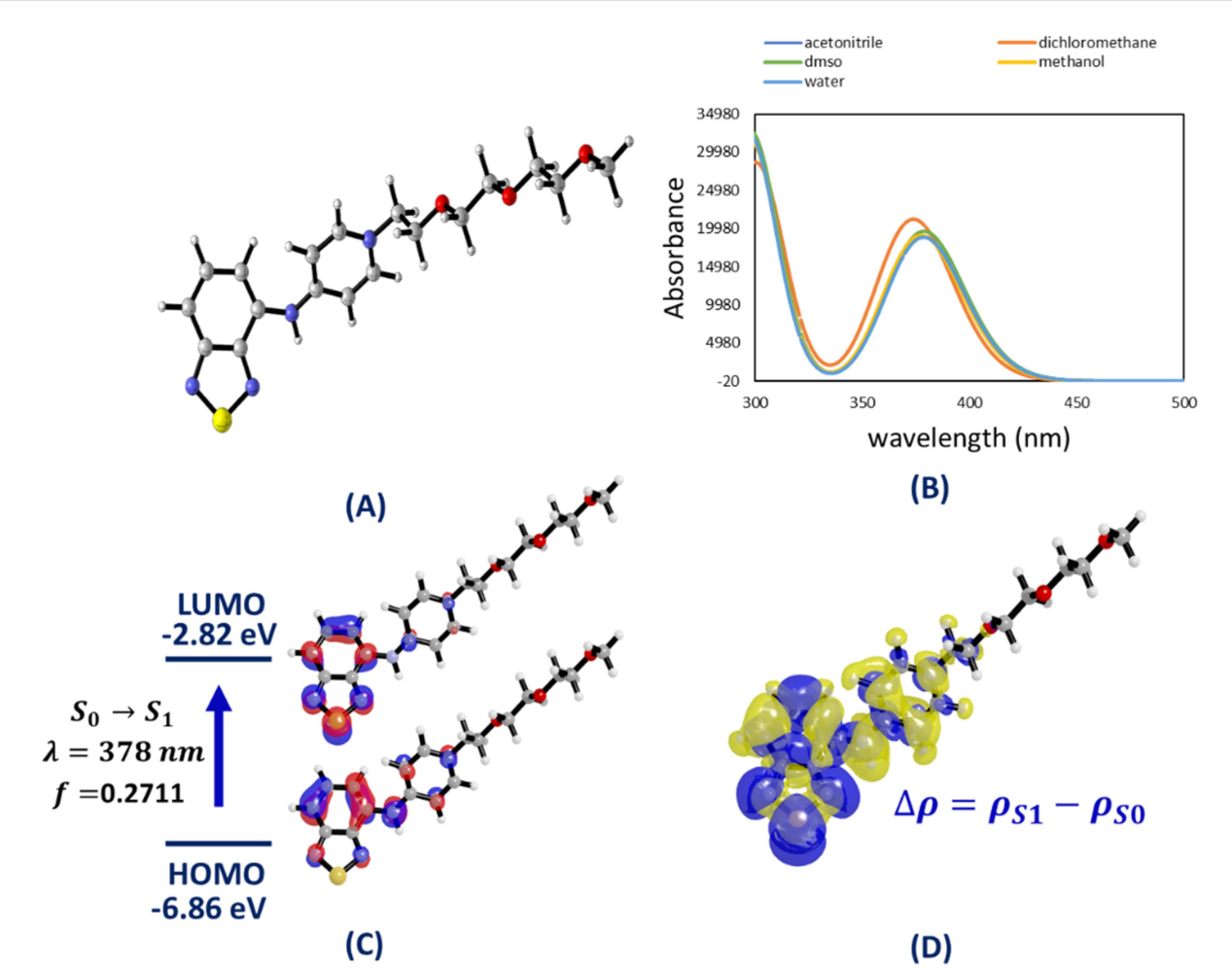

Figure 4: (A) CAM-B3LYP/6-311+G(d) optimized geometry of BTD-4APTEG (implicit DMSO). (B) TD-DFT UV–vis spectra of BTD-4APTEG calculated at the PBE1PBE/6-311+G(2d,p) level of theory. Solvent effects were estimated under the IEF-PCM formalism. (C) PBE1PBE/6-311+G(2d,p)// CAM-B3LYP/6-311+G(d) HOMO and LUMO orbitals of BTD-4APTEG in DMSO involved in the S0→S1 electronic excitation associated with the longest wavelength band. (D) Electron density difference between the first excited and ground states ($\Delta\rho = \rho_{S1} - \rho_{S0}$), where blue regions correspond to density accumulation whereas the yellow means the density depletion.

state S_1 ($\Delta\rho = \rho_{S1} - \rho_{S0}$), as shown in Figure 4D, highlights the directionality of the electron density transfer with a great deal of ICT between the cationic heterocycle and the BTD core, which stabilizes the excited state of the synthesized chromophore. These theoretical results agreed well with the experimental data obtained for the newly developed dye.

DFT calculations were also employed to forecast the lipophilic character of the dye utilizing several XCFs. Experimentally, lipophilicity can be measured by means of the logarithm of the *n*-octanol/water partition coefficient (known as log P_{ow}), which is defined as the equilibrium concentration ratio of the analyte distributed between these two phases [52]. The theoretical logarithm of the partition coefficient for the water/*n*-octanol mixture at both constant temperature and pressure was computed using Equation 1 [53]

$$\log K_{ow} = \frac{\Delta G^{\text{solv}}_{\text{water}} - \Delta G^{\text{solv}}_{n\text{-octanol}}}{2.303RT} \quad (1)$$

calculated at 298 K.

Table 2 summarizes the solvation free energies of BTD-4APTEG in water and *n*-octanol solutions and the log K_{ow} obtained with the solvation model based on solute electron density (SMD) [54]. The DFT calculations qualitatively returned a preference for nonpolar environments only when B97D3 (GGA level) and ωB97XD (long range-corrected hybrid level) XCFs were employed. Both B97D3 and ωB97XD were strongly recommended by a thoroughly benchmarking of DFT methods for thermochemistry by Goerik and Grimme [55].

Table 2: Calculated solvation free energies in water (ΔG^{solv}_{water}), in 1-octanol ($\Delta G^{solv}_{n\text{-octanol}}$) and corresponding partition coefficient log K_{ow} for BTD-4APTEG. Solvent effects included with the SMD solvation model.[a]

XCF	ΔG^{solv}_{water}	$\Delta G^{solv}_{n\text{-octanol}}$	log K_{ow}
B3LYP	−58.70	−57.12	−1.160
B97D3	−54.92	−55.38	0.333
M11	−58.74	−56.91	−1.341
M06-2X	−57.92	−56.18	−1.272
ωB97XD	−58.12	−59.90	1.305
PW6B95	−56.66	−56.57	−0.800
PW6B95-D3	−57.90	−56.81	−0.792
PBE1PBE	−58.89	−58.84	−0.029

[a]All energetic values expressed in kcal mol^{-1}.

The new dye was then submitted to an MTT assay to investigate possible cytotoxicity effects and the concentrations to use the probe without causing any harm to the cells (Figure 5). Only at concentrations up to 100 μM cytotoxic effects were noted and at 10 μM no effect was observed for the designed BTD-4APTEG. For the subsequent bioimaging experiments, the fluorophore was tested at 1 μM, that is at a concentration 100-fold lower than that of the cytotoxic effect.

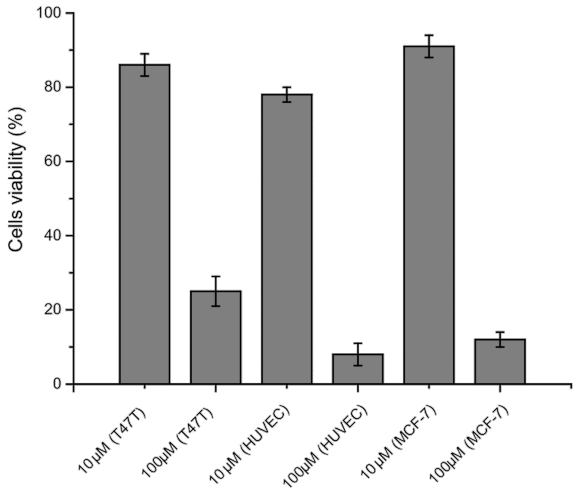

Figure 5: Cellular viability determined by MTT analysis after 24 h treatment with the developed dye BTD-4APTEG. No statistically significant cytotoxic effect was observed after 24 h incubation with the new dye BTD-4APTEG at 10 μM. However, the dye induced strong cytotoxic effects in all tested cell lines at 100 μM ($p < 0.05$).

The new compound was then tested as bioimaging probe in live and fixed cells (Figure 6). As can be seen, the green fluorescent dye BTD-4APTEG was found most concentrated at the plasma membranes of the MCF-7 cells in both, live and fixed cells (Figure 6A,C), and not in the cytosol, thus pointing firmly to its affinity for the plasma membrane.

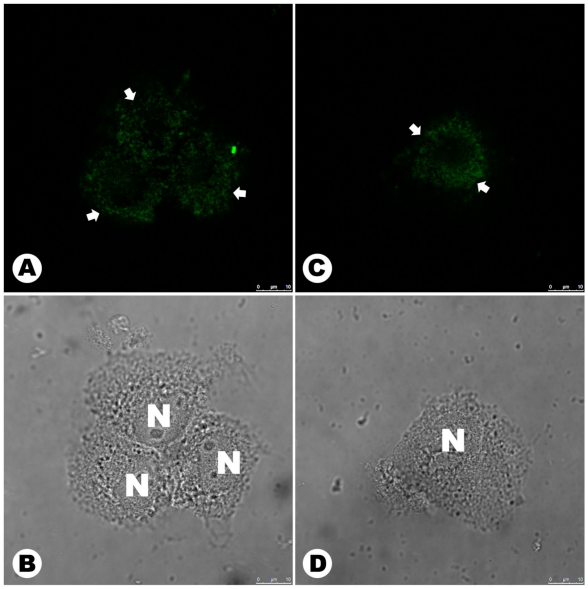

Figure 6: MCF-7 cells incubated with BTD-4APTEG (1 μM) in live (A) and (B) and fixed cells (C) and (D). (A) and (C) show the staining distribution of the new dye BTD-4APTEG in the plasma membrane of the cells. (B) and (D) show the normal morphological aspects of the samples by phase contrast microscopy. The dye was found accumulated in the peripheral region of the cellular membrane (white arrows) in both samples. The letter N indicates the nuclei of the cells (scale bar of 10 μm).

To confirm the selectivity of BTD-4APTEG towards the plasma membrane of both live and fixed cells, co-staining experiments using the commercially available probe known as CellMask were also conducted and the results are shown in Figure 7. Both bioprobes were found in the plasma membranes of the cells and their superposition (Figure 7B showing the images overlay) afforded an orange emission (green plus red).

Although there was no doubt regarding the preference of BTD-4APTEG for the plasma membranes, a Pearson correlation coefficient (PCC) [56-58] analysis between the two fluorescent signals (green and red emissions) from BTD-4APTEG and from CellMask, was performed using ten independent analyses of ten different images. The quantitative PCC showed an agreement of 79% and 77% for live and fixed cells, respectively (see Figures S6 and S7 in Supporting Information File 1). The quantitative results obtained by PCC validate the qualitative analysis shown in Figure 7, therefore supporting the dye's affinity for the plasma membranes. The negative control was performed using BTD-4APTEG 90° counterclockwise rotation [56-58]. The analyses also provided evidence that no random colocalization was taking place (Figures S6 and S7 in Supporting Infor-

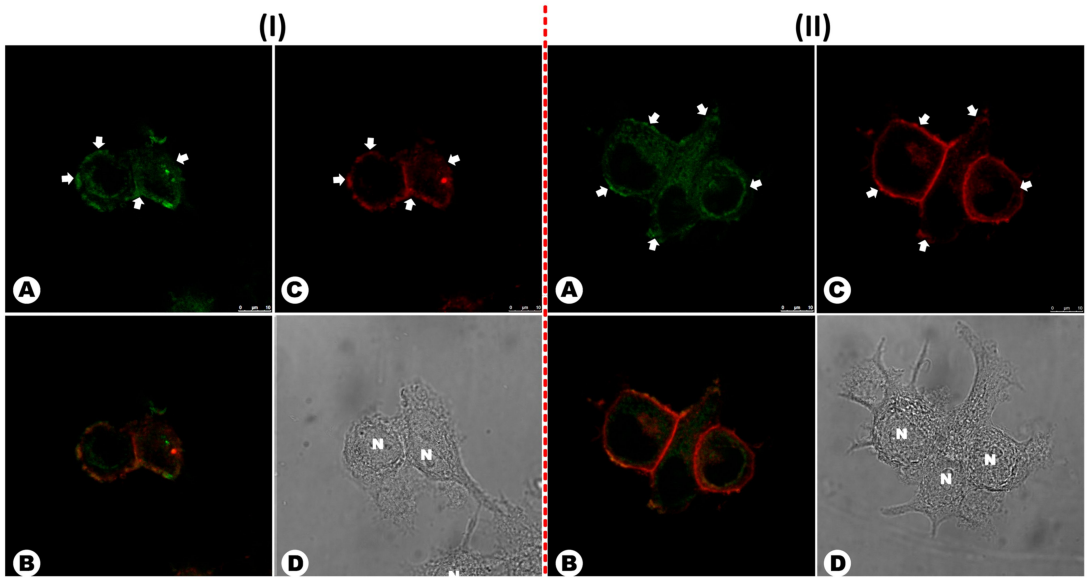

Figure 7: Co-staining experiments using the commercially available CellMask (red emission) and BTD-4APTEG (green emission) in (I) live and (II) fixed MCF-7 cells. (A) Plasma membranes stained with the designed BTD-4APTEG. (B) Overlay of (A) and (C) showing the orange emission as the result of both green and red emissions. (C) Plasma membranes stained with the commercially available CellMask. (D) Shows the normal morphology of the cells by phase contrast microscopy. Arrows indicate the peripherical accumulation of the dyes in the plasma membranes. The letter N indicates the nuclei of the cells (scale bar of 10 μm).

mation File 1). It is known that CellMask is capable of entering the cells to some extent, especially when using fixed cells. Thus its selectivity seems to be smaller than the one observed for the new green emitter.

Although the plasma membrane separates the interior of the cell from the extracellular environment, there is a massive material transfer between both sides [59]. These materials typically are transported by vesicles which assemble large organelles within the cell cytoplasm called endosome. There are at least two different endosome types (i.e., early and late endosome) and one of them is localized near to the plasma membrane (early endosomes) whereas the other is found near to the nucleus (late endosomes) [60-62]. These organelles are formed by plasma membrane invaginations sustaining the structure and composition of the original component. The use of lipophilic dyes for plasma membrane staining will therefore afford additional cytoplasm markers due to endosome formation from the plasma membrane previously stained with the fluorescent compound. There is no way to eliminate this fluorescent signal because of the constitutive presence of endosomes in mammalian cells. Cancer cells have, in addition, an accelerated metabolism and high endocytosis index [63]. Endocytosis is known to be the cellular event that plays a pivotal role in endosome formation and maintenance. The presence of intracellular structures marked with BTD-4APTEG is then explained by endosome formation. The mild fluorescent noise observed over the cells is probably caused by the plasma membrane involving the cells and its fluorescent signal has then contributed to the image formation.

Finally, the developed fluorophore was tested in additional cell lines to show its efficiency. A2780 (human ovarian carcinoma) cells, T47D (human breast tumor) cells and HUVEC (human umbilical vein endothelial) cells were tested and the results are shown in Figure S8 (Supporting Information File 1). Again, the designed fluorophore was capable of selectively stain the plasma membranes with intense green emissions, indicating therefore, the fluorogenic dye efficiency as a new bioprobe for bioimaging experiments.

Conclusion

In summary, a new water-soluble BTD fluorophore BTD-4APTEG was developed and applied as selective probe for bioimaging and stained plasma membranes selectively in the tested cells lines. The features envisaged for the synthesis of the structure proved to be capable of granting the dye water solubility, good photostability and affinity for the plasma membrane as depicted in the imaging (qualitative and quantitative) experiments. Theoretical calculations were found to be in accordance with the experimental data and helped to understand the ICT stabilizing process of the designed fluorophore. The developed green emitter was efficiently applied as selective plasma membrane probe in bioimaging experiments. Co-staining and PCC experiments confirmed the dye's affinity for the plasma membrane and indicated its efficiency as a new bioprobe.

Experimental

NMR spectra were recorded on an NMR instrument using a 5 mm internal diameter probe operating at 400 MHz for ^{1}H and at 100 MHz for ^{13}C NMR. Chemical shifts were expressed in parts per million (ppm) and referenced by the signals of the residual hydrogen atoms of the deuterated solvent, as indicated in the legends. UV–vis absorption (Varian Cary 5000) spectroscopy and fluorescence emission (Cary Eclipse,Varian CA-USA) were acquired using recent prepared solutions (10 μM for all analyses). All reagents and solvents were purchased from commercial sources.

Synthesis of BTD-4APTEG. 2-(2-(2-Methoxyethoxy)-ethoxy)ethyl methanesulfonate (48 mg, 0.2 mmol) and BTD-4AP [41] (11.5 mg, 0.05 mmol) were mixed in MeCN (5 mL) in a sealed Schlenk tube and the reaction mixture was stirred at 80 °C for 24 h. After cooling, the solvent was removed and the crude washed several times with ethyl acetate to remove unreacted reagents. The desired product was obtained in 65% yield. IR (cm^{-1}): 3090, 2870, 1960, 1630, 1514, 1220, 1106, 930; ^{1}H NMR (400 MHz, D_2O) δ (ppm) 8.15 (d, J = 7.2 Hz, 2H), 8.00–7.95 (m, 1H), 7.84–7.65 (m, 2H), 7.13 (d, J = 7.2 Hz, 2H), 4.37 (t, J = 5.2 Hz, 2H,) 3.88 (t, J = 5.2 Hz, 2H,) 3.65–3.44 (m, 8H), 3.21 (s, 3H), 2.74 (s, 3H); ^{13}C NMR (100 MHz, D_2O/CD_3OD 1:1, v/v) δ (ppm) 156.4, 155.8, 144.1, 130.9, 129.2, 126.4, 123.3, 120.1, 111.9. 71.50, 71.47, 70.2, 69.9, 69.3, 38.9; HRMS (ESI-Q-TOF) calcd. for $C_{18}H_{23}N_4O_3S^+$, 375.1485; found, 375.1460.

Theoretical calculations. All DFT calculations were performed using the Gaussian 09 suite of programs [64]. Geometry optimizations were carried out with the long-range corrected density functional CAM-B3LYP with 6-31G(d) Pople's split basis set. Harmonic frequency calculations were performed to verify that a genuine energetic minimum was achieved. Solvent effects on the BTD-4APTEG geometries were assessed using the polarizable continuum model (PCM) in which the solute molecule is enclosed in a cavity embedded in a continuum dielectric medium. The optimized geometries of the ground state (S_0) in the calculated solvents were then used for the single point TD-DFT calculation using density functionals of different flavors to assess the performance of different density functionals: B3LYP, CAM-B3LYP, LC-ωPBE, M06, M06-2X, and PBE1PBE. It was employed the 6-311+G(2d,p) basis set to simulate the excitation spectra of the BTDs. To comprise the solvent effects, the implicit PCM treatment was also included in the TD-DFT calculations.

Biological experiments. The new BTD derivative BTD-4APTEG was diluted in water in the cell medium supplemented with 10% of fetal calf serum. The following cell lines were used: human ovarian cancer cell line A2780, human breast adenocarcinoma cell line MCF-7, breast adenocarcinoma cell line T47D and human umbilical vein endothelial cells, HUVEC. The cells were maintained according to ATCC (American type culture collection) recommendations at 37 °C in an atmosphere containing 5% CO_2.

Cell viability. For cell viability the synthesized compound BTD-4APTEG was tested at two different concentrations, 10 and 100 μM. The cells were incubated with the synthesized BTD for 24 h and analyzed by a standard MTT assay, following the manufacturer's recommendations (R&D System Inc, MN, USA). Briefly, 3×10^3 cells of each cell line were seeded in a 96-well plate and maintained overnight at 37 °C. The samples were incubated with 150 μL of MTT (3-[4,5-dimethylthiazol-2-yl]-2,5-diphenyltetrazolium bromide) solution (0.5 mg mL^{-1}) in cell culture medium for 4 h in the dark at 37 °C (MTT is reduced by metabolically active cells to insoluble purple formazan dye crystals that accumulate inside the cell cytoplasm). Afterwards, the MTT solution is removed and 200 μL of DMSO are added to all samples to solubilize the formazan dye crystals. The plate was read in spectrophotometer and the optimal wavelength for absorbance was 570 nm. The MTT assay was performed in triplicate and also made three independent assays. The cell viability inhibition was determined by evaluation of MTT result obtained for test samples compared with the control samples in the same conditions, following the expression: [survival % = [(tested sample-blank)/(control sample-blank)] × 100].

Bioimaging experiments. The bioimaging experiments were performed in a similar manner to a procedure which have already been published elsewhere [65]. Cells were seeded on 13 mm round glass coverslips on the bottom of a 24-well plate and allowed to adhere overnight. Afterwards, the cells were washed three times with serum-free medium aiming at removing non-adherent cells. After reaching the expected confluence, the cells were separated in two main samples, that is, live samples and fixed samples. Live cells were therefore incubated for 30 minutes with a BTD-4APTEG solution (1 μM) at 37 °C, washed three times with PBS 1X (pH 7.4) at room temperature and fixed in formaldehyde 3.7% for 30 minutes. Again, the cells were washed three times in PBS 1X (pH 7.4) at room temperature and the coverslips were mounted over glass slides using ProLong Gold Antifade (Invitrogen, OR, USA) according to the manufacturer's recommendations. A similar procedure was followed for fixed cells. Fixed cells were washed three times in PBS 1X (pH 7.4) and then fixed in formaldehyde 3.7% for 30 minutes. Afterwards, fixed cells were washed three times in PBS 1X (pH 7.4) at room temperature and incubated for 30 minutes with BTD-4APTEG solution (1 μM) at room tem-

perature, washed three times in PBS 1X (pH 7.4) at room temperature and the coverslips were mounted over glass slides using ProLong Gold Antifade (Invitrogen, OR, USA) according to the manufacturer's recommendations. These two main samples (of live and fixed cells) were analyzed using confocal microscopy and excited using 405 nm wavelength laser emission and the fluorescence images were acquired at 520–550 nm wavelength range. Triplicated assays could be carried out and the procedure was performed as three repetitions for each experimental condition.

Plasma membrane co-staining. The cell membrane staining procedures were performed with CellMask, a specific fluorescent commercial marker indicated to membrane staining. Briefly, live and pre-fixed cells (processed as described above) were incubated with a CellMask solution (prepared according the manufacturer's instructions) or with BTD-4APTEG during 30 minutes at room temperature. Afterwards, the cells were washed three times in PBS and the samples were mounted over glass slides by using antifade agent Prolong Gold (Invitrogen, OR, USA) according to the manufacture's recommendations. The samples were analyzed using confocal microscopy. CellMask was excited at 633 nm wavelength and the fluorescent images were acquired at 680–720 nm wavelength range. BTD-4APTEG was excited at 405 nm wavelength and the fluorescence images were acquired at 520–550 nm wavelength range. All assays were performed in triplicate and it was done three repetitions for each cell sample and experimental condition.

Supporting Information

Supporting Information File 1

Copies of spectra, additional figures, energies and Cartesian coordinates for all calculated structures.
[https://www.beilstein-journals.org/bjoc/content/supplementary/1860-5397-15-257-S1.pdf]

Acknowledgements

This work has been supported by CAPES, CNPq, FINEP-MCT, FAPERGS, FINATEC, FAPDF, and DPP-UnB. BAD Neto also thanks INCT-Transcend group and LNLS. PPGQ-UFRGS is greatly acknowledge by BADN.

ORCID® iDs

Jose R. Correa - https://orcid.org/0000-0003-2752-5395
Daniel F. S. Machado - https://orcid.org/0000-0001-9690-6090
Jackson D. Scholten - https://orcid.org/0000-0002-7433-392X
Brenno A. D. Neto - https://orcid.org/0000-0003-3783-9283

References

1. Edidin, M. *Nat. Rev. Mol. Cell Biol.* **2003,** *4,* 414–418. doi:10.1038/nrm1102
2. Scorrano, L.; De Matteis, M. A.; Emr, S.; Giordano, F.; Hajnóczky, G.; Kornmann, B.; Lackner, L. L.; Levine, T. P.; Pellegrini, L.; Reinisch, K.; Rizzuto, R.; Simmen, T.; Stenmark, H.; Ungermann, C.; Schuldiner, M. *Nat. Commun.* **2019,** *10,* 1287. doi:10.1038/s41467-019-09253-3
3. Murray, L. M. A.; Krasnodembskaya, A. D. *Stem Cells (Durham, NC, U. S.)* **2019,** *37,* 14–25. doi:10.1002/stem.2922
4. Lai, R. C.; Lim, S. K. *J. Lipid Res.* **2019,** *60,* 318–322. doi:10.1194/jlr.r087411
5. Lingwood, D.; Simons, K. *Science* **2010,** *327,* 46–50. doi:10.1126/science.1174621
6. Lingwood, D.; Simons, K. *Nat. Protoc.* **2007,** *2,* 2159–2165. doi:10.1038/nprot.2007.294
7. Sezgin, E.; Levental, I.; Mayor, S.; Eggeling, C. *Nat. Rev. Mol. Cell Biol.* **2017,** *18,* 361–374. doi:10.1038/nrm.2017.16
8. Rello, S.; Stockert, J. C.; Moreno, V.; Gamez, A.; Pacheco, M.; Juarranz, A.; Canete, M.; Villanueva, A. *Apoptosis* **2005,** *10,* 201–208. doi:10.1007/s10495-005-6075-6
9. Shynkar, V. V.; Klymchenko, A. S.; Kunzelmann, C.; Duportail, G.; Muller, C. D.; Demchenko, A. P.; Freyssinet, J.-M.; Mely, Y. *J. Am. Chem. Soc.* **2007,** *129,* 2187–2193. doi:10.1021/ja068008h
10. Laguerre, A.; Schultz, C. *Curr. Opin. Cell Biol.* **2018,** *53,* 97–104. doi:10.1016/j.ceb.2018.06.013
11. Kreder, R.; Oncul, S.; Kucherak, O. A.; Pyrshev, K. A.; Real, E.; Mély, Y.; Klymchenko, A. S. *RSC Adv.* **2015,** *5,* 22899–22905. doi:10.1039/c4ra16225k
12. Collot, M.; Boutant, E.; Lehmann, M.; Klymchenko, A. S. *Bioconjugate Chem.* **2019,** *30,* 192–199. doi:10.1021/acs.bioconjchem.8b00828
13. Jia, H.-R.; Wang, H.-Y.; Yu, Z.-W.; Chen, Z.; Wu, F.-G. *Bioconjugate Chem.* **2016,** *27,* 782–789. doi:10.1021/acs.bioconjchem.6b00003
14. Collot, M.; Kreder, R.; Tatarets, A. L.; Patsenker, L. D.; Mely, Y.; Klymchenko, A. S. *Chem. Commun.* **2015,** *51,* 17136–17139. doi:10.1039/c5cc06094j
15. Lee, M.; Tremblay, M. S.; Jockusch, S.; Turro, N. J.; Sames, D. *Org. Lett.* **2011,** *13,* 2802–2805. doi:10.1021/ol200328p
16. Model, M. A.; Reese, J. L.; Fraizer, G. C. *Cytometry, Part A* **2009,** *75A,* 874–881. doi:10.1002/cyto.a.20787
17. Koo, C.-K.; Wong, K.-L.; Man, C. W.-Y.; Tam, H.-L.; Tsao, S.-W.; Cheah, K.-W.; Lam, M. H.-W. *Inorg. Chem.* **2009,** *48,* 7501–7503. doi:10.1021/ic9007679
18. Heek, T.; Nikolaus, J.; Schwarzer, R.; Fasting, C.; Welker, P.; Licha, K.; Herrmann, A.; Haag, R. *Bioconjugate Chem.* **2013,** *24,* 153–158. doi:10.1021/bc3005655
19. Neto, B. A. D.; Carvalho, P. H. P. R.; Correa, J. R. *Acc. Chem. Res.* **2015,** *48,* 1560–1569. doi:10.1021/ar500468p
20. Neto, B. A. D.; Lapis, A. A. M.; da Silva Júnior, E. N.; Dupont, J. *Eur. J. Org. Chem.* **2013,** 228–255. doi:10.1002/ejoc.201201161
21. Neto, B. A. D.; Corrêa, J. R.; Silva, R. G. *RSC Adv.* **2013,** *3,* 5291–5301. doi:10.1039/c2ra21995f
22. Carvalho, P. H. P. R.; Correa, J. R.; Guido, B. C.; Gatto, C. C.; De Oliveira, H. C. B.; Soares, T. A.; Neto, B. A. D. *Chem. – Eur. J.* **2014,** *20,* 15360–15374. doi:10.1002/chem.201404039
23. Jiang, Q.; Zhang, Z.; Lu, J.; Huang, Y.; Lu, Z.; Tan, Y.; Jiang, Q. *Bioorg. Med. Chem.* **2013,** *21,* 7735–7741. doi:10.1016/j.bmc.2013.10.019

24. Garcia, L.; Lazzaretti, M.; Diguet, A.; Mussi, F.; Bisceglie, F.; Xie, J.; Pelosi, G.; Buschini, A.; Baigl, D.; Policar, C. *New J. Chem.* **2013,** *37,* 3030–3034. doi:10.1039/c3nj00380a
25. Yao, S.; Kim, B.; Yue, X.; Colon Gomez, M. Y.; Bondar, M. V.; Belfield, K. D. *ACS Omega* **2016,** *1,* 1149–1156. doi:10.1021/acsomega.6b00289
26. Appelqvist, H.; Stranius, K.; Börjesson, K.; Nilsson, K. P. R.; Dyrager, C. *Bioconjugate Chem.* **2017,** *28,* 1363–1370. doi:10.1021/acs.bioconjchem.7b00048
27. Yang, D.; Wang, H.; Sun, C.; Zhao, H.; Hu, K.; Qin, W.; Ma, R.; Yin, F.; Qin, X.; Zhang, Q.; Liang, Y.; Li, Z. *Chem. Sci.* **2017,** *8,* 6322–6326. doi:10.1039/c7sc02698f
28. Han, X.; Wang, Z.; Cheng, Q.; Meng, X.; Wei, D.; Zheng, Y.; Ding, J.; Hou, H. *Dyes Pigm.* **2017,** *145,* 576–583. doi:10.1016/j.dyepig.2017.06.039
29. Dyrager, C.; Vieira, R. P.; Nyström, S.; Nilsson, K. P. R.; Storr, T. *New J. Chem.* **2017,** *41,* 1566–1573. doi:10.1039/c6nj01703g
30. Chen, C.; Hua, Y.; Hu, Y.; Fang, Y.; Ji, S.; Yang, Z.; Ou, C.; Kong, D.; Ding, D. *Sci. Rep.* **2016,** *6,* 23190. doi:10.1038/srep23190
31. Wang, S.; Li, Z.; Liu, Y.; Feng, G.; Zheng, J.; Yuan, Z.; Zhang, X. *Sens. Actuators, B* **2018,** *267,* 403–411. doi:10.1016/j.snb.2018.04.052
32. Chen, F.; Zhang, J.; Qu, W.; Zhong, X.; Liu, H.; Ren, J.; He, H.; Zhang, X.; Wang, S. *Sens. Actuators, B* **2018,** *266,* 528–533. doi:10.1016/j.snb.2018.03.162
33. Sun, J.; Ling, P.; Gao, F. *Anal. Chem. (Washington, DC, U. S.)* **2017,** *89,* 11703–11710. doi:10.1021/acs.analchem.7b03154
34. Liou, S.-Y.; Ke, C.-S.; Chen, J.-H.; Luo, Y.-W.; Kuo, S.-Y.; Chen, Y.-H.; Fang, C.-C.; Wu, C.-Y.; Chiang, C.-M.; Chan, Y.-H. *ACS Macro Lett.* **2016,** *5,* 154–157. doi:10.1021/acsmacrolett.5b00842
35. Zhang, J.; Konsmo, A.; Sandberg, A.; Wu, X.; Nyström, S.; Obermüller, U.; Wegenast-Braun, B. M.; Konradsson, P.; Lindgren, M.; Hammarström, P. *J. Med. Chem.* **2019,** *62,* 2038–2048. doi:10.1021/acs.jmedchem.8b01681
36. Toscani, A.; Marín-Hernández, C.; Robson, J. A.; Chua, E.; Dingwall, P.; White, A. J. P.; Sancenón, F.; de la Torre, C.; Martínez-Máñez, R.; Wilton-Ely, J. D. E. T. *Chem. – Eur. J.* **2019,** *25,* 2069–2081. doi:10.1002/chem.201805244
37. Jung, K. H.; Kim, S. F.; Liu, Y.; Zhang, X. *ChemBioChem* **2019,** *20,* 1078–1087. doi:10.1002/cbic.201800782
38. D'Angelis do Espirito Santo Barbosa, C.; Corrêa, J. R.; Medeiros, G. A.; Barreto, G.; Magalhães, K. G.; de Oliveira, A. L.; Spencer, J.; Rodrigues, M. O.; Neto, B. A. D. *Chem. – Eur. J.* **2015,** *21,* 5055–5060. doi:10.1002/chem.201406330
39. Diniz, J. R.; Correa, J. R.; Moreira, D. d. A.; Fontenele, R. S.; de Oliveira, A. L.; Abdelnur, P. V.; Dutra, J. D. L.; Freire, R. O.; Rodrigues, M. O.; Neto, B. A. D. *Inorg. Chem.* **2013,** *52,* 10199–10205. doi:10.1021/ic4017678
40. dos Santos, F. S.; Dias, G. G.; de Freitas, R. P.; Santos, L. S.; de Lima, G. F.; Duarte, H. A.; de Simone, C. A.; Rezende, L. M. S. L.; Vianna, M. J. X.; Correa, J. R.; Neto, B. A. D.; da Silva Júnior, E. N. *Eur. J. Org. Chem.* **2017,** 3763–3773. doi:10.1002/ejoc.201700227
41. Carvalho, P. H. P. R.; Correa, J. R.; Paiva, K. L. R.; Baril, M.; Machado, D. F. S.; Scholten, J. D.; de Souza, P. E. N.; Veiga-Souza, F. H.; Spencer, J.; Neto, B. A. D. *Org. Chem. Front.* **2019,** *6,* 2371–2384. doi:10.1039/c9qo00428a
42. Mota, A. A. R.; Correa, J. R.; de Andrade, L. P.; Assumpção, J. A. F.; de Souza Cintra, G. A.; Freitas-Junior, L. H.; da Silva, W. A.; de Oliveira, H. C. B.; Neto, B. A. D. *ACS Omega* **2018,** *3,* 3874–3881. doi:10.1021/acsomega.8b00434
43. Mota, A. A. R.; Carvalho, P. H. P. R.; Guido, B. C.; de Oliveira, H. C. B.; Soares, T. A.; Corrêa, J. R.; Neto, B. A. D. *Chem. Sci.* **2014,** *5,* 3995–4003. doi:10.1039/c4sc01785d
44. Reichardt, C. *Chem. Rev.* **1994,** *94,* 2319–2358. doi:10.1021/cr00032a005
45. Ravi, M.; Soujanya, T.; Samanta, A.; Radhakrishnan, T. P. *J. Chem. Soc., Faraday Trans.* **1995,** *91,* 2739–2742. doi:10.1039/ft9959102739
46. Lee, D.-C.; Jeong, Y.; Brownell, L. V.; Velasco, J. E.; Robins, K. A.; Lee, Y. *RSC Adv.* **2017,** *7,* 24105–24112. doi:10.1039/c7ra03612d
47. Jiang, D.; Chen, S.; Xue, Z.; Li, Y.; Liu, H.; Yang, W.; Li, Y. *Dyes Pigm.* **2016,** *125,* 100–105. doi:10.1016/j.dyepig.2015.10.014
48. Jadhav, T.; Dhokale, B.; Patil, Y.; Mobin, S. M.; Misra, R. *J. Phys. Chem. C* **2016,** *120,* 24030–24040. doi:10.1021/acs.jpcc.6b09015
49. Li, Y.; Scudiero, L.; Ren, T.; Dong, W.-J. *J. Photochem. Photobiol., A* **2012,** *231,* 51–59. doi:10.1016/j.jphotochem.2012.01.011
50. Zhu, W.; Meng, X.; Yang, Y.; Zhang, Q.; Xie, Y.; Tian, H. *Chem. – Eur. J.* **2010,** *16,* 899–906. doi:10.1002/chem.200901855
51. Tomasi, J.; Mennucci, B.; Cancès, E. *J. Mol. Struct.: THEOCHEM* **1999,** *464,* 211–226. doi:10.1016/s0166-1280(98)00553-3
52. Ribeiro, R. F.; Marenich, A. V.; Cramer, C. J.; Truhlar, D. G. *Phys. Chem. Chem. Phys.* **2011,** *13,* 10908–10922. doi:10.1039/c0cp02784g
53. Garrido, N. M.; Economou, I. G.; Queimada, A. J.; Jorge, M.; Macedo, E. A. *AIChE J.* **2012,** *58,* 1929–1938. doi:10.1002/aic.12718
54. Marenich, A. V.; Cramer, C. J.; Truhlar, D. G. *J. Phys. Chem. B* **2009,** *113,* 6378–6396. doi:10.1021/jp810292n
55. Goerigk, L.; Grimme, S. *Phys. Chem. Chem. Phys.* **2011,** *13,* 6670–6688. doi:10.1039/c0cp02984j
56. Stauffer, W.; Sheng, H.; Lim, H. N. *Sci. Rep.* **2018,** *8,* 15764. doi:10.1038/s41598-018-33592-8
57. Moser, B.; Hochreiter, B.; Herbst, R.; Schmid, J. A. *Biotechnol. J.* **2017,** *12,* 1600332. doi:10.1002/biot.201600332
58. Zinchuk, V.; Wu, Y.; Grossenbacher-Zinchuk, O. *Sci. Rep.* **2013,** *3,* 1365. doi:10.1038/srep01365
59. Llanses Martinez, M.; Rainero, E. *Essays Biochem.* **2019,** No. EBC20190014. doi:10.1042/ebc20190014
60. Furusawa, K.; Takasugi, T.; Chiu, Y.-W.; Hori, Y.; Tomita, T.; Fukuda, M.; Hisanaga, S.-i. *J. Biol. Chem.* **2019,** *294,* 10886–10899. doi:10.1074/jbc.ra118.005385
61. Yordanov, T. E.; Hipolito, V. E. B.; Liebscher, G.; Vogel, G. F.; Stasyk, T.; Herrmann, C.; Geley, S.; Teis, D.; Botelho, R. J.; Hess, M. W.; Huber, L. A. *Traffic* **2019,** *20,* 674–696. doi:10.1111/tra.12679
62. Palm, W.; Thompson, C. B. *Nature* **2017,** *546,* 234–242. doi:10.1038/nature22379
63. Gilleron, J.; Gerdes, J. M.; Zeigerer, A. *Traffic* **2019,** *20,* 552–570. doi:10.1111/tra.12670
64. *Gaussian 09,* Revision B.01; Gaussian Inc.: Wallingford, CT, U.S.A., 2009.
65. Raitz, I.; de Souza Filho, R. Y.; de Andrade, L. P.; Correa, J. R.; Neto, B. A. D.; Pilli, R. A. *ACS Omega* **2017,** *2,* 3774–3784. doi:10.1021/acsomega.7b00416

BEILSTEIN JOURNAL OF ORGANIC CHEMISTRY

Emission solvatochromic, solid-state and aggregation-induced emissive α-pyrones and emission-tuneable 1*H*-pyridines by Michael addition–cyclocondensation sequences

Natascha Breuer[1], Irina Gruber[2], Christoph Janiak[2] and Thomas J. J. Müller[*1]

Full Research Paper

Open Access

Address:
[1]Heinrich-Heine Universität Düsseldorf, Institut für Organische Chemie und Makromolekulare Chemie, Universitätsstraße 1, D-40225 Düsseldorf, Germany and [2]Heinrich-Heine Universität Düsseldorf, Institut für Anorganische Chemie und Strukturchemie, Universitätsstraße 1, D-40225 Düsseldorf, Germany

Email:
Thomas J. J. Müller[*] - ThomasJJ.Mueller@uni-duesseldorf.de

* Corresponding author

Keywords:
cyclocondensation; DFT calculations; fluorescence; heterocycles; 1*H*-pyridines; α-pyrones

Beilstein J. Org. Chem. **2019,** *15,* 2684–2703.
doi:10.3762/bjoc.15.262

Received: 16 July 2019
Accepted: 24 October 2019
Published: 12 November 2019

This article is part of the thematic issue "Dyes in modern organic chemistry".

Guest Editor: H. Ihmels

Abstract

Starting from substituted alkynones, α-pyrones and/or 1*H*-pyridines were generated in a Michael addition–cyclocondensation with ethyl cyanoacetate. The peculiar product formation depends on the reaction conditions as well as on the electronic substitution pattern of the alkynone. While electron-donating groups furnish α-pyrones as main products, electron-withdrawing groups predominantly give the corresponding 1*H*-pyridines. Both heterocycle classes fluoresce in solution and in the solid state. In particular, dimethylamino-substituted α-pyrones, as donor–acceptor systems, display remarkable photophysical properties, such as strongly red-shifted absorption and emission maxima with daylight fluorescence and fluorescence quantum yields up to 99% in solution and around 11% in the solid state, as well as pronounced emission solvatochromism. Also a donor-substituted α-pyrone shows pronounced aggregation-induced emission enhancement.

Introduction

A high sensitivity and precise tuneability of fluorescence colors are prerequisites for the application of fluorescent substances in chemistry, medicine and materials science [1]. With this respect emissive small molecules [2], fluorescent proteins [3], and quantum dots have received considerable attention and remarkable progress in their synthesis and photophysics has been achieved [4]. Small molecule organic fluorophores are particularly advantageous due to the potential of a tailored fine-tuning of their photophysical properties through synthetic modifications [5]. Based on their structural features, functionalized organic chromophores, containing N-, O- or S-atoms, are increasingly used in OLEDs [6-10] and LCDs [11-13] of mobile

phones [14]. Fluorescent compounds often intensively emit in solution but only weakly or not in the solid state [15]. Dyes which fluoresce both in the solid state and in solution are still relatively rare, due to the fact that often molecular aggregation in the solid state causes fluorescence quenching [16].

In recent years, we have coined diversity-oriented syntheses of functional chromophores by multicomponent strategies [17,18], opening accesses to substance libraries for systematic studies of structure–property relationships on fluorophores [19], in particular on aggregation-induced emissive polar dyes [20]. Conceptually, many of these consecutive multicomponent syntheses rely on transition-metal-catalyzed heterocyclic syntheses [21]. By virtue of catalytic generation of alkynones [22] we have recently disclosed consecutive alkynylation–Michael addition–cyclocondensation (AMAC) multicomponent syntheses of α-pyrones [23].

While most α-pyrones neither fluoresce in solution nor in the solid state specific substitution patterns have been identified for fluorophore design for this heterocyclic family. Tominaga and co-workers synthesized a series of α-pyrone derivatives with emission maxima between 400 and 675 nm in the solid state and between 486 and 542 nm in chloroform [16,24-26], including fluorescence quantum yields as high as 95% in solution and 58% in the solid state [16,24]. While these fluorophores were synthesized by cyclocondensation with ketene dithioacetals and substituted acetophenones other cyano-containing derivatives became accessible by desymmetrizing cyclocondensation of 1,2-diaroylacetylenes with ethyl cyanoacetate [27], similar to related studies with dialkyl malonates [28]. Here, we report on effects of base and temperature on Michael addition–cyclocondensation sequences in the formation of α-pyrones and/or 1*H*-pyridines starting from diversely substituted alkynones and cyanoethylacetate. This bifurcating domino process furnishes small chromophore libraries which were characterized by photophysical studies (absorption and emission spectroscopy) and the studies on the electronic structure were accompanied by TD-DFT calculations for assigning the dominant longest-wavelength absorption bands.

Results and Discussion

Synthesis and tentative mechanism

Recently, we reported a straightforward access to α-pyrones through a consecutive alkynylation–Michael addition–cyclocondensation (AMAC) multicomponent synthesis [23]. The reaction can be rationalized by a Sonogashira coupling between an acid chloride and a terminal alkyne furnishing an alkynone, which is transformed without isolation by addition of dialkyl malonates in a Michael addition–cyclocondensation to form α-pyrones (Scheme 1).

With this sequence in hand, we envisioned the variation of CH-acidic esters to generate differently 3-substituted α-pyrones. For introducing a cyano substituent we employed benzoyl chloride (**1a**), phenylacetylene (**2a**), and ethyl cyanoacetate (**4**) within the AMAC sequence (Scheme 2). Surprisingly, the desired α-pyrone was not isolated, but two other compounds

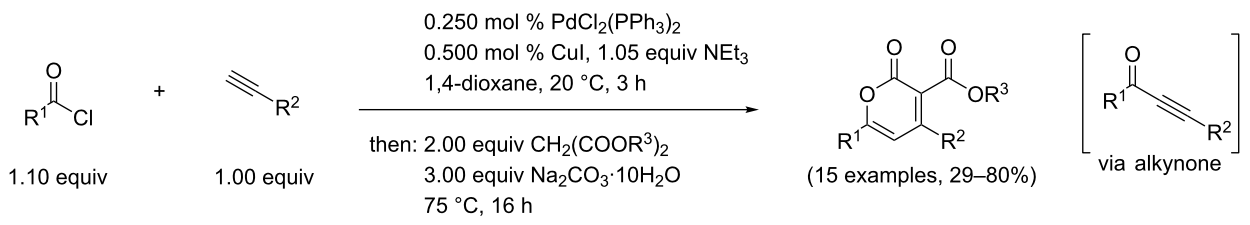

Scheme 1: Consecutive three-component alkynylation–Michael addition–cyclocondensation (AMAC) synthesis of α-pyrones from acid chlorides, terminal alkynes and dialkyl malonates.

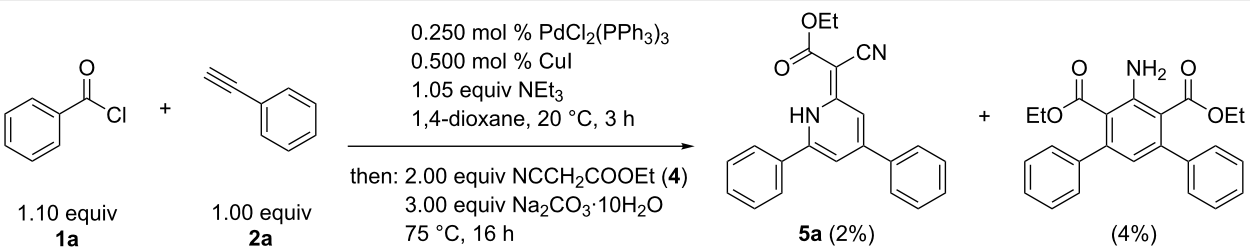

Scheme 2: Consecutive pseudo-four-component alkynylation–Michael addition–cyclocondensation (AMAC) synthesis of 1*H*-pyridines **5a** and an aniline derivative.

were detected. On the one hand a 1*H*-pyridine derivative **5a** (2% yield) and on the other hand an aniline derivative with two ester groups (4% yield). Both compounds indicate that two molecules of ethyl cyanoacetate (**4**) were incorporated in the final structure.

With an increased amount of ethyl cyanoacetate the yield of both products could be increased. By the addition of ethanol as a cosolvent in the second step of the sequence, 1*H*-pyridine **5a** could be isolated in 30% yield, while the aniline derivative was not formed (Scheme 3).

There are only a few known methods for the synthesis of this kind of 1*H*-pyridines. In a cyclocondensation, starting from 1,3-dicarbonyl compounds, Elnagdi and co-workers synthesized 1*H*-pyridines with an additional cyano substituent in the 3-position [29]. Most syntheses generating 1*H*-pyridines make use of ethyl cyanoactate as a starting material. It can react with itself and forms a dimer by selfcondensation, catalyzed by transition metals [30,31].

Intrigued by the unusual pseudo-four-component AMAC synthesis we investigated the reaction conditions of the terminal Michael addition–cyclocondensation step starting from alkynone **3a**. By varying the amount of the base we could observe the formation of 1*H*-pyridine **5a**, but also of α-pyrone **6a** (Scheme 4, Table 1), similarly to the reaction of compound **4** with 1,2-diaroylacetylenes [28].

Table 1: Optimization of the cyclization step of 1,5-diacyl-5-hydroxypyrazoline **5b**.[a]

Entry	Base (equiv)	Compound **5a** (yield)[b]	Compound **6a** (yield)[b]
1	$Na_2CO_3·10H_2O$ (0.80)	20%	50%
2	$Na_2CO_3·10H_2O$ (1.0)	8%	64%
3	$Na_2CO_3·10H_2O$ (1.5)	32%	–
4	$Na_2CO_3·10H_2O$ (2.0)	26%	–
5	Na_2CO_3 (0.80)	3%	41%
6[c]	Na_2CO_3 (0.80)	22%	52%
7[b]	Na_2CO_3 (1.4)	9%	66%

[a]All reactions were carried out on a 0.500 mmol scale (c_0(**3a**) = 0.50 M, c_0(**4**) = 2.0 M; [b]all yields refer to isolated and purified products; [c]additional water (5.6 equiv).

With either 0.8 or 1.0 equiv of $Na_2CO_3·10H_2O$ α-pyrone **6a** is formed as the main product (50–64%), while 1*H*-pyridine **5a** can also be isolated in around 15% yield (Table 1, entries 1 and 2). By increasing the amount of $Na_2CO_3·10H_2O$, exclusively 1*H*-pyridine **5a** can be isolated in low yield (Table 1, entries 3 and 4). Using anhydrous sodium carbonate α-pyrone **6a** is again formed as the main product in 41% yield, but the yield of 1*H*-pyridine **5a** drops to 3% (Table 1, entry 5). By the addition of water, the yield of **6a** could be increased (Table 1, entries 6 and 7).

Next we evaluated the use of a mixture of two bases, sodium carbonate and sodium acetate, and water (Table 2). With

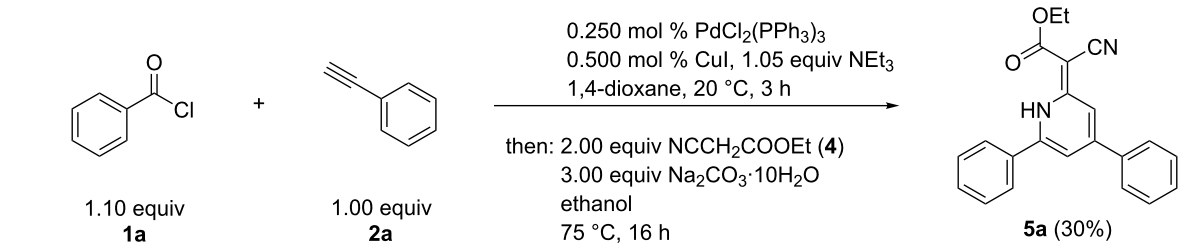

Scheme 3: Consecutive pseudo-four-component alkynylation–Michael addition–cyclocondensation (AMAC) synthesis of 1*H*-pyridines **5a** from acid chlorides **1**, terminal alkynes **2** and ethyl cyanoacetate (**4**).

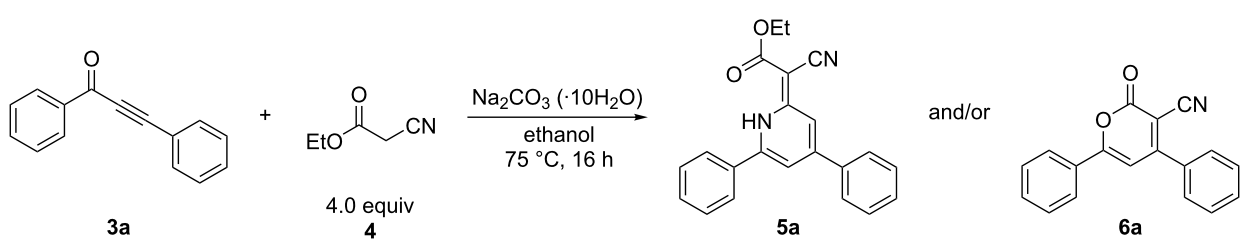

Scheme 4: Model system for the optimization of the Michael addition–cyclocondensation reaction step to 1*H*-pyridine **5a** or/and α-pyrone **6a**.

Table 2: Optimization of the formation of 1*H*-pyridine **5a** or/and α-pyrone **6a** in the Michael addition–cyclocondensation reaction with Na_2CO_3, NaOAc and water.[a]

Entry	Na_2CO_3 [equiv]	NaOAc [equiv]	H_2O [equiv]	Compound **5a** (yield)[b]	Compound **6a** (yield)[b]
1	0.80	0.60	5.6.	56%	–
2[c]	0.80	0.60	5.6	26%	–
3[d]	0.80	0.60	5.6	56%	–
4	0.80	0.60	–	44%	–
5	–	0.60	–	26%	28%
6	–	0.60	5.6	23%	–
7	0.80	0.60	2.8	40%	–
8	0.80	0.60	8.4	40%	20%
9	0.80	0.60	11	38%	28%
10	1.0	0.60	5.6	45%	–
11	0.80	0.80	5.6	43%	–

[a]All reactions were carried out on a 0.500 mmol scale (c_0(**3a**) = 0.50 M, c_0(**4**) = 2.0 M; [b]all yields refer to isolated and purified products; [c]c_0(**4**) = 1.0 M; [d]additional 4.0 equiv of ethyl cyanoacetate (**4**) after 2 h.

0.80 equiv of sodium carbonate, 0.60 equiv of sodium acetate and 5.6 equiv of water 1*H*-pyridine **5a** could be isolated in 56% yield. Decreasing the amount of ethyl cyanoacetate (**4**) the yields drops (Table 2, entry 2), however, increasing the amount of substrate **4** does not improve the yield (Table 2, entry 3). The exclusion of water only causes a decrease in yield (Table 2, entry 4). With sodium acetate as the only base, both 1*H*-pyridine **5a** and α-pyrone **6a** are formed in ca. 25% yield each (Table 2, entry 5). Sodium acetate with additional water gives 1*H*-pyridine **5a** in 23% yield (Table 2, entry 6). It seems to be important that both bases and water are present, but neither a reduction nor an increase of the amount of water increased the yields of 1*H*-pyridine **5a** (Table 2, entries 7–9). The increase of neither sodium carbonate (Table 2, entry 10) nor sodium acetate (Table 2, entry 11) caused an increase in yields.

Only lowering the reaction temperature to 20 °C α-pyrone **6a** was isolated as the main product in 78% yield and 1*H*-pyridine **5a** was obtained in only 7% yield (Scheme 5).

Since base(s) and reaction temperature exert a significant impact on which heterocyclic compound is formed, we also tried to change the electronic nature of the starting material. Therefore, an electron-donating substituent was introduced in the alkynone **3b** and the reaction was performed at 75 °C. To our surprise, we only could isolate α-pyrone **6b** (Scheme 6).

However, when we introduced an electron-withdrawing group 1*H*-pyridine **5b** was the only product (Scheme 7).

For elucidating whether 1*H*-pyridine **5a** is formed from α-pyrone **6a** and ethyl cyanoacetate (**4**) a reaction between α-pyrone **6a** and ethyl cyanoacetate (**4**) under the same reaction conditions as for the 1*H*-pyridine from alkynone **3a** was conducted, but only starting material could be isolated. Another option for the formation of the 1*H*-pyridine **5a** was envisioned by an in situ generation of a dimer of ethyl cyanoacetate (**4**). The dimer **7** can be synthesized by iridium catalysis [30]. With

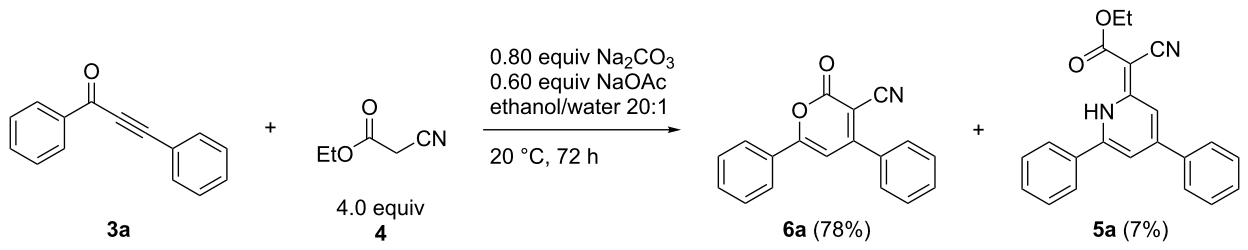

Scheme 5: Formation of α-pyrone **6a** and 1*H*-pyridine **5a** at 20 °C.

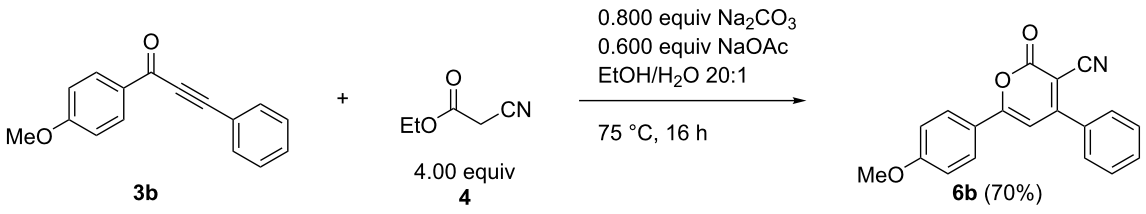

Scheme 6: Formation of α-pyrone **6a** starting from alkynone **3b** having an electron-donating substituent.

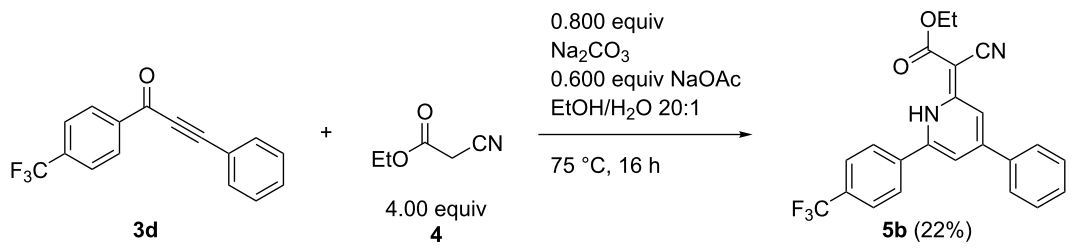

Scheme 7: Formation of 1*H*-pyridine **5b** starting from alkynone **3d** having an electron-withdrawing substituent.

dimer **7** in hand, we performed the reaction at 75 °C for 16 h, but we only could isolate 1*H*-pyridine **8a**, which still contains an ester group (Scheme 8). Therefore, the in situ formation of the dimer starting from the alkynone **3a** and ethyl cyanoacetate (**4**) was excluded for the formation of the 1*H*-pyridine **5a**.

While the in situ generation of dimer **7** does not happen during the formation of 1*H*-pyridine **5a**, we examined the reaction between ethyl cyanoacetate (**4**) and the optimized base system by adding alkynone **3a** to the reaction after different times (Table 3).

In the first attempt, alkynone **3a** was added after 2 h. 1*H*-Pyridine **5a** was isolated in 53% yield (Table 3, entry 1), indicating that the time of addition of the alkynone is not relevant within the first two hours of the reaction. However, if alkynone **3a** was added after 6 h α-pyrone **6a** was the main product and 1*H*-pyridine **5a** could only be isolated in 5% yield (Table 3, entry 2). Upon the addition of alkynone **3a** after 24 h, both 1*H*-pyridine **5a** and α-pyrone **6a** were isolated in only around 3% yield. This finding supports that within the first two hours ethyl cyanoacetate (**4**) is consumed and thereafter the ethyl cyanoacetate concentration is just too low for the formation of 1*H*–pyridine

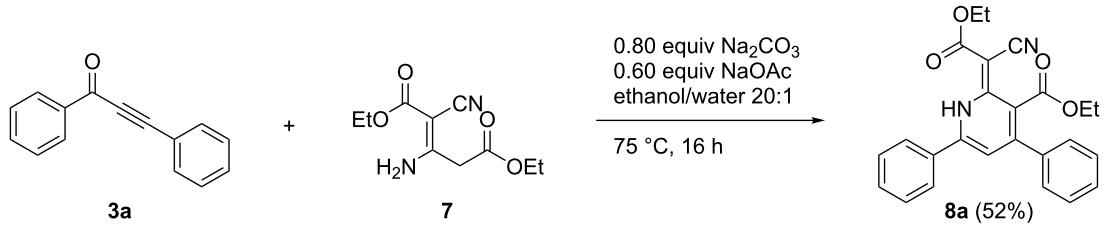

Scheme 8: Formation of 1*H*-pyridine **8a** by Michael addition–cyclocondensation reaction.

Table 3: Influence of the reaction time on the self-condensation of ethyl cyanoacetate (**4**) in the presence of the optimized base system.[a]

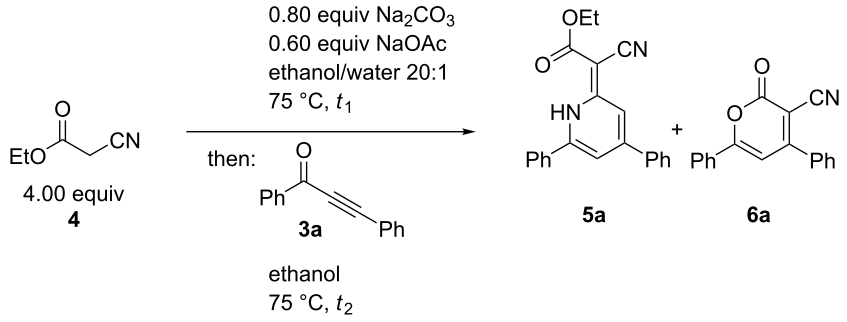

Entry	t_1	t_2	Compound **5a** (yield)[b]	Compound **6a** (yield)[b]
1	2 h	16 h	53%	–
2	6 h	16 h	5%	46%
3	24 h	16 h	3%	2%

[a]All reactions were carried out on a 0.500 mmol scale (c_0(**3a**) = 0.50 M, c_0(**4**) = 2.0 M; [b]all yields refer to isolated and purified products.

5a, therefore α-pyrone **6a** is formed. At longer initial reaction times (6 and 24 h) there is no ethyl cyanoacetate (**4**) left for the formation of any product. Also, ethyl cyanoacetate (**4**) probably does not form dimer **7** because in that case under these conditions 1*H*-pyridine **8a** would have been detected.

Therefore, the tentative mechanistic rationale takes into account that the formation of 1*H*-pyridine **5a** rather proceeds via stepwise condensation of alkynone **3** with two equivalents of ethyl cyanoacetate (**4**) than by reaction with dimer **7** (Scheme 9).

First, a molecule of ethyl cyanoacetate (**4**) attacks the alkynone **3a** in a Michael addition. A second molecule **4** then attacks the cyano substituent and an imine is formed. The ester substituent of the initially reacted more electrophilic ethyl cyanoacetate (**4**) is presumably cleaved by a base-mediated acyl cleavage furnishing directly 1*H*-pyridine **5a** after protonation.

For examining the influence of the electronic nature of the alkynone **3** on the product formation, a range of differently substituted alkynones **3** (for experimental details on their preparation, see chapters 2.1 and 2.2 in Supporting Information File 1) bearing electron-donating and/or electron-withdrawing substituents were synthesized and employed in the cyclocondensation step under the optimized reaction conditions [32-34]. Alkynones **3b–e** with only one electron-donating substituent furnish the corresponding α-pyrones **6b–e**, while the alkynone with a single electron-withdrawing substituent furnishes 1*H*-pyridines **5b–e**. Interestingly, the position of substitution on the alkynone does not affect the outcome (Table 4, entries 2 and 6). Also, for alkynone **3j** bearing an electron-donating substituent on either aryl ring, α-pyrone **6f** is formed likewise (Table 4, entry 10). For electronically unsymmetrically substituted alkynones **3** the product formation depends rather on the strength of the employed electron-donating group. Whereas the *p*-anisyl substituent leads to the formation of 1*H*-pyridine (Table 4, entries 11 and 12), the *N*,*N*-dimethylaminophenyl substituent furnishes α-pyrone **6g** (Table 4, entry 13).

For synthesizing 1*H*-pyridine derivatives **8** with an electron-donating group we employed the isolated dimer **7** and were able to isolate 1*H*-pyridines **8** in 52 and 34% yield (Scheme 10).

Crystal structure of 1*H*-pyridine **5a**

The structure of 1*H*-pyridines **5** was further corroborated by a single crystal X-ray structure determination of compound **5a** (Figure 1) [35]. In the single crystal the carboxyl ester group is oriented to the N–H and via a hydrogen bond. Solid-state torsional/dihedral angles between the 4- and 6-positioned aryl rings differ especially for the 6-positioned phenyl ring with 27° in the X-ray structure and 38° from calculation (for comparison to the DFT calculated ground state structure of 1*H*-pyridine **5a**, see chapter 12.3 in Supporting Information File 1). This is probably due to packing constraints from the involvement of the 6-phenyl ring in C-H···N [36-39] and C-H···π [40-49] interactions (Figure 2, for details, see Supporting Information File 1). It is noteworthy to mention that there are no significant π···π interactions in the solid-state structure of **5a** (for details, see Supporting Information File 1) [50-57].

Photophysical properties

Photophysical properties of 1*H*-pyridines **5** and **8**

1*H*-Pyridine derivatives **5** are yellow or orange compounds under daylight (Figure 3, top) and fluoresce in solution (Figure 3, center) and in the solid state (Figure 3, bottom).

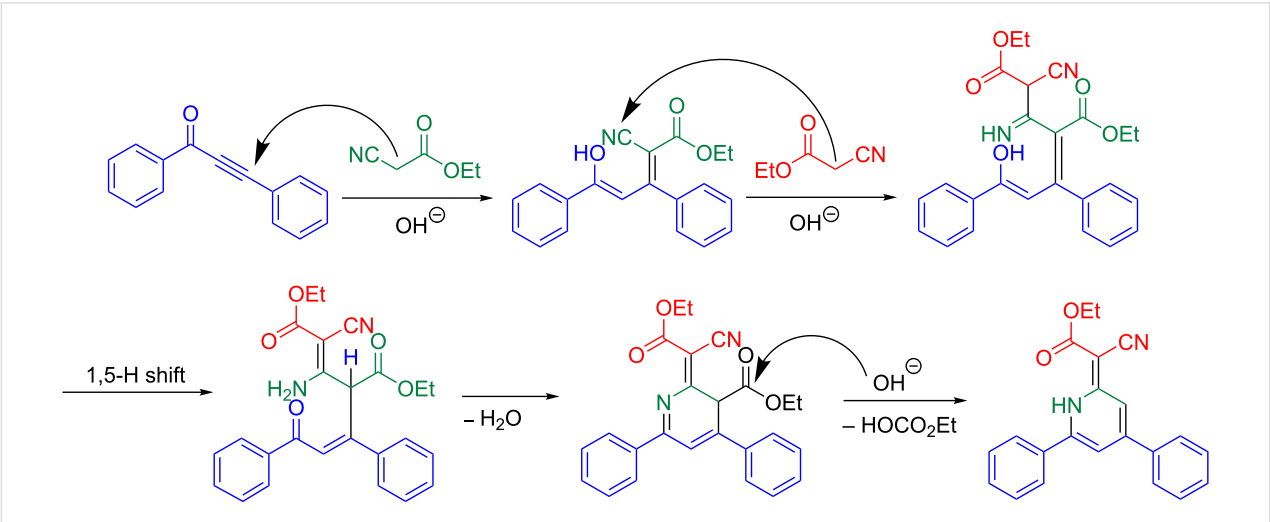

Scheme 9: Mechanistic rationale for the formation of the 1*H*-pyridine **5a**.

Table 4: Michael addition–cyclocondensation synthesis of 1*H*-pyridine **5** or α-pyrone **6**.

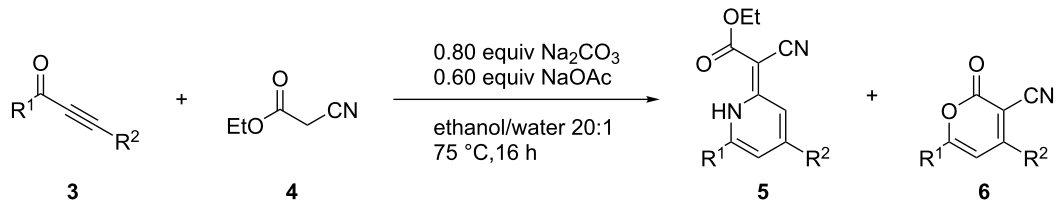

3 **4** **5** **6**

Entry	Alkynone **3**	1*H*-Pyridine **5**[a]	α-Pyrone **6**[a]
1	**3a** (R^1 = Ph, R^2 = Ph)	**5a** (R^1 = Ph, R^2 = Ph, 56%)	–
2	**3b** (R^1 = *p*-$MeOC_6H_4$, R^2 = Ph)	–	**6b** (R^1 = *p*-$MeOC_6H_4$, R^2 = Ph; 70%)
3	**3c** (R^1 = *p*-$Me_2NC_6H_4$, R^2 = Ph)	–	**6c** (R^1 = *p*-$Me_2NC_6H_4$, R^2 = Ph, 12%)
4	**3d** (R^1 = *p*-$F_3CC_6H_4$, R^2 = Ph)	**5b** (R^1 = *p*-$F_3CC_6H_4$, R^2 = Ph, 22%)	–
5	**3e** (R^1 = *p*-NCC_6H_4, R^2 = Ph)	**5c** (R^1 = *p*-NCC_6H_4, R^2 = Ph, 20%)	–
6	**3f** (R^1 = Ph, R^2 = *p*-$MeOC_6H_4$)	–	**6d** (R^1 = Ph, R^2 = *p*-$MeOC_6H_4$, 82%)
7	**3g** (R^1 = Ph, R^2 = *p*-$Me_2NC_6H_4$)	–	**6e** (R^1 = Ph, R^2 = *p*-$Me_2NC_6H_4$, 62%)
8	**3h** (R^1 = Ph, R^2 = *p*-$F_3CC_6H_4$)	**5d** (R^1 = Ph, R^2 = *p*-$F_3CC_6H_4$, 25%)	–
9	**3i** (R^1 = Ph, R^2 = *p*-NCC_6H_4)	**5e** (R^1 = Ph, R^2 = *p*-NCC_6H_4, 2%)	–
10	**3j** (R^1 = *p*-$MeOC_6H_4$, R^2 = *p*-$MeOC_6H_4$)	–	**6f** (R^1 = *p*-$MeOC_6H_4$, R^2 = *p*-$MeOC_6H_4$, 45%)
11	**3k** (R^1 = *p*-$MeOC_6H_4$, R^2 = *p*-$F_3CC_6H_4$)	**5f** (R^1 = *p*-$MeOC_6H_4$, R^2 = *p*-$F_3CC_6H_4$, 37%)	–
12	**3l** (R^1 = *p*-$F_3CC_6H_4$, R^2 = *p*-$MeOC_6H_4$)	**5g** (R^1 = *p*-$F_3CC_6H_4$, R^2 = *p*-$MeOC_6H_4$,, 40%)	–
13	**3m** (R^1 = *p*-$F_3CC_6H_4$, R^2 = *p*-$Me_2NC_6H_4$)	–	**6g** (R^1 = *p*-$F_3CC_6H_4$, R^2 = *p*-$Me_2NC_6H_4$, 71%)
14	**3n** (R^1 = 2-thienyl, R^2 = Ph)	**5h** (R^1 = 2-thienyl, R^2 = Ph, 51%)	–

[a]All yields refer to isolated and purified products.

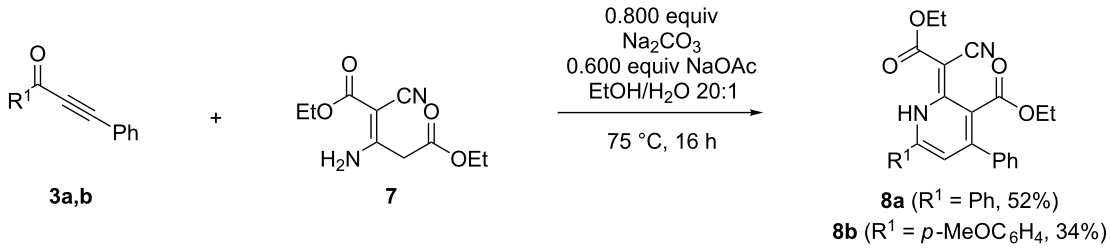

3a,b **7**

8a (R^1 = Ph, 52%)
8b (R^1 = *p*-$MeOC_6H_4$, 34%)

Scheme 10: Formation of 1*H*-pyridine **8a** from alkynone **3b** and dimer **7**.

Therefore, the photophysical properties were studied by absorption and emission spectroscopy (Figure 4, Table 5).

All compounds show three absorption maxima at around 275, 320 and 430 nm, where the longest wavelength absorption maxima exhibit extinction coefficients of around 9500 $L \cdot mol^{-1} \cdot cm^{-1}$ (Table 5). Upon introducing electron-withdrawing substituents on the aryl rings the longest wavelength maxima shift bathochromically (Table 5, entries 2–5). The redshift qualitatively corresponds with the strength of the acceptor group (Table 5, entries 3 and 5). However, as can be seen from entries 2–5 (Table 5), the placement of the acceptor group at the 4 or 6-aryl substituent does not affect the absorption energies. This situation changes to a minor extent upon placing an additional donor substituent at the remaining phenyl substituent (Table 5, entries 6 and 7). A thienyl substituent instead of a phenyl substituent causes a redshift of the longest wavelength absorption maximum (Table 5, entries 1 and 8).

Upon excitation at the longest wavelength absorption band dichloromethane solutions of all compounds **5** fluoresce with emission maxima at around 565 nm (Table 5, entries 2–5). Upon the introduction of electron-withdrawing substituents the maxima are shifted bathochromically, similarly as the absorp-

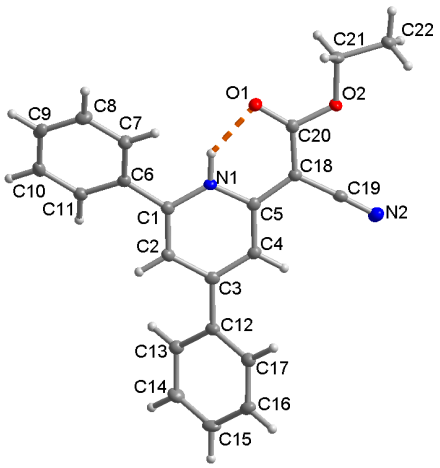

Figure 1: Molecular structure of 1*H*-pyridine **5a** (50% thermal ellipsoids), showing the intramolecular N–H···O bond as dashed orange line. H-bond details N1–H 0.90(2) Å, H···O1 1.87(2) Å, N1···O2 2.624(2) Å, O1–H···O2 140(1)°.

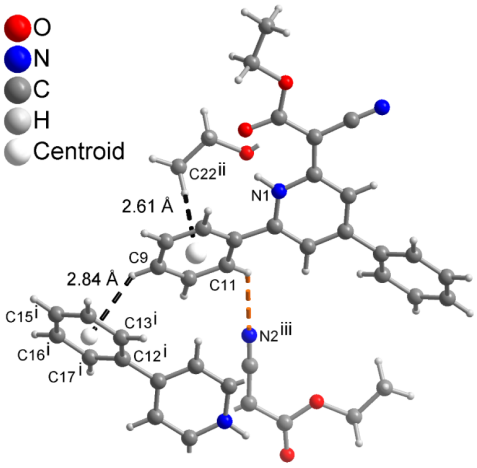

Figure 2: Supramolecular C–H···N [36-39] and C–H···π [40-49] interactions around the 6-positioned phenyl ring in **5a**. Details of C–H···N bond (dashed orange line) C11–H 0.95 Å, H···N2 2.61 Å, C11···N2 3.263(2) Å, C11–H···N2 127°. Symmetry transformations are i = 1−x, 1−y, 1−z; ii = x, 3/2−y, −1/2+z, iii = 1−x, −1/2+y, −1/2−z.

tion maxima, and the shift is qualitatively correlated with the acceptor strength. In comparison, the introduction of another electron-donating substituent does not significantly change the luminescence characteristics (Table 5, entries 2, 4, 6 and 7). The Stokes shifts fall in a range between 5000 and 6100 cm^{-1} and the fluorescence quantum yields of the 1*H*-pyridines **5** account between 1 and 3%.

Besides solution fluorescence all 1*H*-pyridines **5** also luminesce in the solid state (Figure 3, bottom). The emission maxima of two selected 1*H*-pyridines **5** were determined

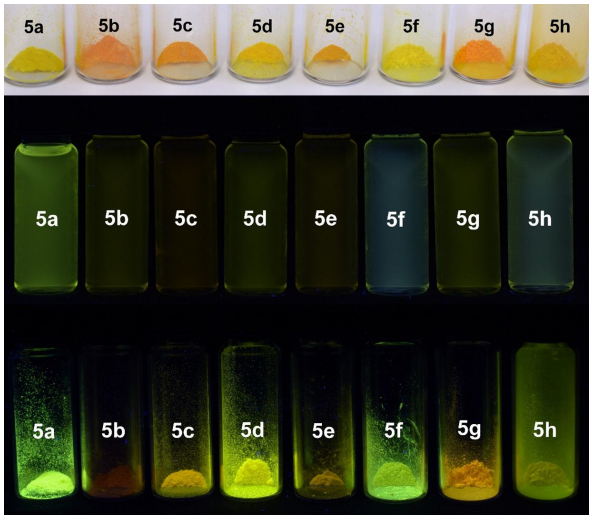

Figure 3: 1*H*-Pyridine derivatives **5** as solids under daylight (top), under UV light (λ_{exc} = 365 nm, c(**5**) = 10^{-4} M) in dichloromethane solution (center), and under UV light (λ_{exc} = 365 nm) in the solid state (bottom).

(Figure 5, Table 6), showing a similar behavior in the solid state as in solution. The emission maximum of the unsubstituted 1*H*-pyridine **5a** appears at 540 nm, while the CF_3-substituted 1*H*-pyridine **5b** emits bathochromically shifted at 604 nm.

In addition, both ester-substituted 1*H*-pyridines **8a** and **8b** also possess interesting photophysical properties (Figure 6, Table 7). Under daylight they are yellow and they fluoresce in solution and in the solid state. The three absorption maxima are found at around 270, 315 and 415 nm. The methoxy group in the spectrum of compound **8b** only has a minor influence on the absorption maximum, however, slightly more on the emission maximum. The fluorescence quantum yields Φ_f of both compounds are lower than 1%.

With the addition of the second ester group in the 3-position to 1*H*-pyridine **8a** the fluorescence in the solid state appears to shift to blue. If the phenyl substituent in the 4-position bears an additional methoxy substituent the fluorescence of the 1*H*-pyridine **8b** appears yellow again (Figure 7).

Photophysical properties of α-pyrones 6

All α-pyrone derivatives **6** are yellow or red under daylight (Figure 8, top) and some of them fluoresce in solution (Figure 8, center) and in the solid state (Figure 8, bottom). Therefore, the photophysical properties were studied by absorption and emission spectroscopy (Figure 9, Table 8).

All compounds show 2–4 absorption maxima and the shortest wavelength maxima appear at around 255 nm. The unsubsti-

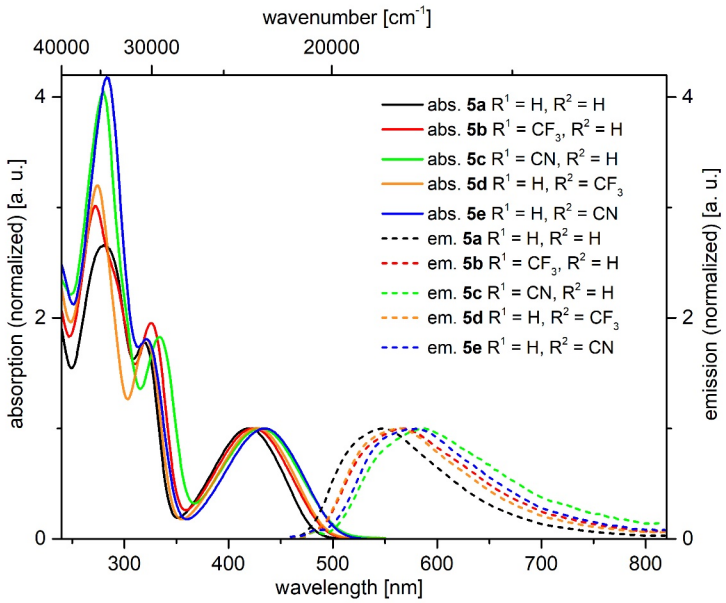

Figure 4: Selected normalized absorption (solid lines) and emission (dashed lines) spectra of 1*H*-pyridines **5a–e** (recorded in dichloromethane at *T* = 298 K).

Table 5: Photophysical properties of 1*H*-pyridines **5**.

Entry	Compound	R^1	R^2	$\lambda_{max,abs}$ [nm][a] (ε [L·mol^{-1}·cm^{-1}])	$\lambda_{max,em}$ [nm][b] (Φ_f)[c]	Stokes shift $\Delta\tilde{\nu}$ [cm^{-1}]
1	**5a**	Ph	Ph	281 (26100), 319 (17400), 418 (9800)	545 (0.02)	5600
2	**5b**	*p*-$F_3CC_6H_4$	Ph	272 (27000), 326 (17500), 424 (8900)	565 (0.01)	5600
3	**5c**	*p*-NCC_6H_4	Ph	280 (37600), 333 (17300), 431 (9500)	585 (0.01)	6100
4	**5d**	Ph	*p*-$F_3CC_6H_4$	274 (32000), 321 (18100), 428 (10000)	565 (0.01)	5700
5	**5e**	Ph	*p*-NCC_6H_4	283 (36000), 322 (15600), 434 (8600)	579 (0.01)	5800
6	**5f**	*p*-$MeOC_6H_4$	*p*-$F_3CC_6H_4$	261 (26200), 306 (28400), 429 (10400)	557 (0.02)	5400
7	**5g**	*p*-$F_3CC_6H_4$	*p*-$MeOC_6H_4$	260 (20300), 324 (43800), 420 (10000)	562 (0.02)	6000
8	**5h**	2-thienyl	Ph	273 (21800), 308 (26700), 433 (9200)	560 (0.03)	5200

[a]Recorded in dichloromethane, *T* = 293 K, *c*(**5**) = 10^{-6} M; [b]recorded in dichloromethane, *T* = 293 K, *c*(**5**) = 10^{-7} M; [c]fluorescence quantum yields were determined relative to coumarin153 (Φ_f = 0.54) as a standard in ethanol [58].

tuted α-pyrone **6a** exhibits its longest wavelength maximum at 381 nm (Table 8, entry 1). A *p*-methoxyphenyl substituent in the 6-position causes a bathochromic shift (Table 8, entry 2), whereas the same substituent in 4-position leads to a hypsochromic shift (Table 8, entry 4). Interestingly, *p*-methoxyphenyl substituents at positions 4 and 6 split the longest absorption band into two maxima at 358 nm (arising from the *p*-methoxyphenyl substituent in the 4-position and at 400 nm arising from the *p*-methoxyphenyl substituent in the 6-position) (Table 8, entry 6). The introduction of a more strongly electron-donating substituent, such as *N*,*N*-dimethylaminophenyl, causes a significant bathochromic shift (Table 8, entries 3 and 5). Donor–acceptor substitution in positions 4 and 6 causes a further bathochromic shift (Table 8, entry 7).

In solution only *N*,*N*-dimethylaminophenyl-substituted derivatives fluoresce (Figure 10). While the 6-substituted α-pyrone **6c** has a fluorescence maximum at 567 nm, the one for the regioisomer **6e** is shifted bathochromically to 634 nm (Table 8, entries 3 and 5). Donor–acceptor substitution in positions 4 and 6 causes a further bathochromic shift to 673 nm (Table 8, entry 7). Most remarkably, the regioisomers **6c** and **6e** differ quite significantly with respect to their fluorescence quantum yields Φ_f. While chromophore **6e** only emits with an efficiency of 1%, the regioisomer **6c** accounts for an extraordinarily high relative quantum yield of 99%.

Furthermore, the *N*,*N*-dimethylaminophenyl-derivative **6c** shows a pronounced emission solvatochromism (Figure 11,

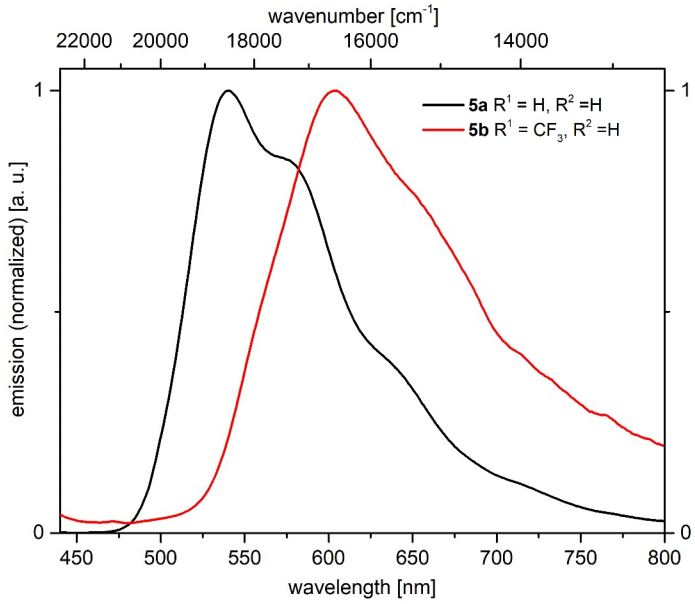

Figure 5: Selected normalized emission spectra of 1*H*-pyridine **5a** and **5b** in the solid state at T = 298 K.

Table 6: Photophysical properties of 1*H*-pyridines **5a** and **5b** in the solid state.

Compound	R^1	R^2	$\lambda_{max,em}$ [nm][a]
5a	H	H	540
5b	CF_3	H	604

[a]λ_{exc} = 420 nm.

Table 9). While the polarity effect on the absorption maximum is only minor within a range of the longest wavelength maximum between 469 and 490 nm, the emission maximum is shifted bathochromically with increasing solvent polarity in a range from green fluorescence (529 nm) in toluene to red fluorescence in DMSO (638 nm) (Figure 12). The observed positive emission solvatochromism is a consequence of a significant change in the dipole moment from the electronic ground to

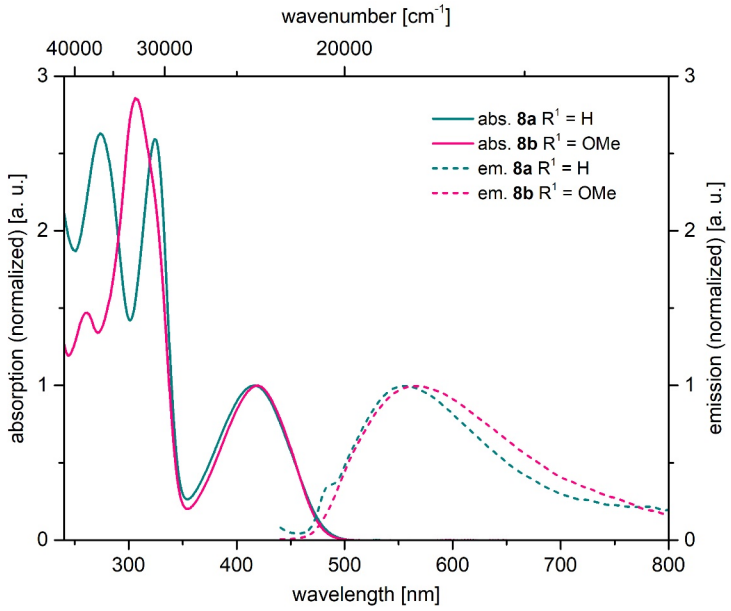

Figure 6: Selected normalized absorption (solid lines) and emission (dashed lines) spectra of 1*H*-pyridines **8a** and **8b** (recorded in dichloromethane at T = 298 K).

Table 7: Photophysical properties of 1*H*-pyridines **8**.

Compound	R^1	R^2	$\lambda_{max,abs}$ [nm][a] (ε [L·mol^{-1}·cm^{-1}])	$\lambda_{max,em}$ [nm][b] (Φ_f)[c]	Stokes shift Δ ṽ [cm^{-1}]
8a	Ph	Ph	274 (20300), 324 (20100), 417 (7700)	557 (<0.01)	6000
8b	*p*-MeOC$_6$H$_4$	Ph	261 (16200), 307 (31300), 419 (11000)	565 (<0.01)	6200

[a]Recorded in dichloromethane, T = 293 K, c(**8**) = 10^{-6} M; [b]recorded in dichloromethane, T = 293 K, c(**8**) = 10^{-7} M (λ_{exc} = 420 nm); [c]fluorescence quantum yields were determined relative to coumarin153 (Φ_f = 0.54) as a standard in ethanol [58].

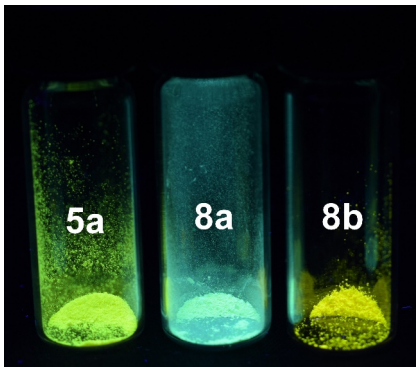

Figure 7: Solid-state luminescence of 1*H*-pyridines **5a**, **8a** and **8b** (λ_{exc} = 365 nm).

the vibrationally relaxed excited state [59]. Plotting Stokes shifts Δṽ against the orientation polarizabilities Δf of the respective solvents (Lippert plot) [60] gives a reasonable linear correlation with a moderate fit of r^2 = 0.970 (Figure 13). The orientation polarizabilities Δf were calculated according to Equation 1

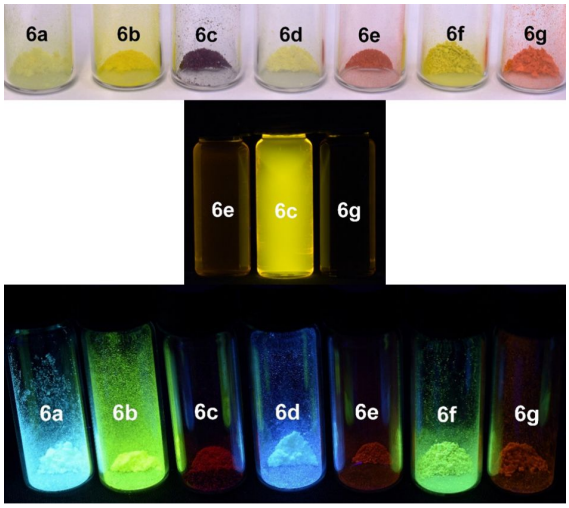

Figure 8: α-Pyrones **6** as solids under daylight (top), selected derivatives under UV light (λ_{exc} = 365 nm, c(**6**) = 10^{-4} M) in dichloromethane solution (center), and under UV light (λ_{exc} = 365 nm) in the solid state (bottom).

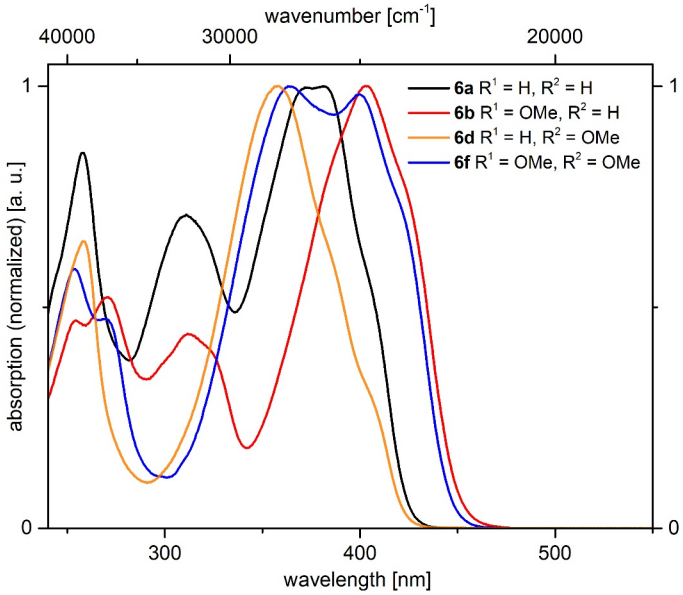

Figure 9: Selected normalized absorption spectra of α-pyrones **6a**, **6b**, **6d**, and **6e** recorded in dichloromethane at T = 298 K.

Table 8: Photophysical properties of α-pyrones **6**.

Entry	Compound	R^1	R^2	$\lambda_{max,abs}$ [nm][a] (ε [L·mol^{-1}·cm^{-1}])	$\lambda_{max,em}$ [nm][b] (Φ_f)[c]	Stokes shift $\Delta\tilde{\nu}$ [cm^{-1}]
1	**6a**	Ph	Ph	258 (15300), 311 (12800), 381 (18000)	–	–
2	**6b**	*p*-$MeOC_6H_4$	Ph	254 (10300), 271 (11500), 312 (9600), 404 (21900)	–	–
3	**6c**	*p*-$Me_2NC_6H_4$	Ph	294 (18800), 482 (47300)	567 (0.99)	3100
4	**6d**	Ph	*p*-$MeOC_6H_4$	258 (19700), 358 (30400)	–	–
5	**6e**	Ph	*p*-$Me_2NC_6H_4$	255 (25600), 289 (23300), 375 (39600), 453 (40600)	634 (0.01)	6300
6	**6f**	*p*-$MeOC_6H_4$	*p*-$MeOC_6H_4$	254 (15000), 364 (25600), 400 (25100)	–	–
7	**6g**	*p*-$F_3CC_6H_4$	*p*-$Me_2NC_6H_4$	251 (16200), 309 (13900), 372 (20200), 465 (21600)	673 (<0.01)	6600

[a]Recorded in dichloromethane, T = 293 K, c(**6**) = 10^{-6} M; [b]recorded in dichloromethane, T = 293 K, c(**6**) = 10^{-7} M (λ_{exc} = 465 nm); [c]fluorescence quantum yields were determined relative to DCM (Φ_f = 0.435) as a standard in ethanol [58].

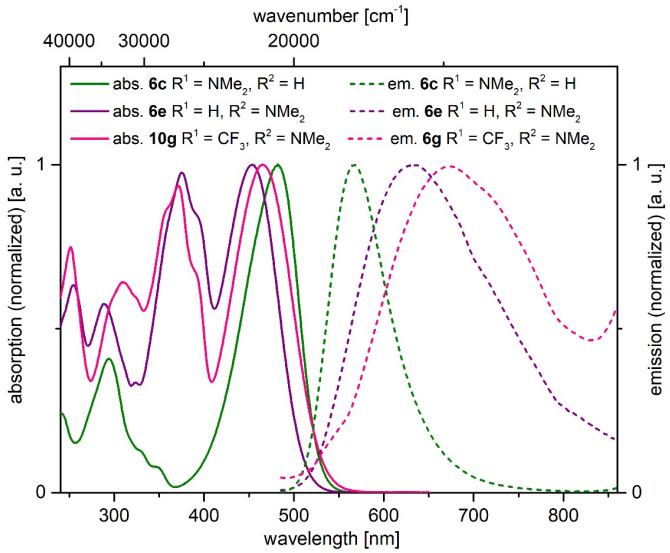

Figure 10: Selected normalized absorption (solid lines) and emission (dashed lines) spectra of α-pyrones **6c**, **6e**, and **6g** recorded in dichloromethane at T = 298 K.

Figure 11: Absorption (top) and fluorescence (bottom) of compound **6c** with variable solvent polarity (left to the right: toluene, ethyl acetate, acetone, DMF and DMSO, c(**6c**) = 10^{-4} M; λ_{exc} = 365 nm, handheld UV lamp).

$$\Delta f = \frac{\varepsilon_r - 1}{2 \cdot \varepsilon_r + 1} - \frac{n^2 - 1}{2 \cdot n^2 + 1} \quad (1)$$

where ε_r is the relative permittivity and n the optical refractive index of the respective solvent.

The change in dipole from the ground to the excited state can be calculated according to the Lippert–Mataga equation (Equation 2)

$$\tilde{\nu}_{abs} - \tilde{\nu}_{em} = \frac{2\Delta f}{4 \cdot \pi \cdot \varepsilon_0 \cdot h \cdot c \cdot a^3} \cdot (\mu_E - \mu_G)^2 + const \quad (2)$$

where $\tilde{\nu}_{abs}$ represents the absorption and $\tilde{\nu}_{em}$ the emission maxima (in m^{-1}), μ_E and μ_G are the dipole moments in the

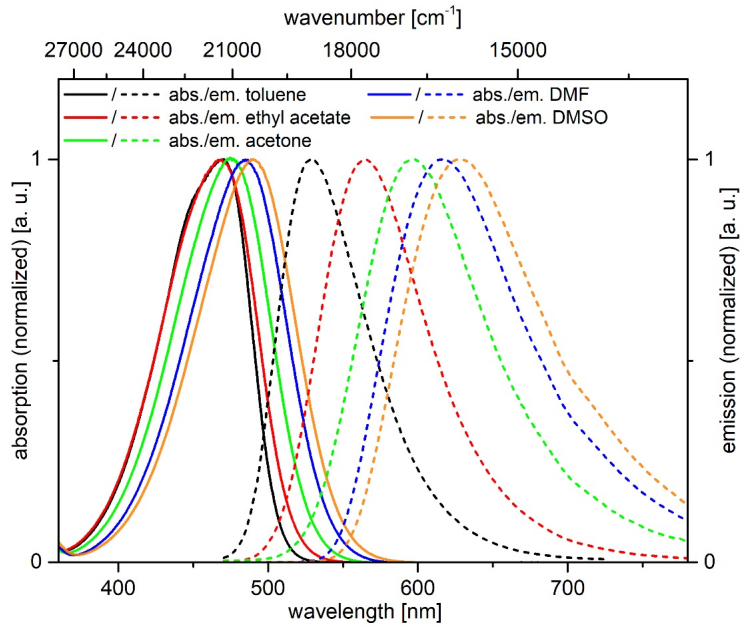

Figure 12: Absorption (solid lines) and emission (dashed lines) spectra of α-pyrone **6c** in five solvents of different polarity (recorded at T = 298 K).

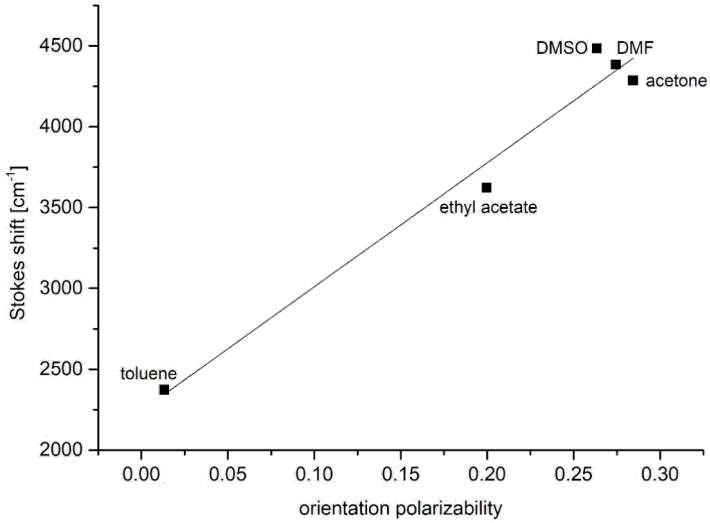

Figure 13: Lippert plot for α-pyrone **6c** (n = x, r^2 = 0.970).

excited and ground state (in C·m), ε_0 ($8.8542 \cdot 10^{-12}$ A·s/V·m) is the vacuum permittivity constant, h ($6.6256 \cdot 10^{-34}$ J·s) is the Planck's constant, c ($2.9979 \cdot 10^{10}$ cm/s) is the speed of light and a is the radius of the solvent cavity occupied by the molecules (in m). The Onsager radius a, assuming a spherical dipole to approximate the molecular volume of the molecule in solution, was estimated from the optimized ground-state structure of compound **6c** obtained by DFT calculations. With an a value of 5.46 Å, the change in dipole moment was calculated to 11.6 D ($3.87 \cdot 10^{-29}$ C·m).

All α-pyrones **6** fluoresce in the solid state (Figure 8, bottom) and for five selected α-pyrones **6** the emission maxima were determined (Figure 14, Table 9). The fluorescence maximum of unsubstituted α-pyrone **6a** lies at 499 nm and the maxima of the monomethoxy-substituted regioisomers **6b** (540 nm) and **6d** (489 nm) appear at quite different energies, similar to their corresponding absorption maxima in solution. In comparison to α-pyrone **6a** the introduction of two methoxy substituents in derivative **6f** results in a bathochromic shift to 526 nm. The solid-state emission of *N*,*N*-dimethylaminophenyl derivative **6c**

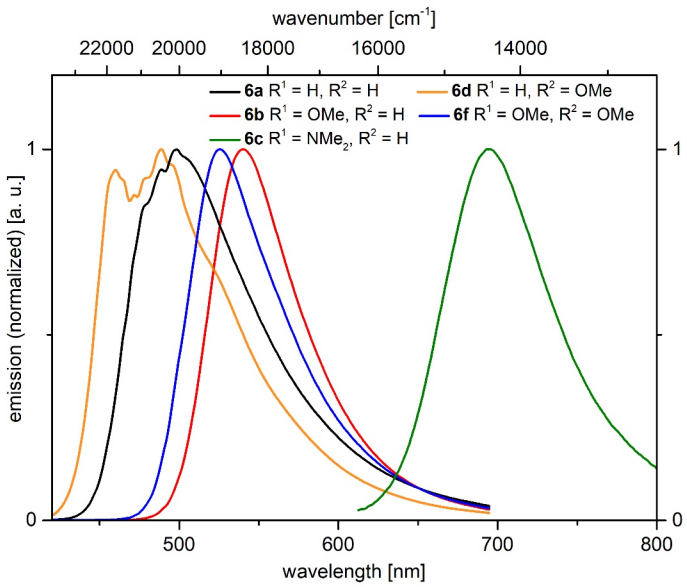

Figure 14: Normalized emission spectra of selected α-pyrones **6a–d**,**f** in the solid state at T = 298 K.

Table 9: Photophysical properties of selected α-pyrones **6** in the solid state.

Compound	R^1	R^2	$\lambda_{max,em}$ [nm][a]
6a	Ph	Ph	499
6b	*p*-$MeOC_6H_4$	Ph	540
6c	*p*-$Me_2NC_6H_4$	Ph	694[b]
6d	Ph	*p*-$MeOC_6H_4$	489
6f	*p*-$MeOC_6H_4$	*p*-$MeOC_6H_4$	526

[a]λ_{exc} = 380 nm; [b]λ_{exc} = 480 nm.

shows an enormous redshift to 694 nm. The solid-state fluorescence quantum yield Φ_f of compound **6c** was determined to 11%.

Interestingly, the α-pyrone **6e** with the *N*,*N*-dimethylaminophenyl substituent in 4-position only fluoresces weakly in solution but shows a strong fluorescence in the solid state. This finding suggests that by restricting intramolecular motion and vibration, which enables radiation-less deactivation of the excited state [61], an AIE (aggregation-induced emission) or AIEE (aggregation-induced enhanced emission), might become operative [62-64].

The AIE or AIEE effect was assessed by measuring the emission spectra of α-pyrone **6e** in THF/water at variable ratios (Figure 15). In pure THF α-pyrone **6e** displays an emission maximum at 644 nm with a relative intensity of 54. The addition of water first quenches the fluorescence and at a water/THF ratio of 80% aggregates are formed and the emission maximum is shifted to 632 nm. The maximal relative intensity of 130 is reached for a ratio of 85%, which is more intense than in pure THF, therefore, an AIEE effect occurs. Further increasing the water content slightly quenches the emission.

Computational studies

Computational studies on 1*H*-pyridines **5** and **8**

For a further elucidation of the electronic structure the geometries of the electronical ground-state structures of the 1*H*-pyridines **5** and **8** were optimized using Gaussian 09 with the B3LYP functional [65-68] and the Pople 6-311G** basis set [69], applying vacuum calculations as well as the polarizable continuum model (PCM) with dichloromethane as a solvent [70] (for details of the DFT calculations, see Supporting Information File 1). The optimized geometries were verified by frequency analyses of the local minima. The electronic absorptions of the 1*H*-pyridines **5** and **8** were calculated on the level of TDDFT theory employing the B3LYP functional and the Pople 6-311G** basis set. The calculated absorption maxima are in accordance with the experimentally determined maxima (for details, see Tables S7 and S8 in Supporting Information File 1). Most characteristically, for all 1*H*-pyridines **5** and **8** the longest wavelength maxima representing the Franck–Condon S_1 states are characterized by HOMO–LUMO transitions and S_2 states are represented by HOMO–LUMO+1 transitions.

The computed Kohn–Sham frontier molecular orbitals show that the coefficient density of the HOMO of the 1*H*-pyridines **5f** and **5g** with an electron-withdrawing and an electron-donating

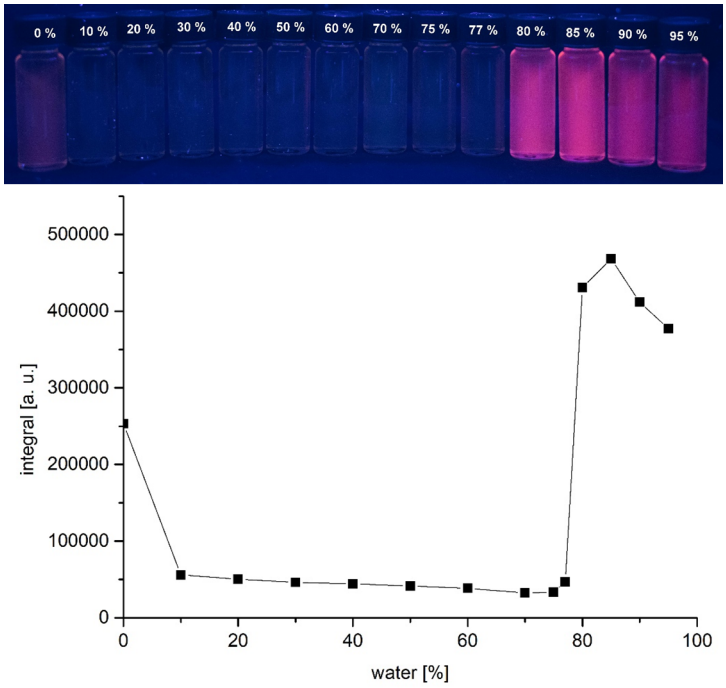

Figure 15: Fluorescence of compound **6e** in different THF/water fractions (top, λ_{exc} = 365 nm, handheld UV lamp) and I/I_0 vs %H_2O of α-pyrone **6e** in THF/water mixtures containing different water fractions (bottom, recorded at T = 298 K).

substituent is located on the 1*H*-pyridine core, the ester and cyano substituents and also on the electron-rich aryl substituent. For the LUMO, the coefficient density is spread over the whole scaffold (Figure 16).

Computational studies on α-pyrones 6

For further elucidation of the electronic structure the geometries of the electronical ground-state structures of the α-pyrones **6** were optimized using Gaussian 09 with the B3LYP functional [65-68] and the Pople 6-311G** basis set [69], applying vacuum calculations as well as the polarizable continuum model (PCM) with dichloromethane as a solvent [70] (for details on the DFT calculations, see Supporting Information File 1). The optimized geometries were verified by frequency analyses of the local minima. The electronic absorptions of the α-pyrones **6** were calculated on the level of TDDFT theory em-

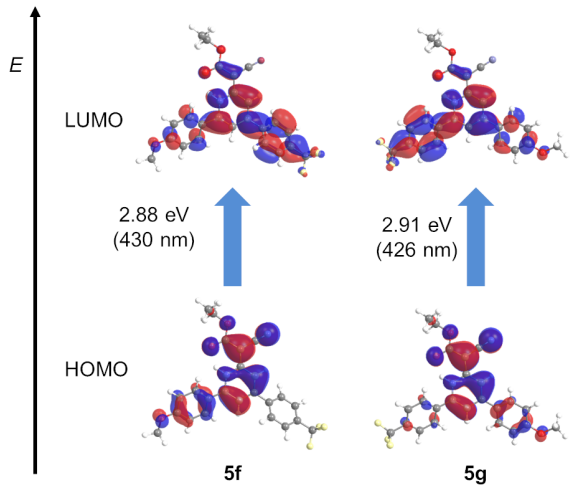

Figure 16: Selected DFT-computed (B3LYP 6-311G**) Kohn–Sham FMOs for 1*H*-pyridines **5f** and **5g** representing contributions of the longest wavelength Franck–Condon absorption bands.

ploying the B3LYP functional and the Pople 6-311G** basis set. The calculated absorption maxima are in accordance with the experimentally determined maxima (for details, see Table S10 in Supporting Information File 1). For all α-pyrones **6** the longest wavelength maxima are characterized by Franck–Condon S_1 states representing HOMO–LUMO transitions (Figure 17).

The computed Kohn–Sham frontier molecular orbitals show that the coefficient density of the HOMO in the parent α-pyrone **6a** is localized on the α-pyrone core and on the phenyl substituent in the 6-position. For an *N*,*N*-dimethylaminophenyl substituent, there is no difference, but for an *N*,*N*-dimethylaminophenyl substituent in the 4-position the coefficient density is shifted towards this substituent. With electron-donating substituents in the 4- and 6-position, the coefficient density is again located on the core and the phenyl substituent in 6-position. Donor substituents in 4-position and acceptor substituents in 6-position cause a coefficient density shift towards the 4-substituent. The coefficient density in the LUMO in all compounds is spread over the whole scaffold.

Conclusion

The cyclocondensation of alkynones and ethyl cyanoacetate, depending on the reaction conditions, the type of base, and the reaction temperature, as well as the electronic nature of the alkynone **3** furnishes either 1*H*-pyridines or α-pyrones. Optimized reaction conditions finally give rise to 8 examples of 1*H*-pyridines and 6 examples of α-pyrones. While the presence of electron-withdrawing substituents mainly furnish 1*H*-pyridines and electron-donating groups lead to the formation of α-pyrones. The strongly electron-donating *p*-*N*,*N*-dimethylaminophenyl group furnishes α-pyrones.

1*H*-Pyridines absorb and emit intensively in solution and in the solid state. While the absorption behavior is not affected by the substitution pattern the emission maxima are shifted bathochromically with increasing acceptor strength. The same trend manifests for the solid-state emission.

For α-pyrones the photophysical properties are considerably depending on the substituent pattern. The absorption and emission maxima are shifted bathochromically with increasing donor strength. α-Pyrones are only weakly fluorescent in solution. However, with distinct *p*-*N*,*N*-dimethylaminophenyl substitution in 6-position, an extraordinarily high fluorescence quantum yield of 99% in solution and 11% in the solid state was achieved. Interestingly, the isomeric *p*-*N*,*N*-dimethylaminophenyl substitution in 6-position represents a system with aggregation-induced emission enhancement. These design principles of luminescent 1*H*-pyridines and α-pyrones as polarity sensitive tunable luminophores and the observed aggregation-induced emission enhancement are currently under further investigation.

Experimental

Typical procedure for the cyclocondensation synthesis of compound 5d

1-Phenyl-3-[4-(trifluoromethyl)phenyl]prop-2-yn-1-one (**3h**, 1.40 g, 5.00 mmol), was placed in a dry Schlenk tube and ethanol (10 mL) was added. Sodium carbonate (430 mg, 4.00 mmol), sodium acetate (250 mg, 3.00 mmol), water

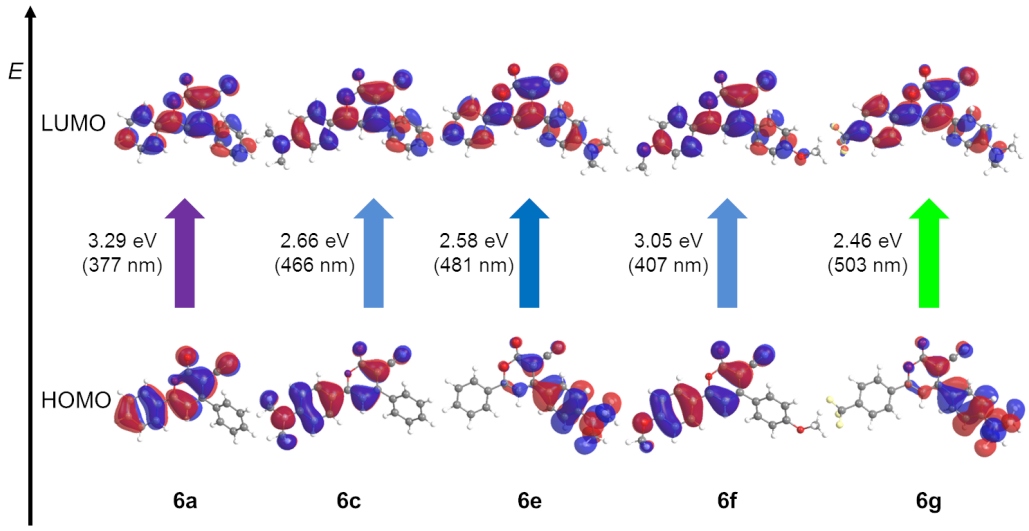

Figure 17: Selected DFT-computed (B3LYP 6-311G**) Kohn–Sham FMOs for 1*H*-pyridines **6a**, **6c**, **6e**, **6f**, and **6g** and representing contributions of the longest wavelength Franck-Condon absorption bands.

(5 mL), and ethyl cyanoacetate (**4**, 2.31 g, 20.0 mmol) were added and the mixture was stirred at 75 °C for 16 h. After the addition of CH_2Cl_2 (5.00 mL) and NaOH/$FeSO_4$ solution (5.00 mL), the solution was extracted with CH_2Cl_2 (3 × 50.0 mL). The combined organic layers were dried (anhydrous $MgSO_4$) and the solvent was removed in vacuo. The residue was purified by flash chromatography on silica gel (*n*-hexane/EtOAc 12:1 to 5:1 to 0:1) and washed with hot ethanol (5 mL) to give compound **5d** (513 mg, 25%) as orange solid. Mp 223–233 °C; ^{1}H NMR (300 MHz, $CDCl_3$) δ 1.38 (t, *J* = 7.1 Hz, 3H), 4.30 (q, *J* = 7.1 Hz, 2H), 7.12 (dd, *J* = 1.5, 1.6 Hz, 1H), 7.44 (dd, *J* = 1.5, 1.6 Hz, 1H), 7.56–7.63 (m, 3H), 7.78–7.84 (m, 6H), 14.57 (s, 1H); ^{13}C NMR (150 MHz, $CDCl_3$) δ 14.7 (CH_3), 60.6 (CH_2), 63.5 (C_{quat}), 109.2 (CH), 116.0 (CH), 119.5 (C_{quat}), 123.9 (q, $J_{C–F}$ = 273 Hz, C_{quat}), 126.1 (CH), 126.2–126.7 (m, CH), 127.8 (CH), 130.1 (CH), 131.6 (CH), 132.3 (C_{quat}), 132.4 (q, $J_{C–F}$ = 32.9 Hz, C_{quat}), 140.6 (C_{quat}), 146.6 (C_{quat}), 151.2 (C_{quat}), 156.0 (C_{quat}), 171.0 (C_{quat}); EIMS (70 eV, *m/z* (%)): 410 ([M]$^+$, 24), 366 (24), 365 ([M − C_2H_5O]$^+$, 100), 339 (12), 338 ([M − $C_3H_5O_2$]$^+$, 53), 337 (38), 308 (8), 240 (23), 149 ([M − $C_{16}H_{12}F_3$]$^+$, 11); IR (ATR) ṽ [cm^{-1}]: 3092 (w), 2992 (w), 2963 (w), 2943 (w), 2876 (w), 2806 (w), 2193 (m), 1625 (m), 1620 (m), 1597 (m), 1577 (m), 1506 (w), 1466 (w), 1413 (w), 1396 (w), 1369 (w), 1308 (m), 1300 (m), 1283 (s), 1258 (m), 1206 (w), 1165 (m), 1115 (s), 1092 (m), 1082 (m), 1071 (m), 1045 (s), 1030 (m), 1015 (m), 980 (m), 976 (m), 968 (w), 920 (w), 885 (w), 874 (w), 837 (s), 829 (m), 764 (s), 745 (w), 727 (w), 685 (m), 662 (w), 655 (w), 650 (w); UV–vis (CH_2Cl_2) λ_{max} [nm] (ε [L·mol^{-1}·cm^{-1}]): 274 (32000), 321 (18100), 428 (10000); emission (CH_2Cl_2) λ_{max} [nm] (Stokes shift [cm^{-1}]): 565 (5700); quantum yield (CH_2Cl_2) Φ_f: 0.01; Anal. calcd for $C_{23}H_{17}F_3N_2O_2$ (410.1): C, 67.31; H, 4.18; N, 6.83; found: C, 67.50; H, 4.32; N, 6.70.

Typical procedure for the cyclocondensation synthesis of compound **6c**

1-[4-(Dimethylamino)phenyl]-3-phenylprop-2-yn-1-one (**3c**, 249 mg, 1.00 mmol) was placed in a dry Schlenk tube and ethanol (2 mL) was added. Sodium carbonate (86.0 mg, 0.80 mmol), sodium acetate (50.0 mg, 0.60 mmol), water (1 mL), and ethyl cyanoacetate (**4**, 462 mg, 4.00 mmol) were added and the mixture was stirred at 75 °C for 16 h. After the addition of CH_2Cl_2 (5.00 mL) and NaOH/$FeSO_4$ solution (5.00 mL), the solution was extracted with CH_2Cl_2 (3 × 50.0 mL). The combined organic layers were dried (anhydrous $MgSO_4$) and the solvent was removed in vacuo. The residue was purified by flash chromatography on silica gel (*n*-hexane/EtOAc 5:1 to 1:1 to 0:1) and washed with hot ethanol (2.00 mL) and compound **6c** (37.0 mg, 12%) was obtained as deep purple solid. Mp 224–253 °C; ^{1}H NMR (300 MHz, $CDCl_3$) δ 3.10 (s, 6H), 6.69 (s, 1H), 6.69–6.75 (m, 2H), 7.51–7.58 (m, 3H), 7.67–7.73 (m, 2H), 7.78–7.85 (m, 2 H); ^{13}C NMR (75 MHz, $CDCl_3$) δ 40.2 (CH_3), 91.1 (C_{quat}), 100.1 (CH), 111.8 (CH), 115.7 (C_{quat}), 116.5 (C_{quat}), 128.0 (CH), 128.8 (CH), 129.3 (CH), 131.6 (CH), 135.3 (C_{quat}), 153.4 (C_{quat}), 160.3 (C_{quat}), 164.1 (C_{quat}), 164.9 (C_{quat}). EIMS (70 eV, *m/z* (%)): 317 (15), 316 ([M]$^+$, 66), 293 (11), 289 ([M − CN]$^+$, 11), 288 ([M − CO]$^+$, 51), 287 (19), 167 ([M − $C_9H_{11}NO$]$^+$, 18), 150 (11), 149 ([M − $C_{11}H_5NO$]$^+$, 100), 148 (20), 144 (13), 127 ([M − $C_{11}H_{11}NO_2$]$^+$, 12), 85 (13), 71 (22), 57 (18), 43 ([M − $C_{18}H_{11}NO_2$]$^+$, 13); IR (ATR) ṽ [cm^{-1}]: 3092 (w), 3048 (w), 2901 (w), 2864 (w), 2812 (w), 2739 (w), 2212 (w), 1708 (m), 1706 (m), 1609 (m), 1589 (m), 1570 (m), 1530 (m), 1497 (m), 1491 (m), 1482 (m), 1478 (m), 1473 (m), 1467 (m), 1458 (m), 1433 (m), 1375 (m), 1360 (m), 1333 (m), 1252 (m), 1209 (m), 1171 (m), 1159 (m), 1125 (m), 1111 (m), 1082 (m), 1059 (m), 1020 (m), 995 (m), 953 (m), 945 (m), 924 (w), 853 (m), 818 (s), 795 (m), 750 (m), 748 (m), 692 (s), 669 (m), 640 (m); UV–vis (CH_2Cl_2) λ_{max} [nm] (ε [L·mol^{-1}·cm^{-1}]): 294 (18800), 482 (47300); emission (CH_2Cl_2) λ_{max} [nm] (Stokes-shift [cm^{-1}]): 567 (3100); quantum yield (CH_2Cl_2) Φ_f: 0.99; emission (solid) λ_{max} [nm]: 694; quantum yield (solid) Φ_f: 0.11; Anal. calcd for $C_{20}H_{16}N_2O_2$ (316.1): C, 75.93; H, 5.10; N, 8.86; found: C, 75.74; H, 5.19; N, 8.56.

Typical procedure for the cyclocondensation synthesis of compound **8a**

1,3-Diphenylprop-2-yn-1-one (**3a**, 103 mg, 0.50 mmol) was placed in a dry Schlenk tube and ethanol (1.00 mL) was added. Sodium carbonate (43.0 mg, 0.40 mmol), sodium acetate (25.0 mg, 0.30 mmol), water (50.0 µL) and diethyl (*Z*)-3-amino-2-cyanopent-2-endioate (**7**, 226 mg, 1.00 mmol) were added and the mixture was stirred at 75 °C for 16 h. After the addition of CH_2Cl_2 (5.00 mL) and NaOH/$FeSO_4$ solution (5.00 mL), the solution was extracted with CH_2Cl_2 (3 × 50.0 mL). The combined organic layers were dried (anhydrous $MgSO_4$) and the solvent was removed in vacuo. The residue was purified by flash chromatography on silica gel (*n*-hexane/EtOAc 5:1 to 1:1 to 0:1) and washed with hot ethanol (5.00 mL) to furnish compound **8a** (108 mg, 52%) as yellow solid. Mp 140–146 °C; ^{1}H NMR (300 MHz, $CDCl_3$) δ 1.08 (t, *J* = 7.2 Hz, 3H), 1.37 (t, *J* = 7.1 Hz, 3H), 4.22 (q, *J* = 7.2 Hz, 2H), 4.31 (q, *J* = 7.1 Hz, 2H), 6.94 (d, *J* = 1.9 Hz, 1H), 7.40–7.48 (m, 5H), 7.55–7.62 (m, 3H), 7.75–7.84 (m, 2H), 15.60 (s, 1H); ^{13}C NMR (75 MHz, $CDCl_3$) δ 13.7 (CH_3), 14.7 (CH_3), 60.9 (CH_2), 62.2 (CH_2), 62.7 (C_{quat}), 112.2 (CH), 118.2 (C_{quat}), 122.8 (C_{quat}), 126.3 (CH), 127.9 (CH), 128.8 (CH), 129.6 (CH), 130.1 (CH), 131.77 (CH), 131.84 (C_{quat}), 137.4 (C_{quat}), 146.1 (C_{quat}), 151.9 (C_{quat}), 153.0 (C_{quat}), 165.1 (C_{quat}), 172.1 (C_{quat}); EIMS (70 eV, *m/z* (%)): 415 ([M + H]$^+$, 26), 414 ([M]$^+$, 97), 369 ([M − C_2H_5O]$^+$, 18), 342 (28), 341 ([M − C_3H_5O]$^+$, 27), 340 ([M − C_3H_6O]$^+$, 12), 314 (20), 313

([M − C_8H_5]$^+$, 57), 298 (24), 297 ([M − $C_5H_9O_3$]$^+$, 27), 296 ([M − $C_5H_{10}O_3$]$^+$, 33), 287 (10), 286 (25), 271 (24), 270 ([M − $C_6H_8O_4$]$^+$, 100), 269 (23), 268 ([M − $C_6H_{10}O_4$]$^+$, 21), 266 (12), 258 ([M − $C_7H_{10}NO_3$]$^+$, 14), 245 (18), 241 (13), 240 (26), 231 (15), 230 ([M − $C_8H_{10}NO_4$]$^+$, 34), 203 (19), 202 (31), 164 (13); IR (ATR) $\tilde{\nu}$ [cm^{-1}]: 2978 (w), 2895 (w), 2197 (m), 1722 (m), 1636 (m), 1593 (s), 1578 (m), 1501 (m), 1489 (w), 1462 (w), 1441 (w), 1420 (w), 1364 (w), 1308 (m), 1288 (m), 1248 (s), 1188 (w), 1169 (m), 1134 (m), 1113 (s), 1092 (m), 1067 (m), 1047 (m), 1028 (w), 1001 (w), 885 (m), 854 (m), 847 (w), 775 (w), 758 (s), 746 (m), 694 (m), 658 (w); UV–vis (CH_2Cl_2) λ_{max} [nm] (ε [$L \cdot mol^{-1} \cdot cm^{-1}$]): 274 (20300), 324 (20100), 417 (7700); emission (CH_2Cl_2) λ_{max} [nm] (Stokes shift [cm^{-1}]): 557 (6000); quantum yield (CH_2Cl_2) Φ_f = < 0.01; Anal. calcd for $C_{25}H_{22}N_2O_4$ (414.2): C, 72.45; H, 5.35; N, 6.76; found: C, 71.97; H, 5.45; N, 6.52.

Supporting Information

For experimental details of the synthesis and analytical data of compounds **3**, **5**, **6**, and **8**, ^{1}H and ^{13}C NMR, and absorption and emission spectra of compounds **5**, **6**, and **8**, solid state emission spectra of compounds **5** and **6**, X-ray structural data of compound **5a**, and DFT/TDDFT calculations of compounds **5** and **6**, see below.

Supporting Information File 1

Additional experimental and calculated data.
[https://www.beilstein-journals.org/bjoc/content/supplementary/1860-5397-15-262-S1.pdf]

Acknowledgements

The authors gratefully acknowledge the Deutsche Forschungsgemeinschaft (DFG, Mu 1088-9/1) and the Fonds der Chemischen Industrie and also cordially thank Arno Schneeweis for measuring the quantum yield of compound **6c** in the solid state in cooperation with Hamamatsu Photonics Deutschland GmbH, Herrsching am Ammersee, Germany.

Statement

The reported results have been summarized in the inaugural dissertation "Diversitätsorientierte Synthese von Heterocyclen über Cyclokondensationen von Alkinonen und CH-aciden Estern" by Dr. Natascha Breuer, Heinrich Heine University Düsseldorf, 2018.

ORCID® iDs

Christoph Janiak - https://orcid.org/0000-0002-6288-9605
Thomas J. J. Müller - https://orcid.org/0000-0001-9809-724X

References

1. Yao, J.; Yang, M.; Duan, Y. *Chem. Rev.* **2014,** *114,* 6130–6178. doi:10.1021/cr200359p
2. Wysocki, L. M.; Lavis, L. D. *Curr. Opin. Chem. Biol.* **2011,** *15,* 752–759. doi:10.1016/j.cbpa.2011.10.013
3. Day, R. N.; Davidson, M. W. *Chem. Soc. Rev.* **2009,** *38,* 2887–2921. doi:10.1039/b901966a
4. Wegner, K. D.; Hildebrandt, N. *Chem. Soc. Rev.* **2015,** *44,* 4792–4834. doi:10.1039/c4cs00532e
5. Zhu, M.; Yang, C. *Chem. Soc. Rev.* **2013,** *42,* 4963–4976. doi:10.1039/c3cs35440g
6. Figueira-Duarte, T. M.; Müllen, K. *Chem. Rev.* **2011,** *111,* 7260–7314. doi:10.1021/cr100428a
7. Forrest, S. R.; Thompson, M. E. *Chem. Rev.* **2007,** *107,* 923–925. doi:10.1021/cr0501590
8. Grimsdale, A. C.; Leok Chan, K.; Martin, R. E.; Jokisz, P. G.; Holmes, A. B. *Chem. Rev.* **2009,** *109,* 897–1091. doi:10.1021/cr000013v
9. Kanibolotsky, A. L.; Perepichka, I. F.; Skabara, P. J. *Chem. Soc. Rev.* **2010,** *39,* 2695–2728. doi:10.1039/b918154g
10. Wang, X.; Zhang, F.; Liu, J.; Tang, R.; Fu, Y.; Wu, D.; Xu, Q.; Zhuang, X.; He, G.; Feng, X. *Org. Lett.* **2013,** *15,* 5714–5717. doi:10.1021/ol402745r
11. de Halleux, V.; Calbert, J.-P.; Brocorens, P.; Cornil, J.; Declercq, J.-P.; Brédas, J.-L.; Geerts, Y. *Adv. Funct. Mater.* **2004,** *14,* 649–659. doi:10.1002/adfm.200400006
12. Hassheider, T.; Benning, S. A.; Kitzerow, H.-S.; Achard, M.-F.; Bock, H. *Angew. Chem., Int. Ed.* **2001,** *40,* 2060–2063. doi:10.1002/1521-3773(20010601)40:11<2060::aid-anie2060>3.3.co;2-8
13. Kartha, K. K.; Babu, S. S.; Srinivasan, S.; Ajayaghosh, A. *J. Am. Chem. Soc.* **2012,** *134,* 4834–4841. doi:10.1021/ja210728c
14. Thimmarayaperumal, S.; Shanmugam, S. *ACS Omega* **2017,** *2,* 4900–4910. doi:10.1021/acsomega.7b00627
15. Park, S.-Y.; Ebihara, M.; Kubota, Y.; Funabiki, K.; Matsui, M. *Dyes Pigm.* **2009,** *82,* 258–267. doi:10.1016/j.dyepig.2009.01.014
16. Hagimori, M.; Mizuyama, N.; Yokota, K.; Nishimura, Y.; Suzuta, M.; Tai, C.-K.; Wang, B.-C.; Wang, S.-L.; Shih, T.-L.; Wu, K.-D.; Huang, Z.-S.; Tseng, S.-C.; Chen, C.-Y.; Lu, J.-W.; Wei, H.-H.; Kawashima, K.; Kawashima, S.; Tominaga, Y. *Dyes Pigm.* **2012,** *92,* 1069–1074. doi:10.1016/j.dyepig.2011.05.014
17. Levi, L.; Müller, T. J. J. *Chem. Soc. Rev.* **2016,** *45,* 2825–2846. doi:10.1039/c5cs00805k
18. Levi, L.; Müller, T. J. J. *Eur. J. Org. Chem.* **2016,** 2902–2918. doi:10.1002/ejoc.201600409
19. Müller, T. J. J. *Drug Discovery Today: Technol.* **2018,** *29,* 19–26. doi:10.1016/j.ddtec.2018.06.003
20. Merkt, F. K.; Müller, T. J. J. *Isr. J. Chem.* **2018,** *58,* 889–900. doi:10.1002/ijch.201800058
21. D'Souza, D. M.; Müller, T. J. J. *Chem. Soc. Rev.* **2007,** *36,* 1095–1108. doi:10.1039/b608235c
22. Gers-Panther, C. F.; Müller, T. J. J. *Adv. Heterocycl. Chem.* **2016,** *120,* 67–98. doi:10.1016/bs.aihch.2016.04.007
23. Breuer, N.; Müller, T. J. J. *Synthesis* **2018,** *50,* 2741–2752. doi:10.1055/s-0037-1610129
24. Tominaga, Y.; Mizuyama, N.; Murakami, Y.; Nagaoka, J.; Kohra, S.; Ueda, K.; Hiraoka, K.; Shigemitsu, Y. *Heterocycles* **2006,** *68,* 1105–1108. doi:10.3987/com-06-10741

25. Mizuyama, N.; Murakami, Y.; Nakatani, T.; Kuronita, K.; Kohra, S.; Ueda, K.; Hiraoka, K.; Tominaga, Y. *J. Heterocycl. Chem.* **2008,** *45,* 265–277. doi:10.1002/jhet.5570450133
26. Tominaga, Y.; Mizuyama, N.; Shigemitsu, Y.; Wang, B.-C. *Heterocycles* **2009,** *78,* 555–570. doi:10.3987/rev-08-642
27. Shankar, R.; Shukla, H.; Singh, U. S.; Thakur, V.; Hajela, K. *Synth. Commun.* **2011,** *41,* 2738–2746. doi:10.1080/00397911.2010.515350
28. Fouli, F. A.; Basyouni, M. N. *Acta Chim. Acad. Sci. Hung.* **1981,** *106,* 297–302.
29. Sadek, K. U.; Fahmy, S. M.; Mohareb, R. M.; Elnagdi, M. H. *J. Chem. Eng. Data* **1984,** *29,* 101–103. doi:10.1021/je00035a033
30. Takaya, H.; Naota, T.; Murahashi, S.-I. *J. Am. Chem. Soc.* **1998,** *120,* 4244–4245. doi:10.1021/ja974106e
31. Hammond, G. B.; Plevey, R. G.; Sampson, P.; Tatlow, J. C. *J. Fluorine Chem.* **1988,** *40,* 81–98. doi:10.1016/s0022-1139(00)83057-2
32. D'Souza, D. M.; Müller, T. J. J. *Nat. Protoc.* **2008,** *3,* 1660–1665. doi:10.1038/nprot.2008.152
33. Götzinger, A. C.; Müller, T. J. J. *Org. Biomol. Chem.* **2016,** *14,* 3498–3500. doi:10.1039/c6ob00483k
34. Karpov, A. S.; Müller, T. J. J. *Org. Lett.* **2003,** *5,* 3451–3454. doi:10.1021/ol035212q
35. CCDC 1944699 (**5a**) contains the supplementary crystallographic data (excluding structure factors) for this paper. These data are provided free of charge by The Cambridge Crystallographic Data Centre.
36. Desiraju, G. R.; Steiner, T. The weak hydrogen bond. *IUCr Monograph on Crystallography;* Oxford Science: Oxford, United KIngdom, 1999; Vol. 9.
37. Desiraju, G. R. *Acc. Chem. Res.* **2002,** *35,* 565–573. doi:10.1021/ar010054t
38. Janiak, C.; Scharmann, T. G. *Polyhedron* **2003,** *22,* 1123–1133. doi:10.1016/s0277-5387(03)00098-6
39. Shivakumar, K.; Vidyasagar, A.; Naidu, A.; Gonnade, R. G.; Sureshan, K. M. *CrystEngComm* **2012,** *14,* 519–524. doi:10.1039/c1ce05997a
40. Anelli, P. L.; Ashton, P. R.; Ballardini, R.; Balzani, V.; Delgado, M.; Gandolfi, M. T.; Goodnow, T. T.; Kaifer, A. E.; Philp, D. *J. Am. Chem. Soc.* **1992,** *114,* 193–218. doi:10.1021/ja00027a027
41. Janiak, C.; Temizdemir, S.; Dechert, S.; Deck, W.; Girgsdies, F.; Heinze, J.; Kolm, M.; Scharmann, T.; Zipffel, O. *Eur. J. Inorg. Chem.* **2000,** 1229–1241. doi:10.1002/(sici)1099-0682(200006)2000:6<1229::aid-ejic1229>3.3.co;2-g
42. N. Laxmi Madhavi, N.; R. Desiraju, G.; K. Katz, A.; L. Carrell, H.; Nangia, A. *Chem. Commun.* **1997,** 1953–1954. doi:10.1039/a705836e
43. Nishio, M. *CrystEngComm* **2004,** *6,* 130–158. doi:10.1039/b313104a
44. Nishio, M. *Phys. Chem. Chem. Phys.* **2011,** *13,* 13873–13900. doi:10.1039/c1cp20404a
45. Nishio, M.; Hirota, M.; Umezawa, Y. *The CH/π interaction (evidence, nature and consequences);* Wiley-VCH: New York, NY, U.S.A., 1998.
46. Nishio, M.; Umezawa, Y.; Honda, K.; Tsuboyama, S.; Suezawa, H. *CrystEngComm* **2009,** *11,* 1757–1788. doi:10.1039/b902318f
47. Steiner, T.; Tamm, M.; Lutz, B.; Van Der Maas, J. *Chem. Commun.* **1996,** 1127–1128. doi:10.1039/cc9960001127
48. Umezawa, Y.; Tsuboyama, S.; Honda, K.; Uzawa, J.; Nishio, M. *Bull. Chem. Soc. Jpn.* **1998,** *71,* 1207–1213. doi:10.1246/bcsj.71.1207
49. Weiss, H.-C.; Bläser, D.; Boese, R.; Doughan, B. M.; Haley, M. M. *Chem. Commun.* **1997,** 1703–1704. doi:10.1039/a704070i
50. Janiak, C. *J. Chem. Soc., Dalton Trans.* **2000,** 3885–3896. doi:10.1039/b003010o
51. Janiak, C.; Uehlin, L.; Wu, H.-P.; Klüfers, P.; Piotrowski, H.; Scharmann, T. G. *J. Chem. Soc., Dalton Trans.* **1999,** 3121–3131. doi:10.1039/a904829d
52. Lozana, V.; Lassahn, P.-G.; Zhang, C.; Wu, B.; Janiak, C.; Rheinwald, G.; Lang, H. *Z. Naturforsch., B: J. Chem. Sci.* **2003,** *58,* 1152–1164. doi:10.1515/znb-2003-1202
53. Wu, H.-P.; Janiak, C.; Rheinwald, G.; Lang, H. *J. Chem. Soc., Dalton Trans.* **1999,** 183–190. doi:10.1039/a807450j
54. Wu, H.-P.; Janiak, C.; Uehlin, L.; Klüfers, P.; Mayer, P. *Chem. Commun.* **1998,** 2637–2638. doi:10.1039/a807522k
55. Yang, X.-J.; Drepper, F.; Wu, B.; Sun, W.-H.; Haehnel, W.; Janiak, C. *Dalton Trans.* **2005,** 256–267. doi:10.1039/b414999h
56. Zhang, C.; Janiak, C. *Z. Anorg. Allg. Chem.* **2001,** *627,* 1972–1975. doi:10.1002/1521-3749(200108)627:8<1972::aid-zaac1972>3.0.co;2-k
57. Zhang, C.; Janiak, C. *J. Chem. Crystallogr.* **2001,** *31,* 29–35. doi:10.1023/a:1013774502147
58. Rurack, K.; Spieles, M. *Anal. Chem. (Washington, DC, U. S.)* **2011,** *83,* 1232–1242. doi:10.1021/ac101329h
59. Lakowicz, J. R. *Principles of Fluorescence Spectroscopy,* 3rd ed.; Springer: Boston, MA, U.S.A., 2006. doi:10.1007/978-0-387-46312-4
60. Lippert, E. *Z. Elektrochem.* **1957,** 962–975.
61. Luo, J.; Song, K.; Gu, F. I.; Miao, Q. *Chem. Sci.* **2011,** *2,* 2029–2034. doi:10.1039/c1sc00340b
62. Mei, J.; Hong, Y.; Lam, J. W. Y.; Qin, A.; Tang, Y.; Tang, B. Z. *Adv. Mater. (Weinheim, Ger.)* **2014,** *26,* 5429–5479. doi:10.1002/adma.201401356
63. Müller, T. J. J. Multicomponent and Domino Syntheses of AIE Chromophores. In *Aggregation Induced Emission: Materials and Applications,* Fujiki, M.; Liu, B.; Tang, B. Z., Eds.; American Chemical Society: Washington, DC, U.S.A., 2016; pp 85–112. doi:10.1021/bk-2016-1226.ch006
64. Liu, B.; Tang, B. Z. *Chem. – Asian J.* **2019,** *14,* 672–673. doi:10.1002/asia.201900185
65. Becke, A. D. *J. Chem. Phys.* **1993,** *98,* 1372–1377. doi:10.1063/1.464304
66. Kim, K.; Jordan, K. D. *J. Phys. Chem.* **1994,** *98,* 10089–10094. doi:10.1021/j100091a024
67. Lee, C.; Yang, W.; Parr, R. G. *Phys. Rev. B* **1988,** *37,* 785–789. doi:10.1103/physrevb.37.785
68. Stephens, P. J.; Devlin, F. J.; Chabalowski, C. F.; Frisch, M. J. *J. Phys. Chem.* **1994,** *98,* 11623–11627. doi:10.1021/j100096a001
69. Krishnan, R.; Binkley, J. S.; Seeger, R.; Pople, J. A. *J. Chem. Phys.* **1980,** *72,* 650–654. doi:10.1063/1.438955
70. Scalmani, G.; Frisch, M. J. *J. Chem. Phys.* **2010,** *132,* 114110. doi:10.1063/1.3359469